

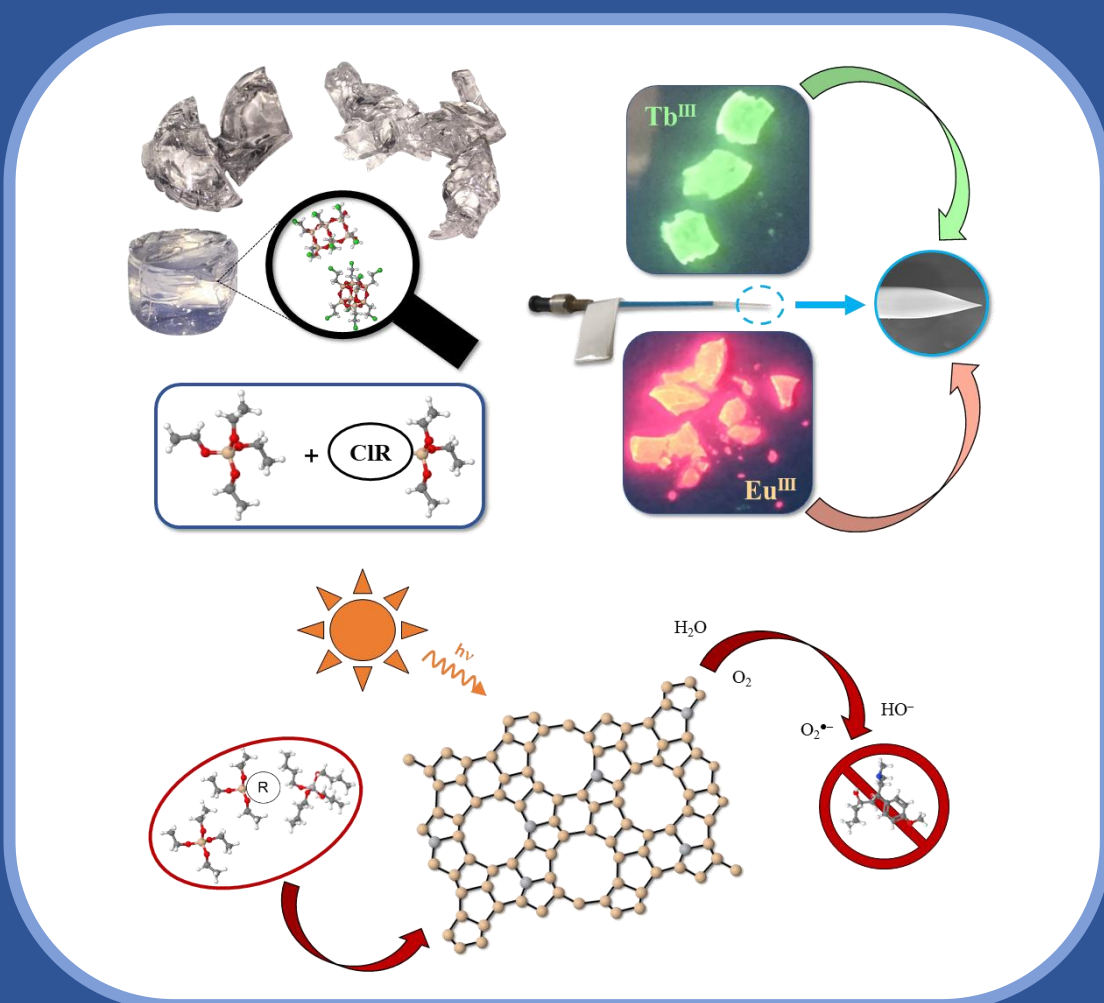
PhD Thesis

Hybrid and Lanthanide-Doped Xerogels, and Modified Titanosilicalites

Synthesis, Characterisation and Application in
Sensorics and Photocatalysis

Guillermo Cruz Quesada

Pamplona, 2024



upna

Universidad Pública de Navarra
Nafarroako Unibertsitate Publikoa

Departamento de Ciencias
Grupo de Química Inorgánica

upna
INAMAT²
Institute for Advanced
Materials and Mathematics

PhD thesis dissertation

**Hybrid and Lanthanide-Doped
Xerogels, and Modified
Titanosilicalites**

**Synthesis, Characterisation, and Application in
Sensorics and Photocatalysis**

Guillermo Cruz Quesada

Supervised by:

Julián J. Garrido Segovia

María Victoria López Ramón

Maialen Espinal Viguri

Pamplona, 10 of February, 2024

upna

Universidad Pública de Navarra
Nafarroako Unibertsitate Publikoa

Departamento de Ciencias
Programa de doctorado en Ciencias
y Tecnologías Industriales

upna
INAMAT²
Institute for Advanced
Materials and Mathematics

upna
Universidad Pública de Navarra
Nafarroako Unibertsitate Publikoa

<https://doi.org/10.48035/Tesis/2454/47982>



D. Julián J. Garrido Segovia, Catedrático de Química Inorgánica del Departamento de Ciencias de la Universidad Pública de Navarra (UPNA), Dña. María Victoria López Ramón, Catedrática de Química Inorgánica del Departamento de Inorgánica y Orgánica de la Universidad de Jaén (UJA), y Dña. Maialen Espinal Viguri, Profesora Contratada Doctora del Departamento de Ciencias de la Universidad Pública de Navarra (UPNA),

HACEN CONSTAR

que la presente memoria titulada:

Hybrid and Lanthanide-Doped Xerogels, and Modified Titanosilicalites: Synthesis, Characterisation, and Application in Sensorics and Photocatalysis

se corresponde con el Proyecto de Tesis aprobado por el Departamento de Ciencias de la Universidad Pública de Navarra (UPNA), y que ha sido realizada por **D. Guillermo Cruz Quesada** en la UPNA bajo nuestra dirección para optar al Grado de Doctor en Química.

Y, asimismo,

AUTORIZAN

la presentación de la citada Memoria de Tesis Doctoral para su defensa y calificación ante el Tribunal correspondiente.

En Pamplona a 21 de diciembre del 2023

GARRIDO
SEGOVIA
JULIAN JOSE -
DNI 24115492S

Firmado digitalmente
por GARRIDO SEGOVIA
JULIAN JOSE - DNI
24115492S
Fecha: 2023.12.26
12:11:22 +01'00'

Fdo. Julián J. Garrido Segovia

LOPEZ RAMON
MARIA
VICTORIA -
23785035E

Firmado
digitalmente por
LOPEZ RAMON
MARIA VICTORIA -
23785035E
Fecha: 2023.12.26
17:12:26 +01'00'

Fdo. M^a Victoria López Ramón

Firmado por Maialen
Espinal Viguri el día
21 de diciembre de
2023 con certificado
digital

Fdo. Maialen Espinal Viguri

FUNDING

This doctoral thesis has been developed thanks to the funding received from Ministerio de Economía y Competitividad (Project MAT2016-78155-C2-2-R) and Ministerio de Ciencia e Innovación (Project PID2020-113558RB-C42) from the Government of Spain.

The author would also like to acknowledge the financial support provided by the Ministerio de Universidades of the Government of Spain, for the predoctoral grant (2020-2024) within the Formación de Profesorado Universitario (FPU) program (FPU18/03467); and the Government of Navarre, for a predoctoral international mobility grant (0011-3564-2022-000035), which allowed the author to complete a three months doctoral stay (2022) in the Faculty of chemical engineering at the University of Porto (FEUP).

PUBLICATIONS AND IMPACT FACTORS OF JOURNALS

This thesis dissertation is a compilation of five already published works.

1. Cruz-Quesada, G.; Espinal-Viguri, M.; López-Ramón, M. V.; Garrido, J. J. Novel Organochlorinated Xerogels: From Microporous Materials to Ordered Domains. *Polymers*, **2021** *13*(9), p. 1415. Doi: 10.3390/polym13091415.
2. Cruz-Quesada, G.; Espinal-Viguri, M.; López-Ramón, M. V.; Garrido, J. J. Hybrid Xerogels: Study of the Sol-Gel Process and Local Structure by Vibrational Spectroscopy. *Polymers* **2021**, *13*(13), p. 2082. Doi: 10.3390/polym13132082.
3. Cruz-Quesada, G.; Espinal-Viguri, M.; López-Ramón, M. V.; Garrido, J. J. Novel Silica Hybrid Xerogels Prepared by Co-Condensation of TEOS and ClPhTEOS: A Chemical and Morphological Study. *Gels* **2022**, *8*, p. 677. Doi: 10.3390/gels8100677.
4. Cruz-Quesada, G.; Rosales-Reina, B.; López-Torres, D.; Reinoso, S.; López-Ramón, M. V.; Arzamendi, G.; Elosua, C.; Espinal-Viguri, M.; Garrido, J. J. From Fundamental Materials Chemistry to Sensing Applications: Unravelling the Water Adsorption Mechanism of a Luminescent Optical Fibre Sensor Membrane. *Sensors and Actuators, B* **2024**, *406*, p. 135369. Doi: 10.1016/j.snb.2024.135369.

5. Cruz-Quesada, G.; Sampaio, M. J.; Espinal-Viguri, M.; López-Ramón, M. V.; Garrido, J. J.; G. Silva, C.; Faria, J. L. Design of Novel Photoactive Modified Titanium Silicalites and Their Application for Venlafaxine Degradation Under Simulated Solar Irradiation. *Solar RRL* **2023**. Doi: 10.1002/solr.202300593.

The impact and quality factors of the JCR indexes journals of these articles, are contained in the following table:

Article	Cites (12/2023)	Journal	Publisher	Impact factor	Category	Journals in category	Ranking in category
1 (2021)	3	Polymers	MDPI	4.967	Polymer science	90	16 (Q1)
2 (2021)	10	Polymers	MDPI	4.967	Polymer science	90	16 (Q1)
3 (2022)	4	Gels	MDPI	4.600	Polymer science	86	16 (Q1)
4 (2024)	-	Sensors & Actuarors B: Chemical	Elsevier	8.400 (2022)	Instruments & Instrumentation	63	1 (Q1)
5 (2023)	-	Solar RRL	Wiley	7.900 (2022)	Materials Science, Multidisciplinary	342	71 (Q1)

STAYS AT I+D RESEARCH CENTRES

International stay at the Laboratory of Separation and Reaction Engineering and Laboratory of Catalysis and Materials (LSRE-LCM) in the Faculty of engineering at the University of Porto (FEUP), under the guidance of Professor Cláudia Sofia Castro Gomes da Silva and Joaquim Luís Bernardes Martins de Faria, from September 1 to December 1, 2022 (3 months). During the stay, the titanosilicalite materials previously synthesised and characterised at UPNA underwent further characterisation (UV-Vis diffuse reflectance and photoluminescence emission spectroscopy) and were tested in the photodegradation of the emerging pollutant venlafaxine in aqueous media under simulated solar light irradiation. These studies resulted in an article that has been published in the high-impact scientific journal Solar RRL (Wiley) and constitutes one of the chapters of this dissertation. Additionally, titanosilicalite-carbon nitride composites were prepared, characterised, and used as photocatalysts, obtaining promising results for a future manuscript in collaboration with the research group at the University of Porto.

ACKNOWLEDGEMENTS/AGRADECIMIENTOS

Me voy a tomar la licencia de escribir esta sección en castellano, ya que tenéis inglés para rato en el resto de la memoria y me parece más cercano usar mi lengua materna para agradecer a todas las personas que han contribuido en mi proceso de maduración (no solo científica) durante estos 5 años.

Lo primero es expresar mi enorme gratitud hacia mis tres directores de tesis, Julián Garrido, Maialen Espinal y María Victoria López. Julián he de agradecerte por todo el apoyo y facilidades que he tenido durante estos años de investigación, por tu jovialidad contagiosa que tanto te caracteriza y por el gran trato humano recibido. Gracias Maialen por toda la paciencia que has tenido conmigo, por enseñarme a trabajar de forma ordenada y rigurosa, y por haberme apoyado en algunos de mis peores momentos, te lo agradezco de corazón. María Victoria, te agradezco tu continua predisposición a echar una mano y por la necesaria dosis de pragmatismo a la hora de tomar decisiones.

En cuanto al resto de personas que integran o han integrado el grupo de investigación de Química Inorgánica, quisiera primero agradecer a Paula Moriones por instruirme en el quehacer diario del laboratorio y por su amabilidad y asistencia cuando era un recién llegado en Pamplona. A mi compañera Beatriz Rosales, sin la cual la investigación concerniente a los sensores de fibra óptica no hubiera sido posible, y con quien se me hicieron más amenas las prácticas de laboratorio. Por último, agradezco a Santiago Reinoso por haberme mostrado que no puedes fiarte del Mendeley, por su buen gusto a la hora de diseñar gráficas (he tomado nota) y por las siempre entrañables conversaciones.

Durante estos años en la UPNA han ido y venido varias personas a las que quiero mostrarles mi gratitud, de todos he aprendido algo (ya sea profesional y/o humano): a Mikel, Beñat, Leticia, Maitane, Blanca, Lucía García, Paulo, Elisa, Isaac, Uxua, Edu, Deborah, Jonathan, Joseph, Yaneth, Soufiane, Sarah, Laura, Itziar, David, Vinícius, Arantxa, Amaia, Iván, Lucía Grande, Majo, Edwin, Rui....; A mis compañeros/as que están con las tesis, les deseo muchos ánimos, no tengo dudas de que serán tesis cojonudas. También quiero agradecer a los/as habituales de la hora del carbón (me niego llamar café a eso) y de las comidas en el comedor, por los agradables momentos de distensión en los que se hablaba de actualidad, de cómo arreglar el mundo y de cualquier temática en

general (dan para un podcast un tanto amateur, pero, en definitiva, entretenido). También quiero expresar mi agradecimiento a todo el personal docente del departamento de ciencias (Alfonso, Nerea, Irene, Sophia, Andoni, Eneko, Antonio, Alberto...), que me trataron muy amablemente y se interesaron por cómo iba la tesis; a las dos técnicas de laboratorio (Zuberoa e Idoia); a los técnicos de la unidad científico técnica de apoyo a la investigación (Pablo y Elena); y a las trabajadoras del comedor y la cafetería. También me gustaría agradecer la colaboración con César Elosua y Diego López del grupo de Sensores de Ingeniería de telecomunicaciones de la UPNA.

En general a todo el personal de la UPNA, mila esker;;

Agradezco enormemente a la Dra. Claudía Gómes da Silva, a la Dra. Maria José Sampaio y al Prof. Joaquim L. Faria su gran acogida durante mi estancia doctoral en el grupo LSRE-LCM de la facultad de ingeniería de la Universidad de Oporto (FEUP). También quiero mencionar a los doctorandos y post-doc con los que coincidí en Oporto, que contribuyeron a que fueran tres meses muy buenos también en el ámbito social: Manu, Irene, Ana María, André, Hanane, Marcia, Juan Carlos, Jorge, Miguel...

A mis queridos e inolvidables amigos de Jaén: Curro, Juanjo, Marina, Cristina, Carlos, Pepe, Pablo, Fernando, Moreno, Ure...; Aunque no nos hemos visto mucho durante estos años me habéis demostrado lo sólidos que son los vínculos que nos unen, os agradezco de corazón vuestra amistad, hay pocas cosas que valore más, todos de una manera u otra formáis parte de mí. GRACIAS.

Por último, no hay palabras suficientes para expresar el amor y profundo agradecimiento que siento hacia mi familia, a los que siempre tengo presentes en mi día a día. A mi padre Alfonso por su continuo soporte emocional y por ayudarme siempre con su increíble capacidad resolutive. A mi madre Inma que es una campeona y un ejemplo de integridad que me ha enseñado a no rendirme nunca pese a la adversidad. A mis hermanos Alfonso y Jesús, personas indispensables en mi vida cuyo afecto y carácter (sois tontísimos; en el buen sentido) han sido como un bálsamo para mi cada vez que bajaba a casa. A Mía, mi querida cabra disfrazada de perra. A José Antonio (alias padrino). Y, por último, a mis abuelos Juan y Ana, mis ejemplos a seguir como ser humano.

A la memoria de mi abuela Ana

“The most important step a man can take. It's not the first one, is it?

It's the next one. Always the next step”

— Brandon Sanderson, Oathbringer

ABSTRACT

The research presented in this doctoral dissertation is focused on the synthesis of hybrid silica xerogels and modified titanium silicalites using different organic precursors, and on the study of their influence on the textural and chemical properties of the new materials. The main goal is to obtain versatile and well-adapted materials for specific applications, which are the preparation of membranes for optical fibre sensors and the photocatalytic degradation of venlafaxine.

Therefore, three well-defined groups of materials were prepared: (i) hybrid silica inorganic-organic xerogels (HXG), (ii) luminescent silica xerogels doped with lanthanide cations and an antenna ligand (Ln-AL), and (iii) modified titanium silicalites-1 (TSR%). Regarding the inorganic-organic hybrid silica xerogels, four series were synthesised by the sol-gel method through the co-condensation of tetraethoxysilane (TEOS) with a chloroalkyl or chloroaryltriethoxysilane (CIRTEOS, R = methyl [M], ethyl [E], propyl [P], or phenyl [Ph]) at different CIRTEOS:TEOS molar percentages. The obtained HXGs monoliths were characterised employing Fourier-transform infrared spectroscopy (FTIR), X-ray diffraction (XRD), ^{29}Si nuclear magnetic resonance (NMR), and gas adsorption of N_2 ($-196\text{ }^\circ\text{C}$) and CO_2 ($0\text{ }^\circ\text{C}$). The results were studied and compared with the results of their non-chlorinated analogues (RTEOS) previously published by the Inorganic chemistry research group at UPNA, with the aim of understanding the steric effect exerted by the alkyl chain or aryl group, and the inductive effect by the chlorine atom. It was demonstrated that the chlorinated precursors yield more microporous xerogels with a lower specific surface area and a narrower pore size distribution than their non-chlorinated analogue precursors. Moreover, the XRD patterns and the deconvolution studies of their FTIR spectra indicate that CIRTEOS precursors produce a more efficient nano-structurization than RTEOS because they favour the formation of 4-fold ring species (SiO_4) within the amorphous matrix. These species are the main constituents of ordered structures such as cage-like (T_8) or short ladder polyoctahedral silsesquioxanes (POSS). Finally, by comparing the four series, it is observed that the bulkier the precursor, the less condensed and more microporous the xerogels. However, CIETEOS precursor has the biggest impact on the internal structure, yielding non-porous and the most ordered xerogels, probably due to the conjugation of the electrostatic effect of the chlorine atom and the lower degree of freedom of the ethyl chain.

The luminescent xerogels (Ln-AL) were prepared following the same sol-gel method as that of the HXGs, but using only the TEOS precursor. Lanthanide trivalent cations were selected as the luminophores because their monochromatic emission is not dramatically affected by the coordination environment and their intensity gradually decreases upon exposition to certain analytes, instead of being instantly deactivated. However, they do not have an intense luminescent emission on their own, thus, their coordination with an antenna ligand (AL) to be sensitised is needed. Therefore, two series of Eu^{III} - or Tb^{III} -doped xerogels, each comprising eight materials varying in the pyridine-based AL type (chelidamic acid, picolinic acids with different functional groups, and a pybox molecule), were prepared. Once characterised, the two xerogels doped with the pybox antenna ligand 2,2'-(4-(2-Ethoxyethoxy)pyridine-2,6-diyl)bis(4,5-dihydrooxazole) (PB) were selected and used to prepare the membranes of two water-vapour optical fibre sensors, and after a preliminary trial, the sensor bearing the Tb-PB membrane (OFSTb-PB) was selected to conduct the measurements of the study. The response of the OFSTb-PB sensor towards water vapour concentration ($C_{\text{H}_2\text{O}}$) was recorded at three different temperatures, and it could be observed that it follows a linear trend up to a certain $C_{\text{H}_2\text{O}}$ value, beyond which the response deviates abruptly from linearity to a third-grade polynomial tendency, and also, the desorption curve yields a hysteresis loop. The isosteric enthalpies of adsorption of water (ΔH_{ads}), both the one of the sensor membrane and the monolithic xerogel present negative values confirming the exothermic nature of the process. When it is reached the $C_{\text{H}_2\text{O}}$ where the linear tendency is lost, the ΔH_{ads} values do not vary, are asymptotic to the concentration axis, and are close to the value of the water enthalpy of condensation in a flat surface (ΔH_{cond}). This confirms that the measurement mechanism is composed of two steps, the adsorption in the micropores of the material (the linearity of the calibration curve) and the capillary condensation taking place in the mesopores (non-linear response). It can be said that a textural characterisation of the membrane was accomplished if we consider the membrane as the adsorbent and the water molecules as the adsorbate. Furthermore, water retention in the membrane eases the contact between the quenching molecules and the luminophores, and thus, causes the abrupt decay of the luminescence.

Titanium silicalites (TSS) are Ti-containing microporous zeolites that are mainly used as catalysts in industrial oxidation reactions of great relevance. Additionally, due to their photoactivity under UV-Vis irradiation, these materials have also been used as photocatalysts, however, their performance does not excel because their microporosity and rigidity limit the diffusion of substrates through their porous channels. Therefore, in this research, three series of modified TS (TSR%) were prepared involving the use of triethoxysilanes (RTEOS, R = methyl [M], propyl [P], or phenyl [Ph]) at different RTEOS:TEOS molar percentages, to modify the internal structure of the titanium silicalites seeking an improvement in their photocatalytic performance. The obtained TSR% materials were characterised by FTIR, UV-VIS diffuse reflectance (DRS), UV-Raman and photoluminescence emission (PL) spectroscopies, and other techniques, such as gas adsorption, scanning electron microscopy and XRD. The information gathered from these techniques pointed out that four out of the twelve synthesised materials (TSM5, TSP5, TSPH5 and TSPH10) presented promising properties for efficient photocatalysis. In consequence, the photoactivity of these four materials was tested in the photodegradation reaction of the antidepressant venlafaxine in aqueous media, using simulated solar light irradiation. Contrary to the reference (a titanium silicalite synthesised with no RTEOS precursor), which is not photoactive, the TSP5 and TSPH5 materials were able to eliminate more than 90% of the pollutant in only two hours. These two materials exhibit the narrowest and most homogeneous pore diameter distribution, the smallest particle size, and the higher abundance of superficial hexacoordinated Ti species (TiO_6), confirming that the proposed synthetic approach allows the obtention of structurally modified titanium silicalites with improved photocatalytic properties.

RESUMEN

La investigación presentada en esta memoria tiene como objetivo preparar xerogeles híbridos de silicio y silicalitas de titanio modificadas, utilizando diversos precursores orgánicos, y estudiar la influencia de su naturaleza en las propiedades texturales y químicas de los nuevos materiales, con el fin de controlar su química superficial y textura, buscando la mayor versatilidad y el material mejor adaptado a la aplicación concreta que se le pretende dar, que son, en este estudio, la preparación de membranas de sensores químicos de fibra óptica y la degradación fotocatalítica de venlafaxina.

Para ello, se han preparado tres tipos de materiales: (i) xerogeles híbridos de silicio inorgánicos-orgánicos (HXG); (ii) xerogeles de silicio luminiscentes dopados con lantánidos y ligandos antena (Ln-AL); y, (iii) titanosilicalitas-1 modificadas (TSR%). De los xerogeles híbridos inorgánicos-orgánicos se sintetizaron cuatro series mediante el método sol-gel y la co-condensación de tetraetoxisilano (TEOS) con un cloroalquil- o cloroariltri-etoxisilano (CIRTEOS, R = metil [M], etil [E], propil [P], o fenil [Ph]) en diferentes porcentajes molares de CIRTEOS:TEOS. Los monolitos de HXGs se caracterizaron empleando espectroscopia infrarroja por transformada de Fourier (FTIR), difracción de rayos-X (XRD), resonancia magnética nuclear (NMR) de ^{29}Si , microscopia electrónica de barrido (SEM), y adsorción de gases de N_2 ($-196\text{ }^\circ\text{C}$) y CO_2 ($0\text{ }^\circ\text{C}$). Los resultados se analizaron y compararon con los publicados de series análogas no cloradas (RTEOS, trabajos previos del grupo de Química Inorgánica de la UPNA), con idea de entender el efecto estérico que ejerce la cadena alquílica o el arilo, y el efecto inductivo que ejerce el átomo de cloro en las propiedades de los materiales. Se demostró que los precursores clorados dan lugar a xerogeles más microporosos, con menor área superficial específica, y una distribución de tamaño de poro más estrecha. Es más, los difractogramas de rayos X y los estudios de deconvolución de sus espectros de FTIR indicaron que los precursores CIRTEOS dan lugar a una nano-estructuración más eficiente que los precursores RTEOS, dado que favorecen la formación en la matriz amorfa de anillos de silicio de 4 miembros (SiO_4), que son los constituyentes principales de estructuras ordenadas como silsesquioxanos poliédricos (POSS) en forma de jaula (T_8) o escaleras cortas. Al comparar las cuatro series, se observa que cuanto más voluminoso es el precursor, menos condensado está y más microporosos son los xerogeles. Probablemente,

debido a la conjunción del efecto electroestático del átomo de cloro y el menor grado de libertad de movimiento que presenta el etilo, el precursor ClETEOS es el que produce el mayor impacto en la estructura interna, obteniéndose xerogeles no porosos y con el mayor grado de orden local.

Los xerogeles luminiscentes (Ln-AL) se sintetizaron siguiendo el mismo método sol-gel, con la salvedad de que solo se utilizó TEOS como precursor. Se seleccionaron como luminóforos cationes trivalentes de lantánidos dado que su emisión monocromática es casi independiente del entorno de coordinación, y que su intensidad decae gradualmente -en lugar de desactivarse instantáneamente- cuando se exponen a determinados analitos (osciladores moleculares como el agua). Sin embargo, al no presentar una emisión luminiscente de alta intensidad, requieren coordinarse con ligandos antena (AL) para activar su emisión. Por ello, se prepararon dos series de xerogeles, una dopada con Eu^{III} y otra con Tb^{III} , y cada una formada por ocho materiales con ligandos antena distintos, todos derivados de la piridina (ácido quelidámico, ácidos picolínicos con diferentes grupos funcionales y una molécula de pybox). Después de su caracterización, se seleccionaron los dos xerogeles dopados con el ligando antena pybox 2'-(4-(2-etoxietoxi)piridina-2,6-diyl)bis(4,5-dihidrooxazol) (PB) para preparar las membranas de dos sensores de fibra óptica de vapor de agua, y tras una serie de pruebas preliminares, se seleccionó el sensor con la membrana del xerogel Tb-PB (OFSTb-PB) para realizar las medidas del estudio. La respuesta del sensor se registró a tres temperaturas, y se observó que las curvas de calibrado tienen una tendencia lineal hasta llegar a un determinado valor de $C_{\text{H}_2\text{O}}$, a partir del cual la respuesta se desvía abruptamente de la linealidad para seguir una tendencia polinómica de tercer grado, y también aparece un ciclo de histéresis en la desorción. Las entalpías isostéricas de adsorción de agua (ΔH_{ads}) de la membrana del sensor y del material monolito toman valores negativos, consistente con el carácter exotérmico del proceso. Cuando se alcanzan las $C_{\text{H}_2\text{O}}$ en las que se pierde la linealidad, las ΔH_{ads} no varían y los valores se hacen asintóticos al eje de concentraciones, además de estar muy próximos a la entalpia de condensación de agua en una superficie plana (ΔH_{cond}). Esto confirma que el mecanismo de medida tiene dos etapas, la adsorción en la microporosidad del material (linealidad de la curva de calibrado) y condensación capilar en mesoporos (cuando la respuesta deja de ser lineal). Se puede decir que de este modo se obtiene una caracterización textural de la membrana, si ésta es considerada el adsorbente y el analito el adsorbato. Por otro lado, la retención del agua en la membrana

facilita el contacto con los luminóforos y, por tanto, causa la desactivación de la luminiscencia.

Las titanosilicalitas (TSs) son un tipo de zeolitas microporosas que contienen titanio, y se utilizan principalmente como catalizadores en reacciones industriales de oxidación de gran relevancia. Estos materiales también han sido utilizados como fotocatalizadores debido a que son fotoactivos bajo irradiación UV-Vis, sin embargo, debido a su microporosidad y rigidez, la difusión de los substratos a través de sus canales porosos es bastante limitada, y provoca que su rendimiento fotocatalítico no sea destacable. Por lo tanto, con el objetivo de mejorar su rendimiento fotocatalítico, en esta investigación se prepararon tres series de TSs modificadas estructuralmente (TSR%) utilizando trietoxisilanos (RTEOS, R = metil [M], propil [P], o fenil [Ph]) en diferentes porcentajes molares respecto al TEOS. Los materiales TSR% se caracterizaron con espectroscopias FTIR, de reflectancia difusa UV-Vis, UV-Raman y de emisión fotoluminiscente (PL) y, otras técnicas, como adsorción de gases, microscopia electrónica de barrido y XRD. La información recopilada puso de manifiesto que cuatro de los materiales sintetizados (TSM5, TSP5, TSPH5 y TSPH10), presentan propiedades prometedoras para fotocatalizar de forma eficiente, por lo que se evaluó su actividad fotocatalítica en la reacción de degradación del antidepresivo venlafaxina en medio acuoso, utilizando radiación solar simulada. Al contrario que el material de referencia (una titanosilicalita sintetizada sin utilizar RTEOS), que no es fotoactivo, los materiales TSP5 y TSPH5 fueron capaces de eliminar más del 90% del contaminante en sólo 2 horas. Estos materiales presentan la distribución de tamaño de poro más estrecha y homogénea, el menor tamaño de partículas, y la mayor abundancia de especies superficiales de titanio hexacoordinado (TiO_6), confirmando que la estrategia experimental utilizada permite obtener titanosilicalitas modificadas estructuralmente con propiedades fotocatalíticas mejoradas.

INDEX

CHAPTER 1. INTRODUCTION	1
1.1 STUDY OF THE CHEMICAL AND MORPHOLOGICAL PROPERTIES OF HYBRID SILICA XEROGELS AND SYNTHESIS OF LUMINESCENT XEROGEL COATINGS FOR FIBRE OPTIC SENSORS	2
1.2 MODIFIED TITANIUM SILICALITES PHOTOCATALYSTS	6
1.3 OBJECTIVES	7
1.4 DISSERTATION STRUCTURE	9
1.5 REFERENCES	12
CHAPTER 2. MATERIALS AND METHODS	17
2.1 SYNTHESIS PROCEDURES	17
2.1.1 Synthesis of hybrid xerogels (CIRTEOS series)	17
2.1.2 Synthesis of lanthanide-doped xerogels (Ln-AL series)	21
2.1.3 Synthesis of modified Titanium silicalites (TSR% series)	25
2.2 CHARACTERISATION TECHNIQUES	28
2.2.1 ²⁹ Si Nuclear Magnetic Resonance (²⁹ Si NMR)	28
2.2.2 Fourier-Transform Infrared spectroscopy (FTIR)	29
2.2.3 UV-Vis spectroscopy: Absorption, Photoluminescence emission (PL), Diffuse Reflectance (DR) and UV-Raman	31
2.2.4 X-ray Diffraction (XRD)	33
2.2.5 Helium Pycnometry	34
2.2.6 Gas adsorption (N ₂ at -196 °C; CO ₂ at 0 °C; and H ₂ O(v) at 25, 30 and 30 °C)	35
2.2.7 Scattering Electron Microscopy (SEM)	37
2.2.8 High-Resolution Transmission Electron Microscopy (HR-TEM)	38
2.3 OPTICAL FIBRE SENSORS COATED WITH Ln-AL FILMS	39
2.3.1 Optical Fibre Sensor (OFS) construction	39
2.3.2 Sensing mechanism	41
2.3.3 Photonic experimental set-up	42
2.4 PHOTOCATALYTIC TESTS OF MODIFIED TITANIUM SILICALITES	43
2.5 CALCULATION METHODS	44

2.5.1	²⁹ Si NMR deconvolution methods of HXG	44
2.5.2	FTIR deconvolution methods of HXG	45
2.5.3	Calculation of bandgaps of TSR% materials	47
2.5.4	Adsorption-desorption isotherms data processing	48
2.5.5	Determination of pore size distribution by DFT methods	52
2.6	REFERENCES	53
CHAPTER 3. NOVEL ORGANOCHLORINATED XEROGELS: FROM MICROPOROUS MATERIALS TO ORDERED DOMAINS		57
3.1	INTRODUCTION	58
3.2	RESULTS AND DISCUSSION	60
3.2.1	²⁹ Si nuclear magnetic resonance (NMR)	60
3.2.2	X-Ray Diffraction (XRD)	64
3.2.3	Skeletal density	67
3.2.4	Porous texture	68
3.2.4.1	<i>Adsorption isotherms and textural properties</i>	68
3.2.4.2	<i>Porosity distribution</i>	72
3.2.5	Field-Emission Scanning Electron Microscopy (FE-SEM)	74
3.3	CONCLUSIONS	77
3.4	ACKNOWLEDGEMENTS	77
3.5	REFERENCES	78
CHAPTER 4. HYBRID XEROGELS: STUDY OF THE SOL-GEL PROCESS AND LOCAL STRUCTURE BY VIBRATIONAL SPECTROSCOPY		81
4.1	INTRODUCTION	82
4.2	RESULTS AND DISCUSSION	84
4.2.1	Influence of organochlorine substituents on gelation time	84
4.2.2	Study of the local structure of hybrid xerogels using FTIR and XRD	89
4.2.3	Spectral deconvolution of the 1300–700 cm ⁻¹ region	98
4.3	CONCLUSIONS	108
4.4	ACKNOWLEDGEMENTS	109
4.5	REFERENCES	109

CHAPTER 5. NOVEL SILICA HYBRID XEROGELS PREPARED BY CO-CONDENSATION OF TEOS AND CLPhTEOS: A CHEMICAL AND MORPHOLOGICAL STUDY	113
5.1 INTRODUCTION	114
5.2 RESULTS AND DISCUSSION	116
5.2.1 Infrared spectroscopy (FTIR)	116
5.2.2 ²⁹ Si nuclear magnetic resonance (NMR)	124
5.2.3 X-ray diffraction (XRD)	126
5.2.4 Helium pycnometry	128
5.2.5 N ₂ and CO ₂ adsorption isotherms	129
5.2.6 Microscopy	133
5.2.6.1 <i>Field-Emission Scanning Electron Microscopy (FE-SEM)</i>	133
5.2.6.2 <i>High Resolution-Transmission Electron Microscopy (HR-TEM)</i>	135
5.3 CONCLUSIONS	137
5.4 ACKNOWLEDGEMENTS	138
5.5 REFERENCES	138
CHAPTER 6. FROM FUNDAMENTAL MATERIALS CHEMISTRY TO SENSING APPLICATIONS: UNRAVELLING THE WATER ADSORPTION MECHANISM OF A LUMINESCENT OPTICAL FIBRE SENSOR MEMBRANE	143
6.1 INTRODUCTION	144
6.2 RESULTS AND DISCUSSION	145
6.2.1 Luminescent and textural characterisation of Ln-AL xerogels	145
6.2.2 Selection of the target OFS coating	153
6.2.3 Time-response curve for humidity	157
6.2.4 Water-vapour isotherms of Tb-PB	162
6.2.5 Isosteric enthalpies of adsorption	163
6.3 CONCLUSIONS	166
6.4 ACKNOWLEDGEMENTS	167
6.5 REFERENCES	167

CHAPTER 7. DESIGN OF NOVEL PHOTOACTIVE MODIFIED TITANIUM SILICALITES AND THEIR APPLICATION FOR VENLAFAXINE DEGRADATION UNDER SIMULATED SOLAR IRRADIATION	171
7.1 INTRODUCTION	172
7.2 RESULTS AND DISCUSSION	175
7.2.1 Characterisation analysis of the synthesized materials	175
7.2.1.1 X-ray diffraction (XRD)	175
7.2.1.2 Fourier transformed infrared spectroscopy (FTIR)	177
7.2.1.3 Diffuse reflectance UV-Vis, photoluminescence emission (PL) and UV-Raman spectroscopy	179
7.2.1.4 N ₂ and CO ₂ adsorption	185
7.2.1.5 FE-SEM and EDX	189
7.2.2 Photocatalytic degradation of venlafaxine in the presence of TS	191
7.3 CONCLUSIONS	194
7.4 ACKNOWLEDGEMENTS	195
7.5 REFERENCES	196
CHAPTER 8. CONCLUSIONS/CONCLUSIONES	201/206
ANNEXE A. SOL-GEL PROCESS, SYNTHESIS OF HYBRID SILICA XEROGELS	211
A.1 INTRODUCTION TO SOL-GEL PROCESS	211
A.2 HYDROLYSIS IN ACID MEDIA	213
A.3 CONDENSATION IN ACID MEDIA	215
A.4 SOL-GEL TRANSITION (GELATION)	218
A.5 AGEING AND DRYING	220
A.6 REFERENCES	222
ANNEXE B. SILICA-COATED OPTICAL FIBRE SENSORS (OFS)	225
B.1 FUNDAMENTS OF OPTICAL FIBRES (OF)	225
B.2 OPTICAL FIBRE SENSORS (OFS)	230

B.3 OPTICAL FIBRE CHEMICAL SENSORS (OFCS)	232
B.4 SILICA GEL COATINGS	235
B.5 LANTHANIDE-DOPED SILICA COATINGS FOR OFS	239
B.6 REFERENCES	239
ANNEXE C. PHOTOLUMINESCENCE OF LANTHANIDES	243
C.1 BASIC CONCEPTS OF LUMINESCENCE.....	243
C.2 ELECTRONIC CONFIGURATION OF Ln ^{III}	250
C.3 ABSORPTION AND EMISSION OF Ln ^{III}	253
C.4 SENSITIZATION OF Ln ^{III} BY ANTENNA LIGANDS (AL)	257
C.5 REFERENCES	260
ANNEXE D. MODIFIED TITANIUM SILICALITES AND PHOTOCATALYSIS	263
D.1 INTRODUCTION TO TITANIUM SILICALITES (TS)	263
D.2 SYNTHESIS OF TITANIUM SILICALITES	267
D.3 HETEROGENEOUS PHOTOCATALYSIS.....	271
D.4 TSs AS PHOTOCATALYSTS IN THE PHOTODEGRADATION OF POLLUTANTS	276
D.5. COMPARATIVE OF THE PERFORMANCE OF THE NOVEL MODIFIED TSs WITH OTHER PHOTOCATALYSTS	278
D.6 REFERENCES	282
APPENDIX A. LIST OF ABBREVIATIONS AND SYMBOLS	287
APPENDIX B. LIST OF FIGURES	295
APPENDIX C. LIST OF TABLES	305
APPENDIX D. CONTRIBUTIONS IN OTHER ARTICLES AND IN CONFERENCES	309

CHAPTER 1

INTRODUCTION

CHAPTER 1

INTRODUCTION

The research presented in this doctoral dissertation is focused on the synthesis of siliceous materials, and the study of their use in different applications. These materials are classified into three well-defined groups: silica hybrid inorganic-organic xerogels (HXG), silica xerogels doped with lanthanide complexes (Ln-AL), and modified titanium silicalites-1 (TSR%). Since this doctoral dissertation is related to the development of new materials, before delving into specific topics of each group we should define what materials science is, and which is its field of study.

Material science is a multidisciplinary field of knowledge that emerges as an amalgam resulting from the combination of the basic sciences and the use of different technologies, but first, what is exactly a material? Materials can be defined as any chemical substance that has been used by humankind to craft items or tools that are crucial on a daily basis; in fact, historians have named whole periods based on the main materials used during that time interval (e.g., stone, bronze and iron age). Then, this science is focused on the study of the correlation between the intrinsic properties of the starting material and the macroscopic properties of the fabricated product.

Materials can be simple or composites. Simple materials are classified into three groups: metal and alloys, ceramics, and organic polymers; nowadays it is well-known that their properties such as density, dielectric constants, thermic expansion, elasticity, stress resistance, among others, can be explained by their crystalline structure, their chemical composition, their morphology, their microstructure, and by applying symmetry (space groups) to their atomic or molecular structures [1]. This knowledge has also allowed the design of composite materials whose properties arise as a synergy between their constituents. For example, in polymeric macromolecules the combination of different monomers is responsible for their macroscopic mechanical properties [2,3]; in metal oxide electrodes a slight perturbation in the atomic ratio of the metal leads to a significant change in the morphology and the electric properties [4].

The first and second sections of this introduction aim to provide a general overview of the nature and applications of the silica xerogel materials and the titanium silicalites, respectively. The final subchapter is dedicated to describing the objectives and clarifying the structure of this doctoral dissertation.

1.1 STUDY OF THE CHEMICAL AND MORPHOLOGICAL PROPERTIES OF HYBRID SILICA XEROGELS AND SYNTHESIS OF LUMINESCENT XEROGEL COATINGS FOR FIBRE OPTIC SENSORS

One area of materials science continuously growing is the study of hybrid inorganic-organic materials. These kinds of materials are of most interest because they do not only retain the properties of their separate components, but also arise unique properties such as easily reversible thermochromism [5], higher compaction and enhanced chemical stability [6], or textural characteristics suitable for substantial removal of pollutants in aqueous media [7]. Among the hybrid materials, organically modified silicates (ormosils) are known for the combination of the mechanical, thermal and structural stability conferred by the inorganic skeleton (silicon oxide), and the functionality and flexibility bestowed by the organic compounds [8]. These materials are synthesised through the sol-gel process, which is a nanotechnology synthesis procedure because the obtained solids are nanoparticles, nanocomposites, or simply nanostructured [9].

The sol-gel method is a synthetic procedure based on the inorganic polymerization chemistry and the bottom-up/self-assembly approach, which involves a few steps employing mild conditions. The concepts giving name to this method, sol and gel, refer to the two steps of matter aggregation during the polycondensation process. A “sol” is a dispersion of colloidal particles in a liquid solvent formed by the hydrolysis of molecular precursors and their successive condensation, whereas “gel” refers to a three-dimensional network formed by the inter-linking of the colloids throughout all the synthesis container. The gels undergo an ageing process to strengthen the polymeric network and to prevent cracks during the following drying step, in which the gels yield solids with a wide variety of shapes (powders, monoliths, coatings and fibres) [10]. Furthermore, the properties of the resulting solids (porosity, optical transparency and hydrophobicity, among others) can be tailored by controlling the synthesis parameters and selecting the organic precursors.

Hence, due to the high versatility of the sol-gel method, organically modified silicates (ormosils) have been designed for innumerable applications, such as biosensors and chemical sensors [11,12], matrices for enzymes and proteins for biomedical applications [13], membranes for ionic exchange [14], and supports for catalysts [15].

Among the ormosils, the organic-inorganic hybrid silica gels are synthesised from the hydrolysis and co-condensation of monomeric tetra-functional silicon alkoxides (tetra-alkoxysilanes, e.g., $\text{Si}(\text{OC}_2\text{H}_5)_4$, TEOS) and organosilanes ($\text{R}'_x\text{Si}(\text{OR})_{4-x}$) containing non-hydrolysable organic groups (R'). The reactions take place in a water-alcohol mixture media (alcohol is used as a homogenising agent due to the insolubility of tetra-alkoxysilanes in water) catalysed by mineral acids or bases [16]. Therefore, according to P. Judestein's classification, hybrid silica gels are considered type II hybrid materials, which englobe materials with strong covalent or ionic-covalent bonds connecting the organic and inorganic moieties [8]. The prefixes “xero”, “cryo” and “aero” usually attached to the term “gel” refer to the drying conditions, which deeply affect the textural properties of the obtained solid. On the one hand, by using supercritical conditions, the liquid can be effectively removed without a significant alteration of the gel network, therefore, the resulting “aerogel” retains its macroporosity. Moreover, sub-zero temperatures can also be used to separate the liquid from the gel, obtaining supermacroporous solids named “cryogels”. On the other hand, if more microporous materials are required, the drying step should be performed at atmospheric conditions to obtain a “xerogel (XG)” [17].

Hybrid silica xerogels (HXG) are known for their large specific surface area, high pore volume and small pore size. These properties along with their high biocompatibility make them especially interesting for biomedical applications, such as bone scaffolds [18], or drug deliverers [19–21]. Furthermore, numerous optical usages of these materials can be found in the literature, due to their optical transparency in a wide wavelength range, the ease of controlling their final morphology, and their mechanical and thermochemical stability [22–25].

The first investigations by the Inorganic Chemistry Group at UPNA with siliceous xerogels with entrapped vapourchromic compounds, and their implementation in optical fibre sensors (OFS) for the detection of VOCs, dates back to 1997. The research resulted in two patents, several papers about vapourchromic compounds, the design of an OFS [26–31], and two PhD Thesis (I. Romeo, 2000; A. Luquín, 2004). Afterwards, the group

deepened in the preparation of tetraethoxysilane (TEOS) gels in acidic medium thanks to two projects granted by MCyT (2002) and GN, Government of Navarre (2003), with the study of the sol-gel process, the dispersion of vapochromic compounds in the gel and the preparation of the corresponding OFS as the main focuses [32–34]. Subsequently, a MEC project was awarded (2005) to study the sol-gel process of TEOS in a basic medium and to prepare some sensing elements for H₂O, butylamine, toluene, or chloromethanes vapours, among others [35,36]. A project granted by “Ministerio de Ciencia e Innovación de España (MICINN)” in 2008 meant refocusing the investigations towards the preparation of HXG by co-condensation of TEOS as the reference precursor, with a second RTEOS precursor (R = methyl (M), ethyl (E), propyl (P), and phenyl (Ph)). This approach allowed to achieve gradual modifications of the porosity and surface chemistry of the xerogel materials, and it was the starting point for a subsequent MICINN project (2009) used to complete the studies to obtain more sensitive and selective OFS by controlling the porosity and the surface polarity of the HXGs. Thus, 11 xerogel series were synthesised starting from a 100% TEOS content and increasing the molar percentage of RTEOS at acidic and alkaline pH values, which allowed the preparation of a library of siliceous XGs with tailored properties for the preparation of OFS films as the sensitive element [37–42]. It was demonstrated that these new XGs are non-crystalline solids with a certain order at the nanometric scale (R–SiO_{1.5} species) and polycondensed Si atoms (T³). Moreover, an in-depth study of the formation of ordered domains in their structure and the search for additional applications were carried out. Three additional research projects (MAT-2016, GN in 2016/2017) allowed the identification of the adsorption phenomenon as the key process to explain the measuring mechanism of a given OFS, to synthesise novel HXGs with different organic precursors, to study the kinetics governing the hydrolysis/condensation reactions through ²⁹Si-NMR, and to set up a gas/vapour sorption equipment (Micrometrics ASAP 2020) for the calibration of OFS for VOC vapours and other gases. These investigations are compiled in 3 doctoral dissertations (J. Estella, 2009; X. Ríos, 2013; P. Moriones, 2016).

Considering the background of the research group concerning silica xerogels, two of the three research topics in this PhD dissertation are focused on these materials (both included in the current project of the group (PID2020-113558RB-C42)). The first topic is the synthesis and characterisation of four series of hybrid xerogels prepared by co-condensation of TEOS with chlorinated organosilanes [CIRTEOS precursor (R = methyl

(M), ethyl (E), propyl (P), and phenyl (Ph)] using different CIRTEOS:TEOS molar percentages. These materials were fully characterised, and the results were studied to gather information about the influence of the organic precursor in the texture, surface chemistry, morphology and structure of the resulting xerogels, and to increase the amount of HXG candidates for the preparation of new functionalized OFS. The second topic regarding xerogels is their synthesis and doping with luminescent species (lanthanide trivalent cations), and their application as the chemical zone (sensing element) of a luminescence-based OFS. Due to the novelty of this research line in the group, 100% TEOS gels were used as the coating films. Although in the literature it can be found plenty examples of luminescent substances embedded into silica gel porous networks [43–45], the development of luminescence-based OFS requires the use of a luminophore that fulfils the following specific conditions: (i) it must be soluble in the sol mixture, thus, the one-pot synthesis strategy of the xerogel remains unchanged; (ii) its emission intensity gradually decreases upon exposition to specific analytes; (iii) the emission should be as intense and monochromatic as possible to facilitate data processing; and finally (iv) the resulting sensors should be reusable and stable at least in a mid-term.

Lanthanide ions (Ln) are well-considered in technological applications due to their unique spectroscopy properties. What makes the lanthanide ions such good and valued “chromophores” in luminescent species, is that they produce narrow emission bands at specific wavelengths almost independently of the environment of the metal, thus, they guarantee monochromatic emissions. Therefore, it was decided to use the lanthanide trivalent ions (Ln^{III}) with the highest intensity emission in the visible spectra, Eu^{III} and Tb^{III}, as the luminophores of the silica-coated OFSs. However, the luminescent emission of isolated Ln^{III} is very weak because they cannot absorb much incident light on their own. Therefore, to increase their emission intensity, it is required the use of molecules that can “harvest” and provide photons to them. These substances that activate the luminescence of the Ln^{III} through the formation of coordination complexes are named “antenna ligands” (AL). This topic generated a new inquiry, the search for an antenna ligand that activates efficiently the luminescence and yields water-soluble complexes, since if we wanted to guarantee its homogeneous distribution through the silica matrix, it must be soluble in the sol-gel media.

Thus, a series of TEOS xerogel containing different combinations of ALs and Ln^{III} ions (Eu^{III} or Tb^{III}) were prepared by adding them directly into the silica sol to form *in*

situ lanthanide complexes (Ln-AL) within the silica matrix. Then, their properties were analysed, and in consequence, the optimal gels for the preparation of the optical fibre sensor (OFSLn-AL) were selected. Finally, the sensor was exposed to a relative humidity interval in a climate chamber, and the optical response was used to unravel the adsorption mechanism of water vapour in the silica film of the sensor.

1.2 MODIFIED TITANIUM SILICALITES PHOTOCATALYSTS

The development of heterogeneous photocatalysts is one of the most important fields in material science due to their applications in topics of paramount importance, such as reactions of industrial interest; water splitting to produce H₂, CO₂ and N₂ reduction; and advanced oxidation processes (AOPs) for water waste treatment [46]. Consequently, many efforts have been made to prepare semiconductor photocatalysts that accomplish the following requirements: high photochemical stability and conversion efficiency, low-cost and scalable synthesis to the industrial level, and photoactivity under visible radiation [47–52]. Nowadays, there are few commercial photocatalysts due to the impossibility of accomplishing all the cited criteria. Nevertheless, titanium dioxide (TiO₂), specifically the 75% anatase phase commercial Degussa P25, is a photocatalyst that is widely employed because of its low manufacturing cost, high stability and oxidizing power. However, TiO₂ only absorbs ultraviolet light, which makes it a poor photocatalyst in solar-light driven photocatalytic systems because UV represents only 4% of the solar spectrum [53].

Titanium silicalite-1 (TS-1) is a type of zeolite that contains titanium cations (Ti^{IV}) isomorphously replacing silicon atoms in its modernite framework inverted (MFI) structure. Although this material is mainly known for its high performance as the catalyst in oxidative reactions using hydrogen peroxide, e.g. epoxidation of olefins; ammoximation of cyclohexane or hydroxylation of aromatic compounds [54–58], its Ti^{IV} species like the framework tetracoordinated (TiO₄) or the non-lattice and superficial hexacoordinated (TiO₆) are both photoactive. In fact, TS-1 presents two main advantages compared to TiO₂ in AOPs: the hydrophobic MFI structure, which eases the selective absorption of organic pollutants; and the higher surface area, which allows a better dispersion of the Ti^{IV} active sites [59]. Nevertheless, the substrates usually manifest diffusion limitations within the microporous structure of conventional TS-1 zeolites,

which have led to the development of different strategies to synthesise modified TS-1s with enhanced texture properties to overcome this issue [60–62].

Hence, the third research topic in this PhD dissertation is focused on the preparation of titanium silicalites that can efficiently photodegrade an emerging pollutant in aqueous media. For such purpose, it was proposed to use the main concept of the synthesis of the hybrid xerogels, in the hydrothermal synthesis of the TS-1s, that is, three series of modified titanium silicalites (TSR%) were obtained by adding organotriethoxysilanes [RTEOS precursor (R = methyl (M), propyl (P), and phenyl (Ph))] in different molar percentages respect to TEOS, along with the titanium source (titanium tetrabutoxide, TBOT) and directing agents/templates. After the calcination, an extensive characterization of the TSR% materials confirmed the modification of their texture and the increase in the abundance of TiO_6 species compared to the TS-1 reference. Then, their photoactivity was tested in the photodegradation of the antidepressant venlafaxine under simulated solar light, where two of the synthesised materials showed outstanding efficiency achieving the almost complete elimination of the pollutant in 2 h. Since the TS-1 reference was not photoactive, the results proved that this new synthesis approach allows the obtention of efficient photoactive TS-1 materials for AOPs under solar irradiation.

1.3 OBJECTIVES

The surface chemistry and the porosity of a material are essential properties to predict its behaviour and performance in emerging or novel applications. Thus, the investigation performed in this thesis aims to prepare hybrid xerogels and modified titanium silicalites using a variety of organic precursors and to study the influence of their nature and quantity on the textural and chemical properties of new materials. Once this information is gathered, the most promising materials will be used in emerging technologies: silica xerogel films as matrices for luminescent probes in chemical optical fibre sensors, and titanium silicalites as photocatalysts for the removal of pollutants in aqueous media. The specific objectives are itemised as follows:

1. Synthesise four series of hybrid xerogels prepared by co-condensation of TEOS and a chloroalkyltriethoxysilanes [CIRTEOS; R = methyl (M), ethyl (E), propyl (P), or phenyl (Ph)] at different CIRTEOS:TEOS molar ratios.

2. Determine the influence of the chlorine atom and the length of the alkylic chain on the morphology, structure and texture of the previously synthesised xerogels.
3. Establish a correlation between the gelation time and the microstructure of HXG xerogels by FTIR deconvolution methods.
4. Prepare a series of luminescent TEOS xerogels (Ln-AL) by the addition into the sol-gel media, at a doping scale, of a lanthanide trivalent cation as the doping agent (Eu^{III} or Tb^{III}) and a water-soluble antenna ligand (AL).
5. Study the luminescence and textural properties of the luminescent xerogels to determine which ones are suitable for the preparation of the OFS coatings.
6. Construct a luminescent-based optical fibre chemical sensor (OFSLn-AL) by the dip-coating technique using a TEOS luminescent gel containing the optimal Ln-AL combination.
7. Test the response of the functionalised OFS towards relative humidity using a climate chamber. Establish a correlation between the sensor response and the textural properties of its sensitive silica coating film.
8. Prepare modified titanium silicalites (TSR%) by hydrothermal synthesis and the use of TEOS and alkyltriethoxysilanes [RTEOS; R = methyl (M), propyl (P) or phenyl (Ph)] at different molar percentages.
9. Determine the effect of the organic precursors used in the synthesis of the modified titanium silicalites on their morphology, texture, and UV-Vis light absorption, and evaluate their potential photoactivity under UV-Vis light.
10. Use the selected modified titanium silicalites as photocatalysts for the degradation of an emerging contaminant in aqueous media.

The **objectives** of the thesis are accomplished in the following Chapters:

- Objective 1: Chapters 3 and 5
- Objective 2: Chapters 3 to 5
- Objective 3: Chapters 4 and 5
- Objectives 4–7: Chapter 6
- Objective 8–10: Chapter 7

1.4 DISSERTATION STRUCTURE

The structure of this dissertation comprises 8 chapters, including this introduction as the first chapter. Materials and methods, both experimental and calculations, are described in *Chapter 2*. *Chapters 3 to 7* correspond to published or sent to journals studies regarding the objectives of the thesis, and the general conclusions of all the investigations are summarised in *Chapter 8*. Additionally to the main chapters, 4 annexes are included: (i) *Annexe A* provides an overview of the sol-gel process considering the synthesis parameters in use and the expected impact of the organic precursors in the matrix; (ii) *Annexe B* explains the fundamental topics related to optical fibres with an emphasis on chemical sensors; (iii) *Annexe C* contains an explanation of the luminescence of the lanthanide trivalent cations, and (iv) *Annexe D* gives an overview of titanium silicalites and heterogeneous photocatalysis. Finally, three appendices contain the list of all the abbreviations and symbols, figures and tables included in the dissertation (*Appendix A, B* and *C*, respectively), and *Appendix D* gathers all the contributions made to other published articles and congresses.

Chapter 2 includes all the common materials and methods that have been used and applied in this research. The first section is dedicated to the synthesis procedures of all the materials. The second section englobes all the characterisation techniques applied to the new materials: ^{29}Si nuclear magnetic resonance; Fourier-transform infrared spectroscopy (FTIR); X-ray diffraction; adsorption of N_2 ($-196\text{ }^\circ\text{C}$), CO_2 ($0\text{ }^\circ\text{C}$) and water vapour at different temperatures; high-resolution transmission and field emission scattering electronic microscopies (HR-TEM and FE-SEM, respectively); UV-Vis absorption, emission, UV-Raman and diffuse reflectance spectroscopies; and Helium pycnometry. The third section comprises the preparation method of the OFSs, as well as the sensing mechanism and photonic experimental set-up. The fourth section details the parameters and procedures of the TSR% photodegradation tests, and the fifth and last section explains all the calculation methods: deconvolution of the ^{29}Si NMR spectra for the determination of Si^{IV} species distribution; deconvolution of FTIR spectra for the distribution of $(\text{SiO})_x$ species; Tauc-plot method for bandgaps; Brunauer-Emmett-Teller (BET), Dubinin-Raduskevich (DR) and Brunauer-Joyner-Halenda (BJH) methods for textural parameters; and Density Functional Theory (DFT) for pore size distributions.

Chapter 3 describes the preparation and characterisation of three series of chloroalkyltriethoxysilanes [CIRTEOS; R = methyl (M), ethyl (E) propyl (P)] synthesised with different CIRTEOS:TEOS molar percentages. The influence of the chlorine atom on the properties of HXGs is discussed by their comparison with materials in the same series (xerogels with different molar percentages of the same organic precursor), crossed comparison with analogue TEOS:RTEOS series synthesised in previous works and comparison with the reference material (100% TEOS).

Chapter 4 provides a theoretical study of the correlation between the gelation time and the microstructure of the HXGs synthesised in *Chapter 3*. This approach consists of the deconvolution of the FTIR spectra of the xerogels to determine the distribution of 4-fold rings $[(\text{SiO})_4]$ and 6-fold rings $[(\text{SiO})_6]$ in the silicon matrix of HXGs. This distribution is used to explain the low-angle diffraction maxima ($10^\circ < 2\theta$) observed in the X-ray pattern of the HXG with the highest molar percentage of organic precursor and the evolution of the gelation times of the HXGs series as the molar percentage of CIRTEOS increases.

In **Chapter 5**, both the experimental characterisation techniques of *Chapter 3* and the deconvolution method of *Chapter 4* are used to study the properties of the HXGs synthesised with p-chlorophenyltriethoxysilane (CIPhTEOS) at different CIPhTEOS:TEOS molar percentages. The characterisation results are compared with those of the xerogels studied previously to gather information on the influence of the chlorophenyl moiety on the properties of the material.

Chapter 6 describes the investigations related to the development of a luminescence-based optical fibre chemical sensor (OFSLn-AL) for humidity as the analyte. This chapter details the textural and luminescence characterisation carried out on TEOS monoliths containing 16 possible combinations of lanthanide cations and antenna ligands. Once the one with the optimal combination for the preparation of OFS films has been selected, the time-curve responses of the prepared OFSLn-AL and the water vapour adsorption isotherms of the Ln-AL monoliths are obtained at the same relative humidity range and three different temperatures. The calculated isosteric enthalpies of adsorption for OFSLn and Ln-AL are compared to explain the water vapour adsorption mechanism in the sensor.

Chapter 7 addresses the characterisation and application of new modified titanium silicalites (TSR%) synthesised using a co-condensation approach analogue to that employed in the synthesis of hybrid silica xerogels. The characterisation results were used to discuss the modifications that the organosilanes [RTEOS; R = methyl (M), propyl (P), or phenyl (Ph)] induce in the zeolite structure and the titanium content of the titanium silicalites obtained. The more promising materials were selected and tested in the photocatalytic degradation of venlafaxine, an emerging pollutant in aqueous media.

Annexe A details the theoretical basis ruling the sol-gel process, which is the method selected for the preparation of the xerogels used (Chapters 3 to 6). After a brief historical overview, the mechanisms and chemical events at each step of the process are detailed with emphasis on the influence of the organosilanes in the final structure and chemical properties.

Annexe B details the composition and the mechanism of light transmission through the optical fibres. It continues with a brief explanation regarding optical fibre chemical sensors, their classification and the mechanism of luminescence-based sensors. Finally, the different strategies used to immobilise sensing substances are explored, with a focus on the dip-coating technique, which was selected as the deposition technique for the optical fibre sensors prepared in this research.

Annexe C explains the theoretical basis of the lanthanide trivalent cation's luminescence emissions. Firstly, the mechanisms of the luminescence phenomena are detailed before focusing on the lanthanides. Then, the absorption and emission of these species are explained regarding their electronic configuration and the selection rules of the electronic transitions. Finally, the antenna effect for the sensitisation of the lanthanide cations is briefly commented.

Annexe D focuses on titanium silicalites and their photocatalytic application. This section begins with a short historical background of this family of materials and continues with an explanation regarding their structure, properties and synthesis method. Then, a summary of the concepts and mechanisms involved in heterogeneous photocatalysis and a literature review of this application is provided. To conclude, it is included a brief discussion where the performance of *Chapter 7* materials in the photodegradation of venlafaxine is compared with the performance of other photocatalyst reported in the literature.

Appendix A includes a list of all figures abbreviations and symbols in this dissertation.

Appendix B contains a list of all figures illustrated in this dissertation.

Appendix C shows a list of all the tables displayed in this thesis.

Appendix D gathers all the contributions to other articles and congresses.

1.4 REFERENCES

- [1] Newnham, R. E. Introduction. In *Properties of Materials: Anisotropy, Symmetry, Structure*; Oxford University Press: Oxford, UK, **2004**; p. 1–8.
- [2] Meijer, H. E. H.; Govaert, L. E. *Prog. Polym. Sci.* **2005**, *30*, p. 915–938.
- [3] Lee, Y. L.; Lester, D. W.; Jones, J. R.; Georgiou, T. K. *ACS Omega* **2021**, *7*, p. 786–792.
- [4] Saaudane, I.; Delmas, C. *J. Mater. Chem.* **1996**, *6*, p. 193–199.
- [5] Jia, Q.-Q.; Luo, Q.-F.; Ni, H.-F.; Su, C.-Y.; Fu, D.-W.; Xie, L.-Y.; Lu, H.-F. *J. Phys. Chem. C* **2021**, *126*, p. 1552–1557.
- [6] Nashrah, N.; Putri, R. A. K.; Alharissa, E. Z.; Al Zoubi, W.; Ko, Y. G. *Metals* **2021**, *11*, p. 1043.
- [7] Gaeta, M.; Barcellona, M.; Purrello, R.; Fragalà, M. E.; D’Urso, A. *Chem. Eng. J.* **2022**, *433*, p. 133262.
- [8] Judeinstein, P.; Sanchez, C. *J. Mater. Chem.* **1996**, *6*, p. 511–525.
- [9] Parashar, M.; Shukla, V. K.; Singh, R. *J. Mater. Sci.: Mater. Electron.* **2020**, *31*, p. 3729–3749.
- [10] Sakka, S. *Handbook of Sol-Gel Science and Technology Processing characterization and applications. Volume I: Sol-Gel Processing*; Sakka, S., Kozuka, H., Eds.; 1st ed.; Kluwer Academic Publishers: Osaka, Japan, **2005**.
- [11] Tiwari, I.; Singh, K. P. *Russ. J. Gen. Chem.* **2012**, *82*, p. 157–167.
- [12] Gillanders, R. N.; Campbell, I. A.; Glackin, J. M. E.; Samuel, I. D. W.; Turnbull, G. A. *Talanta* **2018**, *179*, p. 426–429.
- [13] Ronda, L.; Steffano, B.; Steffano, B. *Curr. Org. Chem.* **2015**, *19*, p. 1677–1683.
- [14] Sgreccia, E.; Narducci, R.; Knauth, P.; Di Vona, M. L. *Polymers* **2021**, *13*, p. 1874.
- [15] Shamir, D.; Elias, I.; Albo, Y.; Meyerstein, D.; Burg, A. *Inorg. Chim. Acta.* **2020**, *500*, p. 119225.
- [16] Brinker, C. J.; Scherer, G. W. *Sol-Gel Science*; 1st ed.; Academic Press, INC: San Diego, CA, USA, **1990**.

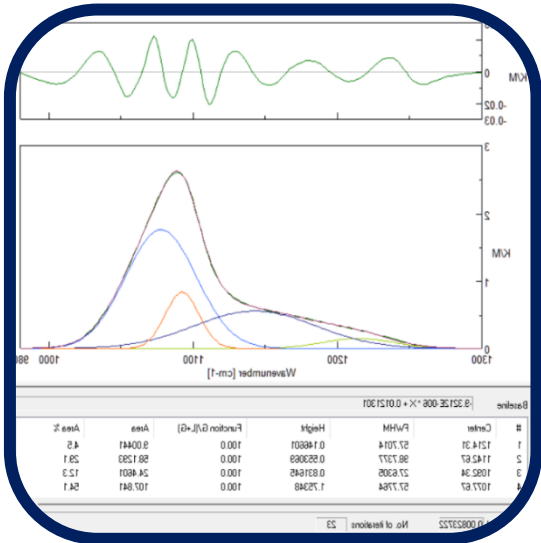
- [17] Nayak, A. K.; Das, B. Introduction to polymeric gels. In *Polymeric Gels Characterization, Properties and Biomedical Applications*; Pal, K., Ed.; Elsevier: Rourkela, India, **2018**; p. 3–27.
- [18] Park, S. J.; Im, S. H.; Kim, D.; Park, D. Y.; Jung, Y.; Han, H. seop; Kim, S. H.; Chung, J. J. *NPG Asia Mater.* **2023**, *15*.
- [19] Guo, X.; Gou, K.; Han, Y.; Pan, Q.; Wang, Y.; Zong, S.; Song, J.; Chen, X.; Li, H. *Mater. Des.* **2022**, *223*, p. 111157.
- [20] Len, A.; Paladini, G.; Románszki, L.; Putz, A.M.; Almásy, L.; László, K.; Bálint, S.; Krajnc, A.; Kriechbaum, M.; Kuncser, A.; Kalmár, J.; Dudás, Z. *Int. J. Mol. Sci.* **2021**, *22*, p. 9197.
- [21] Hatano, K.; Teraki, M.; Nakajima, D.; Yamatsu, T. *Environ. Sci. Pollut. Res.* **2021**, *28*, p. 37562–37569.
- [22] Li, M.; Wang, Y.; Cai, X.; Li, Y.; Li, H.; Yang, Y.; Li, Y. *Mater. Lett.* **2021**, *300*, p. 130177.
- [23] Souto, F. T.; Machado, V. G. *Carbohydr. Polym.* **2023**, *304*, p. 120480.
- [24] Vilela, R. R. C.; Zanoni, K. P. S.; de Oliveira, M.; de Vicente, F. S.; de Camargo, A. S. *S. J. Sol-Gel Sci. Technol.* **2022**, *102*, p. 236–248.
- [25] Julián-lópez, B.; Gonell, F.; Lima, P. P. *Laser Phys. Lett.* **2017**, *14*.
- [26] Contel, M.; Garrido, J.; Gimeno, M.C.; Jimenez, J.; Jones, P.G.; Laguna, A.; L, M. *Inorg. Chem. acta* **1997**, *254*, p. 157–161.
- [27] Contel, M.; Garrido, J.; Jones, P. G.; Jiménez, J.; Laguna, A.; Laguna, M. *J. Organomet. Chem.* **1997**, *543*, p. 71–75.
- [28] Bariáin, C.; Matías, I. R.; Romeo, I.; Garrido, J.; Laguna, M. *Appl. Phys. Lett.* **2000**, *77*, p. 2274–2276.
- [29] Contel, M.; Edwards, A. J.; Garrido, J.; Hursthouse, M. B.; Laguna, M.; Terroba, R. *J. Organomet. Chem.* **2000**, *607*, p. 129–136.
- [30] Luquin, A.; Bariáin, C.; Vergara, E.; Cerrada, E.; Garrido, J.; Matias, I. R.; Laguna, M. *Appl. Organomet. Chem.* **2005**, *19*, p. 1232–1238.
- [31] Casado-Terrones, S.; Elosúa-Aguado, C.; Bariáin, C.; Segura-Carretero, A.; Matías-Maestro, I. R.; Fernández-Gutiérrez, A.; Luquin, A.; Garrido, J.; Laguna, M. *Opt. Eng.* **2006**, *45*, p. 044401.
- [32] Estella, J.; Echeverría, J. C.; Laguna, M.; Garrido, J. J. *J. Non-Cryst. Solids* **2007**, *353*, p. 286–294.
- [33] Estella, J.; Echeverría, J. C.; Laguna, M.; Garrido, J. J. *Microporous Mesoporous Mater.* **2007**, *102*, p. 274–282.
- [34] Estella, J.; Echeverría, J. C.; Laguna, M.; Garrido, J. J. *J. Porous Mater.* **2008**, *15*, p. 705–713.

- [35] Musgo, J.; Echeverría, J. C.; Estella, J.; Laguna, M.; Garrido, J. J. *Microporous Mesoporous Mater.* **2009**, *118*, p. 280–287.
- [36] Estella, J.; De Vicente, P.; Echeverría, J. C.; Garrido, J. J. *Sens. Actuators, B* **2010**, *149*, p. 122–128.
- [37] Rios, X.; Moriones, P.; Echeverría, J. C.; Luquín, A.; Laguna, M.; Garrido, J. J. *Adsorption* **2011**, *17*, p. 583–593.
- [38] Moriones, P.; Ríos, X.; Echeverría, J. C.; Garrido, J. J.; Pires, J.; Pinto, M. *Colloids Surf., A* **2011**, *389*, p. 69–75.
- [39] Echeverría, J. C.; De Vicente, P.; Estella, J.; Garrido, J. J. *Talanta* **2012**, *99*, p. 433–440.
- [40] Rios, X.; Moriones, P.; Echeverría, J. C.; Luquin, A.; Laguna, M.; Garrido, J. J. *Mater. Chem. Phys.* **2013**, *141*, p. 166–174.
- [41] Echeverría, J. C.; Faustini, M.; Garrido, J. J. *Sens. Actuators, B* **2016**, *222*, p. 1166–1174.
- [42] Echeverría, J. C.; Calleja, I.; Moriones, P.; Garrido, J. J. *Beilstein J. Nanotechnol.* **2017**, *8*, p. 475–484.
- [43] Rostami, M.; Zhang, B.; Zhang, Y. *Spectrochim. Acta, Part A* **2023**, *292*, p. 122387.
- [44] Trupp, L.; Marchi, M. C.; Barja, B. C. *J. Sol-Gel Sci. Technol.* **2022**, *102*, p. 63–85.
- [45] Zhang, Q.; Song, Q.; Zhang, Z.; Zhao, C.; Ma, H. *Colloid Polym. Sci.* **2020**, *298*, p. 1587–1596.
- [46] Yang, X.; Wang, D. *ACS Appl. Energy Mater.* **2018**, *1*, p. 6657–6693.
- [47] Guo, S.; Ji, Y.; Li, Y.; Li, H.; An, P.; Zhang, J.; Yan, J.; Liu, S. (Frank); Ma, T. *Appl. Catal., B* **2023**, *330*, p. 122583.
- [48] El hamdaoui, J.; Lakaal, K.; Mazkad, D.; Beraich, M.; El Fatimy, A.; Courel, M.; Pérez, L. M.; Díaz, P.; Laroze, D.; Feddi, E. *Mater. Res. Bull.* **2023**, *164*, p. 112235.
- [49] Islam, M. R.; Islam, M. S.; Zamil, M. Y.; Ferdous, N.; Stampfl, C.; Park, J.; Hossain, M. K. *J. Phys. Chem. Solids* **2023**, *176*, p. 111263.
- [50] Sun, Q.; Li, Z.; Li, J.; Liu, N.; Zhang, M.; Le, T. *J. Alloys Compd.* **2023**, *955*, p. 170234.
- [51] Liane Ücker, C.; San Martins Rodrigues, F.; de Gouveia Cantoneiro, R.; Goetzke, V.; Ceretta Moreira, E.; Meneghetti Ferrer, M.; Wienke Raubach, C.; Cava, S. *J. Photochem. Photobiol., A* **2023**, *441*, p. 114694.
- [52] Villa, K.; Galán-Mascarós, J. R.; López, N.; Palomares, E. *Sustainable Energy Fuels* **2021**, *5*, p. 4560–4569.
- [53] Spasiano, D.; Marotta, R.; Malato, S.; Fernandez-Ibañez, P.; Di Somma, I. *Appl. Catal., B* **2015**, *170–171*, p. 90–123.
- [54] Gao, X.; Luo, B.; Hong, Y.; He, P.; Zhang, Z.; Wu, G. *Front. Chem. Sci. Eng.* **2023**, *17*, p. 772–783.

- [55] Pan, D.; Kong, L.; Zhang, H.; Zhang, Y.; Tang, Y. *ACS Appl. Mater. Interfaces* **2023**, *15*, p. 28125–28134.
- [56] Haghighi, S. K.; Kharat, A. N. *Inorg. Chem. Commun.* **2021**, *125*, p. 108413.
- [57] Li, M.; Shen, X.; Liu, M.; Lu, J. *Mol. Catal.* **2021**, *513*, p. 111779.
- [58] Wang, Y.; Wang, S.; Zhang, T.; Ye, J.; Wang, X.; Wang, D. *Trans. Tianjin Univ.* **2017**, *23*, p. 230–236.
- [59] Ratnasamy, P.; Srinivas, D.; Knözinger, H. Active Sites and Reactive Intermediates in Titanium Silicate Molecular Sieves. In *Advances in catalysis*; Ratnasamy, P., Srinivas, D., Knözinger, B., Eds.; Elsevier INC., **2004**; Vol. 48, p. 1–169.
- [60] Luan, H.; Xu, C.; Wu, Q.; Xiao, F.S. *Front. Chem.* **2022**, *10*, p. 1–12.
- [61] Yuan, W.; Yuan, P.; Liu, D.; Yu, W.; Laipan, M.; Deng, L.; Chen, F. *J. Colloid Interface Sci.* **2016**, *462*, p. 191–199.
- [62] Meng, F.; Ling, Y.; Li, Y.; Guo, M.; Wei, K.; Zhang, M.; Yang, C.; Shi, X.; Tang, B. *Chem. Eng. J.* **2023**, *473*, p. 145200.

CHAPTER 2

MATERIALS AND METHODS



CHAPTER 2

MATERIALS AND METHODS

This chapter gathers and describes all the synthesis procedures of the materials (CIRTEOS and Ln-AL xerogels, and TSR% silicalites), as well as the techniques used for their characterisation. The preparation of the functionalised sensing element of the optical fibre sensors and their experimental setup, the description of photocatalytic tests performed with the TSR% materials and all the calculation methods applied to obtain information about the samples, are also detailed in this chapter. Some methods or procedures are not collected in this chapter but are concisely explained in the corresponding experimental section of *Chapters 3 to 7*.

2.1 SYNTHESIS PROCEDURES

2.1.1 Synthesis of hybrid xerogels (CIRTEOS series)

Hybrid xerogels of *Chapters 3 to 5* were prepared by the sol-gel method through the hydrolysis and polycondensation of tetraethoxysilane (TEOS, purity > 99%, Sigma-Aldrich, St Luis, MO, USA) with one organotriethoxysilane (RTEOS): chloromethyltriethoxysilane (CIMTEOS, purity > 95%, Sigma-Aldrich, St Luis, MO, USA); 2-chlorethyltriethoxysilane (CIETEOS, purity > 95% Flurochem, Glossop, Derbyshire, UK); 3-chloropropyltriethoxysilane (CIPTEOS, purity > 95%, Sigma-Aldrich, San Luis, MO, USA); and (*p*-chlorophenyl)triethoxysilane (CIPhTEOS, purity > 97%, Sigma-Aldrich, St Luis, MO, USA).

The objective was the preparation of transparent meso-microporous xerogels in acid media (pH = 4.5). For this purpose, a procedure described in several previous studies of the Inorganic Chemistry Group at UPNA was performed [1–4], which uses a constant molar ratio of (TEOS + RTEOS):ethanol:water, 1:4.75:5.5 respectively. Four series of xerogels with different RTEOS mixed with TEOS in variable molar ratios were obtained. The synthesis procedure is schematized in Figure 2.1, and a concise description can be found below. In *Annexe A*, all the steps of the sol-gel method considering this synthesis conditions are detailed.

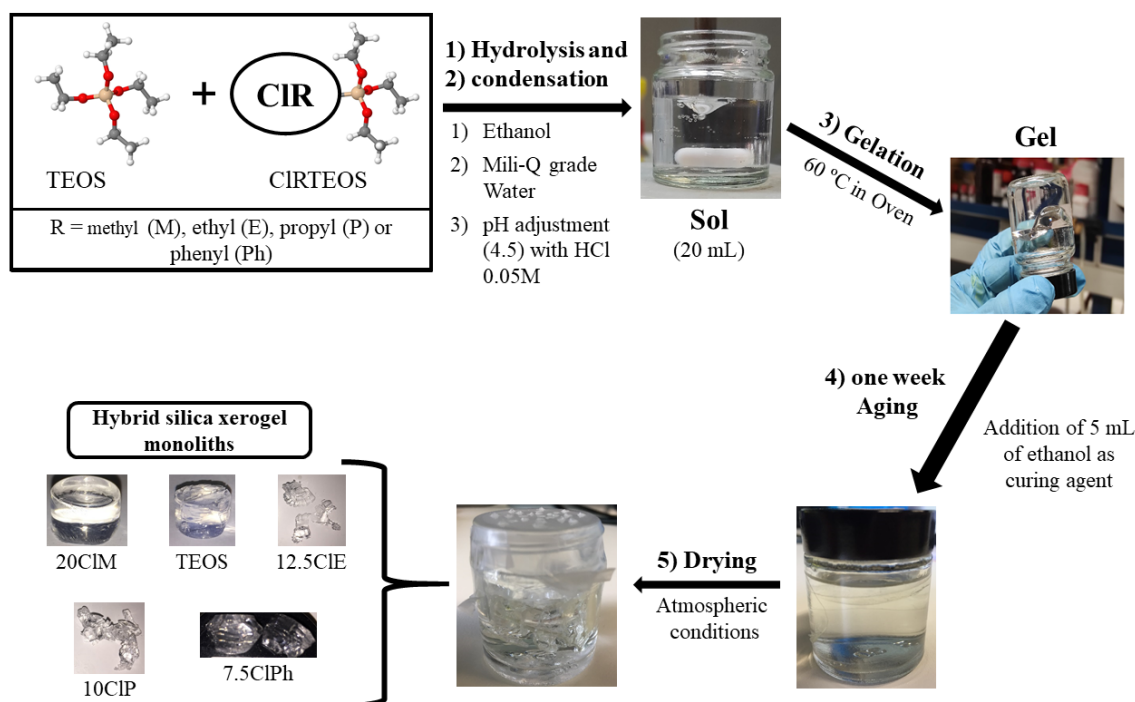


Figure 2.1. Scheme of the synthesis procedure used to prepare the chlorinated hybrid xerogels.

TEOS and RTEOS were mixed in 30 mL vessels (3.5 cm inner diameter, threaded plastic lid, Schrarlab, Barcelona, Spain). Absolute ethanol (EMSURE[®], Merck, Darmstadt, Germany) was then added, followed by the dropwise addition of Milli-Q grade water under magnetic stirring to facilitate miscibility; the amounts of reagent and solvent were adjusted to obtain 20 mL of alcogels. When the pH of the mixtures, which was measured with a pH meter (Metrohm) for ethanolic media, remained unchanged (after approximately 10 min), an automatic burette (Tritino mod. 702 SM, Metrohm, Herisau, Switzerland) was used to set the pH at 4.5 by gradual addition of 0.05 M HCl (37% w/w, Merck, Darmstadt, Germany). The mixtures were stirred for 10 min to ensure homogenization, and then the containers were closed with their plastic lid. Figure 2.2 shows the automatic burette and its coupled pH meter and magnetic stirrer.

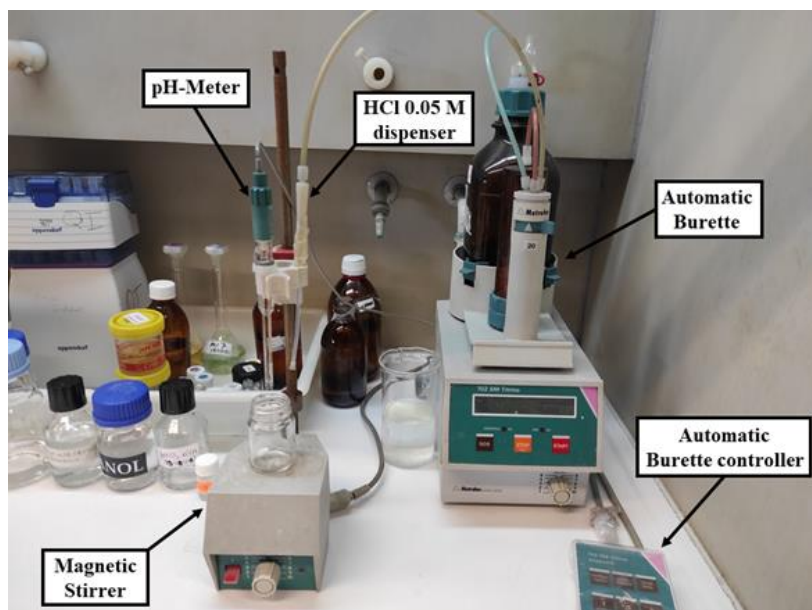


Figure 2.2. 702 SM Titrino Automatic Burette coupled to a magnetic stirrer and a Metrohm pH meter. The apparatus is located in the Science Department of the Public University of Navarre.

The closed vessels were placed in a thermostatised oven at 60 °C (model 2101502, J. P. Selecta S.A, Barcelona, Spain) until gelation (considered the time when the shape of the materials did not change when the vessel was tilted). To overcome possible miscibility problems, higher RTEOS molar percentage xerogels were placed in a reciprocating shaker (SO1-bibby Stuart, Stone, UK) located inside the oven. Subsequently, 5 mL of ethanol was added to cure the alcogels at room temperature for one week. Next, the vessels were opened and covered with PARAFILM[®], perforated with holes to facilitate solvent evaporation, and dried at room temperature under atmospheric pressure. The monolith was considered dried when no significant variation in their mass was observed. Some samples developed cracks and fractures during the drying process, attributable to stress generated by capillary forces within the pores [5]. Finally, the xerogels were further dried, at 90 °C in a heating plate (VacuoTemp, Selecta S. A., Barcelona, Spain) connected to a Vacuum pump (adixen, Pfeiffer Vacuum Pascal 2005SD), and then were grounded in an agate mortar. Figure 2.3 shows the used oven, the heating plate, and the vacuum pump.



Figure 2.3. J.P. Selecta S.A thermostatised oven (*left*), and Selecta S.A heating plate connected to an adixen Pfeiffer vacuum pump (*right*). The apparatuses are located in the Science Department of the Public University of Navarre.

To conclude, Table 2.1 shows all the homogeneous xerogels synthesized in the development of this PhD thesis investigation.

Table 2.1. List of all the homogeneous xerogels synthesized in this PhD thesis.

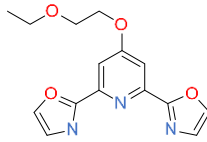
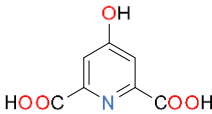
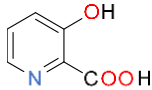
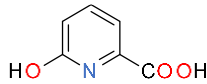
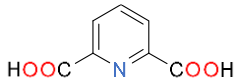
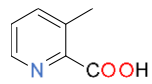
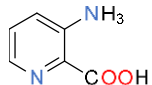
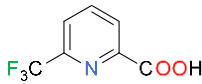
Hybrid xerogel Series	Used molar percentages of CIRTEOS (%)	Chapter
CIMTEOS	0, 1, 3.5, 5, 7.5, 10, 15, 20, 25, 30	3 and 4
CIETEOS	0, 1, 3.5, 5, 7.5, 10, 12.5	3 and 4
CIPTEOS	0, 1, 3.5, 5, 7.5, 10, 15	3 and 4
CIPhTEOS	0, 1, 3.5, 5, 7.5, 10, 15	5

In Table 2.1 and their corresponding chapters, the xerogels were named according to the molar percentage used (i.e., 15CIPh for the xerogel with a molar percentage of 15% of CIPhTEOS). The reference xerogel was synthesized with a 100% molar percentage of TEOS and was labelled as “TEOS” in *Chapters 3 and 4* and as 0CIPh in *Chapter 5*. The maximum molar percentages depended on the miscibility of each CIRTEOS, and the use of higher values than those of the table yielded heterogeneous xerogels or precipitates.

2.1.2 Synthesis of lanthanide-doped xerogels (Ln-AL series)

Luminescent pure TEOS xerogels, or labelled as Ln-AL in *Chapter 6*, were prepared using the reactants and following the procedure described in the previous section, but with slight modifications: (i) no organic precursors (RTEOS) were used, (ii) sol mixture pH was not adjusted by addition of HCl 0.05M, except for the references, and (iii) hexahydrated lanthanide nitrates, $\text{Eu}(\text{NO}_3)_3 \cdot 6\text{H}_2\text{O}$ (Eu purity > 99%, Alfa Aesar, Thermo Fisher Scientific, Ward Hill, Massachusetts, USA) or $\text{Tb}(\text{NO}_3)_3 \cdot 6\text{H}_2\text{O}$ (Tb purity > 99.9%, Strem Chemicals, INC, Newburyport, Massachusetts, USA) were added to the sol media alongside one antenna ligands (AL). All the selected 8 AL have a central pyridinic ring as a common feature (pyridyl groups are well-established chromophores for Ln-sensitisation [6]) are soluble in hydroalcoholic mixtures and provide a variety of chelating coordination modes, from N,N,N- or O,N,O-tridentate to N,O- or O,O-bidentate. AL assigned codes, names, purity, structural formula, and sources are illustrated in Table 2.2.

Table 2.2. List of all the utilized antenna ligands with their purities, formulas and commercial sources.

Assigned code	Name	Purity (%)	Formula		Commercial source
	Nomenclature		Chemical	Structural	
PB	Pybox-EG	-	$C_{15}H_{15}N_3O_4$		^a Non-commercial
	(2,2'-(4-(2-ethoxyethoxy)pyridine-2,6-diyl)bis(4,5-dihydrooxazole))				
CA	Chelidamic Acid	> 99	$C_7H_5NO_5$		^b Sigma-Aldrich
3OHPA	3-hydroxypicolinic acid	> 98	$C_6H_5NO_3$		^b Sigma-Aldrich
6OHPA	6-hydroxypicolinic acid	> 95	$C_6H_5NO_3$		^c Across Organics
DPA	Dipicolinic acid	> 99	$C_7H_5NO_4$		^b Sigma-Aldrich
MPA	3-methylpicolinic acid	> 97	$C_7H_7NO_2$		^b Sigma-Aldrich
APA	3-aminopicolinic acid	> 97	$C_6H_7N_2O_2$		^c Across Organics
FPA	6-trifluoromethylpicolinic acid	> 97	$C_7H_4NO_2F_3$		^b Sigma-Aldrich

^a—was synthesised following the procedure described in the literature [6]; ^b—Sigma-Aldrich (San Luis, MO, USA); ^c—Across Organics, Thermo Fisher Scientific (Ward Hill, Massachusetts, USA).

As can be seen in Table 2.2, all the AL were bought from their respective commercial providers, except for Pybox-EG (PB) which was synthesised following the recipe developed by De Bettencourt-Dias *et al.* (2012) [6]. Figure 2.4 illustrates the reaction steps performed to obtain the PB antenna ligand.

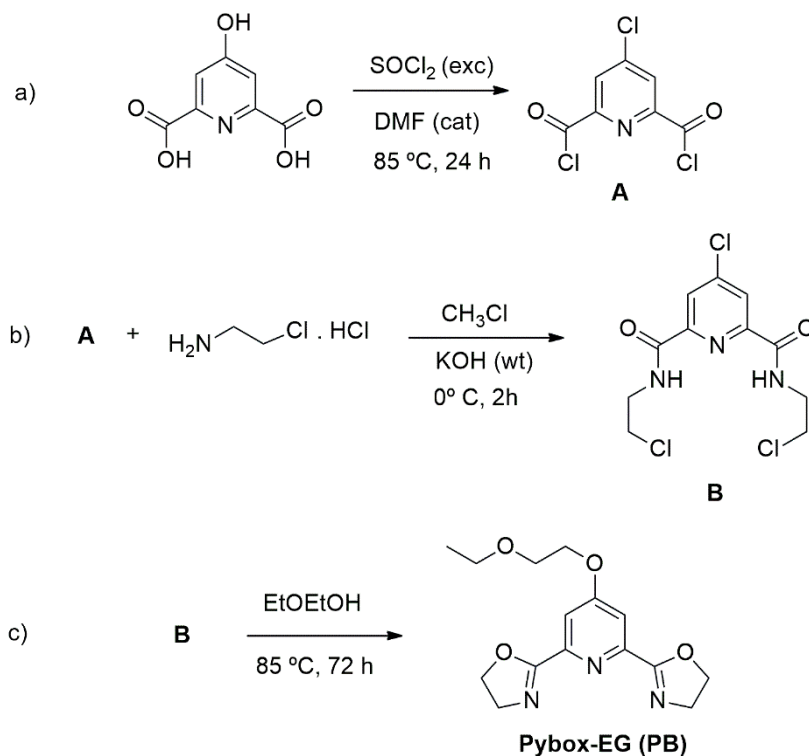


Figure 2.4. Reactions to obtain the PB antenna ligand: (a) chlorination of chelidamic acid, (b) substitution reaction of A with 2-chloroethylamine to yield B, and (c) cyclization of B to yield PB.

The first reaction step (Figure 2.4a) was the chlorination of CA (chelidamic acid, reference in Table 2.2). First, 2 g of CA and two droplets of DMF (dimethylsulfoxide, purity > 99%, Alfa Aesar GmbH & Co. KG, Karlsruhe, Germany) were added to a two-mouth round bottom flask, where they were refluxed in 8 mL of SOCl_2 (thionyl chloride, purity > 99%, Sigma-Aldrich, San Luis, MO, USA) during 24 h, using a bubbler, magnetic stirring and an oil bath at $85\text{ }^\circ\text{C}$. Then, the excess SOCl_2 was removed in a rotary evaporator to obtain 4-chloropyridine-2,6-dicarbonyl dichloride (A), which was used without further purification. In the second step (Figure 2.4b), A was dissolved in 50 mL of CHCl_3 (trichloromethane, purity $\geq 99.8\%$, Honeywell S.A., Levallois-Perret, France) and was immediately added dropwise to a vigorously shaken beaker containing 2.56 g of KOH (flakes, purity > 98%, Alfa-Aesar, GmbH & Co. KG, Karlsruhe, Germany) and 2.78 g of $\text{ClCH}_2\text{CH}_2\text{NH}_2 \cdot \text{HCl}$ (2-chloroethylamine hydrochloride, purity > 98%, Sigma-Aldrich, San Luis, MO, USA) dissolved in a minimum amount of water at $0\text{ }^\circ\text{C}$. The

resulting mixture was kept under magnetic stirring at the same temperature for a further 2 h. Next, 50 mL of CHCl_3 was added to the beaker, whose content was poured into a separatory funnel. The organic phase was washed with mili-Q water ($50 \text{ mL} \times 2$) and with $25 \text{ mL} \times 2$ of a saturated solution of NaHCO_3 , then dried over MgSO_4 , and the solvent was removed in a rotatory evaporator to obtain the solid 4-Chloro- N^2, N^6 -bis(2-chloroethyl) pyridine-2,6-dicarboxamide (**B**). In the last step of the reaction (Figure 2.4c), the obtained amount of **B** was dissolved in 55 mL of EtOEtOH (2-ethoxyethanol, ReagentPlus®, purity > 99%, Sigma-Aldrich, San Luis, MO, USA), and heated at $85 \text{ }^\circ\text{C}$ for three days. Then, the solvent was removed in a rotatory evaporator and the resulting product was refined by flash column chromatography to obtain the solid pybox-EG. Ln-AL xerogels were obtained as monoliths containing luminescent complexes formed by one of the possible 16 combinations of the two Ln^{III} (Eu^{III} or Tb^{III}) ions and one of the 8 ALs. The synthesis procedure is schematized in Figure 2.5 with some antenna ligands as an example.

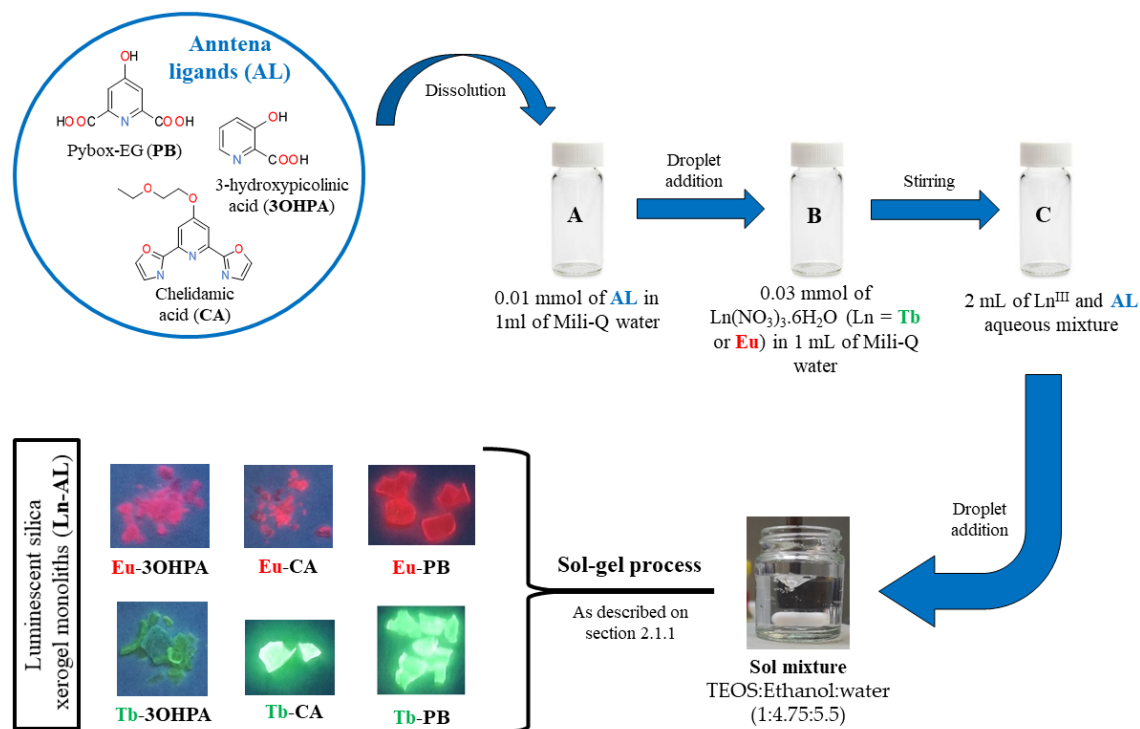


Figure 2.5. Scheme of the synthesis procedure used to prepare the Ln-AL monoliths.

As it can be observed in Figure 2.5, first, a 0.01 M aqueous AL solution (1 mL) was added dropwise to a 0.01 M aqueous solution (1 mL) of $\text{Ln}(\text{NO}_3)_3 \cdot 6\text{H}_2\text{O}$ ($\text{Ln} = \text{Tb}$ or Eu) and the resulting mixture was added to a vessel containing tetraethoxysilane (TEOS, 7.495 mL) and ethanol (9.210 mL) under stirring. Water (1.295 mL) was then added to a total volume of 20 mL containing the sol mixture (TEOS:ethanol:water molar ratio of 1:4.75:5.5). Then, the sols were placed in a thermostatised oven at 60 °C until gelation. The resulting gels were cured for one week with ethanol and finally allowed to dry at atmospheric conditions, obtaining the monolith. Pristine TEOS xerogels without any Ln or AL dopants were analogously synthesised at two different pH values (4.5 and 2.7) to obtain a set of reference materials because, during the synthesis of the Ln-AL xerogels, their sols pH value fluctuated with the AL used. Table 2.3 depicts all the synthesised Ln-AL materials along with the pH of their sols.

Table 2.3. List of all the synthesised Ln-AL monoliths with their respective pH synthesis media.

Antenna ligand (AL)	Monolith xerogel (Ln-AL)		pH
	Eu ^{III}	Tb ^{III}	
None	TEOS-4.5		4.5
None	TEOS-2.7		2.7
PB	Eu-PB	Tb-PB	4.5
CA	Eu-CA	Tb-CA	2.7
3OHPA	Eu-3OHPA	Tb-3OHPA	3.2
6OHPA	Eu-6OHPA	Tb-6OHPA	3.4
DPA	Eu-DPA	Tb-DPA	2.8
MPA	Eu-MPA	Tb-MPA	3.3
APA	Eu-APA	Tb-APA	3.4
FPA	Eu-FPA	Tb-FPA	3.8

2.1.3 Synthesis of modified Titanium silicalites (TSR% series)

The modified titanium silicalites (TSR%) of *Chapter 7*, were synthesised by the hydrothermal synthesis method (see *Annexe D.2*), in which tetraethoxysilane (TEOS, purity > 99%) and hybrid silica precursors (alkyltriethoxysilanes, RTEOS) were mixed with titanium (IV) tetrabutoxide (TBOT, purity > 97%) as silicon and titanium sources, respectively. Additionally, tetrapropylammonium hydroxide (TPAOH, 1M in water) and poly(vinylpolipirrolidone (PVP, ~ 110 µm particle size) were used in the synthesis as structure-directing agents. The three prepared series: TSM%, TSP% and TSPH%, were synthesised using an alkyltriethoxysilanes at different RTEOS:TEOS molar proportions: triethoxymethylsilane (MTEOS, purity > 99%), (n-propyl)triethoxysilane (PTEOS,

purity > 97%), or phenyltriethoxysilane (PhTEOS, purity > 98%), respectively. All reagents were purchased from Sigma-Aldrich (St. Louis, MO, USA). The synthesis method to prepare the titanium silicalites (TS) is based on that described by Ma *et al.* (2021) [7]. Figure 2.6 displays the scheme of the synthesis and the code list for the synthesised materials.

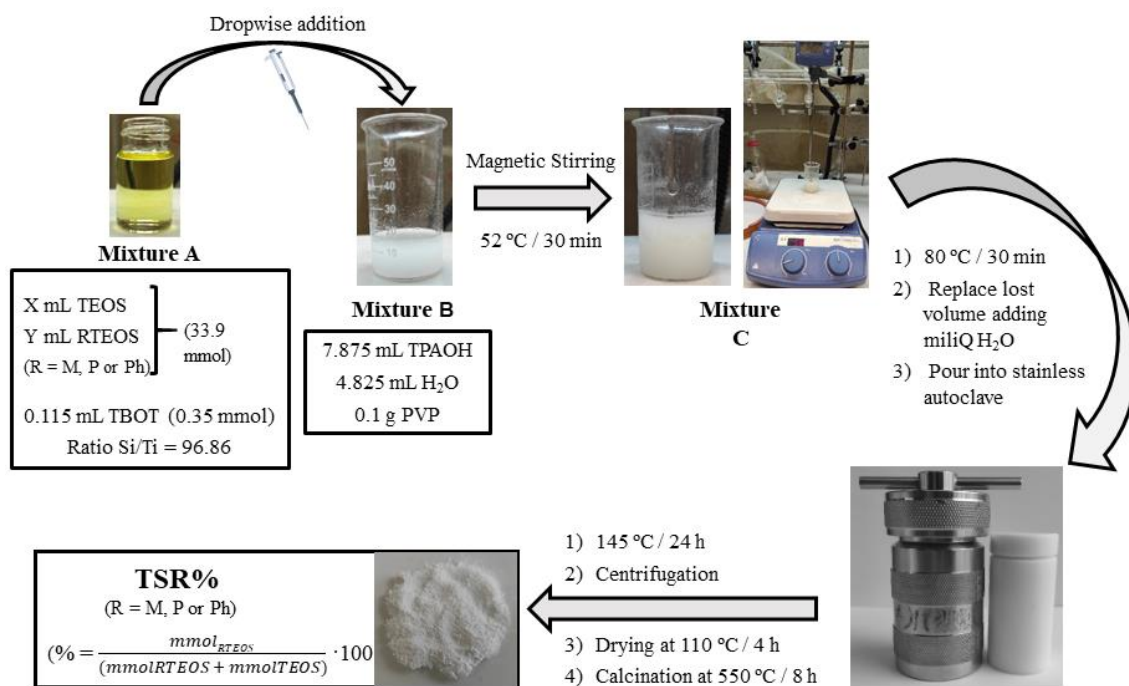


Figure 2.6. Synthesis procedure of the modified titanium silicalites.

Briefly, for the reference sample (TS0, TEOS only), 7.5 mL of TEOS (33.9 mmol) was mixed with 0.115 mL of TBOT (0.35 mmol) and poured dropwise into a 12.7 mL aqueous solution of TPAOH (0.62 mol L^{-1}) containing 0.1 g of PVP. The resulting mixture was stirred at 52 °C for 30 min on a thermostatic magnetic plate. After this time, in which the mixture was homogenized, the temperature was increased to 80 °C to eliminate the alcohols produced by the hydrolysis of the silicon and titanium precursors. Subsequently, water was continuously added to ensure that the total volume remained unchanged for about 30 min. The mixture was then poured into a Teflon-lined autoclave with a stainless-steel jacket (30 mL capacity, Huanyu high-tech CO., LTD, Wenzhou, Zhejiang, China) and kept at 145 °C for 24 h in a stove (model 2001243, J.P. Selecta S.A, Barcelona, Spain). After the hydrothermal process, the obtained white solid was dispersed in water and centrifuged at 5000 rpm for 10 min (Sorvall ST 8 centrifuge, Thermo Fisher Scientific, Waltham, Massachusetts, USA); the centrifuged solid was then dried at 60 °C overnight in a thermostatised oven (model 2101502, J.P. Selecta S.A, Barcelona, Spain).

Finally, the samples were calcined in an oven (model 12PR/300, Hobersal, Barcelona, Spain) at 550 °C for 8 h, obtaining white solids. The modified titanium silicalites (TSR%) were prepared using 5, 10, 20 and 30% molar percentages of an organotriethoxysilane (RTEOS, R = Methyl, M; Propyl, P; or Phenyl, Ph) with respect to TEOS, keeping the amount of TEOS + RTEOS always equals to 33.9 mmol. Table 2.4 displays the list of all TSR% synthesised materials and their nomenclature.

Table 2.4. Nomenclature and list of all the synthesised TSR% materials.

Titanium silicalite	Precursor	% RTEOS ^a
	(RTEOS)	
TSO ^b	None	0
TSM5	MTEOS	5
TSM10		10
TSM20		20
TSM30		30
TSP5	PTEOS	5
TSP10		10
TSP20		20
TSP30		30
TSPH5	PhTEOS	5
TSPH10		10
TSPH20		20
TSPH30		30

^a Molar percentage of RTEOS (TEOS+RTEOS = 100%)

^b Reference Titanium silicalite.

2.2 CHARACTERISATION TECHNIQUES

Several characterisation techniques have been employed to determine the chemical, textural, structural, and morphological characteristics of the synthesised materials. In fact, the xerogels used in *Chapters 3 to 5* require the use of various characterisation techniques due to their amorphous nature [8]. Before delving into each technique, Table 2.5 provides a guide to see which ones have been used in each of the studies contained in *Chapters 3 to 7*.

Table 2.5. Characterisation techniques employed in Chapters 3 to 7.

Characterization techniques	Chapters				
	3	4	5	6	7
²⁹ Si nuclear magnetic resonance (²⁹ Si NMR)	✓		✓		
Fourier-transform infrared spectroscopy (FTIR)	✓	✓	✓	✓	✓
Ultraviolet-visible absorption spectroscopy (UV-Vis)				✓	
Photoluminescence emission spectroscopy (PL)				✓	✓
Diffuse reflectance spectroscopy (UV-Vis DRS)					✓
Ultraviolet-Raman spectroscopy (UV-Raman)					✓
X-ray diffraction (XRD)	✓	✓	✓	✓	✓
Helium pycnometry	✓		✓		✓
N ₂ adsorption at -196 °C	✓		✓	✓	✓
CO ₂ adsorption at 0 °C	✓		✓	✓	✓
Water vapour adsorption (25, 30 and 35 °C)				✓	
Scanning electron microscopy (SEM)	✓		✓	✓	✓
Transmission electron microscopy (TEM)			✓		

All the samples were grinded and dried at 90 °C and under vacuum overnight (using the instruments of Figure 2.3 right) before characterization. However, helium pycnometry and the gas adsorption measurements of CIRTEOS and Ln-AL xerogels were performed with non-grounded samples.

2.2.1 ²⁹Si Nuclear Magnetic Resonance (²⁹Si NMR)

Solid-state nuclear magnetic resonance (NMR) of ²⁹Si gives semi-quantitative information about the different silicon species (atoms with different chemical environments) in the amorphous networks of silica CIPhTEOS xerogels. ²⁹Si NMR spectra are a useful tool to determine the condensation grade and the distribution of the organic moieties in hybrid xerogels. The ²⁹Si NMR measurements were performed in the

“Servicios Centrales de Apoyo a la Investigación (SCAI)” of the University of Jaén. Figure 2.7 shows the used solid NMR equipment.



Figure 2.7. Bruker AV-400 MHz solid-state nuclear magnetic resonance spectrometer (SCAI of the University of Jaén).

^{29}Si Cross Polarization Magic-Angle Spinning (CP MAS) solid-state NMR spectra were recorded on a Bruker AV-400 MHz spectrometer (Billerica, MA, USA) operating at 79.5 MHz. Chemical shifts were expressed in parts per million using TMS (tetramethylsilane) as the reference. The spectra were obtained ^1H decoupled, with a frequency of rotation of 5 kHz and 800 scans per spectrum. For the ^{29}Si NMR studies, the classical notation was employed: T notation for silicon atoms from the organic precursor (bonded to three oxygens capable of forming siloxane bridges), and Q notation for silicon atoms from TEOS (bonded to four oxygens that can yield siloxane bridges). To describe the number of Si–O–Si bridges in each silicon atom, T and Q notations were completed with a superscript i (T^i , $i = 0, 1, 2$ or 3 ; Q^i , $i = 0, 1, 2, 3$ or 4) [9]. The spectra were analysed using the MestReNova software to determine the distribution of Q and T species of each hybrid xerogel. The spectra processing and calculations are detailed in *Chapter 2.5.1*.

2.2.2 Fourier-Transform Infrared spectroscopy (FTIR)

Fourier-transform infrared spectroscopy was used to identify chemical substances and functional groups in the samples by recording their absorption, emission, or reflection of incident infrared radiation. FTIR spectra were acquired using a Jasco spectrometer (mod. 4700, Japan) with a sample holder (Specac, Kent, UK) to measure the absorbance/transmittance of solid samples, and an attenuated-total reflectance (ATR) unit

(ATR Pro one, Jasco, Japan) to measure the reflected infrared radiation of liquid samples. Solid samples were grinded with KBr (spectroscopy grade, sigma-Aldrich, St. Louis, MO, USA) in an agate mortar, and then the pulverized samples were deposited into a tablet press mould (International crystal laboratories, Garfield, New Jersey, USA) that was compressed with a hydraulic press (model 15.011, Specac, Kent, UK) to obtain tablets for the sample holder. Figure 2.8 shows the FTIR spectrometer and all the other equipment used to prepare and measure the samples.

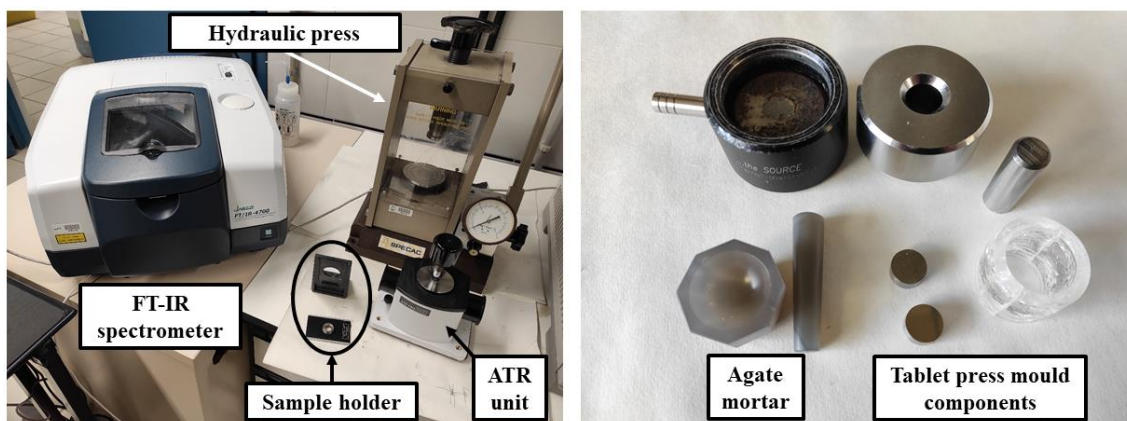


Figure 2.8. Equipment used to obtain the FTIR spectra: (a) Jasco FTIR spectrometer, sample holder, ATR unit and hydraulic press; and (b) agate mortar and components of the tablet press mould. The instrument and components are located in the Science Department of the Public University of Navarre.

Two spectra were obtained for each sample: (i) In the range of $4000\text{--}2200\text{ cm}^{-1}$ using 2 mg of the sample to obtain information on the --OH groups and C--H bonds, and (ii) in the range of $2200\text{--}400\text{ cm}^{-1}$ using 0.6 mg of the sample to avoid saturation of the Si--O--Si asymmetric stretching signal [10]. The samples were dispersed in KBr to create 200 mg tablets, which were dried overnight in an oven at $100\text{ }^{\circ}\text{C}$ under a vacuum (Figure 2.3 right) to remove adsorbed water before the spectra acquisition. Additionally, in the research of *Chapter 4*, a comparison between functional groups of the alkoxy silane precursors in the pure reactant versus xerogel was carried out by using attenuated-total reflectance (ATR) to record spectra directly from droplets of the precursors. The spectra of all the samples, tablets and pure reactant in ATR, were recorded using 25 scans and a resolution of 4 cm^{-1} .

The deconvolution of CIRTEOS infrared spectra using the software of the Jasco spectrometer (SpectraManager) is explained step by step in *Chapter 2.5.2*.

2.2.3 UV-Vis spectroscopy: Absorption, Photoluminescence emission (PL), Diffuse Reflectance (DR) and UV-Raman

UV-Vis spectroscopy is used to detect chromophore substances, i.e. molecules and ions that absorb radiation in the ultraviolet or visible range to promote their electrons to higher energy levels; these electronic mechanisms are detailed in *Annexe C*. Spectrofluorometers measure the absorption/excitation and the photoluminescence emission (PL) of substances; whereas, UV-Vis diffusive reflectance (DR) spectrometers measure the reflected light, both the refracted and the diffusely back-scattered, on the smooth surface of previously pulverized materials. The UV-Vis DR spectra can be used to determine the bandgap of semiconductor materials, therefore, is a standard technique for the characterization of photocatalysts as the TSR% candidate materials. UV-Raman spectroscopy measures the Raman scattering (inelastic dispersion of light) when a sample is irradiated with a monochromatic ray of ultraviolet light, and it is a powerful and standard technique for the characterization of zeolite catalysts [11].

UV-Vis excitation and PL spectra of the Ln-AL xerogels were recorded using a Horiba Fluorolog spectrofluorometer (Horiba, Kyoto, Japan) at the “Servicio General de Apoyo a la Investigación (SAI)” of the University of Zaragoza (Figure 2.9 depicts an image of the model). The spectra were recorded in the range of 300–700 and 250–600 nm for the materials synthesized with Eu^{III} and Tb^{III} , respectively. The operation parameters were: 0.1 s integration time; 1 nm increment; 1 nm of “Side Entrance” or 2 nm of “Exit Slit” for the excitation and emission spectra, respectively.

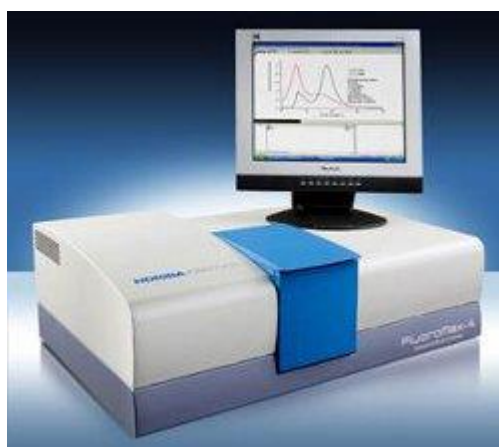


Figure 2.9. Horiba Fluorolog spectrofluorometer. Picture downloaded from the webpage of the SAI of the University of Zaragoza.

All the UV-Vis measurements of TSR% materials were performed at the Laboratory of Separation and Reaction Engineering – Laboratory of Catalysis and Materials (LSR-LCM) of the Faculty of Engineering of the University of Porto (FEUP). UV-Vis DRS were recorded using a Jasco UV-Vis spectrometer (mod V-560, Rev. 1.00), and BaSO₄ was used as a reference material before the measurements (image of the model on the left of Figure 2.10). The absorbance was registered at 100 nm min⁻¹ in the spectral range of 210–800 nm and was transformed into Kubelka-Munk units to estimate the optical bandgap of the materials using the Tauc-plot, calculations are detailed in *Chapter 2.5.3*. Photoluminescence spectra (PL) of these materials were acquired using a Jasco spectrofluorometer (mod FP-8300) equipped with a 150 W Xenon lamp (the right of Figure 2.10 depicts an image of this model). The emission of the samples was registered between 275–500 nm when using 260 nm as excitation (λ_{exc}). The emission and excitation bandwidth were set at 2.5 nm.



Figure 2.10. Spectrometers used at the Faculty of Engineering of the University of Porto: (**left**) Jasco UV-Vis spectrometer mod V-560, image subtracted from the manual of the equipment available online; and (**right**) Jasco spectrofluorometer mod FP-8300, image downloaded from the Jasco.co.uk webpage.

The UV-Raman spectra of the TSR% materials were acquired in a Raman Jasco spectrometer (mod NRS-5100) at the “Servicios Centrales de Apoyo a la Investigación (SCAI)” of the University of Málaga (equipment shown in Figure 2.11). The spectra were registered using an excitation wavelength of 325 nm, and the power of the exciting source ranged from 0.7 to 1.4 mW. The spectral resolution of the measurements was 0.4 cm⁻¹, the acquisition time was 50 s, and 10 scans were acquired per spectra.

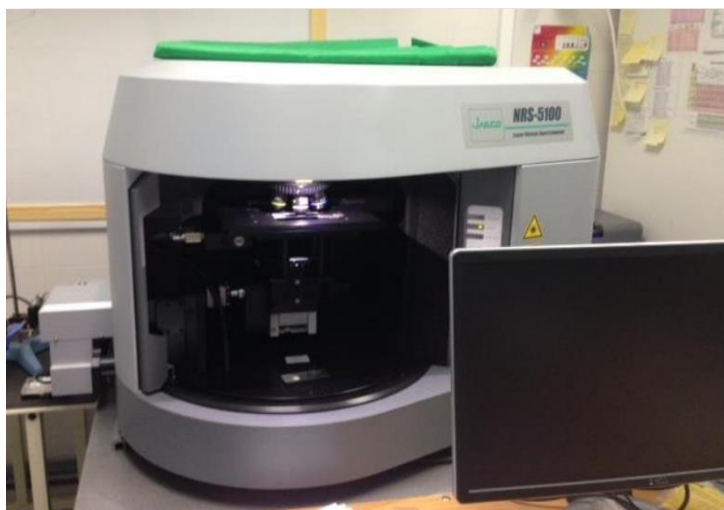


Figure 2.11. NRS-5100 Raman Jasco spectrometer. Image of the equipment located in the SCAI of the University of Málaga.

2.2.4 X-ray Diffraction (XRD)

X-ray diffraction is a technique used to determine the crystalline structure of the different phases that constitute a solid sample. In diffraction patterns, each sharp peak corresponds with a lattice plane of the sample structure (as in the TSR% samples of *Chapter 7*); whereas amorphous samples, such as the silica xerogels of *Chapters 3 to 6* present broad diffraction peaks. Nevertheless, this technique allows the estimation of the crystallinity grade xerogels, since sharp peaks can be observed in the diffraction patterns of some hybrid xerogels.

X-ray diffraction patterns of CIRTEOS xerogels were obtained at the “Servicios Centrales de Apoyo a la Investigación (SCAI)” of the University of Jaén, using a PANalytical Empyrean XRD instrument (Empyrean, Almelo, The Netherlands) with a copper rotating anode and a graphite monochromator (at 45 kV and 40 mA) to select the $\text{CuK}\alpha_{1/2}$ wavelength at 0.154 nm. Measurements were performed in a stepped scan mode (steps of 0.013°), in the range of $2 \leq 2\theta \leq 50^\circ$ at a rate of 0.5 steps s^{-1} [12]. The diffraction patterns of Ln-AL xerogels were acquired by applying the same parameters but using the Bruker D8-Advance powder XRD instrument (Bruker, USA) at the “Unidad Científico Técnica de Apoyo a la Investigación (UCTAI)” of the Public University of Navarre (UPNA). Figure 2.12 depicts the X-ray diffractometers used to analyse the samples.



Figure 2.12. X-ray diffractometers: (**left**) PANalytical Empyrean XRD in the SCAI of the University of Jaén, and (**right**) Bruker D8-Advance powder XRD instrument in the UCTAI of the Public University of Navarre.

The Bruker D8-Advance powder XRD instrument (Bruker, USA) was also used to acquire the diffraction patterns of the TSR% materials. Measurements were performed in a stepped scan mode (steps of 0.013°), in the range of $5 \leq 2\theta \leq 35^\circ$ at a rate of 0.5 steps s^{-1} .

2.2.5 Helium Pycnometry

Helium pycnometry allows the determination of the real or skeletal density of a material, i.e. the volume that occupies the mass of a solid material without considering the volume of open pores. The measurement mechanism is based on the volume-pressure equilibrium that occurs when the inert helium gas penetrates all pores and empty spaces of a sample; thus, the required volume of He depends on the sample composition and compaction. Figure 2.13 shows the helium pycnometer used to measure and calibrate the samples and the cells.



Figure 2.13. (left) AccuPyc 1330 Helium pycnometer, and (right) multivolume kit and calibration standards for skeletal density measurements. The instrument and components are located in the Science Department of the Public University of Navarre.

The skeletal density of CIRTEOS xerogels and TSR% materials was measured using a helium pycnometer (AccuPyc 1330, Micromeritics, Norcross, GA, USA) by performing a routine instrument calibration before analysis (20 purges and 10 measurements) using the calibration standards (a 12 cm³ cell and two 6.37 cm³ metal spheres). Then, a precision calibration (20 purges and 20 measurements) was performed using the 1 cm³ measurement cell and its volume calibration sphere (0.72 cm³). Once the instrument was calibrated, the sample was weighed into the 1 cm³ cell, which was filled as full as possible to reduce measurement inaccuracies caused by dead volumes. Each sample was analysed using 10 purges and 5 measurements, whose standard deviation was checked to discard false readings produced by incomplete degasifications or leaks.

2.2.6 Gas adsorption (N₂ at –196 °C, CO₂ at 0 °C, and H₂O(v) at 25, 30 and 35 °C)

Gas adsorption analysis was used to determine the porous texture of the materials. Two gases were employed for the measurements of all samples, N₂ at –196 °C and CO₂ at 0 °C, since their adsorption-desorption isotherms provide different but complementary information; N₂ is used to measure wide micropores and narrow mesopores, while CO₂ can reach the narrowest micropores or ultramicropores. Additionally, in Chapter 6, water vapour [H₂O(v)] adsorption-desorption isotherms of a Ln-AL xerogel were acquired at three different temperatures (25, 30, and 35 °C). All the isotherms were determined with a volumetric adsorption system (ASAP2020, Micromeritics, Norcross, GA, USA), shown in Figure 2.14.

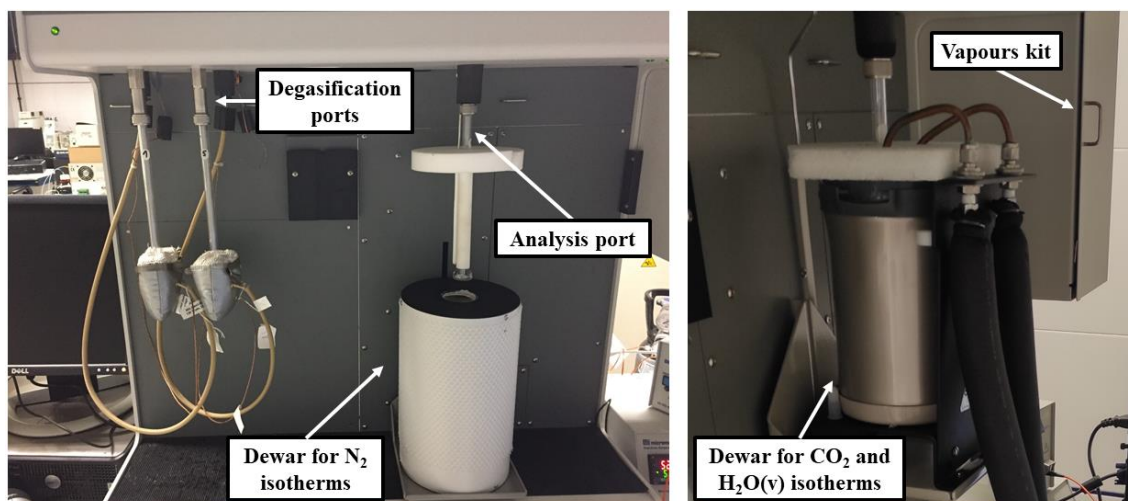


Figure 2.14. (left) ASAP2020 gas adsorption equipment, setups for measuring N_2 isotherms, and (right) CO_2 and $H_2O(v)$ isotherms.

For the acquisition of the isotherms, 150 mg of each sample were precisely weighted and placed into straight-walled Pyrex glass tubes. There, the xerogels and the TSR% were degassed for 3–6 hours at 150 °C and 200 °C respectively, to achieve a residual vacuum of less than 0.66 Pa. Once degassed, the tubes were connected to the analysis port where after a series of preliminary tests (leak test, calculation of free space, among others), were supplied analyte volumes corresponding to each assigned partial pressure (p/p°) until the equilibrium between adsorbed gas (n_a) and free gas was reached. When equilibrium was reached at $p/p^\circ \sim 0.99$, the instrument started to apply vacuum to register the equilibria at decreasing partial pressure values. The recording of n_a at increasing p/p° values is denominated the adsorption curve, whereas the curve obtained with decreasing p/p° values is the desorption curve, and together both curves constitute the adsorption-desorption isotherms. The time needed for the analysis ranged from 14 to 55 h for N_2 adsorption, from 2.5 to 9 h for CO_2 adsorption, and 45 to 60 h for $H_2O(v)$ adsorption.

For the N_2 isotherms, the tubes were covered with a Teflon isothermal jacket and immersed in a dewar with liquid nitrogen; whereas, for CO_2 analysis a metal isothermal jacket and a dewar connected to a thermostatised recirculation bath (PolyScience, Niles, IL, USA) were used, using 50% ethylene glycol/water mix as refrigerant. $H_2O(v)$ isotherms were obtained using the same setup as the one used for CO_2 , and the water vapour was provided by the ASAP2020 vapour kit equipment; Mili-Q water was completely degassed using the equipment's vacuum pumps before being used as an analyte and was replaced weekly. The values of absolute pressure (p°) for N_2 isotherms

were calculated at each isotherm point by the saturation pressure tube, however, for CO₂ and H₂O_(v) analysis the value of p^o was calculated considering the temperature, which was kept constant (p^o is 3485.3142 kPa for CO₂ at 0 °C; for H₂O vapour at 25, 30 and 35 °C is 3.171, 4.248 and 5.63 kPa respectively).

The shape of N₂ isotherms was interpreted and classified according to the IUPAC classification [13]. The recorded adsorption-desorption isotherms data of the three analytes were analysed with the ASAP2020 software (Microactive, version 4.06), adjusting the parameters as appropriate for each of the calculation models that are explained in *Chapter 2.5.3*.

2.2.7 Scanning Electron Microscopy (SEM)

SEM provides images that allow the observation of the morphology and surface characteristics of materials. In fact, high-resolution images, acquired by field-emission scattering electron microscopy (FE-SEM), are used to determine the size of particles, and even quantify the size of macro and mesopores in porous materials. Additionally, SEM instruments usually have installed energy-dispersive X-ray (EDX) detectors, which are used to reveal the atomic distribution of elements of interest on the surface of materials. Figure 2.15 shows the two microscopes used, a FE-SEM (“Servicios Centrales de Apoyo a la Investigación (SCAI)” of the University of Jaén) and a SEM (“Unidad Científico Técnica de Apoyo a la Investigación (UCTAI)” of the Public University of Navarre).



Figure 2.15. Scanning electron microscopes: (left) FE-SEM Carl Zeiss microscope located in the SCAI of the University of Jaén; and (right) SEM Zeiss EVO microscope at the UCTAI of the Public University of Navarre.

High-resolution micrographs of CIRTEOS xerogels and TSR% materials were obtained using a FE-SEM microscope (Carl Zeiss SMT, Oberkochen, Germany) with detectors for secondary and retro-dispersed electrons (SE InLens and EsB InLens, respectively), which operates at 2 kV. The instrument was equipped with an Energy Dispersive X-ray (EDX) detector (Oxford Inca Energy 350X-MAX 50, Oxford Instruments, Abingdon, UK) with a linear resolution of 127 eV, which allowed the observation of the atomic distribution of carbon, silicon, oxygen, chlorine and titanium on the materials. CIRTEOS xerogels were coated with gold due to their high static charge, however, TSR% do not require coatings since they are semiconductors. The micrographs were obtained with an image magnification of 37280.

Micrographs of Ln-AL materials were obtained with a SEM microscope (Zeiss EVO 15, Zeiss, Oberkochen, Germany). The distribution of the lanthanides within the xerogel matrices was studied with a Zeiss SMART EDX detector at 5 kV.

2.2.8 High-Resolution Transmission Electron Microscopy (HR-TEM)

Transmission electron microscopes form pictures from the electrons that have been transmitted through a sample. It is used to observe the inner structure and aggregates of the primordial particles that comprise a material.

HR-TEM images of CIPhTEOS xerogels were obtained at 200 kV with a Jeol-2000 FXII microscope (Jeol Ltd., Tokyo, Japan) with a 0.28 nm point-to-point spatial resolution. Since the beam of electrons hardly penetrates the bulk materials, the CIPhTEOS powders were suspended in isopropanol and deposited on graphite grids to decrease their static charge. The instrument was equipped with an EDX INCA 200 spectrometer (Oxford Instruments, Abingdon, UK), which allowed the observation of the atomic distribution of carbon, silicon, and chlorine on the CIPhTEOS xerogels of *Chapter 5*. These measurements were performed at the “Servicios Científico-Técnicos (SCT)” at the University of Oviedo (equipment depicted in Figure 2.16).

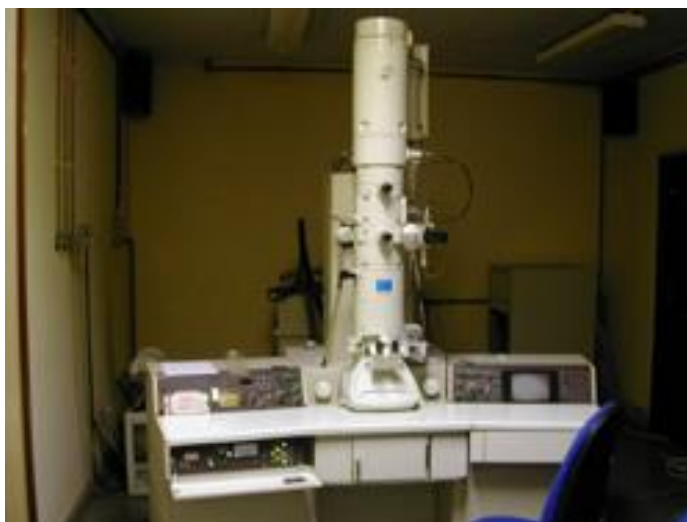


Figure 2.16. Jeol-2000 FXII high-resolution transmission electron microscope located in the SCT of the University of Oviedo.

2.3 OPTICAL FIBRE SENSORS COATED WITH Ln-AL FILMS

As indicated in *Chapter 6*, optical fibre sensors were prepared using gels containing a combination of lanthanide trivalent ion ($\text{Ln}^{\text{III}} = \text{Tb}^{\text{III}}$ or Eu^{III}) and an antenna ligand. The Ln-AL monoliths, whose synthesis was described in *Chapter 2.1.2*, were characterised to select the most-suited materials to build the sensors in terms of porous texture and luminescence. As a result, gels containing the pybox-EG (PB) antenna ligand, were selected. A total of three sensors were prepared: one sensor coated with a TEOS gel synthesised at pH 4.5 (OFSTEOS-4.5), as a reference, and the two sensors coated with the Ln-PB gels (OFSTb-PB and OFSEu-PB). These sensors were used to measure the water vapour concentrations in a climatic chamber to unravel the adsorption mechanism of water on silica xerogel coatings. This objective was achieved through the correlation between the volume of adsorbed vapour and the decrease in the fluorescence emission intensity.

2.3.1 Optical Fibre Sensor (OFS) construction

Ln-AL thin films were deposited onto the tips of 1000 μm core plastic-clad silica fibres (10000UMT with numerical aperture of 0.39, purchased from Thorlabs Inc.) with a cladding thickness of $35 \pm 15 \mu\text{m}$ and a High -OH doping to ensure UV transmission, the fibres can be observed in Figure B.1 of *Annexe B*. To couple the highest possible luminescence emission, the fibre ends were tapered into a conical geometry (scanning electron micrograph in Figure 2.17) that has been demonstrated optimal for

luminescence-based sensors [14]. For the tapering process, the tip of a fibre pigtail was first cut and polished to obtain a smooth, perpendicular surface, and then, the fibre was placed in a dip-coater robot (ND DC 150 m by Nadetech Innovations) and its planar end was subjected to 40 consecutive immersion-withdrawal cycles in HF (Hydrofluoric acid, 48% w/w, Sigma-Aldrich) at constant speed rates of 100 and 1 mm min⁻¹ (Figure 2.17). Finally, the resulting tapered fibre end was cleaned with ethanol and water [15].

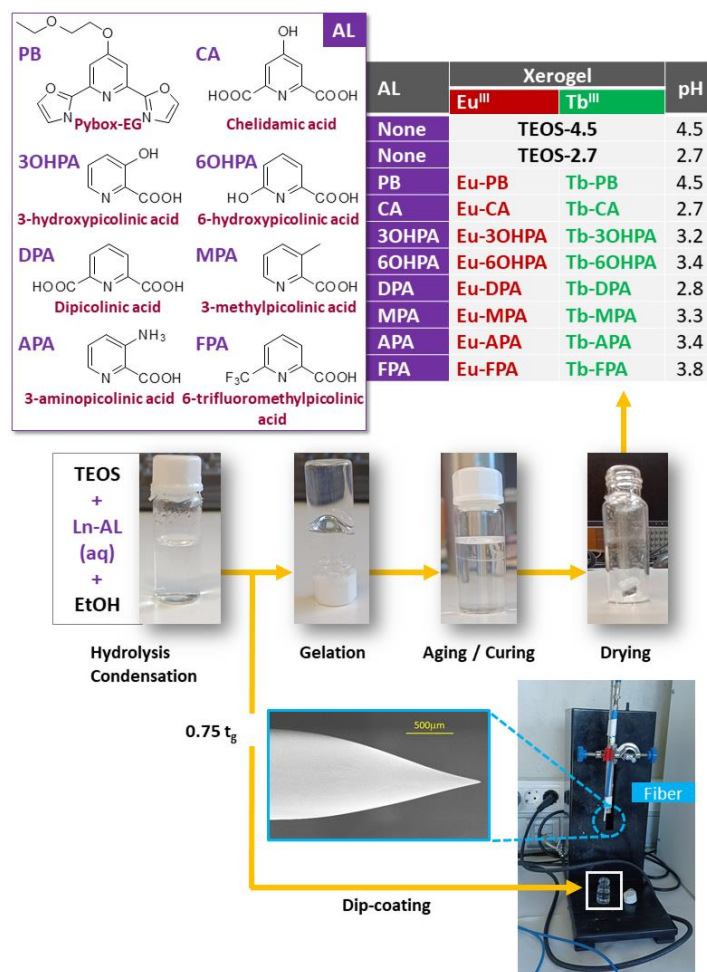


Figure 2.17. Scheme of the chelating AL molecules, synthesis of Ln-AL materials, and fibre coating set-up.

To deposit Ln-AL films by dip-coating, the tapered fibres were immersed for 10 s into sol-gel mixtures at 75% of the gelation time to ensure optimal rheological properties [16,17]. The fibres were then pulled out at a constant speed of 150 mm min⁻¹ and the emission spectra were registered to confirm film deposition (the photonic experimental setup is described in *Chapter 2.3.3*). This sequence was repeated until maximising the intensity of the luminescent signal, which was in all cases achieved after the third sequence repetition (no significant increase of the most intense luminescent maxima was observed upon the third immersion). The resulting sensor was stored for 2 days under a

controlled atmosphere (25 °C, 40% humidity) for the gelation process to complete. The thickness of the resulting layer is 109.2 ± 13.4 nm, as determined by ellipsometry (Uvisel2, Horiba Scientific) on a film deposited onto a silicon wafer following the same procedure used to construct the sensor.

2.3.2 Sensing mechanism of OFS

The sensing mechanism is based on the change in the luminescent intensity emission when water vapour is adsorbed on the silica xerogel film covering the tip of the optical fibre. The water molecules diffuse through the coating and interact with the luminescent species entrapped in the silica matrix. The water adsorption-desorption process reversibly quenches the luminescent emission, thus, working as an on-and-off transduction mechanism for the sensor [18]. As lanthanides have several emission peaks, the one with the highest signal-to-noise ratio was used for the characterisation (545 nm for Tb^{III} and 615 nm for Eu^{III}, see *Chapter 6.3.1*).

The intensity of the luminescent emission was affected by photobleaching, the effect of which was mathematically removed from the sensor response as it led to exponential decay. The sensor response was characterised by referencing the variation of intensity of the selected luminescence emission peak for each RH value ($\Delta I = I_{RH} - I_{ref}$) to I_{ref} , which is the intensity corresponding to the lowest RH value (20%). The reference intensity I_{ref} showed the highest level among all intensities registered, therefore the sign of the normalised intensity variations ($\Delta I/I_{ref}$) was reverted for the resulting values to be always positive, which eases its comparison with humidity dynamic changes (see Equation 2.1). This approach matches the sensor behaviour better than other models [19] and has already been successfully proposed by other authors [20]. Finally, the resulting $-\Delta I/I_{ref}$ values were represented against the water vapour molar concentration (C_{H_2O}) instead of time to correlate the sensor calibration with the water vapour isotherms. The water vapour molar concentration values (mM) were calculated using Equation 2.2 to obtain the absolute humidity (W) and Equation 2.3.

$$\frac{-\Delta I}{I_{ref}} = -\frac{I_{RH} - I_{ref}}{I_{ref}} \quad (2.1)$$

$$W \left(\frac{kg \text{ vapour}}{kg \text{ dry air}} \right) = \frac{\varphi \times RH \times P_w}{101325 - (RH \times P_w)} \quad (2.2)$$

$$C \left(\frac{\text{kmol}}{\text{m}^3} \right) = \frac{W \times V_{\text{dry air}}}{MW_{H_2O} \times V_{c.c}} \quad (2.3)$$

where W is the absolute humidity, ϕ is a factor equal to 0.622 [21], RH is the relative humidity, P_w is the water vapour pressure at a given temperature, C is the water vapour molar concentration, $V_{\text{dry air}}$ is de dry air volume, MW_{H_2O} is the molecular weight of water, and $V_{c.c}$ is the climatic chamber volume [17].

2.3.3 Photonic experimental set-up for OFS

A reflection setup (Figure 2.18) based on a 600 μm bifurcated fibre (High OH Fiber bundle, BFY1000HS02, from ThorLabs Inc.) was used for characterising both the sensor construction and its response. The diameter of the bifurcated fibre ensures the maximum signal coupling [22]. The optical fibre pigtail was connected to the common branch of the bifurcated fibre (Figure 2.18. Point 3) with a SMA-SMA connector and the optical source (a LED centred at the excitation wavelength of the material, purchased from Pyroistech) and an LSL Maya spectrometer (obtained from Ocean Insight) to the other two branches, respectively.

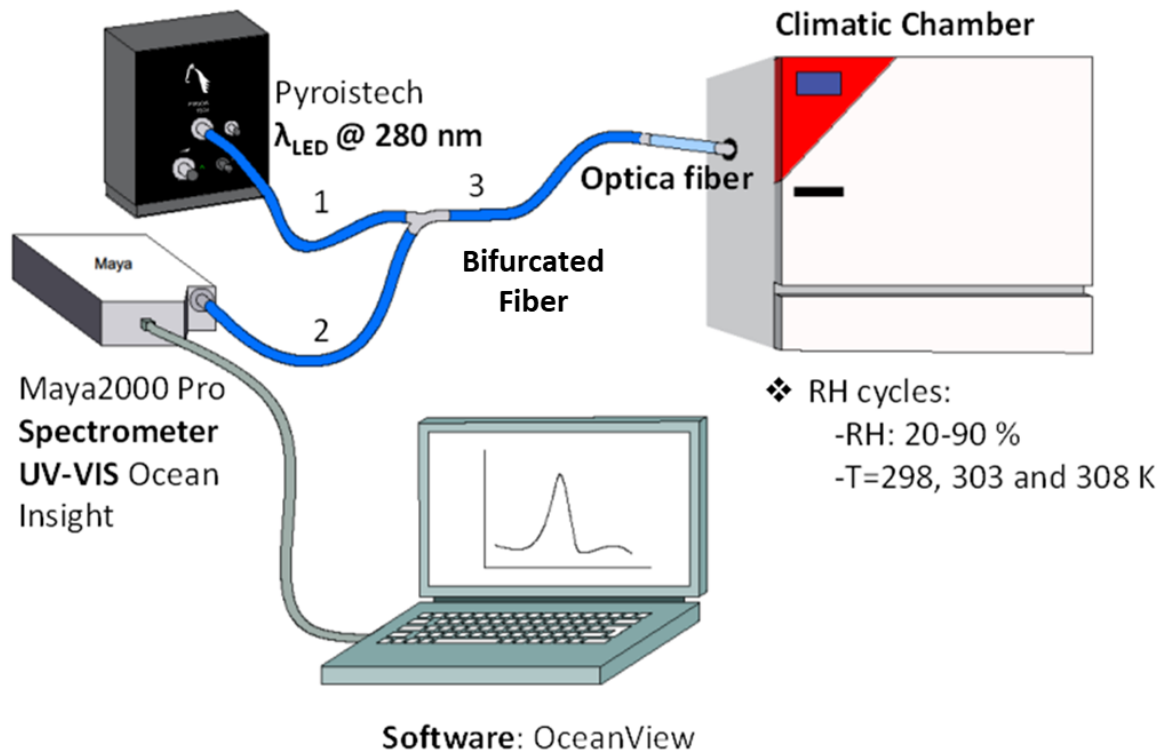


Figure 2.18. Experimental set-up to register the sensor response.

To analyse the response towards humidity and temperature, the sensor was placed in a climatic chamber (KMF-115 by Binder) and evaluated employing relative humidity cycles ranging from 20 to 90% at three different temperatures (25, 30 and 35 °C). Data were recorded using the Ocean View 2.0 software (Ocean Insight) installed on a PC using an integration time of 500 ms. The Limits of Detection (LoD) of the OFSTb-PB sensor were calculated using Equation 2.4 [23].

$$LoD = \frac{k(signal) \times std_A}{B} \quad (2.4)$$

where $k(signal)$ is a numerical value that depends on the level of reliability chosen (in our case, $k(signal) = 3$, corresponding to a reliability level of 99.86 %), B is the slope of the calibration curve in the linear region, and std_A is the standard deviation of the intercept of the linear fitting equation (see Table 6.3).

2.4 PHOTOCATALYTIC TESTS OF MODIFIED TITANIUM SILICALITES

All the photodegradation experiments of venlafaxine (venlafaxine hydrochloride, purity > 99%, Sigma-Aldrich, St. Louis, MO, USA) of *Chapter 7* were performed in ultrapure water (18.2 MΩ cm), with 50 mL of contaminant solution (5 mg L⁻¹), under magnetic stirring, continuously purged with airflow, a fixed photocatalyst dose of 1 g L⁻¹ and 2 h under simulated solar light using a Solarbox 1500e (CO.FO.ME.GRA) equipped with a 1500 W Xenon lamp (500 W m⁻²). During the experiments, aliquots of 0.5 mL were taken with a 5 mL syringe and a 0.45 μm filter and poured into an HPLC insert.

The venlafaxine concentration of the aliquots was determined by Ultra-High-Pressure Liquid Chromatography (UHPLC) using a Shimadzu Nexera X2 LC-30AD apparatus with a SPD-M20A diode array detector, equipped with a Kinetex XB-C18 100 Å column (100 × 2.1 mm; 1.7 μm particle diameter). An isocratic method with a mobile phase of 25/75 %v Acetonitrile/Ultrapure water (with 1 %v of formic acid) at a flow rate of 0.25 mL min⁻¹ at 35 °C was used. The excitation wavelength for venlafaxine was 275 nm and the resulting absorption bands were integrated using the HPLC software to obtain their areas. Then, the concentration of venlafaxine at a given degradation time was obtained using a calibration curve. Additionally, the identification of common organic

carboxylic acids was also assessed by HPLC (Hitachi Elite LaChrom apparatus equipped with a diode array detector).

2.5 CALCULATION METHODS

2.5.1 ^{29}Si NMR deconvolution methods of HXG

First, using the MestReNova software, the ^{29}Si NMR spectra were apodised (exponential function, 70 Hz) and smoothed (normal, Savitzky-Golay), the spectra line bases were automatically corrected (Whittaker smoother), and the bands were normalized with respect to the more intense peak of the set (Q^3). Once the spectra were processed, the -65 to -125 ppm spectral range was selected with the analysis tool to perform a curve fitting that automatically generates Gaussian bands, whose combination yields a theoretical spectrum. Then, the height and width of the bands are manually modified and, if necessary, additional bands are added, to obtain a theoretical spectrum that overlaps with the experimental one yielding a low residual error (~ 1). In Figure 2.19 the curve fitting of the ^{29}Si NMR spectrum of the 15CIMTEOS xerogel is illustrated as an example.

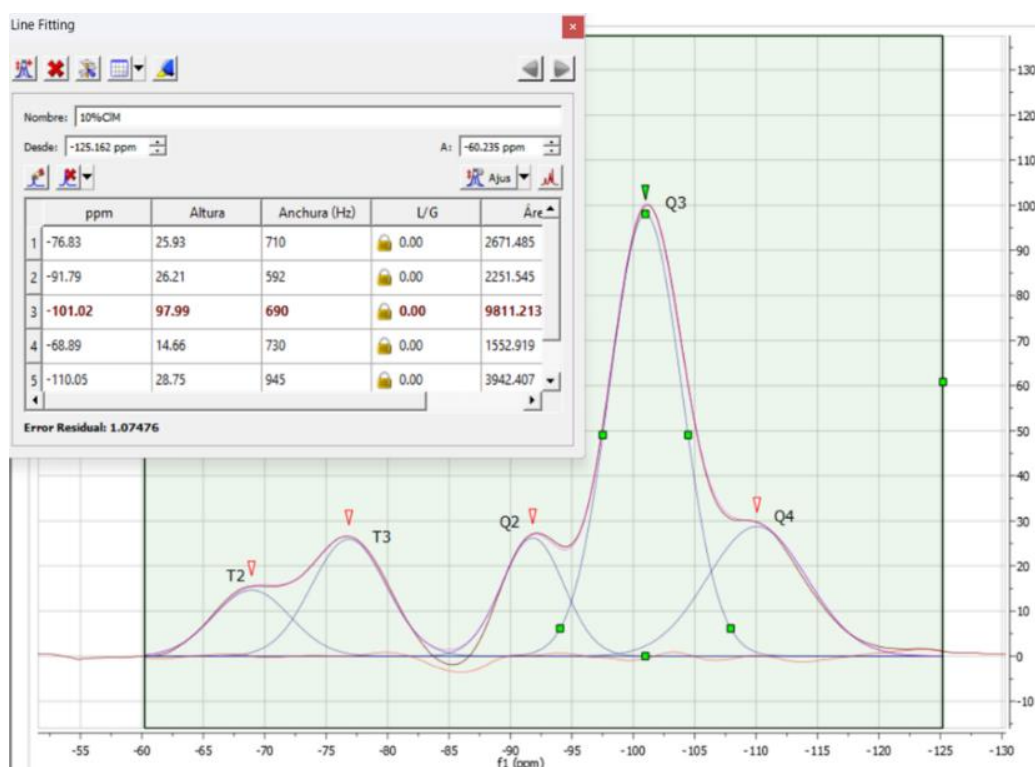


Figure 2.19. MestReNova screenshot of the curve fitting of 15CIMTEOS xerogel ^{29}Si NMR spectrum in the -60 to -130 ppm spectral range.

Each Gaussian band obtained in the curve fitting of hybrid xerogels spectra was assigned to a Q^i or T^i silicon species (TEOS and CIRTEOS species, respectively) considering the chemical shift values that have been reported in the literature [3,9]. The proportion of each species is given by the value of its area divided by the sum of all the areas of the bands.

2.5.2 FTIR deconvolution methods of HXG

The infrared absorbance of the CIRTEOS xerogels spectra was transformed into Kubelka–Munk units with the internal software of the Jasco infrared spectrometer (Spectramanager, SMII FTIR Rev 216A ver2.15A), to allow its deconvolution (curve fitting) by a previously reported method that can provide structural information of the xerogels [24].

This methodology assumes that the broad infrared absorption band that can be observed on silica materials spectra, which occupies the 1300–980 cm^{-1} spectral range, results from the combination of the asymmetric stretching vibration bands of siloxane bonds ($\nu_{\text{as}} \text{Si-O-Si}$) belonging to the different species that constitute the amorphous silica matrix (some of these species are illustrated on Figure A.5 of *Annexe A*). Each silica species (oligomers and rings) has its specific $\nu_{\text{as}} \text{Si-O-Si}$ bands due to its specific bond distances and angle torsions. For calculations, this method only considers the main species that are present on silica matrices, which are 4 and 6-fold rings, $(\text{SiO})_4$ and $(\text{SiO})_6$, respectively. The relative abundance of both species in a silica material depends on the synthesis parameters of the sol-gel method (*see Annexe A.3*). Additionally, since siloxane asymmetric stretching vibrations are sensitive to coulomb interactions, they present two optical modes: transversal mode (TO), from 1100 to 1000 cm^{-1} ; and longitudinal mode (LO), from 1250 to 1100 cm^{-1} [25]. Therefore, four bands are considered for this deconvolution method: TO_4 and LO_4 , belonging to the optical modes of $(\text{SiO})_4$ rings; and TO_6 and LO_6 , belonging to the optical modes of $(\text{SiO})_6$ rings.

The minimum square method was used to obtain the four Gaussian-Lorentzian components corresponding to the four bands mentioned above. Synthetic spectra resulting from the combination of the four bands were obtained by fixing a baseline parallel to the abscissa axis (at 0 KM units) and through successive iterations (200 maximum) until the residual error is ≤ 0.1 . Figure 2.20 depicts a screenshot of the SpectraManager curve fitting analysis tool, processing the infrared spectrum of the TEOS xerogels.

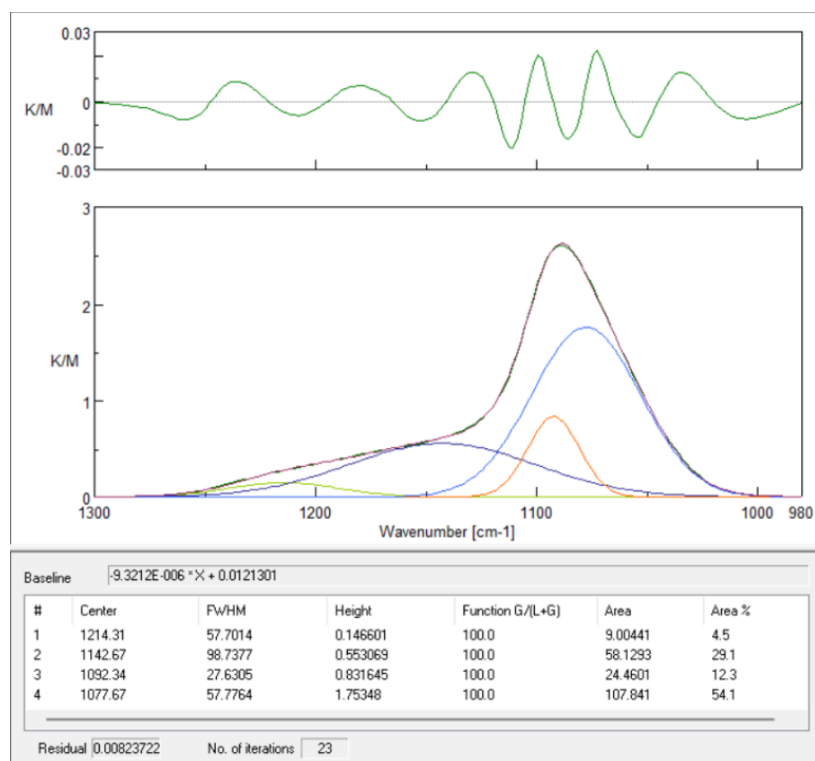


Figure 2.20. SpectraManager screenshot of the curve fitting of TEOS xerogel infrared spectrum in the spectral range 1300–980 cm^{-1} .

The curve fitting of the TEOS xerogel spectrum resulted in an optimized synthetic spectrum that is composed of four bands with maximums at 1214, 1143, 1092 and 1078 cm^{-1} , which were assigned to LO_6 , LO_4 , TO_4 and TO_6 , respectively. This assignment was performed considering the following factors: (i) the previously mentioned ranges of LO and TO optical modes; (ii) the higher spectral range widths of the $(\text{SiO})_6$ optical modes, since those rings have less tensioned angles than the $(\text{SiO})_4$ rings; and (iii) in silica xerogels 4-fold rings are predominant, as is evidenced by the 550 cm^{-1} band observed in their experimental spectra [24,26,27].

The relative abundance of $(\text{SiO})_4$ and $(\text{SiO})_6$ rings was determined with the areas of the four Gaussian-Lorentzian bands $[A(\text{XO})_y; \text{X} = \text{T or L}; y = 4 \text{ or } 6]$ following Equations 2.5 and 2.6, respectively.

$$(\text{SiO})_6, \% = \frac{A(\text{LO}_6) + A(\text{TO}_6)}{A(\text{LO}_4) + A(\text{TO}_4) + A(\text{LO}_6) + A(\text{TO}_6)} \times 100 \quad (2.5)$$

$$(\text{SiO})_4, \% = \frac{A(\text{LO}_4) + A(\text{TO}_4)}{A(\text{LO}_6) + A(\text{TO}_6) + A(\text{LO}_4) + A(\text{TO}_4)} \times 100 \quad (2.6)$$

Deconvolution of CIETEOS and CIPTEOS series spectra were performed applying all the parameters stated above. However, for the CIMTEOS series processing, a fifth band was considered, since the wagging vibration band of the $-\text{ClCH}_2$ functional group (1180 cm^{-1} , C-H wagging [28]) is present in the deconvolution spectral range. In the deconvolution of CIPhTEOS series spectra, the method was modified to generate a maximum of fourteen Gaussian–Lorentzian bands in the $1450\text{--}700\text{ cm}^{-1}$ spectral range, since it was considered all the bands observed in the spectrum of a solid synthesised using 100% of CIPhTEOS precursor (this is explained concisely on *Chapter 5.3.1*)

2.5.3 Calculation of bandgaps of TSR% materials

The bandgaps of the TSR% materials were calculated by applying the Tauc-plot to their UV-Vis diffuse reflectance spectra. In 1966, Jan Tauc realised that the steep slope of the amorphous Germanium UV-Vis absorption spectrum resembled the spectrum of the indirect transitions in crystalline germanium, therefore, he proposed to extrapolate the former spectrum to estimate the optical bandgap of the crystalline-like states [29]. The mathematical method developed by Tauc considers that the energy-dependent absorption coefficient of a material (α) is related to its energy band-gap (E_g) by Equation 2.7.

$$(\alpha \cdot h\nu)^{\frac{1}{r}} = B(h\nu - E_g) \quad (2.7)$$

where h is Planck's constant, ν is the frequency of the adsorbed photons, and r is the factor that denotes the nature of the electronic transitions. r is equal to $\frac{1}{2}$ in direct electronic transitions and to 2 in indirect ones. Equation 2.7 relates bandgap to absorption, but UV-Vis diffuse reflectance spectroscopy (DRS) measures the percentage of reflected radiation ($\%R$) on solid samples, hence, it is necessary to use the Kubelka-Munk faction (Equation 2.8) to obtain absorbance values.

$$F(R) = \frac{K}{S} = \frac{(1 - R)^{\frac{1}{r}}}{2R} \quad (2.8)$$

where K is the absorption coefficient, S is the scattering coefficient, and R is the sample reflectance ($R = \%R/100$). Now, by replacing α with $F(R)$ in Equation 2.7, we obtain Equation 2.9.

$$(F(R) \cdot h\nu)^{\frac{1}{r}} = B(h\nu - E_g) \quad (2.9)$$

Thanks to Equation 2.9, UV-Vis DRS is widely used to estimate the optical bandgap of semiconductors through the value of the x-intersect when the photon energies ($h\nu$ in eV) and $(F(R)\cdot h\nu)^{1/r}$ are represented in the abscissas and ordinates axis, respectively [30]. The UV-Vis DRS spectrometer used to measure the TSR% silicalites can acquire spectra directly in Kubelka-Munk units ($F(R)$), and our titanium silicalites-1 (TS-1) are considered as indirect semiconductors ($r = 2$) [31]. The absorption spectra of an example TSR% material (TSPH5) in Kubelka-Munk units and its Tauc-plot are represented in Figure 2.21.

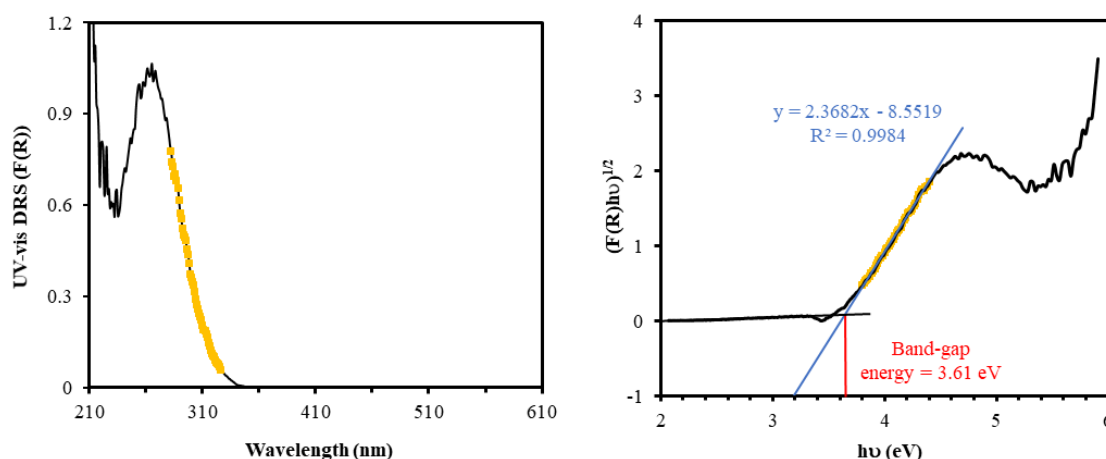


Figure 2.21. (left) UV-Vis diffuse reflectance spectra of TSPH5 in Kubelka-Munk units, and (right) its Tauc-plot analysis.

As can be observed on the Tauc-plot analysis of TSPH5, the bandgap value (3.61 eV) was estimated with the x-intersection of the $(F(R) h\nu)^{1/2}$ function in its linear step region (blue line, Figure 2.21 right), since it corresponds with the slope of the characteristic absorption region (yellow section, Figure 2.21 left) of this semiconductor material.

2.5.4 Adsorption-desorption isotherms data processing

The ASAP2020 instrument registers the amount of physisorbed per mass of sample (n_a), in mmol g^{-1} or $\text{cm}^3 \text{g}^{-1}$ in STP conditions (STP = standard cubic centimetre), at each partial pressure (p/p^0) when the adsorption-desorption equilibrium is reached. Therefore, the first data processing needed to determine the sample pore volumes was to perform the conversion of its recorded n_a in mmol g^{-1} into $\text{cm}^3 \text{g}^{-1}$ considering that the analytes have been adsorbed as liquids in the pores. Equation 2.10 indicates the conversion calculation.

$$n_a \left(\frac{\text{cm}^3}{\text{g}} \right) = \frac{n_a \left(\frac{\text{mmol}}{\text{g}} \right) \cdot MW \left(\frac{\text{g}}{\text{mol}} \right) \cdot \frac{1 \text{ mol}}{1000 \text{ mmol}}}{\rho_l \left(\frac{\text{g}}{\text{cm}^3} \right)} \quad (2.10)$$

where MW is the molecular weight of the analytes (28, 44, 18 g mol⁻¹ for N₂, CO₂ and H₂O, respectively) and ρ_l is the liquid density of the analytes obtained from the literature (0.808, 1.023 and 0.997 g cm⁻³ for N₂, CO₂ and H₂O_(v), respectively [32–34]).

Before stepping into the determination of the pore volumes of the materials it is convenient to define how the pores are classified. IUPAC classifies pores into three categories according to their inner diameter/width (\emptyset) [13]: (i) micropores ($\emptyset \leq 2$ nm), which in turn can be divided into narrow micropores or also called ultramicropores ($\emptyset \leq 0.7$ nm) or wide micropores ($2 \geq \emptyset > 0.7$ nm); (ii) mesopores ($2 < \emptyset \leq 50$ nm); and (iii) macropores ($\emptyset > 50$ nm).

The total pore volume (V_{Total}) and the volume of macropores (V_{macro}) were obtained from isotherm data. V_{Total} is given by the adsorbed amount of analyte at $p/p^\circ = 0.95$, which is a value close enough to p° but avoids selecting volumes corresponding to saturation phenomena; whereas V_{macro} is obtained by subtracting the volume of analyte adsorbed at $p/p^\circ = 0.8$ to V_{Total} . On the other hand, the determination of the volume of micropores (V_{micro}) and the volume of mesopores (V_{meso}), as well as the rest of textural parameter of interest: specific surface areas (a_{BET} and a_{DR}); characteristic energy of adsorption (E_c); and average pore size (APS), required the use of mathematical methods that were applied using the Microactive software (version 4.06).

The specific surface areas (a_{BET} , in m² g⁻¹) of the analysed materials were obtained by applying the well-known BET method, the mathematical model of gas adsorption in multimolecular layers developed by Brunauer, Emmett and Teller in 1938 [35], to their N₂ and H₂O_(v) isotherms. The BET method transforms the adsorption curve of an isotherm into the BET plot by applying Equation 2.11.

$$\frac{p}{n_a(p^\circ - p)} = \frac{1}{q_m C} + \frac{C - 1}{q_m C} \left(\frac{p}{p^\circ} \right) \quad (2.11)$$

By plotting the first term of Equation 2.11 (where n_a , also noted as Q , is in mol g⁻¹) in the ordinate axis and the partial pressure in the abscissa axis, the amount of necessary analyte to fill the theoretical monolayer (q_m , in mol g⁻¹) and the analyte-solid affinity parameter (C) can be easily determined by the values of the slope and the x-

intersection. However, BET plot is only valid in linear partial pressure ranges and when $C > 0$; C parameter is exponentially dependent on the energy of adsorption in the monolayer, and therefore having a negative value has no physicochemical meaning. To guarantee its linear dependence, and according to the Rouquerol criteria [36], the BET plot was applied only at the 0.05–0.3 partial pressure range of the type IV isotherms (IUPAC classification for isotherms of micro-mesoporous materials [13]); whereas, for isotherms of very microporous materials (Type I isotherms), it was possible to select partial pressures below 0.05 providing that their plotting against $n_a(1 - p/p^o)$ yields a linear tendency [37]. Once the value of n_m was obtained from the BET plot, the a_{BET} can be calculated by Equation 2.12.

$$a_{BET} = \frac{q_m N_A \sigma_m}{m} \quad (2.12)$$

where σ_m is the cross-sectional area of N_2 or H_2O molecules (0.162 and 0.125 nm² molecule⁻¹, respectively), N_a is the Avogadro's number (6.022×10^{23} molecule mol⁻¹), and m is the mass of the sample in grams. Although the calculations of Equations 2.11 and 2.12 are automatically performed by the software, the p/p^o ranges were manually assigned to fulfil the linearity and C parameters conditions. Figure 2.22 shows as an example the BET surface area and Rouquerol BET plots of the N_2 isotherm of the 20CIMTEOS xerogel.

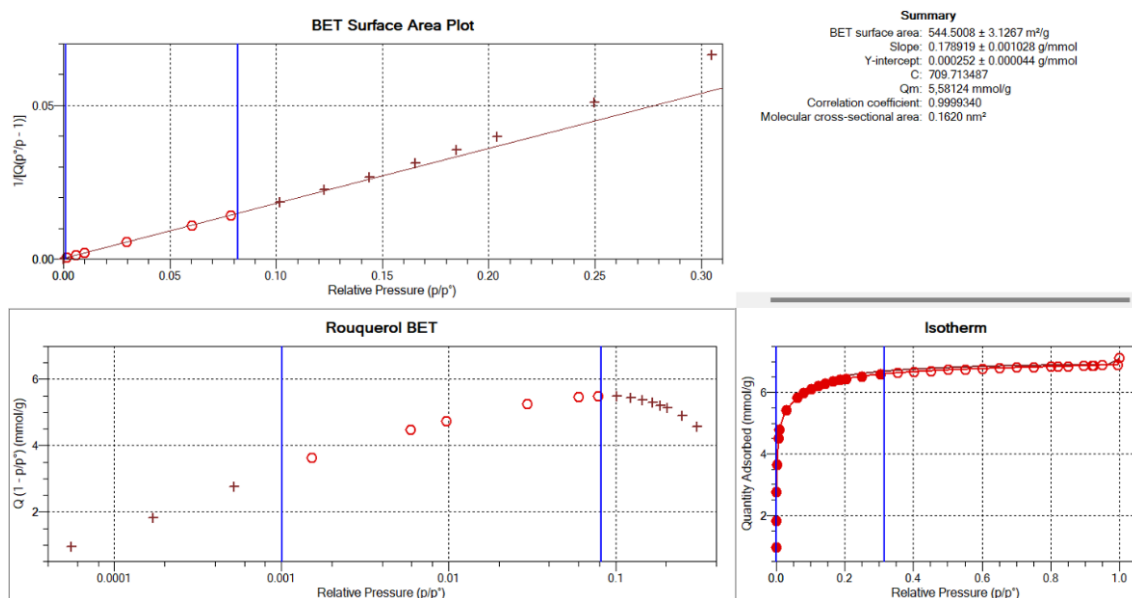


Figure 2.22. Relative pressure range section on Microactive software for the determination of the specific surface area.

The volume of micropores (V_{micro}) and the characteristic energy of adsorption (E_c) of the samples were from the adsorption isotherms of the three analytes by applying the Dubinin-Raduskevich (DR) method with the modification suggested by Kaganer (DRK) [38]. The DR method is used to describe the adsorption mechanism, whether it is physical or chemical, on microporous homogeneous systems. Since is based on Polanyi's potential theory, it assumes the characteristic curve principle and that the pores adsorption potential of an adsorbent follows a Gaussian energy distribution, therefore, it considers that the adsorbed analytes form a plane monomolecular layers that cover the micropores surfaces [39,40]. The basic Dubinin-Polanyi theory equation correlates the amount of adsorbed analyte (n_a) with the adsorption potential (A) and characteristic energy (E_c) as follows

$$n_a = n_0 e^{-k\left(\frac{A}{E_c}\right)^2} \quad (2.13)$$

where n_0 is the micropore capacity, also known as the volume of micropores (V_{micro}), and k is a parameter that reflects the function of the distribution of the volume of the pores according to sizes. The adsorption potential, A , is given by Equation 2.14.

$$A = 2.303RT \left[\log\left(\frac{p^0}{p}\right) \right]^2 \quad (2.14)$$

where T is the temperature in kelvin, and R is the universal gas constant ($0.0083 \text{ kJ K}^{-1} \text{ mol}^{-1}$). If Equation 2.14 is substituted in Equation 2.13, after some mathematical operations we can obtain the DRK equation (Equation 2.15), which is the one that the Microactive software applies to the isotherms data.

$$\log n_a = \log n_0 - D \left[\log\left(\frac{p^0}{p}\right) \right]^2; D = 2.303 \left(\frac{RT}{E_c}\right)^2 \quad (2.15)$$

where n_0 , was obtained from the y-intersection when this equation was plotted. However, to determine n_0 it was required to select values of $\log^2(p^0/p)$ ranging from 1 to 8 in the Microactive software since this interval corresponds to the p/p^0 interval of the isotherm (0–0.3) that is, assigned to microporosity. The D is the Dubinin parameter, which represents a measurement of the average size distribution of micropores, which can be obtained from the slope in the plot of Equation 2.15. Once the value of the D parameter is known, the characteristic energy (E_c) is calculated by Equation 2.16.

$$E_c = \frac{2.303RT}{\sqrt{2.303D\beta}} \quad (2.16)$$

where β is the affinity coefficient or scale factor, which depends on each adsorbate (0.330, 0.461 and 1.030 for N₂, CO₂ and H₂O, respectively [32,41]). The value of the E_c parameter depends on the packaging of the adsorbates and the average pore size of the adsorbate micropores. In addition to V_{micro} and E_c , the specific surface area was calculated with the DR method (a_{DR}) with CO₂ adsorption data by replacing n_a with its calculated n_0 in Equation 2.12; σ_m value of CO₂ is 0.17 nm² molecule⁻¹.

The lacking pore volume, the volume of mesopores (V_{meso}) of the materials, was calculated by subtracting V_{macro} and V_{micro} from V_{total} .

To conclude, the average pore size (APS) of the samples was calculated using the method developed by Barret, Joyner and Halenda in 1951 [42]. BJH method takes into consideration the BET multilayer theory and the capillary condensation within the pores of adsorbent materials. Hence, average pore sizes were calculated with the N₂ desorption curves, the adsorption curve selected if the desorption branch does not close the adsorption-desorption loop and selecting the Kruk-Jaroniec-Sayari curve fittings and corrections in the Microactive software.

2.5.5 Determination of pore size distribution by DFT methods

The pore size distribution (PSD) of the materials was calculated by SAIEUS software (copyright © Jacek Jagiello), which applies a namesake mathematical method developed by Jacek Jagiello [43], and a series of non local density functional theory (NLDFT) models (Micromeritics Instrument Corp) to the N₂ and CO₂ isotherms recorded by the ASAP2020 instrument. PSD was not determined with the H₂O_(v) isotherms data, because there was no model available in the software that considered H₂O as an adsorbate.

Due to the lack of NLDFT models specifically designed for silica materials, the models designed for carbon materials were selected for PSD calculations of CIRTEOS and Ln-AL xerogels; the model applied to the N₂ isotherm data was “carbon-N2-77, 2D-NLDFT heterogeneous Surface”, whereas “carbon-CO2-273, 2D-NLDFT Het Surface, pp max = 10 atm” was the one selected for CO₂ isotherms data. For TSR% materials, the models “Zeolite(H-form)-N2-77, NLDFT, cylindrical model” and “carbon-N2-77, 2D-NLDFT heterogeneous Surface” were applied to the N₂ adsorption data of crystalline and amorphous samples, respectively. The model “Carbon-CO2-273, 2D-NLDFT Het surface, pmax = 10 atm” was applied to all CO₂ isotherm data of TSR% materials.

Once the isotherm data was loaded and a model was selected, the SAIEUS software automatically estimates a suitable value for the smoothing parameter (λ) and provides an optimized PSD (in $\text{cm}^3 \text{g}^{-1} \text{\AA}^{-1}$) from 3.6 to a maximum of 500 \AA ; then the units were converted to $\text{cm}^3 \text{g}^{-1} \text{nm}^{-1}$ to prepare the PSD graphs depicted in *Chapters 3* and *5–7*. Figure 2.23 shows, as an example, the SAIEUS calculation of the pore size distribution of a TEOS xerogel from its N_2 isotherm data.

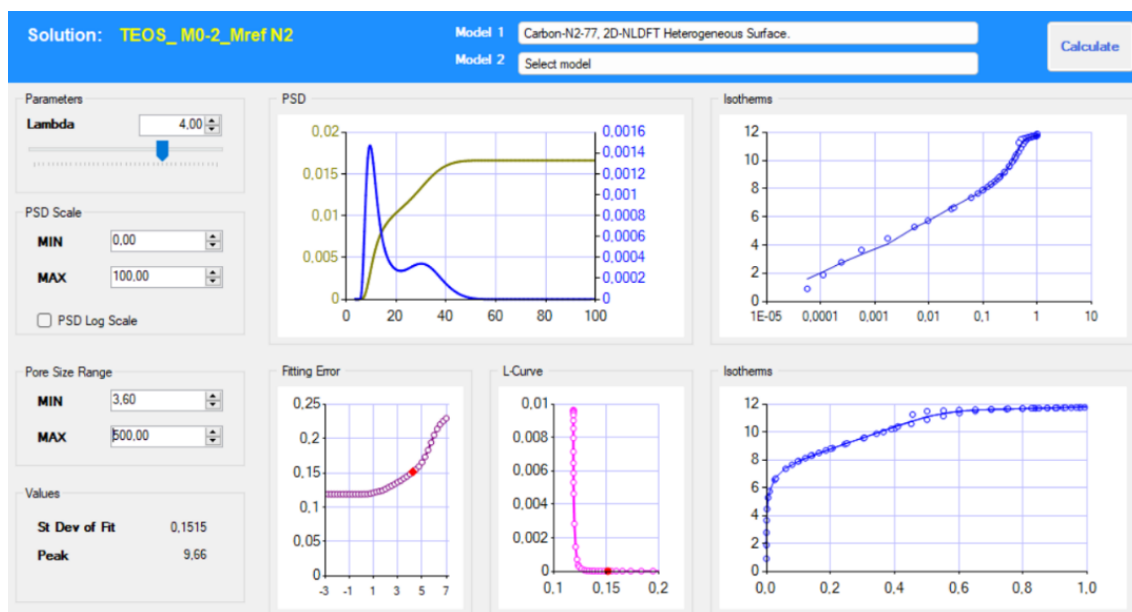


Figure 2.23. SAIEUS Screenshot of the calculated pore size distribution of a material.

2.6 REFERENCES

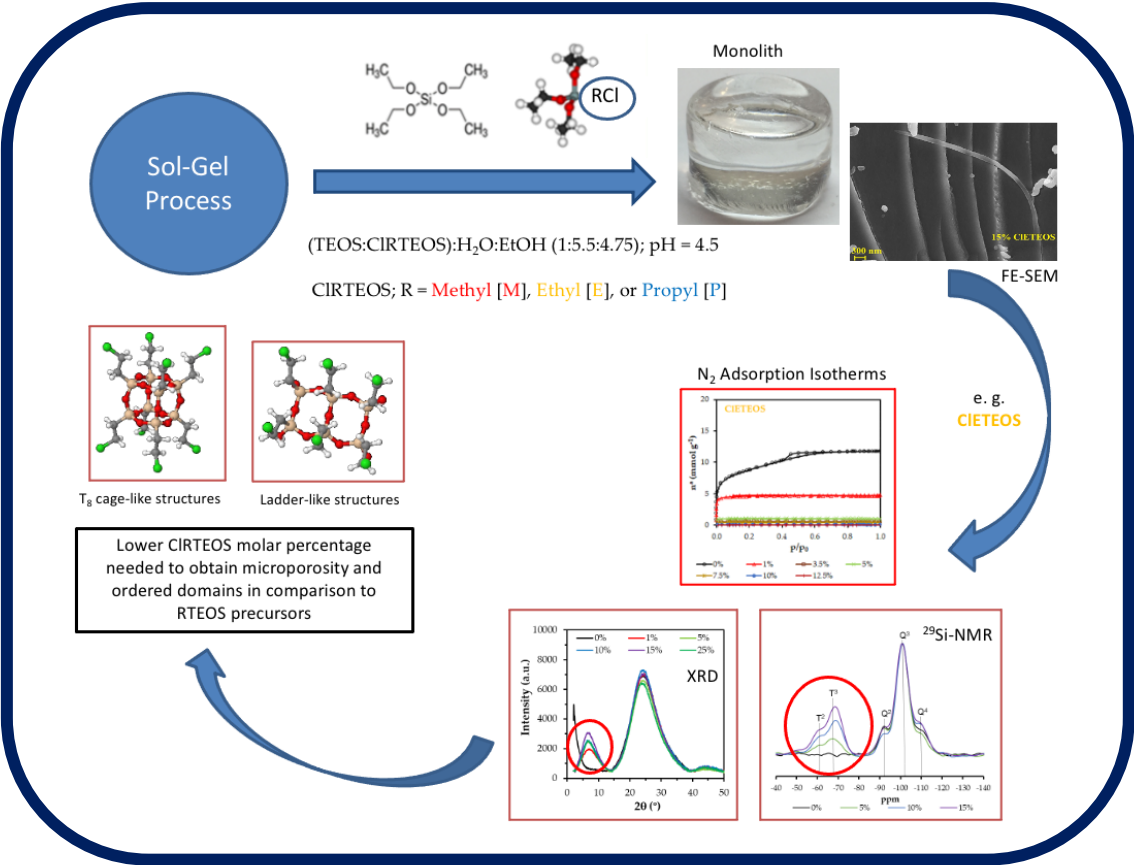
- [1] Estella, J.; Echeverría, J. C.; Laguna, M.; Garrido, J. J. *J. Non-Cryst. Solids* **2007**, *353*, p. 286–294.
- [2] Rios, X.; Moriones, P.; Echeverría, J. C.; Luquín, A.; Laguna, M.; Garrido, J. J. *Adsorption* **2011**, *17*, p. 583–593.
- [3] Rios, X.; Moriones, P.; Echeverría, J. C.; Luquin, A.; Laguna, M.; Garrido, J. J. *Mater. Chem. Phys.* **2013**, *141*, p. 166–174.
- [4] Moriones, P.; Echeverria, J. C.; Parra, J. B.; Garrido, J. J. *Adsorption* **2020**, *26*, p. 177–188.
- [5] Brinker, C. J.; Scherer, G. W. *Sol-Gel Science*; 1st ed.; Academic Press, INC: San Diego, CA, USA, **1990**.
- [6] De Bettencourt-Dias, A.; Barber, P. S.; Bauer, S. *J. Am. Chem. Soc.* **2012**, *134*, p. 6987–6994.
- [7] Gao, J.; Gao, L.; Zhang, B.; Wang, H.; Ma, W. *Can. J. Chem. Eng.* **2021**, *99*, p. S596–S604.

- [8] Kickelbick, G. *Hybrid Materials Synthesis, Characterization, and Applications*; Wiley-VCH Verlag GmbH & Co. KGaA, **2007**.
- [9] Vasil'ev, S. G.; Volkov, V. I.; Tatarinova, E. A.; Muzafarov, A. M. *Appl. Magn. Reson.* **2013**, *44*, p. 1015–1025.
- [10] Torres-Luna, J. A.; Carriazo, J. G. *Solid State Sci.* **2019**, *88*, p. 29–35.
- [11] Stair, P. C. *Adv. Catal.* **2007**, *51*, p. 75–98.
- [12] Sakka, S. *Handbook of Sol-Gel Science and Technology: Processing, Characterization and Applications. Volume II: Characterization of Sol-Gel Materials and products*; Sakka, S., Almeida, R. M., Eds.; 1st ed.; Kluwer Academic Publishers: Osaka, Japan, **2005**.
- [13] Thommes, M.; Kaneko, K.; Neimark, A. V.; Olivier, J. P.; Rodriguez-Reinoso, F.; Rouquerol, J.; Sing, K. S. W. *Pure Appl. Chem.* **2015**, *87*, p. 1051–1069.
- [14] Elosua, C.; Arregui, F. J.; Del Villar, I.; Ruiz-Zamarreño, C.; Corres, J. M.; Barriain, C.; Goicoechea, J.; Hernaez, M.; Rivero, P. J.; Socorro, A. B.; Urrutia, A.; Sanchez, P.; Zubiate, P.; Lopez-Torres, D.; De Acha, N.; Ascorbe, J.; Ozcariz, A.; Matias, I. R. *Sensors* **2017**, *17*, p. 2312.
- [15] De Acha, N.; Elosúa, C.; Arregui, F. J. *Sensors* **2020**, *20*, p. 2372.
- [16] Echeverría, J. C.; Faustini, M.; Garrido, J. J. *Sens Actuators, B* **2016**, *222*, p. 1166–1174.
- [17] Echeverría, J. C.; Calleja, I.; Moriones, P.; Garrido, J. J. *Beilstein J. Nanotechnol.* **2017**, *8*, p. 475–484.
- [18] Omary, M. A.; Patterson, H. H. Luminescence, theory. In *Encyclopedia of Spectroscopy and Spectrometry*; Elsevier Ltd., **2016**; pp. 636–653.
- [19] Aguayo-López, M. L.; Capitán-Vallvey, L. F.; Fernández-Ramos, M. D. *Talanta* **2014**, *126*, p. 196–201.
- [20] Li, X. M.; Wong, K. Y. *Anal. Chim. Acta* **1992**, p. 262, 27–32.
- [21] Singh, R. P.; Heldman, D. R. Psychrometrics. In *Introduction to Food Engineering: Fifth Edition*; Academic Press, **2014**; pp. 593–616.
- [22] Elosúa, C.; De Acha N.; Hernaez, M.; Matias, L. R.; Arregui, F. J. *Sens Actuators, B* **2015**, *207*, p. 683–689.
- [23] Butler, L. R. P.; Laqua, K.; Strasheim, A. *Spectrochim. Acta, Part B* **1986**, *41*, p. 507–544.
- [24] Fidalgo, A.; Ciriminna, R.; Ilharco, L. M.; Pagliaro, M. *Chem. Mater.* **2005**, *17*, p. 6686–6694.
- [25] Tan, C. Z.; Arndt, J. J. *Chem. Phys.* **2000**, *112*, p. 5970–5974.
- [26] Fidalgo, A.; Ilharco, L. M. *Chem. - Eur. J.* **2004**, *10*, p. 392–398.
- [27] Caresani, J. R.; Lattuada, R. M.; Radtke, C.; Dos Santos, J. H. Z. *Powder Technol.* **2014**, *252*, p. 56–64.

- [28] Launer, P. J.; Arkles, B. Infrared Analysis of Organosilicon Compounds. In *Silicon Compounds: Silanes and Silicones (3rd edition)*; Arkles, B., Larson, G. L., Eds.; Gelest, INC: Morrisville, PA; USA, **2013**; p. 175–178.
- [29] Tauc, J.; Grigorovici, R.; Vancu, A. *Phys. Status Solidi* **1966**, *15*, p. 627–637.
- [30] Makuła, P.; Pacia, M.; Macyk, W. *J. Phys. Chem. Lett.* **2018**, *9*, p. 6814–6817.
- [31] Shang, Q.; Liu, X.; Zhang, M.; Zhang, P.; Ling, Y.; Cui, G.; Liu, W.; Shi, X.; Yue, J.; Tang, B. *Chem. Eng. J.* **2022**, *443*, p. 136354.
- [32] Garrido, J.; Linares-solano, A.; Martìn-Martínez, J. M.; Molina-Sabio, M.; Rodríguez-Reinoso, F.; Torregrosa, R. *Langmuir* **1987**, *3*, p. 76–81.
- [33] García-Martínez, J.; Cazorla-Amorós, D.; Linares-Solano, A. *Stud. Surf. Sci. Catal.* **2000**, *128*, p. 485–494.
- [34] Duan, S.; Geng, L.; Li, G.; Ling, X. *Fluid Phase Equilib.* **2022**, *563*, p. 113583.
- [35] Brunauer, S.; Emmett, P. H.; Teller, E. *J. Am. Chem. Soc.* **1938**, *60*, p. 309–319.
- [36] Rouquerol, F.; Rouquerol, J.; Sing, K. S. W.; Llewellyn, P.; Maurin, G. Chapter 6- Assessment of Surface Area. In *Adsorption by Powders and Porous Solids Principles, Methodology and Applications*; San Diego, **1999**; pp. 165–189.
- [37] Rouquerol, J.; Llewellyn, P.; Rouquerol, F. *Stud. Surf. Sci. Catal.* **2007**, *160*, p. 49–56.
- [38] Gregg, S.J.; Sing, K.S.W. *Adsorption, Surface Area and Porosity*; Second edi.; Academic Pres, INC: London, UK, **1982**.
- [39] Polanyi, M. *Trans. Faraday Soc.* **1932**, *28*, p. 1–18.
- [40] Dubinin, M. M. *Chem. Rev.* **1960**, *60*, p. 235–241.
- [41] Tamon, H.; Murakami, N.; Okazaki, M. *J. Chem. Eng.* **1997**, *30*, p. 735–741.
- [42] Barrett, E. P.; Joyner, L. G.; Halenda, P. P. *J. Am. Chem. Soc.* **1951**, *73*, p. 373–380.
- [43] Jagiellot, J. *Langmuir* **1994**, *10*, p. 2778-2785.

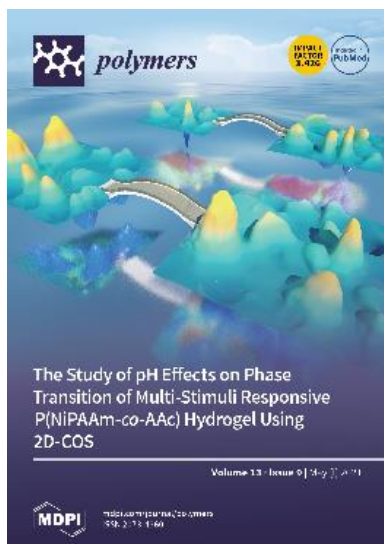
CHAPTER 3

NOVEL ORGANOCHLORINATED XEROGELS: FROM MICROPOROUS MATERIALS TO ORDERED DOMAINS



CHAPTER 3

“NOVEL ORGANOCHLORINATED XEROGELS: FROM MICROPOROUS MATERIALS TO ORDERED DOMAINS”



Published article

Authors: Guillermo Cruz-Quesada, Maialen Espinal-Viguri, María Victoria López-Ramón and Julián J. Garrido

Reference: *Polymers* **2021**, *13*(9), p. 1415.
Doi: 10.3390/polym13091415

Publication date: 04/27/2021

Keywords: xerogels; hybrid materials; TEOS; chloroalkyltriethoxysilane; inductive effect; textural properties; ORMOSILs.

Abstract: Hybrid silica xerogels combine the properties of organic and inorganic components in the same material, making them highly promising and versatile candidates for multiple applications. They can be tailored for specific purposes through chemical modifications, and the consequent changes in their structures warrant in-depth investigation. We describe the synthesis of three new series of organochlorinated xerogels prepared by co-condensation of tetraethyl orthosilicate (TEOS) and chloroalkyltriethoxysilane (CIRTEOS; R = methyl [M], ethyl [E], or propyl [P]) at different molar ratios. The influence of the precursors on the morphological and textural properties of the xerogels was studied using ^{29}Si NMR (Nuclear Magnetic Resonance), FTIR (Fourier-Transform Infrared Spectroscopy), N_2 , and CO_2 adsorption, XRD (X-ray Diffraction), and FE-SEM (Field-Emission Scanning Electron Microscopy). The structure and morphology of these materials are closely related to the nature and amount of the precursor, and their microporosity increases proportionally to the molar percentage of CIRTEOS. In addition, the influence of the chlorine atom was investigated through comparison with their non-chlorinated analogues (RTEOS, R = M, E, or P) prepared in previous studies. The results showed that a smaller amount of precursor was needed to detect ordered domains (ladders and T_8 cages) in the local structure. The possibility of coupling self-organization with tailored porosity opens the way to novel applications for this type of organically modified silicates.

3.1 INTRODUCTION

The demand for materials with specific physicochemical properties has markedly increased over the past decade. Research has focused on the design of hybrid solids in which organic and inorganic species coexist on a nanometric scale, with the aim of generating synergistic effects and tailored materials. Organically modified silicates (ORMOSILs) are hybrid silicon xerogels that combine the mechanical, thermal, and structural rigidity and stability of inorganic materials with the flexibility and functionality of organic molecules [1]. These properties favour their utilization as chemical and optical sensors [2–7], catalysts [8,9], coatings [10–14], chromatographic agents [15,16], nanoprobess, and photo-voltaic cells [17,18], among others.

The most widely adopted approach to hybrid xerogel synthesis is the sol-gel method (see *Annexe A*) [19], using either (i) “silane coupling agents” to provide a functional surface group that can be substituted or act as a bridge to other structural units [3,10,11,15] or (ii) co-condensation reactions or condensation between monomers of silicon tetraalkoxides (e.g., tetramethoxy- or tetraethoxysilane (TMOS, TEOS)) and one or more mono-, di-, or tri-alkylalkoxysilanes ($R_xSi(OR')_{4-x}$). This procedure yields hybrid silicon materials based on a silica matrix with organic groups that modify the network, permitting the production of materials with specifically designed chemical and textural properties in a single process [20–22]. The incorporation of organic groups is known to promote the formation of ordered domains induced by intermolecular forces (e.g., hydrogen bonds, hydrophobic or electrostatic interactions, or π – π stacking) [23]. Although these forces may be weak at molecular level, they are capable of directing the nanostructuring mechanism at macromolecular level. This approach may offer a simple and efficient option for the preparation of transparent materials with controlled structure and porosity that can also have different morphologies (membranes, monoliths, and fibres, among others) [24]. The structure and texture of materials produced by the sol–gel method are known to be influenced by the molar percentage of $R_xSi(OR')_{4-x}$ [25,26], the pH [27], the proportions of $H_2O/TEOS$ and $EtOH/TEOS$ [18,26,27], and the curing and drying methods [28,29]. Changes in these factors can produce significant variations in the density and porosity of the resulting xerogel. In this way, the properties of these materials can be controlled by acting on their molecular structure and morphology.

In previous studies, the formation of ordered domains in the amorphous structure of hybrid silicon xerogels was evidenced by: (i) a signal in the X-ray diffraction patterns

at $2\theta < 10^\circ$, (ii) the appearance in the NMR spectra of $T^{2,3}$ structures (T^n , notation used for silicon atoms bonded to three oxygen atoms and Q^n , for silicon atoms bonded to four bridged oxygen atoms) [30,31], and (iii) a band at around 1150 cm^{-1} in the Fourier-transform infrared spectroscopy (FTIR) spectra [20–22]. These observations are consistent with data obtained by mass spectrometry (MS) [21], simulations of the FTIR spectra, and inelastic neutron spectroscopy (INS). We also constructed a theoretical cage model to explain the presence of ordered domains in these materials and increase knowledge of the properties and the processes involved in their formation [32].

The aim of the present study was to determine the influence of the alkyl chain and chlorine atom on the morphological and textural properties of various hybrid materials produced by co-condensation. For this purpose, three new series of organochlorinated xerogels were prepared and characterised using TEOS and a chloroalkyltriethoxysilane (CIRTEOS; R = methyl [M], ethyl [E], or propyl [P]) at different molar ratios; the synthesis and characterisation techniques are described in *Chapters 2.1.1* and *2.2*, respectively. These chlorinated precursors have been used as silane coupling agents or in the preparation of polyhedral oligomeric silsesquioxanes (POSS) [33–35]; however, to our best knowledge, they have not been studied in co-condensation with tetraalkoxysilanes. Development of the structure and morphology of these materials was characterised by ^{29}Si NMR (Nuclear Magnetic Resonance), XRD (X-ray Diffraction), FTIR (Fourier-Transform Infrared Spectroscopy), helium pycnometry, FE-SEM (Field-Emission Scanning Electron Microscopy), and N_2 and CO_2 adsorption. The influence of the halogen was also explored by comparison with results previously obtained for analogous alkyl xerogels (RTEOS:TEOS) [20–22]. The ultimate application of these materials is to use them as coatings for optical fibre sensors, for which a labile and specific interaction with the analyte is necessary, hence the importance of increasing knowledge on their properties to be able to develop siliceous materials with tailored properties and porosities.

3.2 RESULTS AND DISCUSSION

3.2.1 ^{29}Si Nuclear magnetic resonance (NMR)

^{29}Si NMR spectra were obtained to study the effect of chloroalkyl precursors on the relative abundance of silicon species in hybrid xerogels. In all cases, they showed the characteristic bands of the different species of silicon that can be found in this type of material, represented in Figure 3.1a.

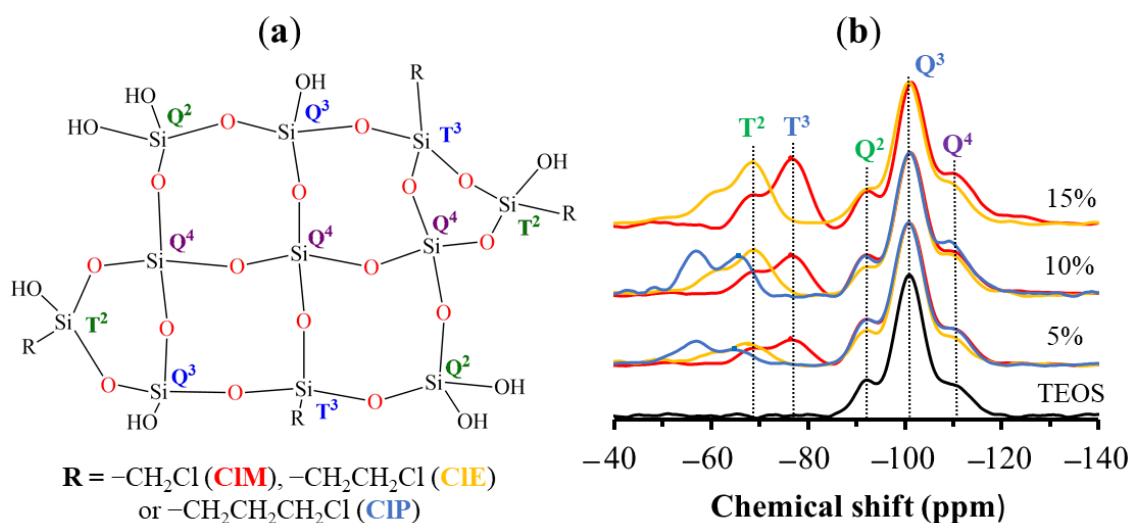


Figure 3.1. (a) Silicon environments present in chloroalkyltriethoxysilane (CIRTEOS):tetraethoxysilane (TEOS) xerogels, and (b) normalized ^{29}Si NMR spectra of the hybrid xerogels synthesised with 5%, 10%, and 15% of CIRTEOS (chloromethyltriethoxysilane (CIMTEOS) (•), chloroethyltriethoxysilane (CIETEOS) (▲), and chloropropyltriethoxysilane (CIPTEOS) (□)).

Figure 3.1b depicts ^{29}Si NMR spectra for the three series of CIRTEOS:TEOS xerogels, normalized with respect to the Q³ signal, which was always the most intense signal and corresponds to the dominant species in these materials synthesised in acid media. Q¹ and T¹ signals are not detected [20], and the proportions of T² and T³ species vary according to the precursors. Thus, T³ species are more abundant than T² species at all molar percentages in xerogels prepared with CIMTEOS and CIETEOS, indicating that these xerogels are preferably formed by the most condensed species. Spectra for the series prepared with CIPTEOS show a predominance of T² species, implying that more silicon atoms are partially condensed and attached to hydroxyl groups. Spectra for the Q species reveal a decrease in Q³ and Q² species with an increase in the molar percentage of chlorinated precursor.

Figure 3.2 depicts the relative abundance of species detected in the spectra for the three series of hybrid xerogels CIRTEOS:TEOS (its calculation is explained in *section 2.5.1*). It shows the time course of the total proportion of Q ($Q^2 + Q^3 + Q^4$) and T ($T^2 + T^3$) species as a function of the percentage of CIRTEOS and the time course of each individual species. It can be observed that Q^2 and Q^3 species always decrease with increased molar percentage of the chlorinated precursor, while the results for Q^4 differ according to the precursor used, with a lower abundance in the CIMTEOS series and a slightly higher abundance in the CIPTEOS series.

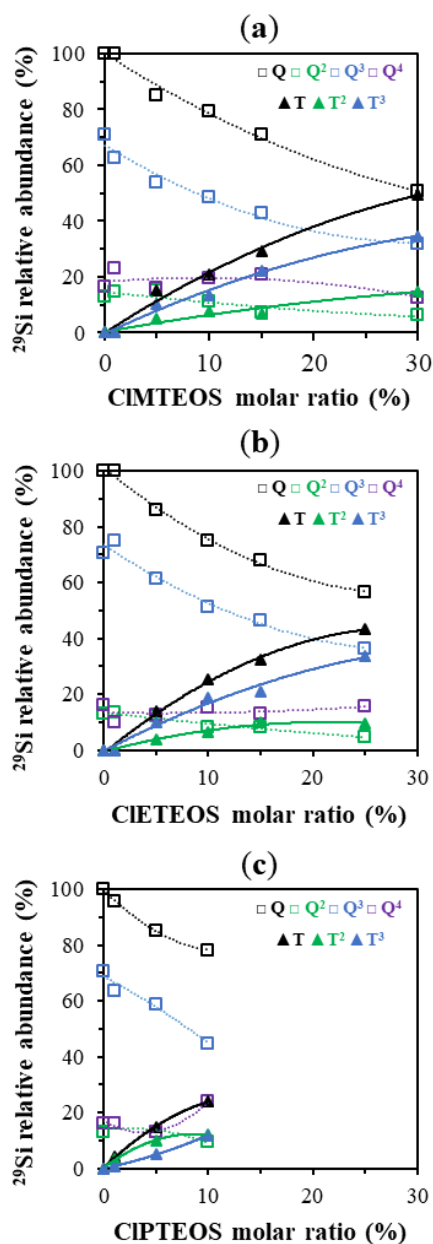


Figure 3.2. Variation in the relative abundance of the condensed species of Si^{IV} with respect to percentage CIRTEOS obtained by integrating the ^{29}Si NMR spectra for: (a) CIMTEOS, (b) CIETEOS, and (c) CIPTEOS.

Figure 3.2 also shows that T³ species predominate over T² species in the CIMTEOS and CIETEOS series, whereas T² species predominate in the CIPTEOS series. This is attributable to the steric hindrance exerted by the chloropropyl chain in the condensation reactions, hampering complete condensation around the Si^{IV}. The chloropropyl chain also influences the surface charge of the colloids and generates repulsion between them, consistent with the exponential increase in gelation times of this series at the highest molar percentages (Table 3.1).

Table 3.1. Gelation time (t_g) of CIRTEOS: TEOS materials.

CIRTEOS molar percentage (%)	t_g (h)
CIMTEOS 5	6
CIMTEOS 15	8
CIMTEOS 25	11
CIETEOS 5	141
CIETEOS 15	357
CIETEOS 25	815
CIPTEOS 5	13
CIPTEOS 15	1199
CIPTEOS 25	4769

Chen *et al.* (2015) reported that T³ and Q⁴ species are predominant in POSS synthesised with CIMTEOS [35]. In the present study, T³ species are associated with rings formed by cyclic tetramers of (SiO)₄ that build T₈ cages, while Q⁴ would be the silicon atoms at the vertex that bind T₈ structures together. The minor signal detected in the POSS, T², is related to the presence of partially open cages (T₇). The proportion of Q species has also been associated with the FTIR spectra, with reports that Q², Q³, and Q⁴ species present their asymmetric Si–O–Si stretching vibration mode at different frequencies (1000–1030, 1100, and 1150–1200 cm⁻¹, respectively) [36,37] and that the aforementioned polycyclic structures ((SiO)₄ and T₈ cages) are related to bands at 1090 and 1150 cm⁻¹, respectively [38]. It can therefore be concluded that the presence of these structures in the materials is consistent with the increase in T³, Q³, and Q⁴ species when the amount of precursor is larger and with the shoulder at 1150 cm⁻¹ observed in the FTIR spectra (Figure 3.3).

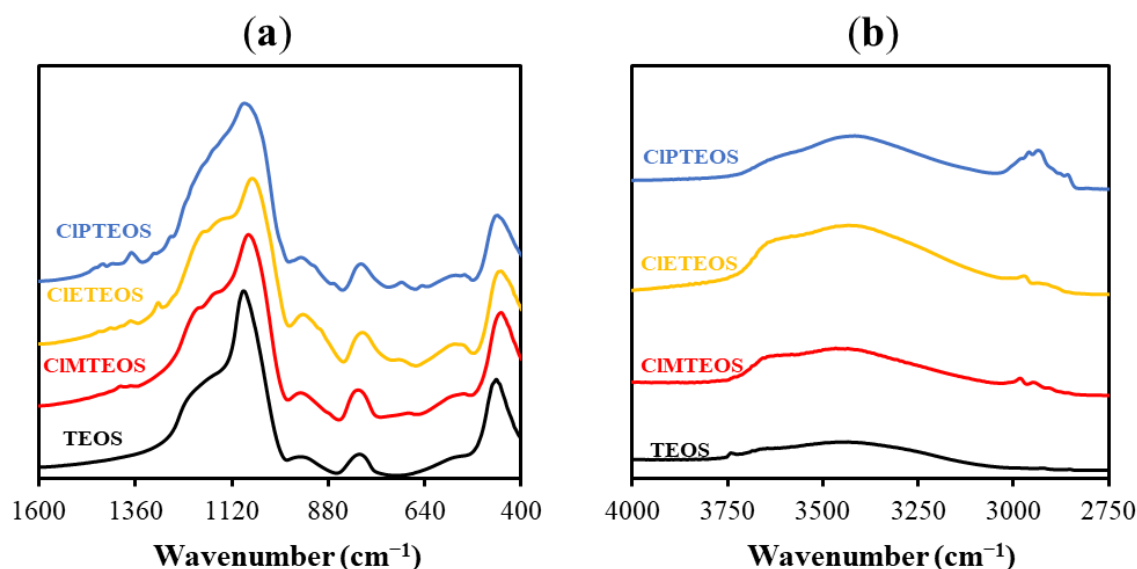


Figure 3.3. FTIR spectra of xerogels synthesised with 15% precursor within the range of (a) 1600–400 cm^{-1} and (b) 4000–2750 cm^{-1} .

Table 3.2 exhibits the chemical shifts for the different Si^{IV} of each hybrid xerogel, showing that T and Q signals are not affected in any series by the increase in molar percentage of CIRTEOS or RTEOS, because there is no significant change in the silicon environment. However, a marked shift in T signals is observed in the comparison of different series with the same percentage of precursor. This is attributable to a shielding effect in which the organic precursor acts by adding or removing charge density to the silicon atom, thereby shifting the signal to a higher or lower field [39,40]. The chlorine atom removes charge density, reducing the donor capacity of the alkyl chains and increasing the positive charge of the silicon atom, and this effect is reflected in the shift of its signal to lower ppm. Likewise, the further the chlorine is from the Si^{IV} , the lesser is the shift of the signal. This trend is readily observed by comparing the average T^3 chemical shift between the chloroalkyl and the alkyl series: (i) -12.2 ppm when chlorine is in carbon α position (MTEOS vs. CIMTEOS), (ii) -4.4 ppm when it is in β position (ETEOS vs. CIETEOS), and (iii) -0.45 ppm when it is in γ position (PTEOS vs. CIPTEOS).

Table 3.2. Signals from the ^{29}Si NMR spectra of the hybrid xerogels chloroalkyltriethoxysilane (CIRTEOS):tetraethoxysilane (TEOS) and alkyltriethoxysilane (RTEOS): tetraethoxysilane (TEOS) ($R = \text{methyl, ethyl, and propyl}$) [20–22].

Precursor molar percentage (%)	^{29}Si chemical shift (ppm)				
	T ²	T ³	Q ²	Q ³	Q ⁴
CIMTEOS 5	-68.5	-76.6	-92	-100.9	-110.4
CIMTEOS 10	-68.9	-76.8	-91.8	-101.0	-110.1
CIMTEOS 15	-68.3	-76.7	-92.9	-101.3	-110.4
CIETEOS 5	-60.2	-67.7	-91.7	-100.8	-109.7
CIETEOS 10	-60.3	-68.8	-91.7	-100.8	-109.7
CIETEOS 15	-60.3	-68.7	-91.9	-100.9	-109.5
CIPTEOS 5	-57.0	-65.0	-91.6	-100.8	-110.3
CIPTEOS 10	-57.4	-65.5	-91.9	-100.7	-109.6
MTEOS 30	-54.8	-63.1	-91.7	-101.1	-110.9
MTEOS 70	-56.3	-64.6	a	-100.9	-109.6
MTEOS 100	-57.0	-65.8	a	a	a
ETEOS 10	-54.6	-63.2	-92.5	-101.7	-110.7
ETEOS 30	-55.7	-63.8	-92.3	-101.3	-109.9
ETEOS 60	-56.4	-65.0	a	-101.9	-110.0
PTEOS 10	-56.4	-64.1	-92.2	-100.9	-110.2
PTEOS 30	-56.1	-64.6	-90.9	-100.3	-109.4
PTEOS 60	-56.8	-65.7	a	-101.4	-110.4

a—Not detected

3.2.2 X-ray diffraction (XRD)

Figure 3.4 displays the XRD diffraction patterns of the xerogels synthesised with CIMTEOS, CIETEOS, and CIPTEOS. The diffraction pattern shows a broad signal at around $2\theta = 24^\circ$, characteristic of amorphous silica. This signal corresponds to the distance between silicon atoms connected by siloxane bonds [39]. It can be observed that the intensity of this signal is reduced with an increased molar percentage of the precursor and that another signal arises with higher molar percentage of CIMTEOS and CIPTEOS (30% and 10%, respectively) at $2\theta < 10^\circ$. The behaviour of the CIETEOS series is different, observing the presence of this signal at the lowest molar percentage (1%) and an increase in its intensity with a larger amount of precursor. The $2\theta < 10^\circ$ signal is associated with the formation of ordered structures composed of T₈ cages or ladders, which are, in turn, related to lamellar morphologies [41–43]. The distances calculated from this maximum correspond to the distance between the organic substituents in these structures [32]. The three series show this band at lower molar percentages in comparison to those previously observed for their alkyl equivalents, being detected in 70% of

MTEOS, 30% of ETEOS, and 10% of PTEOS series [20–22]. This indicates a higher tendency for the chloroalkyl precursors to form ordered domains in the amorphous matrix. There is also a broad low-intensity signal at $2\theta \sim 45^\circ$. According to Bragg's law, these bands correspond to replicas of the signal at $2\theta = 24^\circ$, which supports the presence of local periodicity in the silica matrix.

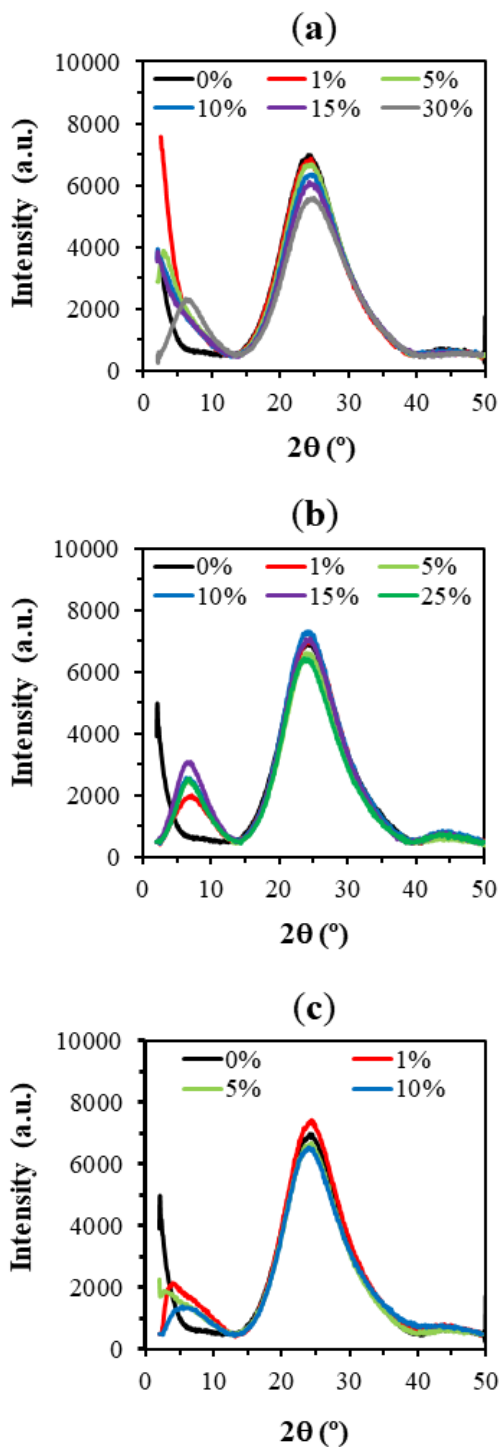


Figure 3.4. X-ray diffraction patterns of the hybrid xerogels CIRTEOS:TEOS at different molar percentages: (a) CIMTEOS, (b) ClETEOS, (c) ClPTEOS.

Table 3.3. Bragg angles (2θ), band area (A), and bond distance (d_1 and d_2 (nm)) calculated from the XRD bands of the xerogels synthesised with different precursors and molar percentages.

CIRTEOS molar percentage (%)	Diffraction maximum $2\theta < 10^\circ$			Diffraction maximum $10^\circ < 2\theta < 30^\circ$		
	$2\theta_1$ ($^\circ$)	A_1	d_1 (nm)	$2\theta_2$ ($^\circ$)	A_2	d_2 (nm)
0	a	a	a	24.16	68,812	0.368
CIMTEOS 1	a	a	a	24.26	66,451	0.367
CIMTEOS 5	a	a	a	24.30	65,847	0.366
CIMTEOS 10	a	a	a	24.54	62,627	0.363
CIMTEOS 15	a	a	a	24.42	60,377	0.365
CIMTEOS 30	6.52	10,217	1.35	24.78	56,217	0.359
CIETEOS 1	7.17	8,594	1.23	24.56	68,577	0.362
CIETEOS 5	6.92	15,879	1.28	24.30	74,258	0.366
CIETEOS 10	6.76	16,568	1.31	24.14	81,785	0.369
CIETEOS 15	6.76	19,509	1.31	24.22	78,157	0.367
CIETEOS 25	6.76	15,780	1.31	23.90	71,722	0.372
CIPTEOS 1	a	a	a	24.22	73,819	0.367
CIPTEOS 5	a	a	a	23.98	65,782	0.371
CIPTEOS 10	5.80	5,514	1.52	24.06	66,143	0.370

a—Not detected

Table 3.3 displays the angles of each signal (2θ), the area of the diffraction maxima, and the Si–O–Si bond distances. It shows the shift of the amorphous silica signal ($2\theta \sim 24^\circ$) as a function of the precursor and its molar percentage. There is a shift to larger angles in the CIMTEOS series, which results in a shortening of the Si–O–Si bond distance (0.368 nm for 0% and 0.359 nm for 30%), whereas there is a shift to smaller angles in the CIETEOS and CIPTEOS series, resulting in longer bond distances (0.372 nm for 25% CIETEOS and 0.370 nm for 10% CIPTEOS). These modifications of bond distances are attributable to inductive and steric effects generated by the chloroalkyl substituents of the precursors. The shorter bond distances for the CIMTEOS series result from the predominance of the inductive effect of the chlorine atom, which removes electron density from the silicon atom and therefore polarizes the adjacent Si–O bond. On the contrary, in CIETEOS and CIPTEOS series, the effect of the alkyl chain predominates over the inductive effect of the chlorine atom, thus elongating the adjacent Si–O bond as occurred with their non-chlorinated analogues.

3.2.3 Helium pycnometry

Helium pycnometry reveals the skeletal density of the synthesised xerogels. Figure 3.5 depicts the variation in skeletal density as a function of the molar percentage of the precursor for the chloroalkyl series (Figure 3.5a) and for the analogous alkyl series prepared in previous studies (Figure 3.5b). The density of the chloroalkyl xerogels decreases with a greater proportion of the precursor, because the precursor blocks one of the hydrolysis and condensation positions, reducing the degree of cross-linking. Another influencing factor is the nature of the substituent, observing a lower skeletal density with a longer alkyl chain due to greater steric hindrance. In the previously studied alkyl xerogels, the XRD diffraction patterns show an elongation of the siloxane bonds consistent with the donor effect of the carbon atom directly bound to silicon, leading to lesser compaction and therefore, lower skeletal density [20–22]. In the chloroalkyl series, densities are higher than those of their non-chlorinated analogues at the same molar percentages due to the attractor effect of chlorine. For example, at a molar percentage of 10%, the density value is 1.91 g cm^{-3} for the CIMTEOS xerogel vs. 1.7 g cm^{-3} for the MTEOS xerogel.

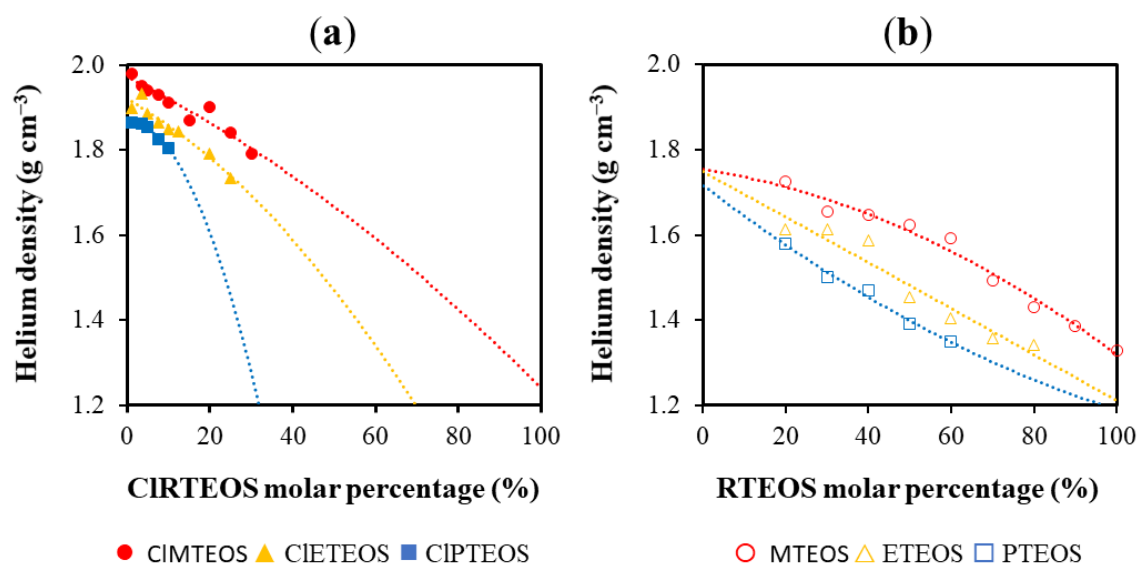


Figure 3.5. Skeletal density of the materials according to the precursor molar percentage for: (a) CIRTEOS series (CIMTEOS, CIETEOS, and CIPTEOS) and (b) RTEOS series (MTEOS, ETEOS, and PTEOS) in previous studies [20–22]. Reference material density (100%TEOS) = 1.96 g cm^{-3} .

3.2.4 Porous texture

3.2.4.1 Adsorption isotherms and textural properties

The nitrogen adsorption isotherms of the CIRTEOS:TEOS series are exhibited in Figure 3.6. The isotherm of the reference material has a flat knee (Type I(b) isotherm), an adsorption branch with a positive slope, and a hysteresis loop in the desorption branch (H2(a)), typical of type IV(a) isotherms. It is therefore a material with a mixed Type I(b)-IV(a) isotherm, indicating micro-mesoporosity [44].

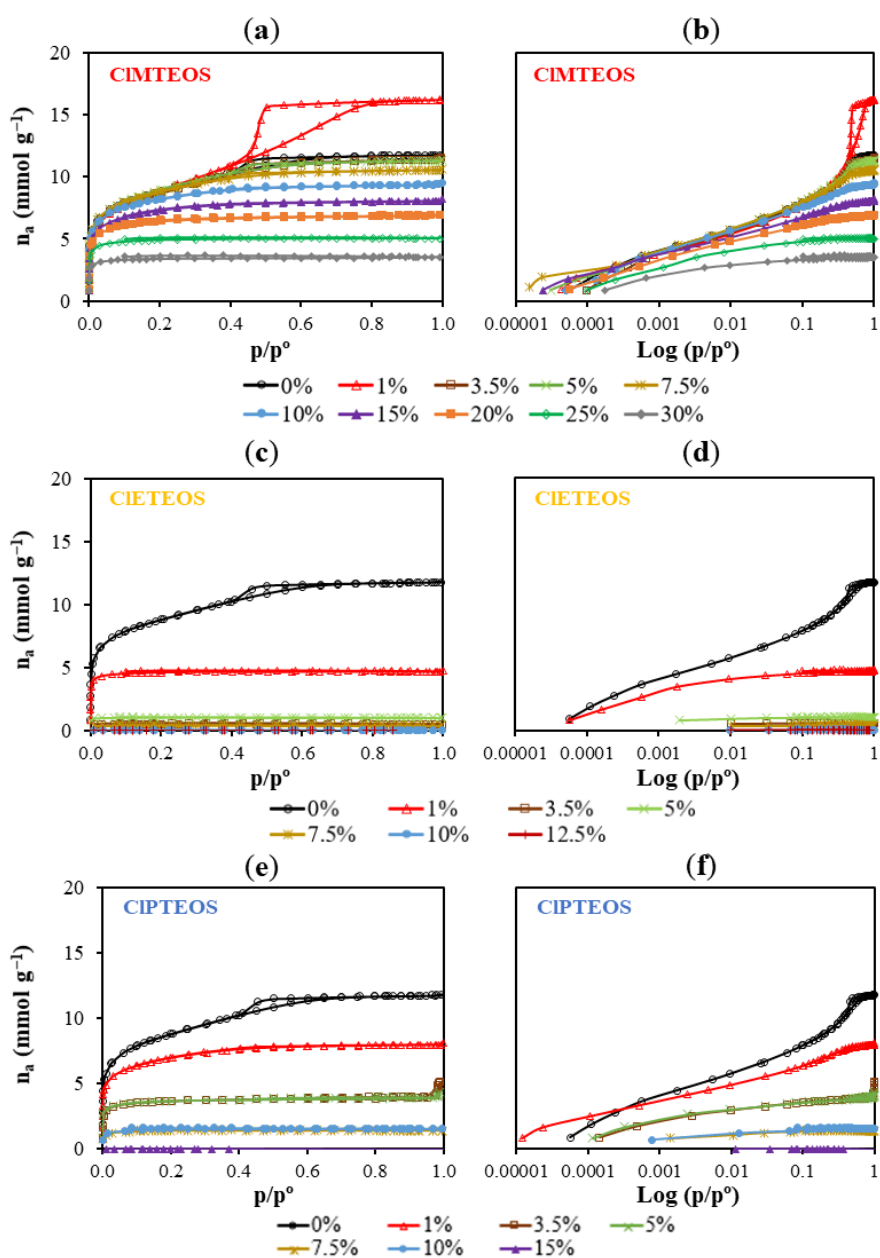


Figure 3.6. Decimal scale (left) and semi-logarithmical scale (right) of the N_2 isotherms ($-196\text{ }^\circ\text{C}$) of chloroalkyl materials at different molar percentages of: (a, b) CIRTEOS, (c, d) CIETEOS, and (e, f) CIPTEOS.

With respect to the reference material, the isotherms of the hybrid xerogels prepared in this study show that they adsorbed a smaller amount of N₂, gradually becoming more microporous. The knees are sharper, the plateaus are practically parallel to the abscissa axis, and the hysteresis loop disappears. Figure 3.6 depicts the N₂ isotherms of the three series of chloroalkyl xerogels. In the CIMTEOS series (Figure 3.6a), Type IV isotherms become Type I(b) and I(a) with an increased molar percentage of the precursor (10% and 30%, respectively), and N₂ adsorption ceases when the highest molar percentage is reached (35%) (Table 3.4). In contrast, Figure 3.6a depicts the striking observation of a Type IV(a) isotherm for the material containing 1% CIMTEOS, showing a similar knee but wider hysteresis loop in comparison to the reference material (Type H1). Dudás *et al.* (2020) prepared hybrid xerogels with low proportions of MTEOS and also observed increased N₂ adsorption, associated with the transition from cone to ink-bottle shaped pores that is responsible for the Type H1 hysteresis loop [45]. The CIETEOS series (Figure 3.6c) has a type I(a) isotherm at a precursor molar percentage of 1%, whereas N₂ adsorption is very low at higher percentages and ceases at 12.5%. The CIPTEOS series (Figure 3.6e) changes from Type I(b) at a percentage of 1% to Type I(a) at percentages up to 10%, with a cessation of adsorption at higher percentages, as in the case of the CIETEOS xerogels. The isotherms on the right of Figure 3.6 are depicted on semi-logarithmic scale on its right side to visualize more clearly the development of the microporosity at higher molar percentages of the precursor. Hence, the incorporation of chlorinated precursors into the structure of TEOS modifies its porosity, reducing the size, volume, and shape of the pores in the following order: CIETEOS > CIPTEOS > CIMTEOS.

At least two adsorbates are required to characterize the porosity of a material. N₂ adsorption (196 °C) has long been complemented by CO₂ adsorption (0 °C), allowing differentiation between microporosity below 0.7 nm and that above 0.7 nm (associated with cooperative processes of the adsorbate molecules). The isotherms displayed in Figure 3.7 show a similar trend for all of the materials, evidencing lesser adsorption of CO₂ at higher molar percentages of the precursor.

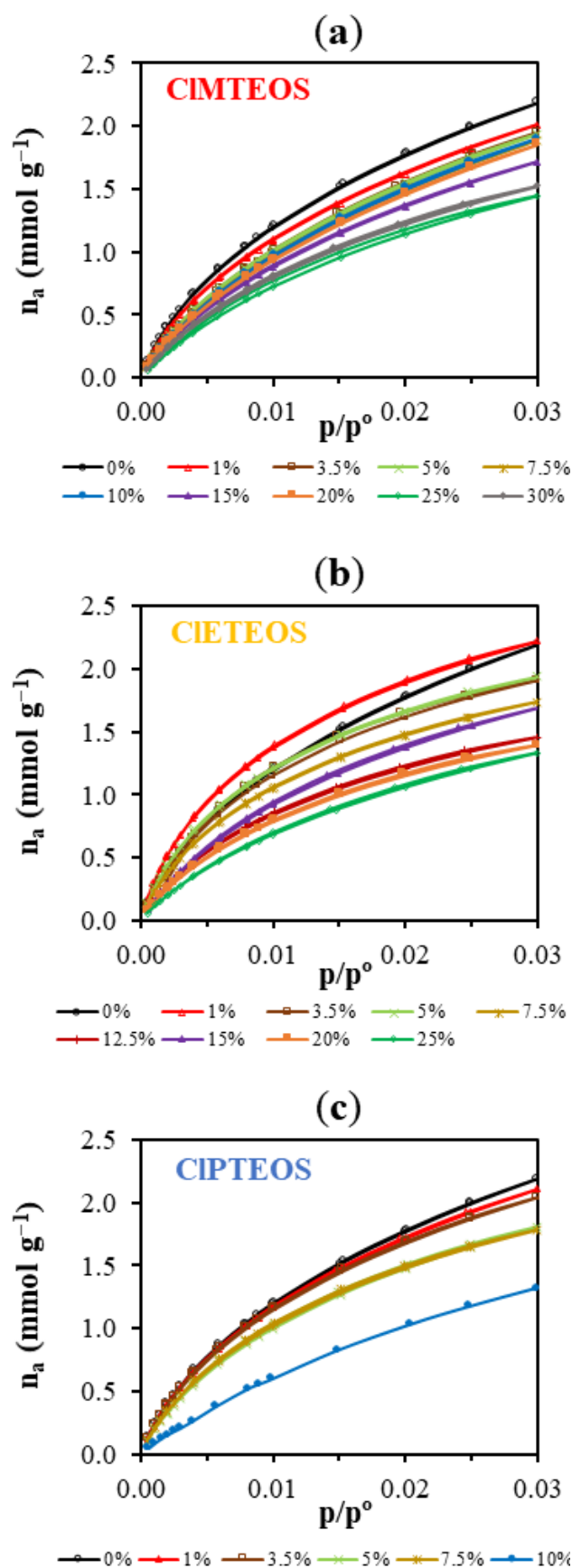


Figure 3.7. CO₂ isotherms (0 °C) of chloroalkyl materials at different molar percentages of: (a) CIMTEOS, (b) CIETEOS, and (c) CIPTEOS.

Table 3.4 displays the textural values calculated from N₂ and CO₂ isotherms, the calculation procedures are described in detail in *Chapter 2.5.4*. A reduction in the specific surface areas a_{BET} (N₂) and a_{DR} (CO₂) can be observed with a higher percentage of CIRTEOS. The pore volume data confirm the essentially microporous nature of the material, given that $V_{micro}(N_2) > V_{meso}(N_2)$, and V_{meso} tend towards zero with a higher percentage of the precursor. Notably, the material becomes ultramicroporous at CIETEOS molar percentages above 1%, explaining the lack of N₂ adsorption. Higher and more constant adsorption characteristics energies (E_c , calculated by DR method) were observed for CO₂ than for N₂, consistent with kinetic restrictions of N₂ entry into the narrowest pores. However, it should be noted that E_c calculated with CO₂ is lower than that calculated with N₂ at the xerogels with the higher molar percentages of CIMTEOS (25 and 30%), and at the material with the lowest percentage of CIETEOS (1%). This is because in these materials the N₂ retention mechanism within the narrow micropores ($\emptyset < 0.7$ nm) is based on the overlap of pore wall potentials when $r_{pores}/r_{adsorbate} \sim 1.1$, as in CO₂ adsorption. This behaviour was also described in analogous non-chlorinated xerogels [46].

Table 3.4. Textural parameters of chloroalkyl materials at different molar percentages.

CIRTEOS molar percentage (%)	$a_{\text{BET}} (\text{N}_2)$	$V_{\text{micro}} (\text{N}_2)$	$V_{\text{micro}} (\text{CO}_2)$	$V_{\text{meso}} (\text{N}_2)$	$V_{\text{total}} (\text{N}_2)$	BJH APS ^a	$E_c (\text{N}_2)^b$	$E_c (\text{CO}_2)^b$
	($\text{m}^2 \text{g}^{-1}$)	(cm ³ g ⁻¹)			(nm)	(kJ mol ⁻¹)		
0	697	0.283	0.195	0.074	0.407	3.61	15.27	19.71
CIMTEOS 1	700	0.289	0.178	0.210	0.560	4.21	14.27	19.77
CIMTEOS 3.5	691	0.285	0.182	0.061	0.394	3.55	14.82	18.93
CIMTEOS 5	702	0.293	0.177	0.052	0.390	3.51	14.93	19.15
CIMTEOS 7.5	693	0.288	0.175	0.036	0.364	3.41	15.26	18.98
CIMTEOS 10	662	0.274	0.180	0.022	0.324	3.38	15.67	18.77
CIMTEOS 15	591	0.248	0.164	0.013	0.278	3.30	15.81	18.82
CIMTEOS 20	534	0.226	0.177	0.009	0.239	3.15	16.42	18.71
CIMTEOS 25	422	0.175	0.146	0.002	0.174	2.56	18.32	18.29
CIMTEOS 30	294	0.121	0.137	0.003	0.123	2.09	20.47	18.32
CIMTEOS 35	c	c	0.132	c	c	c	c	18.04
CIETEOS 1	410	0.164	0.193	0.001	0.164	2.32	22.17	20.80
CIETEOS 3.5	c	c	0.178	c	c	c	c	20.05
CIETEOS 5	c	c	0.172	c	c	c	c	20.64
CIETEOS 7.5	c	c	0.157	c	c	c	c	20.25
CIETEOS 10	c	c	0.142	c	c	c	c	d
CIETEOS 12.5	c	c	0.136	c	c	c	c	19.69
CIETEOS 15	c	c	0.164	c	c	c	c	19.05
CIETEOS 20	c	c	0.134	c	c	c	c	19.29
CIETEOS 25	c	c	0.132	c	c	c	c	18.55
CIPTEOS 1	555	0.232	0.189	0.018	0.282	3.39	16.50	19.74
CIPTEOS 3.5	312	0.129	0.184	0.004	0.136	2.96	18.48	19.80
CIPTEOS 5	318	0.129	0.167	0.004	0.136	2.85	19.98	19.49
CIPTEOS 7.5	118	0.050	0.165	0.000	0.048	2.09	17.37	19.72
CIPTEOS 10	132	0.056	0.137	0.000	0.053	2.18	15.72	17.69

^a—Average Pore Size; ^b—Characteristic energy from Dubinin-Raduskevich; c—The samples did not adsorb N₂; d—Not calculated.

3.2.4.2 Porosity distribution

Two distinct theoretical approaches were adopted to explore the effect on the porosity of the precursors. The BJH method was used to calculate the mean pore size from the desorption branch of the isotherms. Application of this method showed a reduction in mean pore size proportional to the precursor molar percentage (Table 3.4), from 4.21 to 2.09 nm of CIMTEOS and from 3.39 to 2.18 nm of CIPTEOS. In the CIETEOS series, N₂ adsorption is only observed at a molar percentage of 1%, and this material has a value of 2.32 nm.

The DFT was also applied to calculate porosity distributions from N₂ and CO₂ adsorption data (depicted in Figure 3.8 left and right, respectively), showing a similar

influence of the precursor in both cases. Thus, N_2 isotherm data show a progressive narrowing of the pores and a loss of mesoporosity with a higher percentage of precursor, and the CO_2 isotherm data also show a sharpening of the micropore distribution. Note should be taken of the aforementioned irregular behaviours of: (i) 1% CIMTEOS material (Figure 3.8a), which has an increased pore size in comparison to the reference material, becoming more mesoporous, and (ii) the CIETEOS series (Figure 3.8c), whose ultramicroporous nature means that pore distribution values can only be obtained for the material with a molar percentage of 1%, observing a gradual loss of porosity with higher percentages of the precursor (Figure 3.8d).

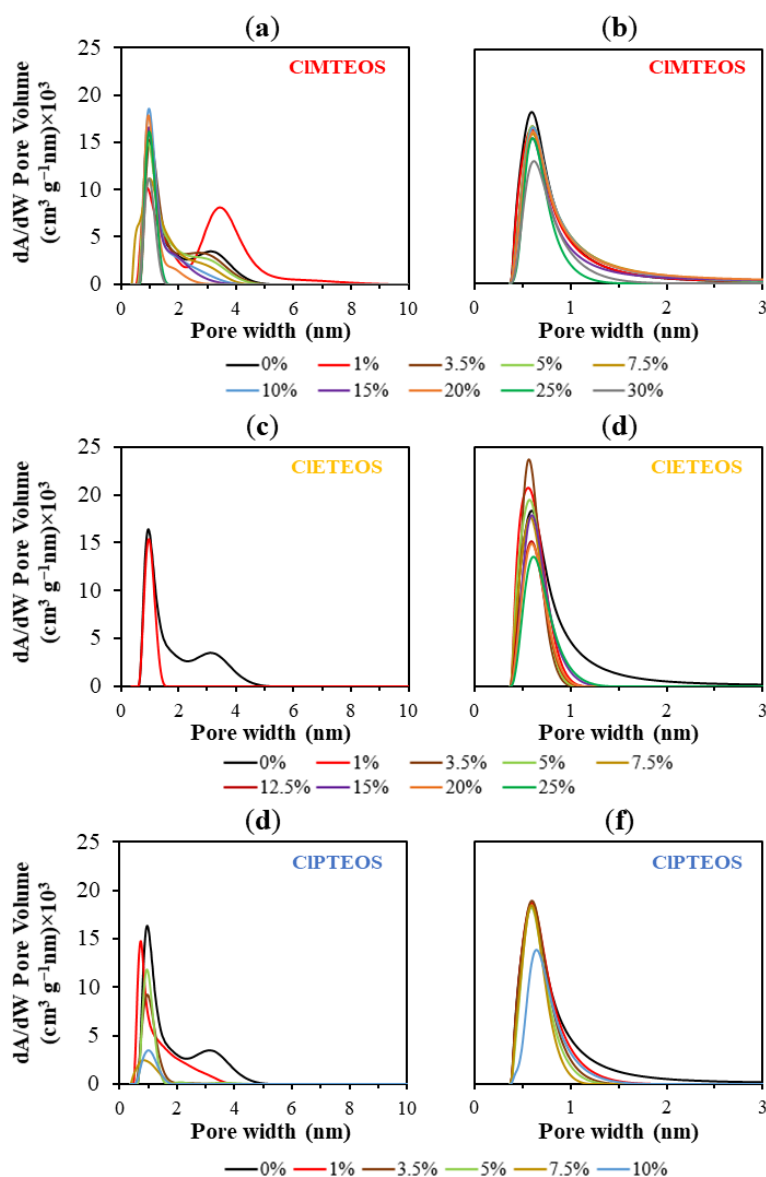


Figure 3.8. Density-functional theory (DFT) porosity distribution obtained from N_2 isotherms (left) and CO_2 isotherms (right) of: (a, b) CIMTEOS:TEOS series, (c, d) CIETEOS:TEOS series, and (e, f) CIPTEOS:TEOS series.

3.2.5 Field-Emission Scanning Electron Microscopy (FE-SEM)

Figure 3.9 depicts FE-SEM micrographs of the reference material and a sample of each series synthesised with chloroalkyl precursors. The surface of samples in Figure 3.9 was studied with energy-dispersive X-ray spectroscopy (EDX) to confirm that the chlorine atoms of the chloroalkyl precursors are homogeneously distributed on their surface (Figure 3.10).

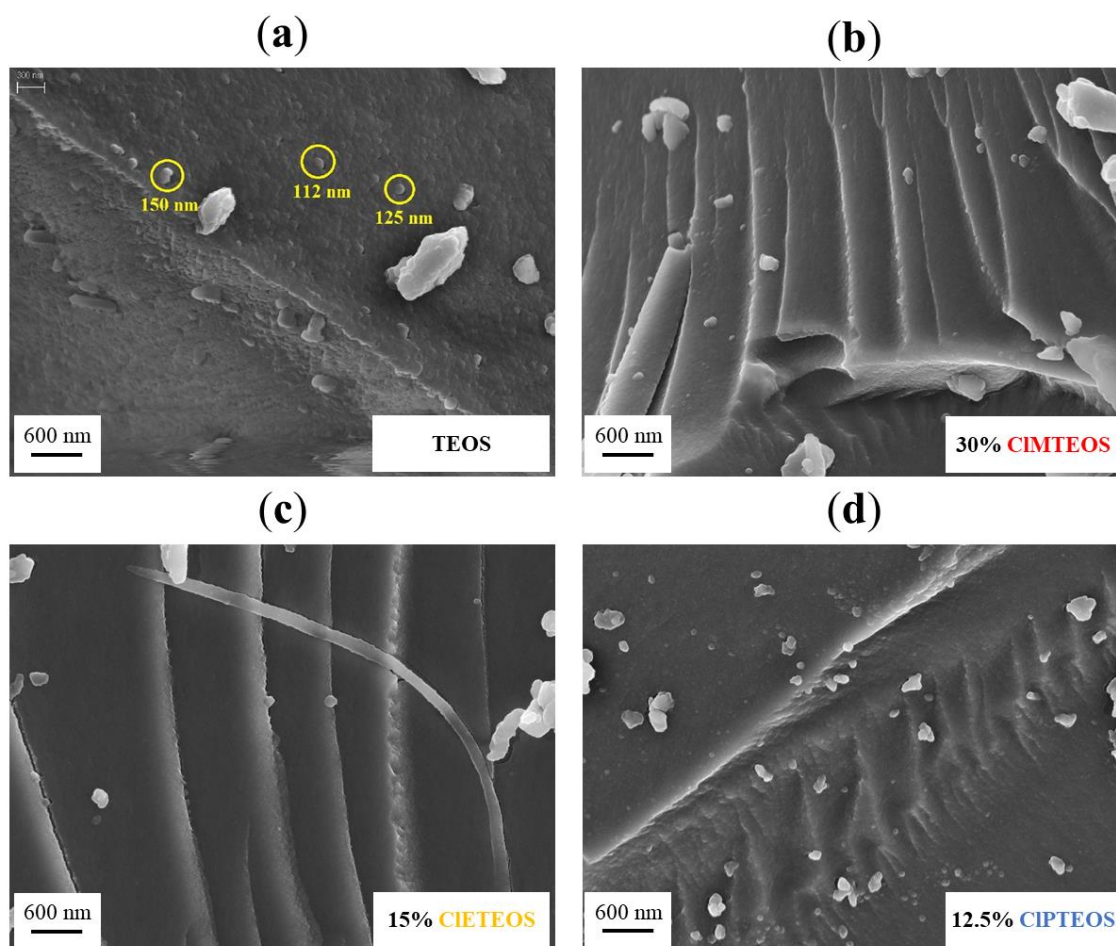


Figure 3.9. FE-SEM micrographs of: (a) reference xerogel (100% TEOS), (b) xerogel synthesised with 30% of CIMTEOS, (c) xerogel synthesised with 15% CIETEOS, and (d) xerogels synthesised with 12.5% CIPTEOS.

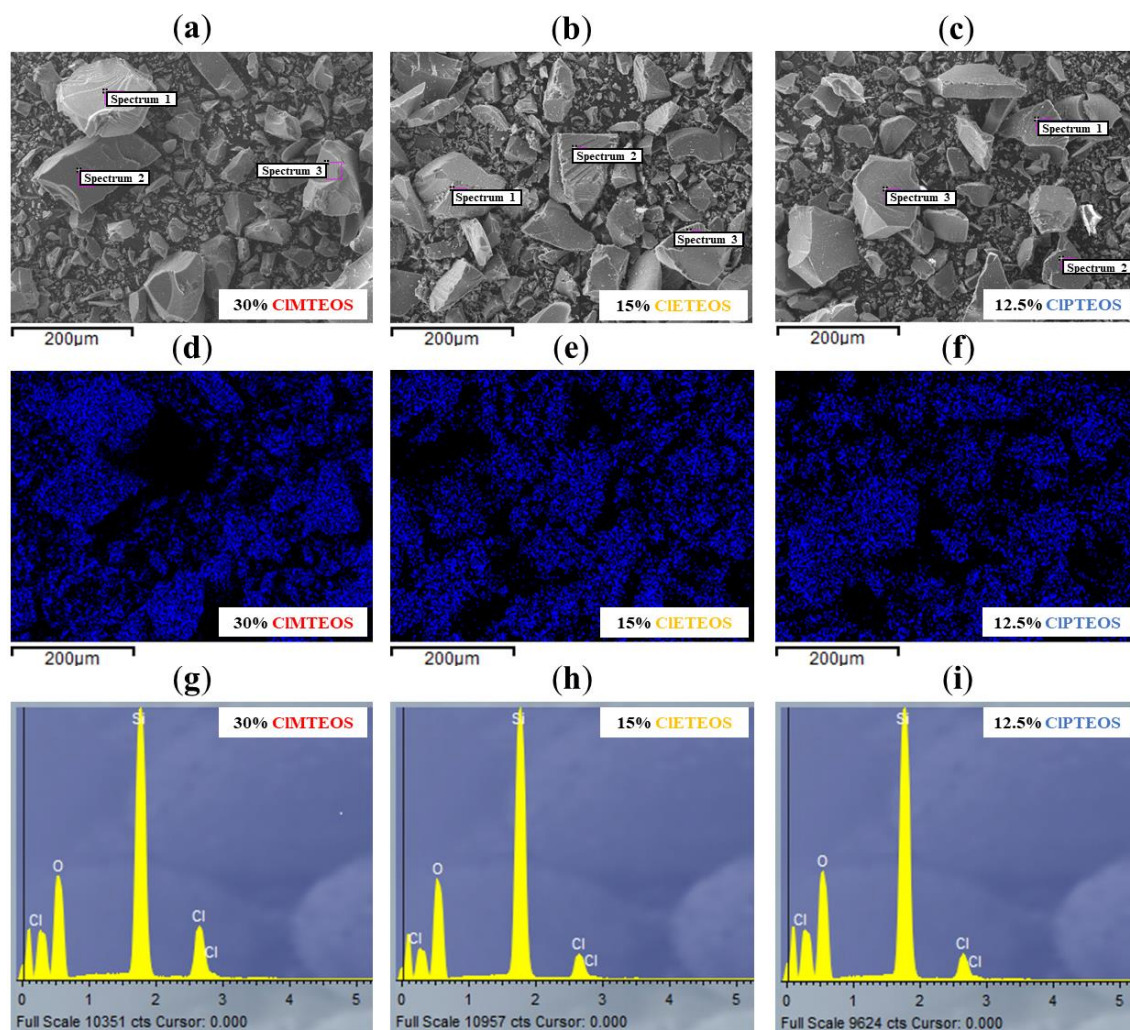


Figure 3.10. SEM micrographs of the chloroalkyl materials, (a-c) Distribution of chlorine atoms on the surface of xerogels obtained by applying EDX, (d-f) Sum of EDX spectra obtained by analyzing different points of the micrographs (g-i).

The reference material (Figure 3.9a) has a rough surface made up of globular particles that melt, giving it a scaly appearance. The particle diameter ranges from 110 to 150 nm, and the inter-particle spacing correlates with the narrow mesoporosity recorded by the isotherm [47]. Figure 3.11 depicts the micrographs of the lower molar percentages xerogels. The surface of the xerogel synthesised with 1% CIMTEOS (Figure 3.11a) is also formed by globular particles, which are smaller and difficult to detect. This morphological change results from both the increase in pore volume and the transition from cone to ink-bottle shaped pores. The surface particles fade with an increased molar percentage of CIMTEOS, which gives rise to thin layers that overlap and intersect, yielding a highly microporous and compact material in accordance with its isotherm (Type I(a)).

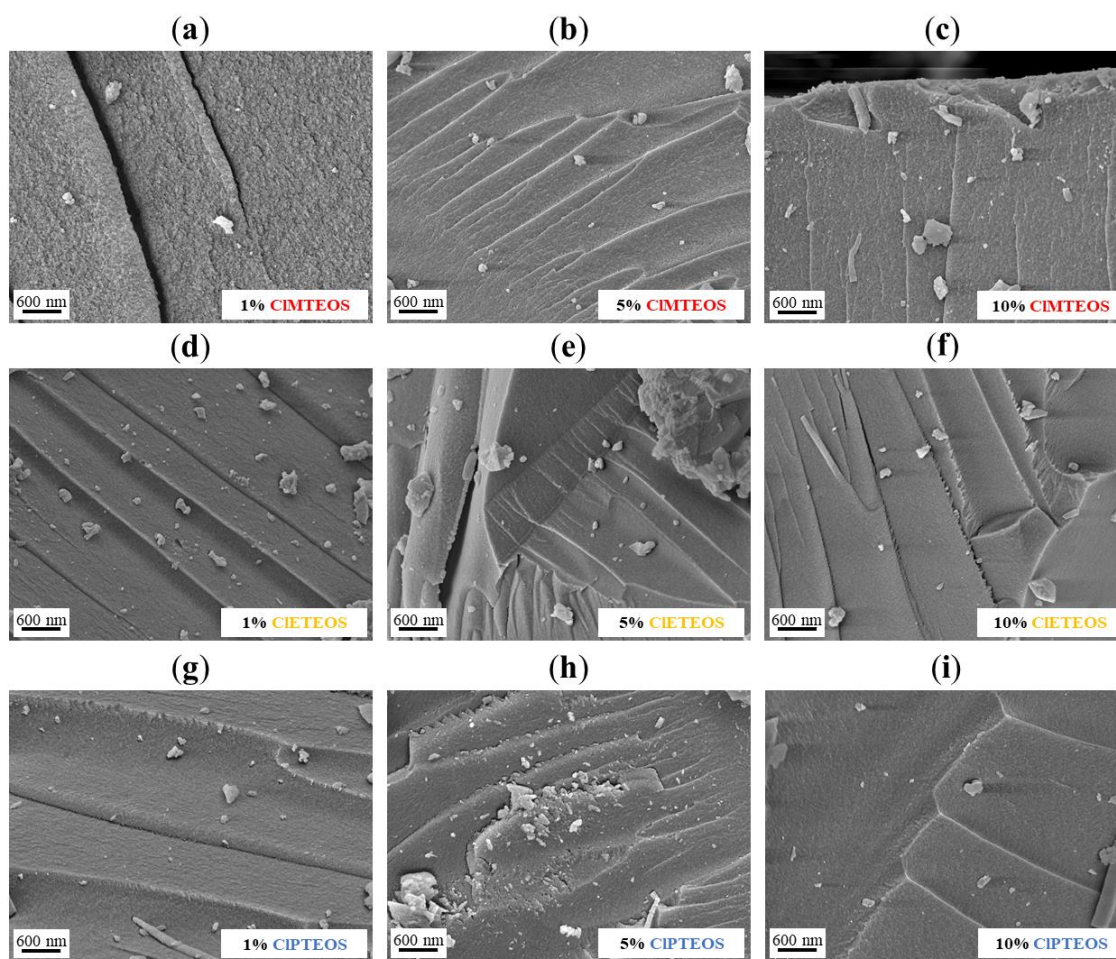


Figure 3.11. FE-SEM micrographs of (a-c) CIMTEOS:TEOS materials, (d-f) CIETEOS:TEOS materials, and (g-i) CIPTEOS:TEOS materials.

Micrographs of the CIETEOS series (Figure 3.9c and Figure 3.11d–f) show smooth flake-like surfaces consistent with the lack of N_2 adsorption of these xerogels. The same pattern is observed in the CIPTEOS series (Figure 3.9d and Figure 3.11g–i), although a larger amount of precursor is needed to bring about these changes.

In all three CIRTEOS series, the particle size decreases with higher percentages of the precursor. This effect is associated with the lower degree of triethoxysilane cross-linking in comparison to TEOS and with the nanostructuring generated to minimize the repulsion between colloids caused by the surface chloroalkyl groups. The decrease in particle size results in the formation of compact but less dense sheets that are responsible for the lower mesoporosity and lesser N_2 adsorption of these materials.

3.3 CONCLUSIONS

Hybrid CIRTEOS:TEOS xerogels were prepared at pH = 4.5 up to molar percentages of 35% (CIMTEOS) and 25% (CIETEOS and CIPTEOS). Signals of triethoxysilanes (T^n) in ^{29}Si NMR spectra confirm the presence of the chloroalkyl substituents in the silicon matrix, indicating the stability of Si–C bonds under the synthesis conditions used. These signals are mainly found for the most condensed species (T^3) in the CIMTEOS and CIETEOS series, observing a greater proportion of condensed species of TEOS, Q^3 , and Q^4 , with a higher percentage of the precursor. This predominance of the most condensed species is consistent with the presence of a signal at a small angle ($2\theta < 10^\circ$) in the XRD spectra and with the shortening of Si–O–Si bonds compared with their non-chlorinated analogues, indicating the presence of ordered domains constituted by tight and compact structures, such as short ladders and T_8 cages. The three series of xerogels show higher skeletal densities in comparison to their analogous non-chlorinated series due to the electronic and steric effects of the chloroalkyl precursor. With regard to the texture of the materials, FE-SEM micrographs show changes in their surface morphology from a granular to a smoother and more compact texture with higher precursor percentages. These modifications also reflect the decrease in N_2 and CO_2 adsorption capacity recorded by the isotherms with a higher percentage of precursor, allowing materials with different pore sizes to be tailored. XRD spectra show that the chloroalkyl moiety of the precursors more efficiently promotes the ordering of the local structure in comparison to the alkyl chain in their non-chlorinated analogues. Strikingly, a very small amount of precursor (1% molar percentage) is required in the CIETEOS series to induce periodic domains formed by well-defined ladders and T_8 cage-like structures, producing a significant change in both structural and textural properties with respect to the reference material. The synthesis of these new locally nanostructured hybrid materials with tunable porosities opens up a very promising path for their use in a wide range of applications such as membranes, conductive films, absorbents, catalysis, optoelectronics, and coatings for optical sensors.

3.4 ACKNOWLEDGMENTS

The authors gratefully acknowledge the financial support received from the Ministerio de Economía y Competitividad from Spain (Project MAT2016-78155-C2-2-R). G.C. is thankful to MINECO and “Ministerio de Ciencia, Investigación y

Universidades” of Spain government for the “Formación de Profesorado Universitario (FPU)” grant (FPU18/03467). M.E. is thankful to the “Departamento de Industria y Tecnología, Comercio y Trabajo” of Navarre Government for a grant. The authors would also like to acknowledge the use of the “Centro de Instrumentación Científico-Técnica” at the University of Jaén and UCTAI at the Public University of Navarre.

3.5 REFERENCES

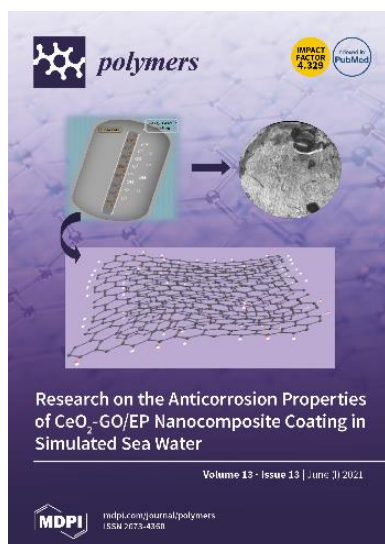
- [1] Judeinstein, P.; Sanchez, C. *J. Mater. Chem.* **1996**, *6*(4), p. 511–525.
- [2] Pastore, A.; Badocco, D.; Pastore, P. *Talanta* **2020**, *212*, p. 120739.
- [3] Gillanders, R. N.; Campbell, I. A.; Glackin, J. M. E.; Samuel, I. D. W.; Turnbull, G. A. *Talanta* **2018**, *179*, p. 426–429.
- [4] Li, Z.; Suslick, K. S. *ACS Appl. Mater. Interfaces* **2018**, *10*, p. 15820–15828.
- [5] Echeverría, J. C.; De Vicente, P.; Estella, J.; Garrido, J. J. *Talanta* **2012**, *99*, p. 433–440.
- [6] Echeverría, J. C.; Calleja, I.; Moriones, P.; Garrido, J. J. *Beilstein J. Nanotechnol.* **2017**, *8*, p. 475–484.
- [7] Niu, L.; Zhou, G.; Miao, X.; Yuan, X.; Kumar, R.; Liu, H.; Jiang, Y.; Zou, X.; Zhou, H.; Lü, H. *Adv. Condens. Matter Phys.* **2018**, *2018*, p. 1–6.
- [8] Shamir, D.; Elias, I.; Albo, Y.; Meyerstein, D.; Burg, A. *Inorg. Chim. Acta.* **2020**, *500*, p. 119225.
- [9] Ponamoreva, O. N.; Afonina, E. L.; Kamanina, O. A.; Lavrova, D. G.; Arlyapov, V. A.; Alferov, V. A.; Boronin, A. M. *Appl. Biochem. Microbiol.* **2018**, *54*, p. 736–742.
- [10] Lin, W.; Zhang, X.; Cai, Q.; Yang, W.; Chen, H. *Cellulose* **2020**, *27*, p. 7805–7821.
- [11] Liu, Z.; Tian, S.; Li, Q.; Wang, J.; Pu, J.; Wang, G.; Zhao, W.; Feng, F.; Qin, J.; Ren, L. *ACS Sustainable Chem. Eng.* **2020**, *8*, p. 6786–6797.
- [12] Scotland, K. M.; Shetranjiwalla, S.; Vreugdenhil, A. J. *J. Coat. Technol. Res.* **2020**, *17*, p. 977–989.
- [13] Bouvet-Marchand, A.; Graillet, A.; Abel, M.; Koudia, M.; Boutevin, G.; Loubat, C.; Grosso, D. *J. Mater. Chem. A* **2018**, *6*, p. 24899–24910.
- [14] Yue, D.; Feng, Q.; Huang, X.; Zhang, X.; Chen, H. *Coatings* **2019**, *9*, p. 556.
- [15] Malek, S. K.; Nodeh, H. R.; Akbari-Adergani, B. *J. Sep. Sci.* **2018**, *41*, p. 2934–2941.
- [16] Moriones, P.; Ríos, X.; Echeverría, J. C.; Garrido, J. J.; Pires, J.; Pinto, M. *Colloids Surf., A* **2011**, *389*, p. 69–75.
- [17] Zanut, A.; Palomba, F.; Rossi Scota, M.; Rebecani, S.; Marcaccio, M.; Genovese, D.; Rampazzo, E.; Valenti, G.; Paolucci, F.; Prodi, L. *Angew. Chem., Int. Ed.* **2020**, *59*, p. 21858–21863.

- [18] Meroni, D.; Ardizzone, S.; Cappelletti, G.; Ceotto, M.; Ratti, M.; Annunziata, R.; Benaglia, M.; Raimondi, L. *J. Phys. Chem. C* **2011**, *115*, p. 18649–18658.
- [19] Alemán, J.; Chadwick, A. V.; He, J.; Hess, M.; Horie, K.; Jones, R. G.; Kratochvíl, P.; Meisel, I.; Mita, I.; Moad, G.; *et al. Pure Appl. Chem.* **2007**, *79*, p. 1801–1829.
- [20] Rios, X.; Moriones, P.; Echeverría, J. C.; Luquín, A.; Laguna, M.; Garrido, J. J. *Adsorption* **2011**, *17*, p. 583–593.
- [21] Rios, X.; Moriones, P.; Echeverría, J. C.; Luquin, A.; Laguna, M.; Garrido, J. J. *Mater. Chem. Phys.* **2013**, *141*, p. 166–174.
- [22] Moriones, P. *Síntesis y Caracterización de Xerogeles Silíceos Híbridos (RTEOS/TEOS; R = P, Ph)*. Universidad Pública de Navarra: Pamplona, Spain, **2015**. Available online: <https://academica-e.unavarra.es/handle/2454/20351> (accessed on 14 November 2020).
- [23] Chemtob, A.; Ni, L.; Croutxé-Barghorn, C.; Boury, B. *Chem. - Eur. J.* **2014**, *20*, p. 1790–1806.
- [24] Chen, Y.; Shi, J. *Adv. Mater.* **2016**, *28*, p. 3235–3272.
- [25] Clara Gonçalves, M. *J. Sol-Gel Sci. Technol.* **2015**, *75*, p. 508–518.
- [26] Ramezani, M.; Vaezi, M. R.; Kazemzadeh, A. *Appl. Surf. Sci.* **2015**, *326*, p. 99–106.
- [27] Estella, J.; Echeverría, J. C.; Laguna, M.; Garrido, J. J. *J. Non-Cryst. Solids* **2007**, *353*, p. 286–294.
- [28] Estella, J.; Echeverría, J. C.; Laguna, M.; Garrido, J. J. *Microporous Mesoporous Mater.* **2007**, *102*, p. 274–282.
- [29] Flores-López, S. L.; Villanueva, S. F.; Montes-Morán, M. A.; Cruz, G.; Garrido, J. J.; Arenillas, A. *Colloids Surf., A* **2020**, *604*, p. 125248.
- [30] Yoshitake, H.; Kodate, T.; Takagi, T.; Kawamura, I.; Naito, A. *React. Funct. Polym.* **2016**, *99*, p. 9–16.
- [31] Zacca, M. J.; Laurencin, D.; Richeter, S.; Clément, S.; Mehdi, A. *Molecules* **2018**, *23*, p. 2510.
- [32] Ospino, I.; Luquin, A.; Jiménez-Ruiz, M.; Pérez-Landazábal, J. I.; Recarte, V.; Echeverría, J. C.; Laguna, M.; Urtasun, A. A.; Garrido, J. J. *J. Phys. Chem. C* **2017**, *121*, p. 22836–22845.
- [33] Tran, J. A.; Shea, K. J.; Loy, D. A. *J. Mater. Sci.* **2014**, *49*, p. 5006–5016.
- [34] Siritwong, C.; Sae-Oui, P.; Sirisinha, C. *Polym. Test.* **2014**, *38*, p. 64–72.
- [35] Chen, G.; Zhou, Y.; Wang, X.; Li, J.; Xue, S.; Liu, Y.; Wang, Q.; Wang, J. *Sci. Rep.* **2015**, *5*, p. 1–14.
- [36] Sun, Y.; Zhang, Z. *Metall. Mater. Trans. B* **2015**, *46*, p. 1549–1554.
- [37] El Felss, N.; Gharzouni, A.; Colas, M.; Cornette, J.; Sobrados, I.; Rossignol, S. *J. Sol-Gel Sci. Technol.* **2020**, *96*, p. 265–275.

- [38] Park, E. S.; Ro, H. W.; Nguyen, C. V.; Jaffe, R. L.; Yoon, D. Y. *Chem. Mater.* **2008**, *20*, p. 1548–1554.
- [39] Uhlig, F.; Marsman, H. C. ²⁹Si NMR - Some Practical Aspects. In *Gelest catalogue*; Gelest INC, Morrisville, PA. USA, **2008**, p. 208–222. Available online: <https://www.pascal-man.com/periodic-table/29Si.pdf> (accessed on 14 November 2020).
- [40] Vasil'ev, S. G.; Volkov, V. I.; Tatarinova, E. A.; Muzafarov, A. M. *Appl. Magn. Reson.* **2013**, *44*, p. 1015–1025.
- [41] Ivanovski, V.; Mayerhöfer, T. G.; Kriltz, A.; Popp, J. *Spectrochim. Acta, Part A* **2017**, *173*, p. 608–617.
- [42] Park, S.; Kim, J. Y.; Choi, W.; Lee, M. J.; Heo, J.; Choi, D.; Jung, S.; Kwon, J.; Choi, S. H.; Hong, J. *Chem. Eng. J.* **2020**, *393*, p. 124686.
- [43] Li, Q.; Guo, L.; Qiu, T.; Ye, J.; He, L.; Li, X.; Tuo, X. *Prog. Org. Coat.* **2018**, *122*, p. 19–29.
- [44] Thommes, M.; Kaneko, K.; Neimark, A. V.; Olivier, J. P.; Rodriguez-Reinoso, F.; Rouquerol, J.; Sing, K. S. W. *Pure Appl. Chem.* **2015**, *87*, p. 1051–1069.
- [45] Dudás, Z.; Len, A.; Ianăși, C.; Paladini, G. *Mater. Charact.* **2020**, *167*, p. 33–36.
- [46] Echeverría, J. C.; Estella, J.; Barbería, V.; Musgo, J.; Garrido, J. J. *J. Non-Cryst. Solids* **2010**, *356*, p. 378–382.
- [47] Liu, Q.; Zhang, J.; Sun, W.; Xie, Q. R.; Xia, W.; Gu, H. *Int. J. Nanomed.* **2012**, *7*, p. 999–1013.

CHAPTER 4

“HYBRID XEROGELS: STUDY OF THE SOL-GEL PROCESS AND LOCAL STRUCTURE BY VIBRATIONAL SPECTROSCOPY”



Published article

Authors: Guillermo Cruz-Quesada, Maialen Espinal-Viguri, María Victoria López-Ramón and Julián J. Garrido

Reference: *Polymers* **2021**, *13*(13), p. 2082.
Doi: 10.3390/polym13132082

Publication date: 06/24/2021

Keywords: ORMOSILs; xerogels; hybrid materials; chloroalkyltriethoxysilanes; inductive effect; (SiO)_x structures; FTIR.

Abstract: The properties of hybrid silica xerogels obtained by the sol-gel method are highly dependent on the precursor and the synthesis conditions. This study examines the influence of organic substituents of the precursor on the sol-gel process and determines the structure of the final materials in xerogels containing tetraethyl orthosilicate (TEOS) and alkyltriethoxysilane or chloroalkyltriethoxysilane at different molar percentages (RTEOS and CIRTEOS, R = methyl [M], ethyl [E], or propyl [P]). The intermolecular forces exerted by the organic moiety and the chlorine atom of the precursors were elucidated by comparing the sol-gel process between alkyl and chloroalkyl series. The microstructure of the resulting xerogels was explored in a structural theoretical study using Fourier-transformed infrared spectroscopy and deconvolution methods, revealing the distribution of (SiO)₄ and (SiO)₆ rings in the silicon matrix of the hybrid xerogels. The results demonstrate that the alkyl chain and the chlorine atom of the precursor in these materials determine their inductive and steric effects on the sol-gel process and, therefore, their gelation times. Furthermore, the distribution of (SiO)₄ and (SiO)₆ rings was found to be consistent with the data from the X-ray diffraction patterns, which confirm that the local periodicity associated with four-fold rings increases with higher percentage of precursor. Both the sol-gel process and the ordered domains formed determine the final structure of these hybrid materials and, therefore, their properties and potential applications.

4.1 INTRODUCTION

Organically modified silicon xerogels (ORMOSILs) are attracting considerable interest for their application in new-generation technologies, being utilized in chemical and optical sensors [1–6], for catalysis [4,5], in coatings [6–10], for chromatography [11,12], and in pharmacy [13]. They have great chemical versatility and can be efficiently modified for specific applications due to their combination of highly varied mechanical, optical and textural properties [14].

The sol-gel method is the most widely used approach to the synthesis of hybrid silicon xerogels (see *Annexe A*). It is based on co-condensation between monomers of traditional alkoxides ($\text{Si}(\text{OR})_4$) such as tetramethoxy- or tetraethoxysilane (TEOS and TMOS, respectively) and one or more mono-, di- or trialkoxysilanes ($\text{R}_x\text{Si}(\text{OR}')_{4-x}$) [15]. In hybrid xerogels, the addition of organic molecules or functional groups in the silica network restricts the three-dimensional growth of the material and blocks a condensation position, favouring the preferential formation of $(\text{SiO})_4$ and $(\text{SiO})_6$ rings in the amorphous structure of the silica materials [16,17] and even leading to the formation of structures with a higher degree of order [18]. However, although the sol-gel process has been widely studied [19], some questions have yet to be adequately settled. For instance, multiple reactions take place simultaneously in the process, making it difficult to extract information from experimental procedures [20]. To date, many studies have attempted to elucidate the influence of precursors on the hydrolysis, condensation reactions, and crosslinking by applying different characterization and analysis techniques, including gas chromatography (GC) [21], nuclear magnetic resonance ^{29}Si NMR [22,23], Raman spectroscopy [24], and Fourier transform infrared spectroscopy (FTIR) [25,26]. Among these approaches, FTIR not only provides complementary information on the bonds and structures formed during the synthesis process but also, when combined with deconvolution methods, yields valuable data on the microstructure of siliceous materials [27–29]. Knowledge obtained by these means is of major interest because it allows for the prediction of: (i) the physical properties of xerogels derived from their structure [30]; (ii) the catalytic activity of metals supported in silica matrices [31]; and (iii) the correlation of the silica species in the membrane of a fibre optic sensor with its efficacy [32].

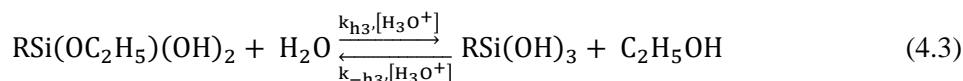
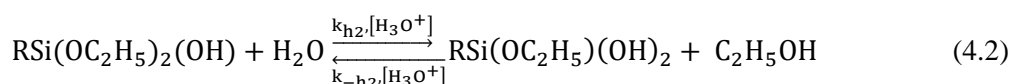
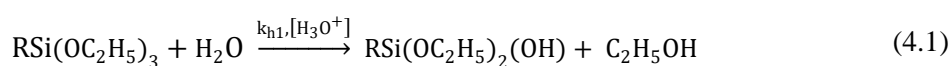
The ultimate application of these materials is as membranes in fibre optic sensors, on which the analyte is specifically and reversibly adsorbed. Physisorption of the analyte on the surface of the material generates a modification of the refractive index and produces a change in the reflected optical power, which determines the analyte concentration in the medium. For this reason, it is important to prepare materials with different porosities and surface chemistries in which the interaction between the membrane (chemical area of a sensor) and the analyte is specific and labile. To date, our research group has prepared membranes with hybrid xerogels obtained using different molar ratios of TEOS:RTEOS (R = methyl or phenyl) [33,34]. Given the results obtained and following this line of reasoning, the addition of a chlorine atom to the organic moiety of a silane emerged as a highly appealing approach because of the inductive effects of the chlorine, which generates a more active chemical surface and favours functionalization with other compounds. For these reasons, CIRTEOS precursors were used to synthesize three series of xerogels analogous to those prepared in previous studies [35].

The objective of this study was to determine the influence of the alkyl and chloroalkyl substituents of the precursors on: (i) the gelation time, and (ii) the microstructure of the synthesised materials, obtained by deconvolution of the FTIR spectra. The study used six series of hybrid xerogels prepared (in previous studies) with tetraethoxysilane (TEOS) and a chloroalkyl or alkyl precursor at different molar percentages (CIRTEOS or RTEOS: R = methyl [M], ethyl [E]; and propyl [P]) [35–38]. Theoretical study of the deconvolution of the band at 1300–980 cm^{-1} in the FTIR spectra yielded semi-quantitative information on the proportion of $(\text{SiO})_4$ and $(\text{SiO})_6$ rings related to periodic structural domains and amorphous silica, respectively. This allows the local internal order of materials to be determined and the influences of the organic substituent and chlorine atom to be predicted. The ultimate application of these materials is as membranes in fibre optic sensors, constituting the chemical area of the sensor, where the analyte is specifically and reversibly adsorbed. Physisorption of the analyte on the surface of the material generates a modification of the refractive index and produces a change in the reflected optical power, which determines the analyte concentration in the medium. This study is of crucial importance because: (i) precise knowledge of the gelation time is essential to effectively impregnate the fibres [33,34], and (ii) complete characterization of the xerogels allows prediction, to a large extent, of their properties and the a priori selection of the xerogel best suited to the characteristics of the analyte of interest [32].

4.2 RESULTS AND DISCUSSION

4.2.1 Influence of organochlorine substituents on gelation time

The gelation time (t_g) is the period between the initial mixture of reagents and the formation of the gel; it comprises hydrolysis, condensation, and gelation (stabilization of colloids and crosslinking) stages, with gelation being the limiting stage [39]. Density functional theory (DFT) studies of TEOS in acidic media showed that the overall process of hydrolysis presents a pseudo-first order mechanism (SN_1) with lesser energy barriers in comparison to condensation [20]. Moreover, each consecutive hydrolysis reaction presents a barrier with less energy, which is consistent with the hydrolysis rates observed in ^{29}Si NMR experiments on various organoalkylsilanes [23]. The hydrolysis reactions of RTEOS are described in the following equations:



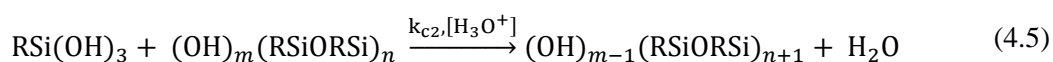
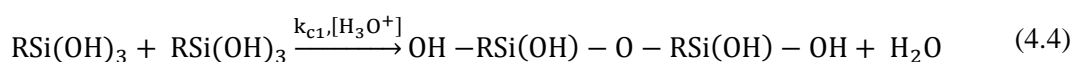
Reaction rates in the acidic hydrolysis of triethoxysilanes depend on the competition between the steric hindrance and inductive effects of the organic moieties [16]. The reaction rate decreases with an increase in the volume of the organic moiety [40], while electron donating groups (+I) stabilize the pentacoordinated transition state and increase the electronic charge of the ethoxide in the hybrid precursor, facilitating the attack of the acidic proton (Equations 4.1–4.3) [20,41]. In previous studies, it was confirmed that the hydrolysis rates increase with a longer alkyl chain in the precursor due to the enhanced inductive effect of the moieties [23]. Given that chloroalkyltriethoxysilanes contain chlorine, an electron withdrawing group (–I), hydrolysis rates are expected to be lower than their non-chlorinated analogues, as can be deduced from the partial charges of the ethoxide groups (δ_{OEt} values of Table 4.1).

Table 4.1. Electronegativities and partial charges of the chloroalkyl precursors and their alkyl analogues calculated from the Pauli electronegativities and application of the equations of Livage and Henry [42].

Precursor	R	X	δ_{Si}	δ_{R}	δ_{OEt}
TEOS	OC ₂ H ₅	2.32	0.32	-	-0.08
MTEOS	CH ₃	2.29	0.31	0.20	-0.17
ETEOS	C ₂ H ₅	2.29	0.31	0.28	-0.20
PTEOS	C ₃ H ₇	2.28	0.30	0.35	-0.22
CIMTEOS	CH ₂ Cl	2.32	0.32	-0.09	-0.08
CIETEOS	C ₂ H ₄ Cl	2.31	0.32	0.02	-0.11
CIPTEOS	C ₃ H ₆ Cl	2.30	0.31	0.11	-0.14

X—molecule electronegativity; δ —partial charge.

However, the condensation reactions determine the overall speed of the gelation process. The following equations exhibit the S_N2 mechanism for the first and consecutive acidic condensation reactions of RTEOS:



In contrast to the hydrolysis reactions (Equations 4.1–4.3), the first condensation between hydrolysed molecules is kinetically favoured (Equation 4.4), leading initially to the formation of long and slightly branched chains and subsequently to intra-molecular condensations and cyclization [16,43,44]. The successive condensations (Equation 4.5) form the polymeric network and the first colloidal particles (10–100 nm), which give rise to a spontaneous and homogeneous nucleation process when their critical radius is reached. It should be noted that gelation of the hybrid material is slower because triethoxysilanes have only three potential directions of polymerization. Unlike in the hydrolysis process, where the more the substituent of the precursor is withdrawn, the more favoured is the condensation, because it favours nucleophilic attack on the silicon atom of a neighbouring molecule. In this way, the condensation rate increases in the order MTEOS > ETEOS > PTEOS for the alkyl series and CIMTEOS > CIETEOS > CIPTEOS for the chloroalkyl series. In addition, chloroalkyl groups restrict the crosslinking between oligomers due to electrostatic repulsions, which destabilize the colloids and prevent the gelling process above a given molar percentage. Thus, it was possible to synthesize hybrid xerogels with molar percentages of up to 35%, 25% and 25% for the chloroalkyl series (CIMTEOS, CIETEOS and CIPTEOS, respectively (the synthesis procedure is described

in *Chapter 2.1.1.* and the images of the monoliths are shown in Figure 4.1), while the molar percentages were substantially higher for the alkyl series [36–38].

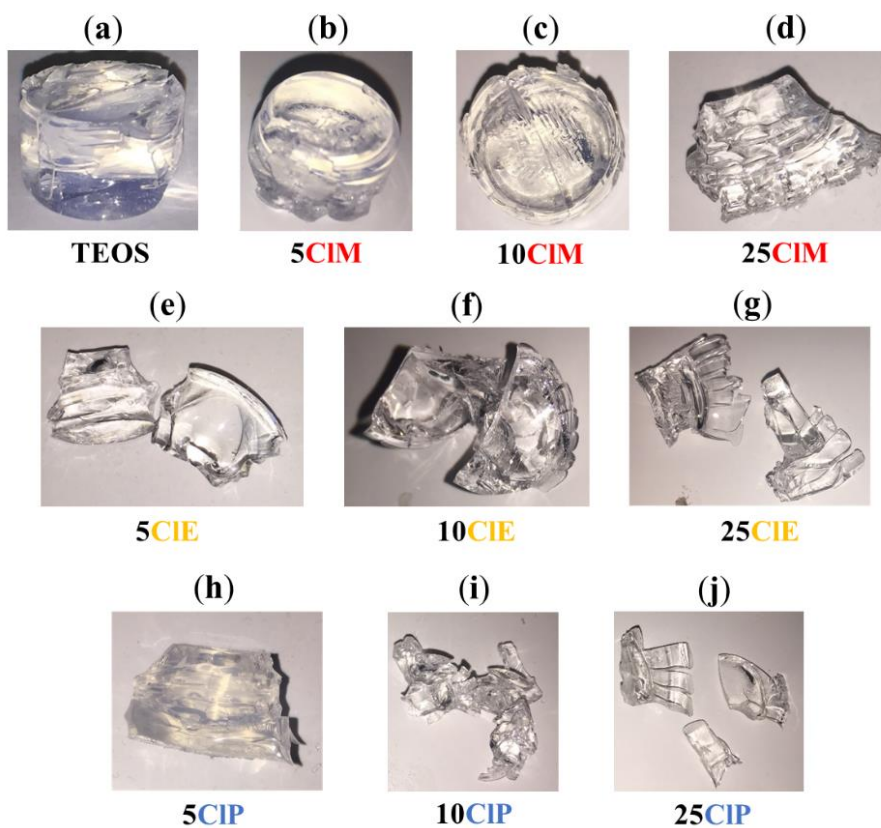


Figure 4.1. Images of the synthesised xerogels where a change in morphology is observed with an increasing percentage of organic precursors: (a) TEOS, (b-d) CIMTEOS, (e-g) CIETEOS, and (h-j) CIPTEOS.

Hence, regarding the gelation times of the synthesised materials, there is a balance between the inductive/steric effects of the organic substituents of the precursor and the electrostatic effect between colloids. This electrostatic effect was a determining factor in the gelation times of chloroalkyl xerogels with a high percentage of precursor, due to the chlorine atom. The corresponding data are displayed in Figure 2a, which depicts the variation in gelation times of the chloroalkyl xerogels as a function of the molar percentage of precursor. It should be noted that gelation times for percentages higher than 10% have been omitted for the CIPTEOS series because they do not follow the trend observed for 0 to 10 molar percentages due to the limitations imposed by steric and electrostatic factors. In all cases, an increase in the molar percentage lengthens the gelation time, and this trend is also observed in xerogels prepared with analogous alkyl precursors, as shown in Figure 2b [36–38]. Figure 2c compares gelation times between the chloroalkyl xerogels and their non-chlorinated analogues, showing that the effect of the chlorine atom is more pronounced in the CIETEOS and CIPTEOS series, besides being opposite to the effect in the CIMTEOS series. This is because the alkyl chain is longer in the CIETEOS and CIPTEOS, increasing the steric effect and the repulsions between colloids created by the chlorine atom, which markedly lengthens the gelation time in comparison to their analogous non-chlorinated series. The chain is shorter in the CIMTEOS series; therefore, the steric effect is less pronounced and the repulsion between colloids is lower, favouring crosslinking in comparison to the longer chain chloroalkyl series. Furthermore, the withdrawing effect of the chlorine atom on the adjacent silicon atom is maximized, favouring condensation. Accordingly, the gelation times for the CIMTEOS series are reduced with respect to the analogous non-chlorinated series.

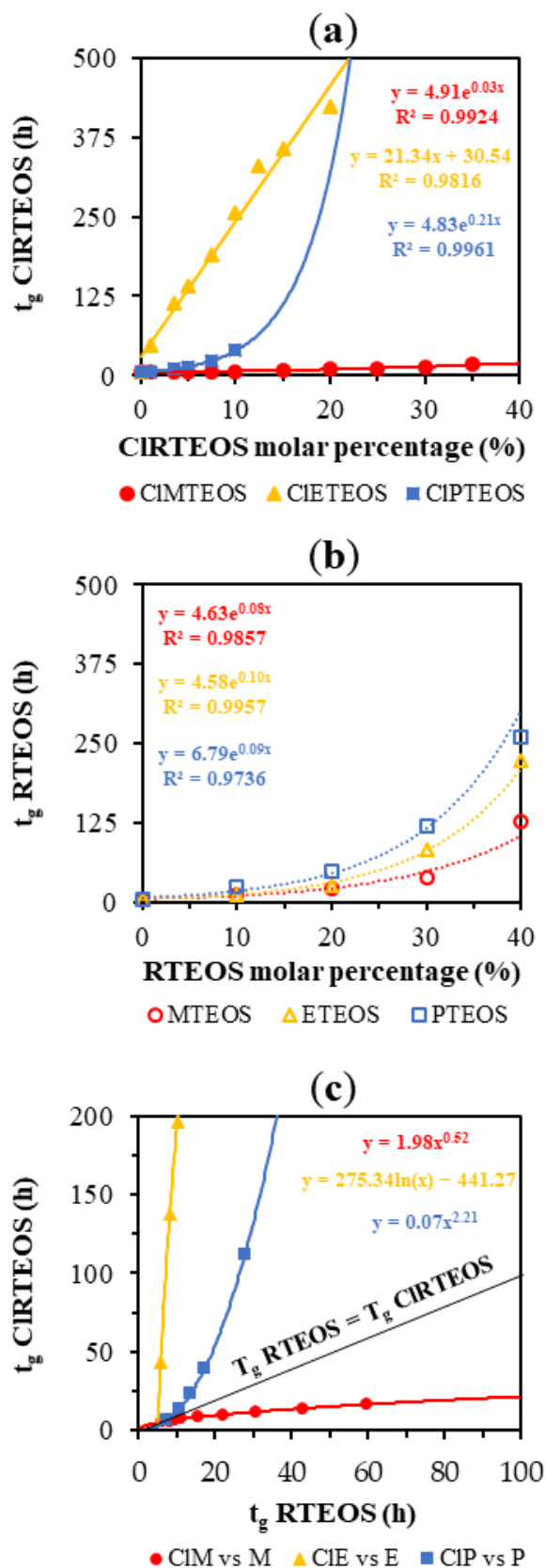


Figure 4.2. (a) t_g as a function of the percentage of precursor in the TEOS:CIRTEOS series, (b) t_g as a function of the percentage of precursor in the TEOS:RTEOS series, and (c) t_g of the CIRTEOS versus RTEOS series.

It should be noted that t_g values are higher for the CIETEOS series than for the other two chloroalkyl series and fit a linear rather than exponential trend (Figure 2a). This is because the length of the chloroethyl chain is not as short as in the CIMTEOS series or as long as in the CIPTEOS series, which has greater flexibility and freedom of movement. As demonstrated below, the behaviour of this substituent is different because its size and nature necessarily place it in the network at fixed positions, minimizing repulsions. The lack of freedom of movement hinders and slows crosslinking, markedly increasing gelation times and forming periodic structures that create ordered domains in the silica network, as explained below.

4.2.2 Study of the local structure of hybrid xerogels using FTIR and XRD

Figure 4.3 depicts, as an example, the FTIR spectra of the three chloroalkyl series with a 20% molar percentage of the precursor in two wavelength ranges: (i) 4000–2750 cm^{-1} and (ii) 1600–400 cm^{-1} . Whereas Figure 4.4 shows the spectra obtained for the xerogels prepared with different molar percentages of chloroalkyl precursor in each series. The different modes of vibration are reported in Table 4.2 with corresponding citations from the literature.

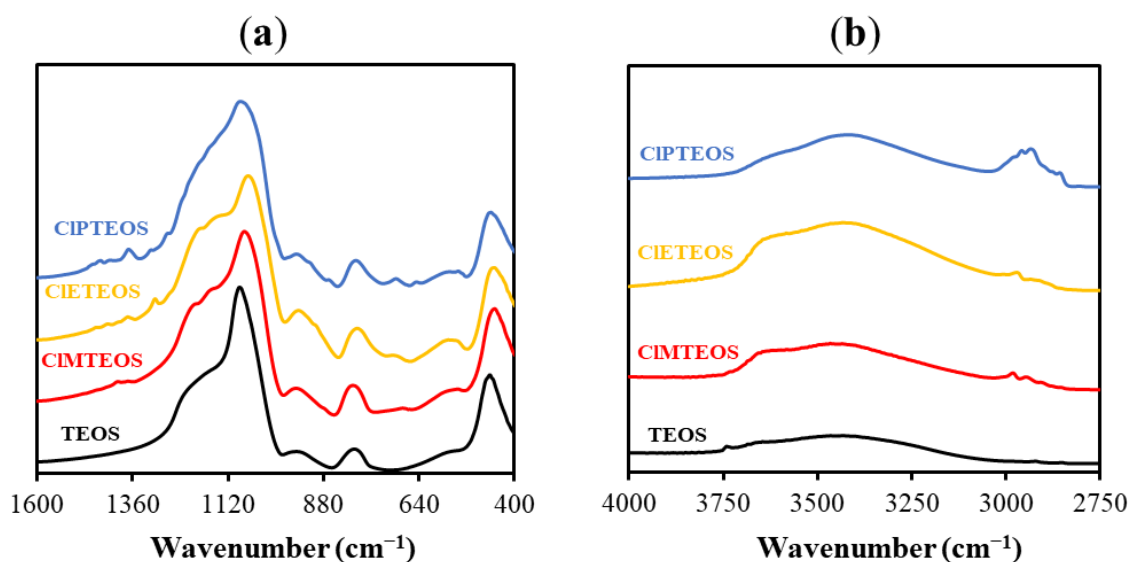


Figure 4.3. FTIR spectra of xerogels synthesised with a 20% molar percentage of precursor in the range of (a) 1600–400 cm^{-1} and (b) 4000–2750 cm^{-1} .

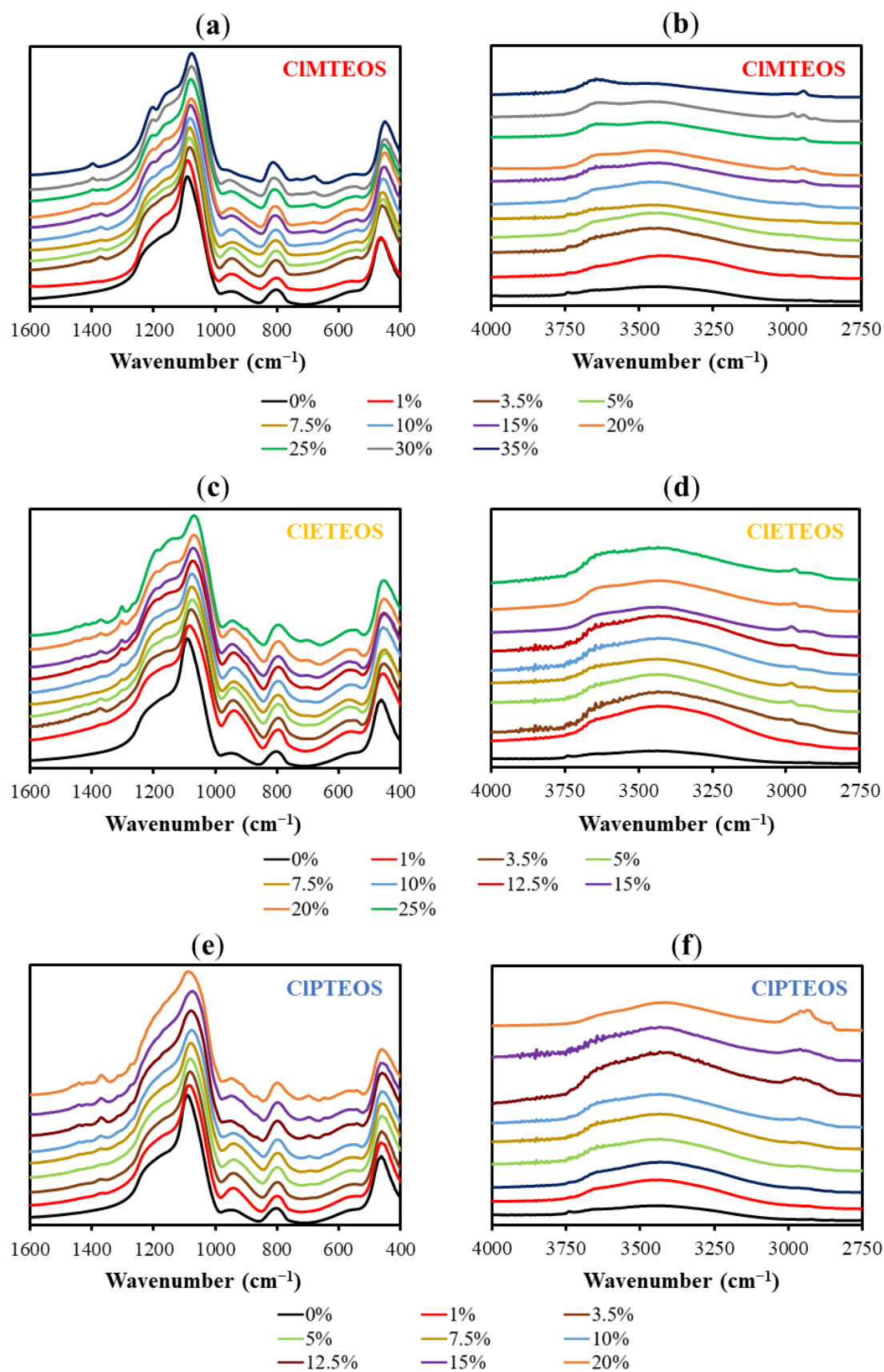


Figure 4.4. FTIR spectra of the CIRTEOS:TEOS xerogels in the ranges of 1600–400 and 4000–2750 cm^{-1} : (a,b) CIMTEOS, (c,d) CIETEOS, and (e,f) CIPTEOS.

Table 4.2. FTIR spectra band assignment of spectra of figures 4.3 and 4.4.

Wave number (cm ⁻¹)	Type of vibration	Structural unit	References
3645	ν (OH-H)	SiO-H	[45]
3465	ν (OH-H)	SiO-H (H-Bridge)	[45]
2980	ν_{as} (C-H)	CH ₃ /CH ₂ -Cl	[35-38]
2945	ν_{as} (C-H)	CH ₃ /CH ₂ -Cl	[35-38]
2928	ν_{as} (C-H)	CH ₂	[35-38]
2900	ν_{s} (C-H)	CH ₃ /CH ₂ -Cl	[35-38]
2850	ν_{s} (C-H)	CH ₂	[35-38]
1640	δ (O-H)	H ₂ O	[46]
1480	τ (C-H)	CH ₃ /CH ₂ -Cl	[46]
1445	τ (C-H)	R-CH ₂ -R	[46]
1420	τ (C-H)	Si-CH ₂ -R	[46]
1395	δ (C-H)	CH ₃ /CH ₂ -Cl	[46-48]
1370	δ (C-H)	CH ₃ /CH ₂ -R	[46,47]
1310	δ (C-H)	Si-CH ₂ -R	[46-48]
1270	ω (C-H)	CH ₃ /-CH ₂ -Cl	[46-48]
1180	ω (C-H)	Si-CH ₂ -Cl	[46-48]
1200	ν_{as} (Si-O-Si mode LO)	$\equiv\text{Si-O-Si}\equiv$	[27,49]
1150	ν_{as} (Si-O-Si)	$\equiv\text{Si-O-Si}\equiv$ (T ₈)	[50]
1090	ν_{as} (Si-O-Si mode TO)	$\equiv\text{Si-O-Si}\equiv$	[27,45,49]
955	ν (Si-O)	$\equiv\text{Si-O-H/}\equiv\text{Si-O-}$	[27,47]
915	ν (C-C)	Si-CH ₂ -CH ₂ -R	[47]
865	ν (C-C)	R-CH ₂ -CH ₂ -Cl	[47]
800	ν_{s} (Si-O)	$\equiv\text{Si-O-Si}\equiv$	[45]
735	ν_{as} C-Cl	CH ₂ -Cl	[49,50]
680	ν_{s} C-Cl	CH ₂ -Cl	[46,48]
560	ν Si-O	Si-O ₂ (T ₄)	[50]
455	ρ Si-O	O-Si-O	[45,47]

ν —stretching vibration; ν_{s} —symmetric stretching; ν_{as} —antisymmetric stretching; δ —bending; τ —twisting; ω —wagging; ρ —rocking; LO—longitudinal optical; TO—transverse optical; T₈—cubic octamer; T₄—four-fold siloxane rings.

Figure 4.3a depicts the characteristic FTIR bands of the silica lattice: (i) rocking of O–Si–O (ρ O–Si–O) at 455 cm^{-1} , (ii) symmetric stretching vibration of Si–O–Si (ν_s Si–O–Si) at 800 cm^{-1} , (iii) stretching of the Si–O bond belonging to surface silanes (ν_s Si–OH) at 955 cm^{-1} , (iv) asymmetric stretching vibration Si–O–Si at 1090 cm^{-1} (ν_{as} Si–O–Si), and (v) a broad and intense shoulder at 1200 cm^{-1} related to various modes of vibration of the Si–O–Si bonds [51]. Additionally, materials synthesised using silsesquioxanes typically show a set of Si–O–Si vibrations belonging to different structures: (i) bicyclic species at 1007 cm^{-1} , (ii) linear species at 1020 cm^{-1} , and (iii) cyclic species at 1050 cm^{-1} [52]. As can be observed in the figure, bands associated with bicyclic and linear species do not appear to overlap with the band at 1090 cm^{-1} , indicating that these structures are present in lower proportions than are the cyclic structures. Figure 4.3b displays the bands of isolated (or non-interacting) surface silanols and silanols interacting by hydrogen bonds at 3660 cm^{-1} and 3450 cm^{-1} , respectively. These bands, which are also characteristic of silicon xerogels, indicate the hydrophobic or hydrophilic nature of the material [53]. In addition to the aforementioned bands, a shoulder is observed at 550 cm^{-1} in all spectra, associated with the presence of 4-membered siloxane rings, $(\text{SiO})_4$ [45,50], which is consistent with the aforementioned assumption of the predominance of cyclic species.

The presence of organic groups in these hybrid materials is revealed by the bond vibrations of the alkyl chain: (i) C–H, (ii) C–C; and (iii) C–Cl. In Figure 4.3b, the characteristic bands of symmetric and asymmetric stretching of C–H are clearly observed between 2890 and 2975 cm^{-1} , showing an increase in intensity with longer chain length from being practically null in TEOS to being readily identifiable in CIPTEOS. The same can be seen in Figure 4.3a for the region between 1250 and 1400 cm^{-1} , which shows the bands of deformation modes related to C–H bonds (δ C–H) [46]. The symmetric stretching band C–C (ν_s C–C) of chloroethyl was detected in CIETEOS series at 900 cm^{-1} [47], while two well-differentiated bands were detected at 920 and 870 cm^{-1} in the CIPTEOS series, corresponding to the C–C bond contiguous to the chlorine and silicon atom, respectively (Table 4.2). This figure also depicts C–Cl stretching vibration bands (ν C–Cl) in the region between 750 and 650 cm^{-1} [47,48], with an increased intensity at higher molar percentages of CIRTEOS, as expected (Figure 4.4). It should be noted that it was not possible to detect the spectral band of the wagging vibration of the Si–CH₂ bond (ω C–H) in the region between 1300 and 980 cm^{-1} and the band corresponding to

the out-of-plane deformation of the Si–C bond due to overlap with the frequencies of the bending vibration of the Si–O bond at 800 cm^{-1} . However, both vibrations can be clearly observed in the attenuated total reflection (ATR) spectrum of the pure precursor (Figure 4.5).

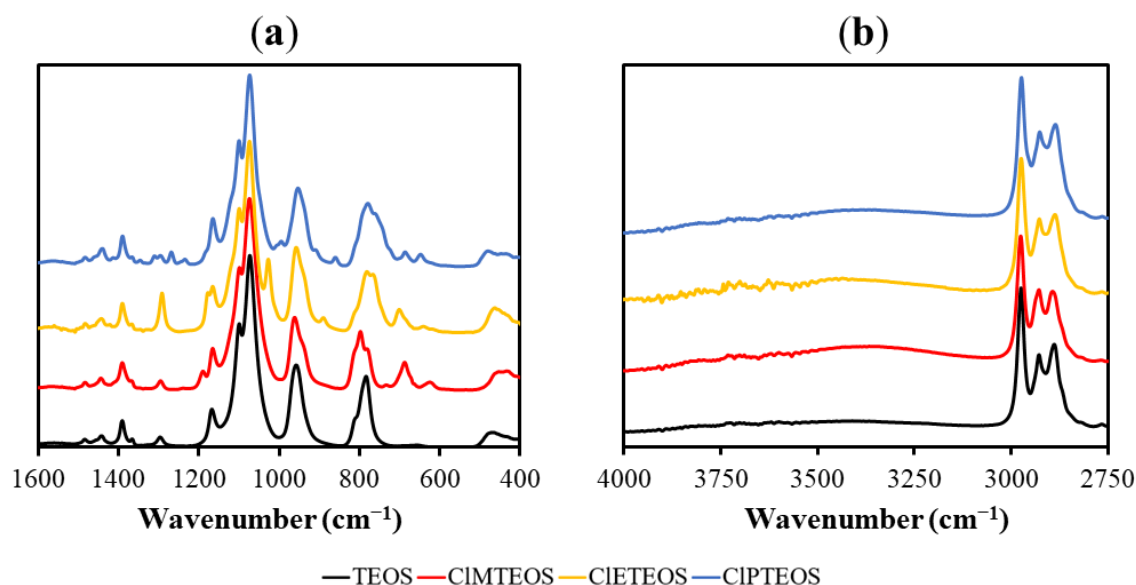


Figure 4.5. FTIR-ATR spectra of the precursors (TEOS, CIMTEOS, CIETEOS and CIPTEOS) in the ranges: (a) $1600\text{--}400\text{ cm}^{-1}$ and (b) $4000\text{--}2750\text{ cm}^{-1}$.

In the alkyl series previously studied by our research group (RTEOS:TEOS, R = M, E or P), a splitting of the band is observed at high percentages of alkyl precursor, moving the original band to lower frequency values due to the inductive effect of alkyl groups [36–38]. In the ETEOS series, for example, the band at 1092 cm^{-1} shifts to 1043 cm^{-1} and a new band appears at 1128 cm^{-1} , increasing its relative absorbance with a higher molar percentage of ETEOS. The appearance of this band is related to the presence of highly symmetric structures within the amorphous silica matrix (Figure 4.6). These structures comprise four-membered silicon rings $(\text{SiO})_4$ and are described as closed or open cages (T_8 and T_7 , respectively) and short ladders [48,54]. The intensity of this new band increases with a higher molar percentage of the chloroalkyl precursor due to the stabilisation of the rings $(\text{SiO})_4$ and the minimisation of the electrostatic repulsions produced by the chlorine atoms. In the chloroalkyl series, the asymmetric Si–O–Si vibration also shifts towards lower frequency values with an increased proportion of the precursor. The bands are not resolved in this case because the molar percentage reached is lower than in the alkyl series; instead, shoulders are observed at around 1200 cm^{-1} .

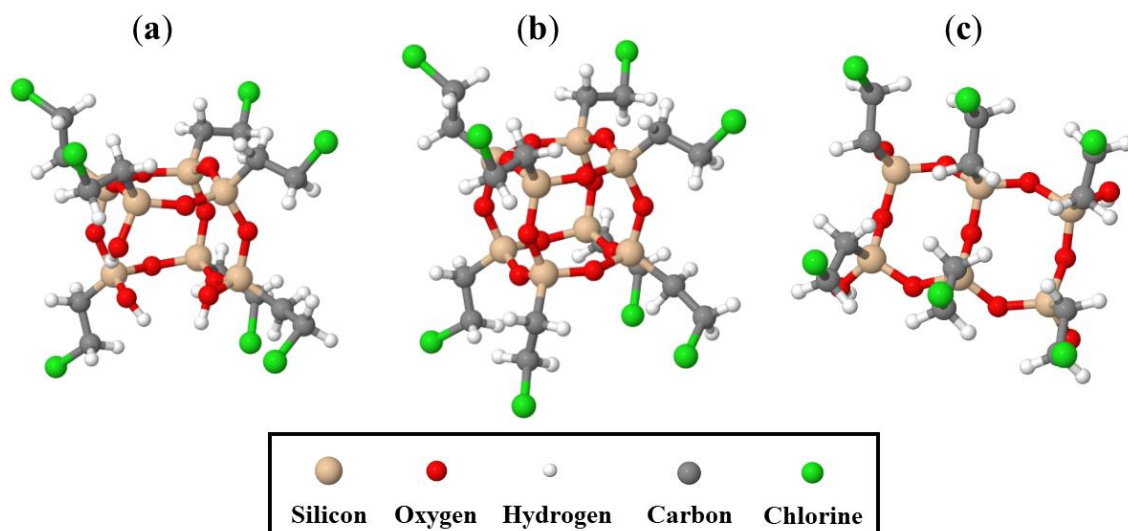


Figure 4.6. Ordered structures in the silica matrix built by $(\text{SiO})_4$ rings in CIETEOS as an example: (a) open cage (T_7), (b) cage (T_8), and (c) short ladders.

The presence of these structures in both RTEOS:TEOS and CIRTEOS:TEOS hybrid xerogels is consistent with the X-ray diffraction patterns obtained for these materials. Figure 4.7 depicts the X-ray diffraction patterns of the CIETEOS:TEOS series (the only series that follows a linear trend in gelation times).

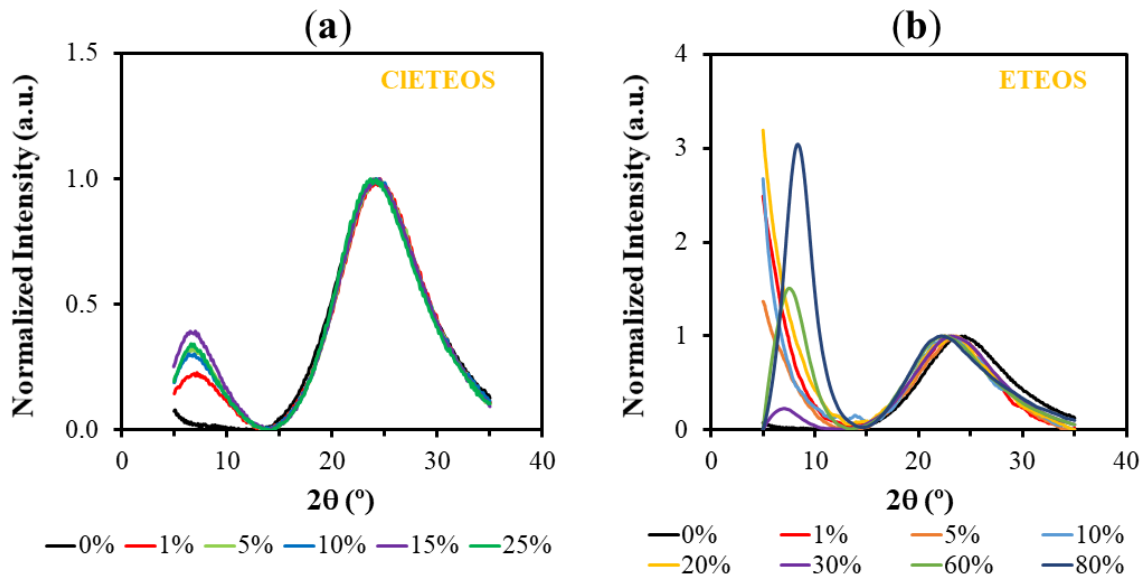


Figure 4.7. X-ray diffraction patterns of the hybrid xerogels at different molar percentages (normalized with respect to the band $2\theta \sim 4^\circ$): (a) CIETEOS:TEOS, and (b) ETEOS:TEOS.

In addition to the characteristic diffraction peak of amorphous silica ($2\theta \sim 24^\circ$) [55,56], another maximum can be observed at $2\theta < 10^\circ$ with only 1% of precursor. This maximum is related to cage-like and ladder-like oligomeric species that form ordered domains within the amorphous matrix of the xerogel [57,58], which, according to computational chemistry studies, are the most thermodynamically stable structures for MTEOS:TEOS hybrid xerogels at pH 4.5 [59]. In the analogous ETEOS series, this diffraction peak is detected above 30% ETEOS and is consistent with the mass spectrometry results, which indicate the presence of ladder-like structures within the silica matrix [37]. Consequently, the appearance of this maximum at much lower molar percentages in the ClETEOS series can be explained by the steric and electronic properties of the chloroethyl substituent, conferring rigidity or freedom of movement restriction to the organic moiety. This compromises the crosslinking and encourages the early formation of ordered periodic domains in the 3D structure. The difficult crosslinking of the colloids or oligomers would explain the anomalous trends in gelation times for this series. The diffraction patterns of the series of hybrid xerogels and the corresponding data are exhibited in Figure 4.8 and Table 4.3, respectively.

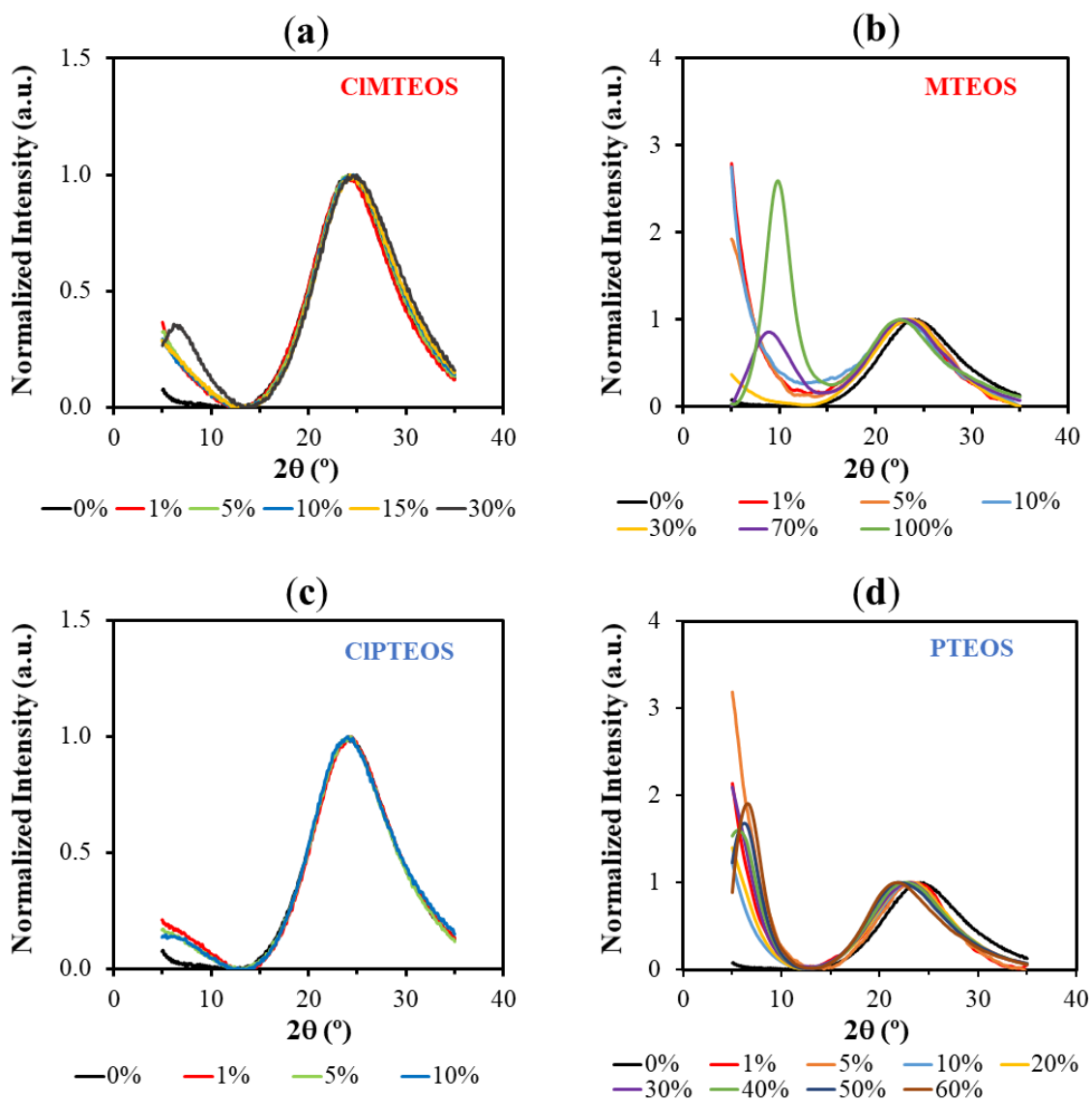


Figure 4.8. X-Ray diffraction patterns of CIRTEOS:TEOS and RTEOS:TEOS xerogels: (a) CIMTEOS, (b) MTEOS, (c) CIPTEOS, and (d) PTEOS.

Table 4.3. Bragg angles (2θ), band area (A), and bond distance (d_1 and d_2 (nm)) calculated from the X-ray diffraction maxima for the xerogels synthesised with CIMTEOS, MTEOS, CIPTEOS and PTEOS.

RTEOS molar percentage (%)	Diffraction maximum $2\theta < 10^\circ$		Diffraction maximum $10^\circ < 2\theta < 30^\circ$	
	2θ ($^\circ$)	d_1 (nm)	2θ ($^\circ$)	d_2 (nm)
0	a	a	24.16	0.368
MTEOS 1	a	a	22.99	0.387
MTEOS 5	a	a	23.85	0.373
MTEOS 10	a	a	22.72	0.391
MTEOS 30	a	a	23.51	0.378
MTEOS 70	8.81	1	22.82	0.39
MTEOS 100	9.83	0.9	22.46	0.396
ETEOS 1	a	a	22.52	0.395
ETEOS 5	a	a	23.58	0.377
ETEOS 10	a	a	22.86	0.389
ETEOS 20	a	a	23.02	0.386
ETEOS 30	7.07	1.25	23.18	0.384
ETEOS 60	7.49	1.18	22.5	0.395
ETEOS 80	8.36	1.06	22.3	0.399
PTEOS 1	a	a	23.38	0.38
PTEOS 5	a	a	23.96	0.371
PTEOS 10	a	a	22.88	0.389
PTEOS 20	a	a	23	0.387
PTEOS 30	a	a	23.12	0.385
PTEOS 40	5.6	1.58	22.67	0.392
PTEOS 50	6.23	1.42	21.8	0.408
PTEOS 60	6.59	1.34	21.86	0.407
CIMTEOS 1	a	a	24.26	0.367
CIMTEOS 5	a	a	24.3	0.366
CIMTEOS 10	a	a	24.54	0.363
CIMTEOS 15	a	a	24.42	0.365
CIMTEOS 30	6.52	1.35	24.78	0.359
CIETEOS 1	7.17	1.23	24.56	0.362
CIETEOS 5	6.92	1.28	24.3	0.366
CIETEOS 10	6.76	1.31	24.14	0.369
CIETEOS 15	6.76	1.31	24.22	0.367
CIETEOS 25	6.76	1.31	23.9	0.372
CIPTEOS 1	a	a	24.22	0.367
CIPTEOS 5	a	a	23.98	0.371
CIPTEOS 10	5.8	1.52	24.06	0.37

a—Not detected

4.2.3 Spectral deconvolution of the 1300–700 cm⁻¹ region

Figure 4.9 depicts the ν_{as} Si–O–Si band at 1090 cm⁻¹ and the associated shoulder at around 1200 cm⁻¹. It shows the shift at lower frequencies of the band at 1090 cm⁻¹ with higher molar percentages of the precursor as well as the overlapping bands derived from the shoulder at 1200 cm⁻¹. These emerging bands are attributable to the different structures that make up the siloxane bonds, mostly forming rings of four or six silicon atoms, (SiO)₄ and (SiO)₆ respectively. The relative abundance of these rings depends on the nature and molar ratio of the precursor: four-fold rings are the predominant species in xerogels and are thermodynamically favoured in the oligomerization of TEOS at acid pH through cyclodimerization processes [43,51], whereas six-fold rings are kinetically favoured over four-membered rings and constitute the main structures of silicates and amorphous silica [17,60,61]. In the deconvolution study, each structure is associated with two optical modes of ν_{as} Si–O–Si vibration in the FTIR spectra due to the Coulomb interactions: (i) transverse mode (TO), between 1100 and 1000 cm⁻¹; and (ii) longitudinal mode (LO), between 1250 and 1100 cm⁻¹ [62].

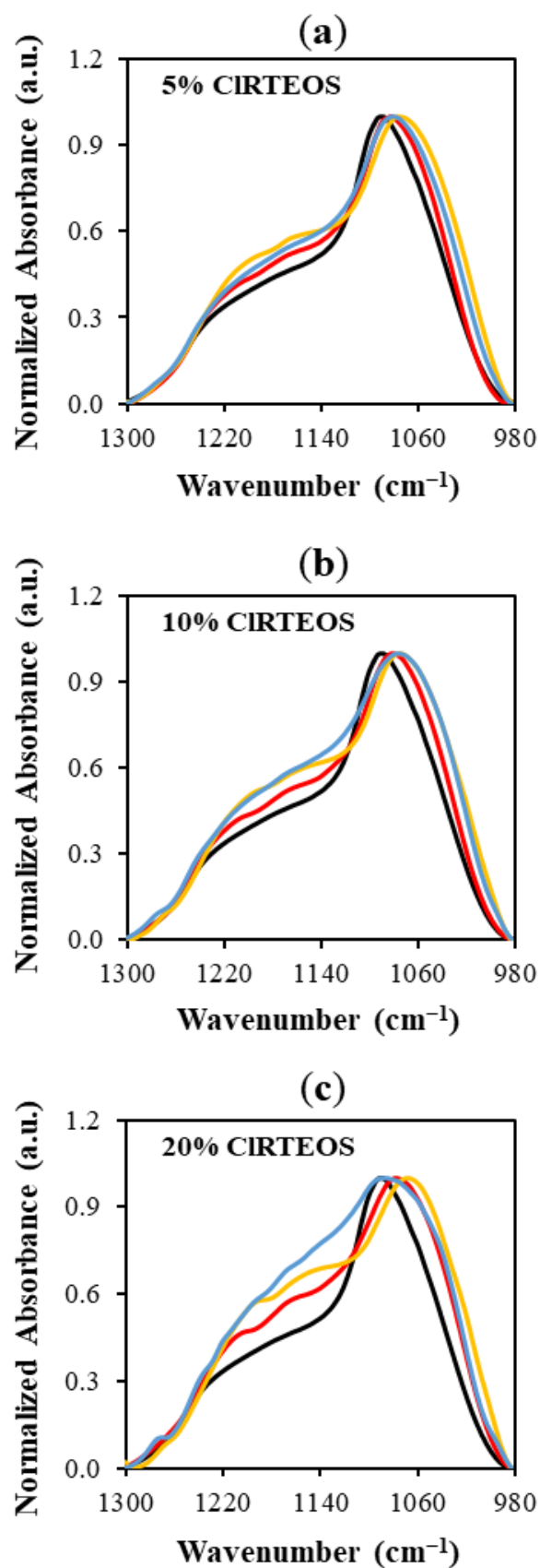


Figure 4.9. Normalized FTIR spectra of the 1300–980 cm⁻¹ region of the TEOS xerogel (**black**), and those of the three chloroalkyl series at different molar ratios: (a) 5%, (b) 10%, and (c) 20%. (ClMTEOS (**red**), ClTEOS (**yellow**), and ClPTEOS (**blue**)).

The changes in these structures as the precursor increases and their relative proportions were studied by deconvolution of the FTIR spectra in the range 1300–980 cm^{-1} , using the non-linear least-squares method to obtain the Gaussian-Lorentzian components (the process is concisely explained in *Chapter 2.5.1*). The different distances and degrees of torsion of Si–O–Si bonds in the structures, along with the optical modes, predict four components of ν_{as} Si–O–Si in the studied range: (i) TO_4 and LO_4 for $(\text{SiO})_4$ rings, and (ii) TO_6 and LO_6 for $(\text{SiO})_6$ rings. Therefore, four components were introduced in the software for deconvolution of the reference material spectrum (100% TEOS xerogel, Figure 4.3). The resulting optimized synthetic spectrum was composed of bells with maxima at 1214, 1143, 1092 and 1078 cm^{-1} , assigned to LO_6 , LO_4 , TO_4 and TO_6 , respectively. This assignation takes account of: (i) the aforementioned frequency ranges of the optical modes; (ii) the predominance of $(\text{SiO})_4$ species evidenced by the shoulder at 550 cm^{-1} in the spectra, and (iii) the broader limiting frequencies in both optical modes for six-fold rings, related to their less tensioned nature (Figure 4.10) [27,49,51].

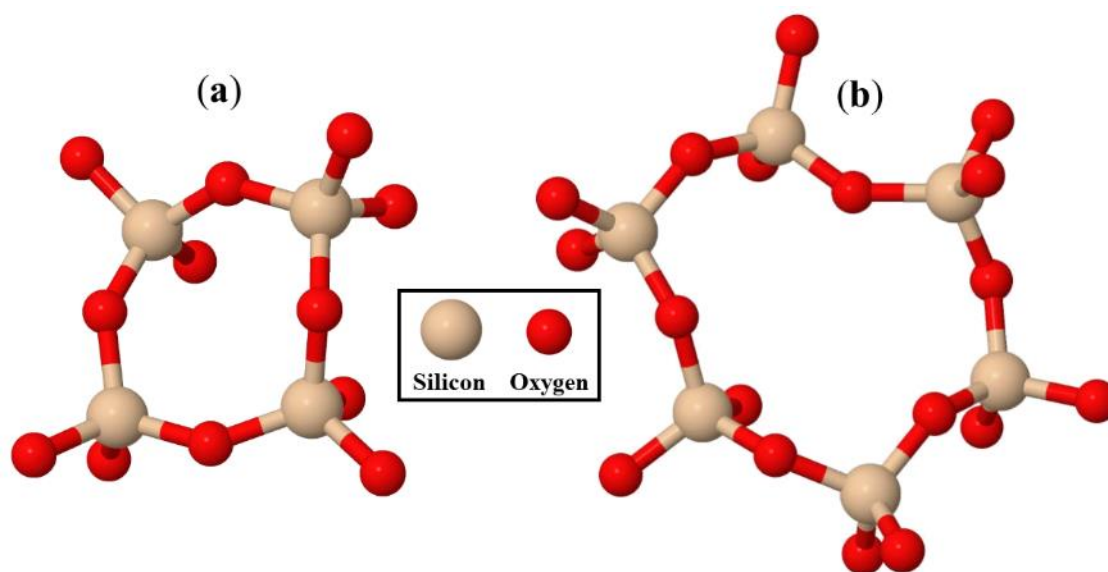


Figure 4.10. Predominant structures within the silica matrix of a xerogel prepared with TEOS: (a) $(\text{SiO})_4$ rings, and (b) $(\text{SiO})_6$ rings.

Spectra of the RTEOS:TEOS and CIRTEOS:TEOS series were deconvoluted using the aforementioned frequencies obtained from the reference material (LO₆, LO₄, TO₄ and TO₆) and the frequencies of C–H wagging vibrations corresponding to the organic moiety of each precursor (Table 4.2). By way of example, Figure 4.11 depicts the synthetic spectra derived from the bell-shaped curves obtained for TEOS (Figure 4.11a) and the organochlorinated xerogels with a 20% molar percentage of precursor (actual FTIR spectra shown in Figure 4.9c).

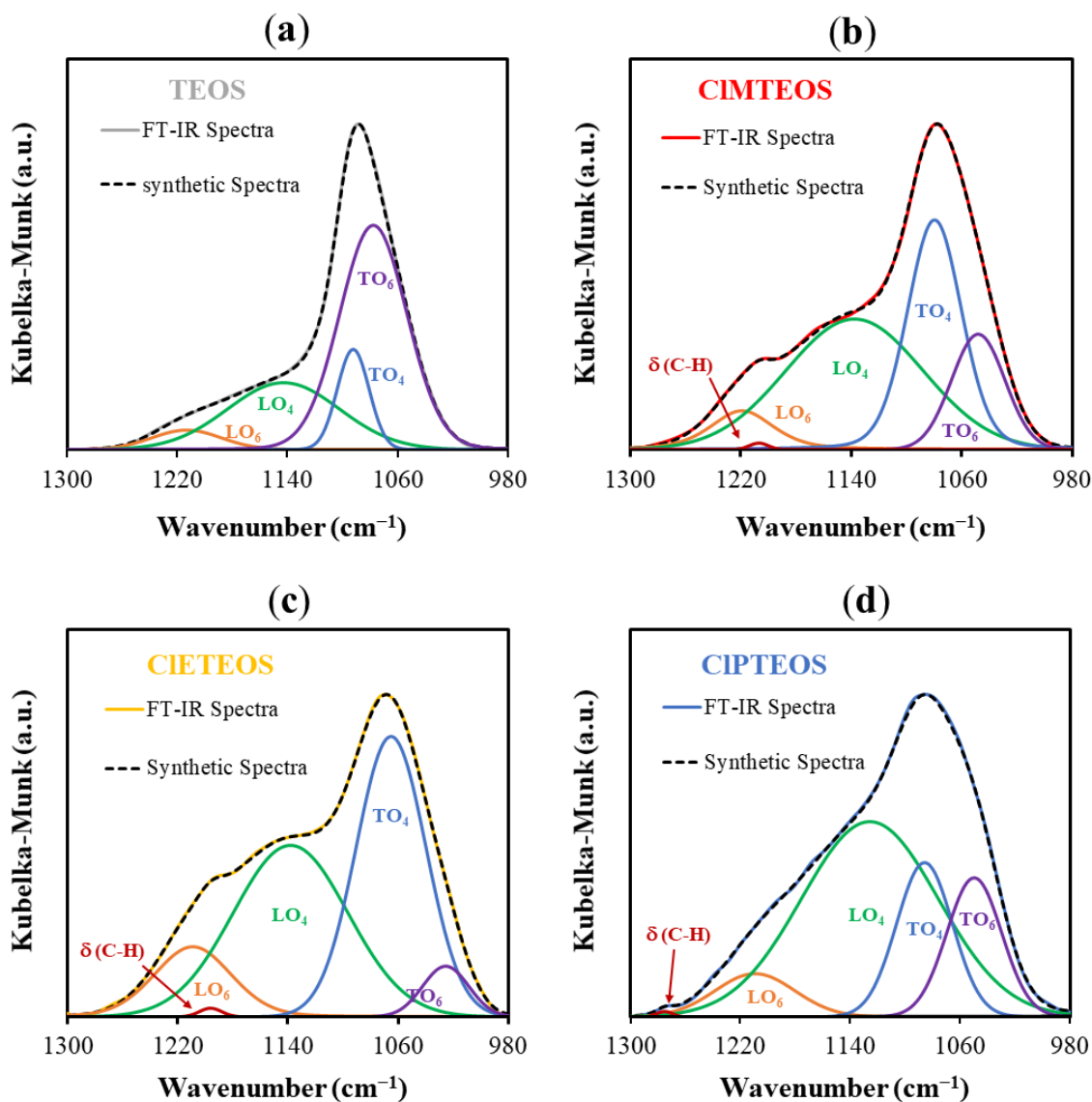


Figure 4.11. Deconvolution and least-squares adjustment of the FTIR spectra of the xerogels: (a) Reference material (100% TEOS), (b) 20% CIMTEOS, (c) 20% CIETEOS, and (d) 20% CIPTEOS.

Based on the integrated areas of the Gaussian-Lorentzian bells, Equations 4.6 and 4.7 were calculated to determine the relative abundance of (SiO)₆ and (SiO)₄ rings (Tables 4.4 and 4.5 for the CIRTEOS:TEOS and RTEOS:TEOS series, respectively).

$$(SiO)_6, \% = \frac{A(LO_6) + A(TO_6)}{A(LO_4) + A(TO_4) + A(LO_6) + A(TO_6)} \times 100 \quad (4.6)$$

$$(SiO)_4, \% = \frac{A(LO_4) + A(TO_4)}{A(LO_6) + A(TO_6) + A(LO_4) + A(TO_4)} \times 100 \quad (4.7)$$

where A(LO₆) is the area of the band at 1220 cm⁻¹, A(LO₄) is the area of the band at 1150 cm⁻¹; A(TO₄) is the area of the band at 1070 cm⁻¹ and A(TO₆) the area of the band at 1050 cm⁻¹.

Table 4.4. Relative areas obtained from the deconvolution of the FTIR spectra of CIRTEOS:TEOS series [35], their calculated (SiO)₄ and (SiO)₆ percentages, and their (SiO)₄/(SiO)₆ ratios. The selected data for the construction of Figure 4.12a are shaded in grey.

CIRTEOS molar percentage (%)	(LO) ₆		(LO) ₄		(TO) ₄		(TO) ₆		(SiO) ₄ ^c	(SiO) ₆ ^d	$\frac{[(SiO)_4]^e}{[(SiO)_6]}$
	ν^a (cm ⁻¹)	(%) ^b	ν^a (cm ⁻¹)	(%) ^b	ν^a (cm ⁻¹)	(%) ^b	ν^a (cm ⁻¹)	(%) ^b	(%)	(%)	
0	1214	4.9	1143	27.3	1093	11.6	1078	56.1	39.0	61.0	0.6
CIMTEOS 1	1216	5.0	1145	32.7	1092	10.8	1082	51.5	43.5	56.5	0.8
CIMTEOS 3.5	1219	6.5	1145	36.3	1089	5.7	1077	51.5	42.0	58.0	0.7
CIMTEOS 5	1221	6.4	1147	36.5	1091	8.2	1076	48.9	44.7	55.3	0.8
CIMTEOS 7.5	1202	14.4	1126	32.1	1087	32.5	1061	21.0	64.6	35.4	1.8
CIMTEOS 10	1218	8.3	1138	42.5	1077	42.9	1043	6.4	85.3	14.7	5.8
CIMTEOS 15	1215	9.2	1137	38.2	1082	37.7	1051	14.9	75.9	24.1	3.1
CIMTEOS 20	1219	9.4	1138	42.6	1080	32.0	1049	15.8	74.6	25.2	3.0
CIMTEOS 25	1218	9.8	1140	39.4	1079	39.1	1048	11.7	78.5	21.5	3.7
CIMTEOS 30	1226	4.7	1136	52.5	1074	33.7	1040	9.1	86.2	13.8	6.3
CIMTEOS 35	1223	4.5	1136	48.6	1076	37.9	1044	9.0	86.5	13.5	6.4
CIETEOS 1	1216	11.3	1139	37.2	1090	18.3	1058	33.1	55.6	44.4	1.3
CIETEOS 3.5	1214	11.2	1137	36.4	1089	14.5	1059	37.9	50.9	49.1	1.0
CIETEOS 5	1212	10.7	1136	39.0	1086	13.8	1058	36.5	52.8	47.2	1.1
CIETEOS 7.5	1210	11.5	1135	40.3	1083	17.1	1053	31.1	57.4	42.6	1.3
CIETEOS 10	1210	12.4	1136	38.5	1078	26.5	1044	22.6	64.9	35.1	1.8
CIETEOS 15	1208	12.8	1134	40.8	1076	28.1	1043	18.3	68.9	31.1	2.2
CIETEOS 20	1209	12.1	1138	41.7	1065	41.3	1025	4.9	83.0	17.0	4.9
CIETEOS 25	1211	7.0	1138	52.2	1062	39.4	1021	1.4	91.6	8.4	10.9
CIPTEOS 1	1220	6.9	1146	34.8	1089	6.0	1074	52.2	40.9	59.1	0.7
CIPTEOS 3.5	1214	8.9	1140	33.3	1085	39.1	1055	18.7	72.4	27.6	2.6
CIPTEOS 5	1216	9.0	1135	40.8	1083	31.2	1049	19.0	71.9	28.1	2.6
CIPTEOS 7.5	1214	9.1	1133	44.0	1079	33.5	1044	13.4	77.4	22.6	3.4
CIPTEOS 10	1219	6.6	1142	42.1	1075	42.7	1039	8.6	84.8	15.2	5.6
CIPTEOS 15	1216	7.7	1145	38.3	1071	51.1	1040	2.9	89.4	10.6	8.4
CIPTEOS 20	1209	7.4	1126	57.6	1086	18.6	1050	16.4	76.2	23.8	3.2
CIPTEOS 25	1199	11.0	1124	45.7	1096	9.7	1064	33.5	55.4	44.6	1.2

^a—Frequency of Gaussian–Lorentzian bands maxima calculated by the spectra curve fitting in the SpectraManager software; ^b—Area percentage of each calculated band with respect to the sum of all (SiO)₄ and (SiO)₆ related bands; ^c—Proportion of (SiO)₄ rings calculated with Equations 4.6; ^d—Proportion of (SiO)₆ rings calculated with Equations 4.7; ^e—Ratio of rings calculated by dividing the percentages of rings.

Table 4.5. Relative areas obtained from the deconvolution of the FTIR spectra of RTEOS:TEOS series [36–38], their calculated (SiO)₄ and (SiO)₆ percentages, and their (SiO)₄/(SiO)₆ ratios. The selected data for the construction of Figure 4.12b are shaded in grey.

RTEOS molar percentage (%)	(LO) ₆		(LO) ₄		(TO) ₄		(TO) ₆		(SiO) ₄ ^c	(SiO) ₆ ^d	$\left[\frac{(\text{SiO})_4}{(\text{SiO})_6}\right]^e$
	ν^a (cm ⁻¹)	(%) ^b	ν^a (cm ⁻¹)	(%) ^b	ν^a (cm ⁻¹)	(%) ^b	ν^a (cm ⁻¹)	(%) ^b	(%)	(%)	
0	1214	4.9	1143	27.3	1093	11.6	1078	56.1	39.0	61.0	0.6
MTEOS 10	1228	6.9	1147	32.8	1094	5.3	1071	55.0	38.1	61.9	0.6
MTEOS 20	1124	4.1	1142	38.5	1088	29.5	1053	27.8	68.1	31.9	2.1
MTEOS 30	1221	3.7	1137	44.1	1066	44.1	1026	11.1	85.1	14.9	5.7
MTEOS 40	1216	2.8	1139	44.9	1059	51.7	1020	0.6	96.6	3.4	28.4
MTEOS 50	1212	4.0	1137	43.6	1067	30.6	1034	21.8	74.2	25.8	2.9
ETEOS 5	1210	3.9	1135	32.5	1087	7.1	1070	56.5	39.6	60.4	0.7
ETEOS 10	1228	4.6	1149	34.5	1094	7.2	1071	53.6	41.8	58.2	0.7
ETEOS 20	1209	6.6	1117	38.9	1080	45.7	1051	8.8	84.6	15.4	5.5
ETEOS 30	1216	2.1	1131	54.4	1062	40.9	1044	2.6	95.3	4.7	20.3
ETEOS 40	1212	3.2	1119	68.0	1089	9.1	1052	19.7	77.1	22.9	3.4
ETEOS 50	1209	3.7	1125	62.3	1066	25.1	1041	8.9	87.4	12.6	6.9
ETEOS 60	1201	6.4	1129	54.6	1063	27.8	1040	11.2	82.4	17.6	4.7
ETEOS 70	1197	7.5	1127	60.2	1059	25.7	1038	6.6	85.9	14.1	6.1
PTEOS 5	1217	3.3	1143	31.2	1086	5.2	1068	60.3	36.4	63.6	0.6
PTEOS 10	1224	4.5	1134	39.7	1084	43.1	1052	12.8	82.7	17.3	4.8
PTEOS 20	1023	12.4	1132	28.7	1080	34.9	1048	24.0	63.6	36.4	1.7
PTEOS 30	1212	6.2	1128	44.5	1080	19.7	1050	29.6	64.2	35.8	1.8
PTEOS 40	1204	9.1	1134	34.7	1069	43.0	1046	13.2	77.8	22.2	3.5
PTEOS 50	1199	3.2	1122	60.4	1054	35.7	1027	0.6	96.2	3.8	25.0

^a—Frequency of Gaussian–Lorentzian bands maxima calculated by the spectra curve fitting in the SpectraManager software; ^b—Area percentage of each calculated band with respect to the sum of all (SiO)₄ and (SiO)₆ related bands; ^c—Proportion of (SiO)₄ rings calculated with Equations 4.6; ^d—Proportion of (SiO)₆ rings calculated with Equations 4.7, ^e— Ratio of rings calculated by dividing the percentages of rings.

Figure 4.12 graphically depicts the $(\text{SiO})_4/(\text{SiO})_6$ ratio as a function of the molar percentage of chloroalkyl and alkyl precursor (Figure 4.12a and 4.12b, respectively). The graphs have been constructed with the data of Tables 4.4 and 4.5 that yielded the best exponential adjustment (data shaded in grey).

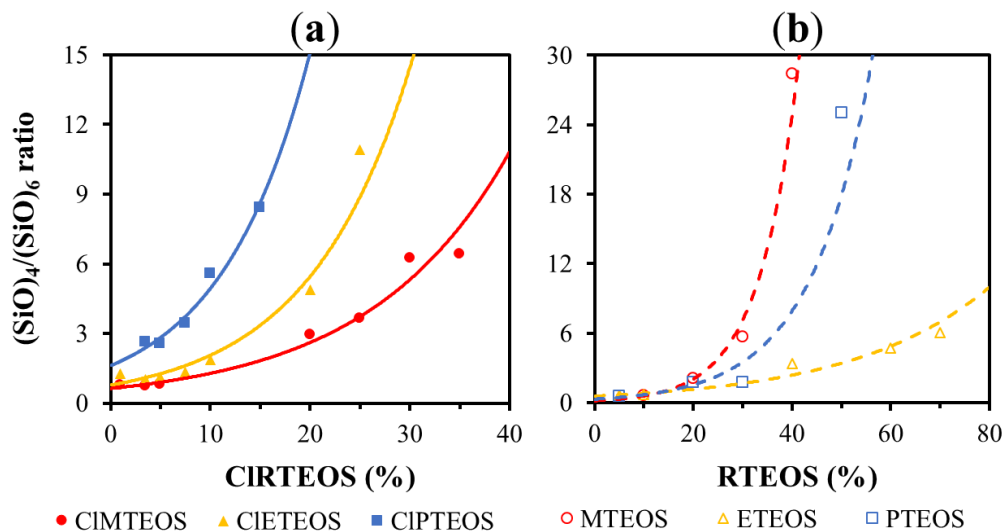


Figure 4.12. Variation in $(\text{SiO})_4/(\text{SiO})_6$ ratio as a function of the molar percentage of precursor in (a) CIRTEOS:TEOS and (b) RTEOS:TEOS xerogels.

Figure 4.12.a shows that the formation of $(\text{SiO})_4$ rings is more favoured with a longer chloroalkyl chain for a given molar percentage of precursor. The $(\text{SiO})_4/(\text{SiO})_6$ ratio increases exponentially with a higher percentage of precursor in the three series. These trends are not expected, because the entry of organic molecules or substituents into the network should produce an increase in the proportion of $(\text{SiO})_6$ species, which minimises steric tension, increases the volume, and markedly reduces the skeletal density (Table 4.6).

Table 4.6. Skeletal density for the hybrid xerogels obtained from Figure 3.5 of Chapter 3.2.3. Reference material skeletal density (100%TEOS) = 1.96 g cm^{-3} .

Xerogel series precursor	Skeletal density ($\text{cm}^3 \text{ g}^{-1}$) at each molar percentage of precursor		
	5%	10%	20%
CIMTEOS	1.94	1.91	1.90
CIETEOS	1.88	1.85	1.79
CIPTEOS	1.85	1.80	a
MTEOS	1.82	1.80	1.72
ETEOS	1.80	1.76	1.61
PTEOS	1.86	1.76	1.58

a—Not enough sample to measure.

Accordingly, Fidalgo *et al.* (2005) found that the proportion of (SiO)₆ rings increase with higher molar percentage of RTEOS (R = M, E and P), reaching an abundance of almost 85% for samples with a precursor percentage of 75% [27]. However, the synthesis of these materials was performed in basic medium, explaining the greater abundance of six-membered rings from crosslinking between more branched chains. In the case of the present xerogels, the higher proportion of (SiO)₄ rings in the chloroalkyl series would be related not only to their synthesis in acidic medium but also to the formation of ordered domains at very low molar percentages of precursor. The data in Table 4.4 for the three chloroalkyl series show that the contribution of the LO₄ band (attributable to the total percentage of (SiO)₄ rings) increases with higher percentage of precursor. This is a relevant finding, given that this band is also associated with the presence of ordered structures in the literature [5,50,63]. Its presence is closely related to a decrease in the degree of crosslinking in the xerogel, in agreement with the shifts at lower wavelengths of the TO₄ band, which is associated with the silicon network [13]. Another factor that supports the formation of these ordered structures is the decrease in the intensity of the LO₆ band (see Table 4.4), because this band is generally associated not only with (SiO)₆ rings but also with the non-silica porous skeleton [64].

The way in which the chlorine atom affects the ring distribution was studied in greater depth by performing interpolations using the equations of the exponential curves shown in Figure 4.12. These equations were used to obtain (SiO)₄/(SiO)₆ ratios for percentages of the precursor in the range of 1–35% in both the chlorinated series and their non-chlorinated analogues (the adjustment equations used are exhibited in Table 4.7).

Table 4.7. Equations obtained from the exponential adjustment of the curves depicted in the graphs of Figure 4.12.

Xerogel series precursor	Exponential adjustment	
	Equation ^a	R ²
CIMTEOS	$y = 0.6317e^{0.0711x}$	0.9813
CIETEOS	$y = 0.7789e^{0.0974x}$	0.9457
CIPTEOS	$y = 1.6182e^{0.1117x}$	0.9612
MTEOS	$y = 0.1685e^{0.1249x}$	0.9911
ETEOS	$y = 0.5691e^{0.0358x}$	0.9652
PTEOS	$y = 0.3052e^{0.0814x}$	0.9188

^a—where $y = (\text{SiO})_4/(\text{SiO})_6$ ratio, and $x =$ precursor molar percentage (%)

Figure 4.13 compares $(\text{SiO})_4/(\text{SiO})_6$ ratios between the CIRTEOS:TEOS series and the RTEOS:TEOS series to show how the chlorine atom affects the relative proportion of species. A discontinuous black straight line has been added in this figure to depict the hypothetical case in which the ratio of $(\text{SiO})_4/(\text{SiO})_6$ rings is the same for the alkyl and chloroalkyl series at the same molar percentage of precursor, which would indicate that the chlorine atom in the CIRTEOS precursor has no effect on the $(\text{SiO})_4/(\text{SiO})_6$ ratio with respect to its counterpart, RTEOS. Above this line, the effect of the chlorine on the $(\text{SiO})_4/(\text{SiO})_6$ ratio is positive, favouring the formation of $(\text{SiO})_4$ rings. Below this line, the effect of the chlorine is negative, favouring the formation of $(\text{SiO})_6$ structures.

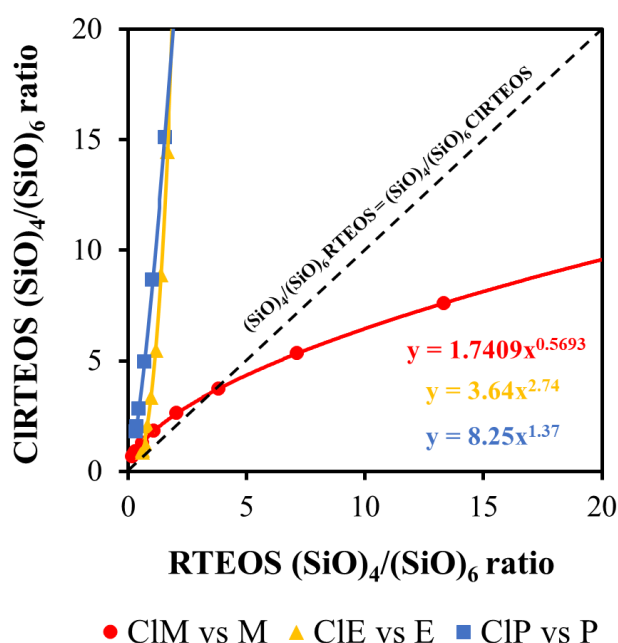


Figure 4.13. Variation in the proportion of structures $(\text{SiO})_4/(\text{SiO})_6$ of the chloroalkyl series with respect to the alkyl series at different molar percentages of precursor.

The figure shows that this ratio is lower in the CIMTEOS than in the MTEOS series. This trend is consistent with the behaviour observed in Figure 4.2c, which shows that the CIMTEOS series has shorter gelation times, closely related to the size of the chloroalkyl chain. This not only fails to produce a significant steric or electrostatic effect to disfavour the formation of $(\text{SiO})_6$ rings (kinetically favoured species), but also accelerates condensation due to the inductive effect of the chlorine, which reduces gelation times and gives rise to lower $(\text{SiO})_4/(\text{SiO})_6$ ratios. Unlike the CIMTEOS series, the $(\text{SiO})_4/(\text{SiO})_6$ values for the CIETEOS and CIPTEOS series are higher than those of their analogues throughout the region, which is in turn consistent with the longer gelation

times displayed in Figure 4.2c. In these two series, the steric factor and the electrostatic repulsions between colloids significantly increase the crosslinking time, disfavours $(\text{SiO})_6$ ring formation. The slope of these curves is much steeper than the slope observed for CIMTEOS series, implying that the addition of a higher percentage of precursor increases the influence exerted by the chlorine atom on the structure of the synthesised materials, which is maximized in CIPTEOS:TEOS, the series with the longest chain. It should be noted that, although the $(\text{SiO})_4/(\text{SiO})_6$ ratio is slightly lower in the CIETEOS versus CIPTEOS series, the former has longer gelation times and peaks at small angles ($10^\circ < 2\theta$) in all X-ray diffraction patterns. According to these findings, the chloroethyl moiety in this material is more efficient in directing the formation of ordered domains and nanostructuring the material, even when it has fewer $(\text{SiO})_4$ rings (related to periodic cages or ladder-type structures), consistent with the results of all techniques used to characterize these hybrid materials [35].

4.3 CONCLUSIONS

In general, an increase in the molar percentage of the precursor (CIRTEOS and RTEOS) translates into an increase in gelation times due to conjugation of the steric and inductive effects of the organic substituents. The gelation times of the chloroalkyl series are longer than those of their analogous alkyl series for long alkyl chains (CIETEOS and CIPTEOS), although they are slightly shorter for the shortest alkyl chain (CIMTEOS). This is explained by the maximization of the inductive effect of the chlorine atom due to its proximity to the silicon atom, which exerts a positive influence on the condensation and crosslinking reactions, the slowest step in the sol-gel process. On the other hand, a larger number of carbons in the alkyl chain reduces the inductive effect of the chlorine on the silicon atom and increases the steric effect exerted by the chain to form the silica network; this effect is maximized in the series bearing ethyl, chloroethyl, propyl and chloropropyl groups. Unexpectedly, the CIETEOS series have the highest gelation times, explained by: (i) the lack of flexibility of the chloroethyl group due to the steric tension caused by its size; (ii) the electrostatic repulsions exerted by chlorine, forcing the formation of kinetically disfavoured structures in order to minimize its energy; and (iii) the X-ray diffraction patterns of this series (1–25%), which reveal a maximum of diffraction at a small angle ($2\theta < 10^\circ$), consistent with the presence in their structure of periodic domains that require more time for their formation. The FTIR spectra of each

hybrid xerogel yielded data for a semi-quantitative determination of the proportions of (SiO)₄ and (SiO)₆ rings by deconvolution methods. These findings reveal a competitive process between the two species that is dependent on the precursor and its molar ratio, observing similar trends to those obtained for the gelation times. In the CIMTEOS series, the presence of the chlorine atom favours the formation of six-fold rings. An opposite trend is observed in the CIETEOS and CIPTEOS series, favouring the formation of 4-fold rings; in addition, the chlorine atom exerts a stronger influence in the CIETEOS and CIPTEOS series, consistent with their longer gelation times and the presence of periodic structures. According to these results, the substitution of a hydrogen atom by a halogen functional group (e.g., chlorine) in hybrid xerogels produces relevant changes in its microstructure due to the intermolecular forces generated by the chlorine atom in the sol-gel process.

4.4 ACKNOWLEDGEMENTS

The authors gratefully acknowledge the financial support received from the Ministerio de Economía y Competitividad of Spain (Project MAT2016-78155-C2-2-R). G.C. thanks MINECO and the “Ministerio de Ciencia, Investigación y Universidades” of Spain for his “FPU” grant (FPU18/03467). The authors also acknowledge the use of the “Centro de Instrumentación Científico-Técnica” at the University of Jaén and UCTAI at the Public University of Navarre.

4.5 REFERENCES

- [1] Pastore, A.; Badocco, D.; Pastore, P. *Talanta* **2020**, *212*, p. 120739.
- [2] Gillanders, R. N.; Campbell, I. A.; Glackin, J. M. E.; Samuel, I. D. W.; Turnbull, G. A. *Talanta* **2018**, *179*, p. 426–429.
- [3] Li, Z.; Suslick, K. S. *ACS Appl. Mater. Interfaces* **2018**, *10*, p. 15820–15828.
- [4] Shamir, D.; Elias, I.; Albo, Y.; Meyerstein, D.; Burg, A. *Inorg. Chim. Acta.* **2020**, *500*, p. 119225.
- [5] Ponamoreva, O. N.; Afonina, E. L.; Kamanina, O. A.; Lavrova, D. G.; Arlyapov, V. A.; Alferov, V. A.; Boronin, A. M. *Appl. Biochem. Microbiol.* **2018**, *54*, p. 736–742.
- [6] Lin, W.; Zhang, X.; Cai, Q.; Yang, W.; Chen, H. *Cellulose* **2020**, *27*, p. 7805–7821.
- [7] Liu, Z.; Tian, S.; Li, Q.; Wang, J.; Pu, J.; Wang, G.; Zhao, W.; Feng, F.; Qin, J.; Ren, L. *ACS Sustainable Chem. Eng.* **2020**, *8*, p. 6786–6797.

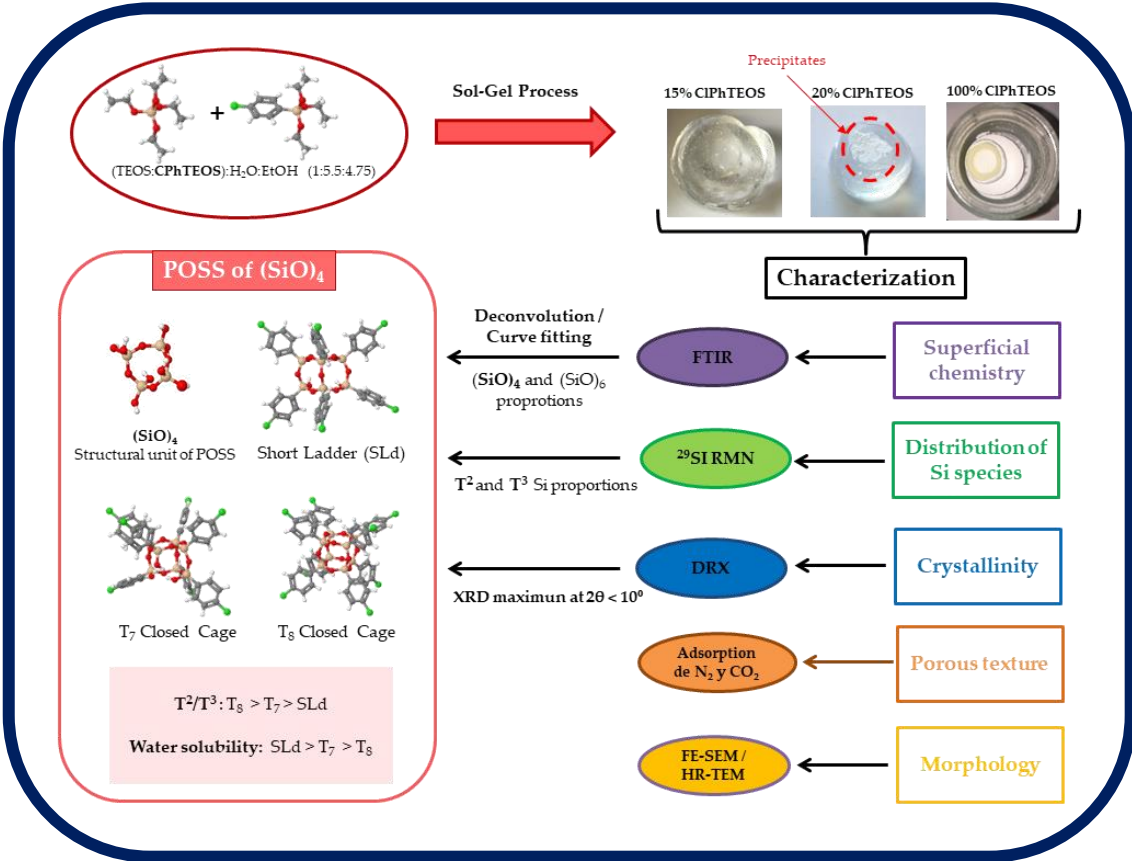
- [8] Scotland, K. M.; Shetranjiwalla, S.; Vreugdenhil, A. J. *J. Coat. Technol. Res.* **2020**, *17*, p. 977–989.
- [9] Bouvet-Marchand, A.; Graillot, A.; Abel, M.; Koudia, M.; Boutevin, G.; Loubat, C.; Grosso, D. *J. Mater. Chem. A* **2018**, *6*, p. 24899–24910.
- [10] Yue, D.; Feng, Q.; Huang, X.; Zhang, X.; Chen, H. *Coatings* **2019**, *9*, p. 556.
- [11] Malek, S. K.; Nodeh, H. R.; Akbari-Adergani, B. *J. Sep. Sci.* **2018**, *41*, p. 2934–2941.
- [12] Moriones, P.; Ríos, X.; Echeverría, J. C.; Garrido, J. J.; Pires, J.; Pinto, M. *Colloids Surf., A* **2011**, *389*, p. 69–75.
- [13] Tran, H. N.; Nghiem, T. H. L.; Duong Vu, T. T.; Pham, M. T.; Nguyen, T. V.; Tran, T. T.; Chu, V. H.; Tong, K. T.; Tran, T. T.; Xuan Le, T. T.; Brochon, J.-C.; Nguyen, T. Q.; Hoang, M. N.; Duong, C. N.; Nguyen, T. T.; Hoang, A. T.; Nguyen, P. H. *Adv. Nat. Sci.: Nanosci. Nanotechnol.* **2013**, *4*.
- [14] Judeinstein, P.; Sanchez, C. *J. Mater. Chem.* **1996**, *6(4)*, p. 511–525.
- [15] Alemán, J.; Chadwick, A. V.; He, J.; Hess, M.; Horie, K.; Jones, R. G.; Kratochvíl, P.; Meisel, I.; Mita, I.; Moad, G.; *et al.* *Pure Appl. Chem.* **2007**, *79*, p. 1801–1829.
- [16] Brinker, C. J.; Scherer, G. W. *Sol-Gel Science*; 1st ed.; Academic Press, INC: San Diego, CA, USA, **1990**.
- [17] Fidalgo, A.; Ilharco, L. M. *J. Non-Cryst. Solids* **2001**, *283*, p. 144–154.
- [18] Chemtob, A.; Ni, L.; Croutxé-Barghorn, C.; Boury, B. *Chem. - Eur. J.* **2014**, *20*, p. 1790–1806.
- [19] Issa, A. A.; Luyt, A. S. *Polymers* **2019**, *11*, p. 537.
- [20] Cheng, X.; Chen, D.; Liu, Y. *ChemPhysChem* **2012**, *13*, p. 2392–2404.
- [21] Issa, A. A.; El-Azazy, M.; Luyt, A. S. *Sci. Rep.* **2019**, *9(17624)*, p. 1–15.
- [22] Echeverría, J. C.; Moriones, P.; Arzamendi, G.; Garrido, J. J.; Gil, M. J.; Cornejo, A.; Martínez-Merino, V. *J. Sol-Gel Sci. Technol.* **2018**, *86*, p. 316–328.
- [23] Moriones, P.; Arzamendi, G.; Cornejo, A.; Garrido, J. J.; Echeverria, J. C. *J. Phys. Chem. A* **2019**, *123*, p. 10364–10371.
- [24] Colin, B.; Lavastre, O.; Fouquay, S.; Michaud, G.; Simon, F.; Laferte, O.; Brusson, J.-M. *Green Sustainable Chem.* **2016**, *6*, p. 151–166.
- [25] Innocenzi, P.; Falcaro, P.; Grosso, D.; Babonneau, F. *Mater. Res. Soc. Symp. Proc.* **2002**, *726*, p. 271–281.
- [26] Ponton, S.; Dhainaut, F.; Vergnes, H.; Samelor, D.; Sadowski, D.; Rouessac, V.; Lecoq, H.; Sauvage, T.; Caussat, B.; Vahlas, C. *J. Non-Cryst. Solids* **2019**, *515*, p. 34–41.
- [27] Fidalgo, A.; Ciriminna, R.; Ilharco, L. M.; Pagliaro, M. *Chem. Mater.* **2005**, *17*, p. 6686–6694.
- [28] Saputra, R. E.; Astuti, Y.; Darmawan, A. *Spectrochim. Acta, Part A* **2018**, *199*, p. 12–20.

- [29] Stocker, M. K.; Sanson, M. L.; Bernardes, A. A.; Netto, A. M.; Brambilla, R. *J. Sol-Gel Sci. Technol.* **2021**, *98*, p. 568–579.
- [30] Fidalgo, A.; Ilharco, L.M. *J. Non-Cryst. Solids* **2004**, *347*, p. 128–137.
- [31] Izaak, T. I.; Martynova, D. O.; Stonkus, O. A.; Slavinskaya, E. M.; Boronin, A. I. *J. Sol-Gel Sci. Technol.* **2013**, *68*, p. 471–478.
- [32] Capeletti, L. B.; Zimnoch, J. H. Fourier Transform Infrared and Raman Characterization of Silica-Based Materials. In *Applications of Molecular Spectroscopy to Current Research in the Chemical and Biological Sciences*; Stauffer, M., Ed.; Intechopen: Kansas, USA, **2016**; pp. 3–22.
- [33] Echeverría, J. C.; Faustini, M.; Garrido, J. J. *Sens. Actuators, B* **2016**, *222*, p. 1166–1174.
- [34] Echeverría, J. C.; Calleja, I.; Moriones, P.; Garrido, J. J. *Beilstein J. Nanotechnol.* **2017**, *8*, p. 475–484.
- [35] Cruz-Quesada, G.; Espinal-Viguri, M.; López-Ramón, M. V.; Garrido, J. J. *Polymers* **2021**, *13*, p. 1415.
- [36] Rios, X.; Moriones, P.; Echeverría, J. C.; Luquín, A.; Laguna, M.; Garrido, J. J. *Adsorption* **2011**, *17*, p. 583–593.
- [37] Rios, X.; Moriones, P.; Echeverría, J. C.; Luquin, A.; Laguna, M.; Garrido, J. J. *Mater. Chem. Phys.* **2013**, *141*, p. 166–174.
- [38] Moriones, P. *Síntesis y Caracterización de Xerogeles Silíceos Híbridos (RTEOS/TEOS; R = P, Ph)*. Universidad Pública de Navarra: Pamplona, Spain, **2015**. Available online: <https://academica-e.unavarra.es/handle/2454/20351> (accessed on 14 November 2020).
- [39] Berrier, E.; Courtheoux, L.; Bouazaoui, M.; Capoen, B.; Turrell, S. *Phys. Chem. Chem. Phys.* **2010**, *12*, p. 14477–14484.
- [40] Brochier Salon, M. C.; Belgacem, M. N. *Colloids Surf., A* **2010**, *366*, p. 147–154.
- [41] Pierre, A. C. *Introduction to Sol-Gel Processing*; Klein, L., Ed.; 1st Ed.; Kluwer Academic Publishers: New York, NY, USA, **1998**.
- [42] Uhlmann, D. R.; Ulrich, D. R. *Ultrastructure Processing of Advance Materials.*; 1st Ed.; John Wiley & Sons, INC.: Tucson, Arizona, US, **1992**.
- [43] Depla, A.; Verheyen, E.; Veyfeyken, A.; Van Houteghem, M.; Houthoofd, K.; Van Speybroeck, V.; Waroquier, M.; Kirschhock, C. E. A.; Martens, J. A. *J. Phys. Chem. C* **2011**, *115*, p. 11077–11088.
- [44] Depla, A.; Lesthaeghe, D.; Van Erp, T. S.; Aerts, A.; Houthoofd, K.; Fan, F.; Li, C.; Van Speybroeck, V.; Waroquier, M.; Kirschhock, C. E. A.; Martens J. A. *J. Phys. Chem. C* **2011**, *115*, p. 3562–3571.
- [45] Innocenzi, P. *J. Non-Cryst. Solids* **2003**, *316*, p. 309–319.
- [46] Coates, J. Interpretation of Infrared Spectra, A Practical Approach. In *Encyclopedia of Analytical Chemistry*; Meyers, R.A., Ed.; John Wiley & Sons Ltd., **2004**; pp. 1–23.

- [47] Launer, P. J.; Arkles, B. Infrared Analysis of Organosilicon Compounds. In *Silicon Compounds: Silanes and Silicones*; Arkles, B., Larson, G.L., Eds.; 3rd Ed.; Gelest, INC: Morrisville, PA; USA, **2013**; pp. 175–178.
- [48] Chen, G.; Zhou, Y.; Wang, X.; Li, J.; Xue, S.; Liu, Y.; Wang, Q.; Wang, J. *Sci. Rep.* **2015**, *5*, p. 1–14.
- [49] Caresani, J. R.; Lattuada, R. M.; Radtke, C.; Dos Santos, J. H. Z. *Powder Technol.* **2014**, *252*, p. 56–64.
- [50] Handke, M.; Kowalewska, *Spectrochim. Acta, Part A* **2011**, *79*, p. 749–757.
- [51] Fidalgo, A.; Ilharco, L. M. *Chem. - Eur. J.* **2004**, *10*, p. 392–398.
- [52] Hayami, R.; Ideno, Y.; Sato, Y.; Tsukagoshi, H.; Yamamoto, K.; Gunji, T. *J. Polym. Res.* **2020**, *27*, p. 316.
- [53] Ramezani, M.; Vaezi, M. R.; Kazemzadeh, A. *Appl. Surf. Sci.* **2015**, *326*, p. 99–106.
- [54] Park, E. S.; Ro, H. W.; Nguyen, C. V.; Jaffe, R. L.; Yoon, D. Y. *Chem. Mater.* **2008**, *20*, p. 1548–1554.
- [55] Kamiya, K.; Dohkai, T.; Wada, M.; Hashimoto, T.; Matsuoka, J.; Nasu, H. *J. Non-Cryst. Solids* **1998**, *240*, p. 202–211.
- [56] García-Cerda, L. A.; Mendoza-González, O.; Pérez-Robles, J. F.; González-Hernández, J. *Mater. Lett.* **2002**, *56*, p. 450–453.
- [57] Hagiwara, Y.; Shimojima, A.; Kuroda, K. *Chem. Mater.* **2008**, *20*, p. 1147–1153.
- [58] Nowacka, M.; Kowalewska, A.; Makowski, T. *Polymer* **2016**, *87*, p. 81–89.
- [59] Ospino, I.; Luquin, A.; Jiménez-Ruiz, M.; Pérez-Landazábal, J. I.; Recarte, V.; Echeverría, J. C.; Laguna, M.; Urtasun, A. A.; Garrido, J. J. *J. Phys. Chem. C* **2017**, *121*, p. 22836–22845.
- [60] Handke, M.; Jastrzębski, W. *J. Mol. Struct.* **2004**, *704*, p. 63–69.
- [61] Shi, Y.; Neufeind, J.; Ma, D.; Page, K.; Lamberson, L. A.; Smith, N. J.; Tandia, A.; Song, A. P. *J. Non-Cryst. Solids* **2019**, *516*, p. 71–81.
- [62] Tan, C. Z.; Arndt, J. *J. Chem. Phys.* **2000**, *112*, p. 5970–5974.
- [63] Choi, S. S.; Lee, A. S.; Lee, H. S.; Baek, K. Y.; Choi, D. H.; Hwang, S. S. *Macromol. Res.* **2011**, *19*, p. 261–265.
- [64] Gallardo, J.; Durán, A.; Di Martino, D.; Almeida, R. M. *J. Non-Cryst. Solids* **2002**, *298*, p. 219–225.

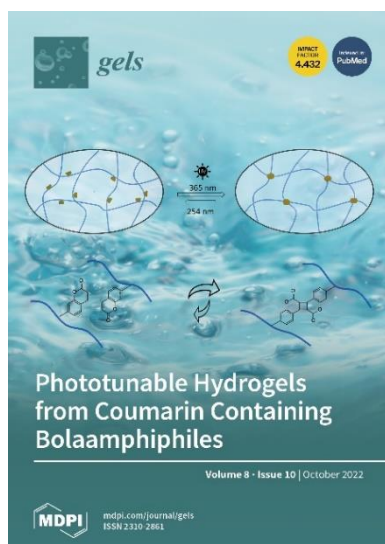
CHAPTER 5

NOVEL SILICA HYBRID XEROGELS PREPARED BY CO-CONDENSATION OF TEOS AND CLPHTEOS: A CHEMICAL AND MORPHOLOGICAL STUDY



CHAPTER 5

“NOVEL SILICA HYBRID XEROGELS PREPARED BY CO-CONDENSATION OF TEOS AND CIPhTEOS: A CHEMICAL AND MORPHOLOGICAL STUDY”



Published article

Authors: Guillermo Cruz-Quesada, Maialen Espinal-Viguri, María Victoria López-Ramón and Julián J. Garrido

Reference: *Gels* **2022**, *8*(10), p. 677.

Doi: 10.3390/gels8100677

Publication date: 20/10/2022

Keywords: xerogels; hybrid materials; TEOS; chlorophenyltriethoxysilane; chemical-textural properties; ORMOSILs; ordered structures; silica species.

Abstract: The search for new materials with improved properties for advanced applications is, nowadays, one of the most relevant and booming fields for scientists due to the environmental and technological needs of our society. Within this demand, hybrid siliceous materials, made out of organic and inorganic species (ORMOSILs), have emerged as an alternative with endless chemical and textural possibilities by incorporating in their structure the properties of inorganic compounds (i.e., mechanical, thermal, and structural stability) in synergy with those of organic compounds (functionality and flexibility), and thus, bestowing the material with unique properties, which allow access to multiple applications. In this work, synthesis using the sol-gel method of a series of new hybrid materials prepared by the co-condensation of tetraethoxysilane (TEOS) and 4-chlorophenyltriethoxysilane (CIPhTEOS) in different molar ratios is described. The aim of the study is not only the preparation of new materials but also their characterization using different techniques (FTIR, ^{29}Si NMR, X-ray Diffraction, and N_2/CO_2 adsorption, among others) to obtain information on their chemical behaviour and porous structure. Understanding how the chemical and textural properties of these materials are modulated with respect to the molar percentage of organic precursor will help to envisage their possible applications: From the most conventional such as catalysis, adsorption, or separation, to the most advanced in nanotechnology such as microelectronics, photoluminescence, non-linear optics, or sensorics.

5.1 INTRODUCTION

Silica hybrid gels are among the so-called organic modified silica (ORMOSILs). Nowadays, these materials are being used for multiple applications such as the adsorption of metals in water [1–3], catalyst support [4–6], support for luminescent compounds [7–9], anti-corrosive or fungicide coatings [10–13], and biomedicine [14–19]. The key behind the tunability of the properties of these materials is the synergetic effect that generates the coexistence, at a nanometric scale, of an inorganic skeleton with flexible and functional organic constituents [20,21]. The hybrid gels are prepared by the sol-gel method (see *Annexe A*), a very versatile synthetic technique that allows different approaches: (i) Anchoring of organic molecules in the porous of the already-formed solid gel [1,2,7–9], (ii) grafting of organic moieties on the surface of a silica material [4,22,23], (iii) co-condensation of an organosilane ($\text{SiR}_x(\text{OR}')_{4-x}$), with a carbon precursor, to form Si–O–C xerogels [16,18,24,25], or finally, (iv) classic co-condensation of a tetraalkoxysilane ($\text{Si}(\text{OR})_4$), usually tetraethoxysilane (TEOS), with one or more organosilanes [8–10]. In the latter approach, to obtain materials with the desired properties, it is of paramount importance to control the precursors' hydrolysis and condensation reactions (Figure 5.1), due to their susceptibility to the media conditions (pH, solvents, use or not of catalyst, proportions of H_2O /precursor or organosilane/tetraalkoxysilane) [26–30].

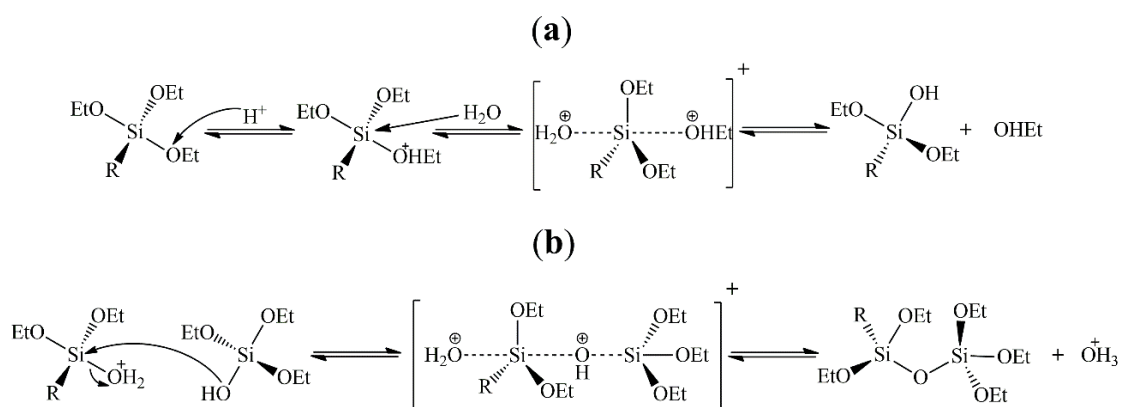


Figure 5.1. Mechanism in acidic media of (a) the first hydrolysis reaction of tetraethoxysilane ($R = \text{OEt}$) or triethoxysilane ($R = \text{alkyl or aryl}$), and (b) the co-condensation reaction of tetraethoxysilane with a triethoxysilane ($R = \text{alkyl or aryl}$).

The influence of these parameters in the synthesis of silica xerogels has been studied by our research group in recent years [31–34], with special emphasis on the nature and molar proportion of organosilanes in hybrid xerogels [35–37]. Using different techniques, such as mass spectroscopy, inelastic neutron scattering, and infrared spectra deconvolution, it was confirmed that ordered domains of polyhedral oligomeric silsesquioxanes (POSS) are formed within the silica matrix of the hybrid materials, due to the blocking of the condensation direction in the organic precursor RTEOS (RTEOS = alkyl/chloroalkyl triethoxysilanes) and the intermolecular forces (e.g., hydrophobic or electrostatic interactions) exerted by the organic moieties [38–40]. In fact, ordered domains were detected at lower molar percentages of organic precursor when chloroalkyltriethoxysilanes (CIRTEOS) were used instead of their analogous alkoxysilanes [37,40]. The knowledge acquired in those studies has been used to prepare optical fibre sensors (OFS) by dip-coating, using selected gels with specific properties. These sensors have a labile and specific interaction with different adsorbates, such as vapour of water and volatile organic compounds (COVs), allowing their detection and monitoring [41–43].

Following this line of research, the present work aims to study the morphological, textural, and chemical properties of silica hybrid xerogels containing a chlorophenyl moiety, and to evaluate their use as coatings for OFS in the future. For this purpose, a new series of transparent hybrid xerogels were prepared by co-condensation, in acidic media, of TEOS with (*p*-chlorophenyl) triethoxysilane (CIPhTEOS) at different molar percentages (the synthesis process is described in *Chapter 2.1.1*). The resulting materials were fully characterised by ^{29}Si NMR (Nuclear Magnetic Resonance), XRD (X-ray Diffraction), FTIR (Fourier-Transform Infrared Spectroscopy), Helium Pycnometry, FE-SEM (Field-Emission Scanning Electron Microscopy), HR-TEM (High-Resolution Transmission Spectroscopy), and the adsorption of N_2 ($-196\text{ }^\circ\text{C}$) and CO_2 ($0\text{ }^\circ\text{C}$). In addition, a modified and adjusted deconvolution method of the FTIR spectra was used to acquire semi-quantitative information about the proportion of $(\text{SiO})_4$ and $(\text{SiO})_6$ rings [40,44], which are related to ordered structures and amorphous silica, respectively. Finally, the results were compared with those of the previously studied xerogels to remark on the influence of the chlorophenyl moiety on the properties of the materials.

5.2 RESULTS AND DISCUSSION

5.2.1 Infrared spectroscopy (FTIR)

Figure 5.2 depicts the FTIR spectra in the spectral ranges of 1600–400 and 4000–2750 cm^{-1} of the hybrid xerogels synthesised at different molar percentages of organic precursor.

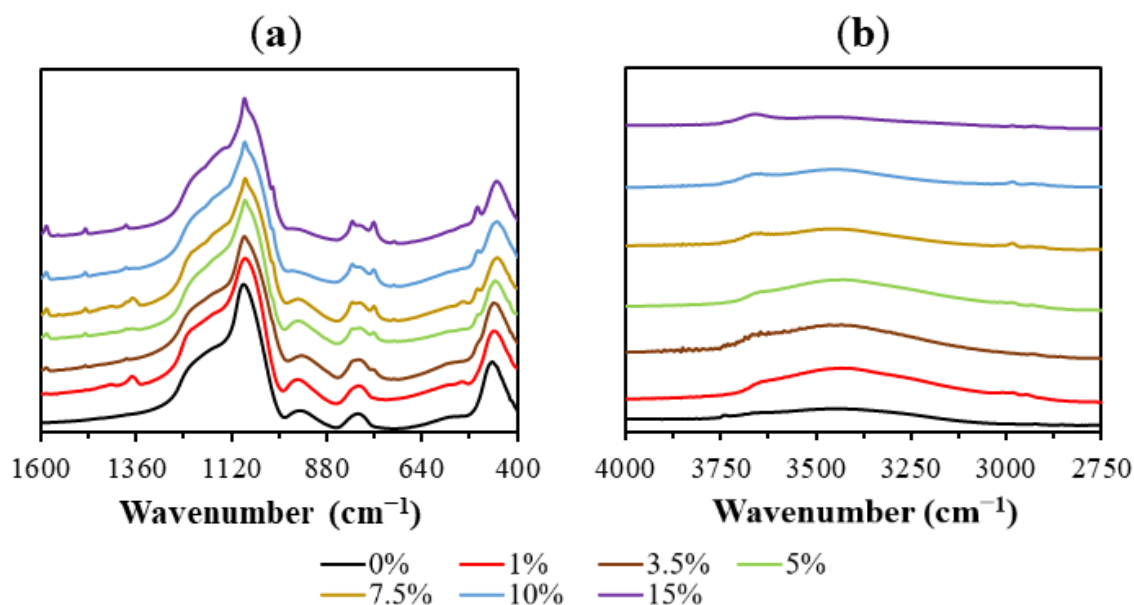


Figure 5.2. FTIR spectra of the reference (100%TEOS, 0% in the graphs) and the hybrid materials at different molar percentages of organic precursor (ClPhTEOS) within the range of (a) 1600–400 cm^{-1} and (b) 4000–2750 cm^{-1} .

In Figure 5.2a, the characteristic bands of the amorphous silica matrix can be observed: (i) rocking of O–Si–O at 455 cm^{-1} (ρ O–Si–O), (ii) symmetric Si–O–Si stretching vibration at 800 cm^{-1} (ν_s Si–O–Si), (iii) Si–O bond stretching vibration of the silanols on the surface at 955 cm^{-1} (ν_s Si–OH), (iv) asymmetric Si–O–Si stretching vibration at 1090 cm^{-1} (ν_{as} Si–O–Si), and (v) a wide and intense shoulder from 1350 to 1120 cm^{-1} associated with various vibrational modes of the Si–O–Si [45]. Additionally, a slight shoulder at 550 cm^{-1} can be observed, which is associated with the presence of 4-member siloxane rings, $(\text{SiO})_4$ [46]. In the spectra, as the molar percentage of organic precursor gradually increases, a new incipient shoulder becomes more evident at 1140 and 1155 cm^{-1} , and the band at 1080 cm^{-1} narrows and stands out, similar to an emerging peak. These changes could indicate that the organic precursor is favouring the formation, within the silica matrix, of new structures with vibration modes (ν_{as} Si–O–Si) at different specific frequencies [40]. In the spectral region of 400–2750 cm^{-1} (Figure 5.2b), it is

possible to observe the stretching bands of superficial silanols (ν Si–OH at 3450 cm^{-1}) and those resulting from the interaction of these groups through hydrogen bonds (ν Si–OH–H at 3660 cm^{-1}) [45].

The presence of the chlorophenyl moiety in the hybrid materials can be confirmed by a set of bands observed in the spectra: (i) the stretching bands of the hydrogens of the benzene ring in the range of $3090\text{--}3010\text{ cm}^{-1}$ (ν (C–H), Figure 5.2b), (ii) three C=C bond stretching bands in the spectral range of $1450\text{--}1000\text{ cm}^{-1}$ (1380 , 1085 and 1015 cm^{-1}), and finally, (iii) three bands corresponding to the deformation vibrations of the C–H bonds in the aromatic rings (at 815 , 760 , and 500 cm^{-1}), and a band due to the stretching vibration of the C–Cl bond (at 710 cm^{-1}) [43,47,48]. It should be noted that the spectrum of the xerogel 20ClPh is not shown in Figure 5.2 because a heterogeneous monolith with two well-differentiated phases was obtained: A non-coloured transparent phase above (monolith) and an opaque phase below (precipitate), whose spectra turned out to be very different (Figure 5.3c). This difference might be because the organic precursor favours the formation of structures with lower solubility in the reaction media, and thus precipitates. To test this hypothesis and obtain information on those structures, a material using only ClPhTEOS was synthesized, resulting in a white, soft, and extremely hydrophobic solid (100ClPh) (Figure 5.3d).

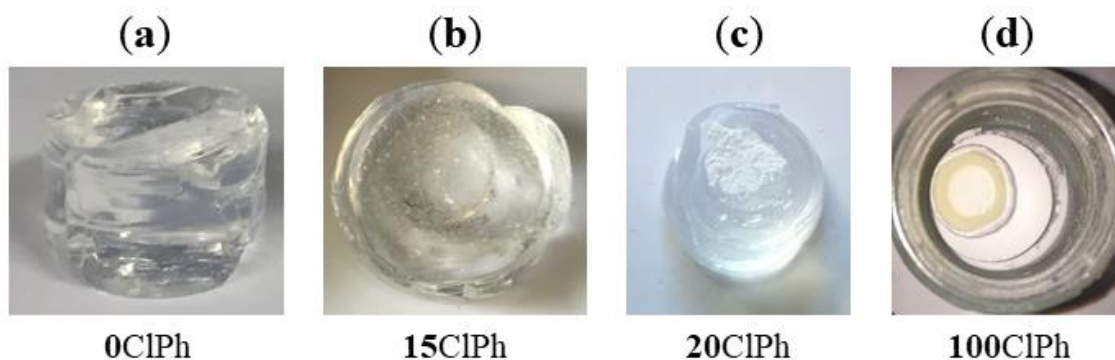


Figure 5.3. Pictures of ClPhTEOS materials: (a) 0ClPh, (b) 15ClPh, (c) 20ClPh, and (d) 100ClPh.

Figure 5.4 depicts the FTIR spectra of the reference, 15ClPh, 20ClPh (monolith and precipitate), and 100ClPh, while Table 5.1 displays the list of bands observed in the spectrum of 100ClPh, the vibrations and structures assigned to those bands, and the literature consulted for the assignment.

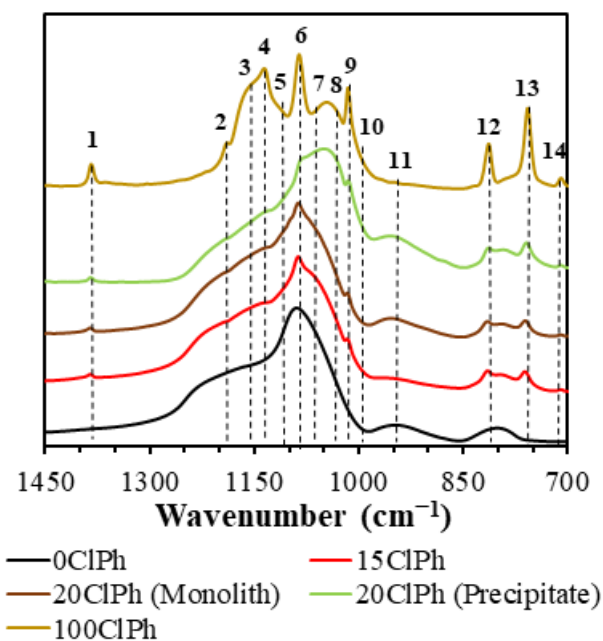


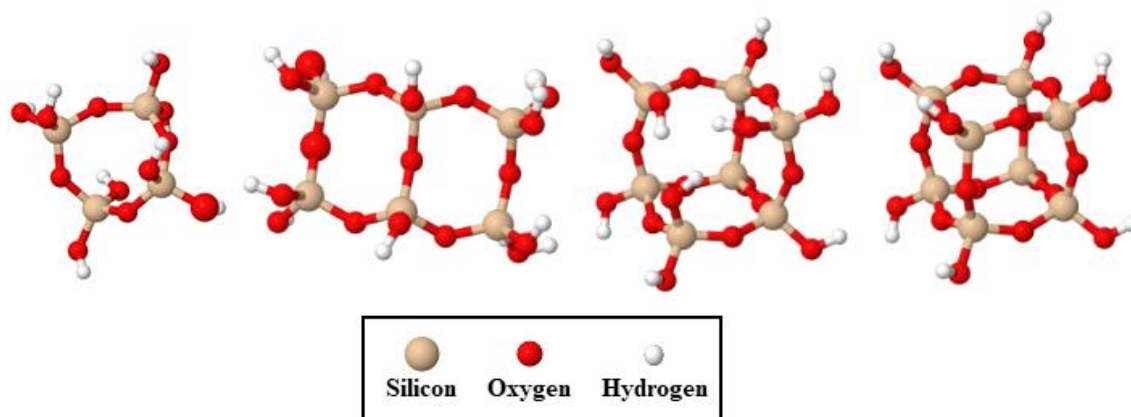
Figure 5.4. FTIR spectra (range 1400–900 cm^{-1}) of the reference, 15ClPh, and both phases of 20ClPh and 100ClPh.

The bands due to the vibrations of ν_{as} (Si–O–Si) in the spectral range of 1400–1000 cm^{-1} (Table 5.1) correspond to simple structures (linear siloxane chains and $(\text{SiO})_4$ or $(\text{SiO})_6$ rings) and more compact and complex structures (i.e., polyhedral oligomers of silsesquioxanes, POSS). Oligomers known as open or closed cages (T_7 and T_8 , respectively) and short ladders (SLd) are among the best-known POSS, which are formed by the fusion of two or more four-membered rings ($(\text{SiO})_4$) (Figure 5.5 depicts these structures formed by TEOS) [49–53].

Table 5.1. List of bands observed in the spectrum of 100ClPh and the proposed assignation of vibrations and structures.

Band number	Wavenumber (cm ⁻¹)	Vibration Assignation	Structural Unit	Reference
1	1380	ν (C=C)	Si-Ph-Cl	[36,48]
2	1190	ν_{as} (Si-O-Si), LO mode	(SiO) ₆	[40,44]
3	1160	$\nu_{ring-as}$ (Si-O-Si), LO mode	(SiO) ₄ ; T ₇	[54]
4	1135	$\nu_{ring-as}$ (Si-O-Si), LO mode	(SiO) ₄ ; T ₈	[40,44,54-56]
5	1120	ν_{ring-s} (Si-O-Si), LO mode	(SiO) ₄ ; T ₇ , Sld	[54]
6	1085	ν_{as} (C=C)	Si-Ph-Cl	[48]
7	1050	ν_{as} (Si-O-Si), TO mode	(SiO) ₄ , Sld	[40,44,54,56]
8	1030	ν_{as} (Si-O-Si), TO mode	(SiO) ₆	[40,44]
9	1015	ν_s (C=C)	Si-Ph-Cl	[48]
10	1005	ν_{as} (Si-O-Si)	Linear siloxane	[55]
11	950	ν (Si-O/Si-OH)	Si-OH	[40,44,46]
12	815	T _{δ,y} C-H	Si-Ph-Cl	[36,48]
13	760	Φ C-H	Si-Ph-Cl	[36]
14	710	C-Cl	Si-Ph-Cl	[36,47]

ν —Stretching vibration; ν_s —Symmetric stretching vibration; ν_{as} —Asymmetric stretching vibration; ν_{ring-s} —Antiparallel displacements of O atoms on opposite sides of a (SiO)_x ring; $\nu_{ring-as}$ —Parallel displacements of O atoms on opposite sides of a (SiO)_x ring; T _{δ,y} C-H—wagging out and inside the plane; Φ —deformation out and inside the plane; LO—Longitudinal optical vibration mode; TO—Transversal optical vibration mode; (SiO)₄—4-fold ring; (SiO)₆—6-fold ring; T₇—Open cage-like silsesquioxane; T₈—Cage-like silsesquioxane; SLd—Ladder-like silsesquioxane.

**Figure 5.5.** From left to right: 4-fold ring [(SiO)₄], short ladder (SLd), open-cage (T₇), and close-cage (T₈).

The formation of the rings that constitute these structures ((SiO)₄) is thermodynamically favoured in the oligomerization of siloxanes in acidic media [45,57], in contrast to the six-membered rings ((SiO)₆), kinetically favoured and typical of amorphous materials [39,58]. To study how the precursor affects the formation of ordered structures, it is necessary to know the proportion of (SiO)₄ in the silica matrix. For this purpose, the deconvolution of the FTIR spectra in the range of 1300–980 cm⁻¹ was performed using the non-linear least-squares method, obtaining the Gaussian–Lorentzian components. The different distances and degrees of torsion of Si–O–Si bonds in (SiO)₄ and (SiO)₆ rings allow us to distinguish bands belonging to the optical modes of vibration; two in transverse mode between 1100 and 1000 cm⁻¹ (TO₄ and TO₆) and two in longitudinal mode between 1250 and 1100 cm⁻¹ (LO₄ and LO₆) [40,44,59,60]. In this work, a modification of this method has been carried out, consisting of the adjustment of additional bands (Table 5.1) corresponding to (i) C=C and C–H vibrations of the chlorophenyl (1450–700 cm⁻¹); (ii) vibrations of the siloxane groups and Si–O bonds, characteristic of amorphous silica (950 and 800 cm⁻¹, respectively); (iii) vibrations of the (SiO)₄ rings that make up the POSS: $\nu_{\text{ring-s}}$ and $\nu_{\text{ring-as}}$ for the “open” species (T₇ and short ladders), and only $\nu_{\text{ring-as}}$ for the “closed” species (T₈), due to the $\nu_{\text{ring-s}}$ vibration mode being forbidden [54]; and (iv) ν_{as} (Si–O–Si) vibration of linear siloxanes. The calculated spectra and the bands generated for the reference xerogel, 5CIPh, 10CIPh, 15CIPh, the two phases of 20CIPh and 100CIPh are displayed in Figure 5.6.

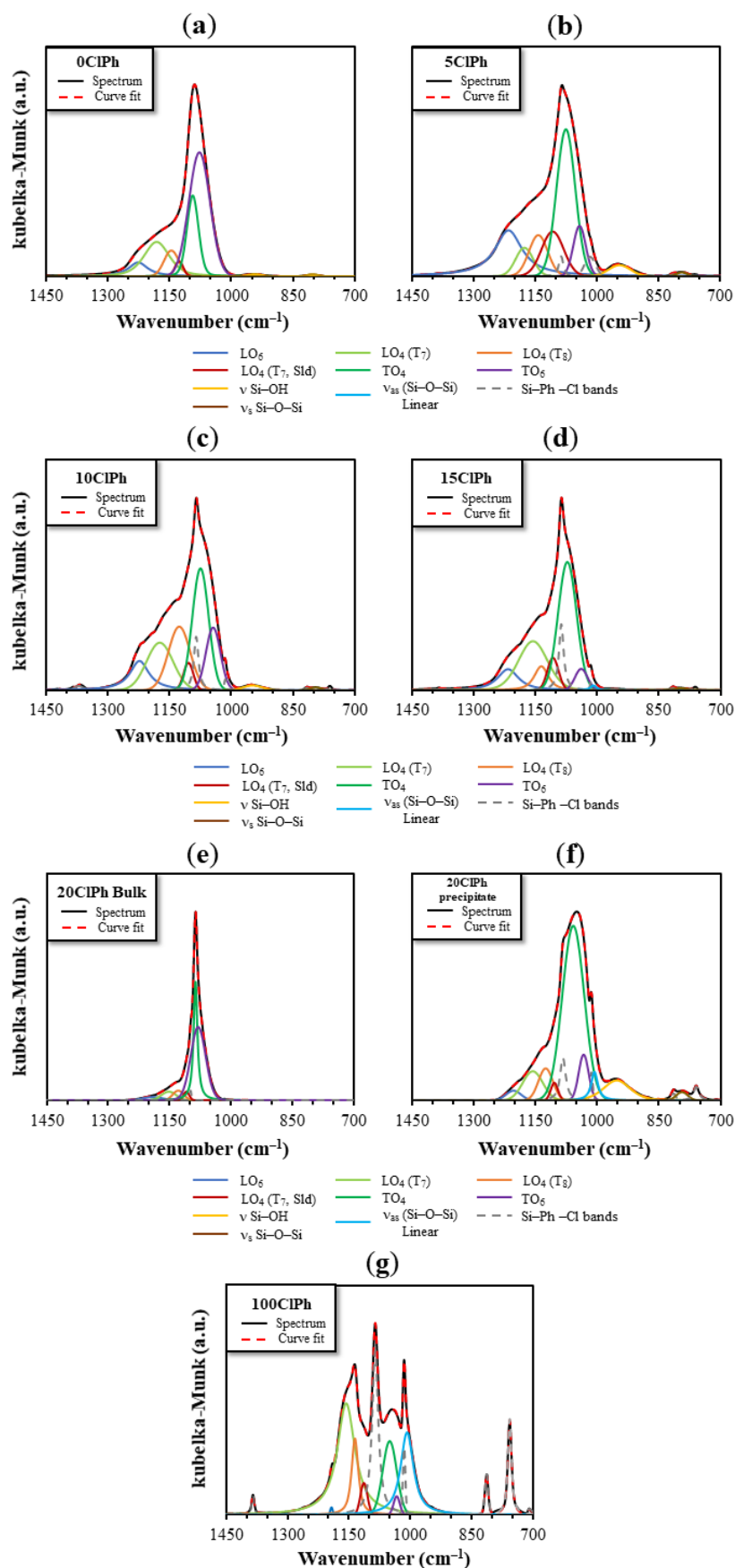


Figure 5.6. Synthetic spectra and Gaussian-Laurentzian bands generated in the curve fitting for: (a) 0CIPh, (b) 5CIPh, (c) 10CIPh, (d) 15CIPh, (e) 20CIPh(monolith), (f) 20CIPh(Precipitate), and (g) 100CIPh.

The percentage area of each component and the residual value (difference between the real spectrum and the fit) are exhibited in Table 5.2.

Table 5.2. Wavelength (ν) and percentual area (A) of the generated band in the curve fitting for each ClPhTEOS material, and their curve fitting parameters: number of iterations (I), and residual value (RV).

Band	0CIPh		5CIPh		10CIPh		15CIPh		20CIPh (Monolith)		20CIPh (Precipitate)		100CIPh	
	ν (cm^{-1})	A (%)	ν (cm^{-1})	A (%)	ν (cm^{-1})	A (%)	ν (cm^{-1})	A (%)	ν (cm^{-1})	A (%)	ν (cm^{-1})	A (%)	ν (cm^{-1})	A (%)
1	a	-	a	-	1371	0.6	1385	0.1	a	-	a	-	1385	0.8
2	1227	6.9	1216	23.3	1223	11.6	1193	14.5	1192	3.3	1204	2.1	1193	0.2
3	1182	19.4	1177	6.1	1174	17.4	1157	34.8	1153	5.9	1157	8.2	1157	32.8
4	1146	6.7	1143	9.5	1127	19.1	1135	6.4	1129	5.1	1126	6.4	1135	7.9
5	1127	2.1	1108	12.1	1104	3.7	1114	9.6	1110	2.4	1105	1.8	1114	2.5
6	a	-	1088	1.5	1085	5.1	1086	10.1	1099	0.7	1084	4.9	1086	16.4
7	1094	17.9	1076	33.6	1075	27.3	1050	39.8	1087	30.7	1059	53.3	1050	11.3
8	1077	46.2	1043	7.7	1044	12.5	1033	12.6	1081	52.0	1033	6.3	1033	1.3
9	a	-	1017	2.6	1015	0.3	1015	0.4	a	-	1014	0.9	1015	2.0
10	a	-	a	-	1007	0.6	1008	0.7	a	-	1006	3.9	1008	17.0
11	943	0.4	945	2.9	948	1.3	a	-	a	-	953	8.9	a	-
12	a	-	815	0.1	816	0.1	815	0.2	a	-	815	0.5	813	1.7
13	802	0.3	794	0.5	794	0.4	796	0.6	a	-	794	1.4	757	5.7
14	a	-	761	0.1	760	0.2	762	0.3	a	-	759	1.5	708	0.6
I	116		200		200		200		50		200		38	
RV	0.00520836		0.00137787		0.00148709		0.00167645		0.894758		0.00043146		0.000698583	

The percentage of four-membered and six-membered rings was determined by applying the following equations to the Gaussian–Lorentzian bell areas of the TO and LO components:

$$(\text{SiO})_6, \% = \frac{A(\text{LO}_6) + A(\text{TO}_6)}{A(\text{LO}_4) + A(\text{TO}_4) + A(\text{LO}_6) + A(\text{TO}_6)} \times 100 \quad (5.1)$$

$$(\text{SiO})_4, \% = \frac{A(\text{LO}_4) + A(\text{TO}_4)}{A(\text{LO}_6) + A(\text{TO}_6) + A(\text{LO}_4) + A(\text{TO}_4)} \times 100 \quad (5.2)$$

where $A(\text{LO})_6$ is the area of the band at 1190 cm^{-1} , $(\text{TO})_6$ is the area of the band at 1030 cm^{-1} , $A(\text{LO})_4$ is the sum of the areas of the three LO_4 bands, 1160 , 1135 , and 1120 cm^{-1} , and $A(\text{TO})_4$ is the area of the band at 1050 cm^{-1} . Table 5.3 displays the proportion of rings calculated by applying Equations (5.1) and (5.2). It can be observed that increasing the molar percentage of CIPhTEOS in the xerogels favours the formation of $(\text{SiO})_4$ rings (from 46.54% in the reference to 97.35% in 100CIPh).

Table 5.3. Proportion of $(\text{SiO})_4$ and $(\text{SiO})_6$ rings in the hybrid materials.

CIPhTEOS Material	LO ₆	LO ₄	TO ₄	TO ₆	(SiO) ₄	(SiO) ₆
	(%)				(%)	
0CIPh	7.0	28.5	18.1	46.5	46.5	53.5
5CIPh	26.7	31.8	38.6	3.0	70.4	29.6
10CIPh	12.8	43.9	29.8	13.6	73.7	26.3
15CIPh	12.3	43.1	33.9	10.7	77.0	23.0
20CIPh (Monolith)	3.3	13.4	30.9	52.4	44.3	55.7
20CIPh (Precipitate)	2.6	21.0	68.3	8.1	89.6	10.8
100CIPh	0.4	77.2	20.2	2.3	97.4	2.7

Another noteworthy observation is the great difference in the percentage of these rings between both phases of 20CIPh: The monolithic phase has a percentage of rings similar to that of the reference 0CIPh, and the phase that precipitates is similar to 100CIPh. This might be explained by considering that an increase in CIPhTEOS favours the formation of POSS, which are mainly formed by four-membered rings, and, as their abundance increases, there is a critical point at which these species exceed the molar solubility in the reaction media and segregate as a precipitate [61].

5.2.2 ^{29}Si Nuclear Magnetic Resonance (NMR)

^{29}Si NMR spectra of the hybrid materials were obtained to determine the relationship between the molar percentage of the precursor and the relative abundance of silicon species in the xerogels. Figure 5.7a depicts the spectra of the hybrid materials normalized with respect to the signal of the dominant species, Q^3 , the most intense in all cases.

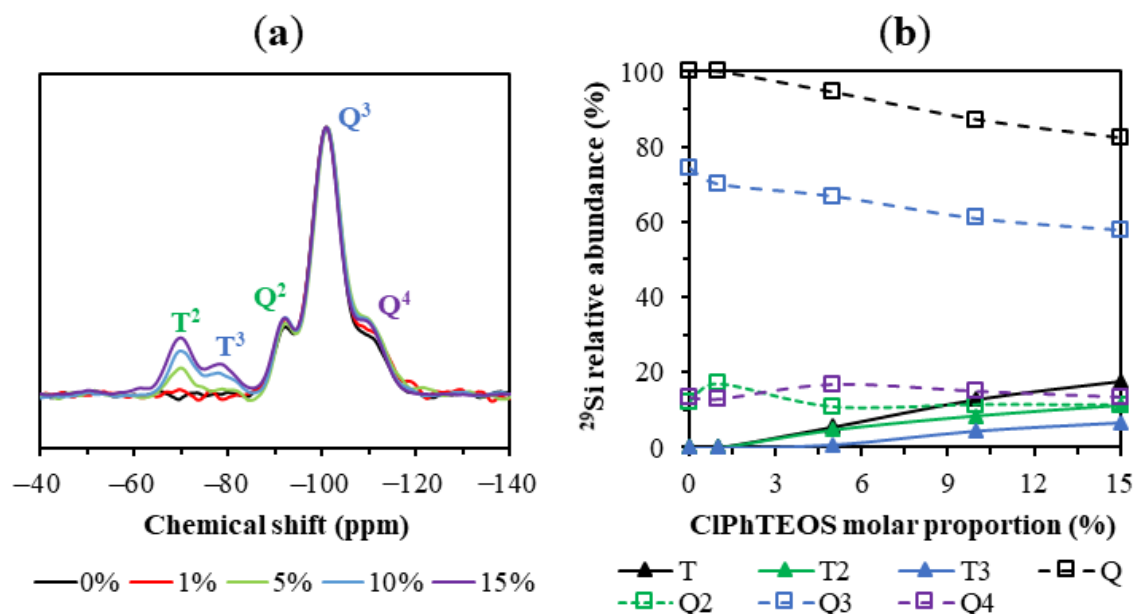


Figure 5.7. (a) Normalised ^{29}Si NMR spectra of the hybrid xerogels. (b) Variation of the relative abundance of the condensed species with respect to the percentage of CIPhTEOS.

The signals associated with the less condensed species (Q^1 and T^1) in Figure 5.7a are not observed. The dominant species corresponding to the hybrid precursor is the semi-condensed T^2 , whose intensity is greater than that of the more condensed T^3 in all the materials. In addition, Figure 5.7b displays both the evolution of the relative abundance of Q ($\text{Q}^2 + \text{Q}^3 + \text{Q}^4$) and T ($\text{T}^2 + \text{T}^3$) species with respect to the molar percentage of CIPhTEOS, as well as that of each species. For example, the Q^2 relative abundance increases slightly to stabilize at 11% and Q^4 increases up to 5% CIPhTEOS and then decreases at higher molar percentages of organic precursor. Table 5.4 exhibits the chemical shifts of each ^{29}Si species in the spectra and the integrals of the T species.

Table 5.4. Chemical shifts and integral areas of the ^{29}Si NMR spectra of the hybrid materials.

Xerogel	^{29}Si NMR (ppm)					Band areas			
	T ²	T ³	Q ²	Q ³	Q ⁴	T	T ²	T ³	T ³ /T ²
0ClPh	a	a	-92.1	-100.9	-109.0	a	a	a	-
1ClPh	a	a	-92.3	-101.0	-109.3	a	a	a	-
5ClPh	-69.8	-78.7	-92.3	-101.1	-109.4	5.5	4.7	0.8	0.2
10ClPh	-69.8	-79.1	-92.2	-101.0	-108.5	12.8	8.4	4.4	0.5
15ClPh	-69.8	-78.2	-92.1	-100.9	-108.6	17.6	11.1	6.5	0.6

^a—Not detected.

There is no significant displacement of the chemical shifts with the increase in ClPhTEOS, indicating that the environment of the silicon atoms does not change substantially. The chemical shifts of the T signals (organic precursor) are less negative than those of the Q signals (TEOS) because the chlorophenyl moiety removes less electronic charge from the silicon atom than oxygen, favouring the Shielding Effect [62,63]. Additionally, a higher positive charge density in the silicon atom favours nucleophilic attacks and therefore condensation [64,65]; however, the more abundant species is the least condensed and not T³, indicating that the inductive effect exerted by the chlorine atom of the chlorophenyl moiety is weaker than its steric effect, preventing total condensation in the materials. The increase in T³ species is related to the presence of POSS in the material, since the silicon atoms that form (SiO)₄ rings are mainly condensed species T³, Q³, or Q⁴ (less condensed structures T₇ and SLd also contain T² and Q²) [54]. In fact, the shifts of T³ species (Table 5.4) are closer to those observed in T₈ structures (-77 ppm) than to those of the aliphatic R-Si-O_{1.5} species (-66 to -67 ppm) [66,67]. Finally, it is worth mentioning that 100ClPh material only contains T units and, as has been verified in the analysis of its FTIR spectra, it is composed almost exclusively of (SiO)₄ rings.

5.2.3 X-ray Diffraction (XRD)

Figure 5.8 depicts the X-ray diffraction patterns of the hybrid materials synthesized at different molar percentages of organic precursor.

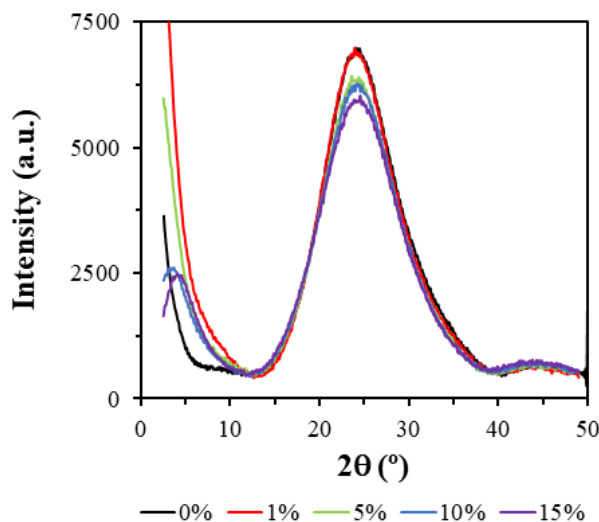


Figure 5.8. XRD diffractograms of the hybrid xerogels (reference, 1CIPh, 5CIPh, 10CIPh, and 15CIPh).

All the diffractograms showed a broad diffraction maximum at $2\theta \sim 24^\circ$, characteristic of the amorphous silica and associated with the distance between the silicon atoms linked by siloxane bridges [68]. This maximum slightly decreases with the increase in the molar percentage of the organic precursor. Interestingly, another maximum can be observed at $2\theta < 10^\circ$ when the molar percentage of the precursor is increased (10CIPh and 15CIPh). This new diffraction maximum is associated, in the literature, with the presence of ordered domains composed of POSS in the form of cages (T_7 or T_8) or short ladders within the amorphous matrix of the material [60]. The emergence of this maximum as the one at 24° decreases is consistent with the greater local structuration of the materials as we increase the molar percentage of the organic precursor. This behaviour was already seen in previously studied CIRTEOS xerogels ($R = M$, methyl; E , ethyl, or P , propyl), where it was found that the maximum at $2\theta < 10^\circ$ appeared at lower molar percentages than their analogous RTEOS. In these chlorinated series, the minimum molar percentages containing the new maximum were 30, 1, and 10% for CIMTEOS, CIETEOS, and CIPTEOS, respectively [37]. The CIPhTEOS series not only share this minimum percentage with the CIPTEOS but also have more T^2 than T^3 species, which could indicate that, although the chlorine atom in the precursors favours the condensation and the subsequent formation of POSS, the steric effect of the bulkier organic moieties (both propyl and phenyl) could generate less condensed POSS, such as T_7 or SLd. In all the

patterns, another low-intensity maximum is observed around 45° , which is associated, according to Bragg's law ($n = 2$ in $n\lambda = 2d \sin \theta$), with a replica of the maximum at $2\theta \sim 24^\circ$, indicating long-range order in the materials. Table 5.5 displays the angles, intensities, and distances calculated from Bragg's law for each maximum in the diffractograms of Figure 5.8.

Table 5.5. Bragg angles (2θ), band area (A), and bond distance (d_1 and d_2 (nm)) calculated from XRD maxima of hybrid xerogels at different molar percentages of organic precursor (ClPhTEOS).

Xerogel	Diffraction maximum $2\theta < 10^\circ$			Diffraction maximum $10^\circ > 2\theta > 30^\circ$		
	$2\theta_1$ ($^\circ$)	A_1	d_1 (nm)	$2\theta_2$ ($^\circ$)	A_2	d_2 (nm)
0ClPh	a	a	a	24.11	6481	0.369
1ClPh	a	a	a	23.93	6845	0.372
5ClPh	a	a	a	23.58	5921	0.377
10ClPh	3.6	2112	2.43	24.14	5778	0.369
15ClPh	4.1	1985	2.17	24.53	5534	0.363

^a—Not detected.

In 1ClPh and 5ClPh materials, the Si–O–Si bond elongates proportionally to the molar percentage of the precursor (maximum shifts to smaller angles), consistent with what was observed in the ^{29}Si NMR spectra, that is, the increase in T species (from the organic precursor) causes a decrease in the average positive charge density of the silicon atoms, and therefore, the siloxane bonds are less polarized. However, as the molar percentage of the organic precursor increases in 10ClPh and 15ClPh, the bond becomes shorter (the maximum shifts to higher angles). This effect, inverse to the one discussed above, is related to the appearance of a diffraction maximum at $2\theta < 10^\circ$ in 10ClPh and 15ClPh, since this maximum is associated with ordered POSS-type structures, where the siloxane bridges (Si–O–Si) that make up the $(\text{SiO})_4$ rings are more compact than those of the amorphous silica (formed mainly by $(\text{SiO})_6$) [40], thus explaining the decrease in Si–O–Si distances associated with the maximum at $2\theta \sim 24^\circ$. The calculated distances for the additional maximum at $2\theta < 10^\circ$ (displayed in Table 5.5) are similar to those associated with the organic moiety in the cage-like structures (1–3 nm) [39,51], and to that of the interplane between short ladders [53,69]. Additionally, the X-ray diffractogram of 100ClPh is depicted in Figure 5.9. In the diffractogram, a sharp and intense diffraction maximum at $2\theta = 6.84^\circ$ (1.3 nm) can be observed, which confirms that the 20ClPh precipitate contains a large amount of POSS. In a recent study, Nowacka *et al.* (2016)

reported an interplane distance of 1.24 nm for ladder-like phenylsilsesquioxane oligomers, suggesting that these are the species formed in 100CIPh [60].

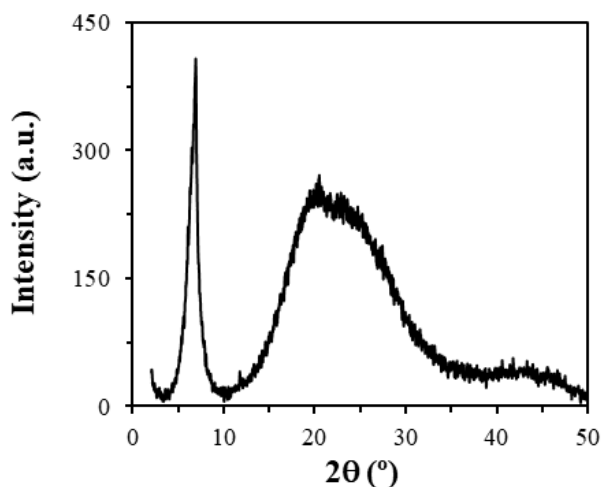


Figure 5.9. XRD diffraction pattern of 100CIPh.

5.2.4 Helium Pycnometry

Helium pycnometry reveals the skeletal density of the synthesized xerogels. Figure 5.10 depicts the variation in the skeletal density as a function of the molar percentage of CIPhTEOS.

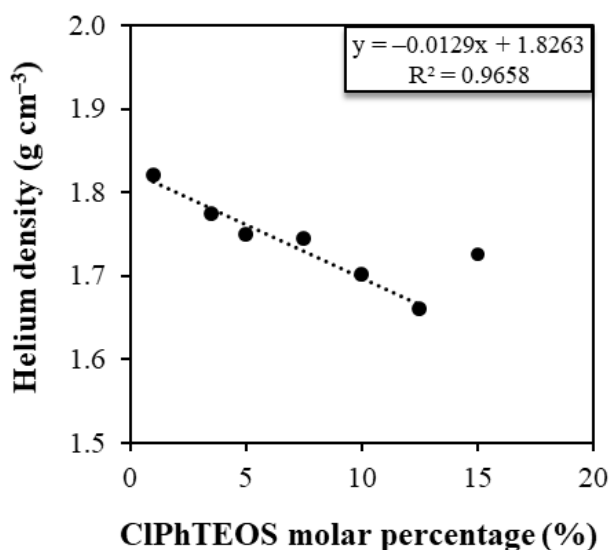


Figure 5.10. Skeletal density of the hybrid materials with respect to the percentage of CIPhTEOS.

A decrease in the skeletal density with respect to CIPhTEOS is observed, since the organic precursor blocks one of the hydrolysis and condensation positions, thus reducing the degree of cross-linking with respect to the reference material (100% tetraethoxysilane, TEOS). The skeletal density of 15CIPh is greater than expected, which indicates that the limit of precursor that the system can assimilate has been reached. This new series has lower values of skeletal density than the previously studied CIRTEOS series (R = methyl, M; ethyl, E; propyl, P). For example, for 10CIPh, the skeletal density is 1.68 in contrast to 1.91, 1.85, and 1.80 g cm⁻¹ for CIMTEOS, CIPTEOS, and CIETEOS, respectively [37]. This result is consistent with the information deduced from the ²⁹Si NMR spectra and the XRD diffractograms (CIPhTEOS favours the less condensed POSS, T₇ and SLd).

5.2.5 N₂ and CO₂ Adsorption Isotherms

N₂ and CO₂ molecules have a similar size; however, the temperature at which the adsorption takes place is very different, being -196 °C for N₂ isotherms and 0 °C for CO₂ isotherms. If the pores are very thin, N₂ molecules cannot access them due to kinetic restrictions; however, CO₂ molecules can. On the other hand, the high saturation pressure of CO₂ vapour (3.5 MPa) allows the finer microporosity to be explored in detail, which is covered at very low relative pressures. This fact makes the data provided by both isotherms complementary and makes it possible to differentiate the micropores of less than 0.7 nm and even the finest mesopores. If there are no kinetic constraints, N₂ adsorption provides the volume of pores of less than 50 nm, CO₂ adsorption of those sized less than 0.7 nm, and the difference of these values would provide the microporosity between 2 and 0.7 nm. This divergence can be explained by the different adsorption mechanisms taking place in both microporous intervals; in the so-called “primary micropore filling”, the ultramicropores are accessed at very low relative pressure ($p/p^{\circ} = 0.03$) and the adsorbent–adsorbate interactions predominate over those of the adsorbate–adsorbate, whereas, in wider micropores, the adsorbate–adsorbate interactions predominate, favouring a cooperative process of adsorption [70,71]. The N₂ adsorption isotherms (at -196 °C) and the CO₂ isotherms (at 0 °C) of the hybrid xerogels are shown in Figure 5.11.

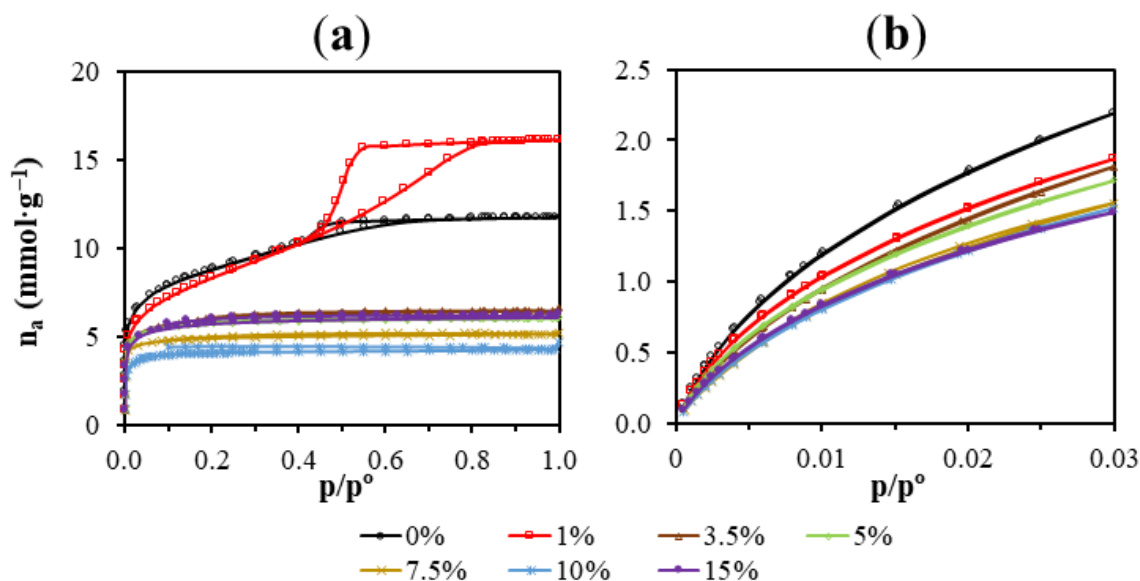


Figure 5.11. Isotherms of the hybrid xerogels: (a) N_2 ($-196\text{ }^\circ\text{C}$), and (b) CO_2 ($0\text{ }^\circ\text{C}$).

The isotherm of the reference material has an open knee, a sign of a wide micropore size distribution, characteristic of type I(b) isotherms. Moreover, its slope is pronounced in the adsorption, and it presents a hysteresis loop in the desorption (H2(a)), which is characteristic of a type IV isotherm typical of mesoporous materials. Therefore, the reference material can be considered micro-mesoporous with a type I(b)-IV(a) mixed isotherm [71]. Except for 1CIPh and 15CIPh materials, the higher the percentage of an organic precursor the smaller the pore volume, obtaining a type I(a) isotherm in all cases, typical of microporous materials with a narrow pore distribution. The isotherm of 1CIPh is a type IV(a) with an H1 hysteresis loop, indicating that, in this case, the organic precursor increases the total volume of pores and mesopores with respect to the reference, an effect that was also observed in analogous hybrid materials previously reported, which is associated with a change in the morphology of the pores, from cone-shaped to inkwell-shaped pores [27,37]. The 15CIPh isotherm is type I(a) but, surprisingly, it adsorbs more N_2 than 10CIPh, 7.5CIPh, and CIPh5. This fact is consistent with the value obtained for its skeletal density (Figure 5.10), which suggests that in this material, the limit of the organic precursor that the xerogel accepts is practically reached and is therefore heterogeneously distributed in the silicon matrix. Table 5.6 exhibits the textural parameters obtained from the adsorption isotherms.

Table 5.6. Textural parameters of the hybrid xerogels.

Xerogel	a_{BET}	a_{DR}	V_{micro}	V_{micro}	V_{meso}	V_{total}	BJH APS ^a	E_c ^b	E_c ^b
	(N ₂)	(CO ₂)	(N ₂)	(CO ₂)	(N ₂)	(N ₂)		(N ₂)	(N ₂)
	(m ² g ⁻¹)		(cm ³ g ⁻¹)				(nm)	(KJ mol ⁻¹)	
0ClPh	697	510	0.283	0.195	0.074	0.407	3.61	15.27	19.71
1ClPh	656	426	0.253	0.163	0.222	0.557	4.38	15.57	19.97
3.5ClPh	504	429	0.205	0.164	0.007	0.223	3.33	18.73	19.28
5ClPh	493	400	0.205	0.153	0.006	0.209	3.40	18.11	19.77
7.5ClPh	431	388	0.176	0.148	0.004	0.177	3.29	19.49	18.92
10ClPh	367	363	0.151	0.139	0.003	0.147	2.05	16.24	19.29
15ClPh	497	358	0.208	0.137	0.007	0.212	3.11	15.61	19.55

^a—Average Pore Size from desorption loop; ^b—Characteristic energy from Dubinin-Raduskevich.

A decrease in the specific surface area (a_{BET}) with the increase in the molar percentage of ClPhTEOS is observed, except for 15ClPh, which has a larger area than expected. Additionally, the table displays the volume of micropores obtained from the N₂ adsorption data ($V_{\text{micro(N}_2)}$), and of the narrowest micropores ($V_{\text{micro(CO}_2)}$, where $\phi < 0.7$ nm), determined by applying the Dubinin–Raduskevich equation to the CO₂ adsorption data. Both volumes decrease with an increase in the molar percentage of ClPhTEOS. The average pore size determined by the Barrett–Joyner–Halenda method (BJH APS) indicates that their mesoporosity narrows with the molar percentage of ClPhTEOS until microporous materials are obtained. In comparison with the ClRTEOS materials with the same percentage of the organic precursor, 10ClPh has a higher surface area and $V_{\text{micro(N}_2)}$ than those of ClPTEOS and ClTEOS, but lower than that of ClMTEOS [37]. This implies, once again, that these materials are less condensed due to the predominance of T² over T³ species and the bulky nature of the chlorophenyl group.

Figure 5.12 depicts the pore size distribution by applying DFT calculations to the N_2 and CO_2 isotherm data. All the materials are microporous, with an internal width close to 1 nm. The distribution shows that the materials do not present a significant volume of mesopores, except for the reference and 1CIPh.

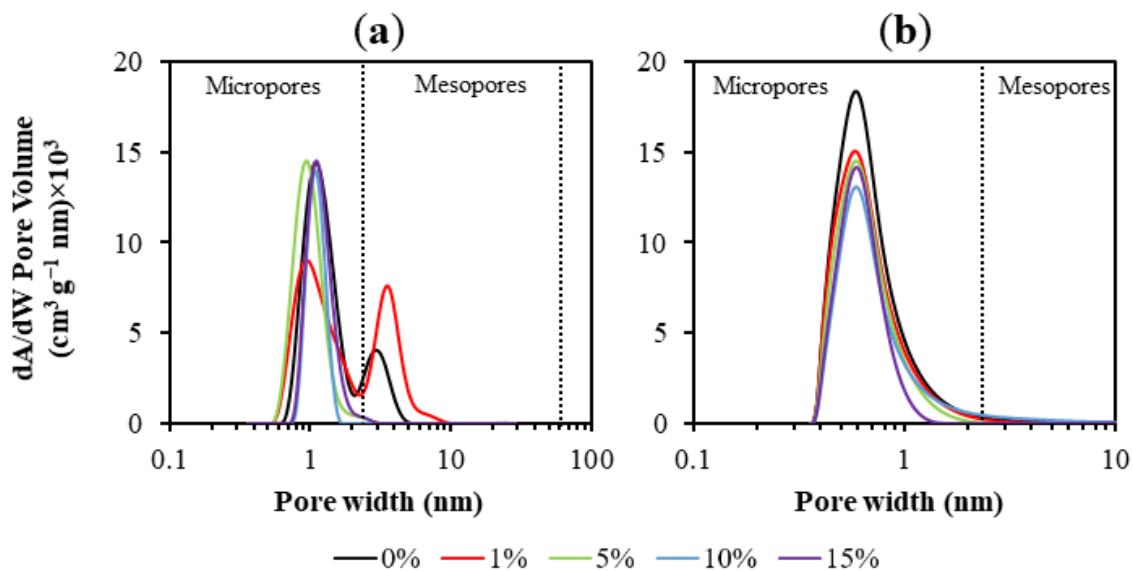


Figure 5.12. Pore size distribution of the materials calculated from (a) N_2 isotherms and (b) CO_2 isotherms.

5.2.6 Microscopy

5.2.6.1 Field-Emission Scanning Electron Microscopy (FE-SEM)

To determine the influence of the precursor on the texture, micrographs of the materials were acquired using scanning electron spectroscopy (SEM). The micrographs of the whole series are displayed in Figure 5.13.

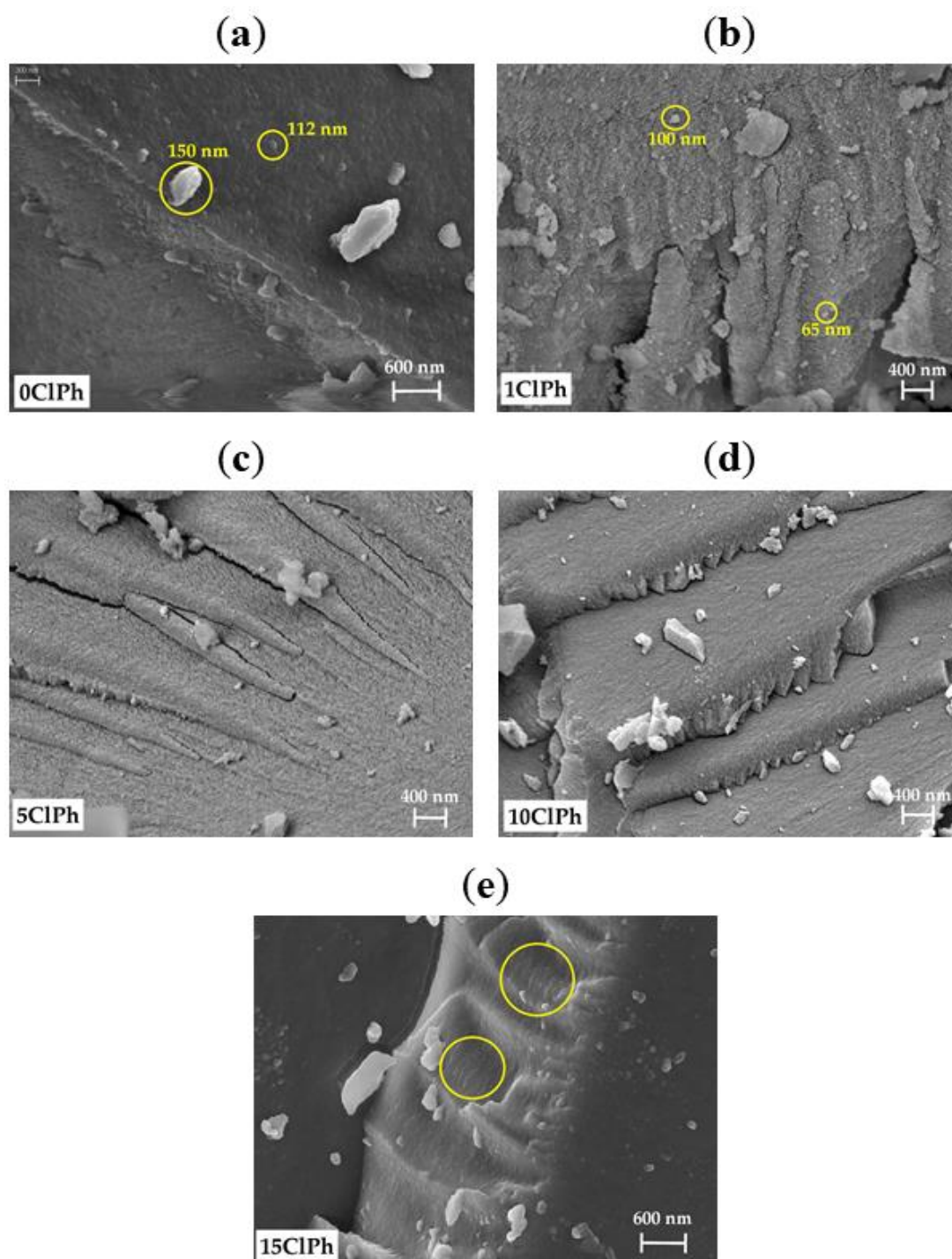


Figure 5.13. FE-SEM micrographs of: (a) 0ClPh, (b) 1ClPh, (c) 5ClPh, (d) 10ClPh, and (e) 15ClPh.

The micrograph of the reference material (Figure 5.13a) exhibits a rough morphology composed of small intersecting globular particles in a chainmail-like surface (110–150 nm). The space between the particles corresponds to the narrow mesoporosity of this material, consistent with the N₂ adsorption isotherm. Figure 5.13b shows how the use of only 1% of the organic precursor in the synthesis of 1CIPh results in a remarkable change: The surface is rougher, and the constituent particles are smaller (30–100 nm), justifying why the isotherm of this material reflects a greater specific surface area and mesoporosity than the reference material (0CIPh). In Figure 5.13c and 5.13d, respectively, CIPh5 and CIPh10 display a progressive smoothing of the surface with the increase in the organic precursor, which is consistent with the loss of mesoporosity and pore volume reduction deduced from their isotherms. A stratification of the surface can also be observed in overlapped compacted sheets to give mainly microporous materials. In CIPh15 (Figure 5.13e), the layers of compacted sheets, which are related to the stacking of the ladder POSS [53], can be better appreciated.

5.2.6.2 High Resolution-Transmission Electron Microscopy (HR-TEM)

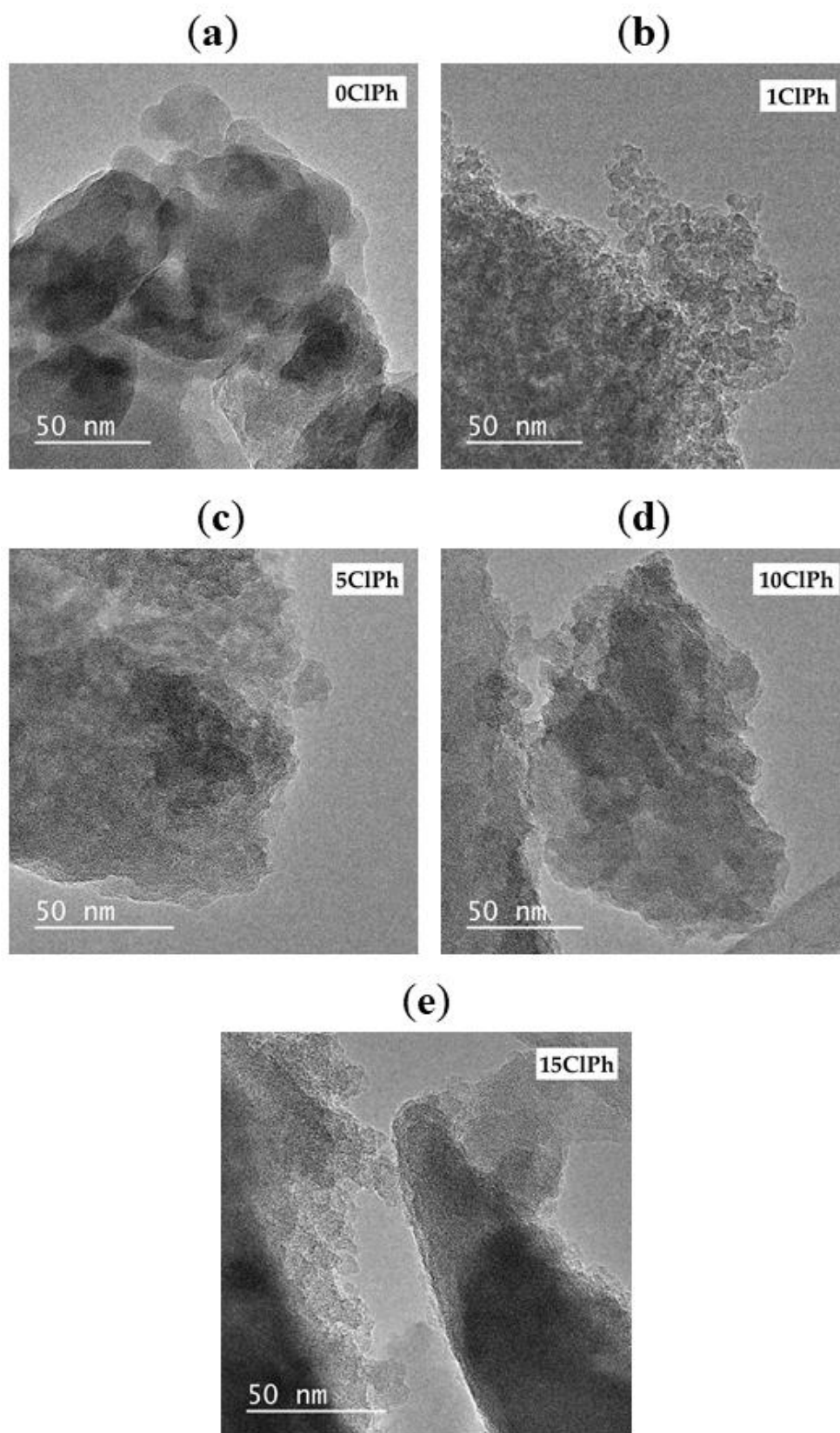


Figure 5.14. HR-TEM micrographs of (a) 0ClPh, (b) 1ClPh, (c) 5ClPh, (d) 10ClPh, and (e) 15ClPh.

The micrograph of the reference material (Figure 5.14a) exhibits a morphology formed by an agglomerate of large particles of several tens of nm, which leave holes that are related to the mesoporosity of the material. In the following micrograph (Figure 5.14b, 1CIPh), particles of smaller size are interconnected, but they are still identifiable, unlike in the micrographs of the materials with a higher percentage of CIPhTEOS. To determine the degree of precursor distribution in the material, a mapping of the weight percentage of chlorine in the materials was carried out by X-ray energy dispersion. Table 5.7 displays the experimental and theoretical weight percentage of chlorine obtained for each material.

Table 5.7. Average weight percentage of chlorine determined theoretically and by EDX of the hybrid materials.

Xerogels	Weight percentage of chlorine		E/T
	(wt %)		
	Theoretical (T)	Experimental (E)	
1CIPh	0.37	0.29	0.77
5CIPh	1.68	1.20	0.72
10CIPh	2.97	2.80	0.94
15CIPh	3.99	2.28	0.57

The weight percentages (wt%) of chlorine in Table 5.7 are the average of the values recorded in different particles of the sample and reflect that the actual content of chlorine in the materials is lower than the theoretical. However, most of the chlorophenyl precursor is found as part of 1CIPh, 5CIPh, and 10CIPh materials, in contrast to 15CIPh, where approximately half of the amount of precursor used for the synthesis is present in the material. This is consistent with what was observed in the rest of the characterization techniques since the results obtained are characteristic of a material with a lower molar percentage of the organic precursor than the actual amount used for its preparation.

5.3 CONCLUSIONS

A new series of hybrid xerogels has been prepared via the co-condensation of TEOS and ClPhTEOS as the organic precursor at different molar percentages. From the FTIR spectra of the materials and by applying a deconvolution method, the percentages of $(\text{SiO})_6$ and $(\text{SiO})_4$ rings in the silica matrix of the materials were determined, the former associated with amorphous silica and the latter with ordered structures such as polysilsesquioxanes (POSS). The study determined that increasing the molar percentage of the organic precursor leads to an increase in the proportion of four-membered rings, $(\text{SiO})_4$. The presence of POSS is consistent with the XRD diffractograms, where an additional maximum at $2\theta < 10^\circ$ associated with ordered domains is observed for the materials with the highest ClPhTEOS content. The ^{29}Si NMR spectra indicate that the most abundant silicon species from the organic precursor (T) are the semi-condensed (T^2), likely due to the steric and electronic effect exerted by the chlorophenyl groups during the crosslinking of the colloids. Regarding the textural properties, it has been determined that an increase in the organic precursor in the materials results in a loss of mesoporosity and specific surface area, and a narrower pore size distribution. This is closely related to the smoothing of the material's surface and the decrease in particle size observed in the FE-SEM and HR-TEM when increasing the molar percentage of ClPhTEOS. It is suggested that the layers that the micrographs exhibit are due to the stacking of the less condensed POSS (T_7 open cages and short ladders), whereas condensed ones (T_8 close cages) containing only hydrophobic chlorophenyl groups in their T^3 silicon atoms precipitate and cause the heterogeneity observed in the 20ClPh material. In fact, the aromatic moiety together with the electronic properties of the chlorine atom opens the door to a more specific interaction with volatile aromatic compounds, and thus, for the application of these materials in sensorics for the detection of pollutants in the atmosphere. The study of the chemical and textural properties of these novel hybrid materials is the prelude to their use in different relevant fields. In fact, the aromatic moiety together with the electronic properties of the chlorine atom opens the door to a more specific interaction with volatile aromatic compounds, and thus, to the application of these materials in sensorics for the detection of pollutants in the atmosphere.

5.4 ACKNOWLEDGEMENTS

The authors gratefully acknowledge the financial support received from “Ministerio de Ciencia e Innovación” from Spain (PID2020-113558RB-C42). G.C.-Q is thankful to “Ministerio de Universidades” of the Spanish government for the “Formación de Profesorado Universitario (FPU)” grant (FPU18/03467). The authors would also like to acknowledge the use of the “Centro de Instrumentación Científico-Técnica” at the University of Jaén, UCTAI at the Public University of Navarre and “Servicios Científico-Técnicos” at the University of Oviedo.

5.5 REFERENCES

- [1] Hannachi, Y.; Hafidh, A.; Ayed, S. *Chem. Eng. Res. Des.* **2019**, *143*, p. 11–23.
- [2] Kobylinska, N. G.; Kessler, V. G.; Seisenbaeva, G. A.; Dudarko, O. A. *ACS Omega* **2022**, *7*, p. 23576–23590.
- [3] Wojciechowska, P.; Cierpiszewski, R. *Appl. Sci.* **2022**, *12*, p. 1258.
- [4] Didó, C. A.; Coelho, F. L.; Closs, M. B.; Deon, M.; Horowitz, F.; Bernardi, F.; Schneider, P. H.; Benvenuti, E. V. *Appl. Catal., A* **2020**, *594*, p. 117444.
- [5] Estevez, R.; Luna, D.; Bautista, F. M. *Catal. Today* **2022**, *390–391*, p. 12–21.
- [6] Liu, M.; Wang, L.; Zhang, L.; Zhao, Y.; Chen, K.; Li, Y. *small* **2022**, *18*, p. 202104934.
- [7] Song, L.; Jia, Y.; Jin, X.; Wang, X.; Chen, M.; Wu, Y. *J. Lumin.* **2022**, *250*, p. 119071.
- [8] Vilela, R. R. C.; Zanoni, K. P. S.; de Oliveira, M.; de Vicente, F. S.; de Camargo, A. S. *S. J. Sol-Gel Sci. Technol.* **2022**, *102*, p. 236–248.
- [9] Santos, J. F. M.; Zanuto, V. S.; Ventura, M.; Bramorski, C. B.; Catunda, T. *Phys. Rev. Mater.* **2019**, *3*, p. 115201.
- [10] Alcántara-garcía, A.; García-casas, A.; Jiménez-morales, A. *Prog. Org. Coat.* **2020**, *139*, p. 105418.
- [11] Scotland, K. M.; Shetranjiwalla, S.; Vreugdenhil, A. J. *J. Coat. Technol. Res.* **2020**, *17*, p. 977–989.
- [12] Rodič, P.; Milošev, I.; Lekka, M.; Andreatta, F.; Fedrizzi, L. *Prog. Org. Coat.* **2018**, *124*, p. 286–295.
- [13] Hao, S.; Hu, C.; Lin, X. *Materials* **2021**, *14*(3), p. 577.
- [14] Wang, H.; Yue, W.; Zhang, S.; Zhang, Y.; Li, C.; Su, W. *catalysts* **2021**, *11*(12), p. 1463.
- [15] Hatano, K.; Teraki, M.; Nakajima, D.; Yamatsu, T. *Environ. Sci. Pollut. Res.* **2021**, *28*, p. 37562–37569.

- [16] Pérez-Moreno, A.; Reyes-Peces, M. virtudes; Vilches-Pérez, J. I.; Fernández-Montesinos, R.; Pinaglia-Tobaruela, G.; Salido, M.; de la Rosa-Fox, N.; Piñero, M. *Int. J. Mol. Sci.* **2021**, *22*(15), p. 8321.
- [17] Kapusuz, D. *J. Mater. Res.* **2019**, *34*, p. 3787–3797.
- [18] Goel, H.; Santhiya, D. *Mater. Chem. Phys.* **2022**, *281*, p. 125828.
- [19] Wendels, S.; de Souza Porto, D.; Avérous, L. *Polymers* **2021**, *13*(23), p. 4256.
- [20] Judeinstein, P.; Sanchez, C. *J. Mater. Chem.* **1996**, *6*(4), p. 511–525.
- [21] Kaya, G. G.; Deveci, H. *J. Ind. Eng. Chem.* **2020**, *89*, p. 13–27.
- [22] Kolle, J. M.; Sayari, A. *Microporous Mesoporous Mater.* **2022**, *343*, p. 112195.
- [23] Jahandar, M.; Ziaei-azad, H.; Sayari, A. *Chem. Eng. J.* **2022**, *450*, p. 138393.
- [24] Yan, J.; Kuang, M.; Zhu, Y.; Chen, Y.; Zhang, C.; Ma, H.; Zhang, X.; Kong, L. *J. Porous Mater.* **2022**, *30*, p. 103–113.
- [25] Flores-López, S. L.; Villanueva, S. F.; Rey-Raap, N.; Arenillas, A. *Materials* **2022**, *15*(1), p. 265.
- [26] Ramezani, M.; Vaezi, M. R.; Kazemzadeh, A. *Appl. Surf. Sci.* **2015**, *326*, p. 99–106.
- [27] Dudás, Z.; Len, A.; Ianăși, C.; Paladini, G. *Mater. Charact.* **2020**, *167*, p. 33–36.
- [28] Mageste, R. L.; Sampaio, D.; Mayrink, T. F.; Ahmed, H.; Palhares, H. G.; Nunes, E. H. M.; Houmard, M. *Microporous Mesoporous Mater.* **2022**, *342*, p. 112114.
- [29] Innocenzi, P. *The Sol-Gel Transition; 2^o Edition.*; Springer: Sassari, Italy, **2019**.
- [30] Zhao, X.; Wang, Y.; Luo, J.; Wang, P.; Xiao, P.; Jiang, B. *Silicon* **2021**, *13*, p. 3413–3421.
- [31] Estella, J.; Echeverría, J. C.; Laguna, M.; Garrido, J. J. *J. Non-Cryst. Solids* **2007**, *353*, p. 286–294.
- [32] Musgo, J.; Echeverría, J. C.; Estella, J.; Laguna, M.; Garrido, J. J. *Microporous Mesoporous Mater.* **2009**, *118*, p. 280–287.
- [33] Echeverría, J. C.; Estella, J.; Barbería, V.; Musgo, J.; Garrido, J. J. *J. Non-Cryst. Solids* **2010**, *356*, p. 378–382.
- [34] Echeverría, J. C.; Moriones, P.; Arzamendi, G.; Garrido, J. J.; Gil, M. J.; Cornejo, A.; Martínez-Merino, V. *J. Sol-Gel Sci. Technol.* **2018**, *86*, p. 316–328.
- [35] Rios, X.; Moriones, P.; Echeverría, J. C.; Luquín, A.; Laguna, M.; Garrido, J. J. *Adsorption* **2011**, *17*, p. 583–593.
- [36] Moriones, P.; Echeverría, J. C.; Parra, J. B.; Garrido, J. J. *Adsorption* **2020**, *26*, p. 177–188.
- [37] Cruz-Quesada, G.; Espinal-Viguri, M.; López-Ramón, M. V.; Garrido, J. J. *Polymers* **2021**, *13*, p. 1415.
- [38] Rios, X.; Moriones, P.; Echeverría, J. C.; Luquín, A.; Laguna, M.; Garrido, J. J. *Mater. Chem. Phys.* **2013**, *141*, p. 166–174.

- [39] Ospino, I.; Luquin, A.; Jiménez-Ruiz, M.; Pérez-Landazábal, J. I.; Recarte, V.; Echeverría, J. C.; Laguna, M.; Urtasun, A. A.; Garrido, J. J. *J. Phys. Chem. C* **2017**, *121*, p. 22836–22845.
- [40] Cruz-Quesada, G.; Espinal-Viguri, M.; López-Ramón, M. V.; Garrido, J. J. *Polymers* **2021**, *13*, p. 2082.
- [41] Estella, J.; De Vicente, P.; Echeverría, J. C.; Garrido, J. J. *Sens. Actuators, B Chem.* **2010**, *149*, p. 122–128.
- [42] Echeverría, J. C.; Faustini, M.; Garrido, J. J. *Sens. Actuators, B Chem.* **2016**, *222*, p. 1166–1174.
- [43] Echeverría, J. C.; Calleja, I.; Moriones, P.; Garrido, J. J. *Beilstein J. Nanotechnol.* **2017**, *8*, p. 475–484.
- [44] Fidalgo, A.; Ciriminna, R.; Ilharco, L. M.; Pagliaro, M. *Chem. Mater.* **2005**, *17*, p. 6686–6694.
- [45] Fidalgo, A.; Ilharco, L. M. *Chem. - Eur. J.* **2004**, *10*, p. 392–398.
- [46] Innocenzi, P. *J. Non-Cryst. Solids* **2003**, *316*, p. 309–319.
- [47] Lin, W.; Zheng, J.; Zhuo, J.; Chen, H.; Zhang, X. *Surf. Coat. Technol.* **2018**, *345*, p. 177–182.
- [48] Launer, P. J.; Arkles, B. Infrared Analysis of Organosilicon Compounds. In *Silicon Compounds: Silanes and Silicones*; Arkles, B., Larson, G.L., Eds.; 3rd Ed.; Gelest, INC: Morrisville, PA; USA, **2013**; pp. 175–178.
- [49] Marchesi, S.; Carniato, F.; Palin, L.; Boccaleri, E. *Dalton Trans.* **2015**, *44*, p. 2042–2046.
- [50] Choi, S. S.; Lee, A. S.; Lee, H. S.; Baek, K. Y.; Choi, D. H.; Hwang, S. S. *Macromol. Res.* **2011**, *19*, p. 261–265.
- [51] Wu, J.; Mather, P. T. *Polym. Rev.* **2009**, *49*, p. 25–63.
- [52] Choi, S. S.; Lee, A. S.; Hwang, S. S.; Baek, K. Y. *Macromolecules* **2015**, *48*, p. 6063–6070.
- [53] Jung, J.; Won, J.; Hwang, S. S. *J. Membr. Sci.* **2020**, *595*, p. 117520.
- [54] Park, E. S.; Ro, H. W.; Nguyen, C. V.; Jaffe, R. L.; Yoon, D. Y. *Chem. Mater.* **2008**, *20*, p. 1548–1554.
- [55] Guo, M.; Kanezashi, M.; Nagasawa, H.; Yu, L.; Yamamoto, K.; Gunji, T.; Ohshita, J.; Tsuru, T. *J. Membr. Sci.* **2019**, *584*, p. 56–65.
- [56] Hayami, R.; Ideno, Y.; Sato, Y.; Tsukagoshi, H.; Yamamoto, K.; Gunji, T. *J. Polym. Res.* **2020**, *27*.
- [57] Depla, A.; Verheyen, E.; Veyfeyken, A.; Van Houteghem, M.; Houthoofd, K.; Van Speybroeck, V.; Waroquier, M.; Kirschhock, C. E. A.; Martens, J. A. *J. Phys. Chem. C* **2011**, *115*, p. 11077–11088.
- [58] Handke, M.; Jastrzębski, W. *J. Mol. Struct.* **2004**, *704*, p. 63–69.

- [59] Hagiwara, Y.; Shimojima, A.; Kuroda, K. *Chem. Mater.* **2008**, *20*, p. 1147–1153.
- [60] Nowacka, M.; Kowalewska, A.; Makowski, T. *Polymer* **2016**, *87*, p. 81–89.
- [61] Blanco, I.; Bottino, F. A.; Abate, L. *Thermochim. Acta* **2016**, *623*, p. 50–57.
- [62] Vasil'ev, S. G.; Volkov, V. I.; Tatarinova, E. A.; Muzafarov, A. M. *Appl. Magn. Reson.* **2013**, *44*, p. 1015–1025.
- [63] Uhlig, F.; Marsman, H. C. ²⁹Si NMR - Some Practical Aspects. In *Gelest catalogue*; Gelest INC, Morrisville, PA. USA, **2008**, p. 208–222. Available online: <https://www.pascal-man.com/periodic-table/29Si.pdf> (accessed on 14 November 2020).
- [64] Cheng, X.; Chen, D.; Liu, Y. *ChemPhysChem* **2012**, *13*, p. 2392–2404.
- [65] Pierre, A. C. *Introduction to Sol-Gel Processing*; Klein, L., Ed.; 1st Ed.; Kluwer Academic Publishers: New York, NY, USA, **1998**.
- [66] Laird, M.; Yokoyama, J.; Carcel, C.; Unno, M.; Bartlett, J. R.; Wong Chi Man, M. *J. Sol-Gel Sci. Technol.* **2020**, *95*, p. 760–770.
- [67] Wu, X.; Qin, Z.; Zhang, W.; Yang, R. *React. Funct. Polym.* **2022**, *177*, p. 105284.
- [68] Kamiya, K.; Dohkai, T.; Wada, M.; Hashimoto, T.; Matsuoka, J.; Nasu, H. *J. Non-Cryst. Solids* **1998**, *240*, p. 202–211.
- [69] Jo, Y. Y.; Lee, A. S.; Baek, K. Y.; Lee, H.; Hwang, S. S. *Polymer* **2017**, *124*, p. 78–87.
- [70] Garrido, J. J.; Linares-solano, A.; Martín-Martínez, J. M.; Molina-Sabio, M.; Rodríguez-Reinoso, F.; Torregrosa, R. *Langmuir* **1987**, *3*, p. 76–81.
- [71] Thommes, M.; Kaneko, K.; Neimark, A. V.; Olivier, J. P.; Rodríguez-Reinoso, F.; Rouquerol, J.; Sing, K. S. W. *Pure Appl. Chem.* **2015**, *87*, p. 1051–1069.

CHAPTER 6

FROM FUNDAMENTAL MATERIALS CHEMISTRY TO SENSING APPLICATIONS: UNRAVELLING THE WATER ADSORPTION MECHANISM OF A LUMINESCENT OPTICAL FIBRE SENSOR MEMBRANE

AL	Xerogel		pH
	Eu ^{III}	Tb ^{III}	
None	TEOS-4.5		4.5
None	TEOS-2.7		2.7
PB	Eu-PB	Tb-PB	4.5
CA	Eu-CA	Tb-CA	2.7
3OHHPA	Eu-3OHHPA	Tb-3OHHPA	3.2
6OHHPA	Eu-6OHHPA	Tb-6OHHPA	3.4
DPA	Eu-DPA	Tb-DPA	2.8
MPA	Eu-MPA	Tb-MPA	3.3
APA	Eu-APA	Tb-APA	3.4
FPA	Eu-FPA	Tb-FPA	3.8

Hydrolysis Condensation: TEOS + Ln-AL (aq) + EtOH

Gelation

Aging / Curing

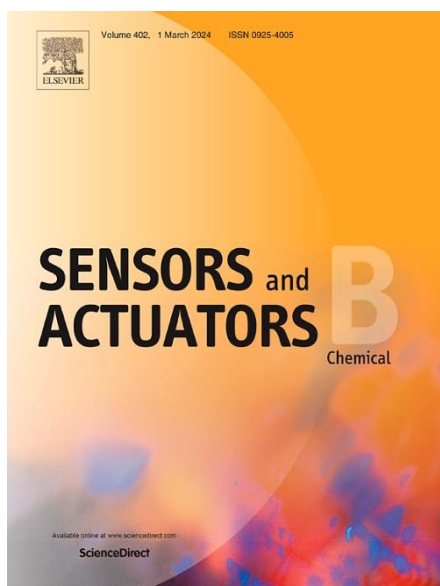
Drying

Dip-coating: 0.75 t_g

Fiber

CHAPTER 6

“FROM FUNDAMENTAL MATERIALS CHEMISTRY TO SENSING APPLICATIONS: UNRAVELLING THE WATER ADSORPTION MECHANISM OF A LUMINESCENT OPTICAL FIBRE SENSOR MEMBRANE”



Published article

Authors: Guillermo Cruz-Quesada, Beatriz Rosales Reina, Diego López Torres, Santiago Reinoso, María Victoria López-Ramón, Gurutze Arzamendi, César Elosua, Maialen Espinal-Viguri, and Julián J. Garrido

Reference: *Sens. Actuators, B* **2024**, 406, p. 135369. Doi: 10.1016/j.snb.2024.135369.

Publication date: 22/10/2024

Keywords: Silica xerogels; water adsorption; optical fibre sensor; isosteric enthalpy; lanthanides; luminescence.

Abstract: This work provides insight into the correlation between the luminescent response of a water-vapour optical fibre sensor and the textural properties of its lanthanide-doped silica coating. To this end, a library of 16 silica xerogels derived from combinations between 2 lanthanide dopants (Eu^{III} , Tb^{III}) and 8 antenna ligands was synthesised and characterised by photoluminescence spectroscopy and N_2 and CO_2 adsorption-desorption isotherms, among others. Based on the best luminescent response and most-suited porous texture, the material doped with Tb^{III} and 2,2'-(4-(2-Ethoxyethoxy)pyridine-2,6-diyl)bis(4,5-dihydrooxazole) was selected to construct the probe. A film of this material was affixed to a commercial silica fibre by dip-coating and the resulting sensor was tested in a climatic chamber with relative humidity ranging from 20 to 90% to obtain normalised time-response and calibration curves at three temperatures. The response was linear up to certain water-vapour concentrations, beyond which abruptly changed to polynomial, acting against the sensor resolution. The adsorption mechanism was elucidated by comparing the isosteric enthalpies of adsorption calculated from the sensor calibration curves to those determined from the monolith water-vapour isotherms, revealing that capillary condensation in the membrane mesopores was the key phenomenon leading to the response deviating from linearity.

6.1 INTRODUCTION

Porous silica xerogels (XGs) are known for their easy sol-gel synthesis and customised chemical and textural properties. This versatility makes them promising materials for a wide range of applications, from the most conventional (catalysts, adsorbents) to the most sophisticated (e.g., electronics). Due to their structural and thermochemical stability, they are also used as matrices to host a variety of functional substances conferring additional properties to the material. Beyond these characteristics, they show additional features suitable to develop coatings for optical fibre sensors (OFS), such as a refractive index analogous to that of optical fibres; transparency in a wide wavelength range, and the possibility of fine-tuning the porous texture and the surface chemistry by including functional guests in their matrix.

Luminophores are ideal functional guests to endow XG host matrices with optical properties. This strategy opens a wide field of research on the sensing response of the resulting materials because the XG porosity and surface chemistry directly affects the luminophore response by influencing the sensitivity towards target analytes. Lanthanide ions (Ln) are widely known for their characteristic luminescent emission originating from forbidden electronic transitions within shielded 4f and 5d orbitals, leading to small absorption coefficients and low emission rates. To overcome these drawbacks, they are usually sensitised through chelating antenna ligands bearing chromophores based on conjugated π -systems, which collect photons upon excitation to transfer charge to the emissive centre [1,2].

Luminescence is one of the transduction mechanisms on which OFS can be based [3]. The emission intensity and lifetime relate to changes in external parameters, allowing the development of pH, temperature, vapours, or humidity sensors [4–8]. The latter has drawn attention due to their application in many industrial processes, such as pharmaceutical, manufacturing, food processing, and paper production [9–11]. Humidity can affect the quality standards of goods as exemplified by some food types, which need constant humidity to avoid spoilage before consumption [12]. Furthermore, the air's relative humidity can significantly impact many physicochemical processes of industrial interest [13,14], making its monitorisation a relevant task for production.

The dependence of the sensor response on the analyte concentration has been widely studied in luminescence-based OFS, but little is currently known about the

influence on the signal of the mechanism governing the analyte adsorption on the coating surface. On this ground, this work was conceived to explore the correlation between the response of a water-vapour OFS and the textural properties of the luminescent XG used as the sensitive coating. Silica films have been previously used to successfully detect the presence of water [15–18], but studies on the prediction of the sensor response and the water adsorption mechanism are yet to be developed for luminescence-based OFS. Thus, we decided to prepare a catalogue of XGs with the desired porosity and surface chemistry and endow them with luminescence through doping with Ln^{III} ions and antenna ligands (AL). More specifically, two series of Eu^{III}- or Tb^{III}-doped XGs, each comprising eight materials varying in the AL type, were prepared (synthesis is detailed in *Chapter 2.1.2*), and the most suited in terms of porosity and luminescent emission was fully characterised and used as a coating to construct a luminescence-based humidity OFS (sensor construction and its sensing mechanism are described in *Chapter 2.3.1* and *2.3.2*, respectively). To evaluate its sensitivity, reproducibility, and reversibility towards humidity, calibration curves were obtained for the OFS at three different temperatures and water-vapour adsorption-desorption isotherms were registered for a monolith of the doped XG. The information gathered from these two techniques indicates that the coating luminescence decay relates to the concentration of adsorbed water and has allowed us to propose a plausible mechanism for the adsorption process with capillary condensation as the key factor.

6.2 RESULTS AND DISCUSSION

6.2.1 Luminescent and textural characterisation of Ln-AL xerogels

The luminescent response of the Ln-AL materials was preliminarily inspected with the bare eye through irradiation with a UV lamp for thin-layer chromatography to discriminate the most suitable materials before performing a full characterisation (Figure 6.1). The xerogel containing 6-trifluoromethylpicolinic acid and europium (Eu-FPA), and the ones containing 3-methylpicolinic acid (Eu-3MPA and Tb-3MPA), and 3-aminopicolinic acid (Eu-3APA and Tb-3APA) were straightforwardly discarded because of their barely perceptible or negligible emission. In the case of the xerogel containing terbium and the 6-trifluoromethylpicolinic acid ligand (Tb-FPA), its luminescence was

reasonable upon drying the monolith under vacuum as shown in Figure 6.1a, but abruptly decayed when it was exposed to the atmospheric humidity (Figure 6.1b). This behaviour led us to discard this material due to not fulfilling the requirement needed for our type of sensor of being gradually deactivated with increasing water vapour concentration. Although showing intense luminescence, the xerogels containing dipicolinic acid (Ln-DPA) were also discarded because the low AL solubility in the XG matrix rendered heterogeneous monoliths. The xerogels containing 2,2'-(4-(2-Ethoxyethoxy)pyridine-2,6-diyl)bis(4,5-dihydrooxazole) pybox (Ln-PB), chelidamic acid (Ln-CA), 3-hydroxypicolinic acid (Ln-3OHPA) and 6-hydroxypicolinic acid (Ln-6OHPA) met the required criteria for phase homogeneity, transparency, and intense emission, but the latter exhibited blue luminescence associated with the emission of the free ligand rather than the characteristic red or green emission of Eu^{III} and Tb^{III} . In contrast to the sharp and intense Ln emission peaks, those originating from hydroxypicolinates alone are known to be weaker and much broader [19], which makes these bands unsuitable for finely monitoring intensity variations as a response to external stimuli. This fact, together with the compositional heterogeneity arising from the presence of different luminophores in a single material, prevented us from selecting Eu-6OHPA for the OFS construction. After this preliminary test, Ln-PB, Ln-CA, and Ln-3OHPA were the materials chosen for further characterisation.

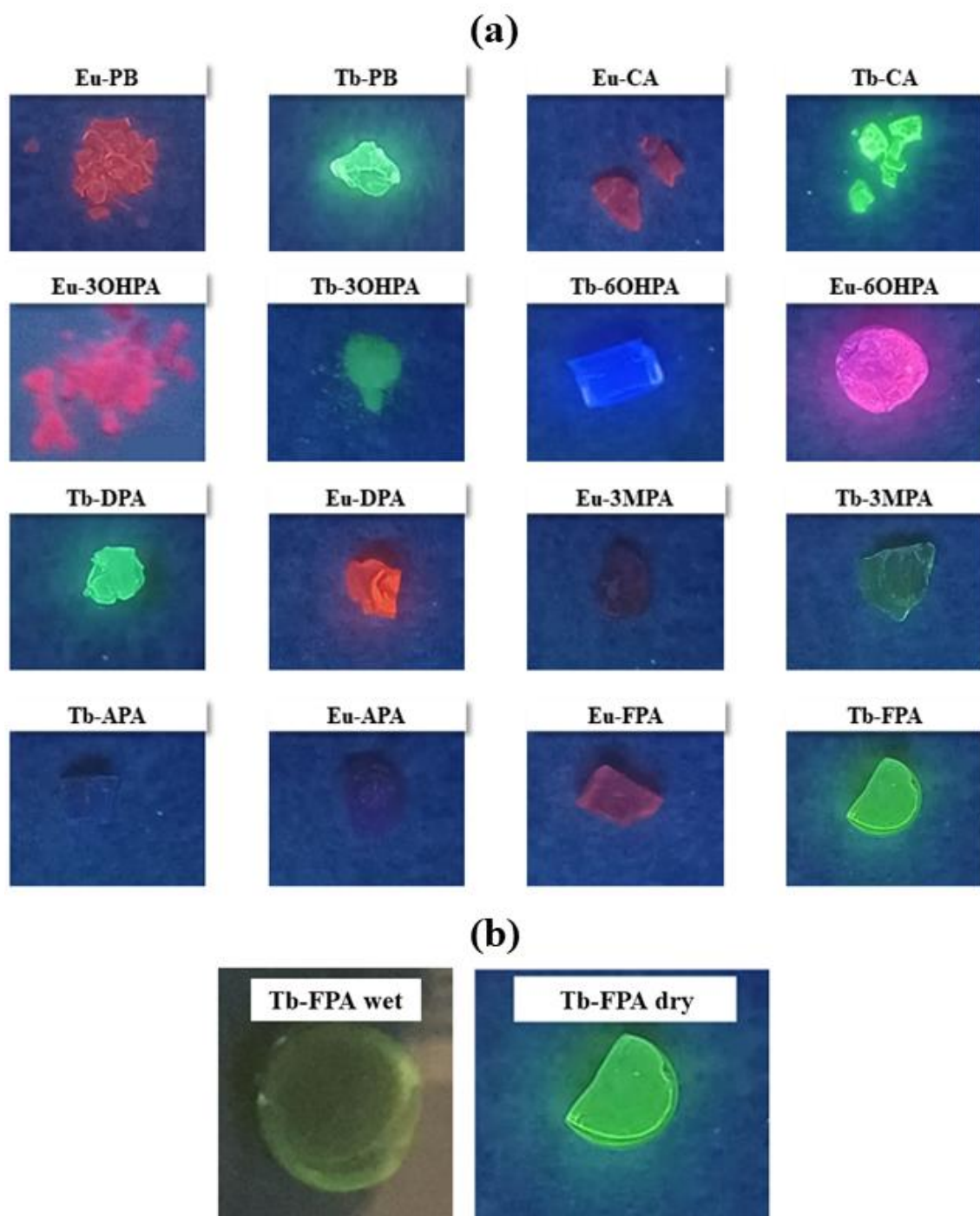


Figure 6.1. (a) Luminescent emission of vacuum-dried (100 °C) Ln-AL materials under UV lamp for thin layer chromatography (Vilber model CN-6 equipped with a VL-6.LC filtered UV lamp, Germany); (b) Luminescent emission of the vacuum-dried Tb-FPA monolith (left) compared to that of a moisturised counterpart (right).

Figure 6.2 displays the room temperature photoluminescence spectra of the selected materials. The excitation spectra were first obtained to determine the excitation wavelength required to optimise the Ln-emission while avoiding spectra overlapping. The emission spectra show the characteristic bands expected for each Ln ion: (i) 590, 615 and 650 nm for Eu^{III} , to $^5\text{D}_0 \rightarrow ^7\text{F}_j$ transitions ($J = 1, 2, \text{ and } 3$, respectively), and (ii) 490, 545 and 585 nm for Tb^{III} , corresponding to $^5\text{D}_4 \rightarrow ^7\text{F}_j$ transitions ($J = 6, 5, 4$, respectively) [20]. In all cases, the most intense emission peaks were those at 615 nm for Eu^{III} and 545 nm for Tb^{III} regardless of AL. Comparing the spectra shows that the Tb-CA and Tb-PB emissions are more intense than those of their Eu-counterparts, although the highest intensity corresponds to Eu-3OHPA. However, Ln-3OHPA materials display a blue emission band (Eu^{III} : 389 nm, Tb^{III} : 407 nm) associated with the free ligand, which indicates some degree of compositional heterogeneity as commented above for Ln-6OHPA. Moreover, the bidentate nature of 3OHPA might not fully prevent molecular oscillators (e.g. water, ethanol) from quenching the luminescence by incorporation into the Ln coordination sphere, in contrast to the coordinative saturation that the tridentate CA or PB can afford. These two aspects combined led us to discard Ln-3OHPA xerogels for the OFS construction at this stage.

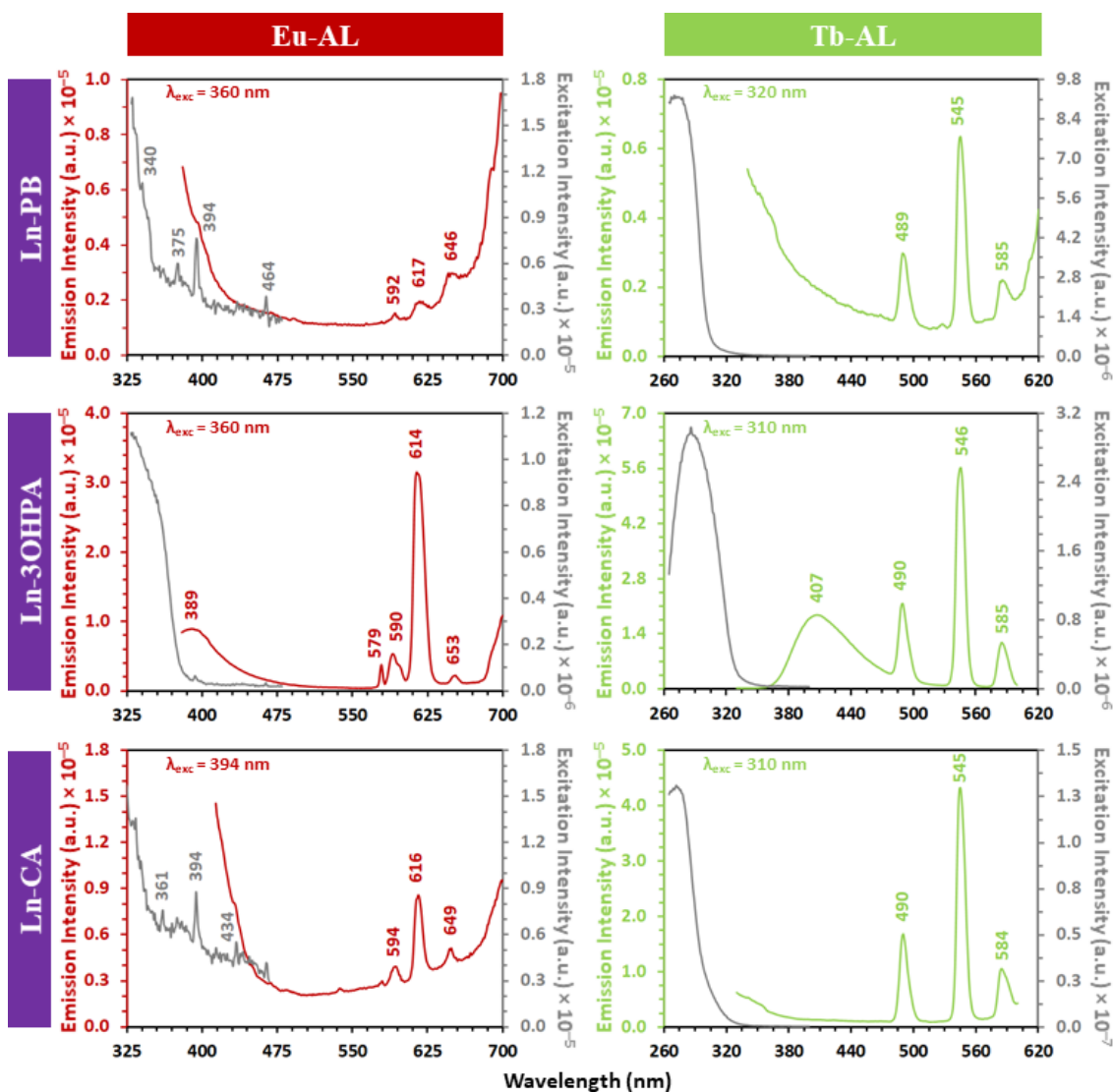


Figure 6.2. Room-temperature excitation (black) and emission (Eu^{III}: red; Tb^{III}: green) spectra of Ln-PB, Ln-3OHPA, and Ln-CA.

Figure 6.3 (top) shows the N₂ adsorption-desorption isotherms (−196 °C) of the selected Ln-AL materials compared to those of their corresponding TEOS references (semilogarithmic scale isotherms are depicted in the centre of Figure 6.3 to facilitate comparison at low partial pressures (p/p°)), while Table 6.1 compiles the textural parameters determined from the adsorption branches. TEOS-4.5 exhibits a mixed isotherm type that can be best described as IV(a)-I(b) according to the IUPAC classification. It is characteristic of micro-mesoporous materials, as evidenced by the positive slope of the adsorption branch at low relative pressures ($p/p^{\circ} < 0.30$), the hysteresis loop between ~ 0.42 and $0.65 p/p^{\circ}$, and the absence of any adsorption in the macroporous range (0.8 to $0.95 p/p^{\circ}$) [21]. Increasing sol acidity is known to be detrimental to the condensation of colloids, preventing the formation of mesopores and

leading to narrower micropores as pH decreases. This agrees with what is observed for TEOS-2.7, which shows a type I(a) isotherm (reaching a plateau at low relative pressures upon a sharp knee) associated with microporous materials showing negligible mesoporosity. Consistently, fewer amounts of adsorbed N_2 and lower pore volumes are observed.

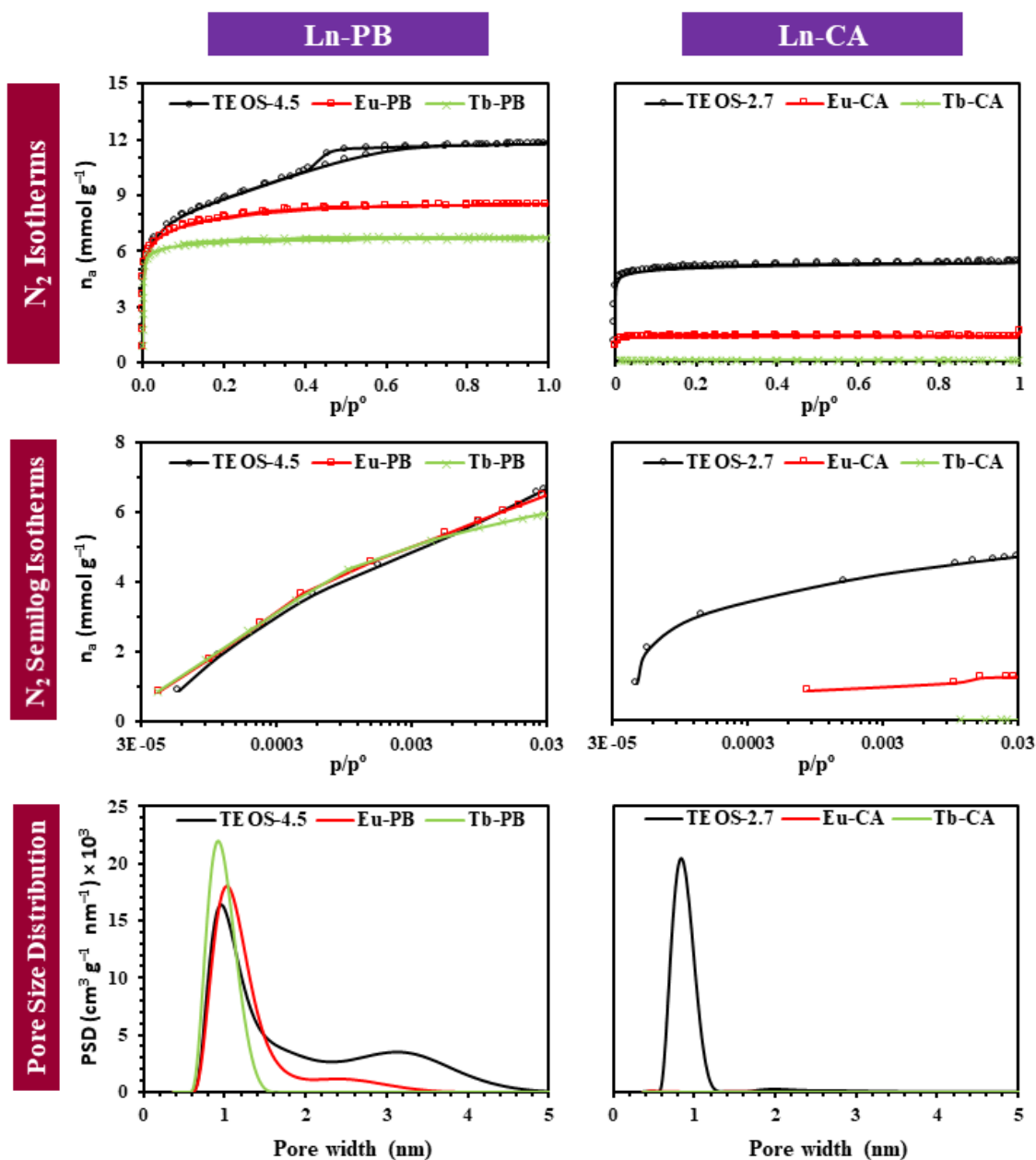


Figure 6.3. N_2 adsorption-desorption isotherms in both scales, (**top**) normal and (**centre**) semi-logarithmic, and (**bottom**) pore size distribution of Ln-PB and Ln-CA compared to those of their TEOS references.

Table 6.1. Textural parameters determined from the adsorption isotherms for Ln-AL materials and their TEOS references.

Ln-AL material	$a_{\text{BET}}^{\text{a}}$	a_{DR}^{b}	$V_{\text{micro}}^{\text{c}}$	$V_{\text{micro}}^{\text{c}}$	$V_{\text{meso}}^{\text{d}}$	$V_{\text{total}}^{\text{e}}$	PSD ^f	PSD ^f	E_{c}^{g}	E_{c}^{g}
	(N ₂)	(CO ₂)	(N ₂)	(CO ₂)	(N ₂)	(N ₂)	Maximum N ₂ ($\phi < 2$ nm)	Maximum (CO ₂)	(N ₂)	(CO ₂)
	(m ² g ⁻¹)		(cm ³ g ⁻¹)				(nm)		(kJ mol ⁻¹)	
TEOS-4.5	697	510	0.29	0.19	0.12	0.41	0.95	0.59	15.5	19.9
Eu-PB	647	439	0.27	0.18	0.01	0.29	1.02	0.61	16.5	19.0
Tb-PB	569	379	0.23	0.16	ⁱ	0.23	0.91	0.59	22.2	19.0
TEOS-2.7	445	494	0.18	0.21	0.01	0.18	0.83	0.59	24.3	20.0
Eu-CA	^h	502	^j	0.21	^j	^j	^h	0.56	^j	20.2
Tb-CA	^h	515	^j	0.22	^j	0.04	0.76	0.56	^j	20.2

^aSpecific surface area obtained from the BET model; ^bSpecific surface area calculated by applying the DR method; ^cMicropore volume obtained from DR; ^dCalculated from the isotherm ($V_{\text{meso}} = V_{\text{total}} - V_{\text{macro}} - V_{\text{micro}}$); ^eTotal pore volume obtained from the isotherm at $p/p_0 = 0.95$; ^fPore size distribution calculated with DFT-based methods; ^gCharacteristic energy from DR; ^hSpecific surface area cannot be calculated using BET; ⁱPore volume lower than 0.01 m²·g⁻¹; ^jInsufficient data for applying DR

The incorporation of Ln and AL guests induces significant changes in the porous texture of the XG host matrices as indicated by the marked differences between TEOS and Ln-AL isotherms. Regardless of the pH, all luminescent materials adsorb less amount of N₂ than their references, having substantially lower specific surface areas and pore volumes. For Ln-PB, this fact is mainly due to the cancellation of mesoporosity accompanied by a slight decrease in the microporous domain when Tb^{III} is used as the dopant. Accordingly, Tb-PB shows a type I(a) isotherm whereas that of Eu-PB (reaching saturation through a smooth slope beyond a flat knee) corresponds to the type I(b), characteristic of microporous materials with a slight volume of micropores ($\phi > 1$ nm). Compared to the TEOS-4.5, the sharper knees at lower pressures in both Ln-PB isotherms indicate the predominance of narrower pores with more similar widths upon doping. Tb-PB has a narrower pore size distribution (PSD) than Eu-PB as evidenced by the sharp knee of its type I(a) isotherm in comparison to the flat knee of the type I(b) isotherm of the latter. The PSD of the xerogels (depicted at the bottom of Figure 6.3), calculated through the density functional theory methods, confirms that Eu-PB has a wider distribution of micropore sizes than Tb-PB and a lower volume of micropores with $\phi < 1$ nm because part of its porosity originates from narrow mesopores. Its maximum pore volume is centred at pore width values higher than those of Tb-PB or even TEOS-4.5 (Table 6.1). For Ln-CA materials, the decrease of specific surface areas and pore volumes upon doping is as substantial as to lead to xerogels that barely adsorb N₂, hence PSD analyses do not provide any reliable information.

To explore the ultramicroporosity ($\emptyset \leq 0.7$ nm) of Ln-AL materials, CO₂ isotherms (0 °C) in both scales, normal and semi-logarithmic (Figure 6.4, top and centre, respectively) [22], and PSD values (Figure 6.4 bottom) were also obtained, revealing slightly opposite trends depending on the ligand.

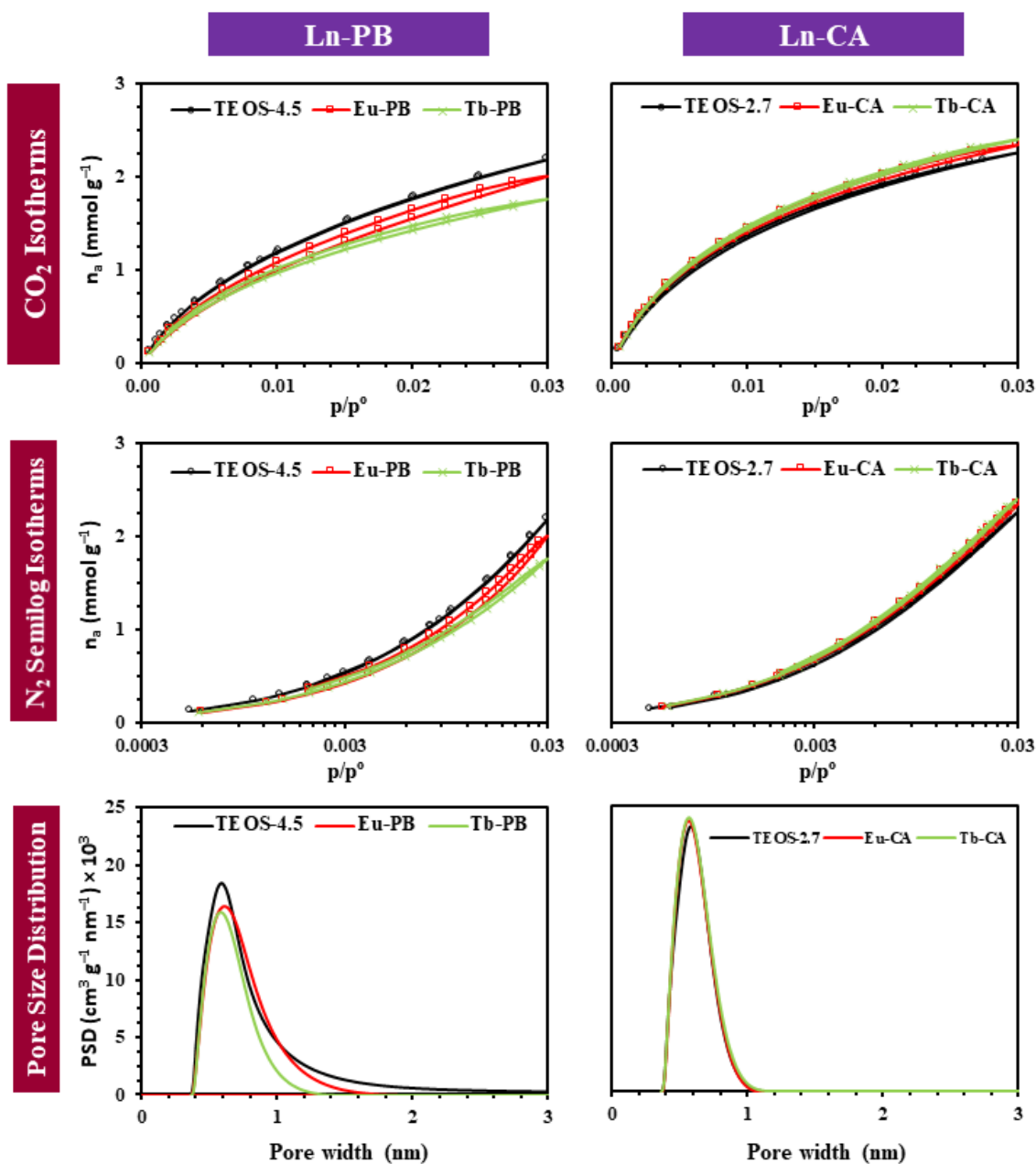


Figure 6.4. CO₂ adsorption-desorption isotherms in both scales, (top) normal and (centre) semi-logarithmic, and (bottom) pore size distribution of Ln-PB and Ln-CA compared to those of their TEOS references.

Both Ln-PB materials adsorb slightly fewer amounts of CO₂ than TEOS-4.5, which originates from subtle reductions of the ultramicroporous volume upon doping, Tb enhancing this effect over Eu as observed for the N₂ isotherms. In contrast, the adsorption of CO₂ in Ln-CA xerogels is slightly higher than that of TEOS-2.7. This implies that Ln-CA are purely ultramicroporous rather than non-porous materials and that the lack of N₂ adsorption is caused by kinetic restraints to diffuse through the pores. PSD analyses show that the Ln-AL microporosity is mainly due to ultramicropores and micropores with 0.7 nm < \emptyset ≤ 1 nm, although Ln-PB have a small contribution of wider pores (\emptyset > 1 nm). For Ln-CA materials, the ultramicroporous texture remains mostly unaffected upon doping, as revealed by the fact that the PSD curves are nearly identical to that of TEOS-2.7.

Overall, the adsorption data obtained with both probe molecules indicate that doping the XG matrix with Ln and AL species noticeably affects the porous texture by reducing the pore volumes and specific surface areas and narrowing the pore diameters. For Ln-PB, it is worth noticing that the Eu-containing xerogel adsorbs more N₂ and CO₂ than the Tb-analogue; Eu^{III} is larger than Tb^{III} due to the lanthanide contraction effect, thereby being more prone to form complexes with higher coordination number that would require larger pores volumes to accommodate within the matrix.

6.2.2 Selection of the target OFS coating

After characterising the Ln-AL materials, the most-suited ligand for preparing a humidity sensor was selected among PB and CA based on both the luminescent and textural properties. Regarding luminescence, all materials exhibited optimal emission for both Ln ions. No free ligand emission was observed in any case, as observed for hydroxypicolinates. Concerning the porous texture, well-defined pore width values and narrow pore size distributions indicate that water molecules with an average size of 0.28 nm could freely enter the pores [23]. However, the purely ultramicroporous nature of Ln-CA xerogels and their lower adsorption capacity could cause kinetic drawbacks during the adsorption-desorption processes. Therefore, PB was found to be the best-suited AL for our purpose based on: (i) PB is a tridentate ligand that effectively sensitises the Ln-luminescence and can saturate the coordination sphere to a degree in which molecular oscillators do not fully quench the emission through non-radiative decay; (ii) the luminescent emission displays sharp peaks of enough intensity to be monitored; and (iii) Ln-PB xerogels present the highest specific surface areas and the widest micropores

among the homogeneous materials studied in this work, while maintaining well-defined PSD, which could lead to a wider dynamic range of the sensor due to a higher adsorption capacity.

Once selected, the morphology of Ln-PB materials was studied by field-emission SEM. The micrographs (Figure 6.5) show smooth layered surfaces consistent with their microporous nature, in contrast to the rougher surface of the micro-mesoporous TEOS-4.5.

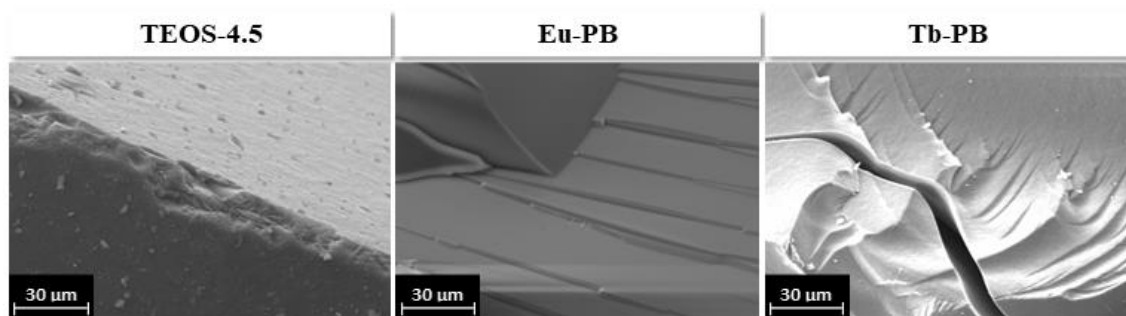


Figure 6.5. SEM micrographs of TEOS-4.5, Eu-PB, and Tb-PB.

EDX spectroscopy was used to inspect the Ln distribution on XG surfaces, which led us to prepare Ln-PB xerogels with higher Ln concentration (3 wt%) due to the detection limit of the equipment. The lanthanide mapping (Figure 6.6) confirms the homogeneous dopant distribution, which should remain also homogenous for a lower Ln quantity, such as that in Ln-PB xerogels.

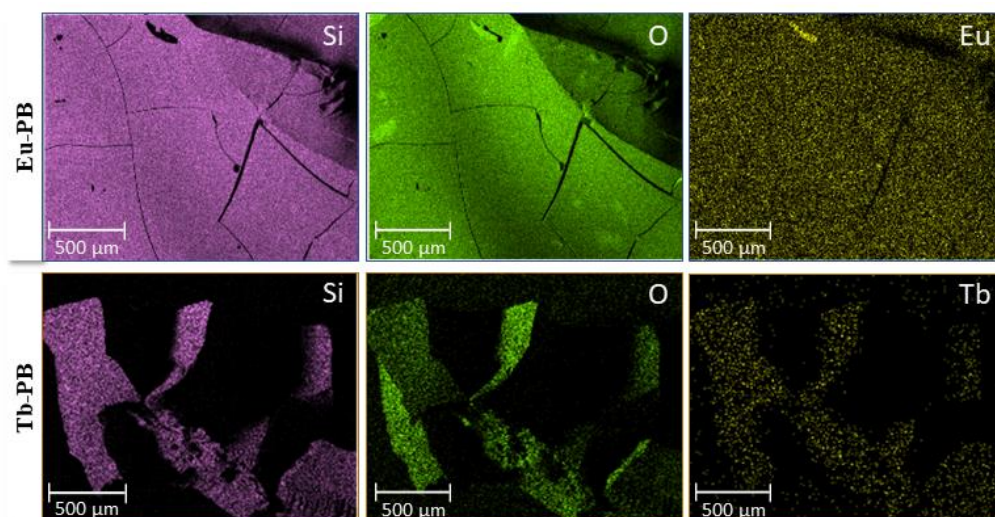


Figure 6.6. EDX mapping of Eu-PB (top) and Tb-PB (bottom) materials containing 3 % in weight of Ln.

This assumption is supported by the powder XRD patterns (Figure 6.7), which are dominated by a very broad signal centred at the 2θ range $22\text{--}24^\circ$ characteristic of amorphous silica. The absence of other sharp diffraction maxima indicates that the dopants must be well-dispersed within the XG matrix without forming crystalline aggregates or inducing any local order.

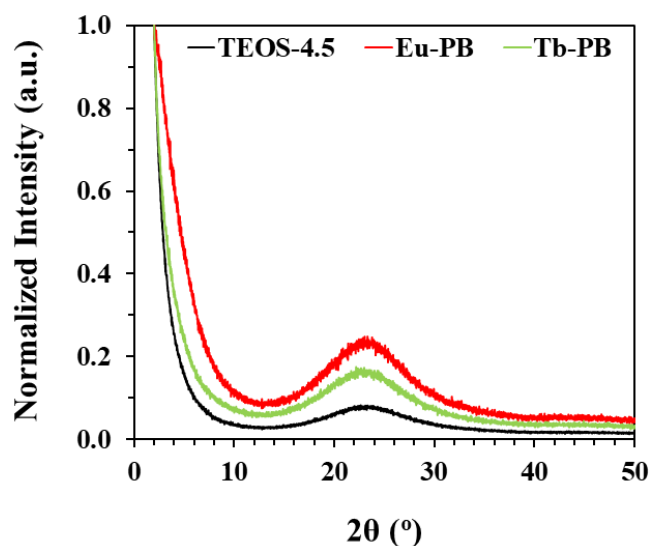


Figure 6.7. Powder X-ray diffraction patterns of Ln-PB materials compared to those of the TEOS-4.5 reference.

The infrared spectra (Figure 6.8) show, besides the characteristic bands of XG matrices and siloxane assemblies within (cyclic, linear, or branched species), additional signals confirming that the TEOS ethoxy groups are not fully hydrolysed (low-intensity C–H stretching peaks in the $2980\text{--}2850\text{ cm}^{-1}$ range) and that Ln-PB xerogels are hydrophilic according to the peaks at ca. 1650 (deformation of physisorbed water) and 3465 cm^{-1} (stretching of water molecules hydrogen-bonded to silanol groups). No signals from free ligands or Ln complexes are detected, other than a narrow peak at 1385 cm^{-1} assigned to nitrate anions from Ln precursors. See Table 6.2 for a full literature-based assignment of the FTIR bands.

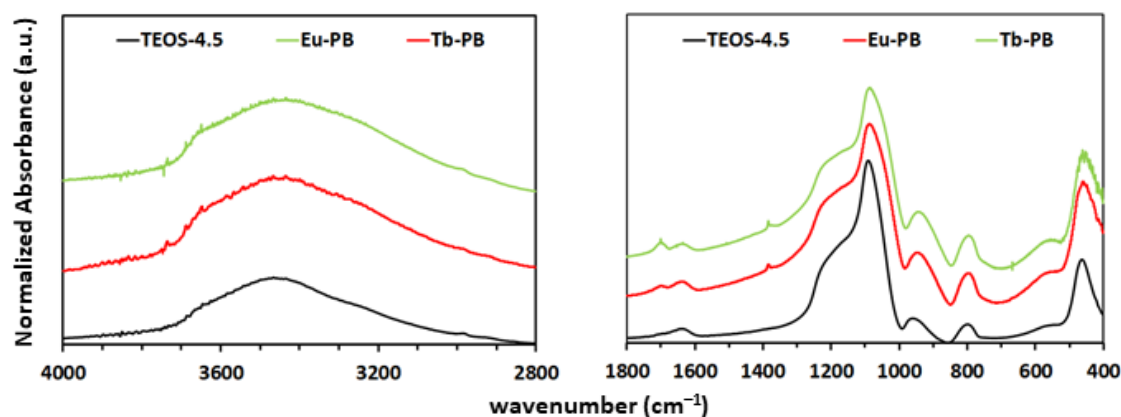


Figure 6.8. Infrared spectra of Ln-PB materials and the TEOS-4.5 reference in the ranges (left) 2800–4000 and (right) 400–1800 cm^{-1} (range from 1800 to 2800 cm^{-1} not included due to the lack of any relevant band).

Table 6.2. Literature-based assignment of FTIR bands (cm^{-1}) in the spectra of Ln-PB materials and the TEOS-4.5 reference.

TEOS-4.5	Eu-PB	Tb-PB	Assignment	Reference
3436	3449	3440	ν (SiO-H)	[24]
-	-	2983	ν_{as} (C-H), $-\text{CH}_3$	[25]
2919	-	-	ν_{as} (C-H), $-\text{CH}_2-$	[25]
2851	-	-	ν_{s} (C-H), $-\text{CH}_2-$	[25]
1621	1637	1634	δ H_2O	[26]
-	1384	1384	ν_{as} ($\text{O}_2\text{N}-\text{O}$)	[27]
1091	1088	1086	ν_{as} (Si-O-Si)	[28,29]
948	946	944	ν (Si-OH)	[30,31]
800	796	796	ν_{s} (O-Si-O)	[24,30]
562	556	562	ν Si-O, T_4	[32]
463	461	457	ρ (O-Si-O)	[33]

Three OFS were prepared: the reference sensor (OFSTEOS-4.5) using the TEOS-4.5 material and the working sensors (OFSEu-PB and OFSTb-PB) using Ln-PB coatings. The sensors were excited with a 280 nm LED to take advantage of the Stokes Shift and to prevent any overlap between the luminescent signals and the emission spectra, in Figure 6.9 were obtained (experimental set-up in Figure 2.18 in Chapter 2.3.3).

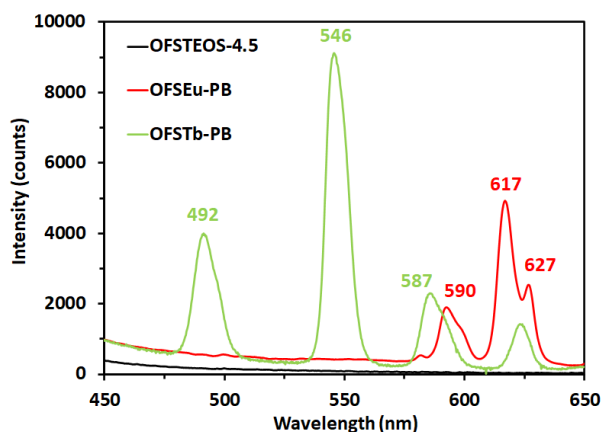


Figure 6.9. Luminescence spectra ($\lambda_{exc} = 280$ nm) of OFSTEOS-4.5, OFSEu-PB and OFSTb-PB.

As expected, the reference OFSTEOS-4.5 does not show any luminescence in the studied range, consistent with the absence of any luminescent doping agents. The spectra of both OFSLn-PB show all the characteristic emission signals of each Ln ion, where the most intense bands were 546 nm and 617 nm for OFSTb-PB and OFSEu-PB, respectively. This observation is consistent with the PL spectra of the Ln-PB monoliths discussed above. Nevertheless, as the OFSTb-PB band at 546 nm is significantly more intense than that of OFSEu-PB at 617 nm, which shows also substantial overlapping with a signal at 627 nm. Thus, OFSTb-PB was selected for exploring its performance towards humidity variations, bearing in mind that the narrower, more intense, and better defined the emission band is, the better signal-noise ratio should be expected for the signal transduction.

6.2.3 Time-response curve for humidity

The OFSTb-PB response (deposited XG film thickness of 136 ± 12 nm) versus relative humidity (RH) at different temperatures was studied using the configuration shown in Figure 2.18 of Chapter 2.3.3. The sensor was exposed to 10 increasing/decreasing cycles of 20-90% RH (0.20–1.00 mM at 25 °C, 0.28–1.40 mM at 30 °C and 0.38–1.80 mM at 35 °C) during 1 h per cycle to ensure time-stability. Figure 6.10 displays the time-response curves at different water molar concentrations (C_{H_2O}) using the two most accurate RH cycles at each temperature. The interrogation of the sensor was carried out by tracking changes in the intensity of the emission peak centred at 546 nm, the value of which was obtained every minute from the emission spectrum. The intensity variation ($\Delta I = I - I_{ref}$) was estimated by subtracting the intensity measured at the lowest RH level (20%, I_{ref}) from the sampled values (I), normalising this variation

by I_{ref} (for more details, see Equation 2.1 in *Chapter 2.3.2*). Two hours were left between experiments at different temperatures to ensure the reference stability.

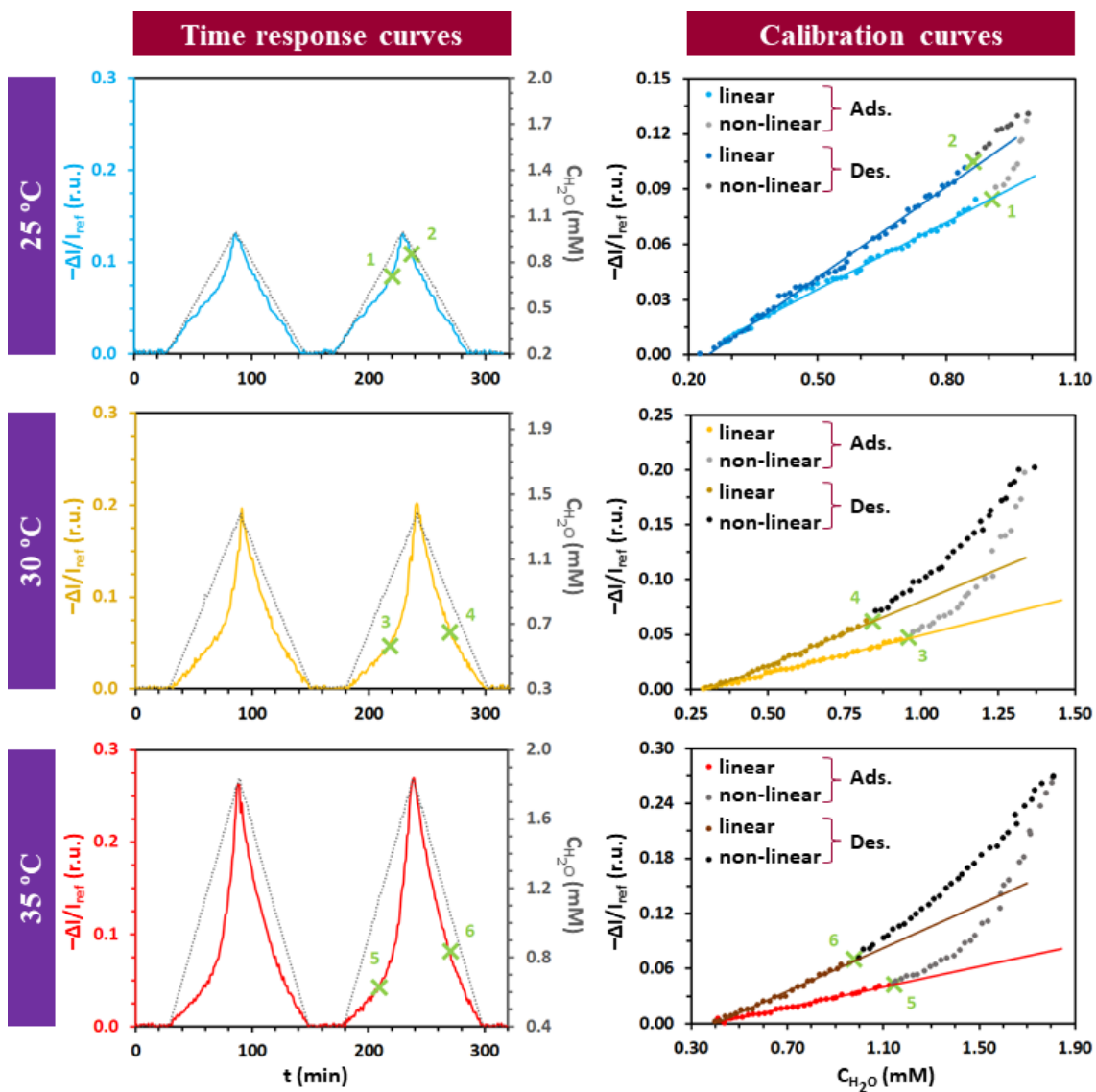


Figure 6.10. (left) Time-response curves for humidity and (right) linear fitting of the calibration curves registered for OFSTb-PB at 25, 30 and 35 °C.

According to the response curves in Figure 6.10, the sensor follows the C_{H_2O} setpoint (see Equations 2.2 and 2.3 in Chapter 2.3.2) in all cycles. The variation in the response of OFSTb-PB increases with C_{H_2O} due to the quenching of luminescence by water molecules [34]. Moreover, the dynamic intensity range of the sensor is also broadened when the temperature increases (from 0.129 at 25 °C to 0.196 and 0.263 at 30 and 35 °C, respectively). This behaviour can be explained by the higher vibration of the electrons when the emission decreases, which in turn, favours alternative non-radiative deactivation pathways [35].

To study the linearity of the response with respect to C_{H_2O} , the calibration curves in Figure 6.10 were registered at the three working temperatures and their linear intervals analysed by calculating the inflection points 1–6 from the tangent of the curves where the latter start deviating from linearity (based on R^2). Table 6.3 compiles the linear fitting parameters and detection limits for each temperature, which are determined from the sensor sensitivity (fitting parameter B, see Equation 2.4 in Chapter 2.3.3).

Table 6.3. Linear fitting parameters of OFSTb-PB calibration curves ($y = A + Bx$).

T ^a (°C)	Linear intervals ^b (mM)	A (r.u.)	B (mmol g ⁻¹)	R ²	LoD ^c (mM)
25 ^{ads}	0.282–0.906	−0.025±0.001	0.121±0.002	0.993	0.022
25 ^{des}	0.863–0.226	−0.040±0.001	0.164±0.002	0.995	0.018
30 ^{ads}	0.292–0.957	−0.020±0.010	0.070±0.001	0.995	0.022
30 ^{des}	0.839–0.300	−0.037±0.001	0.117±0.002	0.995	0.023
35 ^{ads}	0.413–1.143	−0.022±0.001	0.056±0.001	0.988	0.048
35 ^{des}	0.999–0.399	−0.047±0.002	0.118±0.002	0.992	0.038

^a–ads: adsorption branch; des: desorption branch; ^b–water vapour molar concentration ranges in which the calibration curves are linear; ^c–Limits of Detection, calculated through Equation 2.4.

The dynamic behaviour displayed in Figure 6.10 confirms that the sensor kinetics are able to follow relative humidity change rates of (at least) ±0.02% per second, which expressed in water vapour molar concentration is equal to ±13, ±14 and ±21 μM s⁻¹ for 25, 30 and 35 °C, respectively.

On the one hand, the OFSTb-PB response for the adsorption branches follows a linear trend at all temperatures up to C_{H_2O} values in the range from 0.91 mM at 25 °C to 0.96 mM at 30 °C and 1.14 mM at 35 °C (RH = 81.7, 64.3 and 57.6%, respectively). Beyond these values (points 1, 3 and 5 in Figure 6.10), the response deviates abruptly from linearity to a third-grade polynomial (third-grade polynomial fittings compiled in Figure 6.11 and Table 6.4). On the other hand, while desorption at 25 °C is linear for

almost the whole C_{H_2O} range, those at 30 and 35 °C deviate from linearity at inflection points 4 and 6, as happened for adsorption. It is worth noting that temperature directly affects the linearity of the sensor response, with the inflection points appearing at higher C_{H_2O} as the temperature increases for the adsorption branches.

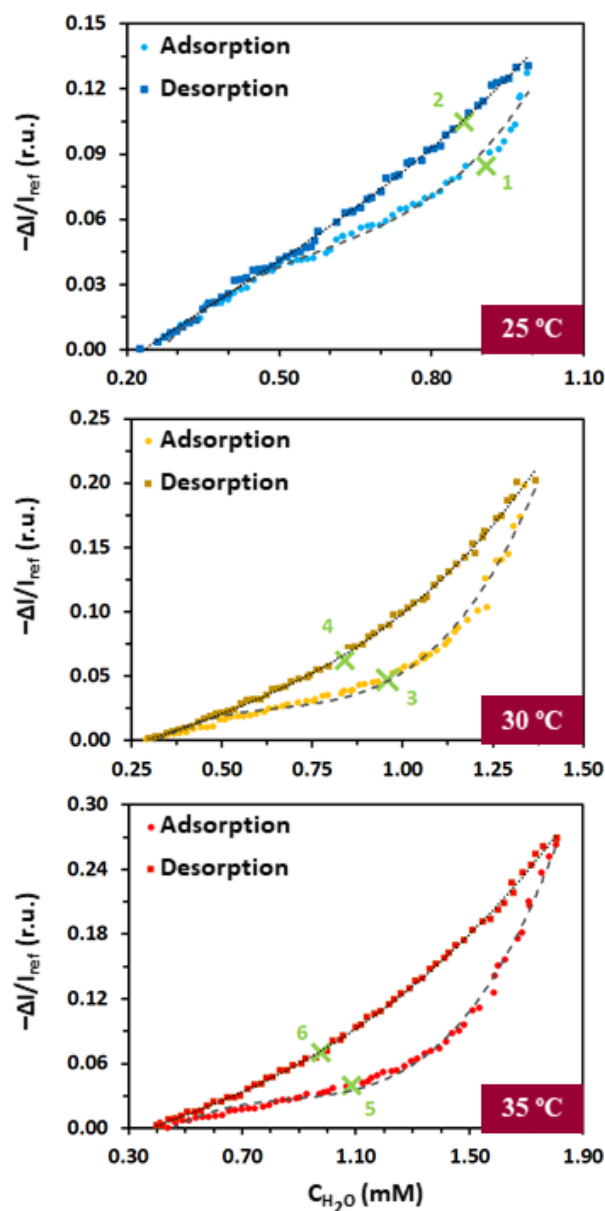


Figure 6.11. Fitting of the OFSTb-PB calibration curves at different working temperatures to third-grade polynomial equations (adsorption branch: dashed grey line; desorption branch: dotted black line).

Table 6.4. Fitting parameters of the OFSTb-PB calibration curves to third-grade polynomial equations ($y = A + B_1x + B_2x^2 + B_3x^3$).

T* (°C)	A (r.u.)	B₁ (mM) ⁻¹	B₂ (mM) ⁻²	B₃ (mM) ⁻³	R²
25 ^{ads}	-0.114±0.014	0.642±0.073	-0.947±0.120	0.540±0.062	0.987
25 ^{des}	-0.040±0.005	0.192±0.031	-0.105±0.053	0.090±0.029	0.997
30 ^{ads}	-0.110±0.012	0.555±0.053	-0.803±0.069	0.410±0.028	0.987
30 ^{des}	-0.030±0.007	0.117±0.028	-0.073±0.036	0.085±0.015	0.998
35 ^{ads}	-0.155±0.014	0.585±0.042	-0.651±0.040	0.252±0.012	0.995
35 ^{des}	-0.030±0.007	0.076±0.021	0.004±0.021	0.026±0.006	0.999

*—ads: adsorption branch; des: desorption branch

The influence of the temperature on the sensor response can be mathematically modelled based on well-established analytical techniques [37], and we plan to apply such methods in the study of sensors with optimised XG coatings in terms of porous texture and surface chemistry. These improved sensors are currently in progress and will be reported in the near future. The performance of the present sensor is compared in Table 6.5 to those of several other humidity optical fibre probes that have been reported in the past few years. In this context, it is worth noting the lack of literature examples of humidity probes based on luminescence as the transduction method, such as our OFSTb-PB sensor.

Table 6.5. Room-temperature performances of literature-reported optical fibre humidity probes compared to that of OFSTb-PB

Material	Transduction	Range (% RH)	Sensitivity	Response Time	References
None	WG Modes	30 - 70	0.23 dB / %RH	240 ms	[38]
PDMS ^a	Fabry Perot	30 - 80	11.39 nm / % RH	125 s	[39]
GO ^b	LPG	20 - 80	0.18 dB / %RH	n/a	[40]
ITO ^c	LMR	30 - 90	116 pm / % RH	n/a	[41]
Agarose	Fabry Perot	50 - 90	0.673 nm / %RH	60 ms	[42]
FIR-53 ^d	Fabry Perot	10 - 90	315 pm / %RH	323 s	[43]
GO ^b	Frequency	30 - 98	34.7 KHz / %RH	64.2 ms	[44]
GO ^b	Sagnac	36 - 78	340 pm / %RH	n/a	[45]
GO ^b	LMR	20 - 90	1.324 nm / %RH	160 ms	[46]
Tb-PB	Luminescence	20 - 90	1.71×10 ⁻³ r.u / %RH ^e	n/a	This work

^a—PDMS: polydimethylsiloxane; ^b—GO: graphene oxide; ^c—ITO: indium tin oxide; ^d—FIR-53: [Zn₂(tipa)₂OH](NO₃)₃·12H₂O MOF, where tipa = tris(4-(1H-imidazol-1-yl)phenyl)amine), ^e—Calculated from the adsorption branch sensitivity datum at 25 °C (Table 6.6) using 0.0141 mM / %RH as the conversion factor.

The differences between the adsorption and desorption branches give rise to significant hysteresis loops, which widen as the temperature increases and relate to the retention of water molecules within the coating. To shed light on the adsorption-desorption mechanism of this film and to get information about the interaction of water molecules within the material pores, variable-temperature water-vapour isotherms were registered for the Tb-PB monolith.

6.2.4 Water-vapour isotherms of Tb-PB

Figure 6.12 depict the water-vapour isotherms in both scales, decimal (left) and semi-logarithmic (right), recorded for the Tb-PB monolith at the three working temperatures to establish a correlation between the sensor response and the textural properties of its coating.

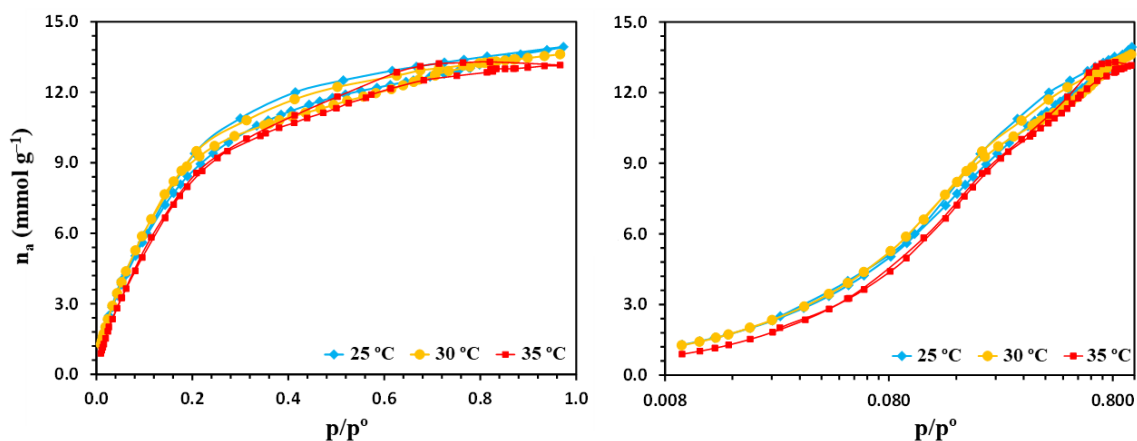


Figure 6.12. Water-vapour adsorption-desorption isotherms of the Tb-PB monolith at different temperatures, and different scales: **(left)** decimal, and **(right)** semi-logarithmic.

The isotherms display a wide knee and a positive slope without *plateau*, the B point being noticeable. Therefore, they could be classified as type II, with a hysteresis loop H5. Tb-PB was found to be mainly microporous using the standard adsorbate N₂, but water molecules are smaller, more polar, and have higher kinetic energy in the adsorption process, hence lower values of partial pressures are required to fill the pores. Thus, the wide micropores for N₂ become mesopores for H₂O. The isotherms show that water molecules are indeed adsorbed following a linear trend at low partial pressures, but also that this behaviour changes when certain p/p° values are reached: 0.09 (25 °C), 0.17 (30 °C), and 0.27 (35 °C). The hysteresis closure relates to a change in the adsorption mechanism from micropore filling to capillary condensation in the mesopores. The higher the temperature is, the higher the p/p° values needed for the hysteresis loop to close, a fact

that agrees with the exothermic nature of the adsorption process [47], as well as with the Tb-PB hydrophilicity due to the interaction between adsorbed water molecules and silanol groups (Figure 6.8).

Table 6.6 displays the thermal effect on several textural parameters determined from the water-vapour adsorption isotherms.

Table 6.6. Textural parameters determined from the water-vapour adsorption isotherms of the Tb-PB monolith.

T (°C)	a_{BET}^{a,b} (m ² g ⁻¹)	V_{micro}^{a,c}	V_{meso}^{a,d} (cm ³ g ⁻¹)	V_{total}^{a,e}	q_m^f (mmol g ⁻¹)	E_c^{a,g} (kJ mol ⁻¹)
25	694	0.15	0.09	0.24	8.9	8.3
30	669	0.15	0.08	0.24	8.9	8.0
35	659	0.13	0.10	0.24	8.8	7.6

^a–Using the H₂O isotherms; ^b–Specific surface area obtained from the Brunauer–Emmett–Teller (BET) model (see Chapter 2.5.4); ^c–Micropore volume obtained from the Dubinin–Raduskevich (DR) method (see Chapter 2.5.4); ^d–V_{meso} = V_{total} – V_{macro} – V_{micro} (negligible macroporosity observed in the 0.8 < p/p^o < 0.95 range); ^e–Total pore volume at p/p^o = 0.95; ^f–Monolayer capacity determined by BET; ^g–Characteristic energy calculated from DR.

These data confirm the presence of a significant mesoporous volume and show that the adsorption monolayer capacity (q_m) increases with temperature. This fact is consistent with the observed decrease in the characteristic adsorption energy (E_c) because the attraction forces between adsorption sites and water molecules become weaker as the temperature increases [48], thereby needing higher C_{H_2O} to reach the monolayer capacity. This phenomenon can explain both the filling of mesopores at higher p/p^o values with increasing temperature, as well as the non-linear nature of the calibration curves beyond the inflection points 1, 3, and 5 (Figure 6.10). All these observations suggest that capillary condensation is a plausible mechanism in the pore filling. To confirm this hypothesis by comparing the strength of water physisorption in both systems, determining the isosteric enthalpies of adsorption (ΔH_{ads}) for both the Tb-PB monolith and the OFSTb-PB sensor became essential.

6.2.5 Isosteric enthalpies of adsorption

ΔH_{ads} is the differential change in energy when a tiny number of molecules are transferred at constant pressure, temperature, and specific surface area of the adsorbent from the bulk gas phase to the adsorbed phase [49]. It is a crucial parameter in adsorption processes and is further used to gain deeper insights into the adsorbate-adsorbent interactions, which are classified as physisorption (weak interactions) and chemisorption

(strong interactions) [50]. Therefore, the sensor response towards humidity could be explained in terms of analyte-adsorbent interactions by a mere comparison between ΔH_{ads} of the XG monolith and that of the XG coating. The Clausius-Clapeyron equation (Equation 6.1) was used to determine the sensor ΔH_{ads} (kJ mol^{-1}) upon assuming that the adsorption is an exothermic process [48]. This equation specifies the temperature dependence of the vapour pressure in phase transitions like capillary condensation (gas-liquid):

$$\ln P = \frac{\Delta H_{ads}}{R} \times \frac{1}{T} + K \quad (6.1)$$

where P = pressure (kPa), R = ideal gas constant ($\text{kJ mol}^{-1} \text{K}^{-1}$), T = temperature (K), and K = constant (y-intercept). To obtain the P_{H_2O} values assuming ideal gas conditions, a least-squared adjustment was performed for the data from both the time-response curves of the sensor OFSTb-PB (Table 6.5) and the water adsorption isotherms of the monolith Tb-PB (Table 6.7 and Figure 6.13).

Table 6.7. Fitting parameters of Tb-PB water vapour adsorption isotherms to a fourth-grade polynomial equation ($y = A + B_1x + B_2x^2 + B_3x^3 + B_4x^4$).

T	A	B ₁	B ₂	B ₃	B ₄	R ²
(°C)	(kPa)	mmol g (kPa) ⁻¹	mmol g (kPa) ⁻²	mmol g (kPa) ⁻³	mmol g (kPa) ⁻⁴	
25 ^{ads}	0.893±0.030	18.932±0.182	-13.106±0.263	4.265±0.133	-0.507±0.022	0.999
30 ^{ads}	0.733±0.043	15.951±0.190	-9.519±0.201	2.604±0.075	-0.255±0.009	0.999
35 ^{ads}	0.398±0.040	11.586±0.146	-4.987±0.129	1.040±0.040	-0.081±0.004	0.999

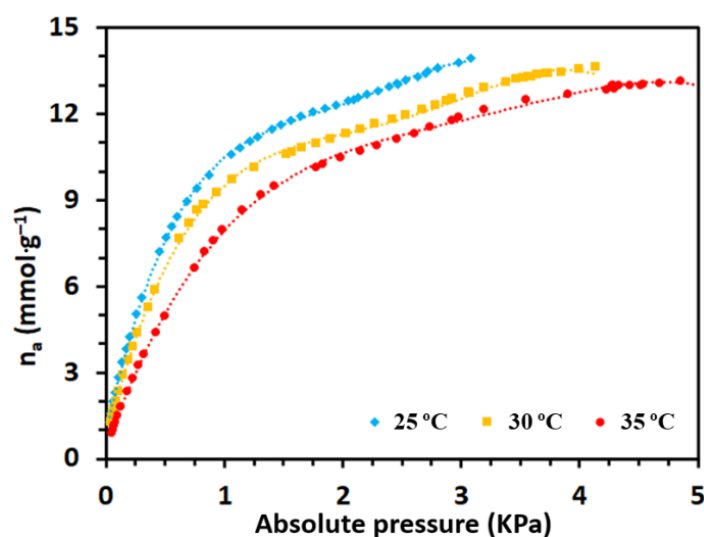


Figure 6.13. Best-fitting of water vapour adsorption isotherms for the Tb-PB monolith.

Thereafter, the logarithm of P_{H_2O} was plotted against $1/T$, thus obtaining isosteres in the ranges $-\Delta I/I_{ref} = 0.03$ – 0.18 range for OFSTb-PB and $n_a = 1.5$ – 10.0 (n_a : mmols of water adsorbed per gram of material) for Tb-PB. The isostere slopes allowed the determination of the corresponding ΔH_{ads} values, which were represented as a function of $-\Delta I/I_{ref}$ and n_a to study the strength of the adsorbate-adsorbent binding energy as C_{H_2O} increases (Figure 6.14).

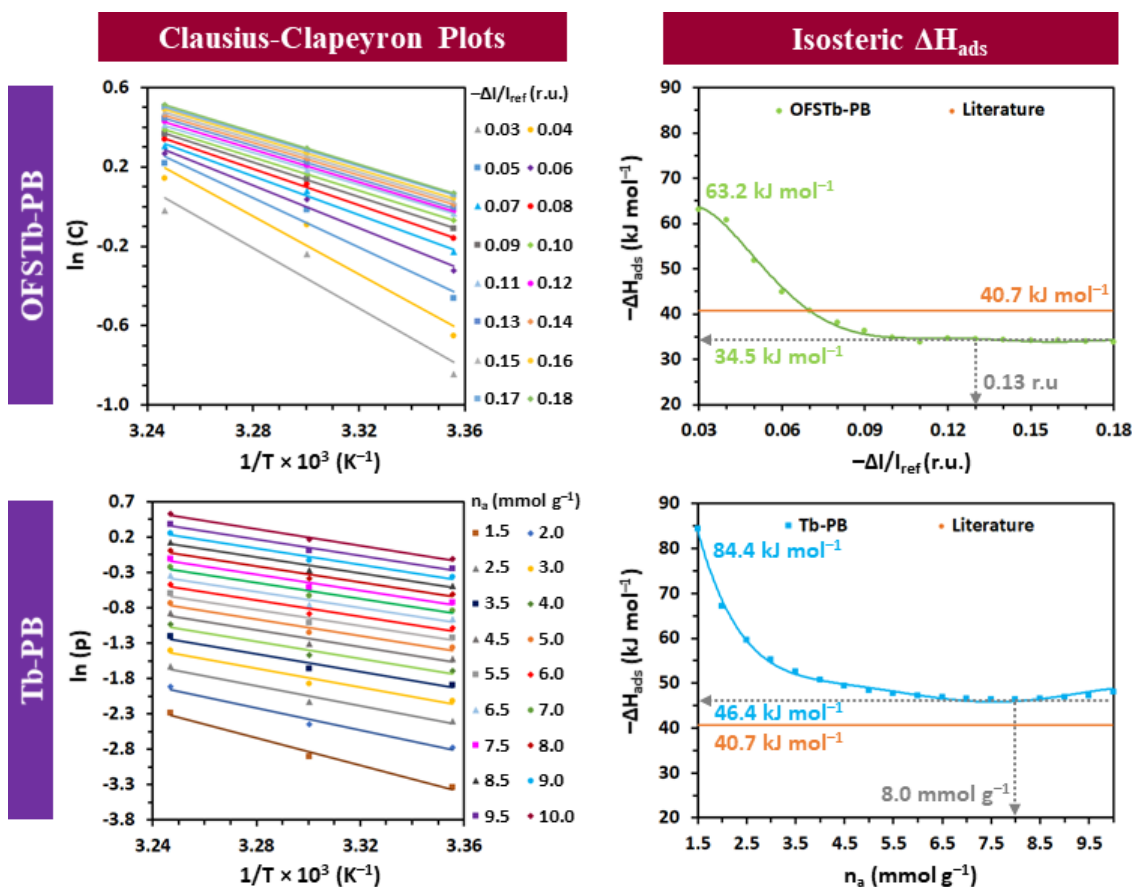


Figure 6.14. (Left) Clausius-Clapeyron plots for the OFSTb-PB response towards humidity changes ($-\Delta I/I_{ref} = 0.03$ – 0.18) and for water-vapour adsorption isotherms of the Tb-PB monolith ($n_a = 1.5$ – 10.0 mmol g⁻¹). (Right) Isosteric enthalpies of adsorption calculated for both the sensor and the monolith.

Figure 6.14 shows that ΔH_{ads} becomes less negative with increasing $-\Delta I/I_{ref}$ until reaching a plateau at -34.5 kJ mol⁻¹. This fact is consistent with a less exothermic process as more water molecules are adsorbed. Values higher than the theoretical one corresponding to water condensation ($\Delta H_{cond} = -40.7$ kJ mol⁻¹, orange line [51]) agree with the predominance of condensation (adsorbate-adsorbate interactions) over adsorption (adsorbate-adsorbent interactions). Below $-\Delta I/I_{ref} = 0.07$, the ΔH_{ads} magnitude remain above the energetic threshold given by ΔH_{cond} , which indicates a mechanism of

physisorption in the micropores ruling the linear range of the OFSTb-PB response in the adsorption calibration curves (Figure 6.10). Conversely, ΔH_{ads} is observed to be less negative than ΔH_{cond} when $-dI/I_{ref}$ is above 0.07, and this fact suggests that the inflection points leading to non-linear trends in the sensor calibration curves match with the beginning of the capillary condensation in the mesopores.

Figure 6.14 also depicts the correlation between ΔH_{ads} calculated for the Tb-PB and the amount of adsorbed water (n_a). In close analogy to what has been commented above, ΔH_{ads} gradually increases with n_a to reach a *plateau* at n_a 7.5–8.0 mmol g⁻¹. This value is similar to those calculated for the monolayer capacities (q_m) from the water adsorption isotherms (Table 6.6) and correlates in the graph with $\Delta H_{ads} = -46.4$ kJ mol⁻¹. Although ΔH_{ads} in the *plateau* does not surpass ΔH_{cond} , this phenomenon can be expected when considering the morphological difference between the sensor coating (a thin film of the material) and a monolith (the bulk material), as the total volume of pores is higher in the latter. The key parameter to consider is the ΔH_{ads} increment until reaching the *plateau*, which is comparable in both cases (28.7 kJ mol⁻¹ for the coating vs. 38.0 kJ mol⁻¹ for the monolith). The information extracted from the comparison of both isosteric enthalpies of adsorption reinforces the hypothesis that the loss of linearity in the OFSTb-PB response originates from the beginning of capillary condensation of water in the mesopores.

6.3 CONCLUSIONS

Two series of Eu^{III} - or Tb^{III}-doped silica xerogels were prepared by the sol-gel method and their luminescence was sensitised using eight pyridine-based antenna ligands. Out of a catalogue of 16 different materials, the xerogel Tb-PB (sensitised with the 2,2'-(4-(2-Ethoxyethoxy)pyridine-2,6-diyl)bis(4,5-dihydrooxazole) ligand) showed the most-suited luminescence and textural properties for a coating in a humidity optical fibre sensor.

The sensor response showed linearity until certain values of water-vapour molar concentration (C_{H_2O}), beyond which shifted to polynomial. Comparing the sensor calibration curves with the water-vapour adsorption isotherms of the bulk material recorded at three different temperatures and calculating their isosteric enthalpy of adsorption (ΔH_{ads}), the linear-to-polynomial shift was found to originate from capillary

condensation of water molecules in the mesopores. When the membrane is exposed to low level of C_{H_2O} , the molecules first interact with the hydrophilic silanol groups on the micropore surface and quench the luminescence linearly while ΔH_{ads} increases, making the adsorption process less exothermic. Once C_{H_2O} is high enough to complete the monolayer, water molecules are then physisorbed forming multilayers in the mesopores due to their larger size compared to micropores. When $\Delta H_{ads} \geq \Delta H_{cond}$, water molecules condense, which critically eases their contact with the luminophores, causing an abrupt decay in the luminescence that breaks the linearity of the sensor response.

This work has established a correlation between the response of a luminescent probe and its texture and proposes a plausible adsorption mechanism to explain the non-linear response of the sensor based on capillary condensation within the mesopores. The knowledge acquired from this investigation is of paramount importance for improving, based on the porous texture, the design of materials that will be used as coatings where the analyte interacts with the sensor.

6.4 ACKNOWLEDGEMENTS

Financial support from the Spanish MICINN (PID2020-113558RB-C42) and AEI is acknowledged. G.C.-Q thanks the Spanish Ministerio de Universidades for a predoctoral grant within the program Formación de Profesorado Universitario (FPU18/03467). M.V.L-R acknowledges financial support from the FEDER 2014-2020 Operative Program and Junta de Andalucía, Spain (FEDER-UJA-1380629). M.E.-V. thanks UPNA for the project Jóvenes Investigadores UPNA-2022 (PJUPNA18-2022). The authors thank the technical and human resources from UCTAI (UPNA) and SAI (University of Zaragoza).

6.5 REFERENCES

- [1] De Bettencourt-Dias, A.; Barber, P. S.; Bauer, S. *J. Am. Chem. Soc.* **2012**, *134*, p. 6987–6994.
- [2] Lakowicz, J. R. Introduction to Fluorescence. In *Principles of fluorescence spectroscopy*; Lakowicz, J. R., Ed.; 3rd Ed.; Springer: New York, USA, **2006**; pp. 1–5.
- [3] De Acha, N.; Elosua, C.; Matias, I.; Arregui, F. J. *Sensors* **2017**, *17*, p. 2826.
- [4] Lv, H. S.; Huang, S. Y.; Zhao, B. X.; Miao, J. Y. *Anal. Chim. Acta* **2013**, *788*, p. 177–182.

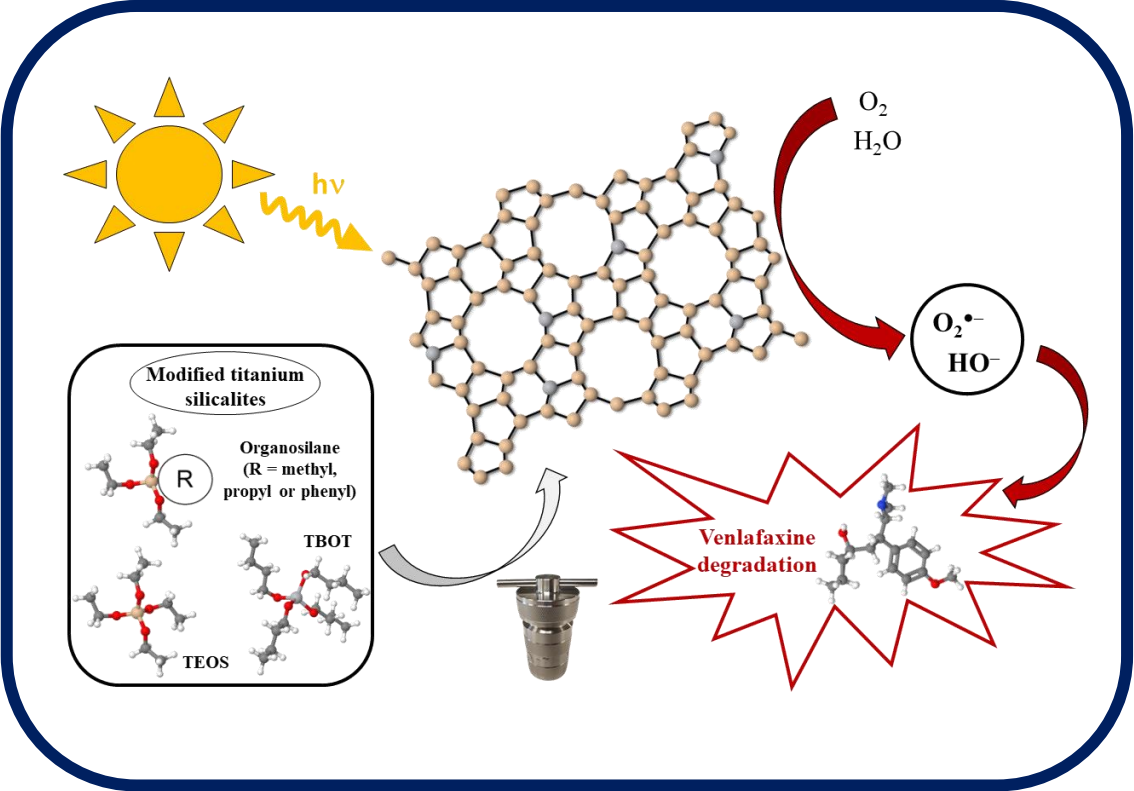
- [5] Li, Y. *Polyhedron* **2020**, *179*, p. 114413.
- [6] Pang, X.; Yu, T.; Shen, F.; Yu, X.; Li, Y. *J. Lumin.* **2018**, *204*, p. 169–175.
- [7] Ross, D.; Gaitan, M.; Locascio, L. E. *Anal. Chem.* **2001**, *73*, p. 4117–4123.
- [8] Yan, J.; Wang, H.; Zheng, Y.; Huang, X.; Meng, H.; Tan, C. *Measurement* **2022**, *187*, p. 110248.
- [9] Ballantine, D. S.; Wohltjen, H. *Anal. Chem.* **1986**, *58*, p. 2883–2885.
- [10] Bridgeman, D.; Corral, J.; Quach, A.; Xian, X.; Forzani, E. *Langmuir* **2014**, *30*, p. 10785–10791.
- [11] Choi, M. M. F.; Ling Tse, O. *Anal. Chim. Acta* **1999**, *378*, p. 127–134.
- [12] Soltani Firouz, M.; Mohi-Alden, K.; Omid, M. *Food Res. Int.* **2021**, *141*, p. 110113.
- [13] Fang, L.; Clausen, G.; Fanger, P. O. *Indoor Air* **1999**, *9*, p. 193–201.
- [14] Sathish, A.; Smith, B. R.; Sims, R. C. *J. Chem. Technol. Biotechnol.* **2014**, *89*, p. 137–142.
- [15] Estella, J.; De Vicente, P.; Echeverría, J. C.; Garrido, J. J. *Sens. Actuators, B Chem.* **2010**, *149*, p. 122–128.
- [16] Zhao, C.; Liu, D.; Xu, G.; Zhou, J.; Zhang, X.; Liao, C.; Wang, Y. *Opt. Fiber Technol.* **2022**, *72*, p. 103000.
- [17] Lu, F.; Wright, R.; Lu, P.; Cvetic, P. C.; Ohodnicki, P. R. *Sens. Actuators, B Chem.* **2021**, *340*, p. 129853.
- [18] Sun, L.; Semenova, Y.; Wu, Q.; Liu, D.; Yuan, J.; Sang, X.; Yan, B.; Wang, K.; Yu, C.; Farrell, G. *IEEE Photonics J.* **2016**, *8*.
- [19] Soares-Santos, P. C. R.; Nogueira, H. I. S.; Félix, V.; Drew, M. G. B.; Sá Ferreira, R. A.; Carlos, L. D.; Trindade, T. *Chem. Mater.* **2003**, *15*, p. 100–108.
- [20] Bünzli, J.-C.G.; Eliseeva, S. V. Basics of Lanthanide Photophysics. In *Lanthanide Luminescence: Photophysical, Analytical and Biological Aspects*; Hänninen, P., Härmä, H., Eds.; Springer-Verlag: Berlin, Germany, **2010**; pp. 1–45.
- [21] Thommes, M.; Kaneko, K.; Neimark, A. V.; Olivier, J. P.; Rodriguez-Reinoso, F.; Rouquerol, J.; Sing, K. S. W. *Pure Appl. Chem.* **2015**, *87*, p. 1051–1069.
- [22] Garrido, J.; Linares-Solano, A.; Martín-Martínez, J. M.; Molina-Sabio, M.; Rodríguez-Reinoso, F.; Torregrosa, R. *Langmuir* **1987**, *3*, p. 76–81.
- [23] Chaplin, M.F. Structure and Properties of Water in its Various States. In *Encyclopedia of Water*; John Wiley & Sons, **2019**; pp. 1–19.
- [24] Innocenzi, P. *J. Non-Cryst. Solids* **2003**, *316*, p. 309–319.
- [25] Estella, J.; Echeverría, J. C.; Laguna, M.; Garrido, J. J. *J. Non-Cryst. Solids* **2007**, *353*, p. 286–294.
- [26] Martra, G.; Coluccia, S.; Marchese, L.; Augugliaro, V.; Loddo, V.; Palmisano, L.; Schiavello, M. *Catal. Today* **1999**, *53*, p. 695–702.

- [27] Verma, S. K.; Deb, M. K. *Anal. Chim. Acta* **2007**, *582*, p. 382–389.
- [28] Fidalgo, A.; Ilharco, L. M. Chemical Tailoring of Porous Silica Xerogels: Local Structure by Vibrational Spectroscopy. *Chem. - Eur. J.* **2004**, *10*, p. 392–398
- [29] Cruz-Quesada, G.; Espinal-Viguri, M.; López-Ramón, M. V.; Garrido, J. J. *Polymers* **2021**, *13*, p. 2082.
- [30] Gallardo, J.; Durán, A.; Di Martino, D.; Almeida, R. M. *J. Non-Cryst. Solids* **2002**, *298*, p. 219–225.
- [31] Hayami, R.; Ideno, Y.; Sato, Y.; Tsukagoshi, H.; Yamamoto, K.; Gunji, T. *J. Polym. Res.* **2020**, *27*.
- [32] Ou, D. L.; Seddon, A. B. *J. Non-Cryst. Solids* **1997**, *210*, p. 187–203.
- [33] Perry, C. C.; Li, X.; Waters, D. N. *Spectrochim. Acta, Part A* **1991**, *47*, p. 1487–1494.
- [34] Dobretsov, G. E.; Syrejschikova, T. I.; Smolina, N. V. *Biophys* **2014**, *59*, p. 183–188.
- [35] Hasegawa, M.; Ohmagari, H.; Tanaka, H.; Machida, K. *J. Photochem. Photobiol., C* **2022**, *50*, p. 100484.
- [36] De Acha, N.; Socorro-Lerános, A. B.; Elosúa, C.; Matias, I. R. *Biosensors* **2021**, *197*, p. 11.
- [37] He, C.; Korposh, S.; Correia, R.; Liu, L.; Hayes-Gill, B. R.; Morgan, S. P. *Sens. Actuators, B* **2021**, *344*, p. 130154.
- [38] Yan, J.; Wang, D. N.; Ge, Y.; Guo, Y.; Xu, B. *J. Lightwave Technol.* **2022**, *40*, p. 2651–2656.
- [39] Chen, H.; Jiang, C.; Zhu, X.; Guo, X.; Li, H.; Sun, S. *IEEE Sens. J.* **2022**, *22*, p. 17845.
- [40] Tsai, Y.; Wu, C.; Tsai, L.; Chiang, C. *J. Lightwave Technol.* **2020**, *39*, p. 4124–4130.
- [41] Fuentes, O.; Corres, J. M.; Matias, I. R.; Del Villar, I. *J. Lightwave Technol.* **2019**, *37*, p. 2300–2306.
- [42] Ma, X.; Zhao, F.; Xu, B.; Zhao, C. L.; Chen, H.; Wang, D. N.; Jin, S. *J. Lightwave Technol.* **2023**, *41*, p. 6824–6830.
- [43] Liu, S.; Zhang, X.; Wang, Q.; Chen, S.; Wang, F.; Wang, J.; Wang, G.; Yang, W.; Huang, M. *IEEE Sens. J.* **2023**, *23*, p. 12906–12914.
- [44] Guo, K.; He, J.; Li, H.; Xu, X.; Du, B.; Liu, S.; Chen, Y.; Ma, D.; Wang, Y.; Xu, G.; Wang, Y. *Opt. Express* **2022**, *30*, p. 15998.
- [45] Li, L.; Wang, Z.; Ma, Q.; Wang, M.; Wu, Q.; Chen, H.; Peng, B. *IEEE Sens. J.* **2021**, *21*, p. 16061–16065.
- [46] Hernaez, M.; Acevedo, B.; Mayesa, A. G.; Melendi-Espina, S. *Sens. Actuators, B* **2019**, *286*, p. 408–414.
- [47] Echeverría, J. C.; Calleja, I.; Moriones, P.; Garrido, J. J. *Beilstein J. Nanotechnol.* **2017**, *8*, p. 475–484.
- [48] Sang, G.; Liu, S.; Elsworth, D. *Water Resour. Res.* **2019**, *55*, p. 7212–7228.

- [49] Atkins, P.W. Adsorption at surfaces. In *Physical Chemistry*; W. H. Freeman and Company: New York, NY, USA, **1986**; pp. 770–777.
- [50] Du, Z.; Nie, X.; Deng, S.; Zhao, L.; Li, S.; Zhang, Y.; Zhao, J. *Microporous Mesoporous Mater.* **2020**, *298*, p. 110053.
- [51] Brini, E.; Fennell, C. J.; Fernandez-Serra, M.; Hribar-Lee, B.; Lukšič, M.; Dill, K. A. *Chem. Rev.* **2017**, *117*, p. 12385.

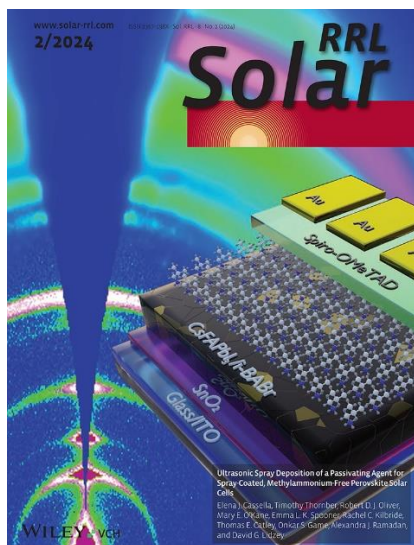
CHAPTER 7

DESIGN OF NOVEL PHOTOACTIVE MODIFIED TITANIUM SILICALITES AND THEIR APPLICATION FOR VENLAFAXINE DEGRADATION UNDER SIMULATED SOLAR IRRADIATION



CHAPTER 7

“DESIGN OF NOVEL PHOTOACTIVE MODIFIED TITANIUM SILICALITES AND THEIR APPLICATION FOR VENLAFAXINE DEGRADATION UNDER SIMULATED SOLAR IRRADIATION”



Published Article

Authors: Guillermo Cruz-Quesada, Maria J. Sampaio, Maialen Espinal-Viguri, María Victoria López-Ramón, Julián J. Garrido, Cláudia G. Silva, Joaquim L. Faria.

Reference: *Sol. RRL* **2023**, 2300593.

Doi: 10.1002/solr.202300593

Publication date: 12/09/2023

Keywords: Modified Titanium-Silicalites; Photocatalysis; antidepressant drug degradation; organotriethoxysilanes; solar radiation.

Abstract: Titanium silicalites (TS) are well-known materials for their use in industrial oxidation reactions, and although they are used as photocatalysts, their activity is limited. Therefore, numerous synthetic strategies have been investigated to improve their photocatalytic activity. In the present work, three series of modified titanium silicalites have been synthesised using tetraethoxysilane (TEOS), titanium tetrabutoxide (TBOT) and three different organotriethoxysilanes [RTEOS, R = methyl (M); propyl (P), or phenyl (Ph)] at different RTEOS:TEOS molar percentages to modify the structure of the zeolite, both at a porous and chemical level, to obtain materials with high photocatalytic activity. The study of their morphological, textural, chemical, and UV-Vis light absorption properties through various characterization techniques has allowed the selection of the best candidates to test their photoactivity in the degradation of venlafaxine, an antidepressant drug that persists as a contaminant in wastewater and has serious neurotoxic effects. Materials synthesised using a 5% molar percentage of RTEOS and 10% of PhTEOS were able to degrade venlafaxine, whereas the reference material (no RTEOS used in the synthesis) did not show any photocatalytic activity. These results lead the way to the use of this synthetic strategy for the development of photoactive titanium silicalites and the optimization of their photocatalytic activity in the degradation reactions of different pollutants.

7.1 INTRODUCTION

In recent decades, a deep interest has arisen in developing more efficient technologies to alleviate the consequences of human activity on the environment. Among the most promising technologies, photocatalysis stands out for its recent advances in contaminant removal [1–4] or hydrogen production [5–7]. With these applications in mind, semiconductor materials of diverse nature and composition have been designed, such as metal-organic frameworks (MOFs) [3,7], metal-carbon composites [2,8], graphitic carbon nitride (g-C₃N₄) composites [5,9], or TiO₂-based materials [4,6], among others. The objectives to be achieved in the preparation of photocatalysts are the improvement of the energy conversion efficiency and photochemical stability, the expansion of the excitation spectral range towards the visible, and the development of simple and low-cost synthesis methodologies that are scalable at the industrial level [10–15]. Due to the difficulty of achieving all these objectives, just a few commercial catalysts are currently available. In this regard, metal oxides, especially titanium dioxide (TiO₂), are among the most promising optical semiconductor materials for applications in photocatalysis, mainly due to their high stability, high oxidizing power, and low manufacturing cost. However, the biggest drawback of TiO₂ is that even the most commercialized photocatalyst (Degussa P25) only absorbs in the UV range, limiting solar applications [16].

Titanium silicalites (TSs), Ti-containing zeolites first synthesised by Tamarrasso *et al.* in 1983 [17], emerged as promising materials for photocatalysis. These materials are mainly known to be used as molecular sieves and as catalysts in industrial reactions of great interest such as olefin epoxidation [18,19], oxidative desulfurization [20], or hydroxylation of alkanes and aromatic compounds [21]. TSs are photoactive materials under excitation with UV-Vis radiation, therefore, besides being useful in the aforementioned oxidation reactions, they have also been used as photocatalysts in the production of H₂ [22–24], in the photodegradation of pollutants in an aqueous media [25–27], and the photo-epoxidation of propylene [28], among others.

The most representative form of titanium in the TSs framework is Ti^{IV}, which exhibits a tetrahedral coordination geometry (TiO₄) and is locally distributed throughout the modernite framework inverted silicalite structure (MFI). When TiO₄ species are excited with UV-Vis light, a charge transfer takes place from one of the coordinating oxygen atoms (O²⁻) to the Ti^{IV} cation, yielding in the process an electron-hole pair as the

excited state ($\text{Ti}^{+3}\text{-O}^-$), which is responsible for the material's photoactivity [29,30]. However, the size difference between Si and Ti atoms makes it difficult to synthesize a TS with a titanium content higher than 2.5 wt% without modifying the crystalline structure [31]. For this reason, defective Ti^{+4} species, such as partially coordinated (TiO_3OH), penta-coordinated (TiO_5), or octahedrally coordinated (TiO_6) species, can be found in TSs [32–34]. Additionally, depending on the synthesis conditions, anatase can be formed (TiO_2 , mainly TiO_6) because the titanium precursors (tetrabutoxides, isopropoxides...) rapidly hydrolyse (5–10 min) and condense with each other rather than with the silicon precursors, which present a slower hydrolyzation (1.5 h) [35]. The presence of anatase in the final material is not desirable because TiO_4 species exhibit much higher photocatalytic activity than TiO_6 [36]. Therefore, the need to obtain TS with a high TiO_4 content is still a challenge and has led to the development of strategies to slow down the hydrolysis of Ti precursors using complexing agents such as H_2O_2 , acetylacetonate, or isopropanol [37]. In this context, Ma *et al.* (2021) reported that polyvinylpyrrolidone (PVP) acts as a structure-directing agent (SDA) in the synthesis of TSs, competing with commonly used surfactants, such as TPAOH, and regulating the nano-structuration of the silica skeleton [38]. In addition, PVP decreases the condensation rate once the titanium precursor is hydrolysed, favouring its crosslinking with the hydrolysed silica precursor.

In the present work, a new synthetic approach is proposed, in which in addition to TPAOH, PVP, tetraethoxysilane (TEOS) and a titanium precursor, different molar proportions of an organotriethoxysilane have been used (RTEOS, R = methyl, M; propyl, P; and phenyl, Ph) yielding three series of modified titanium silicalites (TSR%); the synthesis process of these materials is detailed in *Chapter 2.1.3*. This strategy aims to achieve a change in the internal morphology and structure of the TSR% silica skeleton, as well as in their porous texture, surface chemistry, and proportion of titanium species ($\text{TiO}_4/\text{TiO}_6$) to obtain materials with greater photocatalytic activity. In this regard, RTEOS acts as an additional SDA for the construction of the MFI zeolite skeleton, and its organic moiety blocks one of the positions susceptible to hydrolysing and condensing, thus conditioning the internal structure of the material and yielding a variety of porous textures depending on the organosilane and its molar percentage used in the synthesis. In addition, this organic moiety is less electron withdrawal than the ethoxide groups, and since polycondensation follows a type 2 nucleophilic substitution mechanism (due to the

basicity of the medium), its use will slow down the reaction, which will also affect the final morphology of the materials [39]. After an exhaustive characterization in which the properties of the prepared materials were elucidated and discussed (UV-Vis absorption, photoluminescence emission, nano-structuration, N₂ and CO₂ adsorption capacity, morphology), it was determined that the most promising materials for photocatalysis were those synthesised with 5% RTEOS (TSR5, R = methyl, propyl and phenyl) and the material synthesised with 10% PhTEOS (TSPH10). Once those materials were selected, their activity in the degradation of venlafaxine, a contaminant included in the European Union's Watch List of Substances [40], was tested. The new TSR5 materials, unlike the reference material synthesised under the same conditions without RTEOS, were able to almost degrade venlafaxine completely in less than two hours, confirming that this synthetic approach can lead to an improvement and easy modulation of the photocatalytic properties of titanium silicalites due to the chemical, structural and textural changes derived from the introduction of RTEOS in the synthesis.

7.2 RESULTS AND DISCUSSION

7.2.1 Characterisation Analysis of the Synthesised Materials

7.2.1.1 X-ray diffraction (XRD)

Figure 7.1 depicts the diffraction patterns of the materials obtained in the range $5^\circ < 2\theta < 35^\circ$.

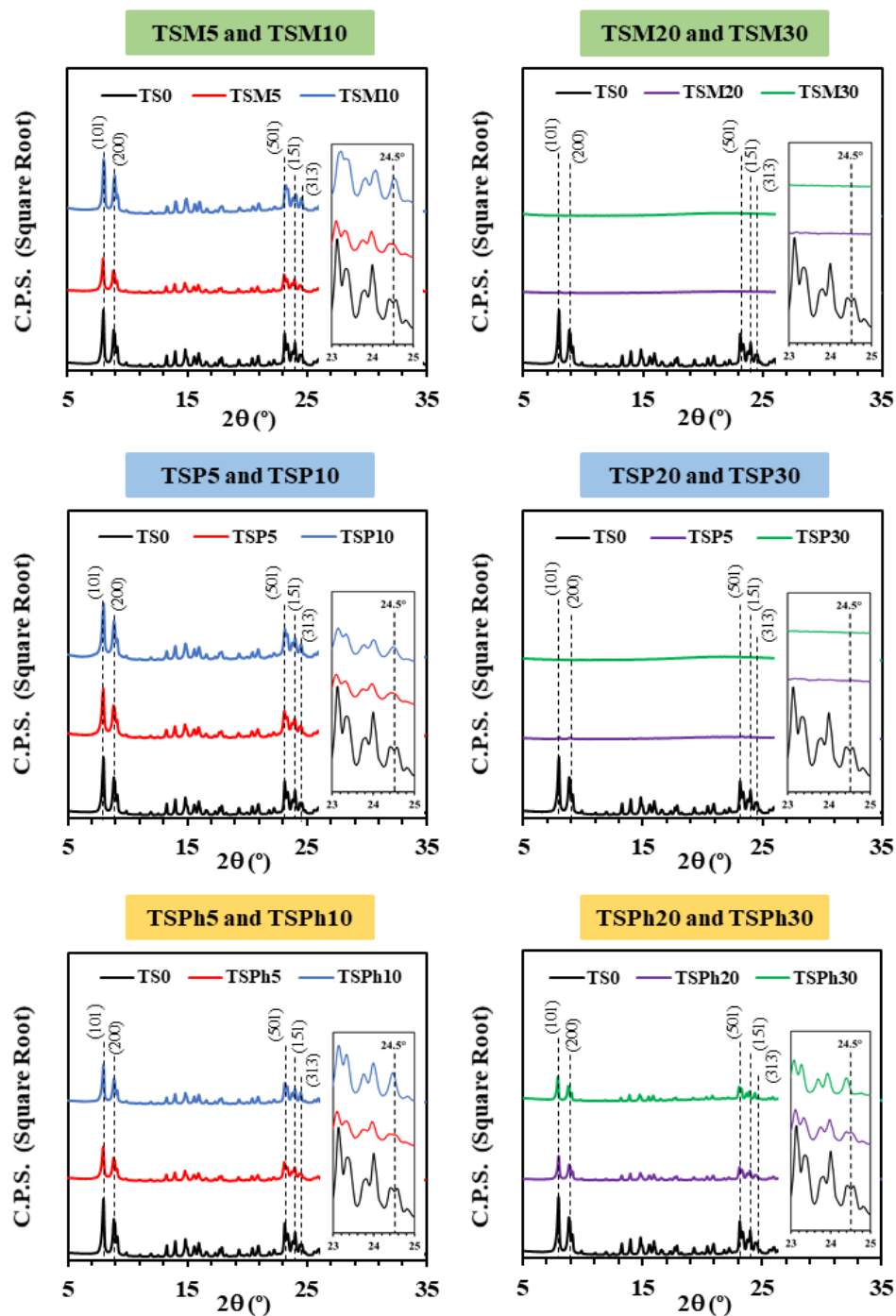


Figure 7.1 XRD diffraction patterns of the reference material (TS0, in black) and the TSR% materials.

The diffraction patterns show that the TSR5, TSR10, TSPH20 and TSPH30 materials present diffraction maxima at 7.8°, 8.9°, 23.1°, 24° and 24.5°, consistent with the standard diffraction patterns of TS-1 (ICDD, JCPDS, file code 70- 4276). In the literature, these maxima are associated with (101), (200), (501), (151), and (313) orthorhombic MFI lattice planes, respectively, where the Ti^{IV} cations are substituting silicon atoms in the framework [26,41]. However, the diffraction pattern of the reference material shows that the diffraction maximum at 24.5° is split, which indicates that this material is monoclinic, as happens with highly pure silicalites ([Si₉₆O₁₉₂]), suggesting that only part of the Ti^{IV} cations are successfully embedded in the silica framework [42]. On the contrary, this split is not observed in the diffraction patterns of the TSR materials and additionally, as the molar percentage of organotriethoxysilane (RTEOS) increases from 5 to 10%, this maximum gets sharper, denoting that the precursor aids the incorporation of Ti^{IV}.

The diffraction patterns of TSPH20 and TSPH30 show the characteristic maxima of titanium silicalite-1 (TS-1), while those of TSM20, TSM30, TSP20 and TSP30 do not present these maxima, and only a broad maximum at 23° is observed (Figure 7.1 right side). This maximum is associated with the siloxane bonds (Si–O–Si) of amorphous silica, indicating that increasing the amount of alkyltriethoxysilane beyond 10% molar percentage restrains the formation of MFI-type structures. It is worth mentioning that the diffraction patterns of all the materials do not present a maximum at $2\theta = 25.4^\circ$, therefore the presence of extra-framework Ti^{IV} in the form of anatase can be ruled out (JCPDS file 73-1764).

7.2.1.2 Fourier Transformed Infrared Spectroscopy (FTIR)

The left side of Figure 7.2 displays the FTIR spectra of the TSR materials in the spectral range between 1600–400 cm^{-1} , and its right side illustrates the spectral region 4000–2750 cm^{-1} . No relevant bands were observed in the 2750–1600 cm^{-1} range.

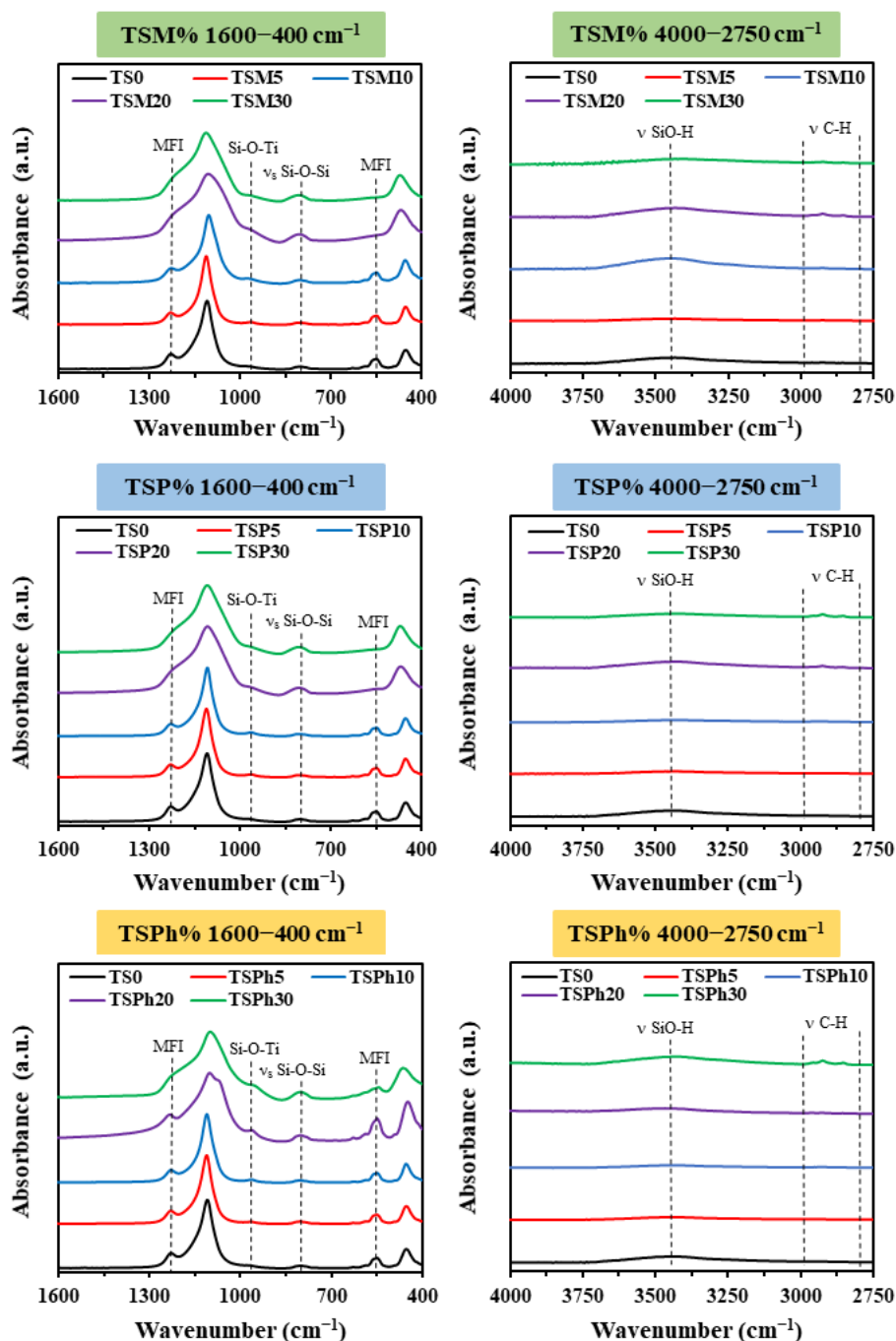


Figure 7.2 FTIR spectra of TSM%, TSP%, and TSPh% in the (left) 1600–400 and (right) 4000–2750 cm^{-1} frequency regions.

The spectra of TSR5 and TSR10 show the specific bands of titanium silicalites (marked in Figure 7.2 left): (i) 1230 cm^{-1} , the vibration of the five-member double ring unit of MFI structure, (ii) 960 cm^{-1} , the stretching vibration of the Si–O bond in SiO_4 units, perturbed by the presence of Ti^{IV} cations (Si–O–Ti), and (iii) 550 cm^{-1} , the asymmetrical stretching vibration of zeolite framework SiO_4 and TiO_4 [43,44]. However, TSR20 and TSR30 (R = M or P) spectra display only the characteristic bands of the silica skeleton: (i) 3430 cm^{-1} , the stretching vibration of surface silanols (Si–OH) in Figure 7.2 right, (ii) 1200 cm^{-1} , a broad shoulder related to vibration modes of the Si–O–Si bonds, (iii) 1090 cm^{-1} , the asymmetrical stretching vibration of Si–O–Si, (iv) 955 cm^{-1} , the stretching vibration of the Si–O bond belonging to surface silanols (Si–OH), (v) 800 cm^{-1} , the symmetrical stretching vibration of Si–O–Si, and (vi) 455 cm^{-1} , the rocking vibration of O–Si–O [45].

It is important to note that, the intensity of the band at 800 cm^{-1} , is a good indicator of the amorphism grade of the material because it corresponds to amorphous silica [46]. On this basis, in the FTIR spectra is easily observable that by increasing the amount of organotriethoxysilane, more amorphous materials are obtained. By comparison with the XRD patterns, it can be stated that TSR20 and TSR30 derived from MTEOS and PTEOS are completely amorphous, whereas those derived from PhTEOS still retain a certain grade of crystallinity. Regarding the FTIR spectra of TSPH20, the simultaneous presence of MFI-structure bands (1230 and 550 cm^{-1}) and the characteristic band of amorphous silica at 800 cm^{-1} suggest that the material is semi-crystalline, although for TSPH30 MFI-structure bands are not observable, indicating that this material is substantially more amorphous, although based on its XRD diffraction pattern (depicted in Figure 7.1 right) it retains a certain grade of crystallinity.

7.2.1.3 Diffuse reflectance UV-Vis, Photoluminescence emission (PL) and UV-Raman spectroscopy

Diffuse reflectance (DR) UV-Vis spectra of the TSR% materials in the range of 210–410 nm are depicted in Figure 7.3.

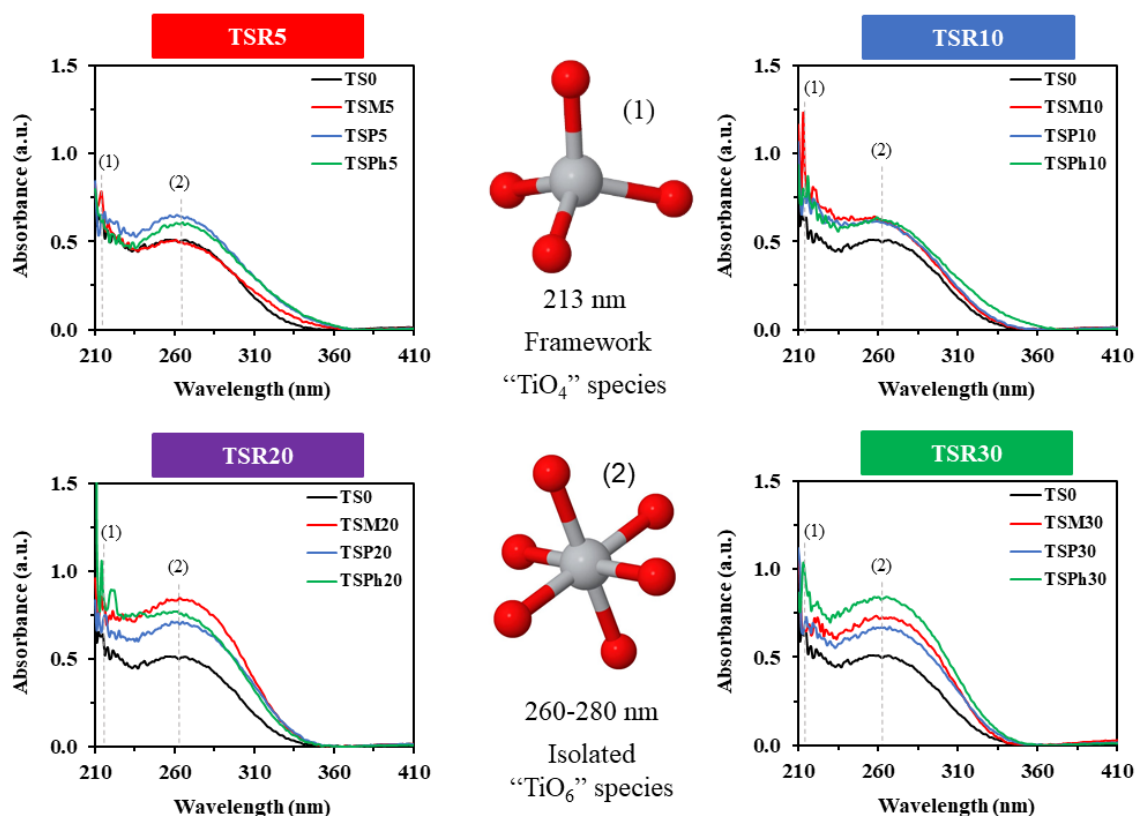


Figure 7.3. DR UV-Vis spectra of reference material and TSR5, TSR10, TSR20, and TSR30.

The DR UV-Vis spectra of the MFI-structured titanium silicalites exhibit a variety of absorption bands in the following ranges: (i) 200–220 nm, attributed to the tetra-coordinated titanium embedded in the framework, and specifically due to the π - π charge transfer between the 2p electron of O^{-2} and the empty 3d orbital of the Ti^{IV} cation [32], (ii) 260–280 nm, generally attributed to the presence of defective titanium species like isolated hexa-coordinated titanium (mononuclear TiO_6 octahedral species) in the MFI structure [32,33], and (iii) 310–330 nm, attributed to the presence of crystalline titanium in the form of anatase [47].

The spectra of the TSR materials synthesised in this work exhibit the bands attributed to the tetra-coordinated titanium embedded in the framework and the extranet hexacoordinated titanium. The band due to the anatase is not observed, thus discarding its presence in the materials, which agrees with the XRD diffraction patterns. The

absorption intensity at ~ 213 nm (tetracoordinated titanium band) and at ~ 265 nm (hexacoordinated titanium band) increases as the amount of RTEOS rises (except for the band at ~ 213 nm of the TSR5 materials), consistent with the non-split narrower maximum at $2\theta = 24.5^\circ$ in the XRD (Figure 7.1). Furthermore, the decay of the ~ 265 nm absorption band is enlarged from 350 nm to 370 nm in the TSR5 and TSPH10 materials, which is translated in a larger range of absorption and will be of great relevance in their photocatalytic activity.

Information on the electronic structure of these materials was obtained by applying the Tauc-plot analysis to the UV-Vis spectra data [48]. Figure 7.4 depicts the plot of $(\alpha h\nu)^{1/n}$ with respect to the energy ($h\nu$), where α is the absorption coefficient of the materials determined from the UV-Vis data in Kubelka-Munk units. The bandgap energy values of the materials (E_g) were calculated from the plot slope by applying $(\alpha h\nu)^{1/n}$, considering $n = 2$ for indirect allowed transitions, and the results obtained are compiled within each of the figures that make up Figure 7.4. The calculation process of the E_g of the materials is explained step by step and in detail in *Chapter 2.5.3*.

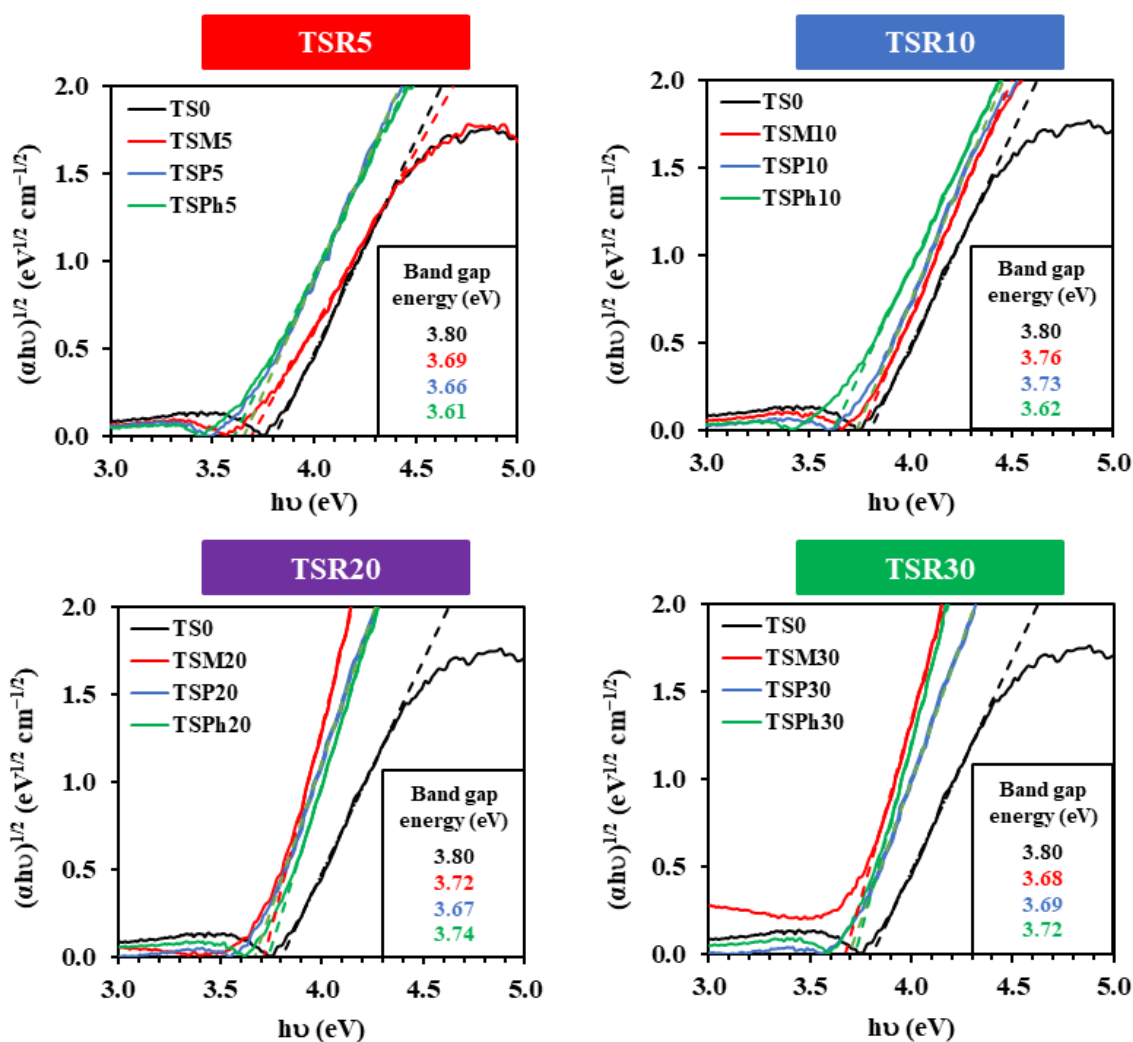


Figure 7.4. Tauc-plot analysis of the reference material and TSR5, TSR10, TSR20, and TSR30.

The indirect band-gap values obtained for the TSR materials are lower than 4 eV, implying that they might exhibit photocatalytic activity, moreover, all the materials yielded lower band-gap values than TS0. Remarkably, TSPH5 and TSPH10 are the materials with the lowest band-gap values when compared to their analogues with the same molar percentage of RTEOS.

The photoluminescence emission spectra of the TSR% materials are illustrated in Figure 7.5.

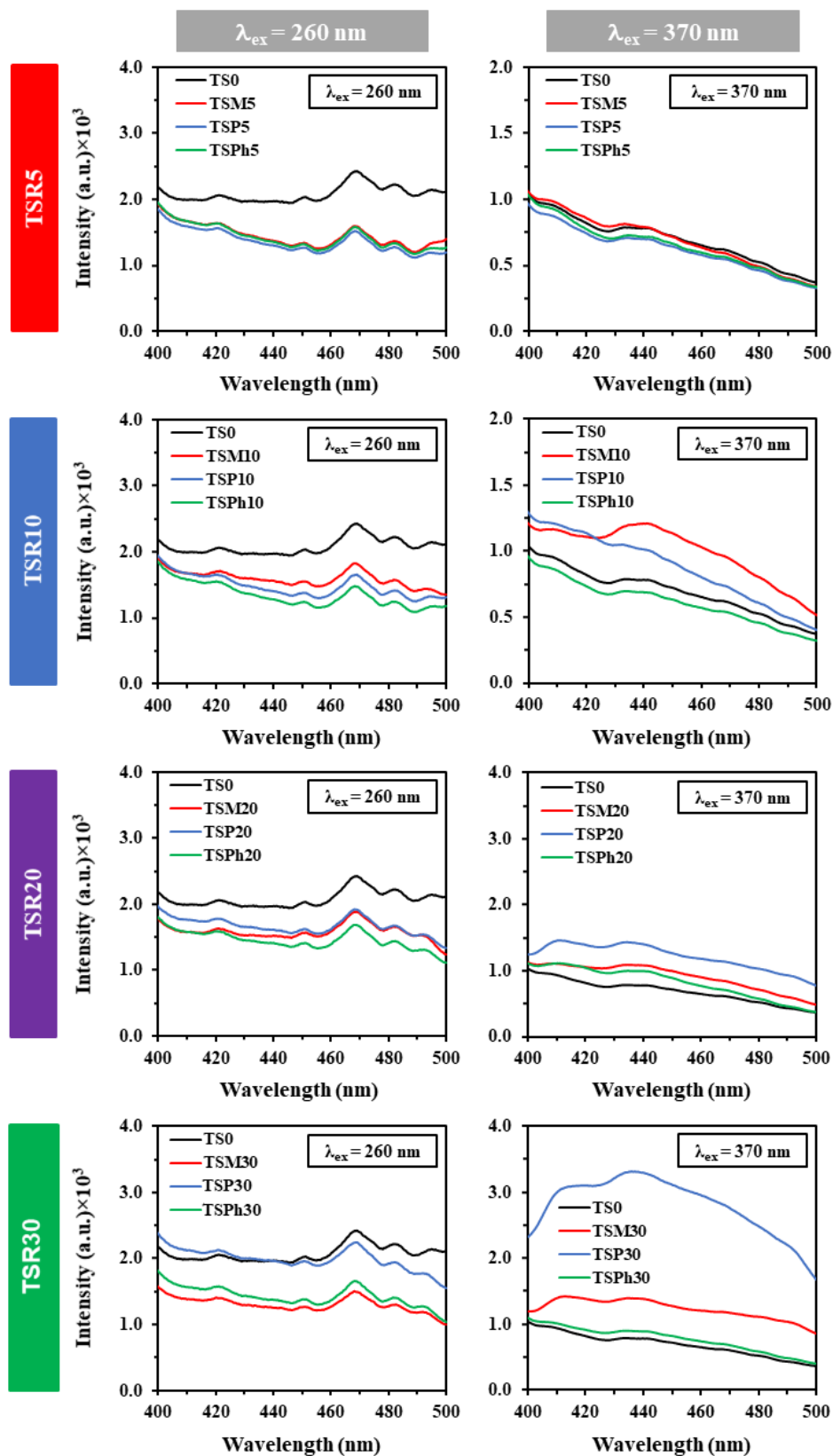


Figure 7.5. Photoluminescent emission spectra of TSR% materials registered at 260 and 370 nm excitation wavelength.

The photoluminescence emission spectra of the materials were obtained at 260 nm, which is the maximum DR UV-Vis absorption of the hexacoordinated Ti species, and 370 nm, which is the limit of UV absorption of TSR5 and TSPH10 (Figure 7.3). When the materials are excited at 260 nm, a set of bands in the range of 400–500 nm is observed, attributed to the radiative decay process from the charge transfer between O^{2-} and Ti^{+4} [49]. At this wavelength, the emission intensity decreases as the molar percentage of RTEOS increases, implying that these modified titanium silicalites present a lower recombination rate of the electron-hole pair than the reference [28]. However, when they are excited at 370 nm, TSM5 presents an intensity similar to that of the reference, whereas TSP5, TSPH5 and TSPH10 intensity is lower than TS0, and TSM10 and TSP10 intensity is higher. These observations, together with the information elucidated by the UV-Vis absorption, suggest that TSP5, TSPH5, and TSPH10 might exhibit the highest photocatalytic activity among the synthesised titanium silicalites.

UV-Raman spectra at 325 nm of TSR5 and TSR10 samples were acquired to further delve into the relative proportion of Ti species in the samples (Figure 7.6).

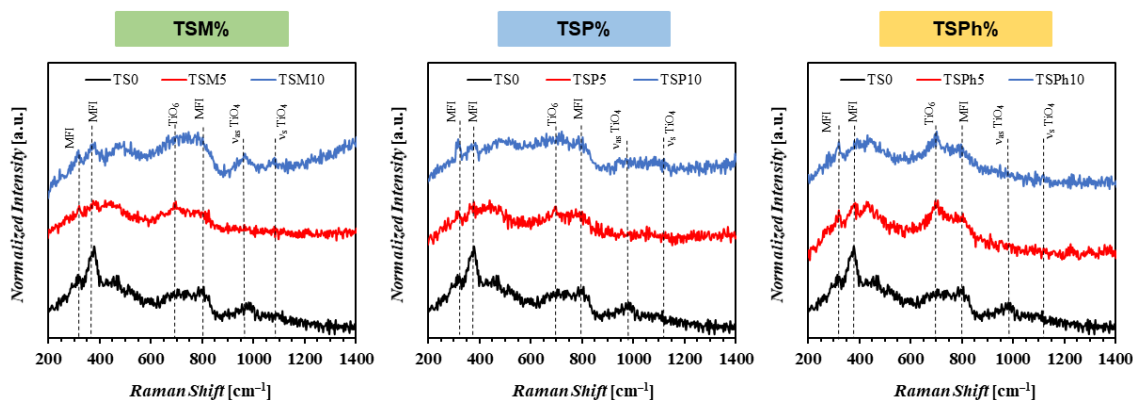


Figure 7.6. UV-Raman spectra of TSR5 and TSR10 registered at 325 nm excitation wavelength.

The UV-Raman spectrum of the reference (TS0) shows some of the characteristic bands of the MFI structures at 290, 380 and 800 cm^{-1} . Additionally, a low-intensity band associated with the asymmetric stretching vibration of TiO_4 species is detected at $\sim 960\text{ cm}^{-1}$, while the symmetric stretching vibration usually reported at 1125 cm^{-1} is not observable [33]. Remarkably, the intensity of the 380 cm^{-1} band of TSR5 and TSR10 is considerably lower, which points to the gradual loss of crystallinity produced by the use of organosilanes. TSM10 spectrum is the only one that clearly depicts the 960 cm^{-1} band, thus confirming the presence of a TiO_4 framework in the material. However, an emerging band at $\sim 700\text{ cm}^{-1}$ in the TSR5 and TSPH10 spectra is noticeable, which is more intense

in the TSPH5 and TSPH10 materials. In the literature, the presence of a band at 695 cm^{-1} has been associated with the UV-Vis absorption band at 270 nm of titanium silicalites, and therefore, with the Ti–O stretching vibration of TiO_6 octahedron species (i.e., amorphous Ti) [33]. Hence, the use of organosilanes in titanium silicalite synthesis, especially phenyltriethoxysilane, is detrimental to the formation of TiO_4 framework species and helps the formation of superficial amorphous TiO_6 species. Thereby, the enlarged UV-Vis absorption range and the lower PL emission intensity of TSR5 and TSPH10 materials are a consequence of the higher proportion of such species.

7.2.1.4 N_2 and CO_2 Adsorption

Figure 7.7 displays the N_2 adsorption isotherms ($-196\text{ }^\circ\text{C}$) of all prepared TSR% materials (top left), as well as the CO_2 adsorption isotherms ($0\text{ }^\circ\text{C}$) of TSR5 and TSR10 materials (top right). The textural parameters of TSR5 and TSR10 materials obtained from the isotherms of both adsorbates are shown in Table 7.1.

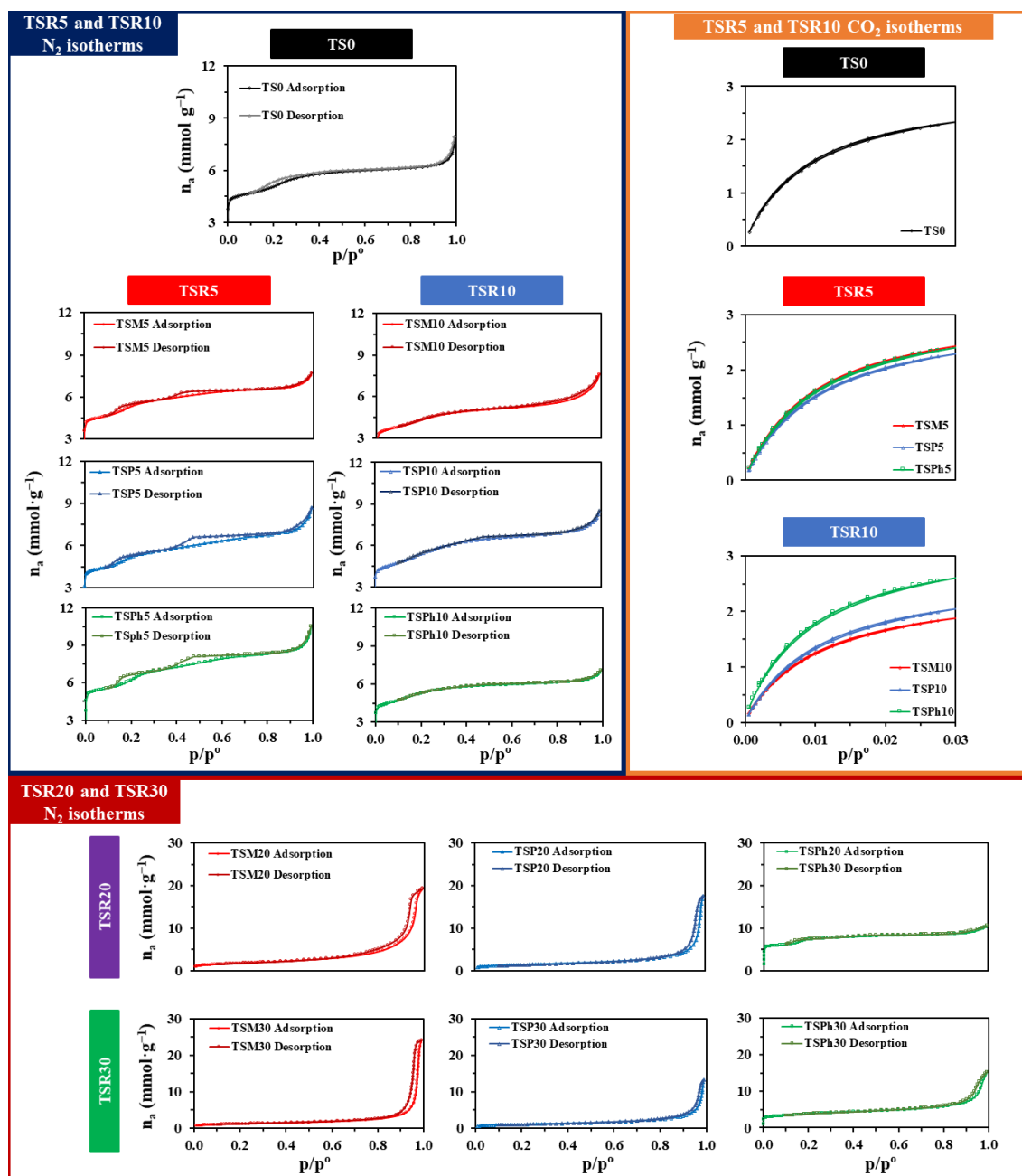


Figure 7.7. N_2 and CO_2 adsorption isotherms of the reference, TSR5, and TSR10 materials (top left and right, respectively), and N_2 isotherms of TSR20 and TSR30 materials (bottom).

Table 7.1. Textural parameters of the reference, TSR5 and TSR10 materials.

In the literature, most of the MFI-structured zeolites show type I N₂ isotherms according to the IUPAC adsorption technical report [50], although in some cases type VI isotherms have been reported for uniform ultramicroporous solids like silicalites or titanium silicalites [51,52]. Whatever the type of N₂ isotherm, it is well reported that MFI zeolites present high adsorption at extremely low partial pressures (p/p°) due to the filling of their inner channels by confinement effects, which typically represents more than 50% of the total amount of adsorbed N₂ [53]. Furthermore, if the material is composed of grain accumulations it will be observable a type H3 hysteresis loop at $p/p^{\circ} > 0.8$ due to the capillary condensation taking place in the interparticle wide mesopores and macropores [43].

In this work, all the materials which are considered zeolites, including the reference, show a type VI N₂ isotherm, a type H3 hysteresis loop at high partial pressures, and high adsorption at $p/p^{\circ} < 0.03$, representing more than half of the N₂ adsorption capacity ($n_a(p/p^{\circ} \leq 0.03)$ in Table 7.1), in agreement with other reported MFI zeolites. The reference material shows a type H4 hysteresis loop at $0.1 < p/p^{\circ} < 0.35$ due to adsorbate-adsorbate interactions inside the pores, leading to a framework structural change produced by the deformation of the non-rigid pore walls [53]. Remarkably, the addition of a 5% molar percentage of RTEOS in the synthesis results in materials with a similar hysteresis loop than the reference at $0.1 < p/p^{\circ} < 0.35$, and a new H4 hysteresis loop located at $0.35 < p/p^{\circ} < 0.8$, consistent with a change in the morphology of the narrow mesopores, from cylindrical to ink-bottle shaped, and thus, creating a retention effect of the adsorbate inside the pores and its capillary condensation [50]. This change in the pore morphology of the TSR5 materials together with their higher pore volume (V_{Total}) and lower amount of N₂ adsorbed at $p/p^{\circ} \leq 0.03$, suggest the possibility of an improvement in the diffusion performance and accessibility of the adsorbates to the active sites during the photocatalysis [24]. On the contrary, the materials prepared with a 10% molar percentage of RTEOS lack the hysteresis at $0.1 < p/p^{\circ} < 0.35$ observed in TSR5, and their isotherms show a partial loss of the narrow mesoporosity, which is translated in the flattening of the hysteresis at $0.35 < p/p^{\circ} < 0.8$. Finally, materials discarded as zeolites due to their substantial amorphous nature (TSM20, TSM30, TSP20, TSP30, and TSP30), present type II isotherms, characteristic of macroporous or non-porous solids (Figure 7.7 bottom). Remarkably, TSP30, which is a semi-crystalline material based on its XRD diffraction

pattern and FTIR spectrum, presents a type VI isotherm with most of its N₂ adsorption below a partial pressure of 0.03, reinforcing the idea that, although it is partially amorphous, most of its skeleton is nanostructured, granting the material MFI zeolite properties. All the titanium silicalites have similar specific surface areas (a_{BET}) to that of the reference, except TSM10 and TSPH5, consistent with their adsorption capacity. The characteristic energy ($E_{c(N_2)}$) decreases with the increase of RTEOS in all the materials, implying a more labile interaction between the surface of the material and the N₂.

Regarding the CO₂ isotherms (top right of Figure 7.7), using 5% of any RTEOS does not significantly affect their micropore volume ($V_{micro(CO_2)}$), as these materials and the reference adsorb similar quantities of CO₂. On the contrary, materials synthesised with 10% RTEOS show relevant changes in the volume of micropores. The micropore volume of TSM10 and TSP10 decreases with respect to the reference, whereas the one of TSPH10 increases. In addition, for all the materials $V_{micro(N_2)} < V_{micro(CO_2)}$ (Table 7.2), confirming that N₂ faces kinetic restraints to enter the narrow micropores. This observation is consistent with their ultramicroporous nature [37], although based on the average pore size determined by the BJH method (BJH APS), all the materials retain a certain degree of mesoporosity.

The pore size distributions (PSD) of the TSR5 and TSR10 materials using both adsorbates, have been determined by DFT methods and are shown in Figure 7.8.

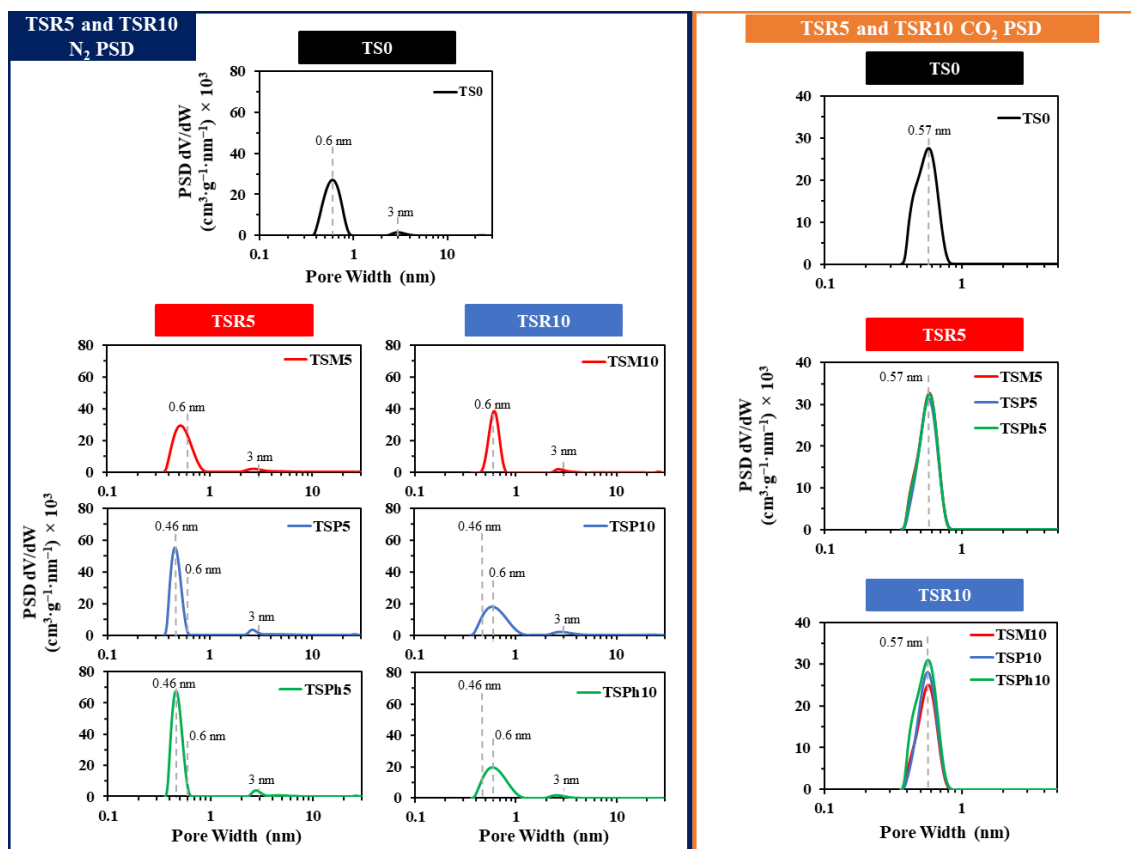


Figure 7.8. Density-functional theory (DFT) and pore size distributions (PSD) calculated of the reference, TSR5, and TSR10 materials obtained from their N_2 and CO_2 adsorption isotherm data (top left and right, respectively).

Figure 7.8 illustrates that most of the pores of TSR5 and TSR10 materials have an internal diameter (\emptyset) centred at approximately 0.6 nm for both adsorbates. This is to be expected since zeolites with MFI-type structures, such as titanium silicalites, are formed of 10-membered rings ($(SiO)_{10}$), with internal diameter channels of $\emptyset = 0.55$ nm [54], which means that only small molecules such as N_2 or CO_2 ($\emptyset = 0.36$ and 0.33 nm, respectively) can access the pores. N_2 PSDs of these materials are characteristic of ultramicroporous materials with a slight portion of narrow mesopores centred at $\emptyset = 2\text{--}4$ nm.

7.2.1.5 FE-SEM and EDX

To determine the particle size and morphology, micrographs of the materials were acquired using field-emission scanning electron microscopy (FE-SEM). The micrographs of TSR5 and TSPH10 are displayed in Figure 7.9.

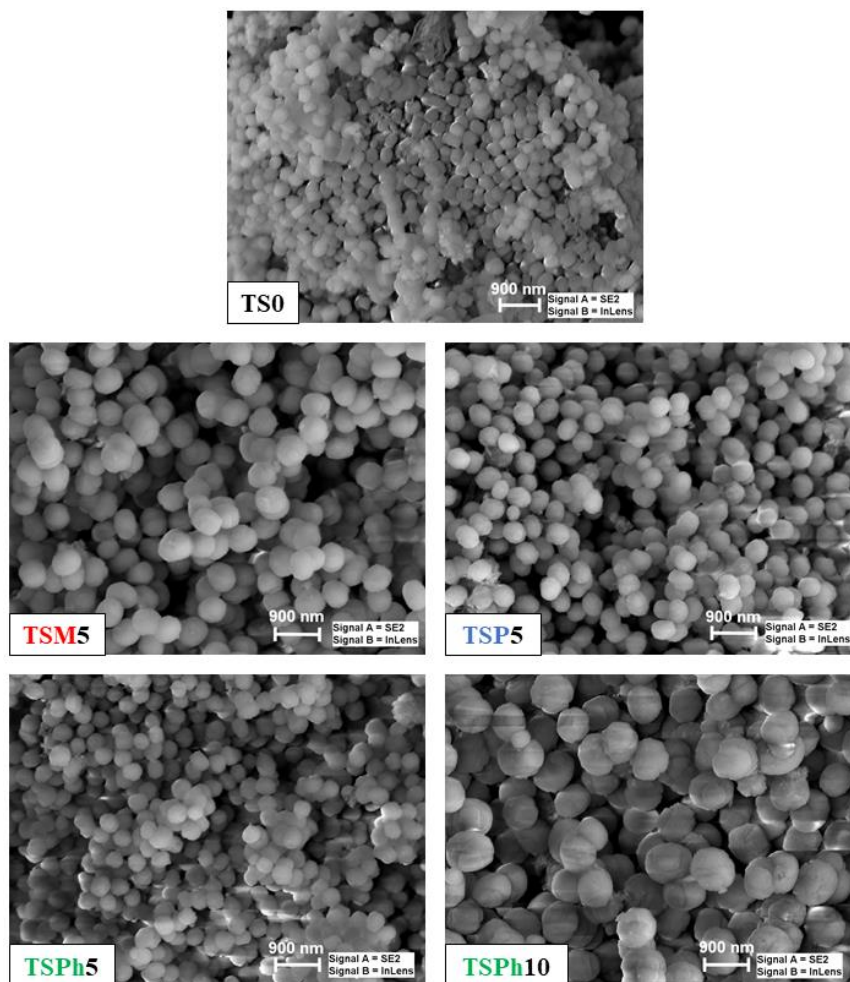


Figure 7.9. FE-SEM micrographs of the reference, TSM5, TSP5, TSPH5, and TSPH10 materials.

The micrograph of TS0 exhibits an agglomeration of ellipsoidal particles with smooth surfaces and variable sizes (ranging from 250 to 320 nm). This morphology differs from the characteristic coffin-like hexagonal crystal shape of titanium-silicalites prepared with TPA⁺ as the only structure-directing agent (SDA) [44]. The shape of the particles in this material derives from the presence of PVP in the synthesis media, which not only slows down the TBOT hydrolysis aiding the introduction of titanium in the matrix but also competes with the TPA⁺ cation acting as a surfactant. This competition changes the crystal growth due to the PVP hydrogen bonding interactions within the TS skeleton [38], yielding flat-cylinder-shaped particles with smaller sizes than titanium

silicalites synthesised by similar procedures (0.5–3 μm) [18,55,56]. The micrographs of the TSR materials show how the use of RTEOS has a big impact on their morphology, as they exhibit bigger, rougher and more spherical-shaped particles than those of TS0, suggesting that the organic moiety of RTEOS hinders the surface interaction of the colloids with the SDAs, which might be the reason why the more the molar percentage of RTEOS is added, the bigger the particles of the material ($\text{TS0} < \text{TSPH5} < \text{TSPH10}$). The hindrance exerted by organosilanes may further explain why materials with a high content of RTEOS (TSR20 and TSR30) gradually lose their crystallinity, and therefore, the skeletal density decreases. Table 7.2 shows the skeletal or real density values of each material determined by helium pycnometry.

Table 7.2. Skeletal density of the materials determined by Helium Pycnometry.

RTEOS	TSM	TSP	TSPH
<i>Molar percentage [%]</i>	<i>Skeletal density [g cm⁻³]</i>		
0*	2.46		
5	2.18	2.18	2.20
10	2.11	2.20	2.18
20	2.11	2.12	2.18
30	2.04	2.11	2.08

*TS0

When the same molar proportion of RTEOS is used, the size of the particles varies depending on the precursor. The material obtained with 5% of PhTEOS exhibits the smallest particle sizes (320–420 nm), whereas the same percentage of MTEOS yields larger particle sizes (550–675 nm), indicating that the methyl group induces a greater steric effect than the phenyl group, hindering the SDAs more effectively, and thus, the growth of the particles. The interparticle space observed in the micrographs constitutes the wide mesoporosity and macroporosity, part of which is displayed as a hysteresis loop above 0.9 p/p^0 in the adsorption-desorption isotherms (top left of Figure 7.7).

To estimate the amount of titanium in the materials, a mapping of the composition was carried out by X-ray energy dispersion. The average values resulting from several mappings are given in Table 7.3.

Table 7.3. Average weight percentage and atomic abundance, estimated by EDX, of C, O, Si and Ti in the reference, TSR5 and TSPH10 materials.

Material	C		O		Si		Ti	
	Weight	Atomic	Weight	Atomic	Weight	Atomic	Weight	Atomic
	(%)		(%)		(%)		(%)	
TS0	7.86	12.15	54.41	63.23	35.77	23.77	0.94	0.36
TSM5	5.63	8.92	53.34	63.53	39.73	27.00	0.90	0.36
TSP5	4.96	7.86	55.14	65.59	37.98	25.74	1.36	0.54
TSPH5	9.59	14.61	54.57	62.37	34.51	22.47	0.88	0.34
TSPH10	7.48	11.33	59.35	67.48	31.96	20.70	0.88	0.33

Results in Table 7.3 show that most of the materials contain approximately 0.9 wt% of titanium, consistent with the previously reported titanium silicalites synthesised under the same conditions [38]. The presence of carbon in the materials is due to the calcination residues from the organic templates, identified as dust in the micrographs. Surprisingly, TSP5 present the highest titanium amount out of all the materials. This fact, together with its high UV-Vis absorption and low PL intensity, suggests that TSP5 could be the best candidate as a photocatalyst. However, TSPH5 displays various properties which must be in consideration for the catalytic activity: it presents the smallest particle sizes, the biggest surface area and the highest pore capacity. Furthermore, its UV-Raman spectrum shows a more intense signal of TiO₆ species than TSP5.

7.2.2 Photocatalytic degradation of venlafaxine in the presence of TS

The photoactivity of TSR materials was tested in the degradation of 5 ppm aqueous solutions of venlafaxine under simulated solar irradiation for 1-hour, detailed experimental conditions and used equipment are provided in *Chapter 2.4*. TS0 was found to be inactive, whereas TSR5 and TSPH10 were able to degrade a significant amount of venlafaxine. Figure 7.10 displays the degradation curves of venlafaxine using these materials as photocatalysts.

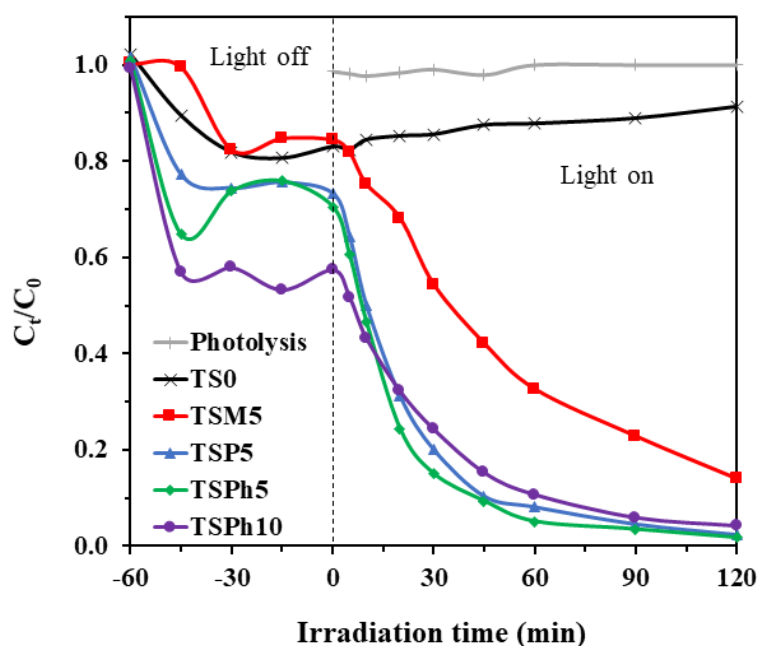


Figure 7.10. Photodegradation of venlafaxine under simulated solar irradiation with the reference, TSM5 and TSPH10 materials. Experimental conditions: $[\text{Venlafaxine}]_0 = 5 \text{ mg L}^{-1}$, photocatalyst load = 1 g L^{-1} , and incident photon irradiance $I = 500 \text{ W m}^{-2}$.

The curves shown in Figure 7.10 show that the materials adsorbed part of the venlafaxine from the solution prior to the irradiation. After 1 h in the absence of light, TSM5 adsorbed a similar amount of venlafaxine than the reference (16 and 19%, respectively), while TSP5 and TSPH5 adsorbed more (28 and 30%, respectively) and TSPH10 the greatest amount (42%), expected as the volume of inter-particle macropores is the highest for this material. Once the adsorption equilibrium was reached, the photocatalytic cycle was performed. Remarkably, the reference material was not photoactive, but all the selected new materials yielded quantitative photodegradation of venlafaxine in 2 h: TSM5 degraded 86%, while TSP5, TSPH5 and TSPH10 degraded practically all the venlafaxine in solution (98%, 98% and 96%, respectively). Besides the common products of the degradation of an organic pollutant (CO_2 and H_2O), HPLC (Shimadzu) confirms the obtention of a small quantity of a degradation intermediate at a retention time of ~ 1.6 min, which was identified as atenolol. As an example, Figure 7.11 shows the HPLC chromatogram profile for the degradation of venlafaxine using TSPH5 as the photocatalyst. Furthermore, using another HPLC equipment (Hitachi) it was possible to detect oxalic, maleic and formic acids.

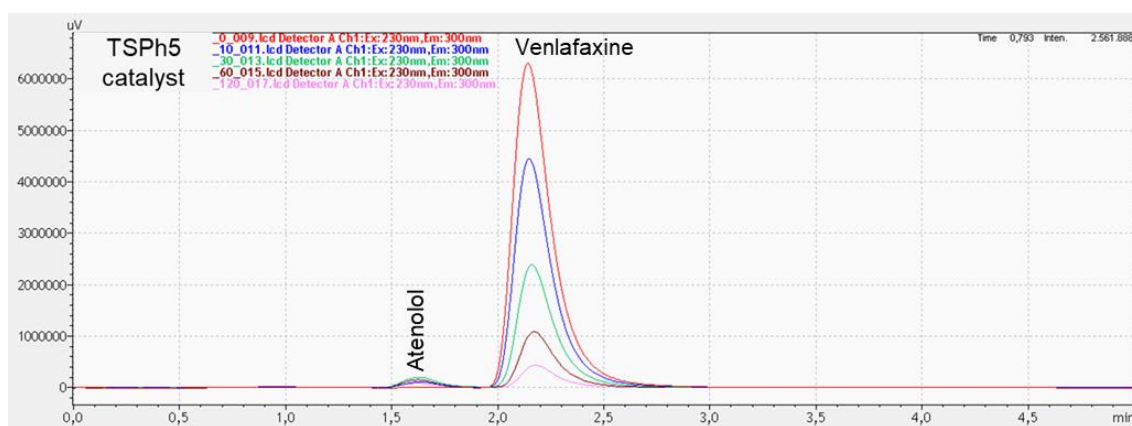


Figure 7.11. HPLC chromatogram profiles for degradation of venlafaxine using TSPH5 photocatalyst over the reaction time.

Once the first photocatalytic cycle was performed to determine that the materials were photoactive, to study and properly compare the photoactivity efficiency of the titanium silicalites, another photocatalytic run was performed, considering the amount of adsorbed venlafaxine of each material prior to the photodegradation, to ensure that the initial concentration before photocatalysis was kept at $\sim 5 \text{ mg L}^{-1}$. Figure 7.12 exhibits the photodegradation curves of venlafaxine after adsorption equilibria (left) and the pseudo-first-order kinetic adjustment (right). The calculated kinetic parameters are displayed in Table 7.4.

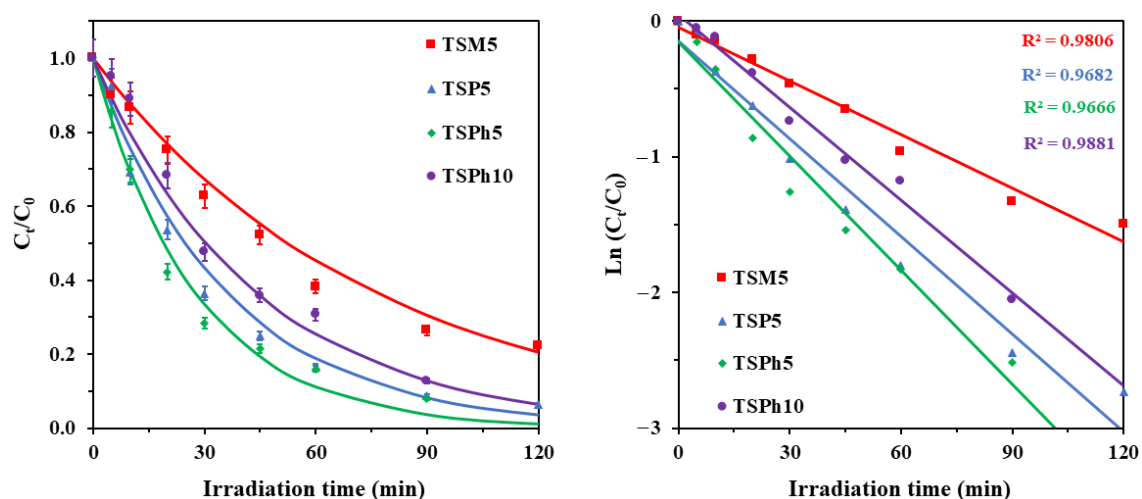


Figure 7.12. (left) Photodegradation of venlafaxine after adsorption equilibria ($[\text{Venlafaxine}]_0 = 5 \text{ mg L}^{-1}$) and (right) pseudo-first-order kinetic adjustment of the photodegradation process.

Table 7.4. Kinetic constants calculated from venlafaxine degradation curves.

Catalyst (1 g L ⁻¹)	k ^a (min ⁻¹)	t _{1/2} ^b (min)
TSM5	0.013	52.53
TSP5	0.028	24.87
TSPH5	0.036	19.09
TSPH10	0.023	30.44

^a-Degradation rate constant; ^b-Half-life time.

Due to the higher initial concentration at the start of venlafaxine photodegradation compared to the first photocatalytic cycle (Figure 7.10), the degraded molar percentage was slightly lower: 78%, 93%, 92% and 87% for TSM5, TSP5, TSPH5 and TSPH10, respectively. TSM5 yielded a lower degradation rate among the tested materials, consistent with its similar UV-Vis absorbance spectra and photoluminescence at $\lambda_{ex} = 370$ nm to those of the reference. Comparing TSPH5 and TSPH10 (materials prepared with the same organotriethoxysilane), the performance of the latter is poorer, probably due to a loss of crystallinity, a greater particle size, and a lower mesopores and total pore volume. TSPH5 and TSP5 exhibit similar photocatalytic activity and are the best among the tested materials. However, from among the two samples, photocatalytic degradation of the pollutant was faster with the TSPH5, with a rate constant 3-fold higher than that of the TSM5 sample, and with a half-life time reduced by almost three times. This could be related to the higher specific surface area and amount of TiO₆ observed in the UV-Raman spectra of TSPH5 compared to TSP5. Although in the literature tetracoordinated TiO₄ species are said to be more active than octahedral TiO₆ species, in the case of the materials synthesized in this study, the latter is more superficial and therefore more accessible to pollutants, which implies an improvement in the kinetics of degradation.

To complement the discussion, in Annexe D the performance of TSP5 and TSPH5 in the photodegradation of venlafaxine is compared with the results achieved by other photocatalysts reported in the literature, whose specifications and experimental conditions used are compiled in Table D.1.

7.3 CONCLUSIONS

Three series of titanium silicalites (TSR%) prepared by a modified hydrothermal synthetic strategy have been obtained. The modification of the method consisted of the addition of an organotriethoxysilane [RTEOS (where R = methyl, propyl or phenyl)], to

the tetraethoxysilane (TEOS) and titanium tetrabutoxide (TBOT) synthesis mixture at various molar percentages with respect TEOS, in an attempt to direct the nano-structuration and to obtain modified titanium silicalites bearing a variety of morphologies and textural properties to improve their photocatalytic activity. XRD diffraction patterns and FTIR spectra confirmed that TSR5 and TSR10 exhibited a crystalline zeolite structure, whereas the addition of higher amounts of RTEOS resulted in amorphous or semi-crystalline materials. Their XRD patterns together with their UV-Vis spectra were consistent with the absence of anatase, the latter indicating also the presence of extra-framework hexacoordinated titanium. It should be noted that a wider spectral range in UV-Vis absorption closer to the visible spectral range was observed for these materials. Materials displaying a lower intensity emission in their photoluminescence spectra than the reference (TSP5, TSP5 and TSP5) were considered better photocatalysts due to a slower hole-electron recombination rate, which was later confirmed in the photodegradation of venlafaxine. These initial photocatalytic studies revealed that, in contrast to the reference, TSR5 and TSP5 were photoactive under simulated solar irradiation. Surprisingly, the TSP5 and TSP5 materials, which exhibit the smallest and most homogeneous pore diameter, as well as the smallest particle size, were the most photoactive of all the series, evidencing how the porous texture is a crucial parameter in their photocatalytic properties. Thus, after this in-depth textural, morphological and chemical study, it can be stated that the proposed synthetic approach yields modified titanium silicalites with improved photocatalytic properties, which efficiently degrade venlafaxine, leading the way to further studies for their optimization.

7.4 ACKNOWLEDGEMENTS

The authors gratefully acknowledge financial support from Ministerio de Ciencia e Innovación, Government of Spain (PID2020-113558RB-C42) and from LA/P/0045/2020 (ALiCE), UIDB/50020/2020 and UIDP/50020/2020 (LSRE-LCM), funded by national funds through the Portuguese Science Foundation FCT/MCTES (PIDDAC).

G.C.-Q thanks Ministerio de Universidades, Government of Spain, for a predoctoral grant within the Formación de Profesorado Universitario (FPU) program (FPU18/03467) and the Government of Navarre, for a predoctoral international mobility grant (0011-3564-2022-000035). M.J.S. acknowledges FCT funding under the Scientific

Employment Stimulus - Institutional Call (CEECINST/00010/2021). M.V.L-R acknowledges financial support from Ministerio de Ciencia e Innovación, Government of Spain (PID2022-142169OB-I00) and from FEDER 2014-2020 Operative Program and Junta de Andalucía, Spain (FEDER-UJA-1380629). M.E.-V. thanks UPNA for the project Jóvenes Investigadores UPNA 2022 (PJUPNA18-2022). The authors would also like to thank the technical and human resources from UCTAI (Unidad Científico Técnica de Apoyo a la Investigación) at UPNA and the use of the “Centro de Instrumentación Científico-Técnica” at the University of Jaén.

7.5 REFERENCES

- [1] Krishnan, A.; Yoosuf, M.; Archana, K.; A. S., A.; Viswam, A. *J. Energy Chem.* **2023**, *80*, p. 562–583.
- [2] Feizpoor, S.; Rahim Pouran, S.; Habibi-Yangjeh, A. *Mater. Sci. Semicond. Process.* **2023**, *162*, p. 107444.
- [3] Wang, L. J.; Dong, P. Y.; Zhang, G.; Zhang, F. M. *Mater. Sci. Semicond. Process.* **2023**, *37*, p. 6323–6347.
- [4] Jabbar, Z. H.; Graimed, B. H.; Okab, A. A.; Issa, M. A.; Ammar, S. H.; Khadim, H. J.; Shafiq, Y. A. *Environ. Nanotechnol., Monit. Manage.* **2023**, *19*, p. 100765.
- [5] Mathew, J.; John, N.; Mathew, B. *Environ. Sci. Pollut. Res.* **2023**, *30*, p. 16817–16851.
- [6] Mumtaz, N.; Javaid, A.; Imran, M.; Latif, S.; Hussain, N.; Nawaz, S.; Bilal, M. *Environ. Pollut.* **2022**, *308*, p. 119690.
- [7] Musial, J.; Mlynarczyk, D. T.; Stanisiz, B. *J. Sci. Total Environ.* **2023**, *856*, p. 159122.
- [8] Wang, M.; Cai, Y.; Zhou, B.; Yuan, R.; Chen, Z.; Chen, H. *J. Sci. Total Environ.* **2022**, *836*, p. 155652.
- [9] Yu, Y.; Huang, H. *Chem. Eng. J.* **2023**, *453*, p. 139755.
- [10] Guo, S.; Ji, Y.; Li, Y.; Li, H.; An, P.; Zhang, J.; Yan, J.; Liu, S. (Frank); Ma, T. *Appl. Catal., B* **2023**, *330*, p. 122583.
- [11] El hamdaoui, J.; Lakaal, K.; Mazkad, D.; Beraich, M.; El Fatimy, A.; Courel, M.; Pérez, L. M.; Díaz, P.; Laroze, D.; Feddi, E. *Mater. Res. Bull.* **2023**, *164*, p. 112235.
- [12] Islam, M. R.; Islam, M. S.; Zamil, M. Y.; Ferdous, N.; Stampfl, C.; Park, J.; Hossain, M. *K. J. Phys. Chem. Solids* **2023**, *176*, p. 111263.
- [13] Sun, Q.; Li, Z.; Li, J.; Liu, N.; Zhang, M.; Le, T. *J. Alloys Compd.* **2023**, *955*, p. 170234.
- [14] Liane Ücker, C.; San Martins Rodrigues, F.; de Gouveia Cantoneiro, R.; Goetzke, V.; Ceretta Moreira, E.; Meneghetti Ferrer, M.; Wienke Raubach, C.; Cava, S. *J. Photochem. Photobiol., A* **2023**, *441*, p. 114694.

- [15] Villa, K.; Galán-Mascarós, J. R.; López, N.; Palomares, E. *Sustainable Energy Fuels* **2021**, *5*, p. 4560–4569.
- [16] Spasiano, D.; Marotta, R.; Malato, S.; Fernandez-Ibañez, P.; Di Somma, I. *Appl. Catal., B* **2015**, *170–171*, p. 90–123.
- [17] Taramasso, M.; Perego, G.; Notari, B. Snamprogetti S.p.A., Milan, Italy. *US Patent No. 4410501-A*, **1983**.
- [18] Wu, W.; Tran, D. T.; Cheng, S.; Zhang, Y.; Li, N.; Chen, H.; Chin, Y. H. (Cathy); Yao, L.; Liu, D. *Microporous Mesoporous Mater.* **2021**, *311*, p. 110710.
- [19] Xiong, G.; Jia, Q.; Cao, Y.; Liu, L.; Guo, Z. *RSC Adv.* **2017**, *7*, p. 24046–24054.
- [20] Du, S.; Chen, H. M.; Shen, H. X.; Chen, J.; Li, C. P.; Du, M. *ACS Appl. Nano Mater.* **2020**, *3*, p. 9393–9400.
- [21] Clerici, M.G. Titanium Silicalite - 1. In *Metal Oxyde catalysis*; Jackson, D., Hargreaves, J.S.J., Eds.; Prentice Hall, **2008**; Vol. 2, pp. 705–754.
- [22] Yin, H.; Su, F.; Luo, C.; Zhu, L.; Zhong, W.; Mao, L.; You, K.; Yin, D. *Appl. Catal., B* **2022**, *302*, p. 120851.
- [23] Zhu, M.; Zhu, C.; Wu, D.; Wang, X.; Wang, H.; Gao, J.; Huang, H.; Shi, C.; Liu, Y.; Kang, Z. *Nanoscale* **2019**, *11*, p. 15984–15990.
- [24] Zhao, Z.; Cheng, D. Guo; Chen, F.; Zhan, X. *Int. J. Hydrogen Energy* **2020**, *45*, p. 33532–33542.
- [25] Ormond, S. P. D.; Ratova, M.; Kelly, P.; Edge, M.; Mihailova, B.; Tosheva, L. *J. Porous Mater.* **2016**, *23*, p. 1421–1429.
- [26] Shang, Q.; Chi, W.; Zhang, P.; Ling, Y.; Liu, X.; Cui, G.; Liu, W.; Shi, X.; Tang, B. *Process Saf. Environ. Prot.* **2022**, *157*, p. 297–305.
- [27] Wu, Q.; Wang, H.; Yi, C. *Optik* **2018**, *158*, p. 1460–1469.
- [28] Li, N.; Yang, B.; Liu, M.; Chen, Y.; Zhou, J. *Chin. J. Catal.* **2017**, *38*, p. 831–843.
- [29] Yamashita, H.; Mori, K. *Chem. Lett.* **2007**, *36*, p. 348–353.
- [30] Yamashita, H.; Mori, K.; Kuwahara, Y.; Kamegawa, T.; Wen, M.; Verma, P.; Che, M. *Soc. Rev.* **2018**, *47*, p. 8072–8096.
- [31] Parker, W.O.; Millini, R. *J. Am. Chem. Soc.* **2006**, *128*, p. 1450–1451.
- [32] Signorile, M.; Braglia, L.; Crocellà, V.; Torelli, P.; Groppo, E.; Ricchiardi, G.; Bordiga, S.; Bonino, F. *Angew. Chem., Int. Ed.* **2020**, *59*, p. 18145–18150.
- [33] Guo, Q.; Sun, K.; Feng, Z.; Li, G.; Guo, M.; Fan, F.; Li, C. *Chem. - Eur. J.* **2012**, *18*, p. 13854–13860.
- [34] Wang, Y.; Yang, H.; Zuo, Y.; Tian, D.; Hou, G.; Su, Y.; Feng, Z.; Guo, X.; Li, C. *Appl. Catal., B* **2023**, *325*, p. 122396.
- [35] Thangaraj, A.; Eapen, M.J.; Sivasanker, S.; Ratnasamy, P. *Zeolites* **1992**, *12*, p. 943–950.

- [36] Li, G.; Dimitrijevic, N. M.; Chen, L.; Nichols, J. M.; Rajh, T.; Gray, K. A. *J. Am. Chem. Soc.* **2008**, *130*, p. 5402–5403.
- [37] Wang, B.; Guo, Y.; Zhu, J.; Ma, J.; Qin, Q. *Coord. Chem. Rev.* **2023**, *476*, p. 214931.
- [38] Gao, J.; Gao, L.; Zhang, B.; Wang, H.; Ma, W. *Can. J. Chem. Eng.* **2021**, *99*, p. S596–S604.
- [39] Moriones, P.; Arzamendi, G.; Cornejo, A.; Garrido, J. J.; Echeverria, J. C. *J. Phys. Chem. A* **2019**, *123*, p. 10364–10371.
- [40] European Commission Establishing a watch list of substances for Union-wide monitoring in the field of water policy according to Directive 2008/105/EC of the European Parliament and of the Council Available online: <https://eur-lex.europa.eu/legal-content/EN/TXT/?uri=CELEX%3A32022D1307>.
- [41] Shi, Y.; Chen, L.; Li, J.; Hu, Q.; Ji, G.; Lu, Y.; Hu, X.; Zhu, B.; Huang, W. *Chem. Phys. Lett.* **2021**, *762*, p. 138116.
- [42] Armaroli, T.; Milella, F.; Notari, B.; Willey, R.J.; Busca, G. *Top. Catal.* **2001**, *15*, p. 63–71.
- [43] Li, Y.; Fan, Q.; Li, Y.; Feng, X.; Chai, Y.; Liu, C. *Appl. Surf. Sci.* **2019**, p. 483, 652–660.
- [44] Díaz, I.; Kokkoli, E.; Terasaki, O.; Tsapatsis, M. *Chem. Mater.* **2004**, *16*, p. 5226–5232.
- [45] Cruz-Quesada, G.; Espinal-Viguri, M.; López-Ramón, M. V.; Garrido, J. J. *Polymers* **2021**, *13*, p. 2082.
- [46] Launer, P. J.; Arkles, B. Infrared Analysis of Organosilicon Compounds. In *Silicon Compounds: Silanes and Silicones*; Arkles, B., Larson, G.L., Eds.; 3rd Ed.; Gelest, INC: Morrisville, PA; USA, **2013**; pp. 175–178.
- [47] Su, J.; Xiong, G.; Zhou, J.; Liu, W.; Zhou, D.; Wang, G.; Wang, X.; Guo, H. *J. Catal.* **2012**, *288*, p. 1–7.
- [48] Tauc, J. *Mat. Res. Bull.* **1968**, *3*, p. 37–46.
- [49] Lamberti, C.; Bordiga, S.; Arduino, D.; Zecchina, A.; Geobaldo, F.; Spanó, G.; Genoni, F.; Petrini, G.; Carati, A.; Villain, F.; Vlaic, G. *J. Phys. Chem. B* **1998**, *102*, p. 6382–6390.
- [50] Thommes, M.; Kaneko, K.; Neimark, A. V.; Olivier, J. P.; Rodriguez-Reinoso, F.; Rouquerol, J.; Sing, K. S. W. *Pure Appl. Chem.* **2015**, *87*, p. 1051–1069.
- [51] Leofanti, G.; Padovan, M.; Tozzola, G.; Venturelli, B. *Catal. Today* **1998**, *41*, p. 207–219.
- [52] Yurdakal, S.; Garlisi, C.; Ozcan, L.; Bellardita, M.; Palmisano, G. (Photo)catalyst Characterization Techniques: Adsorption Isotherms and BET, SEM, FTIR, UV–Vis, Photoluminescence, and Electrochemical Characterizations. In *Heterogeneous Photocatalysis Relationships with Heterogeneous Catalysis and Perspectives*; Marci, G., Palmisano, L., Eds.; Elsevier B.V., **2019**; pp. 87–152.

- [53] Pera-Titus, M.; Llorens, J. *Appl. Surf. Sci.* **2010**, *256*, p. 5305–5310.
- [54] Baerlocher, Ch.; McCusker, L.B. Database of Zeolite Structures. Available online: <http://www.iza-structure.org/databases/> (accessed on Aug 5, **2022**).
- [55] Zuo, Y.; Chen, Y.; Li, T.; Yu, J.; Yang, H.; Liu, M.; Guo, X. *Microporous Mesoporous Mater.* **2022**, *336*, p. 111884.
- [56] Li, J.; Zhang, F.; Zong, L.; Wang, X.; Wei, H. *Catalysts* **2021**, *11*, p. 113.

CHAPTER 8

CONCLUSIONS/CONCLUSIONES

CHAPTER 8

CONCLUSIONS

This section puts into perspective the conclusions reached from *Chapters 3 to 7*.

1. From the study of the influence of the chlorine atom and the alkyl chain length of the organic precursors in the properties of the hybrid xerogels (*Chapters 3 and 5*), the following conclusions have been drawn:
 - Distribution of Si species: For CIMTEOS and CIETEOS series, the condensed species of the organic precursors (T^3) is predominant in the xerogels matrix and increases with the molar percentage. On the other hand, for CIPTEOS and CIPhTEOS series, the semi-condensed species (T^2) predominates over T^3 species due to the higher steric and electronic effect exerted by the organic moieties during the crosslinking of the colloids, thus, yielding less condensed materials compared to CIMTEOS and CIETEOS.
 - Crystallinity: the diffraction maximum at a small angle ($2\theta < 10^\circ$) in the XRD diffraction patterns of silica xerogels indicates the presence of ordered domains within the silica matrix of the materials. The chlorinated series require a significantly lower molar percentage of precursor, compared to their non-chlorinated analogues (MTEOS, ETEOS and PTEOS), for this maximum to emerge (1% in the CIETEOS series). Due to the higher abundance of T^3 species, for CIMTEOS and CIETEOS ordered domains are constituted of cage-like structures, whereas, for CIPTEOS and CIPhTEOS xerogels, open cages and short ladders are the ordered building blocks because those contain higher proportions of T^2 than cage-like structures.
 - Skeletal density: the skeletal density of the four series decreases with the molar percentage of precursor and is always lower than that of the TEOS reference. By comparing the four series it is found that for a given molar percentage, the density values follow the order CIMTEOS > CIETEOS > CIPTEOS \geq CIPhTEOS, which can be explained in terms of the steric effect exerted by the organic moiety.

- Textural properties: for the four series, N₂ and CO₂ isotherms indicate that an increase in the organic precursor in the materials results in a loss of mesoporosity and specific surface area, and a narrower pore size distribution.
 - Morphology: FE-SEM micrographs of the chloroalkyl xerogels show changes in their surface morphology from granular (TEOS reference) to a smoother and more compact texture as the molar percentage of organic precursor increases. This effect is associated with the lower degree of triethoxysilane cross-linking in comparison to TEOS and with the nanostructuration generated by the surface chloroalkyl groups to minimize the repulsion between colloids.
2. *Chapter 4* shows that an increase in the molar percentage of the precursor (CIRTEOS) is translated into an increase in gelation times due to the conjugation of the steric effect of the organic substituent and the inductive effect of the chlorine atom. The gelation times of the chloroalkyl series are longer than those of their analogous alkyl series for CIETEOS and CIPTEOS, and slightly shorter for the shorter for CIMTEOS. This is explained by the maximization of the inductive effect of the chlorine atom due to its proximity to the silicon atom, which exerts a positive influence on the condensation and crosslinking reactions, the slowest step in the sol-gel process. On the other hand, a larger number of carbons in the alkyl chain reduces the inductive effect of the chlorine on the silicon atom and increases the steric effect exerted by the chain to form the silica network; this effect is maximized in the series bearing ethyl, chloroethyl, propyl and chloropropyl groups. Unexpectedly, the CIETEOS series has the highest gelation times, explained by the lack of flexibility of the chloroethyl group due to the steric tension caused by its size, the electrostatic repulsions exerted by chlorine, forcing the formation of kinetically disfavoured structures in order to minimize its energy, and the presence of POSS in all the X-ray diffraction patterns of this series (1–25%). FTIR deconvolution methods for CIMTEOS series show how the presence of the chlorine atom favours the formation of six-fold rings, whereas an opposite trend is observed in CIETEOS, CIPhTEOS and CIPTEOS series, favouring the formation of 4-fold rings, which are the constituents of the POSS. These findings reveal a competitive process between the two species indicating that materials

- with higher amounts of POSS require a higher amount of time to reach the gelation point.
3. The Pybox-EG (PB) containing xerogels synthesised in *Chapter 6* are selected for coatings of a water vapour optical fibre sensor (OFSLn-PB). This selection is based on the absence of free-ligand bands in their photoluminescence spectra and the textural characterization, discarding those ultramicroporous and with lower adsorption capacities.
 4. A sensor coated with the reference gel (only TEOS) synthesised at pH 4.5 (OFSTEOS-4.5), and two sensors coated with the Ln-PB gels (OFSTb-PB and OFSEu-PB) are prepared. Ln-AL thin films are deposited onto the tips of silica fibres through dip-coating at controlled rates. A preliminary photoluminescence emission test of the constructed OFS is performed, which confirms that OFSTb-PB provides a higher emission intensity and better signal-noise ratio than OFSEu-PB, thus, the former was selected as the sensor of study.
 5. The OFSTb-PB response shows linearity luminescent intensity decay until certain values of water-vapour molar concentration (C_{H2O}), beyond which, the response shifts to polynomial. Comparing the sensor calibration curves with the water-vapour adsorption isotherms of the bulk material and calculating the isosteric enthalpies of adsorption (ΔH_{ads}), the linear-to-polynomial shift break in the response is found to be due to capillary condensation of water molecules in the mesopores. When the membrane is exposed to low levels of C_{H2O} , the molecules interact with the hydrophilic silanol groups on the surface of the micropores and enter the Tb^{III} coordination sphere quenching the luminescence linearly, making the adsorption process less exothermic. Once C_{H2O} is high enough to fill the mesoporosity, water molecules condense, causing an abrupt decay in the luminescence by their direct contact with the luminophores, breaking the linearity of the sensor response, and making the ΔH_{ads} constant and parallel to the isosteric enthalpy of condensation of water in a flat surface.
 6. The use of the organic precursors in the synthesis of the modified titanium silicalites of *Chapter 7* has the following effects:

- Crystallinity: TSR5 and TSR10 materials are crystalline, TSPH20 and TSPH30 are semi-crystalline, and TSM20, TSP20, TSM30 and TSP30 are amorphous, implying that phenyltriethoxysilane (PhTEOS) is the precursor that less hinders the formation of titanium silicalite structures during the hydrothermal process.
 - Ti species, UV-Vis absorption and photoluminescence emission: UV-Vis diffuse reflectance spectra of the modified titanium silicalites indicate the absence of anatase and the presence of both, tetra and hexacoordinated species of titanium (213 and 265 nm, respectively). Furthermore, the signals of both species increase as the amount of RTEOS does.
 - Textural properties: the addition of 5% of RTEOS in the titanium silicalites synthesis, produce a change in the morphology of the narrow mesopores, from cylindrical to ink-bottle shaped, and thus, it creates a retention effect of the adsorbate inside the pores and then its capillary condensation. These observations can be directly linked to the possibility of an improvement in the diffusion performance and accessibility of the adsorbates to the active sites during photocatalysis. However, for the other molar percentages, N₂ isotherms indicate that a portion of the narrow mesoporosity in TSR10 and TSPH20 materials is lost, and TSM20, TSP20 and TSR30 are macroporous or non-porous materials.
 - Morphology: The micrographs of the TSR materials show how the use of RTEOS has a big impact on their morphology, as they exhibit bigger, rougher and more spherical-shaped particles than those of the reference, suggesting that the organic moiety of RTEOS hinders the surface interaction of the colloids with the directing agents (TPA⁺ and PVP) used in the synthesis, which might be the reason why the more the molar percentage of RTEOS is added, the bigger the particles of the materials (reference < TSPH5 < TSPH10). TSPH5 is the material with the smallest particle size (320–420 nm) among the TSR5 titanium silicalites.
7. The photodegradation of venlafaxine in aqueous media under simulated solar irradiation is performed using the reference, TSR5 and TSPH10 materials. The references do not show photoactivity, but the modified titanosilicalites achieve a good to very good (78%-93%) venlafaxine degradation in two-hour irradiation,

being TSP5 and TSP_h5 the most photoactive materials. Those materials have the highest abundance of photoactive superficial hexacoordinated Ti species, the narrowest and most homogeneous pore size distributions, and the smallest particle sizes. These results confirm the capability of the RTEOS precursors to effectively modulate the photocatalytic properties of titanium silicalites.

CONCLUSIONES

Esta sección sirve para poner en perspectiva las conclusiones alcanzadas en los *Capítulos 3* al *7*.

1. Se ha estudiado la influencia del átomo de cloro y de la longitud de la cadena alquílica y el arilo de los precursores en las propiedades de los xerogeles híbridos sintetizados en *los Capítulos 3* y *5*. Se llegaron a las siguientes conclusiones:
 - Distribución de especies de silicio: en las series CIMTEOS y CIETEOS, la especie de Si proveniente de los precursores orgánicos (trietoxisilanos) que más abunda, y que además se incrementa con el porcentaje molar de precursor, es la más condensada (T^3). Por el contrario, en las series CIPTEOS y CIPhTEOS, las especies semi-condensadas (T^2) son las más abundantes debido al mayor efecto estérico y electrónico que ejercen sus fragmentos orgánicos durante el entrecruzamiento de los coloides. Esto implica que los materiales de estas últimas series están menos condensados que los de las series CIMTEOS y CIPTEOS.
 - Cristalinidad: el máximo de difracción a ángulo pequeño ($2\theta < 10^\circ$) en los patrones de difracción de rayos X de los xerogeles de silicio, indica la presencia de dominios ordenados dentro de la matriz de sílice de los materiales. Las series de materiales clorados requirieron un porcentaje molar de precursor significativamente menor para que este máximo fuese observable (1% en la serie de CIPTEOS), en comparación con sus series análogas de materiales no-clorados (MTEOS, ETEOS y PTEOS). En las series CIMTEOS y CIPTEOS, debido a la gran abundancia de especies T^3 , los dominios ordenados están principalmente constituidos de estructuras tipo jaulas. En cambio, para los xerogeles de CIPTEOS Y CIPhTEOS, los dominios ordenados están constituidos por jaulas abiertas o escaleras cortas, debido a que dichas estructuras presentan una mayor proporción de especies T^2 que las estructuras tipo jaulas cerradas.
 - Densidad esquelética: la densidad esquelética o real de las cuatro series de materiales clorados, además de ser siempre menor que la de la referencia (100% TEOS) disminuye con el incremento del porcentaje molar de

precursor orgánico. Al comparar las cuatro series, se comprueba que, para un determinado porcentaje molar de precursor, los valores de densidad de los materiales siguen el orden CIMTEOS > CIETEOS > CIPTEOS \geq CIPhTEOS. Dicho orden puede explicarse al considerar el creciente efecto estérico ejercido por los precursores orgánicos en dichas series.

- Propiedades texturales: las isotermas de N₂ y CO₂ de las cuatro series indican que un incremento en el porcentaje molar de precursor orgánico se traduce en una pérdida de la mesoporosidad y del área superficial específica y en un estrechamiento de la distribución de tamaño de poros.
- Morfología: las micrografías FE-SEM de los xerogeles cloroalquílicos muestran cambios en la morfología superficial de los materiales: de una textura granular (referencia TEOS), a texturas cada vez más suaves y compactas conforme se incrementa el porcentaje molar de precursor orgánico. Este fenómeno se asocia al menor grado de entrecruzamiento de los trietoxisilanos en comparación con el tetraetoxisilano, y con la nanoestructuración que generan los grupos cloroalquilo superficiales para minimizar la repulsión entre coloides.

2. En el *Capítulo 4*, se comprueba que el incremento del porcentaje molar de precursor orgánico retarda los tiempos de gelificación debido a la conjugación del efecto estérico e inductivo de los sustituyentes orgánicos. También es importante señalar que los tiempos de gelificación de las series de mayor tamaño de cadena alquílica (CIETEOS y CIPTEOS) son más largos que aquellos registrados por sus series alquílicas análogas (ETEOS y PTEOS), mientras que para CIMTEOS, la serie de menor tamaño de cadena, son un poco más cortos que los de su homólogo sin cloro (MTEOS). Esto se explica por el efecto inductivo que ejerce el átomo de cloro sobre el silicio, maximizado por la proximidad al mismo, y favoreciendo cinéticamente las etapas de condensación y entrecruzamiento, las más lentas del proceso sol-gel. Por otro lado, un mayor número de átomos de carbono en la cadena alquílica reduce el efecto inductivo del cloro en el átomo de silicio, además de incrementar el efecto estérico que ejerce la cadena en la formación de la red de sílice. Este efecto se maximiza en las series que contienen los grupos etil, cloroetil, propil, y cloropropil. Inesperadamente, la serie CIETEOS tiene los tiempos de gelificación más altos, lo que se explica por la falta de flexibilidad de los grupos

cloroetil, debido a la tensión estérica causada por su tamaño, la repulsión electrostática ejercida por el cloro, lo que fuerza la formación de estructuras cinéticamente no favorecidas para minimizar su energía, y la presencia de POSS en los patrones de difracción de rayos X en esta serie (1–25%). Al aplicar los métodos deconvolutivos de FTIR a los espectros de la serie del CIMTEOS se observa que la presencia del átomo de cloro favorece la formación de anillos de 6 átomos de silicio, mientras que la tendencia contraria se observa en las series de CIETEOS, CIPhTEOS, y CIPTEOS, donde se favorece la formación de anillos de 4 átomos de silicio, constituyentes de los POSS. Estos resultados demuestran que existe un proceso competitivo entre ambas especies de anillos e indicaría que los materiales con una mayor proporción de POSS requieren un mayor tiempo para alcanzar el punto de gelificación.

3. Los xerogeles luminiscentes sintetizados con el ligando antena Pybox-EG (PB) en el *Capítulo 6*, se seleccionan para preparar la membrana de un sensor de humedad de fibra óptica (OFSLn-PB). Esta selección se basa en que no hubiera bandas de emisión del ligando libre en los espectros de fluorescencia y en la caracterización textural (descartándose aquellos materiales ultramicroporosos o con poca capacidad de adsorción).
4. Se ha preparado un sensor de fibra óptica recubierto con el gel de referencia (100% TEOS, OFSTEOS-4.5), y dos sensores recubiertos con los geles de Ln-PB (OFSTb-PB y OFSEu-PB). Estas películas finas se han depositado en la punta de las fibras de sílice mediante la técnica de dip-coating a velocidades controladas. Un test preliminar para observar la emisión luminiscente de las fibras ha determinado que OFSTb-PB produce una emisión de mayor intensidad y con mejor relación señal-ruido que OFSEu-PB, por lo que se selecciona como el sensor objeto de estudio.
5. La respuesta del sensor OFSTb-PB muestra un descenso de intensidad de emisión con el incremento de la concentración de vapor de agua (C_{H_2O}) hasta una concentración determinada, a partir de la cual la respuesta pasa a una tendencia polinómica. Al comparar las entalpías de adsorción (ΔH_{ads}) obtenidas a partir de las curvas de calibrado del sensor (OFSTb-PB) con las obtenidas a partir de las isothermas de adsorción-desorción de vapor de agua del monolito (Tb-PB), se

concluye que el cambio de tendencia en la respuesta del sensor se debe a la condensación capilar de las moléculas de agua en los mesoporos. Cuando se expone la membrana a bajos valores de C_{H_2O} , las moléculas de agua interactúan con los grupos silanol hidrofílicos que se encuentran en la superficie de los microporos y producen una desactivación lineal de la luminiscencia (debido a la entrada de H_2O en la esfera de coordinación del ion Tb^{III}), haciendo que el proceso de adsorción sea menos exotérmico. En cambio, cuando C_{H_2O} presenta valores suficientemente altos como para llenar mesoporosidad, las moléculas de agua comienzan a condensar y el valor de ΔH_{ads} permanece constante y paralelo a la entalpía de condensación del agua en una superficie plana.

6. El uso de los precursores orgánicos en la síntesis de las titanosilicalitas modificadas (*Capítulo 7*) tiene los siguientes efectos:

- Cristalinidad: los materiales TSR5 y TSR10 son cristalinos, los materiales TSPH20 y TSPH30 son semi-cristalinos, y los materiales TSM20, TSP20, TSM30 y TSP30 son amorfos, lo que implica que el feniltrietoxisilano (PhTEOS) es el precursor que menos perjudica la formación de una estructura cristalina tipo titanosilicalita durante el proceso hidrotermal.
- Especies de titanio, absorción UV-Vis y emisión fotoluminiscente: los espectros de reflectancia difusa de UV-Vis de las titanosilicalitas mejoradas indican la ausencia de anatasa y la presencia de especies de titanio tanto tetra como hexacoordinadas. Además, las señales de ambas especies se vieron incrementadas con el aumento de RTEOS.
- Propiedades texturales: al utilizar un 5% de porcentaje molar de RTEOS en la síntesis de las titanosilicalitas se produce un cambio en la morfología de los mesoporos estrechos, pasando estos de tener forma cilíndrica a forma de tintero. Esto provoca que se produzca un efecto de retención del adsorbato en los poros y su consecuente condensación capilar. Estas observaciones pueden indicar la posibilidad de que se produzca una mejora en la difusión y accesibilidad del adsorbato a los centros activos durante la fotocatalisis. Sin embargo, al emplear porcentajes molares mayores de RTEOS, las isothermas de N_2 indican que se pierden parte de los mesoporos estrechos de los materiales TSR10 y TSPH20, y que los

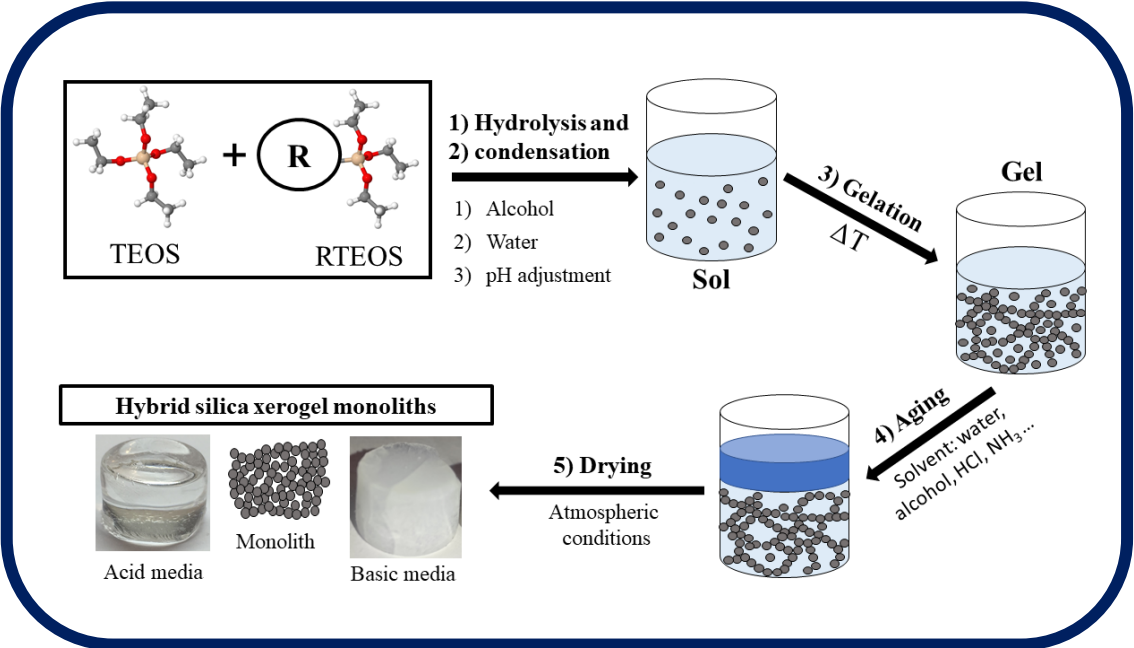
materiales TSM20, TSP20 y TSR30 son directamente macroporosos o no porosos.

- **Morfología:** las micrografías de los materiales TSR mostraron que el uso de RTEOS tiene un gran impacto en la morfología dado que se observan partículas más grandes, rugosas y esféricas que las de la referencia. Esto sugiere que la parte orgánica de los precursores impide la correcta interacción de los agentes directores usados en la síntesis (TPA⁺ y PVP) con la superficie de los coloides, explicando de este modo que a mayor porcentaje de RTEOS, mayor es el tamaño de las partículas del material obtenido (referencia < TSP_h5 < TSP_h10). Por último, al comparar los tamaños entre los materiales TSR5, se comprobó que TSP_h5 presenta el menor tamaño de partículas (320–420 nm).

7. Se han realizado reacciones de fotodegradación del antidepresivo venlafaxina en medio acuoso y bajo radiación solar simulada utilizando el material de referencia y los materiales TSR5 y TSR10 como fotocatalizadores. Aunque la referencia no resultó ser fotoactiva, las titanosilicalitas modificadas consiguieron buenos resultados al eliminar entre un 78 y 93% de venlafaxina en 2 horas de reacción. Los materiales más fotoactivos fueron TSP5 y TSP_h5, que precisamente son los materiales que presentan una mayor abundancia de especies hexacoordinadas de titanio superficiales, distribuciones de tamaño de poro más estrechas y homogéneas, y tamaños de partícula más pequeños. Estos resultados ponen en evidencia la capacidad de los precursores RTEOS para modular eficazmente las propiedades fotocatalíticas de las titanosilicalitas.

ANNEXE A

SOL-GEL PROCESS, SYNTHESIS OF HYBRID SILICA XEROGELS



ANNEXE A

SOL-GEL PROCESS, SYNTHESIS OF HYBRID SILICA XEROGELS

A.1 INTRODUCTION TO SOL-GEL PROCESS

The history of sol-gel technology began in 1846 when Ebelmen observed how a mixture of SiCl_4 and alcohol gelled on exposure to the atmosphere [1]. After that, no application of this technology was explored for nearly 90 years, until 1939 when Geffcken and Berger studied and patented the use of alkoxides in the preparation of oxide films [2]. In the late 60s and early 70s, the ceramic industry showed interest in gel processing due to the facility to obtain multicomponent glass with different morphologies by controlling the hydrolysis and condensation conditions of the alkoxides [3,4]. In 2003, Mackenze published a review compiling all the achievements of the sol-gel method since 1983 [5], in which the sol-gel research was divided into two main periods. During the first period, the field of study was the reactions of the metal alkoxides, while the field of study of the second period was the preparation of inorganic-organic hybrids. Schmidt is considered the pioneer of the second period, due to the development of non-crystalline materials with their organic and inorganic components bonded together [6,7]. Therefore, as part of the second period, hybrid silica gels are considered one of the more interesting synthesis routes in the sol-gel method [8] (Figure A.1).

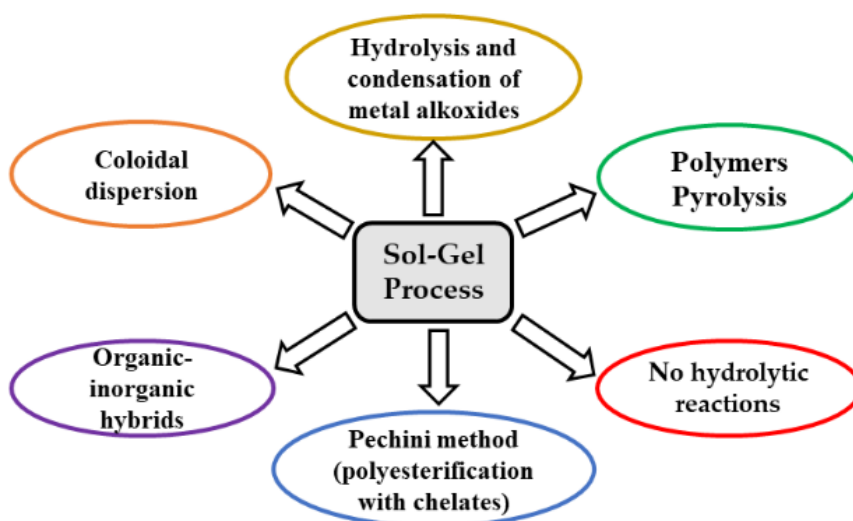


Figure A.1. Sol-gel method routes. Adapted from Dimitriev et al. (2008) [8].

The sol-gel process comprises five marked steps: (i) hydrolysis of the precursors; (ii) condensation of the hydrolysed precursors, which generates a colloidal suspension of small particles (sol); (iii) gelation of the sol, when the colloids stabilise and start interlinking and forming a polymeric network (gel) that occupies more volume than the liquid media; iv) ageing, the interlinking is further promoted to strengthen the network; v) drying, the remaining liquid phase is removed. Drying is the step that differentiates aerogels from xerogels; in the former, the liquid is removed under supercritical conditions, while in the latter it is slowly evaporated under atmospheric conditions. Figure A.2, shows a synthesis scheme of hybrid xerogels using TEOS and triethoxysilanes.

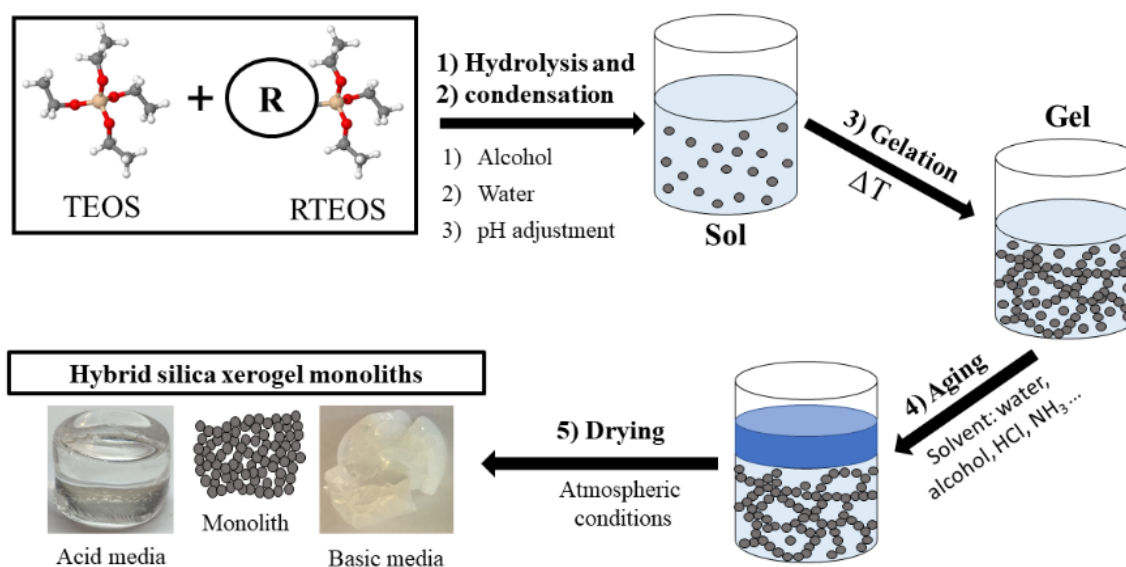


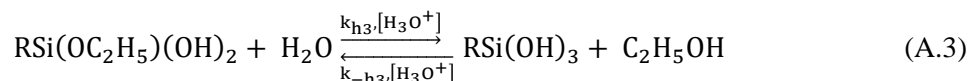
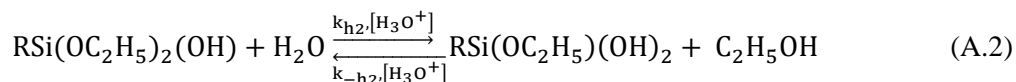
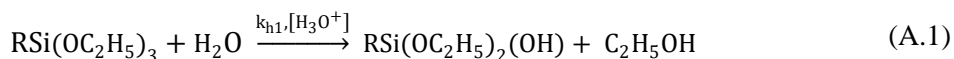
Figure A.2. Synthesis of hybrid silica xerogels.

All the steps are highly dependent on the synthesis parameters and conditions, such as the selected alcohol, the water:alcohol proportion, the selected catalyst, the nature of the precursors, the pH, the gelation temperature, and the ageing time among others. Therefore, each step of the sol-gel process will be addressed considering conditions used during the synthesis of this thesis's hybrid xerogels. The more determining factor on the textural properties of the resulting solids is the pH of the media, for instance, acid media synthesised xerogels are microporous and optically transparent, while those synthesised in basic media are mesoporous and opaque. Given that the main application for the materials would be their use as optical fibre coatings, they have all been synthesised in moderate acid media ($\text{pH} = 4.5$) to ensure their optical transparency. Although the synthesis pH could be nearly above the isoelectric point of silica ($\text{pH} = 2\text{--}4.5$) [9], pH

where positive and negative charges on the material surface are equivalent, the hydrolysis and condensation mechanisms are those of acid media.

A.2 HYDROLYSIS IN ACID MEDIA

The hydrolysis step of the sol-gel process takes place when the alkoxides of the precursors are substituted by an alcohol group assisted by media H^+ . Equations A.1–3, show the successive hydrolysis reactions of organotriethoxysilanes [RTEOS, $RSi(C_2H_5)_3$] or tetraethoxysilane ($R = OC_2H_5$) in acid media.



These hydrolysis reactions follow a second-order nucleophilic substitution (SN_2) mechanism. First, an alkoxide group is rapidly protonated causing a decrease in the electronic density of the silicon atom and favouring the electrophilic attack of an entering water molecule at the opposite site of the leaving protonated alkoxide group. Figure A.3 depicts the first hydrolysis mechanism of organotriethoxysilanes.

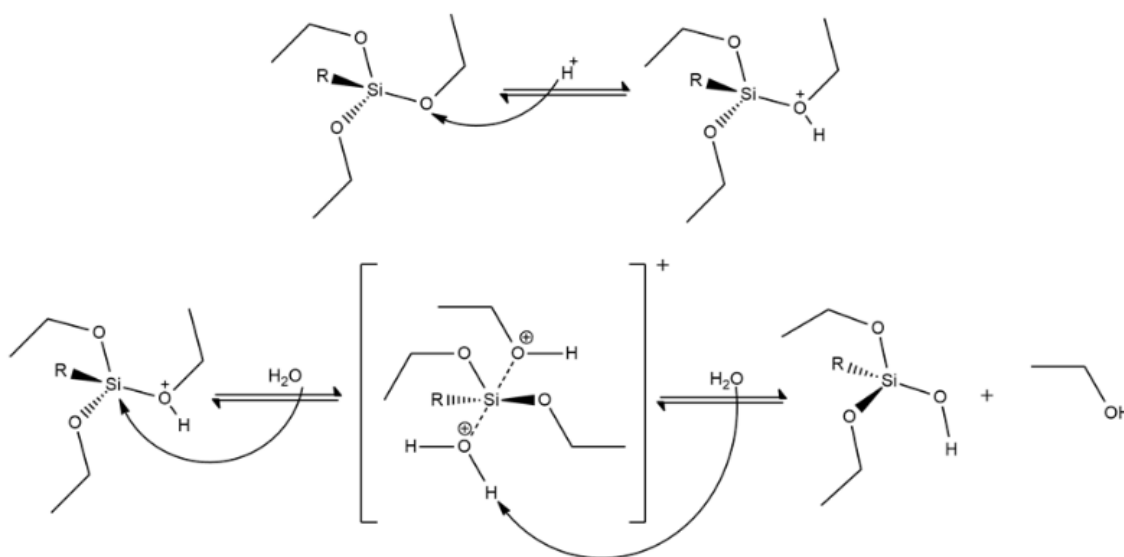


Figure A.3. SN_2 hydrolysis mechanism for RTEOS.

As represented in Figure A.3, SN₂ mechanism contemplates the formation of a positively charged transition state, the stability of which controls the reaction rate. Electron-donating substituents aid the stabilization of the intermediate increasing the rate, therefore, the replacement of alkoxide groups (OR) by the more electron-withdrawing alcohol groups (OH) should act decreasing the rate of the successive hydrolysis steps. However, it has been reported that each consecutive reaction has higher rates than the former ($k_{h1} < k_{h2} < k_{h3}$) for TEOS, due to the lower steric hindrance exerted by the hydroxyl groups compared to the bulkier ethoxides [10]; this remarks that in acid media hydrolysis, the steric factor is more relevant than the inductive factors. In organosilanes, the hydrolysis rate is also highly dependent on the organic moiety, which usually acts as a donor of electronic charge. Equation A.4 shows the silicon electronic density dependence on organosilane substituents.



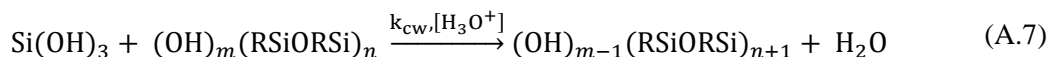
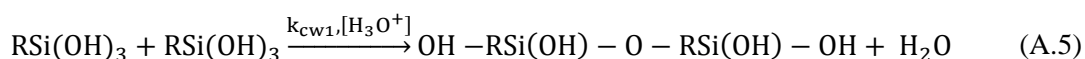
In organotriethoxysilanes the presence of non-hydrolysable organic moiety contributes to a more efficient stabilisation of the transition state in comparison to TEOS, therefore, higher speed rates are to be expected. However, the inductive effect is not the only aspect to be considered, since it has been reported that the size of the organic substituent is inversely proportional to the speed rate [11,12].

Another relevant aspect to consider in the hydrolysis step is the stoichiometric relation of water:ethoxide (r), and to completely hydrolyse a TEOS molecule it is required an $r = 4$. Higher values should increase the hydrolysis rate, however, if r is too high the alkoxides concentration in the medium will decrease and the diffusion would act as a drawback decreasing the hydrolysis rates. The selected water:ethoxide ratio for our synthesis is $r = 5.5$, a high enough water:ethoxide ratio to accelerate the hydrolysis rate and avoid the diffusion issue. But this raises a new issue, alkoxysilanes are insoluble in water, therefore the use of alcohols as solvents and homogenising agents is required [13]. Nevertheless, the use of alcohols presents a new inconvenience, because like water does, they can act like nucleophiles replacing hydroxyl groups with alkoxides, thus, reverting the hydrolysis. This process is called re-esterification if the replacing alkoxide group is equal to the one previously removed by the hydrolysis, and it is called transesterification when the alkoxides are different [14]. These two reactions are not convenient because they compete with the hydrolysis and may yield precursors with different alkoxides

attached $[\text{R}_x\text{Si}(\text{OR}')_{1-x-y}(\text{OR}'')_y]$, which overall decreases the hydrolysis rate and delay the condensation. Transesterification can be easily avoided by using the same alcohol as the alkoxide released during the hydrolysis, thus, ethanol has been used as the solvent since xerogels have been prepared with ethoxysilanes. However, significantly reducing the re-esterification requires the use of a stoichiometric excess of water to favour the hydrolysis, therefore, in all the xerogels syntheses it has been used a molar relation of 1:4.75:5.5 of (TEOS+RTEOS):ethanol:water.

A.3 CONDENSATION IN ACID MEDIA

Following the hydrolysis, the silanols react with another silanol group or alkoxy group, forming siloxane bridges (Si–O–Si) and releasing water or alcohol molecules in a so-called condensation reaction. Equations A.5–7 show the first condensation reaction of totally hydrolysed triethoxysilanes ($\text{RSi}(\text{OH})_3$), between a totally and a partially hydrolysed triethoxysilane, and a general formula for successive condensations, respectively.



Condensation between alkoxy silanes, like hydrolysis, follows an $\text{S}_{\text{N}}2$ mechanism. In acid media, the electronic density of a silicon atom in a monomer decreases when a bounded alcohol is protonated and favours the nucleophilic attack of an alcohol molecule or another monomer's alkoxide. The condensation rates of organotriethoxysilanes are higher than TEOS, because in the condensation a positively charged transition state is also formed like in the hydrolysis. Additionally, bulkier organic moieties would hinder the nucleophilic attack of alcohols or ethoxides, and thus, the formation of the transition penta-coordinated state. Figure A.4 shows an example of the $\text{S}_{\text{N}}2$ condensation mechanism in acid media.

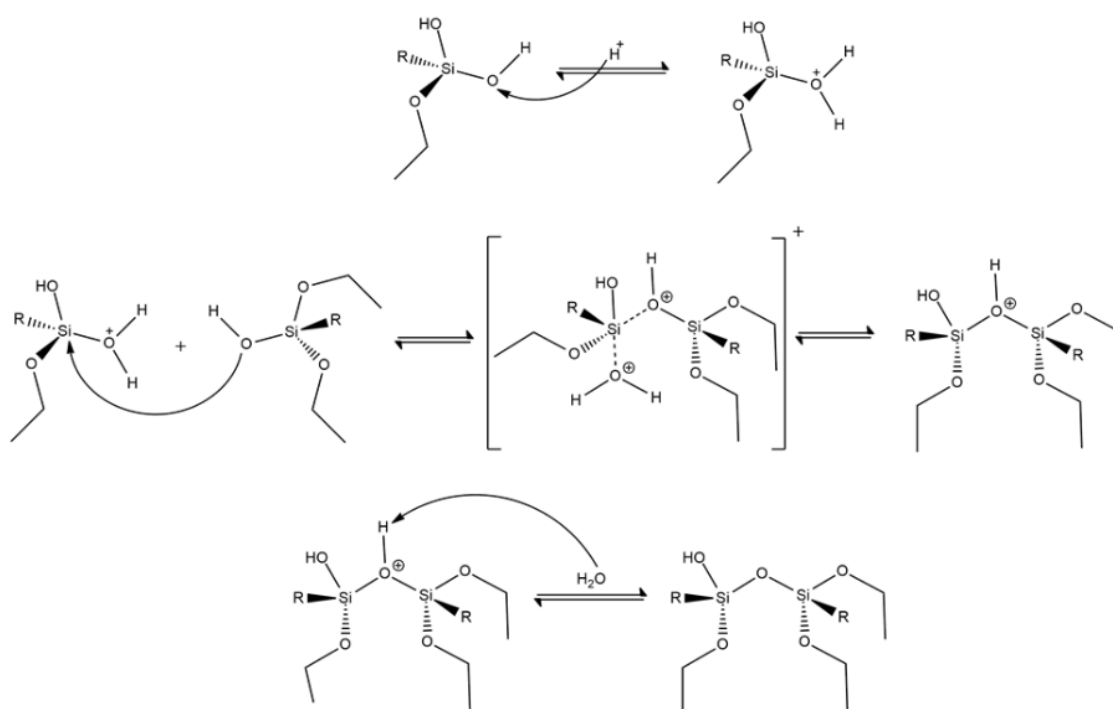


Figure A.4. S_N2 condensation mechanism for RTEOS.

The successive hydrolysis and condensation reactions replace the ethoxide groups with the more electron-withdrawing OH and OSi, respectively, which translates into a less effective stabilization of the positively charged intermediate, and a lower reaction rate in each consecutive condensation reaction ($k_{c1} > k_{c2} > k_{c3}$). This indicates that in acid media the hydrolysis is much faster than condensation ($k_{h1} \gg k_{c1}$) as was confirmed by UV-Raman and ^{29}Si NMR spectroscopy studies [15], and thus, the condensation limits the global sol-gel process rate. The electrophilic character of Si atoms increases with the growth of the Si–O–Si bonds, and at the same time, the more nucleophilic silanols are those present in monomers or slightly branched oligomers, therefore, in acid media the chain-like structures are favoured over branched structures. In the case of our hybrid xerogels synthesis, the use of high water:ethoxide ratio ($r = 5.5$) also contributes to the fast hydrolysis and condensation of monomers, favouring the formation of short-chain oligomers [14].

In a gas chromatography analysis of the species formed during the polymerization of tetramethoxysilane (TMOS) in acid media, M. Yamane *et al.* (1984) determined the presence of three types of species: linear chains, branched chains and cyclic/rings species. Additionally, they also observed that 92% of the species contained one to six silicon tetrahedra, which denotes a narrower distribution of species compared to that observed for basic media [16]. For TEOS, it has been reported that at the early steps of the

hydrolysis and condensation steps, chain-like species predominates, as they are more stable than ring-like species. But, as the condensation further continues, and the monomers and dimers concentration decrease, ring-like species become dominant because they are kinetically favoured over the formation of linear chains [15,17]. Ring species can be formed by intra-condensation of a linear oligomer forming a closed-loop (cyclization) or by intermolecular condensation (cyclodimerization) of dimers or trimers, the latter proposed as the more factual pathway, as the proportion of 4-fold-rings increases at the same time as the linear tetramers proportion [15,18]. Due to their instability, 3-fold rings rapidly disappear as the reaction continues, while the amount of 4 to 6-fold rings increases with time, making the 4-fold rings the most common species [19]. The hydrolysis of siloxane bonds is not favoured in acid media, and besides, the depolymerization rate is hindered by the presence of alcohol molecules [14,20]. Therefore, the ring-like species act as the nucleation centre for the formation of linear or weakly branched species of higher molecular weight that, in turn, form the first 1–2 nm three-dimensional particles or colloids. Figure A.5 depicts the oligomerization routes of TEOS in acid media as proposed in a study published by Depla *et al.* (2011) [18]. In this study, it was demonstrated that increasing water:ethoxide ratio resulted in higher reaction rates, but the reaction paths remained unchanged, and consequently, it is safe to consider that these proposed oligomerization paths apply to our $r = 5.5$ synthesis conditions.

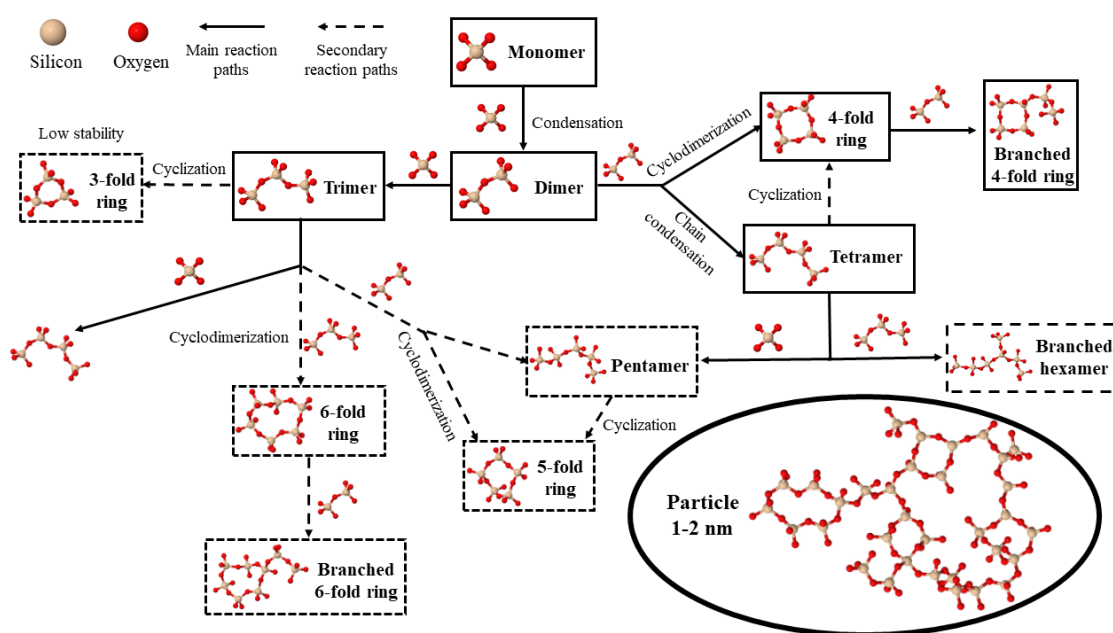


Figure A.5. Scheme of the polymerization routes of TEOS in acid media (H atoms have been removed for the sake of visual clarity). Based on the works of Depla *et al.* (2011) [15, 18].

A.4 SOL-GEL TRANSITION (GELATION)

Under neutral and basic conditions, the concentration of monomers in the medium is significantly higher than under acid conditions. In basic media, the rate of hydrolysis of siloxane bonds is over three orders of magnitude higher than in acid media, which implies a constant redistribution of bonds and formation of monomers, since the hydrolysis occurs preferentially at the less condensed species [14]. Furthermore, in acid media, especially with a high r , silica species are completely hydrolysed at the early stages of the sol-gel process, and thus, monomers are rapidly consumed. The availability of monomers is a crucial factor that determines the growth mechanism of the particles in solution because when there is a shortage of free monomers and dimers in the reaction, the particles grow by the Ostwald ripening mechanism, which consists of the growth of the less soluble large particles (or clusters) by inter-linking with smaller ones [14]. Therefore, in basic media, the particles grow preferentially by the monomer-cluster growth mechanism, which translates into the formation of globular clusters of hundreds of nanometres, whereas in acid media the particles grow by the cluster-cluster mechanism yielding chain-like particles that randomly branch. Once the particles reach submicrometric sizes, the suspension constitutes a viscous liquid designed as “sol”. Figure A.6 shows a scheme of particle growth and transition from sol to gel.

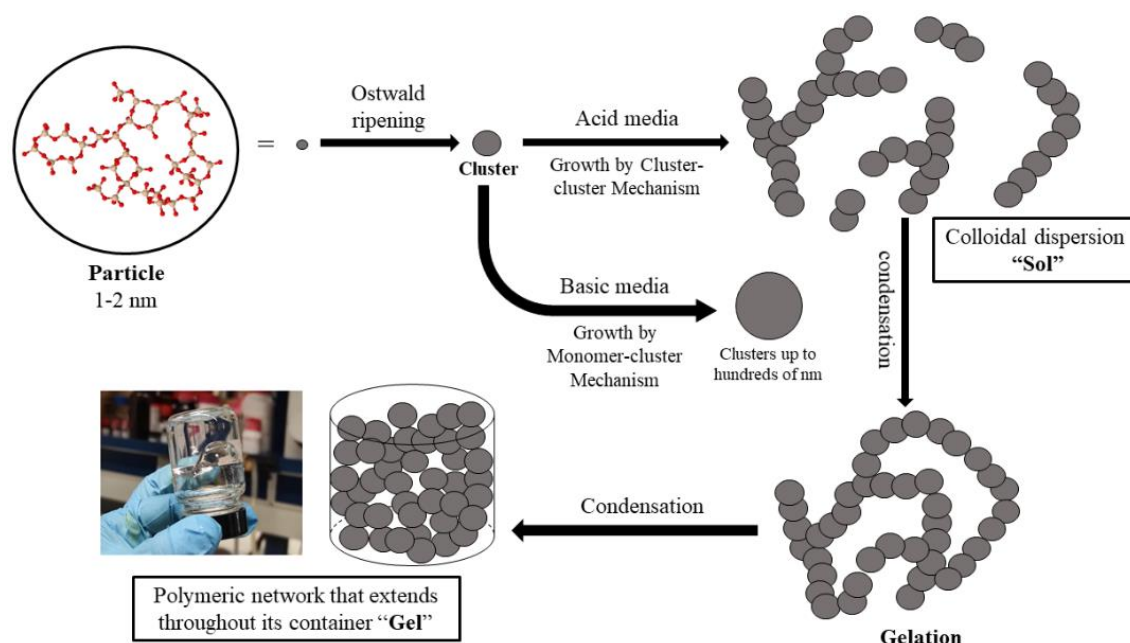


Figure A.6. Scheme of particle growth and sol-to-gel transition.

The scheme represents the formation of the colloids that constitute the sol, as well as the gelation process. This process consists of the inter-linking between colloids in the sol until they reach a critical size, and the “gel”, a polymer network that is interconnected from one side to the other of the container, is formed. If a sol is a system where the solid phase is dispersed in a liquid, a gel is the reverse, liquid entrapped in the pores of a solid continuous phase. Therefore, the system transition can be easily perceived roughly by the sudden alteration of its rheology, which translates into the shift from a viscous liquid to an elastic and stress-resistant solid whose shape is not altered even if the container is put upside down (see image in Figure A.6). The instant in which the rheological change occurs is called gelation time (t_g), nevertheless, the polymeric network is far from being complete, because the colloidal particles that are still present in the liquid phase are progressively connected to the network, increasing the stiffness of the gel.

An important factor in the gelation is the temperature, as it affects the Brownian motion of the colloids and the network speed formation and viscoelastic properties of the gel. In a study ranging from 18 to 50 °C, it was determined that lower temperatures decrease the colloid collision rates, extend the gelation, and favour the efficient contact of clusters to form a strengthened viscoelastic network. On the contrary, higher temperatures contribute to a faster formation of the network, although the resulting structure is weaker and presents liquid-like rheological properties [21]. According to Estella *et al.* (2010), the xerogels synthesised with a TEOS:ethanol:water ratio of 1:4.75:5.5 have their gelation time drastically decreased when 60 °C are used instead of 20 °C (from 882 to 48 h) [22]. Gels prepared with hybrid precursors usually take longer to reach the gelation time compared to those prepared using only tetraalkoxysilanes, due to the lower degree of freedom in the growth of the polymeric network and the steric hindrance exerted by the non-hydrolysable organic moieties (R). Therefore, in hybrid gels, the use of high temperatures is recommended to overcome the kinetic restrictions, hence, in this research 60 °C has been the temperature used in the preparation of the hybrid materials.

A.5 AGEING AND DRYING

Once the system has reached the gel point, the next step in the sol-gel process is ageing, the goal of which is to strengthen the network and prevent cracking during the drying step. The changes that occur during this step are mainly due to three interconnected phenomena: polymerization, phase transformation and coarsening. As commented above in the previous section, the polymeric network is not complete at the t_g , there are still numerous hydroxyl groups that can condense forming bridging bonds that stiffen the network, thus the polymerization process may take even months to complete. The cross-linking between clusters during the polymerization also produces the so-called syneresis that consists of the compaction and shrinkage of the system because of the expulsion of the liquid phase, since the polymers have a better affinity between them than with the solvent molecules. On the contrary, the dissolution-reprecipitation processes (coarsening) of colloids, produce a reduction of the interfacial area of the gel, which contributes to the generation of lower capillary pressures during drying and, therefore, to an enhanced resistance towards shrinkage. However, in acid media shrinkage predominates over coarsening, in opposition to basic media, since condensation rates are low, and the hydrolysis and re-distribution of siloxane bonds are not favoured.

To prevent pore collapse driven by capillary forces, a solvent is added during the ageing step. It has been reported that the use of ammonia increases the mesoporosity and reduces the shrinkage, however, it would dramatically change the media pH and turn the material opaque, thus, its use in this thesis was discarded. Ethanol has also been proven useful as a solvent, if mixed with an aqueous sol, ethanol would preferably evaporate and create an alcohol concentration gradient that promotes interdiffusion of liquids in the gel, reducing the shrinkage stress [23]. Finally, aging time should be considered, higher aging times would result in a higher cross-linked gel, but it would also decrease the pore volume and specific surface area of the resulting materials [24,25]. Figure A.7 depicts the ageing and drying steps of the sol-gel process.

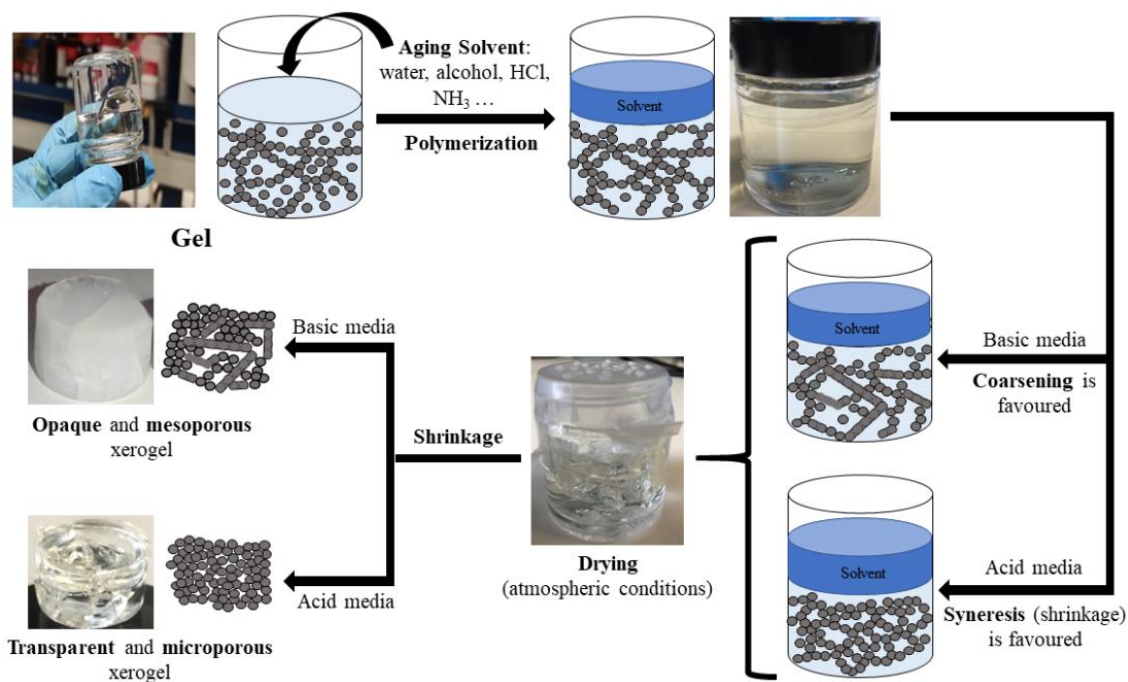


Figure A.7. Scheme of ageing and drying in the sol-gel process.

Finally, during the drying step the liquid phase, the ageing solvent and original sol, is gradually evaporated and removed from the gel. The evaporation produces capillary tension within the pores that is opposed by the compressive stress of the solid, which causes shrinkage and a liquid expulsion from the pores (syneresis process). In the case of our hybrid materials, the liquid is a mixture of two solvents (water and ethanol) with different saturation pressures. Due to its lower saturation pressure, ethanol evaporates preferentially causing a pressure gradient in the pores. Consequently, the gradient produces a non-uniform contraction of the silica skeleton and a drying stress that extends through all the material. Thus, if the evaporation rate is not slowed down, the resulting monolith could crack into several pieces, or the capillary tension could even collapse the pores yielding a non-porous material [26]. Acid-media synthesised xerogels are more prone to cracking than based-media synthesised since the former presents a lower crosslinking grade and therefore, a lower resistance towards shrinkage. In addition to the mild drying conditions (atmospheric pressure and temperature), the evaporation rate of the xerogels synthesised in this thesis has been reduced using pierced thermoplastic lids covering the containers. To ensure the same condition in all the samples, a pierced plastic disc was used as the pattern to make the holes in the thermoplastic lid. The gel shrinks as the drying process continues until the network becomes stiff enough to

withstand the capillary pressure in the pore. The moment at which shrinkage ends is called the critical point and the resulting monolith is known as the xerogel.

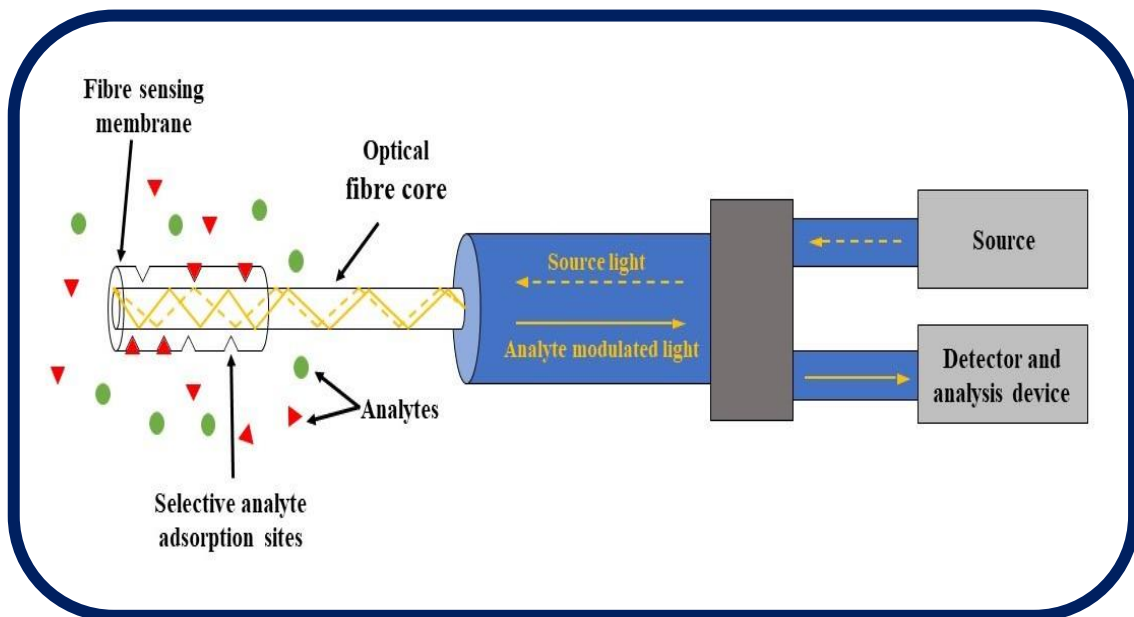
A.6 REFERENCES

- [1] Ebelmen, M. *Ann. Chim. Phys.* **1846**, 16, p. 166.
- [2] Geffken, W. and Berger, E. *German Patent 736 411*, **1939**.
- [3] Levene, L.; Thomas, I. M. *U.S. Patent 3640093*, **1972**.
- [4] Dislich, H. *Angew. Chem., Int. Ed.* **1971**, 10, p. 363–370.
- [5] Mackenzie, J. D. *J. Sol-Gel Sci. Technol.* **2003**, 26, p. 23–27.
- [6] Schmidt, H. *J. Non-Cryst. Solids* **1985**, 73, p. 681–691.
- [7] Schmidt, H. *J. Non-Cryst. Solids* **1989**, 112, p. 419–423.
- [8] Dimitriev, Y.; Ivanova, Y.; Iordanova, R. *J. Univ. Chem. Technol. Metall.* **2008**, 43, p. 181–192.
- [9] Xu, P.; Wang, H.; Tong, R.; Du, Q.; Zhong, W. *Colloid Polym. Sci.* **2006**, 284, p. 755–762.
- [10] Echeverría, J. C.; Moriones, P.; Arzamendi, G.; Garrido, J. J.; Gil, M. J.; Cornejo, A.; Martínez-Merino, V. *J. Sol-Gel Sci. Technol.* **2018**, 86, p. 316–328.
- [11] Brochier Salon, M. C.; Belgacem, M. N. *Colloids Surf., A* **2010**, 366, p. 147–154.
- [12] Moriones, P.; Arzamendi, G.; Cornejo, A.; Garrido, J. J.; Echeverria, J. C. *J. Phys. Chem. A* **2019**, 123, p. 10364–10371.
- [13] Innocenzi, P. *The Sol-Gel Transition*; 2^o Edition.; Springer: Sassari, Italy, **2019**.
- [14] Brinker, C. J.; Scherer, G. W. *Sol-Gel Science*; 1st ed.; Academic Press, INC: San Diego, CA, USA, **1990**.
- [15] Depla, A.; Verheyen, E.; Veyfeyken, A.; Van Houteghem, M.; Houthoofd, K.; Van Speybroeck, V.; Waroquier, M.; Kirschhock, C. E. A.; Martens, J. A. *J. Phys. Chem. C* **2011**, 115, p. 11077–11088.
- [16] Yamane, M.; Inoue, S.; Yasumori, A. *J. Non. Cryst. Solids* **1984**, 63, p. 13–21.
- [17] Voon Ng, L.; Thompson, P.; Sanchez, J.; Macosko, C. W.; McCormick, A. V. *Macromolecules* **1995**, 28, p. 6471–6476.
- [18] Depla, A.; Lesthaeghe, D.; Van Erp, T. S.; Aerts, A.; Houthoofd, K.; Fan, F.; Li, C.; Van Speybroeck, V.; Waroquier, M.; Kirschhock, C. E. A.; Martens, J. A. *J. Phys. Chem. C* **2011**, 115, p. 3562–3571.
- [19] Trinh, T. T.; Jansen, A. P. J.; Van Santen, R. A. *J. Phys. Chem. B* **2006**, 110, p. 23099–23106.
- [20] Berrier, E.; Courtheoux, L.; Bouazaoui, M.; Capoen, B.; Turrell, S. *Phys. Chem. Chem. Phys.* **2010**, 12, p. 14477–14484.

- [21] Amiri, A.; Øye, G.; Sjöblom, J. *Colloids Surf., A* **2011**, *378*, p. 14–21.
- [22] Echeverría, J. C.; Estella, J.; Barbería, V.; Musgo, J.; Garrido, J. J. *J. Non-Cryst. Solids* **2010**, *356*, p. 378–382.
- [23] Estella, J.; Echeverría, J. C.; Laguna, M.; Garrido, J. J. *Microporous Mesoporous Mater.* **2007**, *102*, p. 274–282.
- [24] Steins, P.; Poulesquen, A.; Frizon, F.; Diat, O.; Jestin, J.; Causse, J.; Lambertin, D.; Rossignol, S. *J. Appl. Crystallogr.* **2014**, *47*, p. 316–324.
- [25] Iswar, S.; Malfait, W. J.; Balog, S.; Winnefeld, F.; Lattuada, M.; Koebel, M. M. *Microporous Mesoporous Mater.* **2017**, *241*, p. 293–302.
- [26] Scherer, G. W. *J. Non-Cryst. Solids* **1992**, *147–148*, p. 363–374.

ANNEXE B

SILICA-COATED OPTICAL FIBRE SENSORS



ANNEXE B

SILICA-COATED OPTICAL FIBRE SENSORS

B.1 FUNDAMENTS OF OPTICAL FIBRES (OF)

Optical fibres (OF) are hair-sized flexible and transparent fibres made of silica or plastic, they are designed to allow the passage of light to transmit voice, images and data. The first optical fibres were almost produced simultaneously in 1966 by Kao and Hackman [1], and Werts [2]. Kao, who won the Nobel Prize in Physics in 2009, claimed that using high-purity glass it is possible to create fibres with low light attenuation. This statement was proved true in 1977 when electric and telephone companies started using optical fibres for telephone traffic. In fact, in 1986 Yokota *et al.* were able to propagate light 20 km along an ultra-pure silica optical fibre achieving a reduction of only half of the original intensity signal [3]. Nowadays this technology has become the standard in the communication sector, gradually replacing the old electric communication systems.

There are plenty of optical fibres with different configurations; nevertheless, they all have a core surrounded by a cladding. The core is a transparent cylindrical rod made of drawing glass or plastic and constitutes the medium where the light propagates from the source to the receiving device. The internal diameter of the core ranges from 9 to 62,5 μm , which is close to the diameter of a human hair, and the data transfer rate is proportional to this size. The cladding, which typically has a diameter of 125 μm , is also made of silica or plastic and its function is to contain the light trapped inside the core by making it bounce off the interface between the two components [4]. In the standard commercial OF cables, the cladding is surrounded by a protective coating made up of two plastic layers (acrylate or polyimide). The one that is in contact with the cladding or “soft” layer cushions impacts and prevents damage due to cable bends while the second harder layer is resistant to abrasion [5]. The coating is also protected by a strengthening material, e.g., Kevlar fibres or metal wires, that further protects the core from crushing efforts and tensions [6]. Finally, the outer layer of OF cables is a plastic jacket that keeps the fibre safe from environmental hazards. Figure B.1 depicts two photographs of optical fibres where their compounds can be observed.

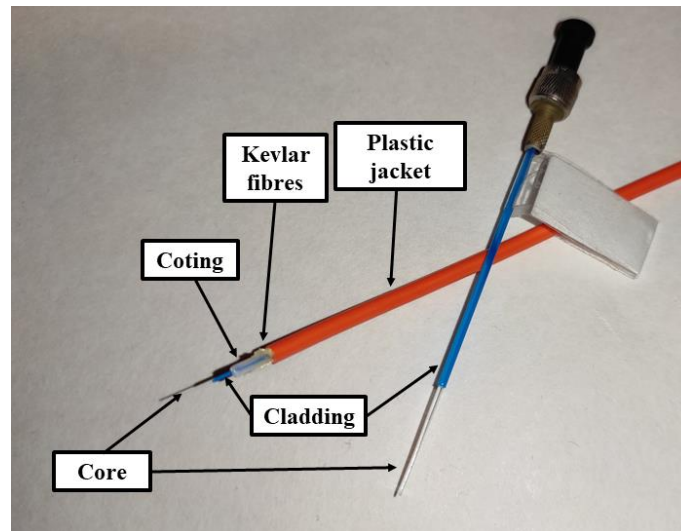


Figure B.1. Optical fibres with their exposed components.

Regarding the light transmission mechanism of optical fibres, from the perspective of the ray theory transmission, it can be said that light is propagated throughout the fibre by total internal reflection in the intersection between the core and the cladding. This is the mechanism because the refractive index of the core ($n \sim 1.5$) is slightly higher than that of the cladding, so, to explain this mechanism it becomes necessary to understand the concept of refractive index. This term refers to the ratio of the speed of light in the vacuum with respect to the velocity of light in a medium; therefore, the denser the medium, the slower the light pierces through, and the higher the value of the refractive index. The optical fibres can be classified as step-index fibres if the refraction index of the core is constant or as graded fibres if the value of the core index decreases with radial distance. The explanation of the light propagation mechanism will be provided from the perspective of step-index fibres because those are the standard commercial optical fibres and are the ones that have been used to prepare the chemical sensors in the research of *Chapter 6*.

In optical fibres, the incidence angle of light (ϕ) and the difference of n between the two continuous dielectric media (the core and cladding), are what decide the process that takes place when light reaches an interface. Refraction is the apparent change in the direction of light when an incident ray reaches the interface; whereas reflection occurs when the light bounces mirror-like and is driven back. Another topic to consider is that the refractive index of a medium can vary with the wavelength, which is the reason behind the dispersion of white light caused by prisms or water droplets. Figure B.2 shows the refraction phenomena and how light propagates in the optical fibre.

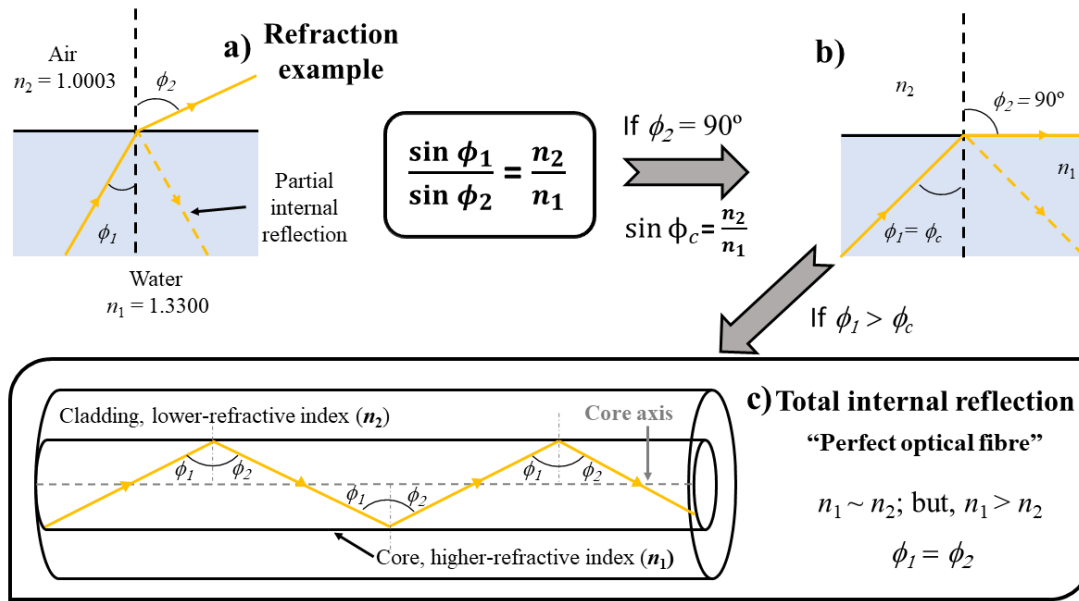


Figure B.2. (a) Refraction example, (b) refraction limit with incident ray at the critical angle, and (c) total internal reflection in a hypothetically perfect optical fibre. Adapted from Senior (2009) [7].

As shown in Figure B.2a, an incident ray propagating through a medium with refractive index n_1 approaches the interface forming the angle ϕ_1 with its perpendicular. If the medium on the other side of the interface has an index (n_2) less than n_1 , the ray is refracted forming the angle ϕ_2 with the perpendicular of the interface in such a way that $\phi_2 > \phi_1$. Nevertheless, a small portion of light may still be reflected to the departure medium, as shown in the figure. In the described system, the relationship between angles and refractive indexes is given by Snell’s law of refraction (Equation B.1), which is expressed as a fraction in Equation B.2 and Figure B.2.

$$n_1 \sin \phi_1 = n_2 \sin \phi_2 \quad (\text{B.1})$$

$$\frac{\sin \phi_1}{\sin \phi_2} = \frac{n_2}{n_1} \quad (\text{B.2})$$

$$\frac{\sin \phi_c}{\sin 90^\circ} = \sin \phi_c = \frac{n_2}{n_1} \quad (\text{B.3})$$

Figure B.2b represents the limiting case of refraction, which occurs when the refracted beam of light is parallel to the interface ($\phi_2 = 90^\circ$). In this situation the angle that is established between the incident light and the interface is called critical angle (ϕ_c), whose value must be below 90° and is given by Equation B.3. In the event of a ϕ_1 higher than 90° , the 99.9% of the photons are reflected to the original medium. This process is called total internal reflection and takes place when light emerging from a medium with

a higher refractive index and an incidence angle higher than ϕ_c reaches the interface with a medium of lower n . Figure B.2c depicts the propagation of light in an optical fibre through the total internal reflection. Finally, it must be pointed out that incident rays coming from the optical source are refracted when they reach the air-core interface. To accomplish the total internal reflection on the core-cladding interface, the light must first reach the air-core interface with such an angle that the exiting ray forms an angle higher than ϕ_c with the core-cladding interface. The incident angles with respect to the core axis that allows the total internal reflection constitute the acceptance angle cone.

The step-index optical fibres are classified as single mode (SM) or multimode (MM), the main difference is that multimode have a much larger diameter core ($\geq 50 \mu\text{m}$) compared to the usual 2–10 μm of the SM fibres. Thanks to their larger core diameter, multimode fibres allow the transmission of multiple rays of light or modes, each with a slightly different incidence angle, whereas SM fibres only allow the propagation of one mode. MM fibres compared to SM fibres provide a higher volume of reliable data, their connections are simpler, can be connected to spatially incoherent optical sources like LEDs, and allow the use of lower-cost transceivers [7]. Nevertheless, contrary to SM fibres, MM fibres experience considerable dispersion due to the different velocities of multiple light modes. In addition, due to this dispersion, MM fibres cannot be used for long-distance communications (200–300 m) because the light is severely attenuated and the maximum bandwidth attainable is restricted [4]. Both Figure B.1 fibres are multimode; in fact, the one with the blue cladding was used to prepare the luminescent-based chemical sensors in this research.

Once the components and mechanism of light propagation have been briefly explained, to conclude it is interesting to highlight the main advantages of the optical fibres compared with traditional electric communications [7,8].

- I. Wide potential bandwidth and low transmission loss: Optical fibres provide greater potential transmission bandwidths than metallic cables because they can cover the range of 10^{13} – 10^{16} Hz (30.000–30 nm) and yield very low attenuation loss in comparison. In optical fibre sensors, these characteristics allow remote measuring of multiple parameters simultaneously.
- II. Small size, flexibility and toughness: As stated, they usually have a diameter no larger than human hair. Additionally, even glassy optical fibres can be bent or twisted without producing significant alterations to their performance, due to their

high tensile resistance. Hence, the storage and handling of optical fibres is easier than those of copper cables.

- III. Electrical isolation and immunity to electromagnetic interference: optical fibres are electric insulators because they are fabricated with silica or plastic; and since the core-cladding interface constitutes a dielectric waveguide, they are shielded against electric, electromagnetic or radiofrequency interferences. For these reasons, optical fibres are ideal as communication systems in environments where the use of conventional electricity wires can be dangerous. In fact, optical fibre sensors have been used to detect leaks in oil and natural gas storage tanks or pipelines [9].
- IV. Temperature and radiation resistance: there are types of optical fibres that are made to withstand harsh conditions such as extremely high temperatures, cryogenic conditions, ionizing radiation, and even the vacuum of outer space [10].
- V. Chemical and biological resistance (silica fibres): silicon dioxide or silica is a compound with relatively high chemical and biological stability. Therefore, silica fibres can be safely used in environments where it is exposed to agents of these kinds. Furthermore, optical fibre sensors are commonly used in biomedical applications due to the biocompatibility of silica.
- VI. High reliability, easy maintenance, and low-cost potential: due to its lower attenuation of light, there is no need to use several intermediate devices, such as amplifiers and repeaters. Fewer devices do not only imply cost reduction but also mean fewer instrumental errors and maintenance. Furthermore, optical fibres are predicted to be able to endure 20–30 years and have the potential to be considerably affordable in the future since their glass core can be produced from sand.

B.2 OPTICAL FIBRE SENSORS (OFS)

As commented before, optical communication is the main application of optical fibres. However, due to the impressive properties of optical fibres, they have been gradually conceived as a valuable resource for preparing sensors. The first optical fibre sensor was documented in 1967, only one year after the original publication of Kao and Hackman [1]. In this published study Menadier *et al.* created a photonic sensor with a bundle of fibres [11]. One of the fibres emitted light onto a surface while the other non-emitting fibre collected the reflected light. The amount of reflected light is proportional to the distance between the fibre and the surface, therefore, it can be used to detect distances and displacements. Later, in 1978, Hill *et al.* discovered photosensitive optical fibres [12]. This article was fundamental for the development of the Fibre Bragg-Grating sensors (FBG), which were first commercially available in 1995 and are still one of the most popular sensors yet due to their versatility.

All optical fibre sensors (OFS) systems have four basic components: (i) an optical source (lasers, LEDs, halogen lamps...), (ii) a sensor or modulator, which can be the optical fibres themselves transducing analytes or stimulus into optical signals, (iii) a detector, and (iv) an analysis device. An OFS measures the changes in the light parameters that propagates within when exposed to certain conditions or media (e.g., intensity, polarization, wavelength). When the light is modified, is reflected as a signal to an analytical device, and then, the light shift is translated into a numerical measurement that can be correlated with its causing variable. In addition to all the benefits of optical fibres as a communication system that were indicated in the previous section, OFS have more advantages regarding their sensor side, because they require less complex setups than other sensors, do not require an electrical supply on the remote sensing location, i.e., they are passive sensors, and they allow the simultaneous measurement of multiple parameters by attaching multiple sensors, each focused to a specific light shift, along the fibre length [13].

OFS can be classified considering the sensor location, application and operating mechanism/modulation scheme. The OFS classifications and types are illustrated in Figure B.3.

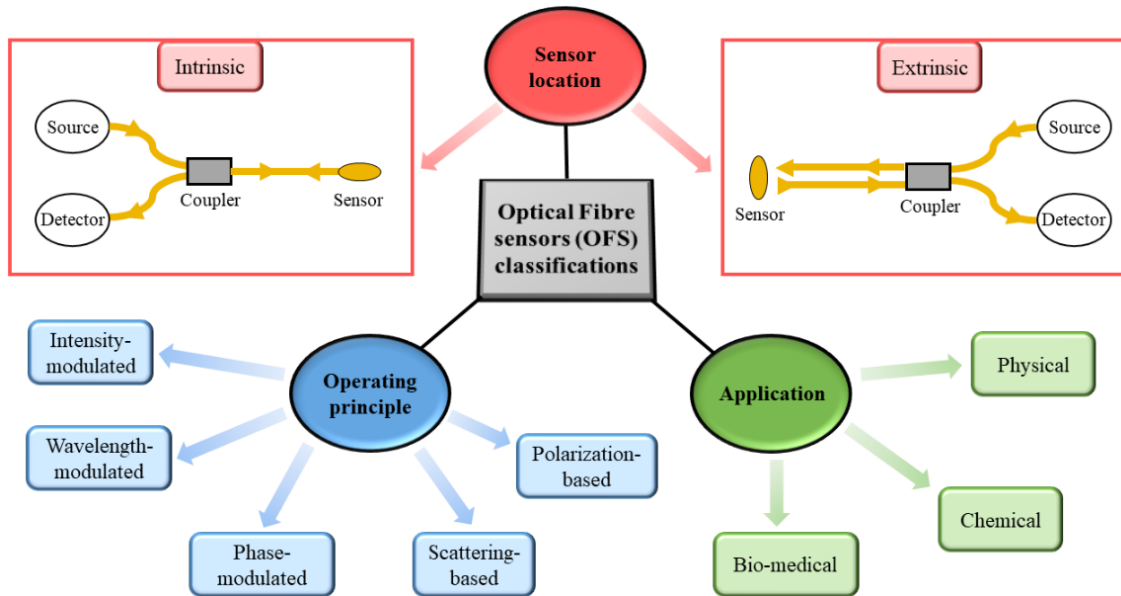


Figure B.3. Scheme of the main three classifications of optical fibre sensors.

The most fundamental of the three mentioned classifications of OFS is the one concerning the sensor location, thus, Figure B.3 represents the two types of sensors considered by this classification: intrinsic and extrinsic sensors [14]. The intrinsic sensors are those where the light is modulated in the optical fibre, the light does not leave the fibre, whereas, in an extrinsic sensor the light is guided to an interaction region external to the fibre, where it is modulated and collected back in the same fibre or other by reflection or scattering. The Menadier's photonic sensor is a perfect example of an extrinsic sensor, likewise, the FBG are an example of an intrinsic sensor.

In the second classification (bottom left of Figure B.3) the sensors are classified based on the operation principle used to obtain the data [15,16]: (i) intensity-modulated, these are the simplest and more affordable sensors. Nevertheless, they require the use of a reference system to correct their fluctuation of optical power loss, (ii) phase-modulated, these sensors measure light interference, and in contrast to intensity-modulated sensors, are quite costly due to their better outputs: sensitivity and accuracy, (iii) polarization-based, they are indirectly based on this light characteristic, since what they measure is the interference caused by the changes produced in the refractive index when the light polarization states are altered, (iv) the changes produced on the light wavelength are measured by the wavelength modulated sensors, and (v) scattering-based sensors are sensors coupled to an optical time domain reflectometer, which enables the detection of scattered light.

The last classification concerns the application, i.e., it is focused on the measurement parameter. Many recent OFS reviews (2021–2023) can be found in the literature that compiles sensors specifically designed to measure physical, chemical or biomedical parameters. Some of the relevant physical parameters transduced by OFS are temperature, strain, water level, or even seismic waves [17–19]. Regarding chemical OFS, they are intended to identify and quantify chemical substances, for instance, they can be used to determine water salinity, concentration of heavy metals in water, or composition of gases, among others [20–22]. Finally, the bio-medical OFS have been used to monitor heart pulse, blood pressure and respiration, and to detect the concentration of O₂ and glucose in blood and proteins [23–25].

B.3 OPTICAL FIBRE CHEMICAL SENSORS (OFCS)

The more important characteristics of an optical fibre chemical sensor (OFCS) are selectivity, sensitivity and reversibility. An OFCS must respond selectively to the desired analyte, to avoid interferences caused by interactions with nontarget species. It has also to be sensitive to the analyte, i.e., it must respond to small concentrations and be able to distinguish between those of similar magnitude to proportion a suitable analyte-dependent response. However, the reusability of OFCS is more challenging to accomplish compared to other OFS because chemical reactions with the analyte can produce irreversible changes. Therefore, OFCS must be designed considering a labile interaction with the analyte. Chemical sensing is a two-step procedure, first, the analytes interact selectively and reversibly with the recognition component of the sensor, which causes the alteration of its physicochemical parameters. Then, in the transduction process, the variation of those parameters is transformed into an analyte-dependent signal output that is amplified and sent toward a detector attached to an analytical device. The most common chemical sensor configuration, and the one that has been used in this research, consists of two fibres fused with a coupler forming a “Y” (as the intrinsic sensor illustrated in Figure B.3). The bifurcated ends are connected to the light source and a detector while the other fibre end acts or contains the sensor. A scheme for an optical fibre indirect chemical sensor for gases and vapours is displayed in Figure B.4.

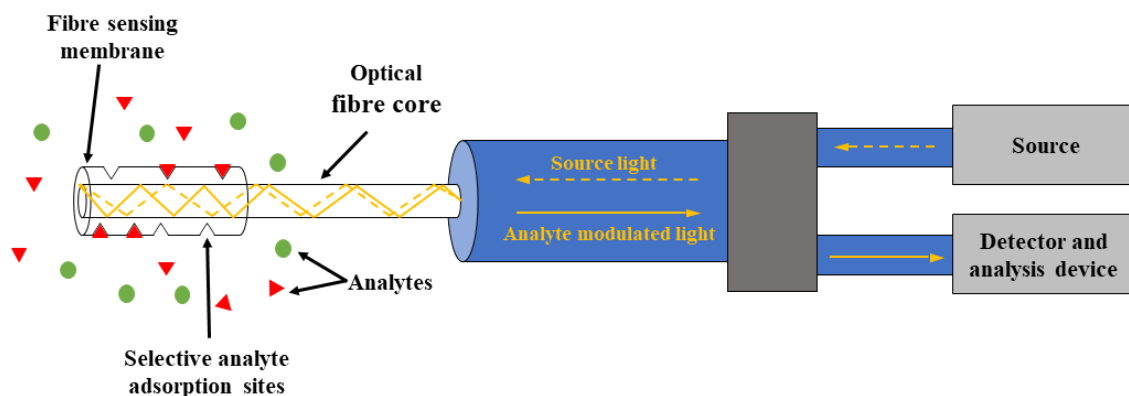


Figure B.4. Scheme of an optical fibre indirect chemical sensor.

The transduction step in an OFCS is performed in the fibre because the light carried within is modulated upon exposition to the analytes. However, OFCS can be classified into two groups depending on who performs the sensing step. In direct sensors the analyte interacts directly with the fibre, therefore, a recognition element is not required whereas in the indirect or complex OFCS, the analytes interact with a sensing material or indicator reagent, which is usually attached to the fibre [14]. Regardless of their type, all gas or vapour sensors operate following a simple principle: the response depends on the adsorption-desorption equilibrium of the analyte (A) in a adsorbent membrane (M) containing a reagent (R) that is selective and sensitive towards the analyte [8]. The equilibrium is given by Equation B.4 and its kinetic law is given by Equation B.5.



$$\frac{-\Delta[A]}{\Delta t} = k_{ads}[A](1 - \theta) - k_{des}\theta \quad (\text{B.5})$$

where, S_M is the number of adsorption sites in the adsorbent membrane, $[A]$ is the concentration of analyte, MA is the the analyte-adsorbent pair formed by the analyte adsorption, k_{ads} is the adsorption rate, k_{des} is the desorption rate. Lastly θ , wich is given by Equation B.6, is the fraction of the total available adsorption sites ($[A]_m$) that are occupied by the anlyte.

$$\theta = \frac{[A]}{[A]_m} \quad (\text{B.6})$$

When MA is formed, perturbations are produced on the light transported within the fibre, therefore, the generated response is modulated by A , and can be caused either by the decrease of the R concentration or by the properties of the generated MA species.

Once the equilibrium is reached ($\frac{-\Delta[A]}{\Delta t} = 0$) and considering Equation B.6, the Equation B.5 can be rearranged and expressed as Equation B.7.

$$\theta = \frac{k_{ads}[A]}{k_{ads}[A] + k_{des}} \quad (\text{B.7})$$

This new equation is the Langmuir adsorption isotherm equation expressed in analyte concentration instead of partial pressures, and by replacing Equation B.6 in Equation B.7 and dividing by k_{des} , the Equation B.8 is obtained.

$$[A] = \frac{K[A]_m[A]}{K[A] + 1} \quad (\text{B.8})$$

where K is the adsorption-desorption equilibrium constant given by the k_{ads}/k_{des} ratio. From all these equations, it can be concluded that a good chemical sensor requires a reagent that can establish selective and labile interactions with the analytes, so the equilibrium allows continuous measurement in a wider range of analyte concentrations.

Among the indirect chemical sensors, those that are based on the interaction of light with the reagent or indicator are quite common. The indicators in these optical chemical sensors interact with specific light wavelengths, generating analyte-dependent light modulations that are studied by a spectroscopic analytical device. The optical phenomena used to transduce the modulation of light into an analyte-dependent signal are absorption, fluorescence, surface plasmon resonance (SPR), and evanescent wave spectroscopy. The humidity OFS constructed in this research is an indirect fluorescence-based sensor, then the mechanism and basic concepts of luminescence will be addressed in the next *Annexe C*. For now, it can be said that the luminescence phenomenon is a two-step process that takes place in some atoms or molecules. First, photons are absorbed, and its energy is invested in the promotion of electrons from fundamental energy levels to excited ones. Then, the electrons radiatively relax back to the fundamental level by emitting photons of lower energy than the absorbed ones. Therefore, the emitted radiation has always a higher wavelength (λ_{em}) than the absorbed or excitation radiation (λ_{exc}), and the intensity of the emitted radiation (I_{em}) is dependent on the intensity of incident radiation (I_0) and the concentration of absorbing species ($[R]$ or $[AR]$). If the luminescent species is the reagent and it is a weakly absorbing species, we can relate I_{em} with a constant I_0 by Equation B.9.

$$I_{em} = K_{\%} \cdot I_0 \cdot \Phi \cdot \mu(\lambda_{exc}) \cdot l \cdot [R] = K_{em} \cdot [R] \quad (\text{B.9})$$

where $K_{\%}$ is the fraction of measurable emission, l is the length of the optical path, $\mu(\lambda_{exc})$ is the molar coefficient of absorption of R, and Φ is the quantum yield of the emission process. An explanation of the last two terms will be also provided in *Annexe C*.

The I_{em} of luminescent reagents fixed to the fibre in an OFCS, such as metal complexes or organic luminophores, can be modulated by quenching species (e.g., O_2 , H_2O , CO_2 , among others), which act as the analytes that form the non-luminescent AR product. The Stern-Volmer equation (Equation B.10), relates the concentration of quenching species [Q] with the luminescent emission intensity [26].

$$\frac{I_{em}^0}{I_{em}} = 1 + K_{SV} \cdot [Q] \quad (\text{B.10})$$

where I_{em} is the emission intensity in the absence of quenching substances I_{em}^0 is the quenched emission intensity, and K_{SV} is the Stern-Volmer constant. This equation reflects the emission intensity decay of a luminescent species that occurs when their promoted electrons are non-radiatively deactivated by collisions with quenching molecules. Therefore, by plotting the emission intensity ratio of the indicator as a function of a known quencher concentration, we can obtain a linear calibration of a luminescence-based OFCS [27]. In the humidity OFS studied in this research (*Chapter 6*), the water molecules are the quenchers that deactivate the luminescent emission of lanthanide complexes embedded in a silica xerogel matrix. In the sensor calibration plots, the intensity emission at the lowest measured relative humidity (20%) is used as the reference intensity (I_{ref}) and $\frac{I_{em} - I_{ref}}{I_{ref}}$ is plotted as a function of water vapour concentration in the climate chamber (C_{H_2O}).

B.4 SILICA GEL COATINGS

There are several ways to fix a sensing material to an optical fibre chemical sensor, although only a few accomplish all the optimal conditions of being simple, reproducible, applied to a wide variety of indicators, avoiding indicator leaching, and not hindering the chemical activity of the indicator. The main immobilization method that fulfils the conditions are adsorption/electrostatic interactions, entrapment, and covalent linking

[27,28]. The easiest method is to adsorb the indicator directly onto the surface of the optical fibre, previously treated to create surface analyte-affine functional groups, or in a polymer film covering the fibre. Nevertheless, this method has a serious drawback, that is, the gradual leaching of the sensing materials. The covalent immobilisation method solves the leaching issue because the indicator is covalently bonded to fibre surface functional groups that have previously undergone functionalization processes, like silinisation with triethoxysilanes. Finally, the entrapment method provides another solution for the leaching problem without requiring a covalent linking with the indicators. In this method the indicator is added to a viscous liquid solution of polymeric precursors, then it is applied to the surface of the optical fibre core where it cross-links and forms a coating upon drying. Thus, the indicator is physically embedded in the coating porous matrix.

Regarding the host matrix in the entrapment method, as commented in *Annexe B.1*, commercial optical fibres may have silicone coatings covering the cladding. Silicones are a family of compounds whose structure is based on a repeating O–SiR₂–O backbone, and they present interesting chemical and physical properties that can be modulated by selecting different functional groups (R). For instance, polydimethylsiloxane (PDMS) is a common silicone with alkyl as the functional group (R = CH₃). Additionally, different monomers can be combined to yield silicone coatings with multiple interesting properties, such as biocompatibility, high temperature and mechanical stability, optical transparency towards UV-Vis radiation, resistivity to strong acids and alkali, low dielectric constant, low light attenuation, and sensitivity towards temperature and humidity. Furthermore, due to their flexibility, elasticity and cross-linking capability, silicone coatings can be easily applied to the optical fibres by pulling the fibre through liquid silicone and then, performing a curing step at 250–500 °C [29,30]. These coatings have been specially conceived as supports for the preparation of gas sensors because they have an extremely high gas permeability. However, although at first glance those properties are attractive for the construction of a humidity intrinsic optical fibre sensor by the entrapment method, silicone porous coatings might not be as convenient for their use as hosts for a sensing material or indicator. Since silicone precursors are hydrophobic, metal complex indicators are insoluble, which makes it necessary to add the indicators trapped inside inorganic fillers (usually silica). Consequently, the luminophore indicators would be surrounded by a highly

heterogeneous medium that will deviate from its linear response [31]. Additionally, the use of fillers can contribute to the formation of high pore-size silicones (from a few to hundreds of μm) [32–34], which would not prevent the gradual leaching of the indicators.

As an alternative to silicone coatings, the sol-gel method can be used to prepare pure inorganic or inorganic-organic hybrid silica films for optical fibre sensors. As can be found in some reviews, the use of this synthesis approach for the preparation of OFS coatings dates to the early 90 s [35,36]. Nowadays, the application of sol-gel technology in OFCS is quite extended due to the ease of preparing transparent optical films with highly tunable chemical and physical properties [37], which allows to embed the sensing species in a porous matrix permeable towards specific analytes. Table B.1 depicts some articles where the sol-gel method was employed to prepare films for OFCS.

Table B.1. Some examples of articles of silica-gel coated optical fibre sensors.

Year	Reference	Film composition	Operation principle	Target analyte
2023	[38]	¹ TEOS aerogel with entrapped ² PAR. Deposited by spin-coating	Colour change by formation of luminophore complex	Vanadium in aqueous media
2021	[39]	Silica (SiO ₂) or gold nanoparticle incorporated silica (Au-SiO ₂) as the sensitive layers. Deposited by dip-coating	Reflection/back-scatter	pH in 8–12 range
2018	[40]	³ LuPc ₂ dispersed in a mesoporous silica matrix synthesised with 75% ¹ TEOS and 25% ⁴ MTEOS. Deposited by dip-coating	Amplitude changes in the reflected spectrum	NO ₂
2018	[41]	Silica synthesised with ¹ TEOS with Nile red entrapped. Deposited by dip-coating	Wavelengths shift in the transmission spectra	VOCs: ethanol and methanol
2015	[42]	Sensitive layers based on ion-pair of ⁵ DHPDS and ⁶ HPTS, immobilized in silica matrixes composed of ⁷ ETEOS and ⁸ GLYMO. Deposited by dip-coating	Fluorescence intensity-based	pH in physiological range
2013	[43]	Composite xerogel: ⁹ (n-propyl-TriMOS)/ ¹ TEOS/ ¹⁰ (Octyl-triEOS) with entrapped ¹¹ PdTFPP. Deposited by dip-coating	Phosphorescence intensity-based	O ₂
2011	[44]	Pure ¹ TEOS coating with methyl blue embedded. Deposited by dip-coating	Evanescent wave scattering and absorption	Humidity

¹-Tetraethoxysilane; ²-4-(2-pyridylazo) resorcinol; ³-Lanthanide bisphthalocyanine; ⁴-Methyltriethoxysilane; ⁵-6,8-dihydroxy-1,3-pyrene disulfonic acid disodium salt; ⁶-8-hydroxypyrene-1,3,6-pyrene trisulfonic acid trisodium salt; ⁷-Ethyltriethoxysilane; ⁸-(3-glycidoxypropyl)-trimethoxysilane; ⁹-n-propyltrimethoxysilane; ¹⁰-n-Octyltriethoxysilane; ¹¹- palladium (II) meso-tetrakis(pentafluorophenyl)porphyrin.

An overall explanation of each step in the sol-gel process has been provided in *Annexe A*; therefore, we shall focus on the deposition technique used to prepare the silica films for OFCS. As can be observed in the examples of Table B.1, almost all the films were deposited by dip-coating. This technique, also known as impregnation or saturation, consists of dipping the tip of the core of an optical fibre (the cladding was previously removed) into a solution between the sol and gel phases at a controlled introduction and withdrawal speed, to create thin, porous and homogeneous membranes covering the fibre core. Figure B.5. depicts a scheme of the dip-coating process.

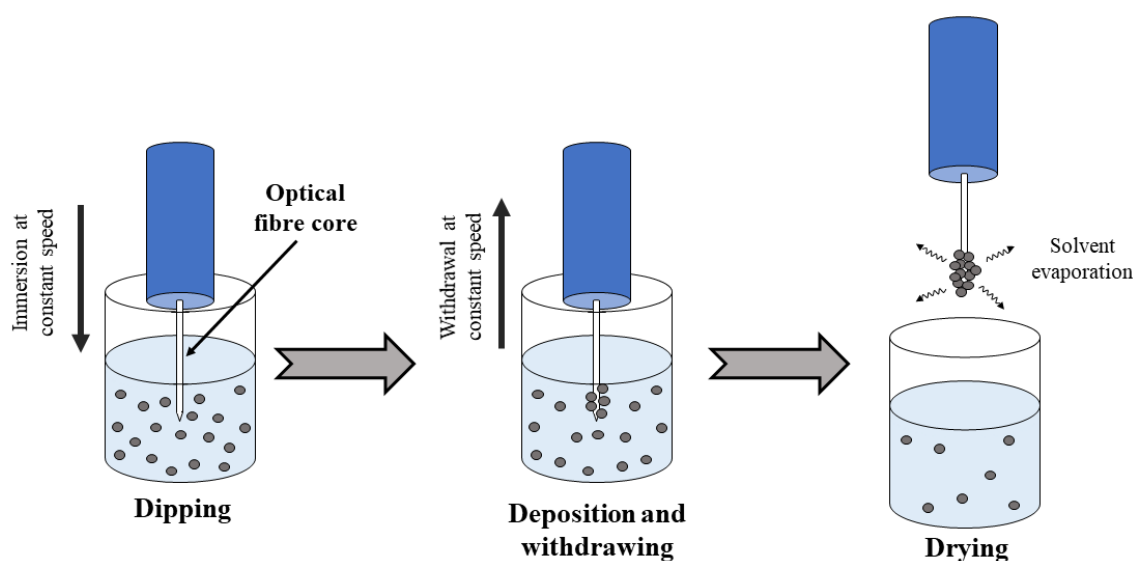


Figure B.5. Scheme of the dip-coating process.

This impregnation method does not produce stress or distort the original fibres, and in addition to its fast implementation, it allows the setup of the thickness and porosity of the films by selecting the pickup speed and the viscosity of the sol. Lower speeds and higher sol viscosities produce films with higher thickness, therefore, coating ranging from a few to hundreds of micrometres can be created. Once the film has been deposited, the sol undergoes the ageing process, and finally, the remaining solvents evaporate gradually at environmental conditions to prevent cracks.

B.5 LANTHANIDE-DOPED SILICA COATINGS FOR OFS

In recent years, Tb^{III} and specially Eu^{III} species (complexes, nanocrystals, MOFs...) have been used to develop specific optical fibre sensors due to their intense radiation at wavelengths within the scope of the human sight (see *Annexe C* to delve into the properties of lanthanide trivalent cations). These sensors have been used to measure concentration of metals in water [45], concentration of gases [46], or even physical parameters such as temperature [47,48], pressure [49] and stress [50]. However, to immobilize lanthanide substances onto the optical fibre surface it is required the use of host materials, and as it was commented in *Annexe B.4*, silica gels have been proven as valuable for such purpose. In the literature, multiple examples of optical applications of silica gels containing lanthanide substances can be found [51–55], however, application in optical fibre technology has been poorly explored since the existing few publications were published decades ago [35,56]. Hence, due to the limited research in this promising field, in *Chapter 6* it was decided to develop silica-coated OFCSs with lanthanide cations as their sensing element, where the signal transduction is based on the luminescence decay of the lanthanides through quenching produced by analyte (water vapour) molecules. Furthermore, the research aims to shed light on the relationship between the adsorption mechanism of the analyte in the silica coating (which is determined by its textural properties) and the luminescent emission response of the sensor, so this knowledge can be applied in the future to develop efficient and selective lanthanide-based OFCSs.

B.6 REFERENCES

- [1] Kao, K. C.; Hockham, G. A. *Proc. Iee* **1966**, *113*, p. 1151–1158.
- [2] Bousquet, P.; Viossat, G. *Bulletin de l'Union des Physiciens*. **1985**, *692*, p. 307–331.
- [3] Yokota, H.; Kanamori, H.; Ishiguro, Y.; Tanaka, G.; Tanaka, S.; Takada, H.; Watanabe, M.; Suzuki, S.; Yano, K.; Hoshikawa, M.; Shimba, H. Ultra low-loss pure silica core single-mode fiber and transmission experiment. In *Optical Fiber Communication Technical Digest Series*; **1986**.
- [4] Osihardware The composition of an optical fiber Available online: <https://www.osihardware.com/wp-content/uploads/2018/08/osi-optics-smartoptics-optical-fibers.pdf> (accessed on Aug 28, **2023**).
- [5] AFL. The basic structure of optical fiber, Available online: <https://learn.aflglobal.com/enterprise/the-basic-structure-of-optical-fiber> (accessed on Aug 28, **2023**).

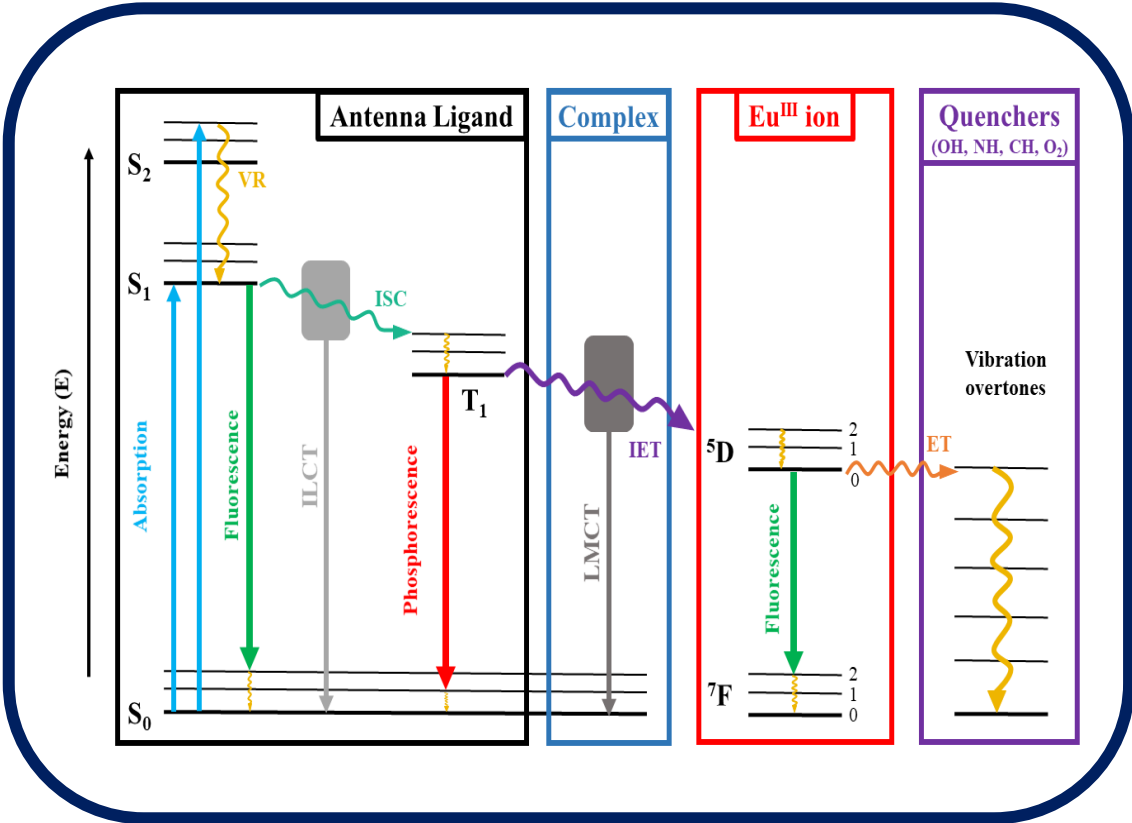
- [6] Urban, J. Anatomy of a Cable – Optical Fiber Available online: <https://blog.biamp.com/anatomy-of-a-cable-optical-fiber/> (accessed on Aug 28, **2023**).
- [7] Senior, J. M. Optical fiber waveguides. In *Optical fiber communications principles and practice*; 3rd ed.; Pearson Prentice Hall: Harlow, England, UK, **2009**.
- [8] del Villar, I.; Matias, I. R. *Optical fibre sensors: Fundamentals for development of optimized devices*; Wiley & Sons, Ltd., **2021**.
- [9] Ashry, I.; Mao, Y.; Wang, B.; Hveding, F.; Bukhamsin, A.; Ng, T. K.; Ooi, B. S. *J. Lightwave Technol.* **2022**, *40*, p. 1407–1431.
- [10] Deng, Y.; Jiang, J. *IEEE Sens. J.* **2022**, *22*, p. 13811–13834.
- [11] Menadier, C.; Kissinger, C.; Adkins, H. *Instrum. Control Syst.* **1967**, *40*, p. 114.
- [12] Hill, K. O.; Fujii, Y.; Johnson, D. C.; Kawasaki, B. S. *Appl. Phys. Lett.* **1978**, *32*, p. 647–649.
- [13] Culshaw, B. *J. Lightwave Technol.* **2004**, *22*, p. 39–50.
- [14] Grattan, K. T. V.; Ning, Y. N. Classification of optical fiber sensors. In *Optical fiber sensor technology. volume 2 devices and technology*; Grattan, K. T. V., Meggitt, B. T., Eds.; Springer-Science+Business Media, B.V.: London, UK, **1998**.
- [15] Pendão, C.; Silva, I. *Sensors* **2022**, *22*, p. 7554.
- [16] Khandelwal, P. *IJLTEMAS.* **2013**, *2*, p. 22–25.
- [17] Yu, J.; Xu, P.; Yu, Z.; Wen, K.; Yang, J.; Wang, Y.; Qin, Y. *sensors* **2023**, *23*, p. 5600.
- [18] Jauregui-Vazquez, D.; Alvarez-Chavez, J. A.; Lozano-Hernandez, T.; Estudillo-Ayala, J. M.; Sierra-Hernandez, J. M.; Offerhaus, H. L. *Photonics* **2023**, *10*, p. 495.
- [19] de Oliveira, L. A.; de Sousa, F. B.; de Sousa, F. M.; Tavares, S. C. C.; Paschoal, W.; Costa, M. B. C. *Opt. Quantum Electron.* **2022**, *54*, p. 1–17.
- [20] Li, G.; Wang, Y.; Shi, A.; Liu, Y.; Li, F. *Sensors* **2023**, *23*, p. 2187.
- [21] Kumar Shakya, A.; Singh, S. *Opt. Laser Technol.* **2022**, *153*, p. 108246.
- [22] Allsop, T.; Neal, R. *Sensors* **2021**, *21*, p. 6755.
- [23] Zhang, X.; Wang, C.; Zheng, T.; Wu, H.; Wu, Q.; Wang, Y. *Sensors* **2023**, *23*, p. 6671.
- [24] Vavrinsky, E.; Esfahani, N. E.; Hausner, M.; Kuzma, A.; Rezo, V.; Donoval, M.; Kosnacova, H. *Biosensors* **2022**, *12*, p. 1–40.
- [25] Lyu, S.; Wu, Z.; Shi, X.; Wu, Q. *Photonics* **2022**, *9*, p. 987.
- [26] Grubbs, T. Fluorescence lifetimes and dynamic quenching Available online: https://chem.libretexts.org/Bookshelves/Physical_and_Theoretical_Chemistry_Textbook_Maps/Exercises%3A_Physical_and_Theoretical_Chemistry/Data-Driven_Exercises/Fluorescence_Lifetimes_and_Dynamic_Quenching (accessed on Sep 5, **2023**).
- [27] Walt, D. R.; Biran, I.; Mandal, T. K. Fiber-optic chemical sensor. In *Encyclopedia of physical science and technology*; 3rd, Ed.; Academic Press, INC, **2003**; pp. 803–829.

- [28] Rudolf Seitz, W.; Sepaniak, M. J. *Crit. Rev. Anal. Chem.* **1988**, *19*, p. 135–173.
- [29] Li, C.; Yang, W.; Wang, M.; Yu, X.; Fan, J.; Xiong, Y.; Yang, Y.; Li, L. *Sensors* **2020**, *20*, p. 1–24.
- [30] Janani, R.; Majumder, D.; Scrimshire, A.; Stone, A.; Wakelin, E.; Jones, A.H.; Wheeler, N. V.; Brooks, W.; Bingham, P.A. *Prog. Org. Coat.* **2023**, *180*, p. 107557.
- [31] Orellana, G.; López-Gejo, J.; Pedras, B. Silicone Films for Fiber - Optic Chemical Sensing. In *Concise Encyclopedia of High Performance Silicones*; **2014**; Vol. 3, p. 339–353.
- [32] Abshirini, M.; Saha, M. C.; Cummings, L.; Robison, T. *Polym. Eng. Sci.* **2021**, *61*, p. 1943–1955.
- [33] Li, Q.; Duan, T.; Shao, J.; Yu, H. *J. Mater. Sci.* **2018**, *53*, p. 11873–11882.
- [34] Yoon, S.; Seok, M.; Kim, M.; Cho, Y. H. *Sci. Rep.* **2021**, *11*, p. 1–11.
- [35] Grattan, K. T. V.; Badini, G. E.; Palmer, A. W.; Tseung, A. C. C. *Sens. Actuators, A* **1991**, *26*, p. 483–487.
- [36] Badini, G. E.; Grattan, K. T. V.; Tseung, A. C. C. *Rev. Sci. Instrum.* **1995**, *66*, p. 4034–4040.
- [37] Figueira, R. B.; De Almeida, J. M.; Ferreira, B.; Coelho, L.; Silva, C. J. R. *Mater. Adv.* **2021**, *2*, p. 7237–7276.
- [38] Zareipour, M.; Rezaei, V. *J. Food Compos. Anal.* **2023**, *115*, p. 104936.
- [39] Lu, F.; Wright, R.; Lu, P.; Cvetic, P. C.; Ohodnicki, P. R. *Sens. Actuators, B* **2021**, *340*, p. 129853.
- [40] Debliquy, M.; Lahem, D.; Bueno-Martinez, A.; Caucheteur, C.; Bouvet, M.; Recloux, I.; Raskin, J. P.; Olivier, M. G. *Sensors* **2018**, *18*, p. 740.
- [41] Liu, D.; Kumar, R.; Wei, F.; Han, W.; Mallik, A.K.; Yuan, J.; Wan, S.; He, X.; Kang, Z.; Li, F.; Yu, C.; Farrell, G.; Semenova, Y.; Wu, Q. *Sens. Actuators, B* **2018**, *271*, p. 1–8.
- [42] Cui, Q.; Podrazký, O.; Mrázek, J.; Proboštová, J.; Kašík, I. *IEEE Sens. J.* **2015**, *15*, p. 4967–4973.
- [43] Chu, C. S. *J. Lumin.* **2013**, *135*, p. 5–9.
- [44] Zhao, Z.; Duan, Y. *Sens. Actuators, B* **2011**, *160*, p. 1340–1345.
- [45] Huang, Z.; Wang, Y.; Yan, X.; Mao, X.; Gao, Z.; Kipper, M. J.; Huang, L.; Tang, J. *Opt. Mater.* **2023**, *135*, p. 113245.
- [46] Xia, T.; Jiang, L.; Zhang, J.; Wan, Y.; Yang, Y.; Gan, J.; Cui, Y.; Yang, Z.; Qian, G. *Microporous Mesoporous Mater.* **2020**, *305*, p. 110396.
- [47] Getz, M. N.; Nilsen, O.; Hansen, P. A. *Sci. Rep.* **2019**, *9*, p. 1–11.
- [48] Zhu, Q.; Li, S.; Wang, Q.; Qi, Y.; Li, X.; Sun, X.; Li, J. G. *Nanoscale* **2019**, *11*, p. 2795–2804.

- [49] Hernandez, C.; Gupta, S. K.; Zuniga, J. P.; Vidal, J.; Galvan, R.; Guzman, H.; Chavez, L.; Lozano, K.; Mao, Y. *J. Mater. Sci. Technol.* **2021**, *66*, p. 103–111.
- [50] Tang, H.; Zhao, L.; Liu, Z.; Peng, Q.; Yu, X.; Wang, Q.; Zhao, F.; Deng, M.; Bai, Y.; Wang, Z.; Wang, T.; Qiu, J.; Xu, X. *Cell Rep. Phys. Sci.* **2022**, *3*, p. 101093.
- [51] Leimane, M.; Krizmane, K.; Bite, I.; Grube, J.; Vitola, V. *Materials* **2023**, *16*, p. 4416.
- [52] Zhao, W.; Feng, X.; Zhang, C.; Zhang, Y. *Appl. Phys. A: Mater. Sci. Process.* **2022**, *128*, p. 1–10.
- [53] Morales, O. G.; Chavira, E.; Rodríguez-rosales, A. A.; Flores-flores, O.; Mata-zamora, M. E.; Ponce, P. *Opt. Mater.* **2022**, *123*, p. 111760.
- [54] Dung, C. T. M.; Giang, L. T. T.; Binh, D. H.; Hieu, L. Van; Van, T. T. T. *J. Alloys Compd.* **2021**, *870*, p. 159405.
- [55] Firmino, E.; da Silva Oliveira, L.; Borges Martins, F. C.; Filho, J. C. S.; Barbosa, H. P.; Andrade, A. A.; Karine de Lima Rezende, T.; de Lima, R. C.; Couto dos Santos, M. A.; Góes, M. S.; Ferrari, J. L. *Opt. Mater.* **2021**, *114*, p. 1–9.
- [56] Zhang, Z. Y.; Sun, T.; Grattan, K. T. V.; Palmer, A. W. *Sens. Actuators, A* **1998**, *71*, p. 183–186.

ANNEXE C

PHOTOLUMINESCENCE OF LANTHANIDES



ANNEXE C

PHOTOLUMINESCENCE OF LANTHANIDES

C.1 BASIC CONCEPTS OF LUMINESCENCE

Throughout history, human beings have struggled to understand different phenomena observed in nature, but until the arrival of quantum mechanics in the last century, a proper explanation for some phenomena could not be provided; this was the case of light-emitting plants, animals, or minerals. This light-emitting characteristic was labelled as luminescence, and comes from the Latin word *Lumen* (light), by the physicist Eilhard Wiedemann in 1888 [1]. Luminescence is one of the two mechanisms of light emission, it occurs when energy is absorbed and light is emitted as a consequence of electronic transitions in atoms; whereas iridescence, the other mechanism, occurs when light is emitted by the vibration of electrically charged molecules when heated. Therefore, the main difference between the two mechanisms is that luminescence is a light emission that takes place at room temperature without generating heat. As stated, luminescence requires energy absorption or excitation from the luminescent substance; this can be achieved by different methods. A prefix accompanies the term luminescence to indicate the exciting method, e.g., *thermo*, by heating; *sono* by ultrasonic irradiation; *galvano*, by electrolysis; and *photo*, by irradiation with UV or visible light [2].

Photoluminescent materials, which are also called luminophores or phosphors, emit light at wavelengths (λ_{em}) that are characteristic of each substance. When a luminophore is excited with a photon with the proper wavelength (λ_{exc}) an electron gains enough energy to be promoted from the ground state (V_0) to an excited state (V_n), this instantaneous transition ($\sim 10^{-16}$ – 10^{-15} s) generates a vacancy in the V_0 that receive the name “hole”. Then, the promoted electron in V_n can be recombined with the hole in V_0 by emitting UV, visible or near-infrared photons, depending on the energy gap (E_g) between V_n and V_0 . All the electronic transitions follow the rule that λ_{exc} must always be shorter than λ_{em} , i.e., emitted radiation always has lower energy than the absorbed one. This phenomenon is called Stokes shift and is due to the non-radiative deactivation processes or vibrational relaxations [3]. For an isolated emitting centre, the dissipated energy corresponds to the energy gap between the two vibrational levels involved in the transition, which can be from the ground state ($\nu_i^0 \neq 0 \rightarrow \nu_0^0$) or an excited state ($\nu_i^n \neq 0 \rightarrow$

ν^0_0). It is also noteworthy that although vibrational relaxations are rapid processes ($\sim 10^{-12}$ – 10^{-10} s), they are slower than the radiative electronic transitions. However, the internal conversion (IC), is an even slower non-radiative process ($\sim 10^{-14}$ – 10^{-11} s) that occurs between two vibrational levels of the same energy. These iso-energetic processes consist of the transfer of an electron in the vibrational ground state of an excited energy level (ν^n_0) to a vibrational level of an inferior excited energy level (ν^{n-1}_i) [4]. The three discussed types of transitions are depicted in the Jablonski diagram of Figure C.1, which represents the electronic transitions of the excitation and emission spectra of a hypothetical molecule.

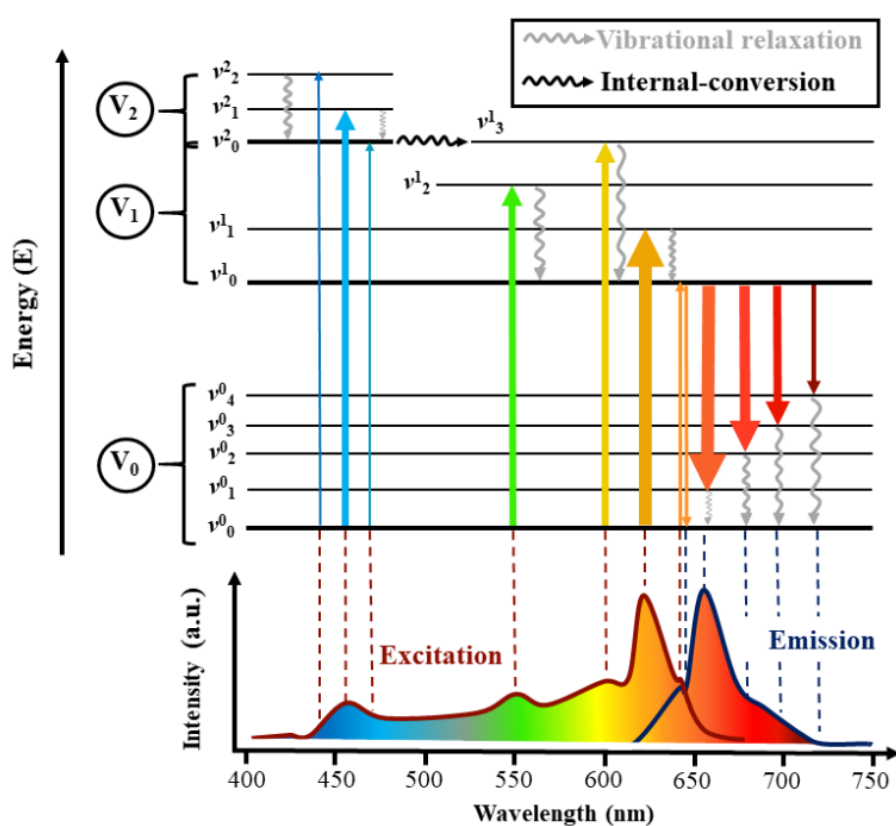


Figure C.1. Jablonski diagram representing the excitation and emission processes that define a luminescence spectrum. Adapted from Pohl in www.enzolifesciences.com (2023) [5].

In Figure C.1, arrows of varying widths illustrate the excitation and emission electronic transitions. The wider arrows represent highly probable transitions that yield intense bands in the corresponding spectrum, while thinner arrows represent unfavourable transitions that produce low-intensity bands. The probability of an electronic transition is given by the application of a series of selection rules considering the specific electronic configuration of the luminophore. If a transition fulfils the selection rules, is highly probable and is marked as “allowed”, whereas if a transition is “forbidden” means that its

probability is very low and is not kinetically favoured. Nonetheless, the rule of the spin multiplicity conservation applies to all the electronic transitions and classifies the photoluminescence phenomena as fluorescence, if the emission is allowed, or phosphorescence, if the emission is forbidden. Before the explanation of this general rule, it becomes necessary to briefly explain the concept of electron spin.

Spin (s) is a quantum number that defines the intrinsic angular momentum of an electron. It can only have a value of $\frac{1}{2}$. The spin angular momentum of an electron (m_s), which is defined as the component of spin quantum momentum parallel to the spatial z-axis, can be up ($+\frac{1}{2}$ or \uparrow) or down ($-\frac{1}{2}$ or \downarrow) oriented. The sum of all m_s electron values in a state is its total spin angular momentum (M_s). The maximum possible value of M_s is denominated total spin angular momentum quantum number (S), and $2S + 1$ gives the spin multiplicity of a state. However, the Pauli exclusion principle states that two electrons with identical m_s values cannot occupy the same quantum state, which implies that two electrons in a single atomic or molecular orbital must be antiparallel ($\uparrow\downarrow$, $S = 0$). For this reason, the multiplicity of the states is usually equal to 1 and is named singlets (S_n). Nevertheless, it can exist metastable excited states named triplets (T_n), whose multiplicity is equal to 3 because their electrons are parallel ($\uparrow\uparrow$ or $\downarrow\downarrow$, $S = 1$).

The spins multiplicity conservation principle establishes that only electronic transitions between states with the same multiplicity are allowed, i.e., a direct transition from a singlet ground state (S_0) to the excited triplet state (T_1), is not possible. However, on the contrary to fluorescence, the phosphorescent emissions do not respect this rule. Figure C.2 depicts a Jablonski diagram representing the mechanism of fluorescence and phosphorescence.

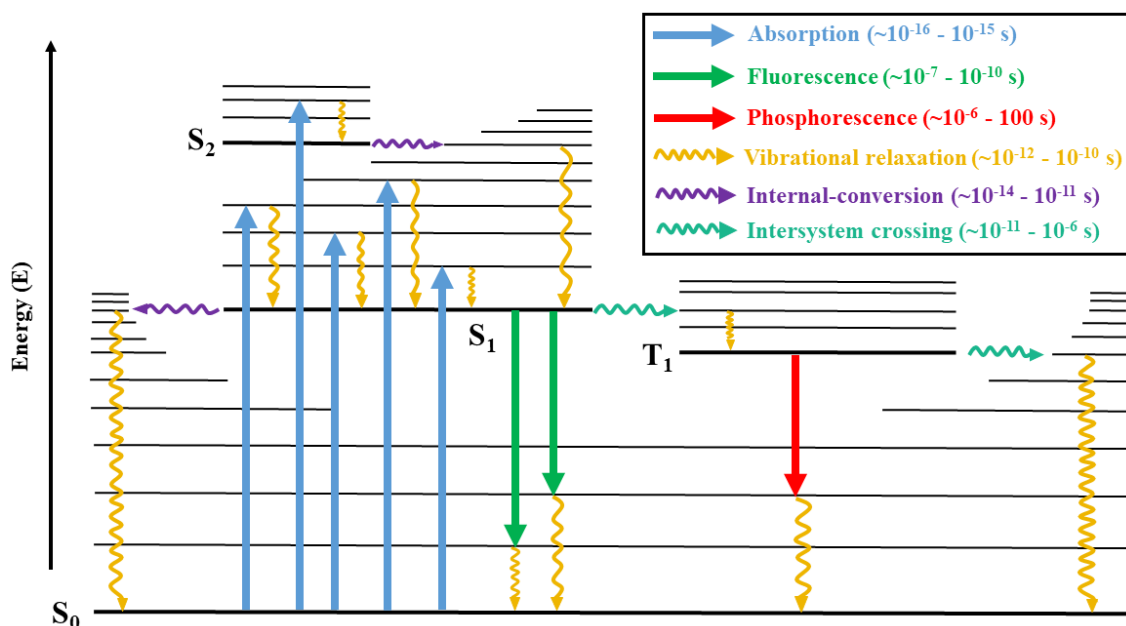


Figure C.2. Jablonski diagram illustrating radiative (fluorescence and phosphorescence) and non-radiative transitions.

As Figure C.2 illustrates, phosphorescence occurs when an electron in a singlet-excited state (S_1) is moved by fast intersystem crossing (ISC, $\sim 10^{-11} - 10^{-6}$ s) to an energetically suitable triplet-excited state (T_1). In the new state, the electrons are parallel, thus, the excited electron must flip its spin to emit a photon and be able to return to the S_0 state. As a result, the electron is deactivated through a forbidden transition, that is not kinetically favoured and will take a considerable amount of time to happen in comparison to fluorescence ($\sim 10^{-6} - 100$ s). Additionally, phosphorescence usually occurs from the vibrational ground level of T_1 to a high vibrational level of S_0 , which means that more energy is spent on vibrational relaxation and the resulting Stokes shift is bigger than fluorescence [6].

All the electronic transitions that take place in an isolated emitting centre have been considered, however, in condensed matter, the emitting centres interact with their neighbouring atoms, which means that a portion of the absorbed energy will be inevitably given up to the vibration of the crystalline lattice or amorphous network. In the lattice, the energy levels of an emitting centre depend on the average distance of the centre to their neighbouring atoms, and configurational coordinates (q_i) define this spatial position. A significant difference between electronic transitions in an isolated or in a lattice emitting centre is that the latter must follow the Franck-Condon principle. This rule establishes that not all the transitions between ground and excited state vibrational levels

are allowed; given that electronic transitions are considerably faster than nuclear motions, the new vibrational level reached by an electron in the excited states ($v^{n_1} \neq 0$) must be compatible with the configurational coordinates (q_i) of the prior vibrational level in the ground state (v^{0_i}) [7]. Figure C.3 depicts an example of a Franck-Condon scheme.

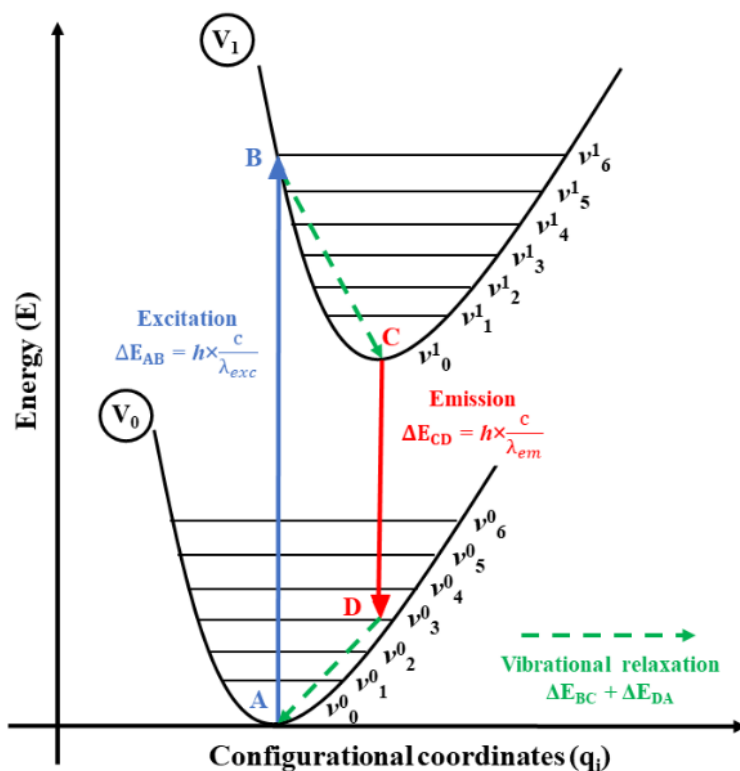


Figure C.3. Frank-Condon scheme. h = Planck's constant, and c = speed of light in vacuum.

As can be observed in Figure C.3, the energy of the excitation radiation (ΔE_{AB}) is higher than the energy of the emitted photon (ΔE_{CD}), being the difference, the non-radiative energy given up to the lattice or Stokes energy ($\Delta E_{BC} + \Delta E_{DA}$). In fact, the energy spent on lattice vibrations is the largest contribution to the Stokes shift experimented by a specific emitting centre in condensed matter, which explains why the excitation and emission spectra depicted in Figure C.1 are composed of bands instead of lines as the free luminophores. On the other hand, the intensity of the bands in photoluminescence spectra is proportional to the number of photons that participate in their corresponding electronic transition, that is, to $N_{em}(\lambda_{em})$ and $N_{exc}(\lambda_{exc})$, which are the number of photons with a specific wavelength emitted or absorbed per unit of time, respectively. However, in a given period, not all the incident photons with a specific wavelength ($N_i(\lambda_{exc})$) contribute to the excitation of the luminophores, for this reason, the emission intensity is higher than the quantum yield (Φ) as expressed in Equation C.1.

$$\Phi = \frac{\text{number of photons emitted}}{\text{number of photon absorbed}} = \frac{N_{em}(\lambda_{em})}{N_{exc}(\lambda_{exc})} = \frac{N_{em}(\lambda_{em})}{N_i(\lambda_{exc})\{1 - e^{[-\mu(\lambda_{exc})x]}\}} = \frac{k_r}{k_r + k_{nr}} \quad (\text{C.1})$$

where $\mu(\lambda_{exc})$ is the molar absorption or attenuation coefficient, which is characteristic of each material and indicates how easily a certain volume of the material can be penetrated by a beam of light of a given λ_{exc} . The thickness of the irradiated sample is given by x , and the terms k_r and k_{nr} refer to the rate constant of the radiative and non-radioactive decay paths, respectively. The term k_{nr} includes the vibrational relaxations, internal conversions, intersystem-crossings, and the energy given to the lattice vibration [8]. In addition to the quantum yield, the radiative lifetime of the excited state (τ_r) is another parameter that indicates the efficiency of a luminophore emission. With the aid of the Frank-Condon scheme of Figure C.3, we can define τ_r as the time an electron spends on point C before it radiates a photon and decays to point D . However, τ_r is not equal to the excited state lifetime (τ), because this last term englobes vibrational relaxation (transition from point B to C) and thermal activation of electrons. The excited state lifetime can be expressed as:

$$\frac{1}{\tau} = \frac{1}{\tau_r} + \frac{1}{\tau_0} e^{\frac{-\Delta E}{K_B T}} + \frac{1}{\tau_Q} \quad (\text{C.2})$$

where the second term of Equation C.2 refers to the probability of thermal activation at temperature T with an activation energy of ΔE and an excited state lifetime at 0 k of τ_0 . The thermal activation of an electron consists of the transition from the ground vibrational level of an excited state (v^n_0 , C in Figure C.3) to a higher vibrational level ($v^n_{i \neq 0}$) when the temperature rises, and once the electron reaches $v^n_{i \neq 0}$, it turns back to v^n_0 by vibrational relaxation. The third term is the probability of other non-radiative processes.

The ratio between τ and τ_r is equal to the quantum yield because they conceptually represent the same thing, i.e., the ratio between the total number of centres in a substance (N_L), and the ones that decay from the excited state by radiative emission ($N_{L,r}$). Since the term N_L is equal to the sum of $N_{L,r}$ and the number of centres that decay through non-radiative pathways ($N_{L,nr}$), the quantum yield can be expressed as follows in Equation C.3.

$$\Phi = \frac{N_{L,r}}{N_L} = \frac{N_{L,r}}{N_{L,r} + N_{L,nr}} = \frac{\tau}{\tau_r} \quad (\text{C.3})$$

Hence, the determination of τ gives relevant information concerning the processes that take place in the excited state. Nowadays, τ can be easily determined by femtosecond time-resolved UV-visible absorption spectroscopy, which is a technique that permits watching the non-radiative process in which the electrons give up part of their energy to the lattice [9–11].

To conclude, it is worth exploring the key factors that decrease the quantum yield and radiative lifetime (τ_r) of an emitting centre, these factors are the temperature, the lattice disorder, the concentration of the emitting centres, quenching by molecular energy transfer, and the size of the material [2]. Each of the following paragraphs focuses on one of the four mentioned factors.

- I. Temperature: when it is increased, the probability of thermal activation rises and, non-radiative processes deactivate the electrons. Therefore, all the emission bands of a spectrum will be broader and less intense.
- II. Order of the lattice: The bands produced by electronic transitions involving orbitals partially mixed with those of the surrounding atoms are considerably broader than the bands generated by unaffected transitions, as can be seen in the emission spectra of amorphous materials, which present bands with heterogeneous broadening. However, lattice disorder has a negligible impact on the emission of lanthanide trivalent cations, as they display sharp and intense emission lines that are almost independent of the chemical environment.
- III. Emitting centres: although the intensity of the emission depends on the total number of centres, the former is not directly proportional to the latter. In fact, a high concentration of emitting centres is detrimental to luminescence since energy transfer between centres is more likely when the average distance between them is shortened. This produces a decrease in the excited state lifetime, and by extension a decrement of the quantum yield, as stated by Equation C.3.
- IV. Quenching effect: it occurs when some molecular groups called oscillators (e.g., OH, NH, O₂ or CH) receive an energy transfer from the luminophore excited state, which consequently deactivates following a non-radiative path. The quenching effect can cause a partial loss of the emission intensity or even the complete suppression of the emission. Molecules containing these groups can be part of the

coordination sphere of a fluorescent metal complex or can be present in the media and collide with the luminophores, hindering the luminescent emission.

C.2 ELECTRONIC CONFIGURATION OF Ln^{III}

Lanthanides, the elements with atomic numbers ranging from 57 to 71, are among the elements commonly known as rare earths. The ground state electronic configuration of their trivalent ions (Ln^{III}) is [Xe] 4f^{*e*}, this means that their valence electrons (*e*) belong to the electronic sub-shell with a principal quantum number (*n*) equal to 4 and angular quantum number (*l*) equal to 3. The number of orbitals within an electronic sub-shell is given by $(2l + 1)$ because each orbital is defined by its magnetic quantum number (*m_l*), whose value varies between $-l$ and $+l$. Since each orbital has a capacity of two electrons, the total electronic capacity of lanthanide ions is 14 electrons. Each of the lanthanides, from Cerium (Ce) to Ytterbium (Yb), have incompletely filled 4f orbitals with a specific number of electrons. This gives them signature energy levels and emission wavelengths that cover all the electromagnetic spectrum: UV (Gd^{III}) [12], visible (e.g., Pr^{III}, Sm^{III}, Eu^{III}, Tb^{III}, Dy^{III}, Tm^{III}) [13–15], and near-infrared (NIR, e.g., Pr^{III}, Nd^{III}, Ho^{III}, Er^{III}, Yb^{III}, Tm^{III}) [16,17]. But the key to the unique spectroscopic and electromagnetic properties of Ln^{III}, is that the 4f orbital shape and energy are slightly affected upon exposition to neighbouring atoms, compared to transition metals, because they are inner orbitals screened by their outer 5s and 5p sub-shells.

For a given Ln^{III}, there are multiple ways to distribute the electrons in the seven 4f wavefunctions. In each possible distribution or microstate, each electron has a defined magnetic quantum number (*m_l*) and a spin quantum number ($m_s = \pm \frac{1}{2}$). Additionally, each microstate can be distinguished by its total orbital and spin angular momentum (M_L and M_S , respectively), resulting from the sum of each electron's respective quantum numbers. The number of possible microstates is the degeneracy or multiplicity of the configuration, moreover, a group of microstates that have the same energy are called a spectroscopic term. The number of these terms allows the prediction of the number of electronic transitions, therefore, the next paragraphs will describe the procedure to determine the spectroscopic terms and their application for the determination of the Eu^{III} and Tb^{III} spectroscopic ground terms.

A spectroscopic term (Γ), is determined by its microstate with the maximum M_L value, which is called total orbital angular momentum quantum number (L). The quantum

number L indicates the number of microstates due to orbital angular momentum in a term ($2L + 1$) because the M_L of a microstate has a value between $+L$ and $-L$. Nevertheless, a term is not only defined by L but the total spin and angular momentum of the microstates (M_S) must be considered as well. The spectroscopic terms are labelled with a capital letter ($\Gamma = S, P, D, F, G, H \dots$) that correspond to the possible values of L ($0, 1, 2, 3, 4, 5 \dots$), however, the term is not complete without considering the spin. The microstate with the maximum M_S value defines the total spin angular momentum quantum number of the term (S), and likewise, the number of microstates due to spin angular momentum or spin multiplicity is equal to $(2S + 1)$ in a term. Finally, if spin multiplicity is considered, the spectroscopic term symbol is written as $(^{2S+1})\Gamma$ and the overall number of microstates in a term is given by $(2L + 1) \times (2S + 1)$ [18]. Several of those spectroscopic terms are contained in the electronic configuration of an element, and the sum of their multiplicities is equal to that of the configuration. However, the only term that can be easily identified is the ground term thanks to Hund's rules, which must be applied in the following order: (i) select the largest spin multiplicity and, (ii) select the largest orbital multiplicity [19]. Regarding the lanthanides, Figure C.4 depicts the procedure commented above applied to determine the Eu^{III} and Tb^{III} ground states and overall multiplicity.

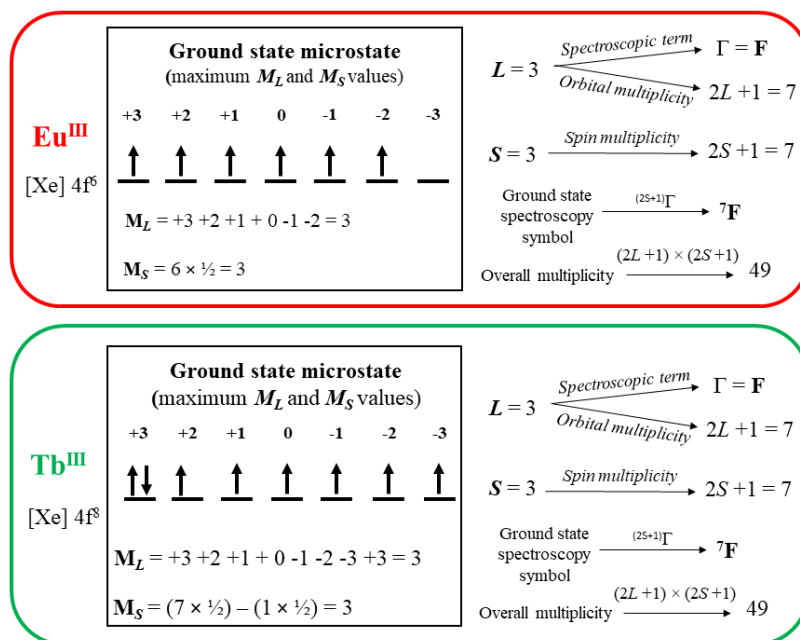


Figure C.4. Ground state spectroscopy symbol and overall multiplicity of Eu^{III} and Tb^{III} .

The procedure depicted in Figure C.4 indicates that the ground spectroscopic term for both lanthanides is the same: 7F . However, orbital and spin angular momentum do not interact with each other, although the two angular motions of the electrons do couple, and it is more relevant the higher the atomic number of the element is. Russel and Saunders defended the need to use an additional quantum number representing the total angular momentum, this new number is J , whose values are ranged from $(L + S)$ to $(L - S)$ [20]. Because of the new quantum number, each spectroscopic term is divided into a series of spectroscopic levels $({}^{2S+1}\Gamma)_J$ with a coupling multiplicity $(2J + 1)$. The sum of the coupling multiplicity is equal to the multiplicity of the term $(2L + 1) \times (2S + 1)$, and it is necessary to apply Hund's third rule to determine which the ground level is. The rule states that if the number of electrons (e) is inferior to $(2l + 1)$, J would have the minimum value (J_{min}) at the ground level, and the set of levels in the term (multiplet) would increase with increasing values of J (regular multiplet). Inversely, if e is higher than $(2l+1)$, J would have the maximum value (J_{max}) at the ground level, and the energy would increase with decreasing values of J (inverted multiplet). Figure C.5 depicts the determination of the ground level (7F_J) of Eu^{III} and Tb^{III} . Contrary to the non-coupling procedure, Eu^{III} and Tb^{III} have different ground levels, and the energy of the 7F levels of Eu^{III} increases from $J = 0$ to 6; whereas, for Tb^{III} the energy order of the levels is reversed.

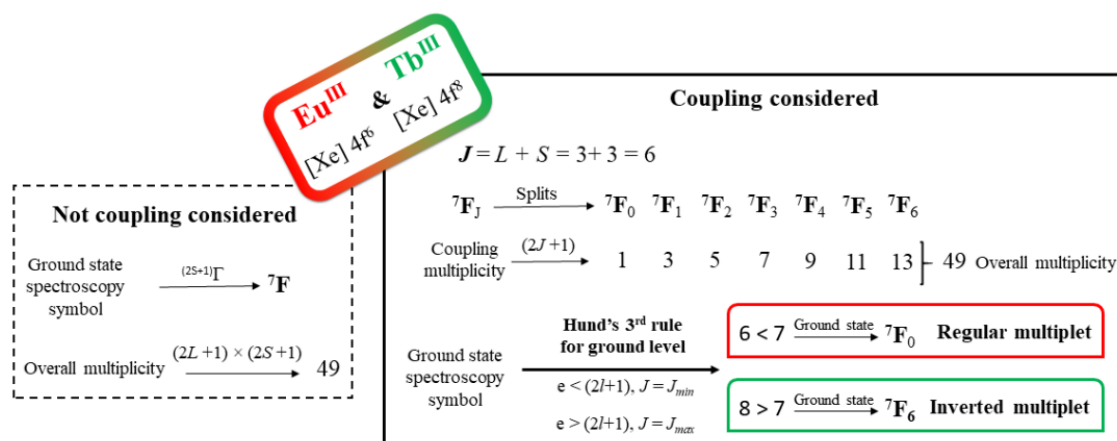


Figure C.5. Ground state spectroscopy symbol of Eu^{III} and Tb^{III} considering coupling.

All of the above refers to isolated ions with a spherical electronic configuration and degenerated $(2J+1)$ multiplicity. Nevertheless, if they are inserted in a chemical environment like a ligand field, the degeneracy of the spectroscopic levels can be partially or completely broken. The crystalline-field theory (CFT) establishes that when a negatively charged ion or ligand approaches a positively charged metal ion, the closer metal orbitals to the ligand will have their energy increased, because of the repulsion between the metal and ligand electrons, and the further orbitals to the contact zone will have their energy decreased. These alterations translate into the inevitable loss of orbital degeneration and the transition from a centrosymmetric system to a non-centrosymmetric system. Additionally, the orbitals are split into ligand-field or Stark sublevels, whose number and energy greatly differ depending on the new symmetry site of the metal: cubic, hexagonal, trigonal, tetragonal, or low symmetry. However, as it has been mentioned, thanks to the screening effect the wavefunctions of the Ln^{III} ions are not directly exposed to the orbitals of the ligands. This results in a minimum orbital mixing compared to other metal ions, which also implies that the energetic differences between levels of the ground spectroscopic term in Ln^{III} are considerably lower [19].

C.3 ABSORPTION AND EMISSION OF Ln^{III}

There electronic transitions that can take place in lanthanide trivalent cations are the intra-configurational 4f–4f transitions, the 4f–5d transitions, and charge-transfer transitions (CT). However, to explain properly these transitions, it becomes necessary to explain the main mechanism involved in the electronic absorption transitions. The mechanism of the absorption depends on which component of the light wavelength, the electric or magnetic fields, is involved in the transition. Some of these mechanisms are “even-parity”, which means that if the spatial coordinates flip during the transition, the sign of the new state wavefunction is not inverted. Inversely, in the “odd-parity” mechanisms, the wavefunction sign does invert when the coordinates are flipped. In other words, in an even-parity mechanism, the electronic transitions occur between states with the same parity (e.g., $1s \rightarrow 2s$, or $2p_x \rightarrow 2p_z$), whereas, odd-parity transitions occur between states with different parity (e.g. $2s \rightarrow 2p$). Hence, each of the transition mechanisms fulfils a parity selection rule, which determines the allowed and forbidden transitions for a given electronic configuration. Nevertheless, independently of the mechanisms, all the electronic transitions follow some common selection rules: $\Delta S = 0$,

and transitions between two $J = 0$ states are forbidden [21]. Table C.1 summarize the parity and selection rules of the main three transition mechanisms: electric-dipole (ED), magnetic-dipole (MD) and electric-quadrupole (EQ).

Table C.1. *Electronic transition mechanism and their parity and selection rules.*

Mechanism	Parity	ΔL	ΔJ	Transition intensity
Electric-dipole (ED)	odd	$0, \pm 1$	$0, \pm 1$	the more intense mechanism is the dominant effect when an electron interacts with light.
Magnetic-dipole (MD)	even	0	$0, \pm 1$	$\sim 10^5$ times weaker than ED
Electric-quadrupole (EQ)	even	$0, \pm 1, \pm 2$	$0, \pm 1, \pm 2$	much weaker than MD

The next paragraphs will focus on the specific electronic absorption transitions of the trivalent cations: the 4f–4f transitions, the 4f–5d transitions, and charge-transfer transitions (CT).

The 4f–4f transitions usually yield sharp absorption spectral bands due to their intra-configurational nature and the screening effect. MD and EQ mechanisms are allowed since 4f–4f are intra-configurational transitions. However, EQ transitions are so weak that they are not usually observed in the emission spectra of Ln^{III} ions. Additionally, although the intensity of MD transitions is practically not affected by the chemical environment, is not high [22]. Conversely, in isolated Ln^{III} ions the ED 4f–4f transitions are forbidden since Laporte's selection rule establishes that for centrosymmetric atoms the electronic transitions between states of the same parity cannot be connected with ED transitions. However, as it was previously explained, when Ln^{III} ions are in a crystalline field the orbitals degeneracy is partially revoked, which allows non-centrosymmetric interactions between electronic states of different parity. Therefore, under the influence of the crystal field, the selection rules of the ED for 4f–4f transitions are more relaxed compared to the ones depicted in Table C.1: $\Delta L \leq 6$, and $\Delta J \leq 6$ if the initial or final J are 0. Nevertheless, the newly induced electric-dipole transitions (IED) are only partially allowed, which implies that their intensity is lower than conventional ED transitions and they usually have the same order of magnitude as MD transitions. Besides, the radiative lifetime of the excited states is very long (1–11 ms for Eu^{III} and 1–9 ms for Tb^{III} transitions) [19]. To conclude, it is worth mentioning that some IED transitions are

hypersensitive to minimal alterations of the Ln^{III} environment like Eu^{III} transitions where $\Delta J = 2$ or 4 [23,24].

In 4f–5d or 4f^e–4f^{e-1}5d¹ transitions the promotion of an electron from one 4f orbital to an external 5d sub-shell occurs through the ED mechanism since a change of state parity is required. These transitions require higher energy than the 4f–4f transitions, and although they have a higher radiative emission probability their radiative lifetime is usually short (10–100 nanoseconds). The energy of 4f–5d transitions largely depends on the environment of the Ln^{III} ion, since the orbitals of the ligands interact directly with the external 5d orbitals; this also explains why the bands associated with these transitions are broad. Another important fact is that 5d–4f emissions are extremely sensitive to temperature because the emission intensity can be quenched even at low temperatures. Additionally, an interesting characteristic of 4f–5d transitions is that their absorption can be produced by ionizing radiation to yield 5d–4f fluorescence emission in return, which is why some lanthanides have been used as dopants in scintillator materials [25]. Finally, it is important to mention that 4f–5d transitions have been mainly observed on Eu^{II} , Ce^{III} , Pr^{III} and Tb^{III} spectra [26,27].

Charge-transfer transitions are intersystem crossing transitions that can be divided into two types depending on the direction of the electronic distribution between the metal and the ligands: ligand-to-metal (LMCT) or metal-to-ligand (MLCT) transitions. LMCT transitions occur when an electron in a bonding σ or π molecular orbital of a ligand, is excited and transferred to one of the 4f orbitals of a Ln^{III} ion; these transitions are relatively common for Eu^{III} ions, nevertheless, the opposite can be said about Tb^{III} [28]. Reversely, MLCT consists of the transfer of an electron from a metal 4f orbital to an antibonding π^* molecular orbital of the ligand. Efficient MLCT transitions have been proven possible from Yb^{III} , Er^{III} and Nd^{III} ions to transition metals (ruthenium, osmium, rhenium and more), however, the energy transfer is inefficient or do not even occur when Eu^{III} and Tb^{III} are used [29].

The 4f–4f emission transitions are the ones that have been considered for the sensor designed in *Chapter 6*. The excitation to a higher 4f level requires the absorption of photons with $\lambda_{\text{exc}} < 578$ nm for Eu^{III} , and $\lambda_{\text{exc}} < 490$ nm for Tb^{III} [24]. Equally to the absorption, 4f–4f emission can be achieved through IED or MD, nevertheless, while all the emission transitions of Tb^{III} consist of combinations of IED and MD mechanisms, some of the Eu^{III} transitions are either purely IED or MD [22]. Sharp bands (almost lines)

form the emission spectra of the Ln^{III} ions contrary to organic molecules (spectrum of Figure C.1). When an electron absorbs a photon and is promoted to a 4f orbital of higher energy, the chemical bonds between ligands and the Ln^{III} are barely affected, since 4f orbitals do not participate actively in the orbital binding between lanthanide ion and the ligands. Consequently, the interatomic distances remain almost unaltered, which is traduced in the sharp lines and low stokes shift (in Figure C.3 Δq_i between points A and C would be lower for Ln^{III}). Additionally, in the emission spectra the bands are spaced by a few nanometres because as mentioned at the end of *Annexe C.2*, the energy gaps between levels of the ground spectroscopic term of Ln^{III} ions are low. The more relevant emission transitions of Eu^{III} and Tb^{III} are shown in Table C.2.

Table C.2. Main 4f–4f emission transitions of Eu^{III} and Tb^{III} ions in aqueous media, corresponding approximate emission wavelengths (λ_{em}), relative emission intensities, mechanisms for each transition, and corresponding energy bandgap between emissive and final state. Data obtained from [19,22,24].

Ln ^{III}	Ground state	Emissive state	Final state	λ_{em} (nm)	Relative intensity	Mechanisms ^a	Energy gap ^b (cm ⁻¹)
Eu	⁷ F ₀	⁵ D ₀	⁷ F ₀	580	weak	IED or MD	17.300
			⁷ F ₁	590	strong	Only MD	16.900
			⁷ F ₂	615	strong	Only IED-H	16.300
			⁷ F ₃	650	very weak	IED or MD	15.400
			⁷ F ₄	720	medium	Only IED-H	14.450
			⁷ F ₅	750	weak	IED or MD	13.450
			⁷ F ₆	820	weak	Only IED	12.300
Tb	⁷ F ₆	⁵ D ₄	⁷ F ₆	460	medium-strong	IED or MD	20.400
			⁷ F ₅	540	strong	IED or MD	18.450
			⁷ F ₄	580	medium	IED or MD	17.100
			⁷ F ₃	620	medium-weak	IED or MD	16.100
			⁷ F ₂	650	weak	IED or MD	15.500
			⁷ F ₁	660	very weak	IED or MD	15.050
			⁷ F ₀	675	very weak	IED or MD	14.800

^a–Mechanism: magnetic-dipole (MD), induced electric dipole (IED), hypersensitive induced electric dipole (IDE-H); ^b–approximate energy band gaps obtained from energy level diagram of [24].

There are some topics about the electronic transitions depicted in Table C.2, which are worth mentioning. In regards to Eu^{III}, some transitions can be used to provide a diagnostic of the ion environment: ⁵D₀ → ⁷F₀ emissions are only allowed when the ion is at a low symmetry site and can yield multiple bands if there are more than one type of emitting Eu^{III} (different complexes or binding sites). Due to the pure MD character of ⁵D₀ → ⁷F₁, its emission intensity is independent of the chemical environment; thus, it can be

used as an internal reference. The $^5D_0 \rightarrow ^7F_1$ and 7F_2 transitions can contribute up to three and five bands in emission spectra, respectively; these bands only yield the maximum number of emission bands when there is a heterogeneity of emitting centres. As has been stated, Eu^{III} emission bands can provide valuable information relative to the metal surroundings, however, that is not the case with Tb^{III} emission bands. To conclude, although none of the Tb^{III} transitions is hypersensitive, the more sensitive to the chemical environment are $^5D_4 \rightarrow ^7F_6$, 7F_4 and 7F_2 . On the other hand, despite the $^5D_4 \rightarrow ^7F_0$ and 7F_1 transitions are not affected by the environment, their emission is always very weak.

C.4 SENSITIZATION OF Ln^{III} BY ANTENNA LIGANDS (AL)

As explained in *Annexe C.1*, once the electrons reach the excited state, they are not only deactivated radiatively but also through non-radiative processes. As stated in the aforementioned section, the relationship between both deactivation pathways is given by the quantum yield (Φ), which is closely related to the radiative lifetime (τ_r). Nevertheless, Φ refers to the balance of the overall emitted photons of a substance, which makes it necessary to define a new parameter, the intrinsic quantum yield ($\Phi_{\text{Ln}}^{\text{Ln}}$) that only considers the photons involved in 4f transitions. This new parameter, which can be calculated using Equation C.1 and Equation C.3, indicates how relevant are the non-radiatively deactivation processes of the excited 4f level.

However, it does not matter if the $\Phi_{\text{Ln}}^{\text{Ln}}$ is high, isolated Ln^{III} ions always yield low-intensity emissions. This is due to the not fully allowed IED mechanism of 4f–4f transitions, which makes improbable the direct excitation to excited 4f levels; in fact, the absorption coefficient of Ln^{III} ions is quite low ($\mu(\lambda_{\text{exc}}) \sim 0.1 \text{ M}^{-1} \text{ cm}^{-1}$) [30]. There are two approaches to solve this obstacle: to use a high-intensity excitation source, which is not an energetically efficient process; or to cause the indirect excitation of the lanthanides through the process named luminescence sensitization or antenna effect. The last approach, which is the standard course of action in Ln^{III} chemistry, consists of embedding a metal ion in a matrix or coordination sphere where one of the components is a good light harvester. Upon irradiation, an electron of the harvester compound is promoted to a higher energy level and then it deactivates non-radiatively through an energy charge transfer to the metal ion.

The light harvesters or antenna ligands (AL) are usually organic molecules that contain a chromophore group with a high $\mu(\lambda_{\text{exc}})$ and usually absorb above 330 nm, such

as aromatic rings or unsaturated bonds that perform $\pi \rightarrow \pi^*$ and $n \rightarrow \pi$ electronic transitions, respectively. In the coordination chemistry of lanthanide ions, the more used AL are heteroaromatic polydentate ligands that can establish more than a stable coordination bond (usually 2 or 3) with the lanthanides to yield chelates. Because lanthanide ions are hard Lewis's acids, bonds with the heteroaromatic ligands are established through their functional groups containing a charged donor atom, such as oxygen, fluoride, sulphur, or nitrogen. Lanthanide coordination complexes or chelates (Ln-AL) usually contain multiple AL, since the coordination number of Ln^{III} (9 for Eu^{III} and 8 for Tb^{III}) allows it [31]. Given the inner character of the 4f orbitals, the bonds that the Ln^{III} forms with the AL are mainly electrostatic, therefore, in Ln-ALs the energy levels are considered ligand or metal-centred. Figure C.6 represent a Jablonski diagram of all the processes that can be involved in the energy transference from the antenna ligand to a Ln^{III} ion (in this case is illustrated with Eu^{III}).

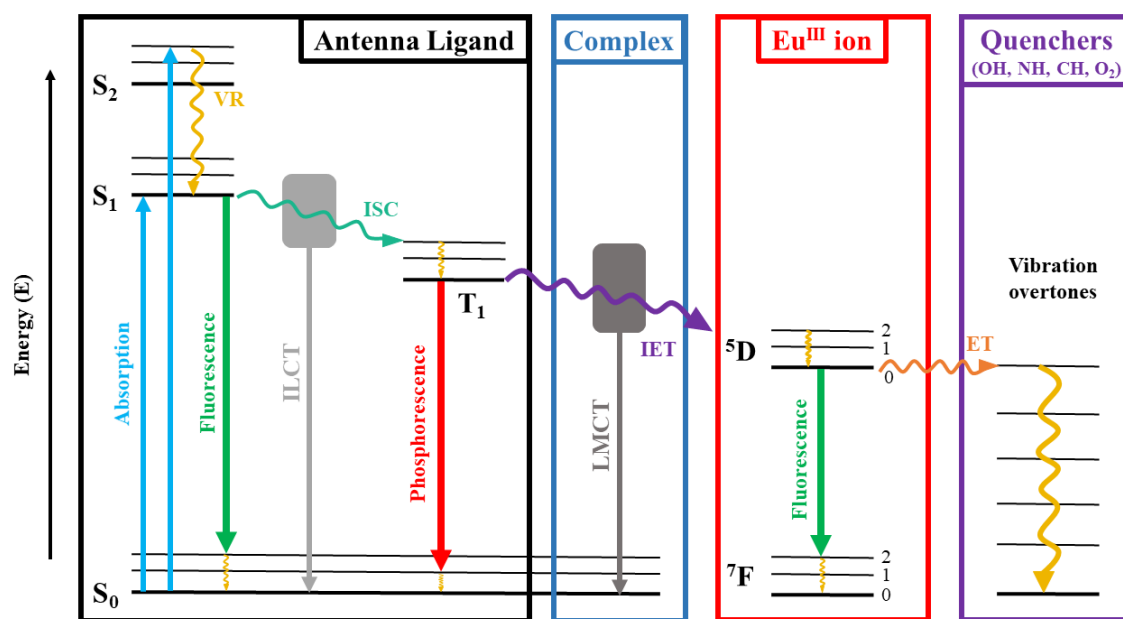


Figure C.6. Jablonski diagram illustrating the possible processes that take place in the sensitization of Ln^{III} through antenna ligand effect, as well as the luminescence quenching by oscillating groups. Flat and curved arrows represent radiative and non-radiative pathways, respectively. S = singlet states, T = triplet state, ILCT = inter-ligand charge transfer, LMCT = ligand-to-metal charge transfer, VR = vibrational relaxation, ISC = intersystem charge transfer, IET = intramolecular energy transfer, ET = energy transfer. Adapted from Capelletti et al. (2017) [32].

As depicted in the Jablonski diagram, the process begins with the promotion of an electron in the singlet ground state (S_0), to a higher singlet energy level (S_1). Then, the electron performs an intersystem crossing (ISC) to reach the long-lasting triplet state (T_1), where intramolecular energy transfer (IET) to Ln^{III} is favoured over the forbidden phosphorescence emission. IET can be produced by two different mechanisms depending on the distance between the ligand and the metal [19]: (i) the Dexter mechanism, which requires short distances (30–50 pm) and consists of the mutual electronic exchange between the metal and the ligand ($T_1 \rightarrow {}^5D_J$ simultaneously to ${}^7F_J \rightarrow S_0$); and (ii) the Förster mechanism, which can operate at a distance up to 1000 pm, and consist on the energy transference from an electron in T_1 to a metal electron in 7F_J . Whichever the mechanism, IET is followed by the ${}^5D_J \rightarrow {}^7F_J$ radiative emission of the Ln^{III} . However, as we can see in Figure C.6, other processes can hinder the energy transference process to the metal, since they produce the non-radiative back energy transfer to the ligands. Those processes are mainly the intra-ligand charge transfers (ILCT) and the ligand-to-metal charge transfers (LMCT). The former is favoured in complexes with low-energy ILCT states, and the latter is common in Ln^{III} with low-energy charge transfer excited states like Eu^{III} [28]. Finally, the quenching effect is also represented in Figure C.6. This occurs when oscillators, chemical bonds in the ligand or the solvent molecules, cause the non-radiative deactivation of the lanthanide's excited state through energy transfer (ET). This quenching effect of the luminescence is the key to our OFSLn-AL measurement mechanism because it allows correlating the decrease of the emission luminescence with the amount of physisorbed water vapour.

To conclude with this section about the luminescence of lanthanides, it should be mentioned that not all chromophores can be used as AL since several conditions must be fulfilled [32].

1. As mentioned above a high $\mu(\lambda_{exc})$ is needed.
2. The T_1 state of the chromophore should have a similar energy to that of the Ln^{III} excited states.
3. The AL's chromophore should be in proximity to the Ln^{III} .
4. A high yield of the chromophore intersystem crossing is required.
5. The AL should saturate the coordination sphere of the Ln^{III} to avoid full deactivation by water.
6. The formed complexes must be thermostable and kinetically inert.

Additionally, to these conditions, in the search for a suitable Ln-AL for our luminescent OFS, we had to focus on water-soluble molecules that can establish strong and non-reversible bonds with the Ln^{III}. The reason is that we need a probe whose luminescent emission can gradually decrease upon exposure to water vapour, thus, we need deactivation by collisional quenching with the physisorbed water molecules rather than instantaneous deactivation by the entry of water molecules in the coordination sphere of the metal.

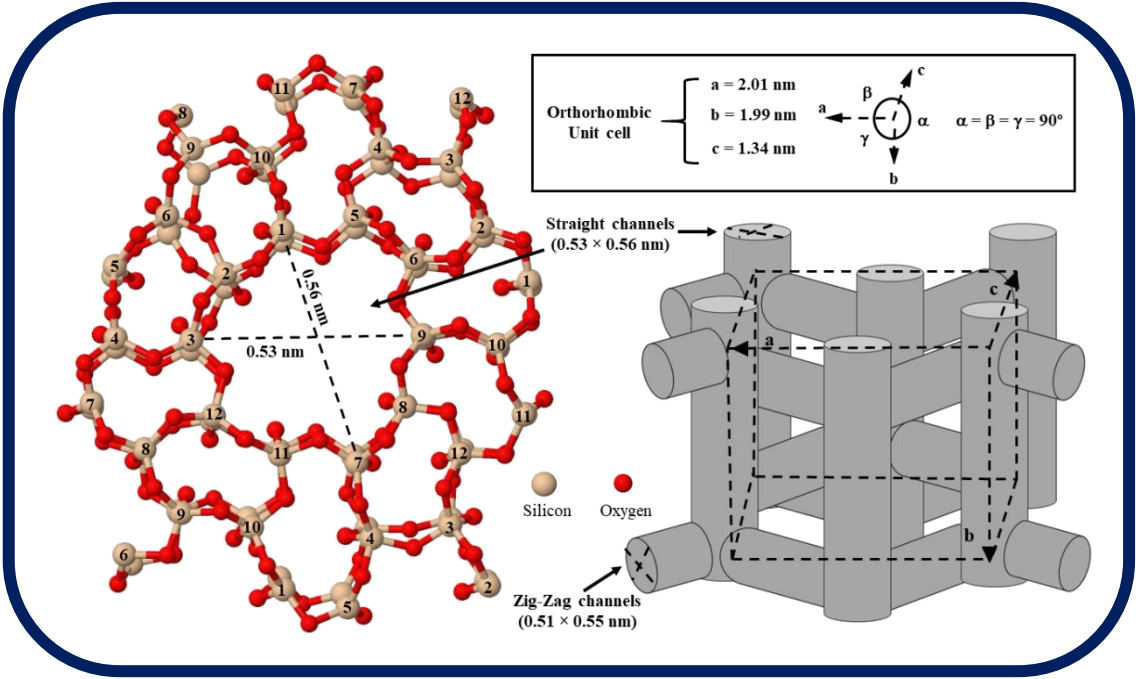
C.5 REFERENCES

- [1] Valeur, B.; Berberan-santos, N. A. *J. Chem. Educ.* **2011**, *88*, 731–738.
- [2] Capelletti, R. Luminescence. In *Encyclopedia of condensed Matter Physics*; Bassani, F., Liedl, G. L., Wyder, P., Eds.; Elsevier Ltd: Parma. Italy, **2005**; p. 178–189.
- [3] Ronda, C. R. *Luminescence From Theory to Applications*; Ronda, C.R., Ed.; Wiley-VCH Verlag GmbH & Co. KGaA, **2008**.
- [4] Lenci, F.; Checcucci, G.; Sgarbossa, A.; Martin, M. M.; Plaza, P.; Angelini, N. Fluorescent Biomolecules. In *Encyclopedia of Condensed Matter Physics*; Elsevier Ltd, **2005**; p. 222–235.
- [5] Pohl, H. What is the difference between fluorescence, phosphorescence and luminescence? Available online: <https://www.enzolifesciences.com/science-center/technotes/2019/december/what-is-the-difference-between-fluorescence-phosphorescence-and-luminescence?/>. (accessed on June, 12, **2023**).
- [6] Lakowicz, J. R. Introduction to Fluorescence. In *Principles of fluorescence spectroscopy*; Lakowicz, J. R., Ed.; Springer: New York, USA, **2006**; p. 1–5.
- [7] Frank, J. *Trans. Faraday Soc.* **1926**, *21*, p. 536–542.
- [8] Wong, K. L.; Bünzli, J. C. G.; Tanner, P. A. *J. Lumin.* **2020**, *224*, p. 117256.
- [9] Malone, R. J.; Miller, A. M.; Kohler, B. *Photochem. Photobiol.* **2003**, *77*, p. 158.
- [10] Martínez-Fernández, L.; Pepino, A. J.; Segarra-Martí, J.; Jovaišaitė, J.; Vaya, I.; Nenov, A.; Markovitsi, D.; Gustavsson, T.; Banyasz, A.; Garavelli, M.; Improta, R. *J. Am. Chem. Soc.* **2017**, *139*, p. 7780–7791.
- [11] Lednev, I. K.; Ye, T. Q.; Matousek, P.; Towrie, M.; Foggi, P.; Neuwahl, F. V. R.; Umapathy, S.; Hester, R. E.; Moore, J. N. *Chem. Phys. Lett.* **1998**, *290*, p. 68–74.
- [12] Pathak, M. S.; Singh, N.; Singh, V.; Watanabe, S.; Rao, T. K. G.; Lee, J. K. *Mater. Res. Bull.* **2018**, *97*, p. 512–516.
- [13] Andres, J.; Chauvin, A. S. Colorimetry of Luminescent Lanthanide Complexes. *Molecules* **2020**, *25*, p. 4022.

- [14] Hong, Z.; Liang, C.; Li, R.; Zang, F.; Fan, D.; Li, W.; Hung, L. S.; Lee, S. T. *Appl. Phys. Lett.* **2001**, *79*, p. 1942–1944.
- [15] Agger, S. D.; Povlsen, J. H. *Opt. Express* **2006**, *14*, p. 50.
- [16] Liu, F.; Liang, Y.; Pan, Z. *Phys. Rev. Lett.* **2014**, *113*, p. 1–5.
- [17] Wu, H.; Yang, Z.; Liao, J.; Lai, S.; Qiu, J.; Song, Z.; Yang, Y.; Zhou, D. *Opt. Letters* **2014**, *39*, p. 918–921.
- [18] Landskron, K. Coordination Chemistry IV - Electronic Spectra. In *Inorganic Coordination Compounds*; LibreTexts: Bethlehem, Pennsylvania, Unites states, **2023**.
- [19] Bünzli, J.-C.G.; Eliseeva, S. V. Basics of Lanthanide Photophysics. In *Lanthanide Luminescence: Photophysical, Analytical and Biological Aspects*; Hänninen, P., Härmä, H., Eds.; Springer-Verlag: Berlin, Germany, **2010**.
- [20] Russell, H. N.; Saunders, F. A. *Astrophys. J.* **1925**, *61*, p. 38–69.
- [21] Karaveli, S.; Zia, R. Optical Frequency Magnetic Dipole Transitions. In *Encyclopedia of Nanotechnology*; Bhushan, B., Ed.; Springer Dordrecht, **2012**; p. 1942–1950.
- [22] Werts, M. H. V.; Jukes, R. T. F.; Verhoeven, J. W. *Phys. Chem. Chem. Phys.* **2002**, *4*, p. 1542–1548.
- [23] Parker, D. Rare Earth Coordination Chemistry in Action: Exploring the Optical and Magnetic Properties of the Lanthanides in Bioscience While Challenging Current Theories. In *Handbook on the Physics and Chemistry of Rare Earths*; Elsevier B.V., **2016**; Vol. 50, p. 269–299.
- [24] Richardson, F. S. *Chem. Rev.* **1982**, *82*, p. 541–552.
- [25] Qin, X.; Liu, X.; Huang, W.; Bettinelli, M.; Liu, X. *Chem. Rev.* **2017**, *117*, p. 4488–4527.
- [26] Zhou, R.; Lin, L.; Liu, C.; Dorenbos, P.; Tao, Y.; Huang, Y.; Liang, H. *Dalton Trans.* **2018**, *47*, p. 306–313.
- [27] Shangda, X.; Tao, C.; Changkui, D. *J. rare earths* **2006**, *24*, p. 400–407.
- [28] Dorenbos, P. *J. Alloys Compd.* **2009**, *488*, p. 568–573.
- [29] D'Aléo, A.; Pointillart, F.; Ouahab, L.; Andraud, C.; Maury, O. *Coord. Chem. Rev.* **2012**, *256*, p. 1604–1620.
- [30] Trupp, L.; Marchi, M. C.; Barja, B. C. *J. Sol-Gel Sci. Technol.* **2022**, *102*, p. 63–85.
- [31] Moore, E. G.; Samuel, A. P. S.; Raymond, K. N. *Acc. Chem. Res.* **2009**, *42*, p. 542–552.
- [32] Capelletti, R.; Kalyani, N. T.; Swart, H.; Dhoble, S. J.; Kalyani, N. T.; Swart, H.; Dhoble, S. J. Luminescence: Basic Principles and Applications. In *Principles and Applications of Organic Light Emitting Diodes (OLEDs)*; Kalyani, N. T., Swart, H., Dhoble, S. J., Eds.; Elsevier Ltd, **2017**.

ANNEXE D

MODIFIED TITANIUM SILICALITES AND PHOTOCATALYSIS



ANNEXE D

MODIFIED TITANIUM SILICALITES AND PHOTOCATALYSIS

D.1 INTRODUCTION TO TITANIUM SILICALITES (TS)

Titanium silicalite-1 (TS-1) is one of the first zeolite containing a transition metal cation (Ti^{IV}) in framework positions, and the first developed material of the big family of catalytic active titanosilicalite zeolites e.g., TS-2, Ti-beta, Ti-ZSM-11, Ti-MWW, among others [1–5]. Nowadays, TS-1 is a well-known catalyst used in the partial oxidation of organic reactants by hydrogen peroxide in aqueous media. This material results as a promising catalyst from an industrial perspective because contrary to other oxide metals of Groups IV-VI, titanium catalytic performance in the cited reaction is excellent, the hydrophobic properties of the TS-1 pores prevent the deactivation of the Ti active sites by water molecules in aqueous media reactions, and they have uniform micropores, high specific surface areas, large pore volumes and good stability [6,7]. As is depicted in the schematic of Figure D.1, some of the main catalytic applications of TS-1 are epoxidation of olefins [8–10], hydroxylation of aromatic compounds [11], oxidation of S-compounds [12], ammoximation of cyclohexanone [13], among others.

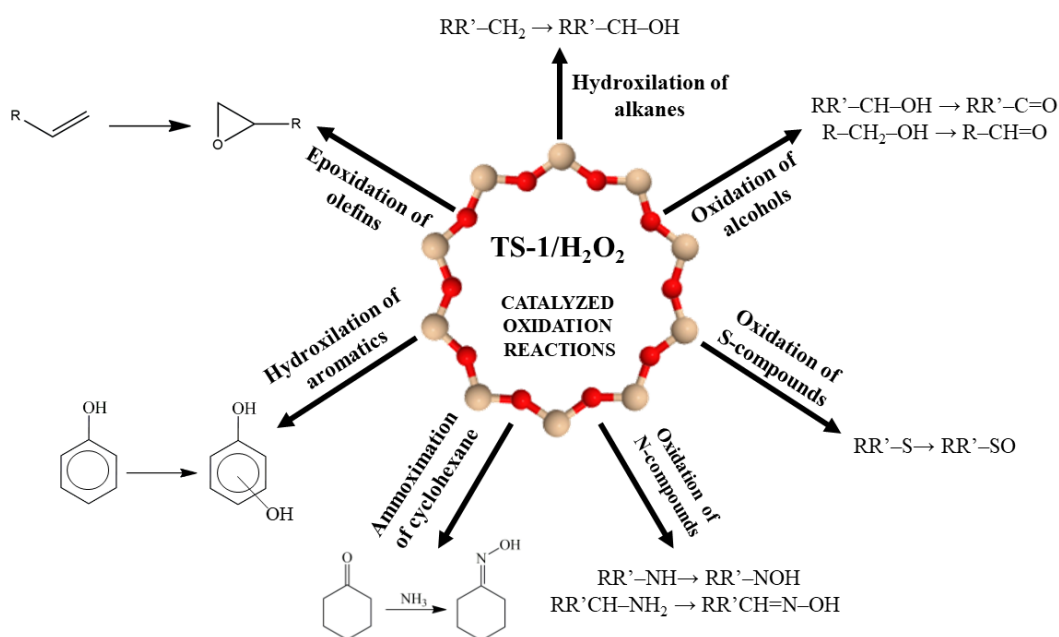


Figure D.1. Main oxidation reactions catalysed by TS-1. Adapted from Millini et. al. (2022) [14].

TS-1 was synthesised for the first time by Taramasso *et al.* (1983) [15], who achieved the isomorphous substitution of Si by Ti in the modernite framework-inverted (MFI) structure of silicalites. Later, in the '90s, research about this material was focused on the different coordination states of Ti [16], and the development of characterisation techniques (XRD diffraction; UV-Vis diffuse reflectance, FTIR and Raman spectroscopies; among others) to ascertain the correct inclusion of Ti in the MFI framework [1]. Nowadays, there is a consensus that the isolated tetrahedrally coordinated Ti^{IV} ions in the Zeolite MFI structure, generate the active sites for plenty of selective oxidation reactions.

The MFI structure of Silicalites-1 (S-1) results from the combination of two interconnected straight and zig-zag channel systems. The channels are composed of 10-member silicon rings $[(\text{SiO})_{10}]$ that arise from the union of pentasil silicalite chains, and the straight channels are directed down the *b* crystallographic axis while the zig-zag channels are connected to the formers through the *a*-axis [17]. The replacement of Si^{+4} from a $(\text{SiO})_{10}$ by Ti^{+4} should not be possible, since the higher ionic radius of tetrahedrally coordinated titanium cations, compared to tetrahedrally coordinated silicon cations ($56 > 41\text{pm}$), is not compatible with the monoclinic unit cell of these materials structure. Nevertheless, the MFI structure is flexible enough to transform the unit cell from monoclinic to orthorhombic to allow the inclusion of Ti^{IV} cations [15]. In fact, neutron diffraction analyses have demonstrated that Ti atoms can occupy simultaneously four or five of the 12 crystallographic tetrahedral sites (T sites) of the MFI structure, although there is still debate about the preferential T-sites of Ti and it has been proposed that they depend on the TS-1 synthesis procedure [18–20]. The MFI orthorhombic structure of TS-1 with its numbered T-sites, as well as the interconnected channel system of the MFI structure, are depicted in Figure D.2.

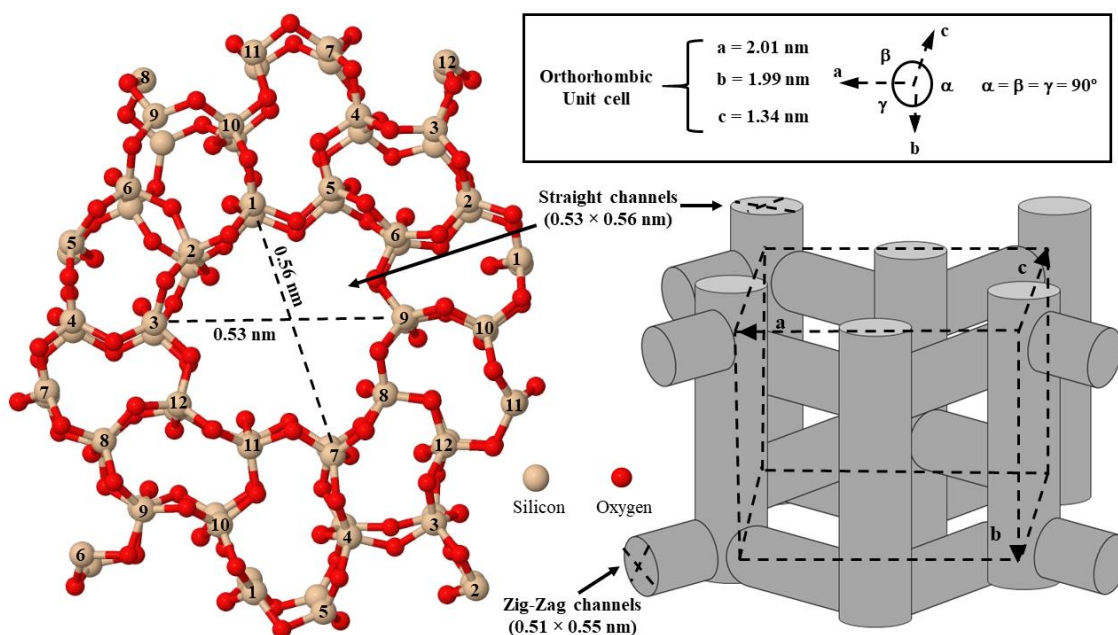


Figure D.2. Orthorhombic TS-1 structure with their different T-sites labelled (*left*) and the interconnected channel system (*right*) with their unit cell parameters.

The replacement causes the expansion of the unit cell volume, but when a certain limit is reached, no more Ti^{IV} is accepted in the framework and extra-framework species are formed. In fact, physicochemical characterizations of TS-1 have demonstrated that a maximum of 2.5 atom % of Ti can be present in these materials in tetrahedral coordination (TiO_4) [21]. Since Ti ions in framework positions are metastable, they are prone to reversely expand their coordination number and change their geometry when they adsorb certain molecules such as H_2O , H_2O_2 and NH_3 ; this explains the remarkable catalytic properties of these Ti species in certain oxidation reactions. For instance, it is widely accepted that in the oxidation of propylene the tetra-coordinated Ti^{IV} cation acts as a Lewis acid site accepting electrons from H_2O_2 and expanding its coordination sphere to generate the Ti-OOH reaction intermediate, which subsequently oxidizes the propylene by oxygen transfer [22,23].

As it was mentioned above, non-framework Ti species can be formed when the amount of Ti surpasses the limit of Ti in the MFI framework. Still, they can also be generated because of the mismatch between the hydrolysis rates of the titanium and silicon sources during the synthesis. Since Ti precursors such as titanium (IV) ethoxide (TEOT); butoxides (TBOT); or isopropoxide (TTIP), have considerably faster hydrolysis rates than silicon precursors such as tetraethoxy or tetramethoxysilanes (TEOS and TMEOS, respectively), they tend to oligomerize and precipitate forming non-framework

hexa-coordinated Ti^{IV} (TiO_6) in form of crystalline TiO_2 anatase [24]. Considerable efforts have been made to avoid the formation of anatase in the synthesis of TS-1 (see *Annexe D.2*), because it can decompose H_2O_2 , severely hindering the catalysed oxidation reactions [25], TiO_4 species exhibit much higher photocatalytic activity than TiO_6 , the predominant species in anatase [26], and it can block the micropores of the TS-1, hindering the diffusion of the reactants or even producing the complete deactivation of the catalyst [27]. Nevertheless, amorphous Ti species can be formed during the synthesis of TS-1 in addition or instead of anatase. In a simultaneously experimental and DFT simulation study of commercial TS-1 sieves, Signorile *et al.* (2020) determined that among the theoretically possible defective Ti-sites in these materials (see Figure D.3), hexa-coordinated Ti species with a local symmetry close to octahedral are present in the materials [28].

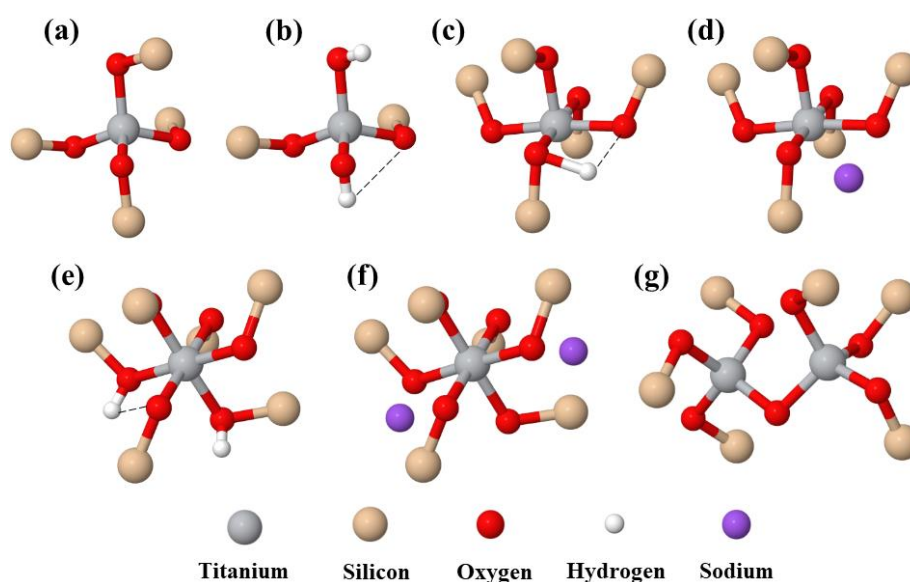


Figure D.3. (a) Tetracoordinated Ti and defective Ti sites in TS-1 structure: (b) bipodal tetracoordinated Ti; (c) H-terminated pentacoordinated Ti; (d) Na-terminated pentacoordinated Ti; (e) H-terminated hexacoordinated Ti; (f) Na-terminated hexacoordinated Ti; and (g) dimeric tetracoordinated Ti. Adapted from Signorile *et al.* (2020) [28].

Interestingly, a thorough UV-Raman spectroscopy study of post-treated TS-1 materials performed by Wang *et al.* (2023), proved that extra-framework penta- and hexa-coordinated Ti^{IV} species are highly active Ti-sites for the epoxidation of propylene [29]. Additionally, Yao *et al.* (2023) achieved excellent results in the alkene epoxidation and in the oxidative desulfurization of dibenzothiophene using a hierarchical TS-1 zeolite with a high concentration of TiO_6 [30]. DFT calculations performed by Gordon *et al.* (2020), suggest that the active Ti centre in epoxidation reactions can be composed of

dimeric Ti species (depicted in Figure D.3g) instead of the traditional perfect tetrahedral Ti framework species [31]. Therefore, although there is still controversy about the role of amorphous Ti species in the oxidation reactions catalysed by TS-1, it is clear that TiO_4 species are not the only active sites.

Aside from the amount and proportion of Ti species, other factors modulate the catalytic efficiency of TS-1 materials, such as the particle size, pore diameter and surface hydrophobicity. Regarding the first factor, van der Pol *et al.* (1992) concluded that particle sizes lower than 0.3 μm are needed to obtain high activity and high production yield in TS-1 catalysed reactions [32]. Small particle sizes, in addition to large surface areas and average pore diameter larger than the standard 0.55 nm channels of the MFI structure, produce a decrease in the diffusion limitations of reactants and more activated catalytic centres [33,34]. However, excessively large mesoporous should be avoided in TS-1 catalysts because it causes instability of the MFI structure and as a consequence, the catalytic activity decreases. Finally, several studies have reported that the modification of superficial Si–OH and Ti–OH bonds increases the hydrophobicity of TS-1 materials and prevents side reactions between water and the active Ti centres. Moreover, it favours the diffusion of reactants through the channels, thus improving the catalytic performance [30,35,36].

D.2 SYNTHESIS OF TITANIUM SILICALITES

Due to the increasing interest in obtaining TS-1 materials with enhanced catalytic performances and lower costs, great efforts have been in the development of new strategies for their synthesis. This is evidenced by the multiple published reviews found in the literature, which are focused on improving different aspects of the resulting materials: cost, regulation of Ti species, mass transfer through control of the porous texture, and so on [37–41]. A scheme of the most used synthesis routes is shown in Figure D.4.

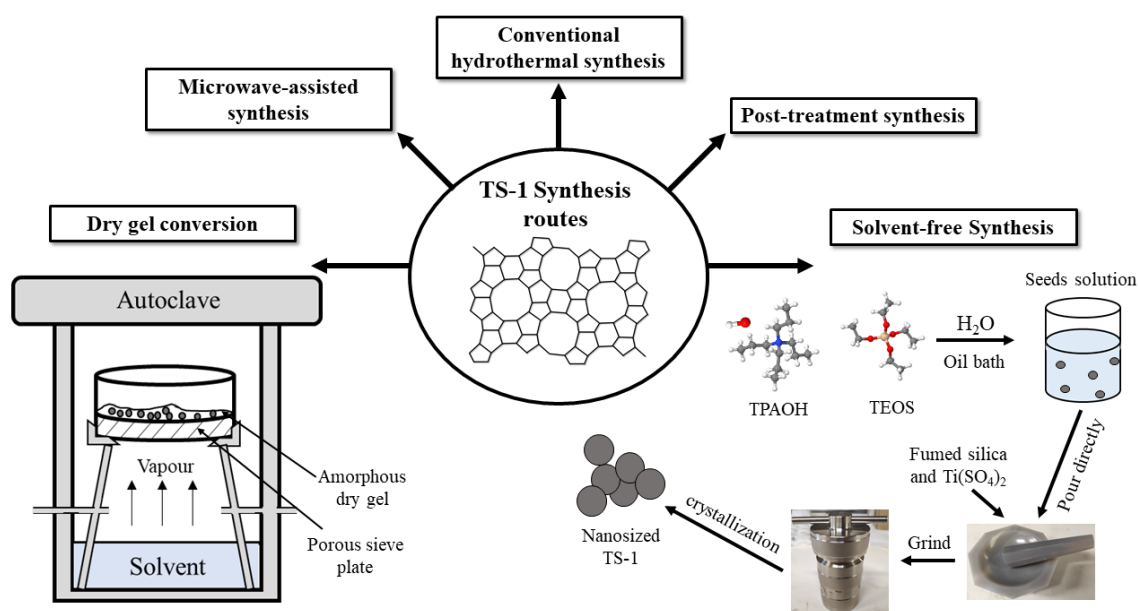


Figure D.4. Scheme of the most used TS-1 synthesis route based on Luan *et al.* (2022) [37]. Dry gel conversion method and solvent-free synthesis schemes adapted from Xu *et al.* (1990) [42] and Liu *et al.* (2022) [43], respectively.

First, the hydrothermal synthesis will be addressed since is the conventional synthesis method and also the one used in the preparation of the modified TS-1 of *Chapter 7*. Then, a brief description of the post-treatment; dry-gel conversion; solvent-free; and microwave-assisted synthesis will be provided.

Hydrothermal synthesis is a two-step conventional synthesis method of TS-1, reported for the first time by Taramasso *et al.* (1983) [15]. The first step is the gelation, where the controlled hydrolysis and co-condensation of titanium and silicon precursors are carried out in the presence of a structure-directing agent (SDA, such as tetrapropylammonium hydroxide (TPAOH) or bromide (TPABr)) which serves as a template for the creation of the MFI channels. In the second step, those reactants are mixed in a hydroalcoholic medium and then, poured inside an autoclave to produce the crystallization of TS-1 under hydrothermal conditions. In such conditions, the growth of single crystals is promoted as a consequence of the insolubility of the reaction products in hot water under high pressure. Inside the growing chamber of an autoclave (the Teflon vessel) a temperature gradient is created where in the hotter and upper parts the solutes dissolve, while in the cooler bottom, the seed crystals are deposited and start growing [44]. A scheme of the hydrothermal synthesis of TS-1 is illustrated in Figure D.5.

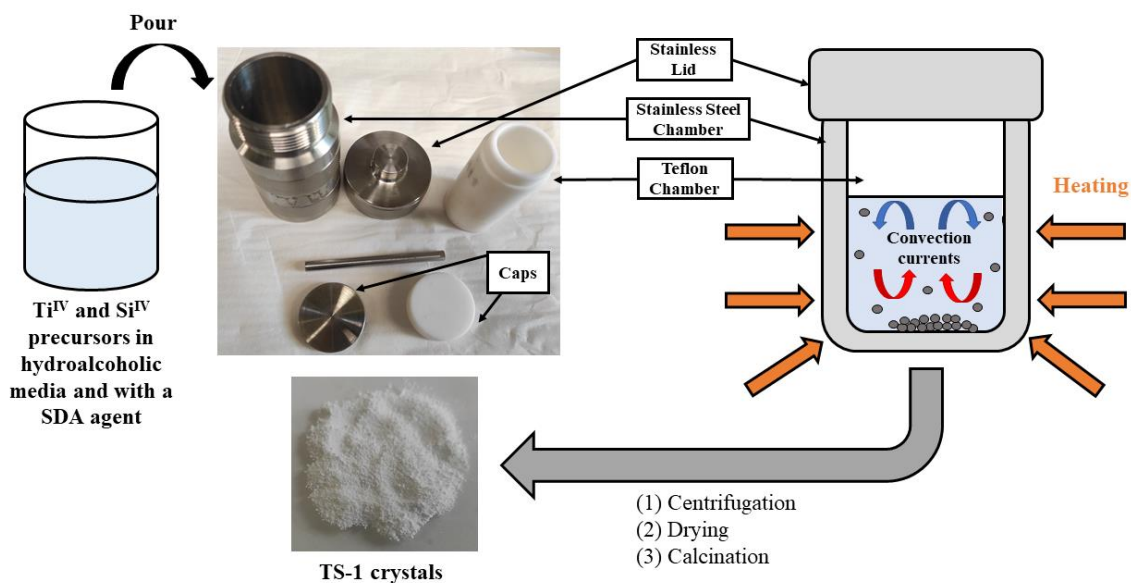


Figure D.5. Scheme of the conventional hydrothermal synthesis of TS-1.

Many modifications of the hydrothermal method have been suggested [45]. Wei *et al.* (2019) used agitation during the crystallization process in the autoclave to further guarantee continuous motion, which resulted in the faster and uniform growth of TS-1 crystals while anatase formation was avoided [46]. Another common modification is the use of additives (e.g., L-lysine; polyvinylpyrrolidone (PVP); Triton-X-100; acetyl acetate; among others) to slow down the hydrolysis rate of the titanium precursors and/or the crystallization and inhibit the formation of amorphous Ti [47–50]. Bai *et al.* (2018) reported that the use of seed crystals (nanosized silicalite-1) in hydrothermal synthesis promotes the formation of mesopores due to grain accumulations of high crystalline TS-1, improving the diffusion of the substrates within the pores, and thus, allowing the obtention of better results in oxidative desulfurization reactions compared to the conventional purely crystalline zeolite [51].

Post-treatment synthesis consists of using a commercial or previously prepared ZSM-5 zeolite as a synthesis precursor that is chemically treated, usually with aqueous HCl, to produce Al or Si lattice vacancies in its structure, which are then filled by Ti. In the first documented application of this methodology, Zhang *et al.* (1999) achieved the isomorphous substitution of Ti through the gas-solid reaction of TiCl₄ vapour with a ZSM-5 zeolite [52]. The advantage of this synthesis route is that the formation of anatase is avoided, although, the treatments may require complex steps.

Dry gel conversion method (scheme depicted on the left of Figure D.4) was first reported for the synthesis of TS-1 in 1990 by Xu *et al.* [42]. The first step of this approach

is the preparation of a synthesis solution containing the Ti and Si precursors, SDAs and additives. Then, the solution is dried to remove the solvent, forming a viscous paste in the process, and upon further heating, an amorphous dry gel is obtained. Later, the dry gel is deposited in a holder placed half-height inside an autoclave reactor that was previously pre-charged with a solvent, usually water. When the autoclave is sealed and heated, the vapours generated inside promote the crystallization of the dry gel, and the TS-1 materials are obtained as a result. Some authors have claimed that this method yields TS-1s with lower cost, higher content of Ti, or higher catalytic activity than the ones prepared by conventional hydrothermal synthesis using the same reactants [53–55].

Solvent-free is a synthesis method first reported by Ren *et al.* (2012) [56]. In this method, the silicon and titanium solid precursors, the SDAs salts and the additives are directly grounded in agate mortars. The prepared synthetic powders are introduced straightforwardly in stainless autoclaves where they crystallize forming the TS-1 zeolites. The example depicted in the right of Figure D.4 is a variation of this method proposed by Liu *et al.* (2002) [43], in which a previously prepared seed solution is poured and grounded along the solid reactants in the mortar; these modifications allowed to easily obtain nanosized TS-1 catalysts.

Microwave-assisted synthesis of TS-1 was reported for the first time by Prasad *et al.* (2002) [57]. The procedure synthesis is identical to the hydrothermal synthesis with the exception that the final gel is transferred to a jar transparent to infrared radiation instead of an autoclave; after the irradiation, the sample is cleaned and calcinated as the conventional method. This approach has the advantage of requiring a considerably lower crystallization time to prepare the TS-1 catalysts, 30 minutes compared to the few days required in hydrothermal synthesis.

D.3 HETEROGENEOUS PHOTOCATALYSIS

Before stepping directly into the application of TS-1 materials as photocatalysts, it becomes necessary to define and provide a brief explanation of the heterogeneous photocatalysis with an emphasis on water treatment application (modified titanium-silicalites prepared in *Chapter 7* have been used to degrade a pollutant in aqueous media).

Photocatalysis can be defined as: “the change rate of a chemical reaction due to the generation of an electron-hole pair in a semiconductor material, as a consequence of its exposure to light” [58]. It is important to differentiate photosynthesis and photocatalysis. In photosynthesis, light is consumed to perform thermodynamically uphill reactions where products of higher energy than the reactants are obtained (the free Gibbs energy change is positive, $\Delta G > 0$), and the light-absorbing material is only considered a photocatalyst if the photons are reactants. In opposition, in photocatalysis, the materials use the absorbed light to ease thermodynamically downhill reactions ($\Delta G < 0$) where only the kinetics of the process is enhanced due to the new reaction route [59]. Examples of photosynthesis are CO_2 reduction and water splitting, while an example of photocatalysis would be the complete oxidation of a substance to CO_2 and water. This difference between photocatalysis and photosynthesis is illustrated in Figure D.6.

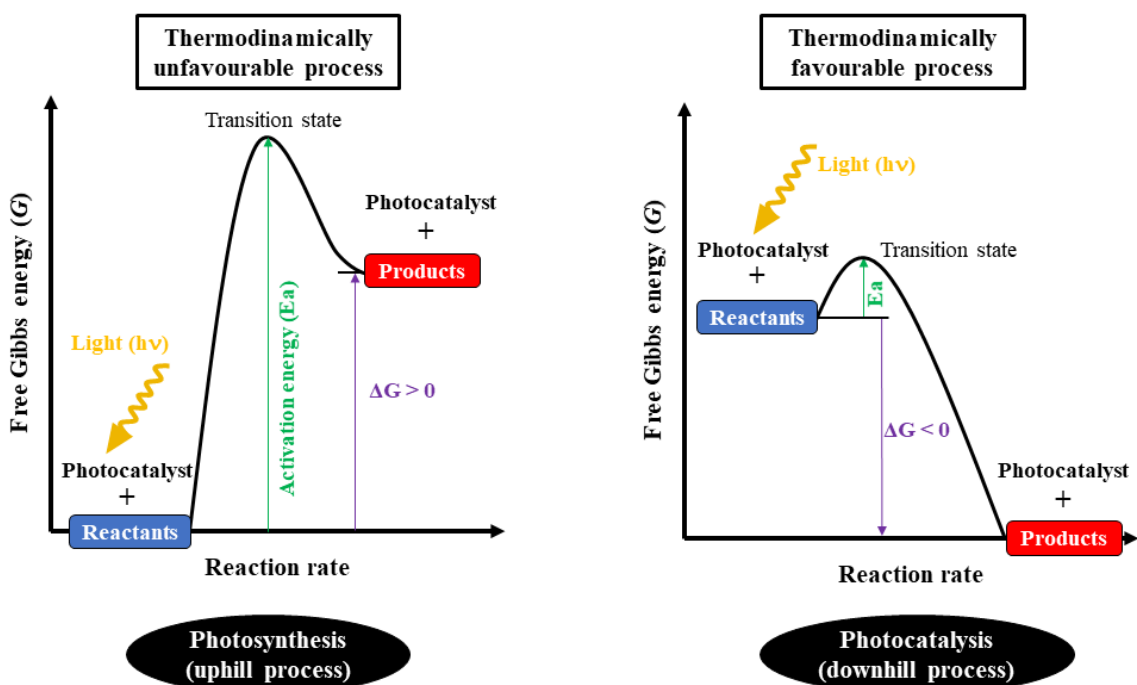


Figure D.6. Thermodynamically unfavourable photosynthesis reaction (*left*) and Thermodynamically favourable photocatalysis reaction (*right*). Adapted from Osterloch (2017) [60].

Photocatalysis can be classified into two categories depending on the state of matter of the reactants and the catalyst: if they are in the same state is designed as homogeneous, while if the state differs it is called heterogeneous. Almost all heterogeneous photocatalysts are solid semiconductors, so we should delve into their electronic properties before addressing photocatalysis.

From the perspective of the molecular orbital theory, the electrons in a molecule contribute equally to the formation of bonds between the atoms and are distributed in energy levels, named molecular orbitals, that are centred around the nuclei of the molecule. The molecular orbitals in solids are formed by the linear combination of all the atomic orbitals, thus, the electrons reside in the available lower energy level, which is known as the “highest occupied molecular orbital (HOMO)” or valence band, while the closer electronic energy level with higher energy is designed as the “lowest unoccupied molecular orbital (LUMO)” or conduction band. The capability of a material to allow the conduction of electricity, i.e. electronic transition from the valence to the conduction band, is given by the energy gap or forbidden bandgap (E_g) between the HOMO and LUMO levels. Conductor materials, such as metals, have no or low E_g values (< 1 eV), so the electrons can move freely between energy levels. On the other hand, the E_g value of an insulator is so high (> 5 eV) that the promotion of electrons from the HOMO to the LUMO is restrained. Semiconductors, as some metal oxides, are materials that have an intermediate E_g value, therefore, they can behave as weak conductors under specific conditions such as low temperature, or light irradiation in the case of photocatalysts. A material is considered a semiconductor when its E_g is ≤ 3 eV, and is considered a wide bandgap semiconductor when its E_g value ranges from 3 to 4 eV [61]. The three kinds of materials are depicted in Figure D.7.

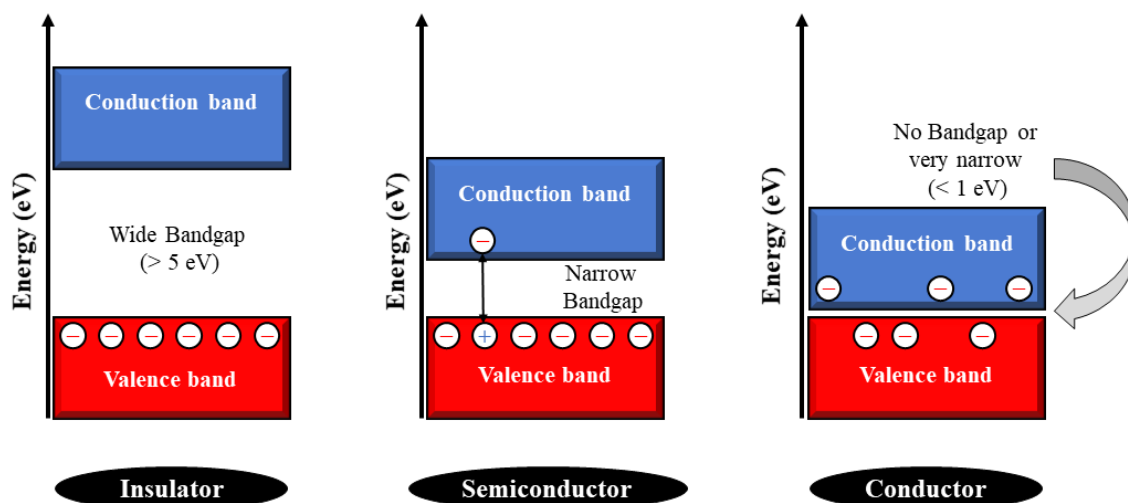


Figure D.7. Scheme of the three types of materials classified according to their electronic conducting capability: insulator (*left*), semiconductor (*centre*) and conductor (*right*).

Before deepening into the electric properties of semiconductors, it becomes necessary to define the Fermi energy (E_F). The E_F is calculated by the Fermie–Dirac distribution function and defines the energy threshold where the energy levels above have less than a 50% probability of being filled by electrons, while in the energy levels below the probability is higher than 50% [62]. In pure semiconductor crystals (intrinsic semiconductor) for each electron (e^-) that gets excited to the conduction band, a positively charged vacancy is generated in the valence band (positive hole, h^+). Since in intrinsic semiconductors the electron density (n) is equal to the density of the holes (p), the Fermi level is located just at the centre of the energy bandgap ($E_g/2$). However, the electric properties of semiconductors are quite sensitive towards lattice defects and impurities. This has been used as an advantage to enhance the conductivity of semiconductors by controlling their n and p through the addition of small quantities of foreign atoms in their crystalline lattice (doping), resulting in the named extrinsic semiconductors. The doping with atoms with an additional valence electron (donor dopant), compared to those of the semiconductor, results in the transfer of an electron and the addition of an extra energy level to the conduction band. In contrast, when a semiconductor is doped with atoms with fewer valence electrons than those of the lattice (accepting donor), it results in the creation of a hole and an additional energy level in the valence band. The semiconductors doped with donor and accepting dopants are known as n -type and p -type semiconductors, respectively. In n -type semiconductors the fermi level is closer to the conduction band while in p -type semiconductors is closer to the valence band. The three types of semiconductors are depicted in Figure D.8.

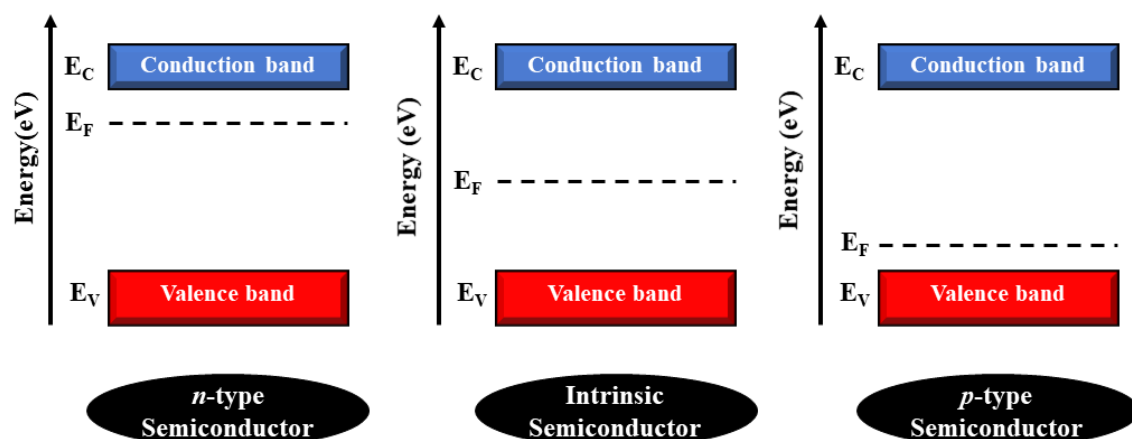


Figure D.8. Scheme of the three types of semiconductors: *n*-type (left), intrinsic (centre), and *p*-type (right). Where E_C is the conduction band edge energy, E_V the valence band edge energy, and E_F is the energy of the Fermi level.

When a semiconductor photocatalyst is exposed to radiation of energy equal to or higher than that of the bandgap (λ_{exc}), the electron-hole pair ($e^- h^+$) is formed. The spatial distribution of the charges in the semiconductors depends on their nature. In *n*-type semiconductors, the electrons migrate to the bulk and holes move towards the surface of the material, whereas the charges migrate to the opposite directions in the *p*-type semiconductors. Then, the electrons in the photoexcited state are either deactivated by the recombination with their holes, resulting in the dissipation of energy as heat or photon emission or are consumed in the reduction of an acceptor molecule, while the holes are employed in the oxidation of donor molecules. The photogenerated potential of the electrons corresponds to the conduction band edge energy (E_C), whereas, the potential of the holes is equal to that of the valence band edge (E_V). When the semiconductors interact with a substrate, four possible scenarios can occur depending on the relative positions of E_C and E_V , compared to the redox level of the substrate (E_{redox}) [58]: (i) the oxidized form of the substrate redox couple is reduced if its redox level (E_{redox}) of the substrate is higher than E_C of the semiconductor, (ii) the reduced form of the substrate redox couple is oxidized if its E_{redox} is lower than E_V of the semiconductor, (iii) no reaction takes place if E_{redox} of the substrate is lower than E_C and higher than E_V of the semiconductor, and (iv) both, the oxidation and reduction reactions, occurs to the substrate redox couple when its E_{redox} is higher than E_C , and lower than E_V of the semiconductor.

To conclude with the semiconductors, the ideal photocatalyst would accomplish all the following properties: (i) chemically and biologically inert, (ii) high absorption coefficient of light, high quantum yields, (iii) absorbs solar radiation, (iv) photocatalytic stability, (v) ease to synthesise and use, (vi) able to efficiently catalyse reactions avoiding generation of side products, (vii) environmentally friendly; (viii) low-cost, (ix) should allow easy product separation, (x) high surface area, (xi) high density of active sites, (xii) it allow to large scale the photocatalytic reaction, (xiii) low surface charge recombination, and (xiv) reusability [59,63]. A known and widely used semiconductor material as a photocatalysts is titanium dioxide (TiO_2), specifically the commercial Degussa P-25 nanoparticles. These particles, composed of 75% of anatase (the more photoactive phase) and 25% of rutile, highlight chemical stability, availability, low-cost, reproducibility and efficient activity in photocatalytic oxidation reactions [64]. However, it is not active under visible radiation (it can only absorb UV, the 4% of the solar spectrum) and its possible impact on the environment is a matter of growing concern [65,66].

Heterogeneous photocatalysis has been proven as a valid advanced oxidative process (AOPs) for the removal of pollutants (pesticides, herbicides, pharmaceutical compounds, and so on) in aqueous media [67–70]. In the conventional photodegradation reaction procedure, the semiconductor in the form of particulate powder is added to a recipient containing an organic pollutant aqueous solution, which is stirred to avoid precipitation and achieve the homogeneous dispersion of the catalyst. The oxidation and reduction reactions occur in close vicinity to the surface of the particulate photocatalyst. The photogenerated e^- reduces the O_2 in the aqueous solution (this is why air is usually bubbled into reactors) yielding superoxide radicals ($\text{O}_2^{\bullet-}$), while photogenerated h^+ oxidizes H_2O molecules and forms hydroxyl radicals (OH^\bullet). Nevertheless, other radicals can be formed by the oxidation and reduction of other molecules or radicals in the solution (H_2O_2 , HO_2^\bullet , OH^\bullet , among others). Due to their long lifetimes and higher oxidizing potential, the generated radicals can degrade the pollutants in solution and, in some cases, can achieve their complete mineralization (transformation to CO_2 and H_2O). The role of the radicals in the AOPs of a pollutant can be evaluated using substances known as scavengers. These inorganic or organic substances tend to react fast and specifically with a radical (or directly with e^- or h^+), forming stable species that are not involved in the degradation of the target pollutant, therefore, they allow to elucidate the effect of the radicals in the reaction [71]. The oxidation and reduction processes that generate the

radicals on the surface of a heterogeneous photocatalyst in aqueous media are displayed in Figure D.9.

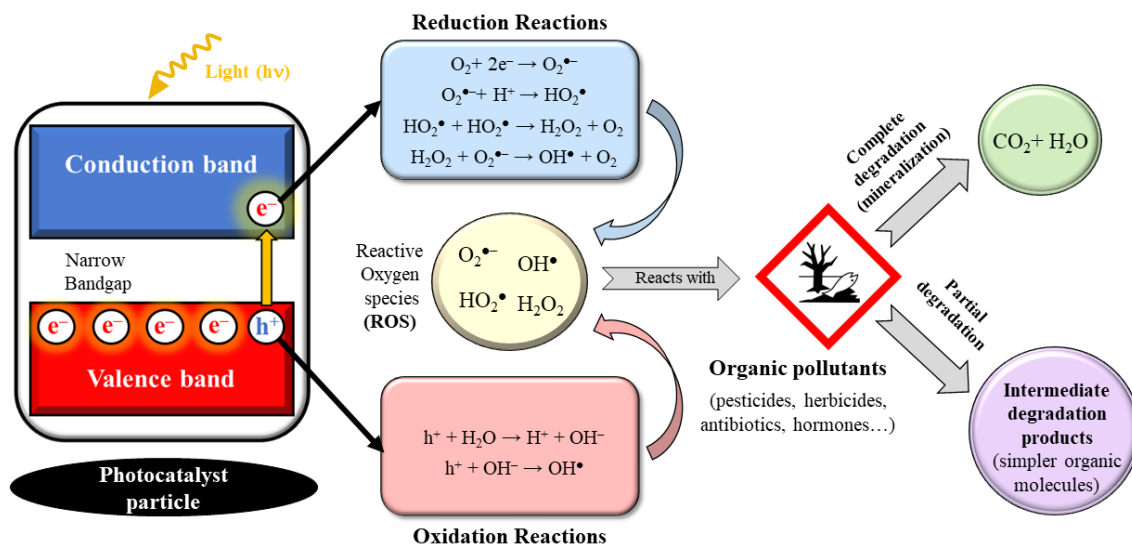


Figure D.9. Scheme of the generation of reactive oxygen species (ROS) by a photocatalyst in aqueous media for the degradation of organic pollutants. Adapted from Shmeis et al. (2022) [72].

D.4 TSs AS PHOTOCATALYSTS IN THE PHOTODEGRADATION OF POLLUTANTS

TiO₂ is an *n*-type semiconductor widely used as a photocatalyst in the removal of water wastes, due to its ease to generate highly oxidant hydroxyl radicals [68]. Many efforts have been made to further improve the photocatalytic performance of TiO₂, and researchers are mainly focused on developing strategies to enlarge the TiO₂ absorption range toward visible radiation to accomplish an efficient excitation with solar light, and on the preparation of composites to enhance the textural properties (specific surface area and pore volume), to reduce the diffusion limitations of the substrate molecules within the catalyst particles and decrease the electron-hole recombination rates [73–75].

TS-1 are materials that contain photoactive Ti species, mainly TiO₄ and TiO₆, distributed within the lattice and surface of a chemically stable structure. Although their use as photocatalysts for the removal of pollutants has not been as prominent as in other oxidation reactions (see *Annexe D.1*), they present two main advantages over conventional TiO₂ in that field. The first advantage is that the silica MFI structure is hydrophobic, and it selectively adsorbs the organic pollutants in a solution, therefore, the catalyst-substrate charge transfer is improved. Another advantage compared with TiO₂ is

that TS-1 materials have a higher surface area and Ti dispersion, and the photoactivity of the metal is more efficient [1].

In the last decade, several interesting works using different strategies to develop modified TS-1 for the degradation of water pollutants are found in the literature. For instance, Ren *et al.* (2012) prepared a hybrid TS-1/graphene material, through *in situ* sol-gel process. In the photodegradation of 4-nitrophenol, the TS-1/graphene hybrids yielded a degradation constant 6–7 times higher than the TS-1/carbon nanotubes hybrid prepared in previous work of the authors, ~25 times higher than pure TS-1, and even higher than the obtained with TiO₂-P25 [76]. Porous TS-1 beads with hierarchical microporous/mesoporous structures were prepared through the resin templating method by Ormond and co-workers (2016). The photocatalytic activity of the materials in the degradation of methyl blue resulted in 1.5 times lower than the commercial CristalACTiVTM PC500 TiO₂, however, due to their macroscopic size, the TS-1 beads could be easily recuperated and used in 4 consecutive cycles without any loss of material [77]. Yuan *et al.* (2016) prepared a hierarchically porous composite by *in situ* hydrothermal coating diatomite with TS-1 nanoparticles. Due to enhanced textural parameters, the TS-1/modified-diatomite composites were able to remove 99.1% of methyl blue after 2 h of photocatalytic reaction with a rate constant more than twice as high as that of pure TS-1 nanoparticles [78]. Qiangshun *et al.* (2018), studied the photoactivity of an iron-supported titanium silicalite (Fe-TS-1) through the photophenton degradation of acid orange seven (AO7) under simulated solar light. The elimination of 97% of AO7 in 40 min when the optimal operational parameters were applied was achieved [79]. Several dyes and antibiotics (rhodamine B, sulforhodamine B, tetracycline, and ciprofloxacin) were successfully removed in 6 h under visible light, by the heterojunction of TS-1 and graphitic carbon nitride (g-C₃N₄) prepared by Kumar and co-workers (2018) [80]. In a work published in 2022, Hsu *et al.* detailed the efficient degradation of phenol using a magnetite/TS-1 composite thin film and oxygen atmosphere [81]. Finally, Meng *et al.* (2023), achieved the synthesis of hierarchical TS-1 using triblock copolymer F127 and a phototreatment synthesis method. The highly crystalline hierarchical TS-1 demonstrated exceptional performance in the removal of the antibiotic erythromycin [82].

To conclude it is noteworthy that modified TS-1 materials have been applied to undergo other photocatalytic processes aside from photodegradation of pollutants. In the

literature, examples of their use in the photocatalytic generation of hydrogen, the selective photo-oxidation of cyclohexane, the photoreduction of CO₂, or the photocatalyzed remote aliphatic C–H oxyfunctionalization can be found [83–86].

D.5 COMPARATIVE OF THE PERFORMANCE OF THE NOVEL TSs WITH OTHER PHOTOCATALYSTS

The photoactivity of the new modified titanium silicalites (TSR%) of *Chapter 7* was tested in the photodegradation process of the emerging pollutant and antidepressant venlafaxine (*Ven*). In those photodegradation trials, 1 g L⁻¹ of TSP5 or TSPH5 silicalites was used to degrade a *Ven* in a 5 mg L⁻¹ solution. After 120 min of simulated solar light irradiation (1500 W Xenon lamp, 500 W m⁻²) a ~ 90% degradation rate of the pollutant was achieved for both catalysts, and apparent pseudo-first order degradation rate constants (k_{app}) of 2.8×10^{-2} and 3.6×10^{-2} min⁻¹ were determined for TSP5 and TSPH5 respectively.

Comparing the obtained results with those reported in the literature for the photodegradation of venlafaxine can be challenging, as it can be appreciated in the variety of operation parameters, photocatalysts and radiation sources depicted in the studies summarized in Table D.1. Lambropoulou *et al.* (2017) also achieved a 90% degradation rate of a 5 mg L⁻¹ solution of *Ven* using a commercial TiO₂-P25 aerioxide, although lower irradiation time (20 min) and catalyst dose (0.4 g L⁻²) were required compared to the TSR%_s [87]. However, it must be pointed out that TSP5 and TSPH5 contains a considerably lower amount of titanium (1.36 and 0.88 wt%, respectively in Table 7.3.) and the radiation source was simulated solar light in contrast to the UV-A lamp used in that study. On the other hand, the TSR%_s yielded higher degradation rates than the Bi⁰-doped Bismuth Oxyhalide catalysts supported in alumina films that were prepared by Dandapat *et al.* (2018), those obtained a 60% degradation of a 0.1 mg L⁻² venlafaxine solution in 60 min of simulated solar light irradiation [88]. Nevertheless, the photodegradation of *ven* by the novel titanium silicalites of *Chapter 7*, do not reach the high performances accomplished by recent developed materials such as supported carbon nitride (CN) photocatalysts [89–91]. This is probably due to their higher adsorption of *ven*, their lower photon absorption in the visible range, and the worse separation of charge carriers compared to the CN materials. Therefore, to overcome those lacks of the TSR%, the preparation of titanium silicalite/CN composites will be addressed in the future.

Table D.1. Most relevant data of publications on the removal of venlafaxine (*Ven*) in aqueous media through photocatalysis.

Year	Catalyst	System	Experimental Conditions	Observations	Ref.
2023	ZIF-67/Ag ₃ VO ₄ based S-scheme heterojunction (ZAV)	Visible light/ZAV	Radiation Source: 300 W Xe lamp with a with a 420 nm cut-off filter. Room Temperature [Ven] ₀ = 20 mg L ⁻¹ [Catalyst] ₀ = 0.05–0.5 g L ⁻¹ Time: 80 min	0.3 g L ⁻¹ of ZAV-30 (30 wt% Ag ₃ VO ₄) degraded 98.5% of venlafaxine in 60 min (^a k _{app} = 1.1×10 ⁻² min ⁻¹). ZAV-30 outperformed bare ZIF-67 and Ag ₃ VO ₄ photocatalysts due to its enhanced photon absorption and improved charge carriers' separation.	[92]
2023	Carbon nitride (CN) photocatalysts immobilized on 3D printed poly(lactic acid) (PLA) cylindrical supports (CN/PLA)	Visible light/C ₃ N ₄ in PLA support	Radiation Source: ox equipped with four perpendicular visible LEDs (average nominal irradiance = 560 W m ⁻² , λ _{max} = 414 nm). Temperature = 20 °C [Ven] ₀ = 5 mg L ⁻¹ Time: 60 min	Negligible <i>Ven</i> adsorption of CN. Bulk CN prepared from urea (CNB-U) achieved above 90% removal of <i>Ven</i> in 30 min (^a k _{app} = 7.54×10 ⁻² min ⁻¹ , ^b t _{1/2} = 9.2 min). Reuse tests confirmed the robust and effective photocatalytic performance of the CNB-U/PLA photocatalyst over multiple cycles.	[91]
2023	Bulk or exfoliated carbon nitride embedded in polyvinylidene fluoride (PVDF) matrix. These photocatalyst were supported in membranes of polytetrafluoroethylene (PTFE)	Visible light/C ₃ N ₄ in PTFE membrane	Radiation Source: 10 W LED emitting at 418 nm (with an irradiance of 11.2 W m ⁻² measured on the position of the membrane). The membranes were tested for venlafaxine (<i>Ven</i>) degradation at a feed concentration of 250 μg L ⁻¹ under continuous flow mode operation Time: 300 h	All the fabricated membranes exhibited similar photocatalytic filtration performance for <i>Ven</i> degradation, resulting in conversions above 95% after 5 h of irradiation and keeping the <i>Ven</i> concentration in the effluent negligible up to 48 h of continuous operation.	[90]

2023	Magnetic reduced graphene oxide (rGO) encapsulated hexagonal FeTiO ₃ (FTO@rGO)	Photo-Phenton Process	<p>Radiation Source: 300 W Xe arc lamp with a 420 nm cutoff filter. The power density of the lamp was measured to be 4.3 mW cm⁻².</p> <p>Temperature = 30 °C</p> <p>[Ven]₀ = 30 mg L⁻¹ in 100 mL</p> <p>[Catalyst]₀ = 0.8 g L⁻¹</p> <p>pH = 7, 20 mM of H₂O₂ added</p> <p>Time: 90 min</p>	<p>Heterogeneous Fenton and photocatalytic (systems achieved less than 25 % Ven degradation. Nevertheless, all FTO@rGO catalysts show higher Ven degradation rate than FTO in photo-Fenton evolution experiments.</p> <p>The FTO@rGO catalysts with rGO loading amount of 5 wt% presents the highest Ven degradation rate (100 % Ven degradation at 90 min), which is attributed to the accelerated migration of photo-generated electrons and the efficient Fe^{II}/Fe^{III} cycle.</p>	[93]
2023	Graphitic carbon nitride (g-C ₃ N ₄) and 1% MoS ₂ /g-C ₃ N ₄ (1MSCN)	UV-Vis/g-C ₃ N ₄ or 1MSCN	<p>Two different radiation Sources: 1) solar simulator apparatus quipped with a xenon lamp (2.2 kW, and 500 Wm⁻² irradiation intensity); and 2) ten UVA lamps (36W. UVA range 340–400 nm, λ_{peak} = 375 nm).</p> <p>Real wastewater samples collected from hospital wastewater treatment plant secondary effluent, spiked with [Ven]₀ = 250 ng L⁻¹.</p> <p>[Catalyst]₀ = 0.1 g L⁻¹</p> <p>Time: 300 min solar simulator, and 360 min UVA Lamps</p>	<p>In all cases, 1MSCN presented higher photocatalytic performance than g-C₃N₄.</p> <p>Under UVA-lamp irradiation 100% Ven was removed after 360 min irradiation using 1MSCN (^ak_{app} = 1.6×10⁻² min⁻¹), similarly to the 97% removal rate achieved after 300 min of simulated solar irradiation (^ak_{app} = 1.5×10⁻² min⁻¹).</p>	[89]
2022	TiO ₂ /Ag nanocatalyst thin films stabilized on glass. Ag/TiO ₂ weight ratio of 0.2.	UV-Vis/TiO ₂ -Ag	<p>Radiation Source: LED lamps (12 v) in both outer shells of an 80 mL reactor.</p> <p>Temperature = 25 °C</p> <p>Time: 180 min</p>	<p>Adsorption removal using TiO₂/Ag thin glass films as an adsorbent was 7%.</p> <p>More than 70% of Ven was removed under optimum conditions: 20 mg L⁻¹ of initial concentration of Ven, pH of 10 under 180 min illumination. ^ak_{app} = 0.76×10⁻² min⁻¹, ^bt_{1/2} = 91.2 min.</p>	[94]

2019	Cobalt-titanate nanowires (Co-TNW)	UV-Vis/ Co-TNW	<p>Radiation Source: 450 W medium-pressure mercury-vapor lamp.</p> <p>Spiked tap water</p> <p>$[Ven]_0 = 10 \text{ mg L}^{-1}$</p> <p>$[Catalyst]_0 = 0.15 \text{ g L}^{-1}$</p> <p>Time: 120 min</p>	<p>Co-TNW do not adsorb <i>Ven</i>.</p> <p>Although photolysis achieved a 99% removal rate of <i>Ven</i> in 90 min, the photocatalyst halved the time needed in the removal of one of the five <i>Ven</i>'s transformation products.</p>	[95]
2018	Bi ⁰ -doped Bismuth Oxyhalide thin films BiOCl _{0.875} Br _{0.125} /alumina film	UV-Vis/ BiOCl _{0.875} Br _{0.125}	<p>Radiation Source: 150 W ozone-free Xe arc lamp solar simulator (incident irradiation of $\sim 500 \text{ W m}^{-2}$ integrated between 280 and 950 nm).</p> <p>$[Ven]_0 = 0.1 \text{ mg L}^{-1}$ in 30 mL of deionized water spiked with a mixture of other six pharmaceutical drugs with the same concentration.</p> <p>Time: 60 min</p>	<p>Adsorption of <i>Ven</i> after 60 min at dark was insignificant.</p> <p>The sample 3% Bi-BiOCl_{0.875}Br_{0.125} showed the highest destruction rate for most of the tested compound, compared to reference TiO₂.</p> <p>After 60 min irradiation, 60% removal of <i>Ven</i> was achieved.</p>	[88]
2017	Aeroxide TiO ₂ -P25	UV/TiO ₂	<p>Radiation Source: UV-A lamp placed in the centre of the reactor inside a double-walled protective quartz tube. Radiation range from 340 and 400 nm with a maximum at 366 nm.</p> <p>Temperature = 25 °C</p> <p>$[Ven]_0 = 2.5\text{--}10 \text{ mg L}^{-1}$ in 500 mL</p> <p>$[Catalyst]_0 = 0.2\text{--}1 \text{ g L}^{-1}$</p> <p>Time: 30 min</p>	<p>Under Optimized operational conditions: 0.6 g L⁻¹ TiO₂, pH 10, and initial <i>Ven</i> concentration 2.5 mg L⁻¹, a 96% degradation efficiency is achieved in 30 min of irradiation, and in addition, a 70% TOC removal is obtained after 240 min.</p> <p>0.4 g L⁻¹ TiO₂ degraded $\sim 90\%$ of 5 mg L⁻¹ in 20 min at pH = 4. $^a k_{app} = 0.18 \text{ min}^{-1}$.</p>	[87]

^a k_{app} = apparent pseudo-first order degradation rate constant; ^b $t_{1/2}$ = degradation half-life time.

D.6. REFERENCES

- [1] Ratnasamy, P.; Srinivas, D.; Knözinger, H. Active Sites and Reactive Intermediates in Titanium Silicate Molecular Sieves. In *Advances in catalysis*; Ratnasamy, P., Srinivas, D., Knözinger, B., Eds.; Elsevier INC., **2004**; Vol. 48, p. 1–169.
- [2] Zou, L.; Zhu, M.; Liu, J.; Chen, L.; Yao, Q.; Hu, N.; Chen, X.; Kita, H. *Microporous Mesoporous Mater.* **2024**, *363*, p. 112823.
- [3] He, Z.; Lei, Q.; Dai, W.; Zhang, H. *J. Catal.* **2023**, *421*, p. 172–184.
- [4] Zhang, F.; Guo, X.; Wang, X.; Li, G.; Zhao, Q.; Bao, X.; Han, X.; Lin, L. *Appl. Catal., A* **2000**, *192*, p. 157–163.
- [5] Chu, J.; Ge, Z.; Peng, J.; Hu, H.; Guo, S.; Chen, X. *Catal. Lett.* **2023**, *153*, p. 348–363.
- [6] Clerici, M. G. Titanium Silicalite-1. In *Metal Oxyde catalysis*; Jackson, D., Hargreaves, J. S. J., Eds.; Prentice Hall, 2008; Vol. 2, p. 705–754.
- [7] Li, Y.; Sun, H.; Wang, Y.; Xu, B.; Yan, Z. *Prog. Chem.* **2015**, *27*, p. 503–510.
- [8] Gao, X.; Luo, B.; Hong, Y.; He, P.; Zhang, Z.; Wu, G. *Front. Chem. Sci. Eng.* **2023**, *17*, p. 772–783.
- [9] Pan, D.; Kong, L.; Zhang, H.; Zhang, Y.; Tang, Y. *ACS Appl. Mater. Interfaces* **2023**, *15*, p. 28125–28134.
- [10] Haghighi, S. K.; Kharat, A. N. *Inorg. Chem. Commun.* **2021**, *125*, p. 108413.
- [11] Li, M.; Shen, X.; Liu, M.; Lu, J. *Mol. Catal.* **2021**, *513*, p. 111779.
- [12] Martausová, I.; Spustová, D.; Cvejn, D.; Martaus, A.; Lacný, Z.; Přeč, J. *Catal. Today* **2019**, *324*, p. 144–153.
- [13] Wang, Y.; Wang, S.; Zhang, T.; Ye, J.; Wang, X.; Wang, D. *Trans. Tianjin Univ.* **2017**, *23*, p. 230–236.
- [14] Millini, R.; Bellussi, G.; Pollesel, P.; Rizzo, C.; Perego, C. *Microporous Mesoporous Mater.* **2022**, *346*, p. 112286.
- [15] Taramasso, M.; Perego, G.; Notari, B. S.p.A., Milan, Italy. *US Patent No. 4410501-A*, **1983**.
- [16] Vayssilov, G. N. *Catal. Rev.: Sci. Eng.* **1997**, *39*, p. 209–251.
- [17] Díaz, I.; Kokkoli, E.; Terasaki, O.; Tsapatsis, M. *Chem. Mater.* **2004**, *16*, p. 5226–5232.
- [18] Hajar, C. A.; Jacubinas, R. M.; Eckert, J.; Henson, N. J.; Hay, P. J.; Ott, K. C. *J. Phys. Chem. B* **2000**, *104*, p. 12157–12164.
- [19] Lamberti, C.; Bordiga, S.; Zecchina, A.; Artioli, G.; Marra, G.; Spanò, G. *J. Am. Chem. Soc.* **2001**, *123*, p. 2204–2212.
- [20] Domoroshchina, E. N.; Svetogorov, R. D.; Kuz'micheva, G. M.; Kravchenko, G. V.; Pirutko, L. V.; Zhukova, A. I.; Utenyshev, A. N.; Bozhenko, K. V. *J. Mater. Sci.* **2023**, *58*, p. 3934–3946.

- [21] Bellussi, G.; Millini, R.; Pollesela, P.; Perego, C. *New J. Chem.* **2016**, *0*, p. 1–3.
- [22] Wu, L.; Zhao, S.; Lin, L.; Fang, X.; Liu, Y.; He, M. *J. Catal.* **2016**, *337*, p. 248–259.
- [23] Wang, L.; Xu, Y.; Zhai, G.; Zheng, Y.; Huang, J.; Sun, D.; Li, Q. *ACS Sustain. Chem. Eng.* **2020**, *8*, p. 12177–12186.
- [24] Thangaraj, A.; Eapen, M. J.; Sivasanker, S.; Ratnasamy, P. *Zeolites* **1992**, *12*, p. 943–950.
- [25] Lousada, C. M.; Johansson, A. J.; Brinck, T.; Jonsson, M. *J. Phys. Chem. C* **2012**, *116*, p. 9533–9543.
- [26] Li, G.; Dimitrijevic, N. M.; Chen, L.; Nichols, J. M.; Rajh, T.; Gray, K. A. *J. Am. Chem. Soc.* **2008**, *130*, p. 5402–5403.
- [27] Liu, Z.; Davis, R. J. *J. Phys. Chem.* **1994**, *98*, p. 1253–1261.
- [28] Signorile, M.; Braglia, L.; Crocellà, V.; Torelli, P.; Groppo, E.; Ricchiardi, G.; Bordiga, S.; Bonino, F. *Angew. Chem., Int. Ed.* **2020**, *59*, p. 18145–18150.
- [29] Wang, Y.; Yang, H.; Zuo, Y.; Tian, D.; Hou, G.; Su, Y.; Feng, Z.; Guo, X.; Li, C. *Appl. Catal., B* **2023**, *325*, p. 122396.
- [30] Yao, Y.; Yang, Z.; Zheng, P.; Diao, Z. *Chem. Eng. J.* **2023**, *475*, p. 146053.
- [31] Gordon, C. P.; Engler, H.; Tragl, A. S.; Plodinec, M.; Lunkenbein, T.; Berkessel, A.; Teles, J. H.; Parvulescu, A. N.; Copéret, C. *Nature* **2020**, *586*, p. 708–713.
- [32] Van der Pol, A. J. H. P.; Verduyn, A. J.; van Hooff, J. H. C. *Appl. Catal., A* **1992**, *92*, p. 113–130.
- [33] Li, Y.; Li, Y.; Zhu, G.; Fan, J.; Feng, X.; Chai, Y.; Liu, C. *Ind. Eng. Chem. Res.* **2020**, *59*, p. 9364–9371.
- [34] Zuo, Y.; Zhang, T.; Liu, M.; Ji, Y.; Song, C.; Guo, X. *Ind. Eng. Chem. Res.* **2018**, *57*, p. 512–520.
- [35] Wang, B.; Han, H.; Ge, B.; Ma, J.; Zhu, J.; Chen, S. *New J. Chem.* **2019**, *43*, p. 10390–10397.
- [36] Li, L.; Wang, W.; Huang, J.; Dun, R.; Yu, R.; Liu, Y.; Hua, Z. *Appl. Catal., A* **2022**, *630*, p. 118466.
- [37] Luan, H.; Xu, C.; Wu, Q.; Xiao, F.S. *Front. Chem.* **2022**, *10*, p. 1–12.
- [38] Wang, B.; Guo, Y.; Zhu, J.; Ma, J.; Qin, Q. *Coord. Chem. Rev.* **2023**, *476*, p. 214931.
- [39] Zhu, K.; Zhou, X. *Curr. Opin. Chem. Eng.* **2015**, *9*, p. 42–48.
- [40] Smeets, V.; Gaigneaux, E. M.; Debecker, D. P. *ChemCatChem* **2022**, *14*, p. 1–25.
- [41] Bai, R.; Song, Y.; Bai, R.; Yu, J. *Adv. Mater. Interfaces* **2021**, *8*, p. 1–13.
- [42] Xu, W.; Dong, J.; Li, J.; Li, J.; Wu, F. *J. Chem. Soc., Chem. Commun.* **1990**, *21*, p. 755–756.
- [43] Liu, H.; Wang, Y.; Ye, T.; Wang, F.; Ran, S.; Xie, H.; Liu, J.; Li, Y.; Li, B.; Liu, Y.; Chai, Y.; Wang, L. *J. Solid State Chem.* **2022**, *307*, p. 122844.

- [44] Kafle, B. P. Introduction to nanomaterials and application of UV–Visible spectroscopy for their characterization. In *Chemical Analysis and Material Characterization by Spectrophotometry*; Elsevier Inc., **2019**; p. 171–173.
- [45] Wang, B.; Guo, Y.; Zhu, J.; Ma, J.; Qin, Q. *Coord. Chem. Rev.* **2023**, *476*, p. 214931.
- [46] Wei, X.; Wang, Y. J.; Ren, T. Q.; Wang, H. Y.; Wei, M. *RSC Adv.* **2019**, *10*, p. 1015–1020.
- [47] Wang, Y.; Li, L.; Bai, R.; Gao, S.; Feng, Z.; Zhang, Q.; Yu, J. *Chin. J. Catal.* **2021**, *42*, p. 2189–2196.
- [48] Gao, J.; Gao, L.; Zhang, B.; Wang, H.; Ma, W. *Can. J. Chem. Eng.* **2021**, *99*, p. S596–S604.
- [49] Du, S.; Li, F.; Sun, Q.; Wang, N.; Jia, M.; Yu, J. *Chem. Commun.* **2016**, *52*, p. 3368–3371.
- [50] Zhao, J.; Shen, B.; Xiao, W.; Zhang, C.; Wang, L. *Energy Sources, Part A* **2009**, *31*, p. 108–117.
- [51] Bai, R.; Sun, Q.; Song, Y.; Wang, N.; Zhang, T.; Wang, F.; Zou, Y.; Feng, Z.; Miao, S.; Yu, J. *J. Mater. Chem. A* **2018**, *6*, p. 8757–8762.
- [52] Zhang, F. Z.; Guo, X. W.; Wang, X. S.; Li, G. Y.; Zhao, Q.; Bao, X. H.; Han, X. W.; Lin, L. W. *Mater. Chem. Phys.* **1999**, *60*, p. 215–220.
- [53] Soekiman, C. N.; Miyake, K.; Hayashi, Y.; Zhu, Y.; Ota, M.; Al-Jabri, H.; Inoue, R.; Hirota, Y.; Uchida, Y.; Tanaka, S.; Kong, C. Y.; Nishiyama, N. *Mater. Today Chem.* **2020**, *16*, p. 100209.
- [54] Ke, X.; Xu, L.; Zeng, C.; Zhang, L.; Xu, N. *Microporous Mesoporous Mater.* **2007**, *106*, p. 68–75.
- [55] Zhang, H.; Fan, Y. F.; Huan, Y. H.; Yue, M. B. *Microporous Mesoporous Mater.* **2016**, *231*, p. 178–185.
- [56] Ren, L.; Wu, Q.; Yang, C.; Zhu, L.; Li, C. *J. Am. Chem. Soc.* **2012**, *134*, p. 15173–15176.
- [57] Ramakrishna Prasad, M.; Kamalakar, G.; Kulkarni, S.J.; Raghavan, K. V.; Narasimha Rao, K.; Sai Prasad, P. S.; Madhavendra, S. S. *Catal. Commun.* **2002**, *3*, p. 399–404.
- [58] Ameta, R.; Solanki, M. S.; Benjamin, S.; Ameta, S. C. Photocatalysis. In *Advanced Oxidation Processes for Wastewater Treatment: Emerging Green Chemical Technology*; Academic Press, **2018**; p. 135–175.
- [59] Yang, X.; Wang, D. *ACS Appl. Energy Mater.* **2018**, *1*, p. 6657–6693.
- [60] Osterloh, F. E. *ACS Energy Lett.* **2017**, *2*, p. 445–453.
- [61] Loddo, V.; Bellardita, M.; Camera-Roda, G.; Parrino, F.; Palmisano, L. Heterogeneous Photocatalysis. In *Current Trends and Future Developments on (Bio-) Membranes: Photocatalytic Membranes and Photocatalytic Membrane Reactors*; Elsevier Inc., **2018**; p. 1–43.

- [62] Dalven, R. Review of Semiconductor Physics. In *Introduction to Applied Solid State Physics*; Springer: Boston, MA, USA, **1990**; p. 1–25.
- [63] Augugliaro, V.; Palmisano, G.; Palmisano, L.; Soria, J. Heterogeneous photocatalysis and catalysis: An overview of their distinctive features. In *Heterogeneous Photocatalysis: Relationships with Heterogeneous Catalysis and Perspectives*; Elsevier B.V., **2019**; p. 1–24.
- [64] Ibhaddon, A. O.; Fitzpatrick, P. *Catalysts* **2013**, *3*, p. 189–218.
- [65] Shah, S. N. A.; Shah, Z.; Hussain, M.; Khan, M. *Bioinorg. Chem. Appl.* **2017**, *2017*, p. 12.
- [66] Ayorinde, T.; Sayes, C. M. *J. Hazard. Mater. Lett.* **2023**, *4*, p. 100085.
- [67] Friedmann, D. *Water* **2022**, *14*, p. 3588.
- [68] Paumo, H. K.; Dalhatou, S.; Katata-Seru, L. M.; Kamdem, B. P.; Tijani, J. O.; Vishwanathan, V.; Kane, A.; Bahadur, I. *J. Mol. Liq.* **2021**, *331*, p. 115458.
- [69] Bruckmann, F. S.; Schnorr, C.; Oviedo, L. R.; Knani, S.; Silva, L. F. O.; Silva, W. L.; Dotto, G. L.; Bohn Rhoden, C. R. *Molecules* **2022**, *27*, p. 6261.
- [70] Zhang, Y.; Zhou, B.; Chen, H.; Yuan, R. *Sci. Total Environ.* **2023**, *856*, p. 159048.
- [71] Schneider, J. T.; Firak, D. S.; Ribeiro, R. R.; Peralta-Zamora, P. *Phys. Chem. Chem. Phys.* **2020**, *22*, p. 15723–15733.
- [72] Abu Shmeis, R. M. Nanotechnology in wastewater treatment. In *Comprehensive Analytical Chemistry*; Elsevier, **2022**; Vol. 99, p. 105–134.
- [73] Arora, I.; Chawla, H.; Chandra, A.; Sagadevan, S.; Garg, S. *Inorg. Chem. Commun.* **2022**, *143*, p. 109700.
- [74] Dong, H.; Zeng, G.; Tang, L.; Fan, C.; Zhang, C.; He, X.; He, Y. *Water Res.* **2015**, *79*, p. 128–146.
- [75] Park, H.; Park, Y.; Kim, W.; Choi, W. *J. Photochem. Photobiol., C* **2013**, *15*, p. 1–20.
- [76] Ren, Z.; Kim, E.; Pattinson, S. W.; Subrahmanyam, K. S.; Rao, C. N. R.; Cheetham, A. K.; Eder, D. *Chem. Sci.* **2012**, *3*, p. 209–216.
- [77] Ormond, S. P. D.; Ratova, M.; Kelly, P.; Edge, M.; Mihailova, B.; Tosheva, L. *J. Porous Mater.* **2016**, *23*, p. 1421–1429.
- [78] Yuan, W.; Yuan, P.; Liu, D.; Yu, W.; Laipan, M.; Deng, L.; Chen, F. *J. Colloid Interface Sci.* **2016**, *462*, p. 191–199.
- [79] Wu, Q.; Wang, H.; Yi, C. *Optik* **2018**, *158*, p. 1460–1469.
- [80] Kumar, A.; Samanta, S.; Srivastava, R. *ACS Omega* **2018**, *3*, p. 17261–17275.
- [81] Hsu, H. L.; Roselin, L. S.; Savidha, R.; Selvin, R. *J. Saudi Chem. Soc.* **2022**, *26*, p. 101538.
- [82] Meng, F.; Ling, Y.; Li, Y.; Guo, M.; Wei, K.; Zhang, M.; Yang, C.; Shi, X.; Tang, B. *Chem. Eng. J.* **2023**, *473*, p. 145200.

- [83] Zhang, X.; Jin, Z.; Li, Y.; Li, S.; Lu, G. *Appl. Surf. Sci.* **2008**, *254*, p. 4452–4456.
- [84] Zhong, W.; Qiao, T.; Dai, J.; Mao, L.; Xu, Q.; Zou, G.; Liu, X.; Yin, D.; Zhao, F. *J. Catal.* **2015**, *330*, p. 208–221.
- [85] Zhu, M.; Zhu, C.; Wu, D.; Wang, X.; Wang, H.; Gao, J.; Huang, H.; Shi, C.; Liu, Y.; Kang, Z. *Nanoscale* **2019**, *11*, p. 15984–15990.
- [86] Sun, Y.; Li, G.; Gong, Y.; Sun, Z.; Yao, H.; Zhou, X. *J. Hazard. Mater.* **2021**, *403*, p. 124019.
- [87] Lambropoulou, D.; Evgenidou, E.; Saliverou, V.; Kosma, C.; Konstantinou, I. *J. Hazard. Mater.* **2017**, *323*, p. 513–52.
- [88] Dandapat, A.; Horovitz, I.; Gnayem, H.; Sasson, Y.; Avisar, D.; Luxbacher, T.; Mamane, H. *ACS Omega* **2018**, *3*, p. 10858–10865.
- [89] Rapti, I.; Boti, V.; Albanis, T.; Konstantinou, I. *Catalysts* **2023**, *13*, p. 252.
- [90] Valenzuela, L.; Pedrosa, M.; Bahamonde, A.; Rosal, R.; Torres-Pinto, A.; Silva, C. G.; Faria, J. L.; Silva, A. M. T. *Catal. Today* **2023**, *418*, p. 114042.
- [91] Peñas-Garzón, M.; Sampaio, M. J.; Manrique, Y.; Silva, C. G.; Faria, J. L. *J. Environ. Chem. Eng.* **2023**, *11*, p. 111343.
- [92] Sharma, S. K.; Kumar, A.; Dhiman, P.; Sharma, G.; Stadler, F. J. *Opt. Mater.* **2023**, *146*, p. 114541.
- [93] Wang, D.; Giannakis, S.; Tang, J.; Luo, K.; Tang, J.; He, Z.; Song, S.; Wang, L. *Chem. Eng. J.* **2023**, *478*, p. 147319.
- [94] Mokhtari, N.; Nazar, A. R. S.; Farhadian, M.; Eskandari, P.; Jeon, B. *Int. J. Environ. Sci. Technol.* **2022**, *19*, p. 12465–12476.
- [95] Osawa, R. A.; Barrocas, B. T.; Monteiro, O. C.; Oliveira, M. C.; Florêncio, M. H. *Chem. Eng. J.* **2019**, *373*, p. 1338–1347.

APPENDIX A

LIST OF ABBREVIATIONS AND SYMBOLS

APPENDIX A**LIST OF ABBREVIATIONS AND SYMBOLS**

3OHPA	<i>3-Hydroxypicolinic acid</i>
6OHPA	<i>6-Hydroxypicolinic acid</i>
a_{BET}	<i>Specific surface area calculated by BET method ($m^2 g^{-1}$)</i>
a_{DR}	<i>Specific surface area calculated by DR method ($m^2 g^{-1}$)</i>
AL	<i>Antenna Ligand</i>
AOPs	<i>Advance Oxidation Processes</i>
APA	<i>3-aminopicolinic acid</i>
APS	<i>Average Pore Size</i>
ATR	<i>Attenuated-total reflectance</i>
BET	<i>Brunauer-Emmett-Teller</i>
BJH	<i>Barrett-Joyner-Halenda</i>
CA	<i>Chelidamic acid</i>
C_{H_2O}	<i>Water-vapour molar concentration</i>
CI TEOS	<i>(2-Chloroethyl)triethoxysilane</i>
CIMTEOS	<i>Chloromethyltriethoxysilane</i>
CIPTEOS	<i>(3-Chloropropyl)triethoxysilane</i>
CIPhTEOS	<i>(p-Chlorophenyl)triethoxysilane</i>
CIRTEOS	<i>Chloro-akyl or aryl-triethoxysilane</i>

COV	<i>Volatile Organic Compound</i>
DFT	<i>Density Functional Theory</i>
DMF	<i>Dimethylsulfoxide</i>
DPA	<i>Dipicolinic acid</i>
DR	<i>Dubinin-Raduskevich</i>
DRK	<i>Dubinin-Raduskevich-Kaganer</i>
DRS	<i>Diffusive Reflectance Spectroscopy</i>
E_c	<i>Adsorption characteristic energy calculated by DR method (kJ mol^{-1})</i>
ED	<i>Electronic-dipole electronic transition</i>
EDX	<i>Energy-Dispersive X-ray spectroscopy</i>
E_g	<i>Optical bandgap energy</i>
EQ	<i>Electric-Quadrupole electronic transition</i>
ETEOS	<i>Ethyltriethoxysilane</i>
FBG	<i>Fibre Bragg-Grating sensor</i>
FE-SEM	<i>Field-Emission Scanning Electron Microscopy</i>
FPA	<i>6-Trifluoromethylpicolinic acid</i>
FTIR	<i>Fourier-Transform Infrared Spectroscopy</i>
h^+	<i>Positive hole</i>
HR-TEM	<i>High-Resolution Transmission Electron Microscopy</i>
HPLC	<i>High-Pressure Liquid Chromatography</i>
HXG	<i>Hybrid Xerogels</i>
I	<i>Intensity in humidity time-response curves</i>

IED	<i>Induced Electric-Dipole transitions</i>
IET	<i>Intramolecular Energy Transfer</i>
ILCT	<i>Intra-Ligand Charge Transfer</i>
I_{ref}	<i>Reference intensity in humidity time-response curves</i>
ISC	<i>Inter-Crossing charge transfer</i>
IUPAC	<i>International Union of Pure and Applied Chemistry</i>
LED	<i>Light-emitting diode</i>
LMCT	<i>Ligand-to-Metal Charge Transfer</i>
Ln-AL	<i>Silica xerogels doped with lanthanide complexes</i>
LO	<i>Optical Longitudinal mode</i>
LoD	<i>Limit of Detection</i>
MD	<i>Magnetic-dipole electronic transition</i>
MFI	<i>Modernite Framework Inverted</i>
MLCT	<i>Metal-to-Ligand Charge Transfer</i>
MPA	<i>3-Methylpicolinic acid</i>
MTEOS	<i>Methyltriethoxysilane</i>
n	<i>Refractive index</i>
n_a	<i>Amount of analyte adsorbed (mmol g^{-1})</i>
NLDFT	<i>No Local Density Functional Theory</i>
NMR	<i>Nuclear Magnetic Resonance</i>
OF	<i>Optical Fibre</i>
OFCS	<i>Optical Fibre Chemical Sensors</i>

OFS	<i>Optical Fibre Sensors</i>
OFSLn-AL	<i>Optical Fibre Sensors with xerogel coatings doped with lanthanide complexes</i>
ORMOSIL	<i>Organically modified silicates</i>
PB	<i>Pybox-EG</i>
PhTEOS	<i>Phenyltriethoxysilane</i>
PTEOS	<i>Propyltriethoxysilane</i>
p°	<i>Saturation pressure</i>
P_{H_2O}	<i>Water-vapour pressure</i>
PL	<i>Photoluminescence spectroscopy</i>
p/p°	<i>Relative pressure</i>
POSS	<i>Polyoctahedral Silsesquioxanes</i>
PSD	<i>Pore Size Distribution</i>
PVP	<i>Polyvinylpyrrolidone</i>
q_i	<i>Configurational coordinates: average distance of a light emitting centre to their neighbouring atoms</i>
q_m	<i>Monolayer capacity determined by BET (mmol g^{-1})</i>
r	<i>Stoichiometric relation of water:ethoxide in xerogel synthesis</i>
RH	<i>Relative Humidity</i>
RTEOS	<i>Alkyl or Aryl-triethoxysilane</i>
SDA	<i>Structure-Directing Agent</i>
SEM	<i>Scanning Electron Microscopy</i>

(SiO) ₄	<i>4-Fold siloxane ring</i>
(SiO) ₆	<i>6-Fold siloxane ring</i>
SLd	<i>Short Ladder-like polyoctahedral silsesquioxane</i>
SN ₂	<i>Bi-molecular Nucleophilic Substitution</i>
TEOS	<i>Tetraethoxysilane</i>
TMEOS	<i>Tetramethoxysilane</i>
T ₇	<i>Open Cage-like Polyoctahedral Silsesquioxane</i>
T ₈	<i>Cage-like Polyoctahedral Silsesquioxane</i>
TBOT	<i>Titanium (IV) tetrabutoxide</i>
<i>t_g</i>	<i>Gelation Time</i>
TiO ₄	<i>Tetra-coordinated Ti⁺⁴ species</i>
TiO ₆	<i>Hexa-coordinated Ti⁺⁴ species</i>
TO	<i>Optical transverse mode</i>
TPA ⁺	<i>Tetrapropylammonium cation</i>
TPAOH	<i>Tetrapropylammonium hydroxide</i>
TS	<i>Titanium Silicalite</i>
TSR%	<i>Modified titanium silicalite</i>
T _{δ,y}	<i>Wagging out and inside the plane vibration</i>
<i>V_{macro}</i>	<i>Macropore volume (cm³ g⁻¹)</i>
<i>V_{meso}</i>	<i>Mesopore volume (cm³ g⁻¹)</i>
<i>V_{micro}</i>	<i>Micropore volume (cm³ g⁻¹)</i>
<i>V_{total}</i>	<i>Total pore volume (cm³ g⁻¹)</i>

W	<i>Absolute humidity</i>
XG	<i>Xerogel</i>
XRD	<i>X-ray Diffraction</i>
α	<i>Energy-dependent absorption coefficient of a material</i>
β	<i>Adsorption affinity coefficient/scale factor</i>
ΔH_{ads}	<i>Isosteric enthalpy of adsorption</i>
ΔH_{cond}	<i>Isosteric enthalpy of condensation</i>
ΔI	<i>Intensity variation in humidity time-response curves</i>
δ	<i>Bending vibration</i>
θ	<i>Bragg angle</i>
λ_{em}	<i>Emission wavelength (nm)</i>
λ_{exc}	<i>Excitation wavelength (nm)</i>
$\mu(\lambda_{exc})$	<i>Molar coefficient of absorption or extinction</i>
ν	<i>Stretching vibration</i>
ν_{as}	<i>Asymmetric stretching vibration</i>
$\nu_{ring-as}$	<i>Parallel displacements of O atoms on opposite sides of a $(SiO)_x$ ring</i>
ν_{ring-s}	<i>Antiparallel displacements of O atoms on opposite sides of a $(SiO)_x$ ring</i>
ν_s	<i>Symmetric stretching vibration</i>
ρ	<i>Rocking vibration</i>
σ_m	<i>Cross-sectional area (nm^2 molecule$^{-1}$)</i>
τ	<i>Twisting vibration</i>

τ_r *Radiative lifetime of the excited state*

ϕ *Incidence angle of light*

Φ *Quantum yield*

ω *Wagging vibration*

\emptyset *Inner diameter/pore width (nm)*

APPENDIX B

LIST OF FIGURES

APPENDIX B

LIST OF FIGURES

- Figure 2.1. Scheme of the synthesis procedure used to prepare the chlorinated hybrid xerogels.
- Figure 2.2. 702 SM Titrino Automatic Burette coupled to a magnetic stirrer and a Metrohm pH meter. The apparatus is located in the Science Department of the Public University of Navarre.
- Figure 2.3. J.P. Selecta S.A thermostatised oven (left), and Selecta S.A heating plate connected to an adixen Pfeiffer vacuum pump (right). The apparatuses are located in the Science Department of the Public University of Navarre.
- Figure 2.4. Reactions to obtain the PB antenna ligand: (a) chlorination of chelidamic acid, (b) substitution reaction of A with 2-chloroethylamine to yield B, and (c) cyclization of B to yield PB.
- Figure 2.5. Scheme of the synthesis procedure used to prepare the Ln-AL monoliths.
- Figure 2.6. Synthesis procedure of the modified titanium silicalites.
- Figure 2.7. Bruker AV-400 MHz solid-state nuclear magnetic resonance spectrometer (SCAI of the University of Jaén).
- Figure 2.8. Equipment used to obtain the FTIR spectra: (a) Jasco FTIR spectrometer, sample holder, ATR unit and hydraulic press; and (b) agate mortar and components of the tablet press mould. The instrument and components are located in the Science Department of the Public University of Navarre.
- Figure 2.9. Horiba Fluorolog spectrofluorometer. Picture downloaded from the webpage of the SAI of the University of Zaragoza.
- Figure 2.10. Spectrometers used at the Faculty of Engineering of the University of Porto: (left) Jasco UV-Vis spectrometer mod V-560, image subtracted from the manual of the equipment available online; and (right) Jasco spectrofluorometer mod FP-8300, image downloaded from the Jasco.co.uk webpage.

- Figure 2.11. NRS-5100 Raman Jasco spectrometer. Image of the equipment located in the SCAI of the University of Málaga.
- Figure 2.12. X-ray diffractometers: (left) PANalytical Empyrean XRD in the SCAI of the University of Jaén, and (right) Bruker D8-Advance powder XRD instrument in the UCTAI of the Public University of Navarre.
- Figure 2.13. (left) AccuPyc 1330 Helium pycnometer, and (right) multivolume kit and calibration standards for skeletal density measurements. The instrument and components are located in the Science Department of the Public University of Navarre.
- Figure 2.14. (left) ASAP2020 gas adsorption equipment, setups for measuring N₂ isotherms; and (right) CO₂ and H₂O(v) isotherms.
- Figure 2.15. Scattering electron microscopes: (left) FE-SEM Carl Zeiss microscope located in the SCAI of the University of Jaén; and (right) SEM Zeiss EVO microscope at the UCTAI of the Public University of Navarre.
- Figure 2.16. Jeol-2000 FXII high-resolution transmission electron microscope located in the SCT of the University of Oviedo.
- Figure 2.17. Scheme of the chelating AL molecules, synthesis of Ln-AL materials, and fibre coating set-up.
- Figure 2.18. Experimental set-up to register the sensor response.
- Figure 2.19. MestReNova screenshot of the curve fitting of 15CIMTEOS xerogel ²⁹Si NMR spectrum in the -60 to -130 ppm spectral range.
- Figure 2.20. SpectraManager screenshot of the curve fitting of TEOS xerogel infrared spectrum in the spectral range 1300–980 cm⁻¹.
- Figure 2.21. (left) UV-Vis diffuse reflectance spectra of TSPH5 in Kubelka-Munk units, and (right) its Tauc-plot analysis.
- Figure 2.22. Relative pressure range section on Microactive software for the determination of the specific surface area.
- Figure 2.23. SAIEUS Screenshot of the calculated pore size distribution of a material.
- Figure 3.1. (a) Silicon environments present in chloroalkyltriethoxysilane (CIRTEOS):tetraethoxysilane (TEOS) xerogels, and (b) normalized ²⁹Si NMR

spectra of the hybrid xerogels synthesised with 5%, 10%, and 15% of CIRTEOS (chloromethyltriethoxysilane (CIMTEOS) (●), chloroethyltriethoxysilane (CIETEOS) (▲), and chloropropyltriethoxysilane (CIPTEOS) (■)).

- Figure 3.2. Variation in the relative abundance of the condensed species of Si^{IV} with respect to percentage CIRTEOS obtained by integrating the ²⁹Si NMR spectra for: (a) CIMTEOS, (b) CIETEOS, and (c) CIPTEOS.
- Figure 3.3. FTIR spectra of xerogels synthesised with 15% precursor within the range of (a) 1600–400 cm⁻¹ and (b) 4000–2750 cm⁻¹.
- Figure 3.4. X-ray diffraction patterns of the hybrid xerogels CIRTEOS:TEOS at different molar percentages: (a) CIMTEOS, (b) CIETEOS, (c) CIPTEOS.
- Figure 3.5. Skeletal density of the materials according to the precursor molar percentage for: (a) CIRTEOS series (CIMTEOS, CIETEOS, and CIPTEOS) and (b) RTEOS series (MTEOS, ETEOS, and PTEOS) in previous studies [20–22]. Reference material density (100%TEOS) = 1.96 g cm⁻³.
- Figure 3.6. Decimal scale (left) and semi-logarithmical scale (right) of the N₂ isotherms (-196 °C) of chloroalkyl materials at different molar percentages of: (a, b) CIMTEOS, (c, d) CIETEOS, and (e, f) CIPTEOS.
- Figure 3.7. CO₂ isotherms (0 °C) of chloroalkyl materials at different molar percentages of: (a) CIMTEOS, (b) CIETEOS, and (c) CIPTEOS.
- Figure 3.8. Density-functional theory (DFT) porosity distribution obtained from N₂ isotherms (left) and CO₂ isotherms (right) of: (a, b) CIMTEOS:TEOS series, (c, d) CIETEOS:TEOS series, and (e, f) CIPTEOS:TEOS series.
- Figure 3.9. FE-SEM micrographs of: (a) reference xerogel (100% TEOS), (b) xerogel synthesised with 30% of CIMTEOS, (c) xerogel synthesised with 15% CIETEOS, and (d) xerogels synthesised with 12.5% CIPTEOS.
- Figure 3.10. SEM micrographs of the chloroalkyl materials, (a-c) Distribution of chlorine atoms on the surface of xerogels obtained by applying EDX, (d-f) Sum of EDX spectra obtained by analyzing different points of the micrographs (g-i).
- Figure 3.11. FE-SEM micrographs of (a-c) CIMTEOS:TEOS materials, (d-f) CIETEOS:TEOS materials, and (g-i) CIPTEOS:TEOS materials.

- Figure 4.1. Images of the synthesised xerogels where a change in morphology is observed with an increasing percentage of organic precursors: (a) TEOS, (b-d) CIMTEOS, (e-g) CIETEOS, and (h-j) CIPTEOS.
- Figure 4.2. (a) tg as a function of the percentage of precursor in the TEOS:CIRTEOS series, (b) tg as a function of the percentage of t precursor in the TEOS:RTEOS series, and (c) tg of the CIRTEOS versus RTEOS series.
- Figure 4.3. FTIR spectra of xerogels synthesised with a 20% molar percentage of precursor in the range of (a) 1600–400 cm^{-1} and (b) 4000–2750 cm^{-1} .
- Figure 4.4. FTIR spectra of the CIRTEOS:TEOS xerogels in the ranges of 1600–400 and 4000–2750 cm^{-1} : (a,b) CIMTEOS, (c,d) CIETEOS, and (e,f) CIPTEOS.
- Figure 4.5. FTIR-ATR spectra of the precursors (TEOS, CIMTEOS, CIETEOS and CIPTEOS) in the ranges: (a) 1600–400 cm^{-1} and (b) 4000–2750 cm^{-1} .
- Figure 4.6. Ordered structures in the silica matrix built by $(\text{SiO})_4$ rings in CIETEOS as an example: (a) open cage (T_7), (b) cage (T_8), and (c) short ladders.
- Figure 4.7. X-ray diffraction patterns of the hybrid xerogels at different molar percentages (normalized with respect to the band $2\theta \sim 4^\circ$): (a) CIETEOS:TEOS, and (b) ETEOS:TEOS.
- Figure 4.8. X-Ray diffraction patterns of CIRTEOS:TEOS and RTEOS:TEOS xerogels: (a) CIMTEOS, (b) MTEOS, (c) CIPTEOS, and (d) PTEOS.
- Figure 4.9. Normalized FTIR spectra of the 1300–980 cm^{-1} region of the TEOS xerogel (black), and those of the three chloroalkyl series at different molar ratios: (a) 5%, (b) 10%, and (c) 20%. (CIMTEOS (red), CIETEOS (yellow), and CIPTEOS (blue)).
- Figure 4.10. Predominant structures within the silica matrix of a xerogel prepared with TEOS: (a) $(\text{SiO})_4$ rings, and (b) $(\text{SiO})_6$ rings.
- Figure 4.11. Deconvolution and least-squares adjustment of the FTIR spectra of the xerogels: (a) Reference material (100% TEOS), (b) 20% CIMTEOS, (c) 20% CIETEOS, and (d) 20% CIPTEOS.
- Figure 4.12. Variation in $(\text{SiO})_4/(\text{SiO})_6$ ratio as a function of the molar percentage of precursor in (a) CIRTEOS:TEOS and (b) RTEOS:TEOS xerogels.

- Figure 4.13. Variation in the proportion of structures $(\text{SiO})_4/(\text{SiO})_6$ of the chloroalkyl series with respect to the alkyl series at different molar percentages of precursor.
- Figure 5.1. Mechanism in acidic media of (a) the first hydrolysis reaction of tetraethoxysilane ($\text{R} = \text{OEt}$) or triethoxysilane ($\text{R} = \text{alkyl}$ or aryl), and (b) the co-condensation reaction of tetraethoxysilane with a triethoxysilane ($\text{R} = \text{alkyl}$ or aryl).
- Figure 5.2. FTIR spectra of the reference (100% TEOS, 0% in the graphs) and the hybrid materials at different molar percentages of organic precursor (CIPhTEOS) within the range of (a) $1600\text{--}400\text{ cm}^{-1}$ and (b) $4000\text{--}2750\text{ cm}^{-1}$.
- Figure 5.3. Pictures of CIPhTEOS materials: (a) 0CIPh, (b) 15CIPh, (c) 20CIPh, and (d) 100CIPh.
- Figure 5.4. FT-IR spectra (range $1400\text{--}900\text{ cm}^{-1}$) of the reference, 15CIPh, and both phases of 20CIPh and 100CIPh.
- Figure 5.5. From left to right: 4-fold ring $[(\text{SiO})_4]$, short ladder (SLd), open-cage (T_7), and close-cage (T_8).
- Figure 5.6. Synthetic spectra and Gaussian-Laurentzian bands generated in the curve fitting for: (a) 0CIPh, (b) 5CIPh, (c) 10CIPh, (d) 15CIPh, (e) 20CIPh(monolith), (f) 20CIPh(Precipitate), and (g) 100CIPh.
- Figure 5.7. (a) Normalised ^{29}Si NMR spectra of the hybrid xerogels. (b) Variation of the relative abundance of the condensed species with respect to the percentage of CIPhTEOS.
- Figure 5.8. XRD diffractograms of the hybrid xerogels (reference, 1CIPh, 5CIPh, 10CIPh, and 15CIPh).
- Figure 5.9. XRD diffraction pattern of 100CIPh.
- Figure 5.10. Skeletal density of the hybrid materials with respect to the percentage of CIPhTEOS.
- Figure 5.11. Isotherms of the hybrid xerogels: (a) N_2 ($-196\text{ }^\circ\text{C}$), and (b) CO_2 ($0\text{ }^\circ\text{C}$).
- Figure 5.12. Pore size distribution of the materials calculated from (a) N_2 isotherms and (b) CO_2 isotherms.

- Figure 5.13. FE-SEM micrographs of: (a) 0CIPh, (b) 1CIPh, (c) 5CIPh, (d) 10CIPh, and (e) 15CIPh.
- Figure 5.14. HR-TEM micrographs of (a) 0CIPh, (b) 1CIPh, (c) 5CIPh, (d) 10CIPh, and (e) 15CIPh.
- Figure 6.1. (a) Luminescent emission of vacuum-dried (100 °C) Ln-AL materials under UV lamp for thin layer chromatography (Vilber model CN-6 equipped with a VL-6.LC filtered UV lamp, Germany); (b) Luminescent emission of the vacuum-dried Tb-FPA monolith (left) compared to that of a moisturised counterpart (right).
- Figure 6.2. Room-temperature excitation (black) and emission (Eu^{III}: red; Tb^{III}: green) spectra of Ln-PB, Ln-3OHPA, and Ln-CA.
- Figure 6.3. N₂ adsorption-desorption isotherms in both scales, (top) normal and (centre) semi-logarithmic, and (bottom) pore size distribution of Ln-PB and Ln-CA compared to those of their TEOS references.
- Figure 6.4. CO₂ adsorption-desorption isotherms in both scales, (top) normal and (centre) semi-logarithmic, and (bottom) pore size distribution of Ln-PB and Ln-CA compared to those of their TEOS references
- Figure 6.5. SEM micrographs of TEOS-4.5, Eu-PB, and Tb-PB.
- Figure 6.6. EDX mapping of Eu-PB (top) and Tb-PB (bottom) materials containing 3% in weight of Ln.
- Figure 6.7. Powder X-ray diffraction patterns of Ln-PB materials compared to that of the TEOS-4.5 reference.
- Figure 6.8. Infrared spectra of Ln-PB materials and the TEOS-4.5 reference in the ranges (left) 2800–4000 and (right) 400–1800 cm⁻¹ (range from 1800 to 2800 cm⁻¹ not included due to the lack of any relevant band).
- Figure 6.9. Luminescence spectra ($\lambda_{exc} = 280$ nm) of OFSTEOS-4.5, OFSEu-PB and OFSTb-PB.
- Figure 6.10. (left) Time-response curves for humidity and (right) linear fitting of the calibration curves registered for OFSTb-PB at 25, 30 and 35 °C.

- Figure 6.11. Fitting of the OFSTb-PB calibration curves at different working temperatures to third-grade polynomial equations (adsorption branch: dashed grey line; desorption branch: dotted black line).
- Figure 6.12. Water-vapour adsorption-desorption isotherms of the Tb-PB monolith at different temperatures, and different scales: (left) decimal, and (right) semi-logarithmic.
- Figure 6.13. Best-fitting of water vapour adsorption isotherms for the Tb-PB monolith.
- Figure 6.14. (Left) Clausius-Clapeyron plots for the OFSTb-PB response towards humidity changes ($-\Delta I/I_{\text{ref}} = 0.03\text{--}0.18$) and for water-vapour adsorption isotherms of the Tb-PB monolith ($n_a = 1.5\text{--}10.0 \text{ mmol g}^{-1}$). (Right) Isothermic enthalpies of adsorption calculated for both the sensor and the monolith.
- Figure 7.1. XRD diffraction patterns of the reference material (TS0, in black) and the TSR% materials.
- Figure 7.2. FT-IR spectra of TSM%, TSP%, and TSPH% in the (left) 1600–400 and (right) 4000–2750 cm^{-1} frequency regions.
- Figure 7.3. DR UV-Vis spectra of reference material and TSR5, TSR10, TSR20, and TSR30.
- Figure 7.4. Tauc-plot analysis of the reference material and TSR5, TSR10, TSR20, and TSR30.
- Figure 7.5. Photoluminescent emission spectra of TSR% materials registered at 260 and 370 nm excitation wavelength.
- Figure 7.6. UV-Raman spectra of TSR5 and TSR10 registered at 325 nm excitation wavelength
- Figure 7.7. N_2 and CO_2 adsorption isotherms of the reference, TSR5, and TSR10 materials (top left and right, respectively), and N_2 isotherms of TSR20 and TSR30 materials (bottom).
- Figure 7.8. Density-functional theory (DFT) and pore size distributions (PSD) calculated of the reference, TSR5, and TSR10 materials obtained from their N_2 and CO_2 adsorption isotherm data (top left and right, respectively).

- Figure 7.9. FE-SEM micrographs of the reference, TSM5, TSP5, TSPH5, and TSPH10 materials.
- Figure 7.10. Photodegradation of venlafaxine under simulated solar irradiation with the reference, TSR5 and TSPH10 materials. Experimental conditions: $[\text{Venlafaxine}]_0 = 5 \text{ mg L}^{-1}$, photocatalyst load = 1 g L^{-1} , and incident photon irradiance $I = 500 \text{ W m}^{-2}$.
- Figure 7.11. HPLC chromatogram profiles for degradation of venlafaxine using TSPH5 photocatalyst over the reaction time.
- Figure 7.12. Photodegradation of venlafaxine after adsorption equilibria ($[\text{Venlafaxine}]_0 = 5 \text{ mg L}^{-1}$) and pseudo-first-order kinetic adjustment of the photodegradation process.
- Figure A.1. Sol-gel method routes. Adapted from Dimitriev *et al.* (2008) [8].
- Figure A.2. Synthesis of hybrid silica xerogels.
- Figure A.3. SN_2 hydrolysis mechanism for RTEOS.
- Figure A.4. SN_2 condensation mechanism for RTEOS.
- Figure A.5. Scheme of the polymerization routes of TEOS in acid media (H atoms have been removed for the sake of visual clarity). Based on the works of Depla *et al.* (2011) [15, 18].
- Figure A.6. Scheme of particle growth and sol-to-gel transition.
- Figure A.7. Scheme of ageing and drying in the sol-gel process.
- Figure B.1. Optical fibres with their exposed components.
- Figure B.2. (a) Refraction example, (b) refraction limit with incident ray at the critical angle, and (c) total internal reflection in a hypothetically perfect optical fibre. Adapted from Senior (2009) [7].
- Figure B.3. Scheme of the main three classifications of optical fibre sensors.
- Figure B.4. Scheme of an optical fibre indirect chemical sensor.
- Figure B.5. Scheme of the dip-coating process.

- Figure C.1. Jablonski diagram representing the excitation and emission processes that define a luminescence spectrum. Adapted from Pohl in www.enzolifesciences.com (2023) [5].
- Figure C.2. Jablonski diagram illustrating radiative (fluorescence and phosphorescence) and non-radiative transitions.
- Figure C.3. Frank-Condon scheme. h = Planck's constant, and c = speed of light in vacuum.
- Figure C.4. Ground state spectroscopy symbol and overall multiplicity of Eu^{III} and Tb^{III} .
- Figure C.5. Ground state spectroscopy symbol of Eu^{III} and Tb^{III} considering coupling.
- Figure C.6. Jablonski diagram illustrating the possible processes that take place in the sensitization of Ln^{III} through antenna ligand effect, as well as the luminescence quenching by oscillating groups. Flat and curved arrows represent radiative and non-radiative pathways, respectively. S = singlet states, T = triplet state, ILCT = inter-ligand charge transfer, LMCT = ligand-to-metal charge transfer, VR = vibrational relaxation, ISC = intersystem charge transfer, IET = intramolecular energy transfer, ET = energy transfer. Adapted from Capelletti *et al.* (2017) [32].
- Figure D.1. Main oxidation reactions catalysed by TS-1. Adapted from Millini *et al.* (2022) [14].
- Figure D.2. Orthorhombic TS-1 structure with their different T-sites labelled (left) and the interconnected channel system (right) with their unit cell parameters.
- Figure D.3. (a) Tetracoordinated Ti and defective Ti sites in TS-1 structure; (b) bipodal tetracoordinated Ti; (c) H-terminated pentacoordinated Ti; (d) Na-terminated pentacoordinated Ti; (e) H-terminated hexacoordinated Ti; (f) Na-terminated hexacoordinated Ti; and (g) dimeric tetracoordinated Ti. Adapted from Signorile (2020) *et al.* [28].
- Figure D.4. Scheme of the most used TS-1 synthesis route based on Luan *et al.* (2022) [37]. Dry gel conversion method and solvent-free synthesis schemes adapted from Xu *et al.* (1990) [42] and Liu *et al.* (2022) [43], respectively.
- Figure D.5. Scheme of the conventional hydrothermal synthesis of TS-1.

Figure D.6. Thermodynamically unfavourable photosynthesis reaction (left) and Thermodynamically favourable photocatalysis reaction (right). Adapted from Osterloch (2017) [60].

Figure D.7. Scheme of the three types of materials classified according to their electronic conducting capability: insulator (left), semiconductor (centre) and conductor (right).

Figure D.8. Scheme of the three types of semiconductors: *n*-type (left), intrinsic (centre), and *p*-type (right). Where E_C is the conduction band edge energy, E_V the valence band edge energy, and E_F is the energy of the Fermi level.

Figure D.9. Scheme of the generation of reactive oxygen species (ROS) by a photocatalyst in aqueous media for the degradation of organic pollutants. Adapted from Shmeis *et al.* (2022) [72].

APPENDIX C

LIST OF TABLES

APPENDIX C

LIST OF TABLES

- Table 2.1. List of all the homogeneous xerogels synthesized in this PhD thesis.
- Table 2.2. List of all the utilized antenna ligands with their purities, formulas and commercial sources.
- Table 2.3. List of all the synthesised Ln-AL monoliths with their respective pH synthesis media.
- Table 2.4. Nomenclature and list of all the synthesised TSR% materials.
- Table 2.5. Characterisation techniques employed in Chapter 3 to 7.
- Table 3.1. Gelation time (t_g) of CIRTEOS: TEOS materials.
- Table 3.2. Signals from the ^{29}Si NMR spectra of the hybrid xerogels chloroalkyltriethoxysilane (CIRTEOS):tetraethoxysilane (TEOS) and alkyltriethoxysilane (RTEOS): tetraethoxysilane (TEOS) (R = methyl, ethyl, and propyl) [20–22].
- Table 3.3. Bragg angles (2θ), band area (A), and bond distance (d_1 and d_2 (nm)) calculated from the XRD bands of the xerogels synthesised with different precursors and molar percentages.
- Table 3.4. Textural parameters of chloroalkyl materials at different molar percentages.
- Table 4.1. Electronegativities and partial charges of the chloroalkyl precursors and their alkyl analogues calculated from the Pauli electronegativities and application of the equations of Livage and Henry (1992) [42].
- Table 4.2. FTIR spectra band assignment of spectra of figures 4.3 and 4.4.
- Table 4.3. Bragg angles (2θ), band area (A), and bond distance (d_1 and d_2 (nm)) calculated from the X-ray diffraction maxima for the xerogels synthesised with CIMTEOS, MTEOS, CIPTEOS and PTEOS.

- Table 4.4. Relative areas obtained from the deconvolution of the FTIR spectra of CIRTEOS:TEOS series [35], their calculated (SiO)₄ and (SiO)₆ percentages, and their (SiO)₄/(SiO)₆ ratios. The selected data for the construction of Figure 4.12a are shaded in grey.
- Table 4.5. Relative areas obtained from the deconvolution of the FTIR spectra of RTEOS:TEOS series [36–38], their calculated (SiO)₄ and (SiO)₆ percentages, and their (SiO)₄/(SiO)₆ ratios. The selected data for the construction of Figure 4.12b are shaded in grey.
- Table 4.6. Skeletal density for the hybrid xerogels obtained from Figure 3.5 of section 3.2.3. Reference material skeletal density (100%TEOS) = 1.96 g cm⁻³.
- Table 4.7. Equations obtained from the exponential adjustment of the curves depicted in the graphs of Figure 4.12.
- Table 5.1. List of bands observed in the spectrum of 100CIPh and the proposed assignation of vibrations and structures.
- Table 5.2. Wavelength and percentual area of the generated band in the curve fitting for each CIPhTEOS material, and their curve fitting parameters.
- Table 5.3. Proportion of (SiO)₄ and (SiO)₆ rings in the hybrid materials.
- Table 5.4. Chemical shifts and integral areas of the ²⁹Si NMR spectra of the hybrid materials.
- Table 5.5. Bragg angles (2θ), band area (A), and bond distance (d₁ and d₂ (nm)) calculated from XRD maxima of hybrid xerogels at different molar percentages of organic precursor (CIPhTEOS).
- Table 5.6. Textural parameters of the hybrid xerogels.
- Table 5.7. Average weight percentage of chlorine determined theoretically and by EDX of the hybrid materials.
- Table 6.1. Textural parameters determined from the adsorption isotherms for Ln-AL materials and their TEOS references.
- Table 6.2. Literature-based assignment of FT-IR bands (cm⁻¹) in the spectra of Ln-PB materials and the TEOS-4.5 reference.

Table 6.3.	Linear fitting parameters of OFSTb-PB calibration curves ($y = A + Bx$).
Table 6.4.	Fitting parameters of the OFSTb-PB calibration curves to third-grade polynomial equations ($y = A + B_1x + B_2x^2 + B_3x^3$).
Table 6.5.	Room-temperature performances of literature-reported optical fibre humidity probes compared to that of OFSTb-PB
Table 6.6.	Textural parameters determined from the water-vapour adsorption isotherms of the Tb-PB monolith.
Table 6.7.	Fitting parameters of the water vapour adsorption isotherms of Tb-PB to a fourth-grade polynomial equation ($y = A + B_1x + B_2x^2 + B_3x^3 + B_4x^4$).
Table 7.1.	Textural parameters of the reference, TSR5 and TSR10 materials.
Table 7.2.	Skeletal density of the materials determined by Helium Pycnometry.
Table 7.3.	Average weight percentage and atomic abundance, estimated by EDX, of C, O, Si and Ti in the reference, TSR5 and TSPH10 materials.
Table 7.4.	Kinetic constants calculated from venlafaxine degradation curves.
Table B.1.	Some examples of articles of silica-gel coated optical fibre sensors.
Table C.1.	Electronic transition mechanism and their parity and selection rules.
Table C.2.	Main 4f–4f emission transitions of Eu^{III} and Tb^{III} ions in aqueous media, corresponding approximate emission wavelengths (λ_{em}), relative emission intensities, mechanisms for each transition, and corresponding energy bandgap between emissive and final state. Data obtained from [19,22,24].
Table D.1.	Most relevant data of publications on the removal of venlafaxine (Ven) in aqueous media through photocatalysis.

APPENDIX D

CONTRIBUTIONS TO OTHER PUBLICATIONS AND CONFERENCES

APPENDIX D

CONTRIBUTIONS TO OTHER PUBLICATIONS AND CONFERENCES

Contributions to other publications

Apart from the works compiled in the thesis dissertation, during his PhD student period, the PhD candidate has contributed in the research of the following published articles:

1. Flores-López, S. L.; Villanueva, S. F.; Montes-Morán, M.A.; Cruz, G.; Garrido, J. J.; Arenillas, A. Advantages of microwave-assisted synthesis of silica gels. *Colloids Surf., A* **2020**, *604*, p. 125248. **Contribution:** Methodology—gas adsorption. Doi: 10.1016/j.colsurfa.2020.125248.
2. García, L.; Garaio, E.; López-Ortega, A.; Galarreta-Rodriguez, I.; Cervera-Gabalda, L.; Cruz-Quesada, G.; Cornejo, A.; Garrido, J. J.; Gómez-Polo, C.; Pérez-Landazábal, J. I. Fe₃O₄-SiO₂ Mesoporous Core/Shell Nanoparticles for Magnetic Field-Induced Ibuprofen-Controlled Release. *Langmuir* **2023**, *39*, p. 211–219. **Contribution:** Methodology—gas adsorption. Doi: 10.1021/acs.langmuir.2c02408
3. Rosales-Reina, B.; Cruz-Quesada, G.; Padilla-Postigo, N.; Irigoyen-Razquin, M.; Alonso-Martínez, E.; López-Ramón, M. V.; Espinal-Viguri, M.; Garrido, J. J. Tunability of Hybrid Silica Xerogels: Surface Chemistry and Porous Texture Based on the Aromatic Precursor. *Gels* **2023**, *9*, p. 382. **Contribution:** formal analysis, writing—original draft and writing—review and editing. Doi: 10.3390/gels9050382.

Contributions to Conferences

The research contained in this PhD dissertation have been presented in 8 contributions in several congresses of different geographical scope, and in poster and oral presentation formats. The details of each contribution can be found in the following tables.

N°	Date	Congress	City	Congress scope	Communication type and name	Authors	Related chapter
1	06/24/2021	IV International Congress in Water Soluble Metal Complexes Applications	Online (Zaragoza)	International (no EU)	Poster: Hybrid xerogels doped with Tb (III) and a water-soluble antenna ligand	Espinal-Viguri, M.; Cruz-Quesada, G. ; Abás-Benedí, E.; Crespo, S.; Rosales-Reina, M.B.; Garrido, J.	6
2	06/25/2021	IV International Congress in Water Soluble Metal Complexes Applications	Online (Zaragoza)	International (no EU)	Oral presentation: Luminescent hybrid silicon xerogeles: study on their porous texture	Cruz-Quesada, G. ; Espinal-Viguri, M.; Crespo, S.; Rosales-Reina, M.B.; Abás-Benedí, E.; Garrido, J.	6
3	09/01/2021	XXIV conference on organometallic chemistry (EuCOMC)	Online (Alcalá de Henares)	European Union	Poster: Hybrid xerogels doped with Tb(III) and Eu(III) and a water soluble pybox ligand	Cruz-Quesada, G. ; Espinal-Viguri, M.; Garrido, J.	6
4	09/30/2021	Symposium of the Spanish Royal Society of Chemistry 2021	Online	National	Poster: New hybrid organochlorinated xerogels	Cruz-Quesada, G. ; Espinal-Viguri, M.; López-Ramón, M.V.; Garrido, J.	3 and 4
5	06/30/2022	XXXVIII Reunión Bienal de la Sociedad Española de Química	Granada	National	Poster: Development of an optical fibre relative humidity sensor based on Tb-doped Porous silica xerogel	Rosales-Reina, M.B.; López-Torres, D.; Cruz-Quesada, G. ; Espinal-Viguri, M.; Crespo, S.; López-Ramón, M.V.; Elosua-Aguado, C.; Garrido, J.	6

N°	Date	Congress	City	Congress scope	Communication type and name	Authors	Related chapter
7	06/30/2022	XXXVIII Reunión Bienal de la Sociedad Española de Química	Granada	National	Poster: Synthesis and characterisation of hybrid xerogels doped with Eu(III) or Tb(III) and a water soluble antenna ligand	Espinal-Viguri, M.; Cruz-Quesada, G. ; Garrido, J.; Crespo, S.; Rosales-Reina, M.B.; López-Ramón, M.V.	6
8	09/16/2022	XLII Reunión Ibérica de Adsorción (42° RIA)	Valencia	International (no EU)	Poster: New hybrid (p-chlorophenyl)triethoxysilane xerogels	Garrido, J.; Cruz-Quesada, G. ; Espinal-Viguri, M.; Rosales-Reina, M.B.; Crespo, S.; López-Ramón, M.V.	5

Directed by:

Prof. Julián José Garrido Segovia

Prof. María Victoria López Ramón

Dra. Maialen Espinal Viguri



Arrosadia campus, Public university of Navarre

The research presented in this doctoral dissertation is focused on the synthesis of siliceous materials, which are classified into three well-defined groups: silica hybrid inorganic-organic xerogels (HXG), silica xerogels doped with lanthanides (Ln-AL), and modified titanium silicalites-1 (TSR%). Although, each group of material have been synthesised with a different objective in mind, the overall aim of this dissertation is to study and control the textural properties of the materials to enhance their performance in their selected application: coatings for optical fibre sensors (HXG and Ln-AL), and photocatalysts for the removal of pollutants in aqueous media (TSR%)

